Università degli Studi di Genova

Doctorate in Sciences and Technologies of Chemistry and Materials

XXXVIII cycle

Curriculum: Drug Discovery and Nanobiotechnologies

Small molecule modulators of the activity of non-coding RNAs

Supervisors: Dr. Tiziano Bandiera and Dr. Fabio Bertozzi
Co-supervisor: Prof. Paola Fossa

Riccardo Quaia

Academic Years: 2022-2025

Preface

I hereby declare that the topics and results outlined in this Thesis are the results of the research carried out throughout my three-year Ph.D. course.
This project is part of a scientific collaboration between the research group of Dr. Tiziano Bandiera (IIT, Genoa) and the group of Dr. Maria Duca (University of Cote D'Azur, Nice). The synthesis of the compounds was carried out at IIT, while the fluorescence-based biological tests were performed in Dr. Duca's lab. In the first part of the third year of my Ph.D. course, I moved to the pharma company AstraZeneca, in Sweden, where I had a six-month visiting collaborative experience under the supervision of Dr. Chi Celestine. During this period, I focused my research activities on NMR-structural studies on pre-miR21.

In the following eight Chapters of this Thesis, different topics are presented:
Chapter 1 presents an introduction on microRNAs with a focus on microRNA-21 and the recent strategies used for modulating its levels attempted in the last years.
Chapter 2 presents the rationale, the aim and the preliminary data of the project, such as the ^{19}F-NMR-based screening performed by Dr. Marina Veronesi (IIT) and the fluorescence-based biological assays performed by Dr. Duca's group.
Chapters 3 and **4** present the synthetic design and structure-activity relationship (SAR) evolution of the hit compound.
Chapter 5 describes the synthesis of the fluorinated RNAs required for the NMR-structural studies carried out in AstraZeneca, under the supervision of Dr. Chi Celestine.
Chapter 6 presents the NMR-based biological assay set-up in AstraZeneca and performed with the help of Dr. Marina Veronesi (IIT).
Chapter 7 describes the data of the in-cell evaluation of the identified, most promising compounds performed by Dr. Debora Russo and Dr. Ilaria Penna (IIT).
Chapter 8 provides a summary of the results and the conclusions.

Abstract

The targeting of non-coding RNAs (nc-RNAs) appears as a promising frontier in current drug discovery, since their extended biological pathways are still largely unexplored and could indeed provide opportunities to modulate biological factors that are not targetable with traditional protein-based drug discovery.

Within this context, micro-RNA-21 (miR21) appears as an attractive potential pharmaceutical target, due to its aberrant overexpression in various cancers and its well-established anti-apoptotic role. At IIT, our research focuses on modulating miR21 levels in cells by means of small molecule compounds, thereby establishing a platform for a broader drug discovery campaign.

To achieve this objective, the modulation of miR21 biogenesis was investigated, identifying the precursor of miR21, i.e., pre-miR21, as the biological target of this medicinal chemistry project. Starting from a ^{19}F-NMR-based screening of *circa* 600 low-molecular-weight compounds (*fragments*) (IIT), followed by a fluorescence-based testing of the preliminary hits for binding confirmation (University of Nice), a few initial hit compounds were identified with a promising affinity toward pre-miR21. Among these compounds, hit **1**, featuring a pyrazolo[1,5-a]pyrimidine scaffold, was selected for its chemical tractability and further developed through a ligand-based medicinal chemistry campaign.

During my research activity at IIT, I designed and synthesized 75 analogues of hit **1** with the aim of increasing the affinity of this chemotype toward pre-miR21. Biochemical activity was evaluated using the fluorescence assay developed in Dr. Duca's laboratory, which guided the further evolution of this chemotype. During this process, a well-defined structure–activity relationship (SAR) was established, suggesting possible target engagement.

Ligand–target interactions were further investigated during my research period at AstraZeneca (Sweden) through NMR structural studies. For achieving these outcomes, fluorinated probes were produced through solid-phase synthesis by systematically introducing them into the pre-miR21 structure. These studies provided insights into the RNA secondary structure and demonstrated that the synthesized compounds establish specific interactions with pre-miR21.

Biochemical target engagement was also assessed using an NMR-based assay, providing orthogonal validation to the fluorescence-based method. SAR analysis established across both approaches showed consistent trends, thus confirming the putative modulation of miR21 by small molecule compounds featuring this novel chemotype.

Having confirmed favourable biochemical ligand–target interactions, the cellular activity of the most promising novel compounds was evaluated by assessing modulation of both mature miR21 levels and related targets. The data produced demonstrated that the identified compounds are indeed active in PANC-1 cell-line and exhibit preliminary indications of possible target engagement.

Overall, throughout this activity set-up, fragment-based drug discovery was shown to be effective from initial screening to hit evolution, yielding small molecules that remain amenable to further optimization and that may serve as starting points for a broader medicinal chemistry campaign.

List of abbreviations

^{1}H NMR = Hydrogen 1 nuclear magnetic resonance;
^{1}D = mono-Dimensional; 2D = bi-Dimensional; 3D = tri-Dimensional;
^{13}C-NMR = Carbon 13 nuclear magnetic resonance;
^{19}F-NMR = Fluorine 19 nuclear magnetic resonance;
AcOEt = Ethyl acetate;
AcOH = Acetic acid;
AcOK = Potassium acetate;
AGO = Argonaute;
AZ = AstraZeneca;
Boc = *Tert*-butyloxycarbonyl ;
$CDCl_3$ = Deuterated chloroform;
COSY = COrrelated SpectroscopY;
CH_3CN = Acetonitrile**;**
cryo-EM = Cryogenic electron microscopy;
Cy = Cyclohexane;
DCM = Dichloromethane;
DIPEA = N,N-diisopropylethylamine;
DMAP = 4-Dimethylaminopyridine;
DMF= Dimethyl formamide;
DMT = Dimethoxytrityl;
DMSO-d_6 = Deuterated dimethyl sulfoxide;
DNA = Deoxyribonucleic acid;
dsRNA = double strand RNA;
EtOH = Ethanol;
Et_3SiH = Triethylsilane;
HATU = 1-[Bis(dimethylamino)methylene] -1H-1,2,3-triazolo[4,5-b]pyridinium 3-oxid hexafluorophosphate;
Hb = Hydrogen bond;
HCl= hydrochloric acid;
HMBC = Heteronuclear Multiple-Bond Coherence;
HPLC-MS = High-performance liquid chromatography coupled with mass spectrometry;
HOESY = Heteronuclear Overhauser Effect Spectroscopy;
HSQC = Heteronuclear Single Quantum Coherence;
IC_{50} = Half-maximal inhibitory concentration;
K_2CO_3 = Potassium carbonate;
KI = Potassium iodide;
iPrOH = Isopropanol;
LDA = Lithium diisopropylamide;
LiOH = Lithium hydroxide;
K_d = Dissociation constant;
lcRNA = Long non-coding RNAs;
MeCN = Acetonitrile;
MeOD-d_4 = Deuterated methanol,
MeOH = Methanol;
MeOH*HCl = Methanolic HCl;
MeOH*NH_3 = Methanolic amonia;
mRNA = Messenger RNA;
miR or miRNA = MicroRNA;
miR-21 = MicroRNA 21;
$NaBH(OAc)_3$= Sodium triacetoxyborohydride;
NaH = Sodium hydride;
ncRNA = non-coding RNA;
$NaHCO_3$= Sodium carbonate;
NaI = Sodium iodide;
Na_2SO_4 = sodium sulphate;
NH_4Cl = Ammonium chloride;
NMR = Nuclear Magnetic Resonance;
NOESY = Nuclear Overhauser Effect Spectroscopy;
NBS = *N*-Bromosuccinimide;
PDCD4 = Programmed Cell Death Protein 4;
$Pd_2(dba)_3$= Tris(dibenzylideneacetone)dipalladium(0);
$Pd(PPh3)_3Cl_2$ = bis(Triphenylphosphine)palladium(II) dichloride;
Pd/C = Palladium (10%) on carbon,
PDB = Protein Data Bank;
Ph = Phenyl;
$PhNTf_2$ = bis(Trifluoromethanesulfonyl)aniline;
PyBrop = Bromotripyrrolidinophosphonium hexafluorophosphate;
$POCl_3$ = Phosphorus(V) oxychloride;
pre-mRNA = Precursor messenger RNA;
pre-miRNA or pre-miR = Precursor microRNA;
premiR-21 = Pre-microRNA-21;
pri-miRNA or pri-miR = Primary-microRNA;
PROTAC = Proteolysis Targeting Chimeras;
PTEN = Phosphatase and tensin homolog;
PyBOX = Pyridine-bis(oxazoline);
RIBOTAC = Ribonuclease Targeting Chimeras;
r.t. = Room temperature;
RISC = RNA-Induced Silencing Complex;
RNA = Ribonucleic Acid;
SAR = Structure-Activity Relationship;
SHAPE = Selective 2'-Hydroxyl Acylation analyzed by Primer Extension;
snRNA= Small nuclear RNA;
SQD = Single Quadrupole Detector;
t-BuOK = Potassium *tert*-butoxide;
t-BuOH = *tert*-Butanol;
TBAF = *tetra*-n-Butylammonium fluoride;
TBMS = *tert*-Butyl dimethyl silyl;
TBMSCl = *tert*-Butyl dimethyl silyl chloride;
tBuXPhos = *tert*-Butyl XPhos;
Tf_2O = Trifluoromethanesulfonic anhydride;
TEA = Triethylenetetramine;
TFA = Trifluoro acetic acid;
THF = Tetrahydrofuran;
TLC = Thin layer chromatography;
tRNA = Transfer RNA;
UPLC = Ultra-performance liquid chromatography;
UPLC-MS = Ultra-performance liquid chromatography coupled with mass spectrometry;
UTR = untranslated region;
XPO5 = Exportin

Contents

CHAPTER 1

INTRODUCTION

Chapter 1: Introduction

Ribonucleic acid (RNA) is a ubiquitous biomolecule that fulfils essential functions in all domains of life, serving as a carrier of genetic information, a regulator of gene expression, and, in some cases, a catalyst of biochemical reactions.[1] This functional versatility highlights RNA as a central component of cellular organization and activity.[2]

At the chemical level, RNA is a linear polymer composed of repeating nucleotide units. Each nucleotide consists of a ribose sugar, a phosphate group, and a nitrogenous base, also known as nucleobase. The ribose sugar contains five carbon atoms, labeled 1' through 5', with the nucleobase attached at the 1' position and the phosphate linked to the 5' carbon. RNA contains four standard nucleobases: adenine (A) and guanine (G), which are purines, and cytosine (C) and uracil (U), which are pyrimidines. Nucleotides polymerize through phosphodiester bonds between the 3' hydroxyl of one ribose and the 5' phosphate of the next, forming a sugar–phosphate backbone that carries a net negative charge (**Figure 1.1**).[1] As a polyanionic macromolecule, RNA folding is strongly influenced by the ionic environment, with metal ions such as magnesium or sodium stabilizing the structure by counteracting electrostatic repulsion.[3] The RNA backbone imposes steric and electrostatic constraints on conformational flexibility, while the nucleobases, which are planar aromatic heterocycles with hydrogen-bonding groups, enable diverse intra- and intermolecular interactions. Each nucleotide, therefore, combines charged, polar, and aromatic chemical features, allowing extensive contacts with solvent molecules, metal ions, and neighbouring nucleotides.[4] In aqueous conditions, these properties drive RNA folding and the formation of complex structures.

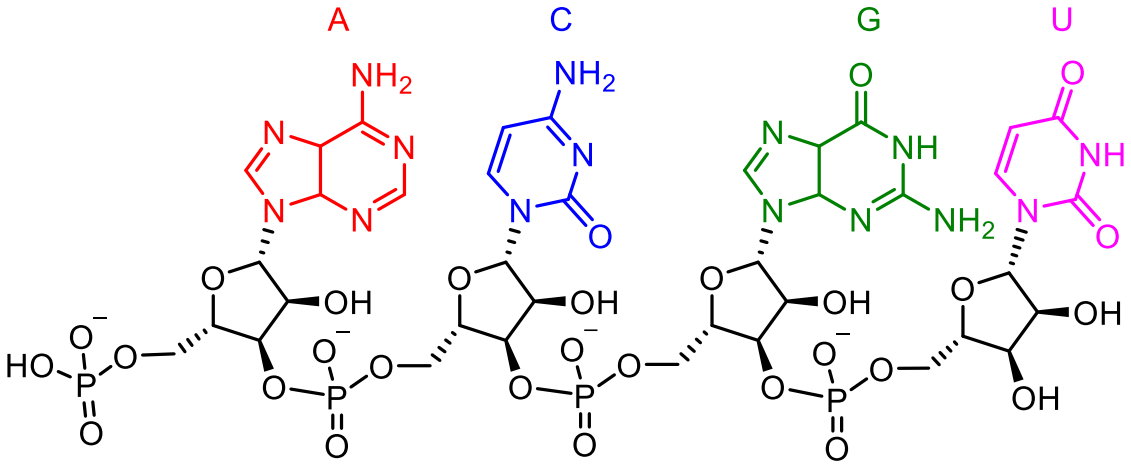

Figure 1.1. *Possible nucleosides in RNA.*

Base pairing further expands the structural repertoire of RNA. Canonical Watson–Crick pairs (A–U and C–G) are the most common, maximizing hydrogen bonding and structural isostericity. Non-canonical interactions, including wobble and Hoogsteen pairings, are also frequently observed and contribute to RNA flexibility (**Figure 1.2A**).[5] Each nucleobase has three potential interaction surfaces: the Watson–Crick edge, the Hoogsteen edge, and the sugar edge. Moreover, glycosidic bonds can adopt cis or trans orientations (**Figure 1.2B**). Combining these possibilities with the four canonical bases yields up to 168 theoretically distinct base-pairing geometries.[6] Several factors, such as steric interactions, protonation states, and metal binding, can further modulate the stability of these interplays, making only some of them happen in the majority of cases.[3] This plethora of interactions brings RNAs to adopt defined conformations. RNAs generally stabilize themselves by forming short intramolecular double-helical

regions, often referred to as “stems,” which arise when complementary sequences within the same strand base-pair with one another. At the same time, RNA molecules feature dynamic elements, such as unpaired nucleotides, mismatches, bulges, and larger loop regions, which interrupt these stems and introduce flexibility into the overall fold (see some examples in **Figure 1.2C**). These unpaired regions are not simply disordered; rather, they often form transient and non-canonical interactions, including hydrogen bonds and base stacking, which contribute to local structure and influence the overall folding landscape. Such interactions within loops and bulges can stabilize specific conformations and facilitate tertiary contacts, playing an important role in RNA folding and function.[7]

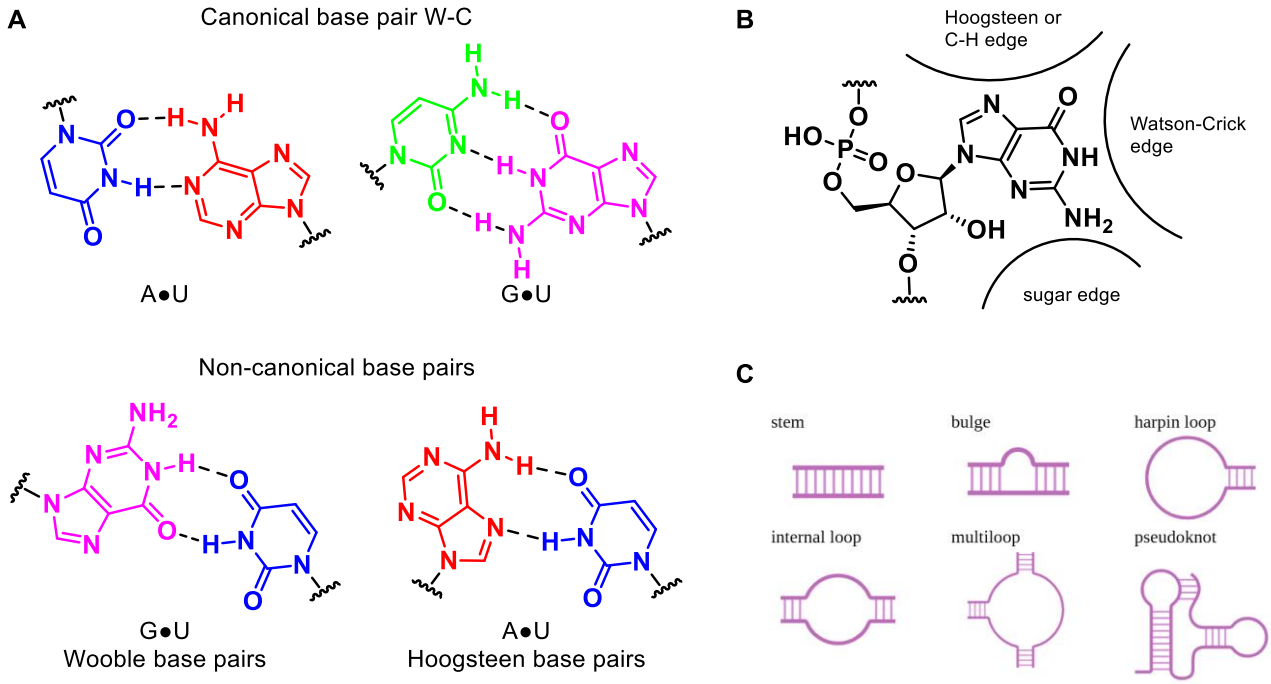

Figure 1.2. *A: Watson-Crick base pairing and Wooble-Hoogsteen base pairing.* ***B****: Representation of the various interaction areas identified in nucleosides.* ***C****: Representation of the possible secondary structure motifs occurring in RNA. Created with biorender.com.*

The combinatorial potential of base pairing gives rise to different RNA structures, which have been historically classified into primary, secondary, and tertiary (**Figure 1.3**). The primary structure is the linear nucleotide sequence. Secondary structure results from local intramolecular base pairing and includes helices, hairpins, internal loops, bulges, and multi-branch junctions. Tertiary structure emerges from long-range interactions between distant secondary elements, including non-canonical pairing, base stacking, and metal ion coordination, stabilizing the native three-dimensional fold.[3,5,8] An example of primary, secondary, and tertiary structures of a shorter model of the precursor of microRNA-21 is reported in **Figure 1.3**.

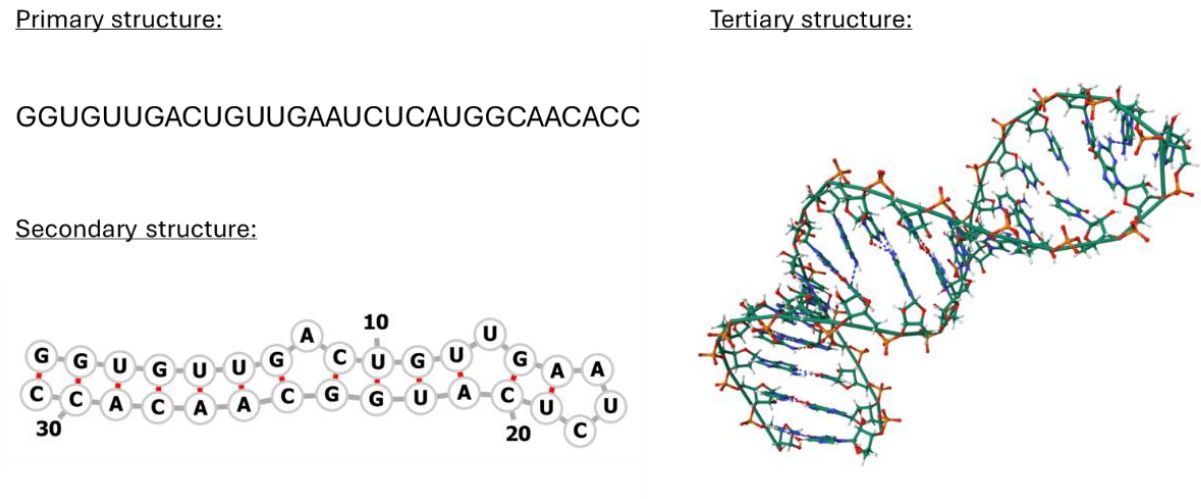

***Figure 1.3**. Primary, secondary, and tertiary structure of the apical loop of the precursor of microRNA-21, entry 5UZT of the protein data bank.*

As stated before, RNA is intrinsically dynamic, existing as an ensemble of interconverting conformations rather than a single rigid structure. Its conformational distribution is influenced by sequence, ionic conditions, and molecular interactions, including both ligand binding and intra- or intermolecular RNA contacts, with molecular crowding further modulating its behaviour.[7] In addition, RNA can undergo in-cell chemical modifications, such as methylation or pseudouridylation, that alter its stability, folding, and functional properties in the cellular context, fine-tuning its functions.[9] This structural flexibility enables RNA to respond to environmental changes and to adopt alternative conformations upon interaction with ligands, metal ions, or proteins, directly linking its plasticity to a wide range of biological functions.[1]

1.1: Non-coding RNAs

A non-coding RNA (ncRNA) is an RNA molecule that is not translated into a protein and instead fulfils a variety of functional roles within the cell.[1] ncRNAs vary widely in length, structure, and mode of action, reflecting a complex layer of gene regulation that is only beginning to be understood.[10] ncRNAs can be classified according to their biological function or their length. Based on function, ncRNAs are commonly divided into structural non-coding RNAs and regulatory non-coding RNAs.[11] According to their length, ncRNAs are instead classified into long non-coding RNAs (lncRNAs) and small non-coding RNAs (small RNAs) (**Figure 1.4**).[10,12] These groups are further subdivided into multiple subclasses based on their specific molecular functions.

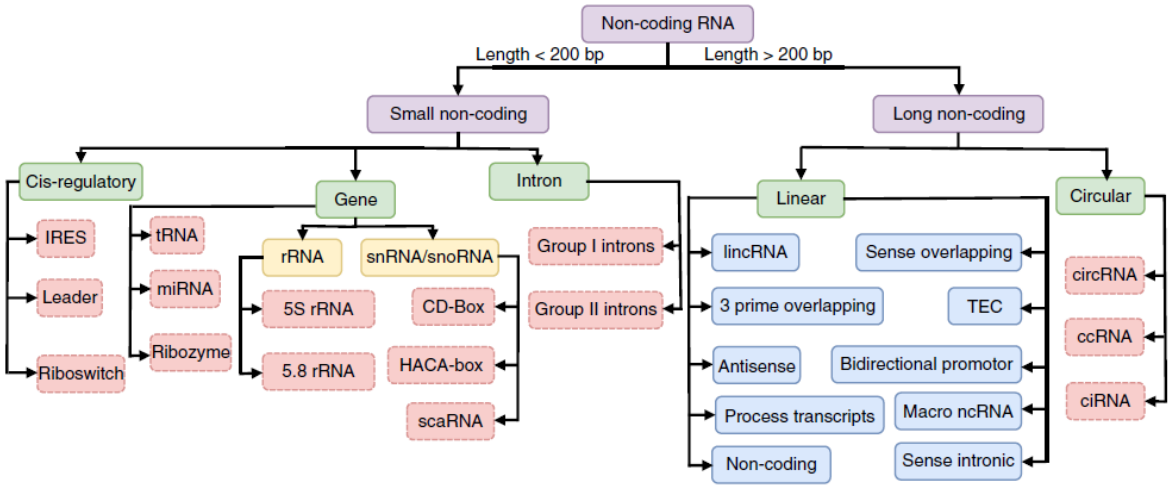

Figure 1.4. *Classification of RNAs according to Amin et al.*[12] *Adapted from reference 12.*

Knowledge of RNA biology is still evolving. The human genome comprises approximately three billion base pairs, the vast majority of which are transcribed into non-coding RNAs, while only about 2% of the genome encodes proteins. Despite their abundance, the functional roles of only a small fraction of ncRNAs have been characterized; indeed, the biological function of the vast majority of ncRNAs remains unknown, making their classification in class and description an always-evolving process.[11–13] Non-coding RNAs (ncRNAs) are particularly attractive from a pharmaceutical perspective. To date, only a very small fraction of the human genome, estimated at approximately 0.05%, is targeted by currently approved protein-directed therapeutics, including small molecules and antibodies. In contrast, the vast majority of the human genome is transcribed into non-coding RNA species, representing a largely unexplored therapeutic landscape, as highlighted in **Figure 1.5**.[14] Moreover, conventional protein-based drug discovery faces intrinsic limitations: it is estimated that up to 85% of proteins lack well-defined binding pockets or clefts suitable for high-affinity small-molecule recognition. As a result, many biologically relevant proteins are considered "undruggable" using traditional approaches.[15] Given their central role in regulating gene expression and cellular pathways, ncRNAs offer an alternative strategy for therapeutic intervention. Targeting ncRNAs may enable modulation of biological processes that are otherwise inaccessible through protein-directed drugs, thereby expanding the scope of druggable space within the genome.[16]

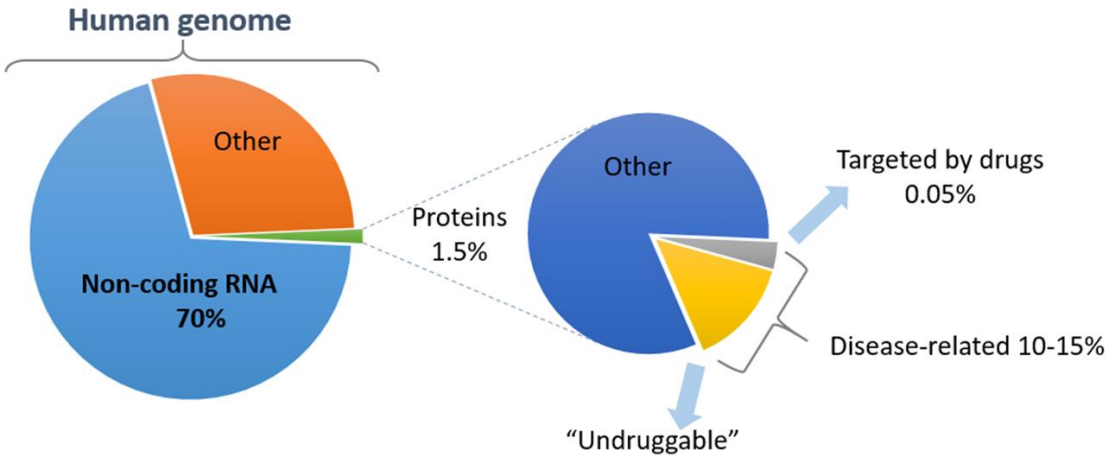

Figure 1.5*. Schematization of the human genome. Reproduced from reference* 17.

Understanding the diversity, abundance, and functional roles of ncRNAs is therefore essential for leveraging their potential as therapeutic targets. Among these, microRNAs have emerged as potential targets due to their widespread regulatory functions and disease associations.

1.2: MicroRNAs

MicroRNAs (miRs) are a class of small, single-stranded non-coding RNAs, 18–25 nucleotides in length, found in both plants and animals.[18–20] miRs are functional ncRNAs that regulate gene expression at the post-transcriptional level, fine-tuning gene expression. This regulation is achieved through partial complementarity between the miR sequence and its target messenger RNA (mRNA), leading ultimately to mRNA modulation, such as degradation or inhibition of translation. In eukaryotes, the complementarity between a miR and its target mRNA is often imperfect, allowing a single miR to target multiple mRNAs and, conversely, enabling a single mRNA to be regulated by multiple miRs, highlighting their role in a complex regulatory system.[21,22] In addition to targeting mRNAs, miRs have been reported to interact with other non-coding RNAs, for example, in miR:miR or miR:primiR interactions, suggesting broader roles in the regulation and coordination of gene expression.[23]

Under normal physiological conditions, miRs play essential roles in safeguarding key biological processes such as proliferation, differentiation, and apoptosis. Deregulation of miRs, due to mechanisms that are not yet fully understood, can contribute to oncogenesis.[21,22] Such deregulation is a common feature of neoplasms, and the analysis of altered miR levels in body fluids has been proposed as a diagnostic and predictive biomarker in cancer.[20]

miRs biogenesis is reported in **Figure 1.6**. miR genes are initially transcribed by RNA polymerase II or III (Pol II/Pol III) into primary transcripts (pri-miRs), which undergo nuclear processing by a microprocessor complex composed of the RNA-binding protein DiGeorge Syndrome Critical Region 8 (DGCR8) and the RNase III enzyme Drosha. DGCR8 recognizes the pri-miR hairpin approximately 11 nucleotides from the basal junction and 22 nucleotides from the apical junction, while Drosha cleaves the pri-miR to generate a precursor miR (nuclear pre-miR).[18,19] This hairpin-structured RNA is subsequently exported to the cytoplasm by Exportin-5, where it is further processed by the RNase III endonuclease Dicer. During this step, the terminal loop is removed, typically by cleavage of approximately 22 nucleotides from both the 5' and 3' ends, resulting in a miR duplex (cytosolic pre-miR).[18,19]

The orientation of the miR strand within the duplex determines the nomenclature of the mature miR. The 5p strand originates from the 5' arm of the pre-miR hairpin, whereas the 3p strand is derived from the 3' arm. Both strands of the miR duplex can be loaded into members of the Argonaute (AGO) protein family. For a given miR, the relative proportion of AGO-loaded 5p and 3p strands can vary substantially depending on the cell type or cellular context, ranging from approximately equal levels to a strong predominance of one strand over the other. In general, the strand characterized by lower thermodynamic stability at its 5' end or by the presence of a 5' uracil is preferentially incorporated into AGO and is referred to as the “guide strand”, whereas the opposing strand is termed the “passenger strand”.[18,19]

Although this represents the canonical miR biogenesis pathway, non-canonical miR biogenesis mechanisms that bypass Drosha processing have also been described.[24]

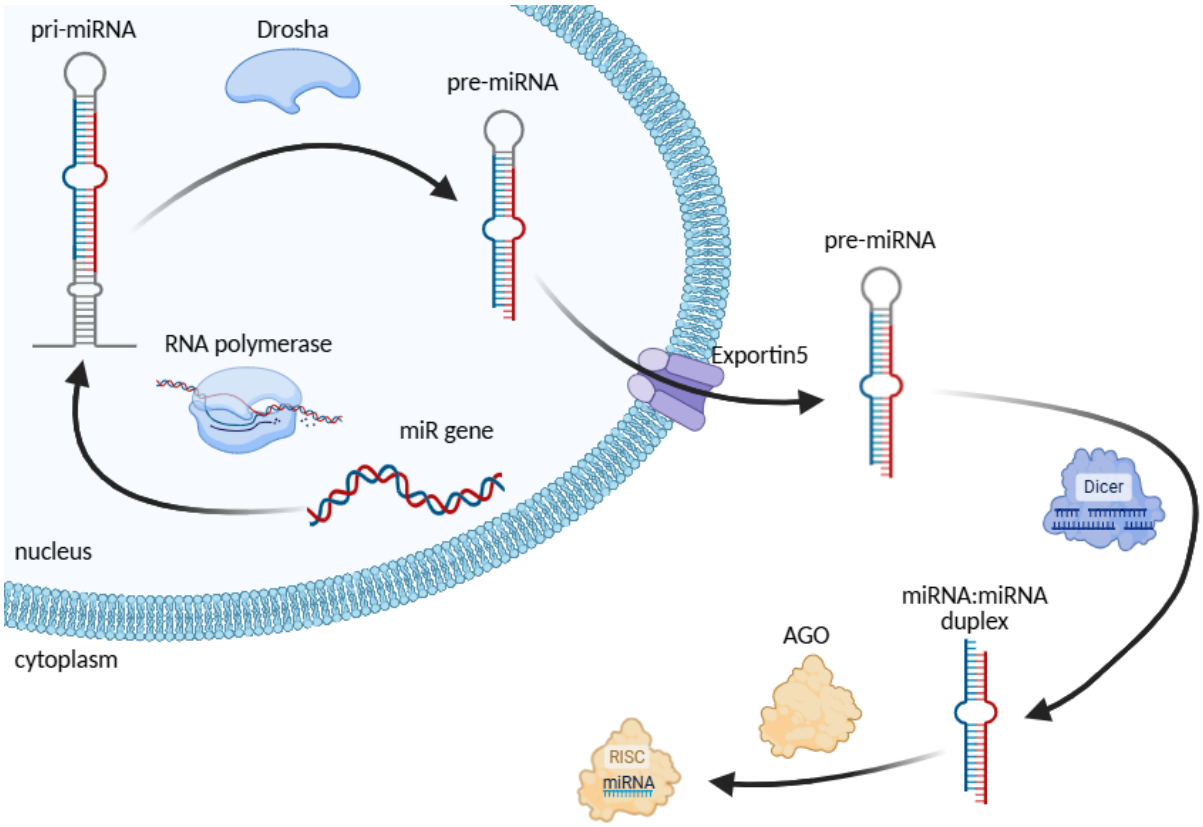

Figure 1.6. *MicroRNA biogenesis. Created with biorender.com.*

Upon binding to an Argonaute (AGO) protein, the minimal miR-induced silencing complex (miRISC) is formed. The miRISC recognizes target mRNAs through sequence complementarity, which in mammals is generally partial. It has been hypothesized that recognition primarily occurs within a so-called "seed region", found in the untranslated region of the mRNA. Three principal mechanisms of miRNA-mediated gene silencing have been described[25] (**Figure 1.7)**, all of which result in modulation of mRNA activity:

1. AGO has been reported to recruit TNRC6, a scaffolding protein capable of interacting with multiple cellular factors.[26] TNRC6, in turn, recruits deadenylase complexes, which remove the poly(A) tail at the 3' end of the mRNA, a construct that normally elongates the mRNA lifetime. This renders mRNA more susceptible to degradation, achieving its silencing indirectly.
2. Eukaryotic mRNAs are typically capped at their 5' end with a 7-methylguanosine moiety. TNRC6, recruited by AGO, can also promote the recruitment of the DCP1/DCP2 decapping complex, which removes the 5' cap structure, another construct used to augment mRNA lifetime. Loss of the cap significantly reduces mRNA stability and facilitates degradation.
3. AGO binding to the target mRNA can also impair ribosome recruitment, thereby inhibiting translation without necessarily inducing immediate mRNA degradation.

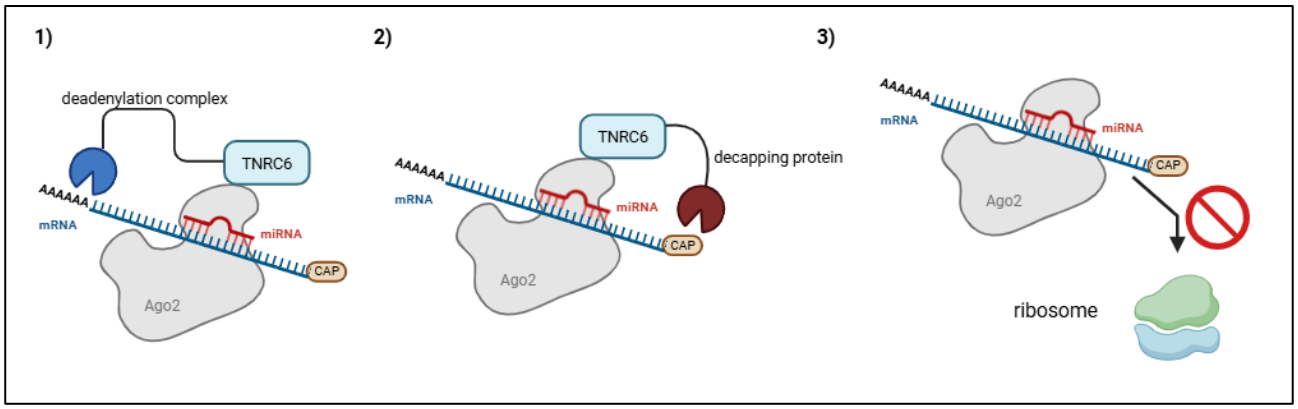

Figure 1.7. *Illustration of the described mRNA modulation mechanism. Created with biorender.com.*

Through Importin-8 or Exportin-1, human Argonaute 2 (AGO2) can shuttle between the nucleus and the cytoplasm.[18] In light of the previously mentioned potential interactions between miRs and other primary miR transcripts, it has been hypothesized that miRs, together with functional proteins such as AGO2, may localize to the nucleus.[18,27] Overall, miRs appear as highly versatile regulators of gene expression, characterized by context-dependent activity, complex biogenesis pathways, and the ability to engage in multifaceted regulatory networks. This intrinsic complexity, coupled with their sensitivity to dysregulation, underlies the significant impact that specific miRs can have on cellular homeostasis and disease-related processes. Consequently, the detailed study of individual miRs has become essential for understanding how alterations in miR-mediated regulation contribute to pathological states.

1.3: miR21

In *Homo sapiens*, the miR21 gene is located at chromosome band 17q23.2, within an intronic region of the vacuole membrane protein 1 (VMP1) locus, also known as transmembrane protein 49 (TMEM49).[28] Following the canonical miR biogenesis pathway described in **Paragraph 1.2**, transcription of the miR21 gene gives rise to a 125-nucleotide-length primary transcript (pri-miR21). This primary transcript is subsequently processed into a 72-nucleotide precursor miR (pre-miR21) hairpin, from which the two mature miR strands, miR21-5p and miR21-3p, are generated, measuring 21 and 20 nucleotides in length, respectively (**Table 1.1**).[29–32] Incorporation into the RISC machinery of -3p or -5p strand is generally tumour-dependent, and no clear trend can be identified.[33]

Table 1.1*. Primary sequences of pri-miR21, pre-miR21, and miR21 mature (both 3p and 5p).*

construct	sequence
Pri-miR21	ACAUCUCCAUGGCUGUACCACCUUGUCGGGUAGCUUAUCAGACUGAUGUUGACUG UUGAAUCUCAUGGCAACACCAGUCGAUGGGCUGUCUGACAUUUUGGUAUCUUUCA UCUGACCAUCCAUAU
Pre-miR21	UGUCGGGUAGCUUAUCAGACUGAUGUUGACUGUUGAAUCUCAUGGCAACACCAGU CGAUGGGCUGUCUGACA
miR21-5p	UAGCUUAUCAGACUGAUGUUGA
miR21-3p	CAACACCAGUCGAUGGGCUGU

miR21 has been predicted to target more than 3,000 human genes,[34] indicating a broad regulatory capacity that spans both normal physiological processes and disease-related pathways. During

development, miR21 expression has been reported to be detectable from early stages, with a marked increase coinciding with embryonic gene activation.[34] miR21 has also been implicated in immune system regulation. In particular, differential expression of miR21 has been observed among T-cell subsets.[35,36] In addition to its roles in normal biological processes, miR21 upregulation has been associated with several pathological conditions, including asthma, Sézary syndrome, and fibrotic processes in cardiac fibroblasts,[30] as well as a wide range of cancers.[37]

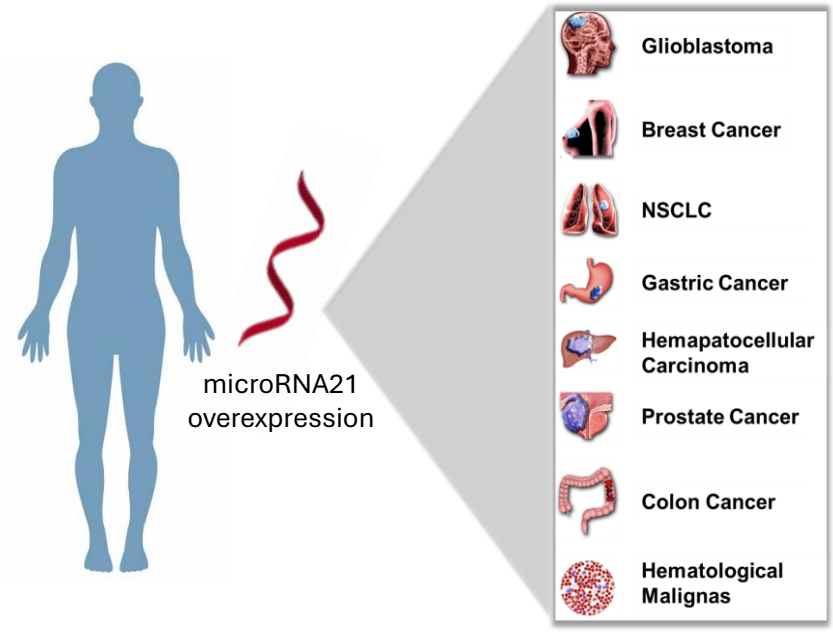

Figure 1.8. *Malignancies associated with miR21 overexpression and possible therapeutic development for miR21 modulation.*

miR21 has been reported to be upregulated in the vast majority of solid tumors, including breast, pancreatic, lung, gastric, prostate, colon, head and neck, and esophageal cancers. It has also been implicated in hematological malignancies, such as leukemia and lymphoma, as well as in glioblastoma, osteosarcoma, and seminoma. Due to this widespread overexpression in cancer, miR21 is considered a prototypical oncomiR.[38] Moreover, miR21 is directly associated with inhibition of cellular apoptosis, as also demonstrated in an in vivo model by Medina and colleagues.[39] Consistently, several of its putative targets are involved in the regulation of apoptosis, further supporting its role in promoting cell survival in tumorigenesis (**Table 1.2**).[40]

Table 1.2*. Selected published miR21 targets validated with experimental data (according to Buscaglia and colleagues). Adapted from reference* 40.

Full name	**Gene**	**Apoptotic role**
Phosphatase and tensin homolog	*PTEN*	Direct
Programmed cell death 4	*PDCD4*	Direct
Tropomyosin 1 (alpha)	*TPM1*	Unknown
Sprouty homolog 1, antagonist of FGF signaling (Drosophila)	*SPRY1*	Indirect
Sprouty homolog 2 (Drosophila)	*SPRY2*	Indirect

As an example, only 5 out of 30 reported, published miR21 targets are indicated.[40]

Given its particular relevance for the in-cell experiments described later (**Chapter 7**), PDCD4 is highlighted in this section. PDCD4 is a tumor suppressor protein that inhibits cell growth, invasion, and metastasis.[41] Downregulation of PDCD4, concomitant with upregulation of miR21, has been reported in multiple cancer types, including leukemia, lung, colon, breast, prostate, and hepatocellular carcinoma.[42,43] Its expression levels have been shown to be inversely correlated with miR21 levels, and restoration of PDCD4 activity can be achieved through inhibition of miR21 activity using small molecules designed to modulate miR21 expression, as described in **Paragraph 1.4**.
Interestingly, Asangani et al.[42] reported an analysis of the complementarity of miR21 and the PDCD4 sequence in different species (**Figure 1.9**). The protein mRNA was screened for complementarity to seed sequences of known miRs via a bioinformatic search, delivering a full match target sequence (>99%) for miR21 at nt 228–249 for all the studied species. A representation of this study is reported in **Figure 1.9**. This data correlates with their subsequent experimental validation, which demonstrated that miR21 specifically downregulates PDCD4 at the post-transcriptional level.

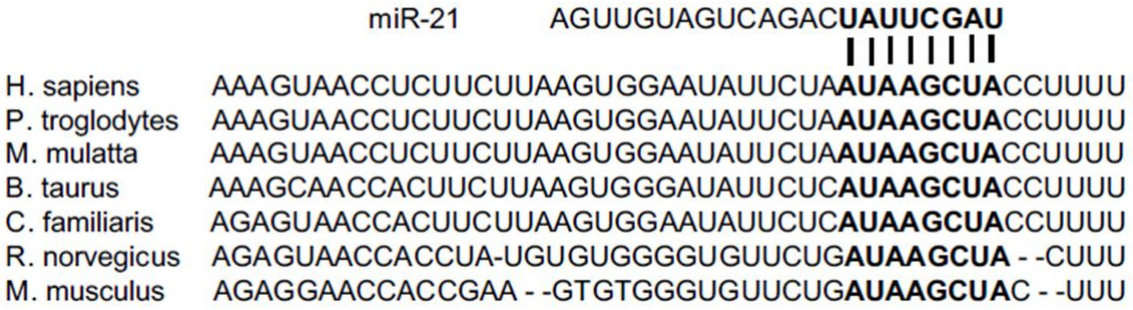

Figure 1.9. *Analysis of the complementarity of miR21 sequence and the PDCD4 sequence in different species.* Adapted from reference 42.

miR21 has been reported to be modulated also by other miRs through miR:miR interactions. Its regulation by miR-145 has been found in colon cancer,[44] while miR-122 has been shown to influence miR21 biogenesis in the liver.[27] These findings underscore that miR21 operates as part of a multi-layered regulatory system, which is not yet fully elucidated, and its levels may be controlled through intricate, context-dependent mechanisms. Despite this complex regulatory system, its oncomir role makes it an interesting potential therapeutic target, and in fact, several groups in recent years have attempted to modulate its levels.

1.3.1: miR proposed inhibition strategies

As stated in **Paragraph 1.2**, miRs generally target multiple genes that may be altered in different diseases. This gives them a unique advantage as therapeutic molecules,[31] since multiple modulations can be achieved by addressing a single biomolecule, making them attractive candidates for targeted intervention. Several strategies have been developed to modulate miR levels, which can be broadly classified into four categories:[45]

1) **Antisense oligonucleotides (ASOs):** complementary oligonucleotides are designed to bind the mature miR sequence, thereby inhibiting its interaction with target mRNAs. While effective in simple models for their high complementarity to the target, ASOs can produce undesired off-target effects, interfere with other RNA species, and provoke immune responses, complicating interpretation and therapeutic use.[46]

2) **miR sponges:** miR sponge strategies involve transgenic overexpression of transcripts containing multiple binding sites for the target miR, effectively "soaking up" the miR. Sponge-based approaches can provide long-term inhibition and may sequester multiple related miRs, which is advantageous when broader network modulation is desired. However, they are time-consuming to develop, difficult to deliver, have poor in vivo stability, and may inadvertently suppress non-intended miRs, perturbing regulatory networks beyond the original target.[47]
3) **Small molecules inhibiting miR biogenesis:** These compounds target either the pri-miR or pre-miR, depending on their ability to permeate the nucleus and the structural characteristics of the target. Advantages of small-molecule inhibitors include reasonable assessment of drug-like profiles, reversibility, relatively low production cost, and ease of delivery, provided that high-affinity and specific binding to the target can be achieved.[48]
4) **Small molecules targeting AGO2/RISC assembly:** These molecules interfere with the incorporation of miRs into the RNA-induced silencing complex (RISC), preventing target mRNA repression. While potentially affecting multiple miRs simultaneously, this approach carries a high risk of off-target effects since AGO2 is central to the function of many miRs, and perturbation of RISC assembly can broadly affect gene regulatory networks.[49]

1.4: Reported miR21 inhibiting compounds

As discussed in **Paragraph 1.3**, miR21 represents an attractive potential pharmaceutical target and, accordingly, several groups have attempted to modulate its levels. As this is a medicinal chemistry PhD project, only small molecule-based approaches will be briefly discussed in this section. Examples of biologic strategies such as miR sponges[50] or nanoparticle-mediated delivery systems[51] have also been reported in the literature.

1.4.1: Antisense oligonucleotides approach for miR21 modulation

Antisense oligonucleotides (ASOs) provide the most direct approach to inhibit miR function. These molecules bind to the target miR through sequence complementarity, which can disrupt its natural folding, prevent interactions with downstream targets, and recruit endogenous cellular machinery to cleave the RNA (RNAases).[16]

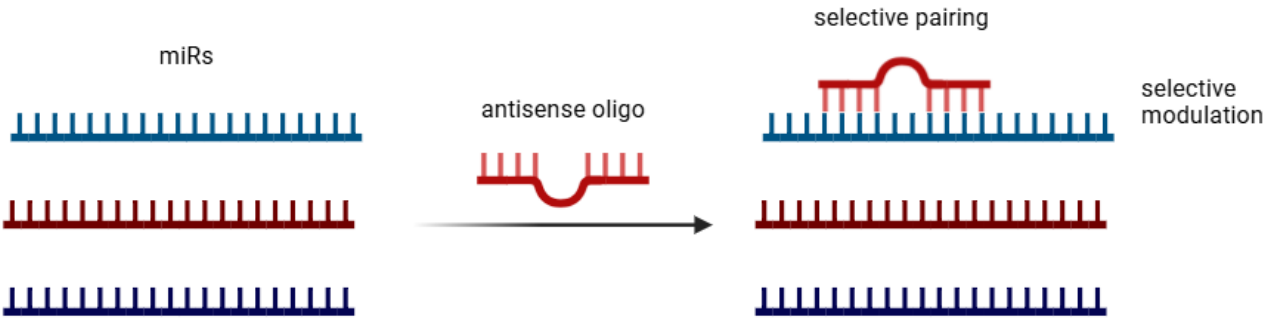

***Figure 1.10**. Illustration of an antisense inhibition mechanism. Created with biorender.com.*

For miR21, the pharma company Sanofi developed Lasemirsen®, an antisense nucleotide, which reached Phase 2 clinical trials for the treatment of Alport syndrome, a kidney disease.[52] The development of this drug is still ongoing.

Despite these promising developments, anti-miR21 ASOs have generally failed to overcome the tumor microenvironment, due to low metabolic stability limiting their effectiveness in vivo and making ASO-based strategies less ideal for cancer therapy.[31]

1.4.2: Small molecules approach for miR21 modulation

Small-molecule therapeutics offer several advantages, including tunable pharmacokinetic properties and relatively low production costs. Given the high potential of miR21 as a therapeutic target, several groups have reported small molecules as modulators of its levels.[53–58] Both phenotypical and biochemical screening approaches have been employed for their identification. As for the biochemical screening approach, the vast majority of the groups prefer pre-miR21 as the putative target, trying to reduce the biogenesis of miR21 by inhibiting the Dicer-mediated cleavage of its precursor. This preference can be rationalized by its cytosolic localization, which makes it more accessible than the nuclear pri-miR21, as well as by practical considerations related to assay development, including the RNA production costs.

However, the first evidence that miR21 levels could be modulated by small molecules emerged from phenotypic screening approaches. In 2010, Gumireddy and colleagues reported the identification of diazobenzene derivatives (compounds **A** and **B**, **Figure 1.11**) capable of selectively modulating miR21 levels in cells without affecting other control miRs.[53] Although the precise molecular target and mechanism of action were not elucidated, this study provided a proof of concept, demonstrating that miR21 is responsive to small-molecule modulation in a cellular context. A subsequent expanded screen of over 30,000 compounds further reinforced this concept by identifying additional chemotypes and establishing a preliminary structure–activity relationship in cells.[54] Together, these studies positioned miR21 modulation within the realm of classical phenotypic drug discovery.

In parallel, drug repurposing strategies were explored as a putative approach to rapidly identify compounds capable of modulating miR21 levels while potentially bypassing early-stage safety studies. Several clinically used drugs, including streptomycin (compound **C**, **Figure 1.11**), doxorubicin, mitoxantrone, and dovitinib, were reported to reduce miR21 expression while concomitantly restoring the levels of downstream targets such as PDCD4. [55–58] However, despite their translational appeal, these compounds generally failed to modulate miR21 levels with sufficient potency or specificity to support further development. Furthermore, the diverse cellular effects of these compounds made it challenging to determine whether their activity resulted from direct binding to pre–miR21 or from indirect pathways, and the lack of an established structure–activity relationship limited their use as starting point for rational medicinal chemistry programs.

To address these challenges, several groups explored *de novo* discovery strategies focused on directly targeting pre–miR21, with the goal of obtaining biochemical evidence of binding. For example, Shortridge and colleagues identified small molecules capable of interacting with pre–miR21, thus reducing the levels of miR21, and reported a preliminary structure–activity relationship using NMR spectroscopy and cellular assays (compound **D**, **Figure 1.11**).[57] This work highlighted the feasibility of applying rational, target-focused approaches to miR21 modulation by targeting the processing of its precursor, moving beyond purely phenotypic screening.

Structural studies have further strengthened this paradigm. Structural models of pre-miR21 in both its native and ligand-bound states have been deposited in the Protein Data Bank (PDB entries 5UZT and 5UZZ),[59] enabling the application of structure-based drug design methods. In parallel, computational approaches have been developed to predict RNA secondary and tertiary structures and guide ligand

design.[60] These activities led to the identification of additional small molecules, such as AC1MMYR2[61] (compound **E**, **Figure 1.11**), 3,3'-diindolylmethane[62] (compound **F**, **Figure 1.11**), and regorafenib®[63] (compound **G**, **Figure 1.11**), which have been shown to bind pre-miR21 and modulate miR21 levels in cellular models, thus demonstrating the feasibility of also an in-silico-based approach.
Taken together, these studies demonstrate that pre–miR21 can be targeted using a range of established drug discovery strategies, including phenotypic screening, drug repurposing, *de novo* ligand design, and structure-based approaches. This highlights pre–miR21 as a promising target for modulating miR21 levels using structurally diverse small molecules. At the same time, there is still a clear need for small-molecule compounds that combine biological activity with favourable drug-like properties and selectivity, as none of the previously reported compounds advanced to in vivo testing, likely due to limitations in these characteristics.

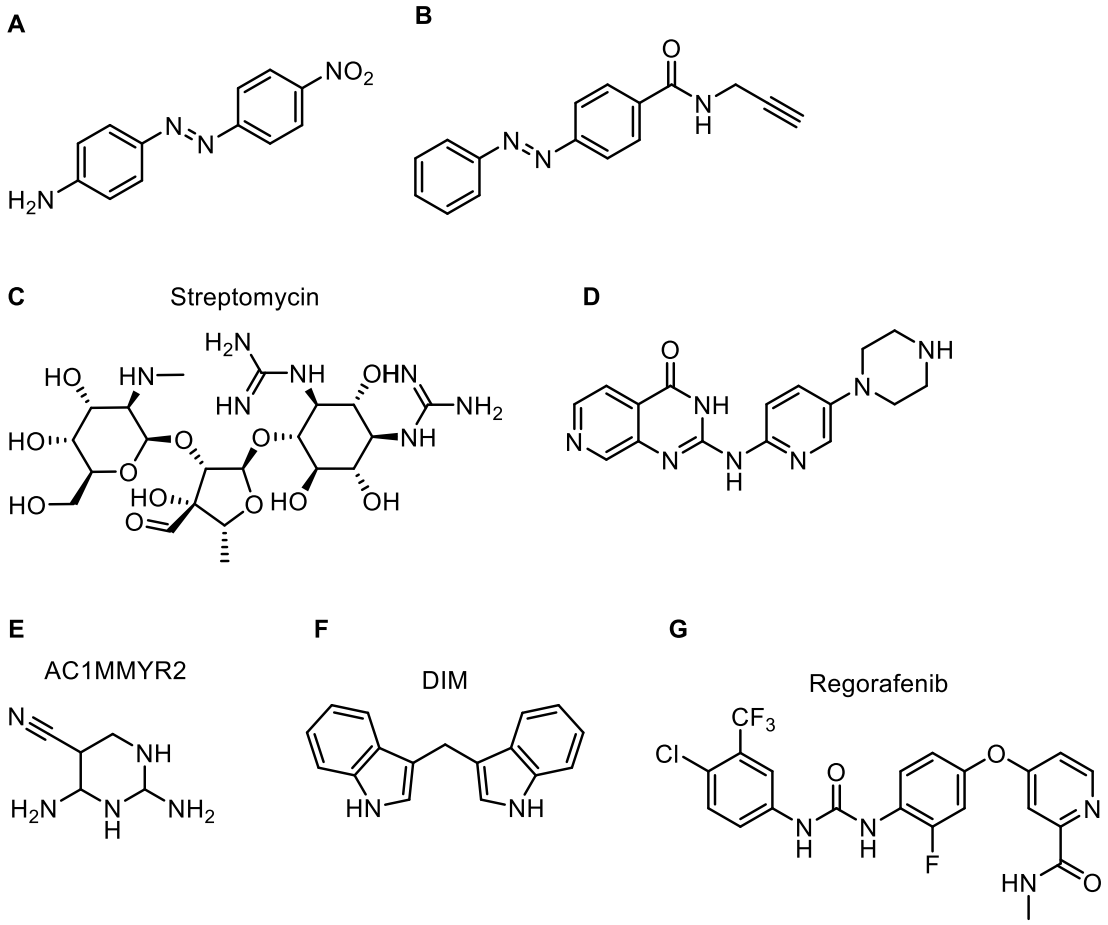

Figure 1.11. *Small molecules proposed as modulators of miR21 levels.*

1.4.3: Novel modalities for modulating miR21 levels

In addition to classical small molecule approaches, novel modalities are being explored for pre–miR21 targeting, including bifunctional compounds that go beyond traditional drug design rules. These molecules take advantage of the spatial proximity of biological macromolecules, a principle often exploited in nature, to either trigger specific biological processes or act as a "molecular glue" between two entities.[64] In this context, bifunctional molecules are designed so that one part confers high affinity for the target RNA, while the other provides a biologically active function.

For pre–miR21, several bifunctional approaches aimed to inhibit Dicer-mediated cleavage. For example, Yan and colleagues[65] designed a dimeric compound combining neomycin, a known pre–miR21 binder, with a Dicer inhibitor, allowing simultaneous engagement of the RNA and the enzyme (compound **H**, **Figure 1.12**). This strategy proved effective, yielding enhanced modulation of miR21 levels in cells compared to neomycin alone.

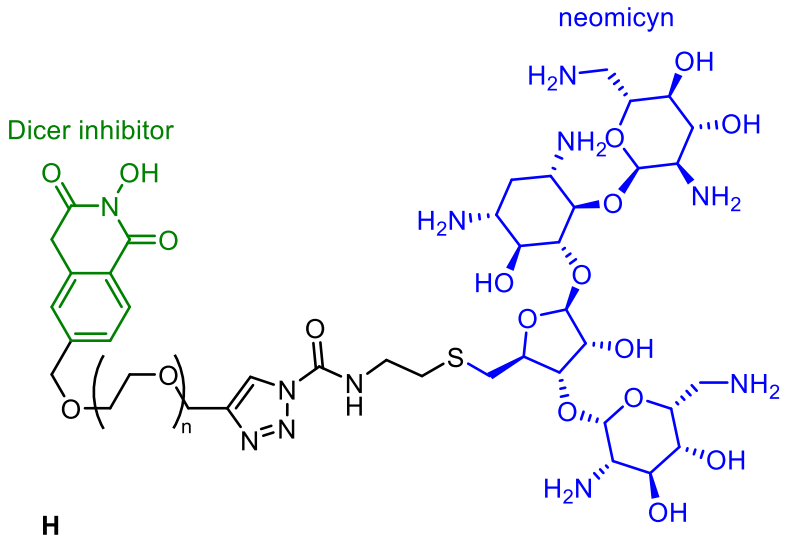

Figure 1.12. *Neomycin-Dicer biofunctional compound **H** proposed by Yan et al.*[65]

Ribonuclease targeting chimeras (RiboTACs) represent another class of bifunctional molecules that expand the toolbox for pre–miR21 targeting. These compounds consist of an RNA-binding small molecule linked to a ribonuclease recruiter, enabling selective degradation of the target RNA via recruitment of RNase L.[66] Compared to conventional small molecules, RiboTACs offer unique advantages, such as sub-stoichiometric activity and an event-driven mechanism of action.[16] Application of this strategy to miR21 has been reported by Disney and colleagues, who demonstrated the modulation of both miR21 levels and downstream targets, such as PDCD4, in cells with compound **J** (**Figure 1.13)**.[67] Similarly, Zhang and co-workers[58] used a derivative of Dovitinib (compound **K**, **Figure 1.13**) as a pre–miR21 binder and conjugated it with an RNase L recruiter to generate a RiboTAC. Compound **K** effectively reduced miR21 levels in cells, further highlighting the potential of RNA-targeted chimeras as a novel modality for miR modulation.

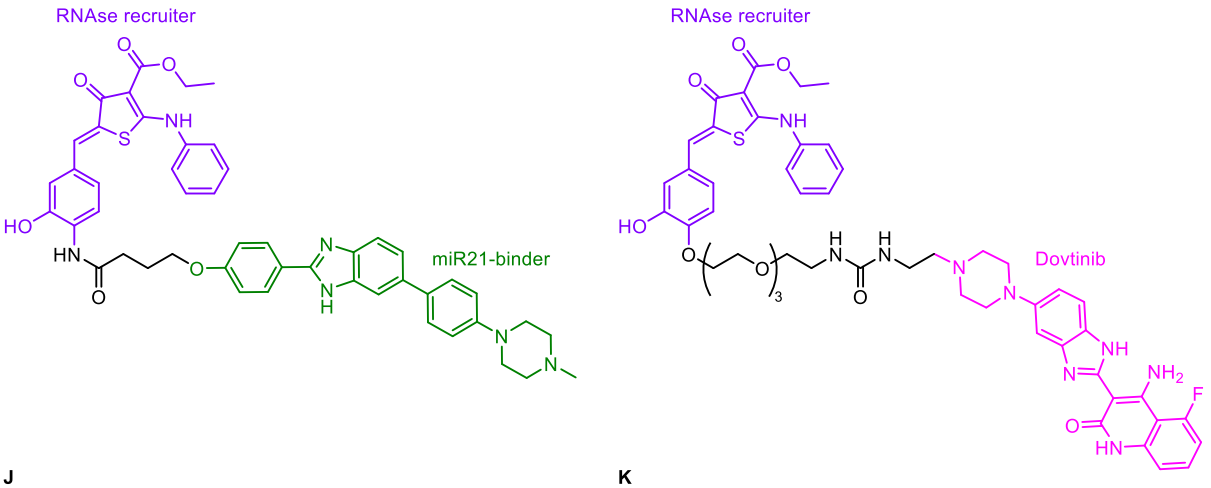

Figure 1.13. *Ribotac compounds targeting pre-miR21 reported by Disney's (J) and Zhang's (K) groups.*

While these bifunctional approaches are often effective in vitro, they frequently exhibit suboptimal pharmacokinetic properties, which can limit their in vivo applicability and present challenges for therapeutic development.[68]

1.5: References

(1) Schowen, R. L. Principles of Biochemistry 2nd Ed. (Lehninger, Albert L.; Nelson, David L.; Cox, Michael M.). *J. Chem. Educ.* **1993**, *70* (8), A223. https://doi.org/10.1021/ed070pA223.1.

(2) Masuki, R.; Liew, D.; Yong, E. H. Hierarchical Analysis of RNA Secondary Structures with Pseudoknots Based on Sections. *PLOS Comput. Biol.* **2026**, *22* (1), e1013904. https://doi.org/10.1371/journal.pcbi.1013904.

(3) Falese, J. P.; Donlic, A.; Hargrove, A. E. Targeting RNA with Small Molecules: From Fundamental Principles towards the Clinic. *Chem. Soc. Rev.* **2021**, *50* (4), 2224–2243. https://doi.org/10.1039/d0cs01261k.

(4) Vicens, Q.; Kieft, J. S. Thoughts on How to Think (and Talk) about RNA Structure. *Proc. Natl. Acad. Sci.* **2022**, *119* (17), e2112677119. https://doi.org/10.1073/pnas.2112677119.

(5) Lee, J. C.; Gutell, R. R. Diversity of Base-Pair Conformations and Their Occurrence in rRNA Structure and RNA Structural Motifs. *J. Mol. Biol.* **2004**, *344* (5), 1225–1249. https://doi.org/10.1016/j.jmb.2004.09.072.

(6) Stombaugh, J.; Zirbel, C. L.; Westhof, E.; Leontis, N. B. Frequency and Isostericity of RNA Base Pairs. *Nucleic Acids Res.* **2009**, *37* (7), 2294–2312. https://doi.org/10.1093/nar/gkp011.

(7) *RNA Structural Dynamics As Captured by Molecular Simulations: A Comprehensive Overview | Chemical Reviews*. https://pubs.acs.org/doi/10.1021/acs.chemrev.7b00427 (accessed 2026-03-10).

(8) Zhang, J.; Fei, Y.; Sun, L.; Zhang, Q. C. Advances and Opportunities in RNA Structure Experimental Determination and Computational Modeling. *Nat. Methods* **2022**, *19* (10), 1193–1207. https://doi.org/10.1038/s41592-022-01623-y.

(9) Roundtree, I. A.; Evans, M. E.; Pan, T.; He, C. Dynamic RNA Modifications in Gene Expression Regulation. *Cell* **2017**, *169* (7), 1187–1200. https://doi.org/10.1016/j.cell.2017.05.045.

(10) Nappi, F. Non-Coding RNA-Targeted Therapy: A State-of-the-Art Review. *Int. J. Mol. Sci.* **2024**, *25* (7). https://doi.org/10.3390/ijms25073630.

(11) Dahariya, S.; Paddibhatla, I.; Kumar, S.; Raghuwanshi, S.; Pallepati, A.; Gutti, R. K. Long Non-Coding RNA: Classification, Biogenesis and Functions in Blood Cells. *Mol. Immunol.* **2019**, *112*, 82–92. https://doi.org/10.1016/j.molimm.2019.04.011.

(12) Amin, N.; McGrath, A.; Chen, Y.-P. P. Evaluation of Deep Learning in Non-Coding RNA Classification. *Nat. Mach. Intell.* **2019**, *1* (5), 246–256. https://doi.org/10.1038/s42256-019-0051-2.

(13) Matsui, M.; Corey, D. R. Non-Coding RNAs as Drug Targets. *Nat. Rev. Drug Discov.* **2017**, *16* (3), 167–179. https://doi.org/10.1038/nrd.2016.117.

(14) Warner, K. D.; Hajdin, C. E.; Weeks, K. M. Principles for Targeting RNA with Drug-like Small Molecules. *Nat. Rev. Drug Discov.* **2018**, *17* (8), 547–558. https://doi.org/10.1038/nrd.2018.93.

(15) Haga, C. L.; Phinney, D. G. Strategies for Targeting RNA with Small Molecule Drugs. *Expert Opin. Drug Discov.* **2023**, *18* (2), 135–147. https://doi.org/10.1080/17460441.2022.2111414.

(16) Costales, M. G.; Childs-Disney, J. L.; Haniff, H. S.; Disney, M. D. How We Think about Targeting RNA with Small Molecules. *J. Med. Chem.* **2020**, *63* (17), 8880–8900. https://doi.org/10.1021/acs.jmedchem.9b01927.

(17) Bellina, F. Study and Development of New RNA-Targeted Probes. **2024**.

(18) O'Brien, J.; Hayder, H.; Zayed, Y.; Peng, C. Overview of MicroRNA Biogenesis, Mechanisms of Actions, and Circulation. *Front. Endocrinol.* **2018**, *9*. https://doi.org/10.3389/fendo.2018.00402.

(19) Ha, M.; Kim, V. N. Regulation of microRNA Biogenesis. *Nat. Rev. Mol. Cell Biol.* **2014**, *15* (8), 509–524. https://doi.org/10.1038/nrm3838.

(20) Esquela-Kerscher, A.; Slack, F. J. Oncomirs — microRNAs with a Role in Cancer. *Nat. Rev. Cancer* **2006**, *6* (4), 259–269. https://doi.org/10.1038/nrc1840.

(21) Jacobsen, A.; Silber, J.; Harinath, G.; Huse, J. T.; Schultz, N.; Sander, C. Analysis of microRNA-Target Interactions across Diverse Cancer Types. *Nat. Struct. Mol. Biol.* **2013**, *20* (11), 1325–1332. https://doi.org/10.1038/nsmb.2678.

(22) Reddy, K. B. MicroRNA (miRNA) in Cancer. *Cancer Cell Int.* **2015**, *15* (1), 38. https://doi.org/10.1186/s12935-015-0185-1.

(23) Hill, M.; Tran, N. miRNA Interplay: Mechanisms and Consequences in Cancer. *Dis. Model. Mech.* **2021**, *14* (4), dmm047662. https://doi.org/10.1242/dmm.047662.

(24) Ruby, J. G.; Jan, C. H.; Bartel, D. P. Intronic microRNA Precursors That Bypass Drosha Processing. *Nature* **2007**, *448* (7149), 83–86. https://doi.org/10.1038/nature05983.

(25) Liu, H.; Lei, C.; He, Q.; Pan, Z.; Xiao, D.; Tao, Y. Nuclear Functions of Mammalian MicroRNAs in Gene Regulation, Immunity and Cancer. *Mol. Cancer* **2018**, *17* (1), 64. https://doi.org/10.1186/s12943-018-0765-5.

(26) Johnson, S. T.; Chu, Y.; Liu, J.; Corey, D. R. Impact of Scaffolding Protein TNRC6 Paralogs on Gene Expression and Splicing. *RNA* **2021**, *27* (9), 1004–1016. https://doi.org/10.1261/rna.078709.121.

(27) *Nuclear miR-122 directly regulates the biogenesis of cell survival oncomiR miR-21 at the posttranscriptional level | Nucleic Acids Research | Oxford Academic*. https://academic.oup.com/nar/article/46/4/2012/4739369 (accessed 2026-03-10).

(28) *MIR21 microRNA 21 [Homo sapiens (human)] - Gene - NCBI*. https://www.ncbi.nlm.nih.gov/gene/406991 (accessed 2026-02-11).

(29) Farasati Far, B.; Vakili, K.; Fathi, M.; Yaghoobpoor, S.; Bhia, M.; Naimi- Jamal, M. R. The Role of microRNA-21 (miR-21) in Pathogenesis, Diagnosis, and Prognosis of Gastrointestinal Cancers: A Review. *Life Sci.* **2023**, *316*, 121340. https://doi.org/10.1016/j.lfs.2022.121340.

(30) Kumarswamy, R.; Volkmann, I.; Thum, T. Regulation and Function of miRNA-21 in Health and Disease. *RNA Biol.* **2011**, *8* (5), 706–713. https://doi.org/10.4161/rna.8.5.16154.

(31) Bautista-Sánchez, D.; Arriaga-Canon, C.; Pedroza-Torres, A.; De La Rosa-Velázquez, I. A.; González-Barrios, R.; Contreras-Espinosa, L.; Montiel-Manríquez, R.; Castro-Hernández, C.; Fragoso-Ontiveros, V.; Álvarez-Gómez, R. M.; Herrera, L. A. The Promising Role of miR-21 as a Cancer Biomarker and Its Importance in RNA-Based Therapeutics. *Mol. Ther. Nucleic Acids* **2020**, *20*, 409–420. https://doi.org/10.1016/j.omtn.2020.03.003.

(32) Kozomara, A.; Birgaoanu, M.; Griffiths-Jones, S. miRBase: From microRNA Sequences to Function. *Nucleic Acids Res.* **2019**, *47* (D1), D155–D162. https://doi.org/10.1093/nar/gky1141.

(33) Pan, C.-Y.; Kuo, W.-T.; Chiu, C.-Y.; Lin, W. Visual Display of 5p-Arm and 3p-Arm miRNA Expression with a Mobile Application. *BioMed Res. Int.* **2017**, *2017*, 6037168. https://doi.org/10.1155/2017/6037168.

(34) Chen, P. Y.; Manninga, H.; Slanchev, K.; Chien, M.; Russo, J. J.; Ju, J.; Sheridan, R.; John, B.; Marks, D. S.; Gaidatzis, D.; Sander, C.; Zavolan, M.; Tuschl, T. The Developmental miRNA Profiles of Zebrafish as Determined by Small RNA Cloning. *Genes Dev.* **2005**, *19* (11), 1288–1293. https://doi.org/10.1101/gad.1310605.

(35) Wu, H.; Neilson, J. R.; Kumar, P.; Manocha, M.; Shankar, P.; Sharp, P. A.; Manjunath, N. miRNA Profiling of Naïve, Effector and Memory CD8 T Cells. *PLOS ONE* **2007**, *2* (10), e1020. https://doi.org/10.1371/journal.pone.0001020.

(36) Ruan, Q.; Wang, P.; Wang, T.; Qi, J.; Wei, M.; Wang, S.; Fan, T.; Johnson, D.; Wan, X.; Shi, W.; Sun, H.; Chen, Y. H. MicroRNA-21 Regulates T-Cell Apoptosis by Directly Targeting the Tumor Suppressor Gene Tipe2. *Cell Death Dis.* **2014**, *5* (2), e1095–e1095. https://doi.org/10.1038/cddis.2014.47.

(37) Rhim, J.; Baek, W.; Seo, Y.; Kim, J. H. From Molecular Mechanisms to Therapeutics: Understanding MicroRNA-21 in Cancer. *Cells* **2022**, *11* (18), 2791. https://doi.org/10.3390/cells11182791.

(38) Physiological and Pathological Functions of Mammalian MicroRNAs. **2010**, 427–446. https://doi.org/10.1016/B978-0-08-046884-6.00223-2.

(39) Medina, P. P.; Nolde, M.; Slack, F. J. OncomiR Addiction in an in Vivo Model of microRNA-21-Induced Pre-B-Cell Lymphoma. *Nature* **2010**, *467* (7311), 86–90. https://doi.org/10.1038/nature09284.

(40) Buscaglia, L. E. B.; Li, Y. Apoptosis and the Target Genes of microRNA-21. *Chin. J. Cancer* **2011**, *30* (6), 371–380. https://doi.org/10.5732/cjc.011.10132.

(41) Brito Querido, J.; Sokabe, M.; Díaz-López, I.; Gordiyenko, Y.; Zuber, P.; Du, Y.; Albacete-Albacete, L.; Ramakrishnan, V.; Fraser, C. S. Human Tumor Suppressor Protein Pdcd4 Binds at the mRNA Entry Channel in the 40S Small Ribosomal Subunit. *Nat. Commun.* **2024**, *15* (1), 6633. https://doi.org/10.1038/s41467-024-50672-8.

(42) Asangani, I. A.; Rasheed, S. a. K.; Nikolova, D. A.; Leupold, J. H.; Colburn, N. H.; Post, S.; Allgayer, H. MicroRNA-21 (miR-21) Post-Transcriptionally Downregulates Tumor Suppressor Pdcd4 and Stimulates Invasion, Intravasation and Metastasis in Colorectal Cancer. *Oncogene* **2008**, *27* (15), 2128–2136. https://doi.org/10.1038/sj.onc.1210856.

(43) Zhu, S.; Wu, H.; Wu, F.; Nie, D.; Sheng, S.; Mo, Y.-Y. MicroRNA-21 Targets Tumor Suppressor Genes in Invasion and Metastasis. *Cell Res.* **2008**, *18* (3), 350–359. https://doi.org/10.1038/cr.2008.24.

(44) Yu, Y.; Nangia-Makker, P.; Farhana, L.; G. Rajendra, S.; Levi, E.; Majumdar, A. P. miR-21 and miR-145 Cooperation in Regulation of Colon Cancer Stem Cells. *Mol. Cancer* **2015**, *14* (1), 98. https://doi.org/10.1186/s12943-015-0372-7.

(45) Van Meter, E. N.; Onyango, J. A.; Teske, K. A. A Review of Currently Identified Small Molecule Modulators of microRNA Function. *Eur. J. Med. Chem.* **2020**, *188*, 112008. https://doi.org/10.1016/j.ejmech.2019.112008.

(46) van Rooij, E.; Kauppinen, S. Development of microRNA Therapeutics Is Coming of Age. *EMBO Mol. Med.* **2014**, *6* (7), 851–864. https://doi.org/10.15252/emmm.201100899.

(47) Boti, M. A.; Diamantopoulos, M. A.; Scorilas, A. RNA-Targeting Techniques: A Comparative Analysis of Modern Approaches for RNA Manipulation in Cancer Research and Therapeutics. *Genes* **2025**, *16* (10). https://doi.org/10.3390/genes16101168.

(48) Deiters, A. Small Molecule Modifiers of the microRNA and RNA Interference Pathway. *AAPS J.* **2010**, *12* (1), 51–60. https://doi.org/10.1208/s12248-009-9159-3.

(49) Lessel, D.; Zeitler, D. M.; Reijnders, M. R. F.; Kazantsev, A.; Hassani Nia, F.; Bartholomäus, A.; Martens, V.; Bruckmann, A.; Graus, V.; McConkie-Rosell, A.; McDonald, M.; Lozic, B.; Tan, E.-S.; Gerkes, E.; Johannsen, J.; Denecke, J.; Telegrafi, A.; Zonneveld-Huijssoon, E.; Lemmink, H. H.; Cham, B. W. M.; Kovacevic, T.; Ramsdell, L.; Foss, K.; Le Duc, D.; Mitter, D.; Syrbe, S.; Merkenschlager, A.; Sinnema, M.; Panis, B.; Lazier, J.; Osmond, M.; Hartley, T.; Mortreux, J.; Busa, T.; Missirian, C.; Prasun, P.; Lüttgen, S.; Mannucci, I.; Lessel, I.; Schob, C.; Kindler, S.; Pappas, J.; Rabin, R.; Willemsen, M.; Gardeitchik, T.; Löhner, K.; Rump, P.; Dias, K.-R.; Evans, C.-A.; Andrews, P. I.; Roscioli, T.; Brunner, H. G.; Chijiwa, C.; Lewis, M. E. S.; Jamra, R. A.; Dyment, D. A.; Boycott, K. M.; Stegmann, A. P. A.; Kubisch, C.; Tan, E.-C.; Mirzaa, G. M.; McWalter, K.; Kleefstra, T.; Pfundt, R.; Ignatova, Z.; Meister, G.; Kreienkamp, H.-J. Germline AGO2 Mutations Impair RNA Interference and Human Neurological Development. *Nat. Commun.* **2020**, *11* (1), 5797. https://doi.org/10.1038/s41467-020-19572-5.

(50) Rama, A. R.; Quiñonero, F.; Mesas, C.; Melguizo, C.; Prados, J. Synthetic Circular miR-21 Sponge as Tool for Lung Cancer Treatment. *Int. J. Mol. Sci.* **2022**, *23* (6). https://doi.org/10.3390/ijms23062963.

(51) Seo, Y.-E.; Suh, H.-W.; Bahal, R.; Josowitz, A.; Zhang, J.; Song, E.; Cui, J.; Noorbakhsh, S.; Jackson, C.; Bu, T.; Piotrowski-Daspit, A.; Bindra, R.; Saltzman, W. M. Nanoparticle-Mediated

Intratumoral Inhibition of miR-21 for Improved Survival in Glioblastoma. *Biomaterials* **2019**, *201*, 87–98. https://doi.org/10.1016/j.biomaterials.2019.02.016.

(52) Gale, D. P.; Gross, O.; Wang, F.; Esteban de la Rosa, R. J.; Hall, M.; Sayer, J. A.; Appel, G.; Hariri, A.; Liu, S.; Maski, M.; Shen, Y.; Zhang, Q.; Iqbal, S.; Kowthalam, M. U.; Lin, J.; Ding, J.; Group, on behalf of the H. C. T. A Randomized Controlled Clinical Trial Testing Effects of Lademirsen on Kidney Function Decline in Adults with Alport Syndrome. *Clin. J. Am. Soc. Nephrol.* **2024**, *19* (8), 995. https://doi.org/10.2215/CJN.0000000000000458.

(53) Gumireddy, K.; Young, D. D.; Xiong, X.; Hogenesch, J. B.; Huang, Q.; Deiters, A. Small Molecule Inhibitors of MicroRNA miR-21 Function. *Angew. Chem. Int. Ed Engl.* **2008**, *47* (39), 7482–7484. https://doi.org/10.1002/anie.200801555.

(54) Naro, Y.; Thomas, M.; Stephens, M. D.; Connelly, C. M.; Deiters, A. Aryl Amide Small-Molecule Inhibitors of microRNA miR-21 Function. *Bioorg. Med. Chem. Lett.* **2015**, *25* (21), 4793–4796. https://doi.org/10.1016/j.bmcl.2015.07.016.

(55) Bose, D.; Jayaraj, G.; Suryawanshi, H.; Agarwala, P.; Pore, S. K.; Banerjee, R.; Maiti, S. The Tuberculosis Drug Streptomycin as a Potential Cancer Therapeutic: Inhibition of miR-21 Function by Directly Targeting Its Precursor. *Angew. Chem. Int. Ed.* **2012**, *51* (4), 1019–1023. https://doi.org/10.1002/anie.201106455.

(56) Tofigh, R.; Akhavan, S.; Tarban, N.; Sadrabadi, A. E.; Jalili, A.; Moridi, K.; Tutunchi, S. Doxorubicin Induces Apoptosis through down Regulation of miR-21 Expression and Increases miR-21 Target Gene Expression in MCF-7 Breast Cancer Cells. *Int. J. Clin. Med.* **2017**, *8* (6), 386–394. https://doi.org/10.4236/ijcm.2017.86036.

(57) Shortridge, M. D.; Chaubey, B.; Zhang, H. J.; Pavelitz, T.; Vidadala, V.; Tang, C.; Olsen, G. L.; Calin, G. A.; Varani, G. Drug-Like Small Molecules That Inhibit Expression of the Oncogenic MicroRNA-21. *ACS Chem. Biol.* **2023**, *18* (2), 237–250. https://doi.org/10.1021/acschembio.2c00502.

(58) *Reprogramming of Protein-Targeted Small-Molecule Medicines to RNA by Ribonuclease Recruitment | Journal of the American Chemical Society*. https://pubs.acs.org/doi/10.1021/jacs.1c02248 (accessed 2026-02-04).

(59) Shortridge, M. D.; Walker, M. J.; Pavelitz, T.; Chen, Y.; Yang, W.; Varani, G. A Macrocyclic Peptide Ligand Binds the Oncogenic MicroRNA-21 Precursor and Suppresses Dicer Processing. *ACS Chem. Biol.* **2017**, *12* (6), 1611–1620. https://doi.org/10.1021/acschembio.7b00180.

(60) *Inforna 2.0: A Platform for the Sequence-Based Design of Small Molecules Targeting Structured RNAs | ACS Chemical Biology*. https://pubs.acs.org/doi/full/10.1021/acschembio.6b00001 (accessed 2026-03-10).

(61) *AC1MMYR2, an Inhibitor of Dicer-Mediated Biogenesis of Oncomir miR-21, Reverses Epithelial–Mesenchymal Transition and Suppresses Tumor Growth and Progression | Cancer Research | American Association for Cancer Research*. https://aacrjournals.org/cancerres/article/73/17/5519/584815/AC1MMYR2-an-Inhibitor-of-Dicer-Mediated-Biogenesis (accessed 2026-02-04).

(62) Junaid, M.; Dash, R.; Islam, N.; Chowdhury, J.; Alam, M. J.; Nath, S. D.; Shakil, M. A. S.; Azam, A.; Quader, S. M.; Zahid Hosen, S. M. Molecular Simulation Studies of 3,3'-Diindolylmethane as a Potent MicroRNA-21 Antagonist. *J. Pharm. Bioallied Sci.* **2017**, *9* (4), 259. https://doi.org/10.4103/jpbs.JPBS_266_16.

(63) *Efficacy, Safety and Cost of Regorafenib in Patients with Metastatic Colorectal Cancer in French Clinical Practice - Fabien Calcagno, Sabrina Lenoble, Zaher Lakkis, Thierry Nguyen, Samuel Limat, Christophe Borg, Marine Jary, Stefano Kim, Virginie Nerich, 2016*. https://journals.sagepub.com/doi/10.4137/CMO.S38335 (accessed 2026-03-10).

(64) Modell, A. E.; Lai, S.; Nguyen, T. M.; Choudhary, A. Bifunctional Modalities for Repurposing Protein Function. *Cell Chem. Biol.* **2021**, *28* (7), 1081–1089. https://doi.org/10.1016/j.chembiol.2021.06.005.

(65) Yan, H.; Bhattarai, U.; Guo, Z.-F.; Liang, F.-S. Regulating miRNA-21 Biogenesis By Bi-Functional Small Molecules. *J. Am. Chem. Soc.* **2017**, *139* (14), 4987–4990. https://doi.org/10.1021/jacs.7b00610.

(66) Zhang, Y.; Zhu, J.; Qiu, L.; Lv, Z.; Zhao, Z.; Ren, X.; Guo, Y.; Chen, Y.; Li, M.; Fan, Y.; Han, Z.; Feng, Y.; Shi, H. Stimulus-Activated Ribonuclease Targeting Chimeras for Tumor Microenvironment Activated Cancer Therapy. *Nat. Commun.* **2025**, *16* (1), 1288. https://doi.org/10.1038/s41467-025-56691-3.

(67) Costales, M. G.; Aikawa, H.; Li, Y.; Childs-Disney, J. L.; Abegg, D.; Hoch, D. G.; Pradeep Velagapudi, S.; Nakai, Y.; Khan, T.; Wang, K. W.; Yildirim, I.; Adibekian, A.; Wang, E. T.; Disney, M. D. Small-Molecule Targeted Recruitment of a Nuclease to Cleave an Oncogenic RNA in a Mouse Model of Metastatic Cancer. *Proc. Natl. Acad. Sci.* **2020**, *117* (5), 2406–2411. https://doi.org/10.1073/pnas.1914286117.

(68) Dey, S. K.; Jaffrey, S. R. RIBOTACs: Small Molecules Target RNA for Degradation. *Cell Chem. Biol.* **2019**, *26* (8), 1047–1049. https://doi.org/10.1016/j.chembiol.2019.07.015.

CHAPTER 2
PH.D. PROJECT OVERVIEW

Chapter 2: PhD project overview

As discussed in **Chapter 1**, miR21 appears to be an interesting potential pharmaceutical target for oncological applications. Among the different approaches to modulate the intracellular levels of miR21, we selected to interfere with its biogenesis. Within the miR21 biogenesis pathway, pre-miR21 represents an appropriate target, as it adopts a defined structure and is predominantly located in the cytosol, making it more accessible than nuclear pri-miR21. In this area, small molecules offer advantages over other therapeutic options due to their high versatility. Nevertheless, a high affinity for the chosen target still needs to be achieved. Based on this rationale, a ^{19}F-NMR driven fragment-based screening campaign was launched in 2020 in the PharmaChemistry (D3P) research line at IIT to identify novel small-molecule compounds targeting pre-miR21.

2.1: Fragment-based drug discovery

Fragment-based drug discovery involves the screening of low–molecular-weight compounds, typically below 250–300 Da, referred to as "*fragments*", against a desired biological target.[1] Although molecules of this size are expected to form weaker interactions due to their limited number of functional groups, they can more efficiently explore the chemical space of a target, making them advantageous in screening.[2] Having less steric hindrance, they can establish specific, albeit weak, interactions with the target. In contrast, complex molecules, such as natural products or large ligands, have a high probability of forming suboptimal interactions due to the higher dimensions, which can hinder productive binding modes.[3] Ligand efficiency[4] has been proposed as a metric to rationalize this concept: it is defined as the free binding energy normalized to the number of heavy atoms, expressed according to **Equation 2.1**, expressing how efficient the binding is in relation to the scaffold extension.[5]

$$(\mathbf{2.1})\ \text{Ligand efficiency} = \frac{\text{Binding free energy}}{\text{Nuber of heavy atoms in the molecule}}$$

Because fragments contain few heavy atoms, they often display higher ligand efficiency than complex molecules, even with lower affinities. Fragments' efficient use of their limited chemical features to engage key interactions with the target makes them well-suited for probing chemical space, provided that the fragment library is carefully designed.

Since fragments typically form weak interactions, sensitive biophysical techniques are required for their detection. Nuclear magnetic resonance (NMR) spectroscopy is particularly well suited for fragment-based screening, as it can reliably detect binding events with dissociation constants in the high micromolar to low millimolar range, often the only observable interactions for challenging targets.[4,6] In addition to hit identification, NMR can be employed to quantify binding affinities and support the establishment of structure–activity relationships.

Although the field of RNA-targeted drug discovery is rapidly advancing, clear guidelines for ligand design and for distinguishing specific binding from nonspecific intercalation are still lacking, and traditional screening approaches often struggle to identify selective RNA binders.[7] In this context, fragment-based NMR spectroscopy has shown promising results, including its application to pre-miR21, as previously reported by Disney and colleagues,[8] highlighting this approach as a valuable strategy for addressing the challenges associated with targeting RNA.

2.2: NMR fragment screening

As described in **Paragraph 2.1**, NMR provides an affordable and reliable approach for screening compounds against RNA targets. Because of this, a screening campaign was conducted in the D3P research line at IIT against pre-miR21 using ^{19}F NMR spectroscopy combined with T_2-filter techniques.[9] ^{19}F NMR offers several advantages for fragment screening. Fluorine is generally absent from biomolecules, resulting in virtually no background signal.[10] Additionally, ^{19}F atoms exhibit a wide spectral window, which allows signals to be well dispersed.[11] Provided that the signals do not overlap, multiple compounds can be screened simultaneously in a mixture, making NMR screening highly efficient.

In NMR spectroscopy, T_2 represents the transverse relaxation time, describing how quickly the transverse component of nuclear magnetization decays due to the loss of phase coherence among nuclear spins, primarily caused by spin–spin interactions and local magnetic field variations.[12] When a fragment binds to RNA, its T_2 relaxation rate decreases proportionally to the molecular weight and dissociation constant of the complex.[8,11] This effect can be exploited using a Carr-Purcell-Meiboom-Gill (CPMG) pulse sequence,[9] which "filters" molecules with short T_2 values by attenuating their signal. In this way, binders can be distinguished from non-binders: interacting compounds show decreased signal intensity, whereas non-interacting compounds' signals remain unaffected.[11] This technique appears advantageous with respect to other fragment screening techniques since it requires a low amount of biological target and does not require immobilization or chemical derivatization of the RNA, maintaining its native conditions.

Following this strategy, over 600 fluorinated fragments from an IIT library, designed to maximize sampling of the chemical space around the fluorine atom (LEF), were screened against pre-miR21. This library consists of compounds bearing a single fluorine atom or a trifluoromethyl group, which are generally bound to an aromatic or a heteroaromatic moiety. Many different scaffolds containing aliphatic, (hetero)cyclic, aromatic and heteroaromatic moieties are present in the library. Typically, only a few compounds per scaffold are included, which differ from each other for the substitution pattern or the type of substituents on the core scaffold. If two or more hits with a common scaffold emerge in a screening campaign, this allows increasing the confidence that the chemical class can be a source of valuable binders/modulators of the target of interest.

For the screening process, a T_2-filter approach was used.[13] As this technique was developed for the rapid screening of large numbers of compounds, only qualitative information was obtained, allowing only the classification of compounds as binders or non-binders. Since this NMR screening campaign is not the primary focus of my PhD work, detailed experimental conditions will not be reported here *(manuscript currently in preparation)*.

The rationale is illustrated in **Figure 2.1**. Individual ^{19}F NMR spectra were first acquired for each compound. Compounds with non-overlapping ^{19}F signals were then combined into mixtures of approximately 25 molecules, and a T_2-filtered experiment was recorded. A second T_2-filtered experiment was performed upon addition of the target RNA. Under these conditions, binding to the RNA results in line broadening and signal attenuation in the T_2-filtered spectrum, whereas non-binding compounds show no significant change in signal intensity. A decrease in signal intensity greater than 10% was used as the threshold for binder identification. Hits identified in the mixture screen were subsequently tested individually to confirm binding.

From this initial screening, approximately 130 compounds were identified as potential hits. Those presenting scaffolds of interest from a medicinal chemistry point of view (primarily chemical

tractability) were subsequently sent to the University of Nice (Dr. Maria Duca's lab) for biochemical activity confirmation.

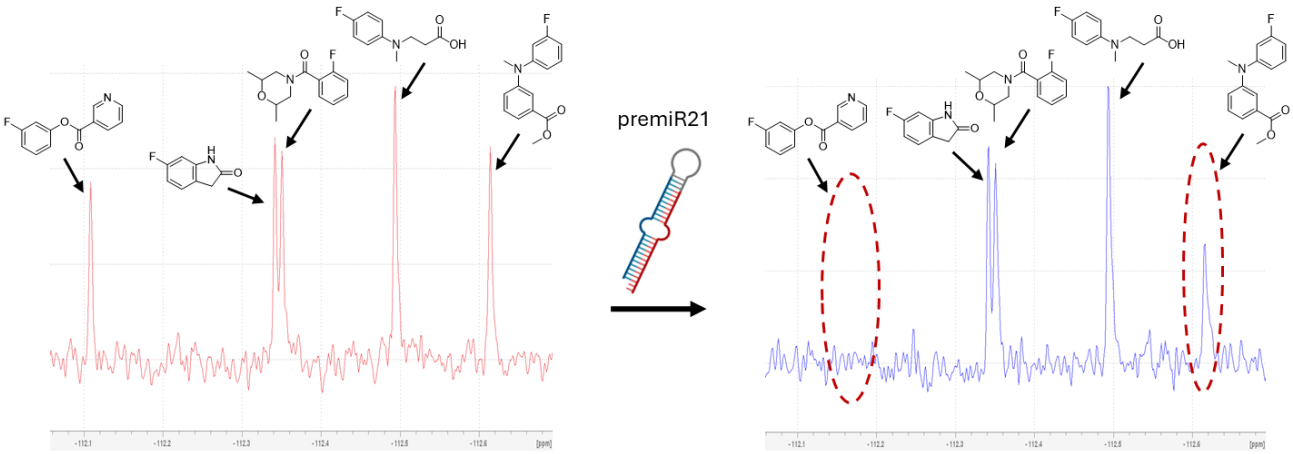

Compounds having different signals are combined in mixture of 20 to 25 each and the spectrum in buffer is registered.

The ^{19}F spectrum of mixtures incubated with pre-miR-21 in buffer is registered. Compounds showing a decrease in their signal are identified as binders.

***Figure 2.1**. Pipeline of the ^{19}F NMR fragment screening conducted at IIT. The compounds illustrated in the figure are just representative and do not correspond to the tested molecules.*

2.3: Biochemical testing

Characterizing a binding event is a challenging process, and the occurrence of false positives is always a possibility. For this reason, the use of an orthogonal technique increases the robustness of binding assessment. When two independent methods, based on different physical principles, detect affinity for the same target, it becomes more likely that the observed interaction represents a genuine binding event rather than an experimental artefact. Following this rationale, a fluorescence-based assay was employed to further evaluate initial hit compounds identified in the NMR screening. The assays were conducted in Dr. Maria Duca's laboratory at the University of Nice, who is a collaborator in this project. The dissociation constant (K_d) was determined using an established fluorescence assay developed in Dr. Duca's laboratory.[14] In this assay, a fluorescently labelled pre-miR21 construct (sequence reported in **Paragraph 1.3**) was used, bearing a carboxyfluorescein derivative (FAM; **Figure 2.2**) at the 5'-end. The resulting 5'-FAM-pre-miR21 construct exhibits intrinsic fluorescence that can change upon ligand binding. Binding is expected to induce conformational rearrangements in the RNA, altering the local environment of the fluorophore and leading to a measurable change in fluorescence. By titrating the selected compounds and applying appropriate mathematical fitting, binding affinity values were calculated.

In parallel, the inhibitory activity of the compounds toward Dicer-mediated processing of pre-miR21 was evaluated by determining IC_{50} values. For this purpose, a fluorescence resonance energy transfer (FRET) assay, previously established in Duca's laboratory, was employed.[14] In this assay, the pre-miR21 construct is labelled with FAM at the 5'-end and with a Dabcyl derivative (DAB; **Figure 2.2**) at the 3'-end, generating a 5'-FAM-pre-miR21-3'-DAB construct. Under normal conditions, cleavage by the Dicer enzyme separates the fluorophore and quencher, resulting in an increase in fluorescence. In contrast, binding of a ligand that inhibits Dicer processing prevents cleavage and blocks the fluorescence

increase. By titrating the compounds and analyzing the fluorescence response, IC_{50} values were determined.[14]

The chosen fluorescence-based and FRET-based assays present the advantage of being performed on a low-cost fluorescence plate reader and requiring only limited amounts of target RNA. Moreover, these assays preserve near-native conditions, as chemical modifications are introduced exclusively at the terminal ends of the RNA construct. Experimental details of these experiments are reported in **Paragraph 4.9**.

An affinity threshold of 100 μM was set, and compounds with K_d > 100 μM were classified as non-binders. This cut-off was chosen because weaker affinities are more likely to correspond to nonspecific interactions, which are not of interest for a medicinal chemistry campaign. Since inhibition of pre-miR21 processing is not a straightforward consequence of binding, compounds exhibiting measurable affinity but lacking inhibitory activity were still considered of interest at the screening stage.

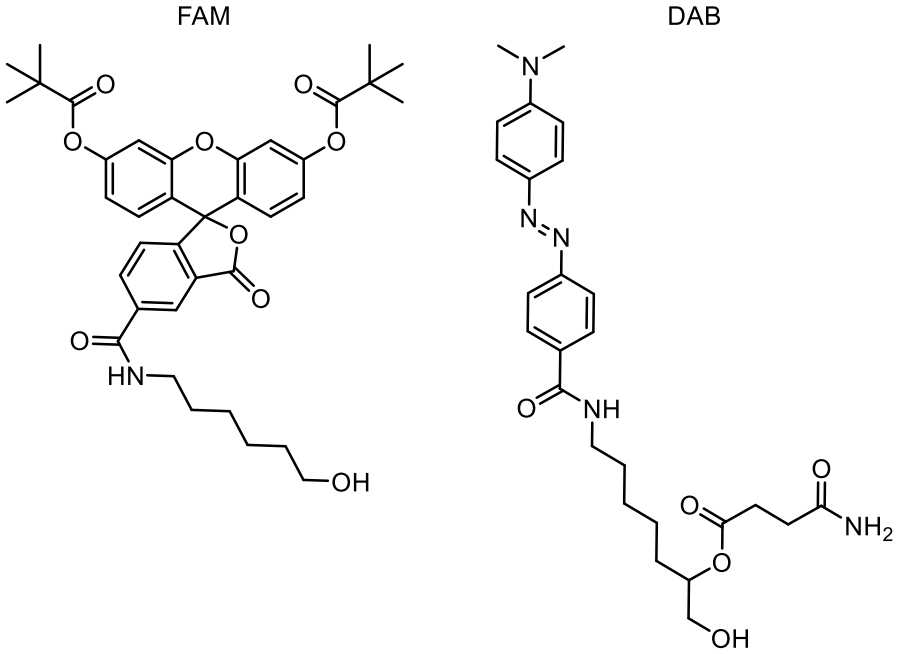

***Figure 2.2**. Chemical modifications introduced into the pre-miR21 construct to test K_d and IC_{50}.*

2.4: Aim of the PhD project

After completion of the screening against pre-miR21, as described in **Paragraph 2.2**, compound **1**, featuring a pyrazolo[1,5-a]pyrimidine scaffold (**Figure 2.3**) emerged as an interesting hit, with a K_d of 8.61 ± 0.49 μM. Although this compound doesn't show any significant inhibitory activity against the cleavage of pre-miR21, it binds the selected RNA target with moderate affinity and features a chemically tractable scaffold.[15] These preliminary considerations made this initial hit a well-suited starting point for a hit-expansion medicinal chemistry campaign.

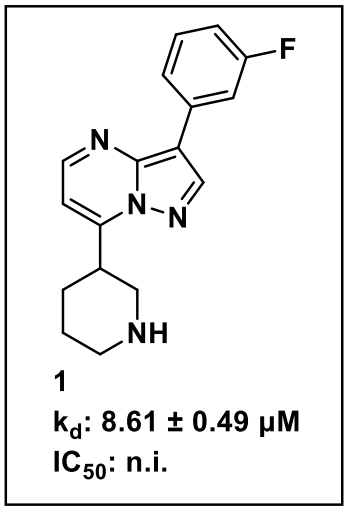

***Figure 2.3**. Hit compound **1** identified in the [19]F-NMR screening. [n.i..=no inhibiting].*

As stated before, the therapeutic rationale underlying this approach is the inhibition of pre-miR21 processing by Dicer through small-molecule-induced conformational perturbation of the RNA, thereby rendering it unrecognizable by the enzyme. A schematization of this concept is reported in **Figure 2.4.** Although direct inhibition of Dicer could, in principle, also suppress miR21 biogenesis, this strategy is not viable due to the essential role of Dicer in the maturation of virtually all miRs and its critical importance for cellular survival.[16]

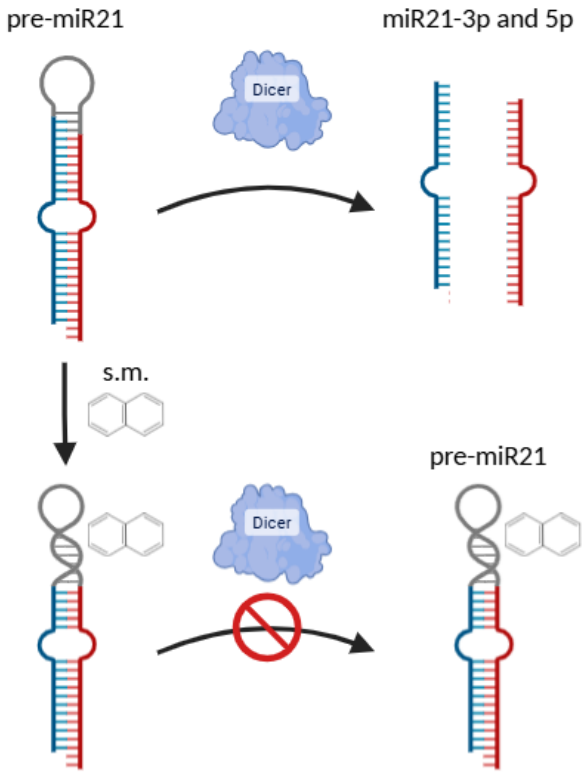

***Figure 2.4.** Rationale behind the targeting of pre-miR21. Under physiological conditions, pre-miR21 is processed by Dicer into the mature miR21-5p and miR21-3p strands. The binding of a small molecule to pre-miR21 can alter its conformation, preventing Dicer recognition and subsequent processing. Created with biorender.com.*

As discussed in **Paragraph 1.4,** this strategy is not novel, since small molecules targeting pre-miR21 have been reported in the literature. However, none of them has yet demonstrated a combination of sufficient affinity and favourable drug-like properties required for effective modulation of miR21 biogenesis, justifying the need for further research in this area. Fragment-derived hits are expected to engage specific interactions with the RNA scaffold (**Paragraph 2.1**) and therefore represent a suitable starting point for a hit expansion process. To my knowledge, a fragment-based optimization strategy has not previously been applied to this target, offering a complementary perspective to address this challenge.

Based on these considerations, a ligand-based medicinal chemistry campaign was initiated at D3P-IIT, which involved most of my PhD work. During my research activity at D3P-IIT, 75 analogues of hit **1** were designed and synthesized (**Chapter 3**), with the aim of increasing the affinity of the identified chemotype toward pre-miR21. Binding affinity and inhibitory activity toward Dicer-mediated processing were evaluated with the fluorescence-based and FRET-based assays developed in Dr. Duca's laboratory (**Paragraph 2.2**), which guided compound optimization (**Chapter 4**).

Target engagement of this chemotype was further investigated by NMR structural studies employing fluorinated probes (**Chapter 5**). Upon confirmation of specific binding and target engagement using an orthogonal biophysical technique (**Chapter 6**), the most promising compounds were evaluated in cellular assays to assess their ability to modulate miR21 levels in a biological context (**Chapter 7**).

While this approach does not directly address pharmacokinetic or selectivity challenges, it provides a robust framework for the identification and optimization of RNA-binding chemotypes. In this context, compounds are considered effective only if they display activity in cellular assays, whereas biochemical affinity is primarily used as a selection criterion to prioritize compounds for in-cell evaluation.

2.5: References.

(1) Xu, W.; Kang, C. Fragment-Based Drug Design: From Then until Now, and Toward the Future. *J. Med. Chem.* **2025**, *68* (5), 5000–5004. https://doi.org/10.1021/acs.jmedchem.5c00424.

(2) Harner, M. J.; Frank, A. O.; Fesik, S. W. Fragment-Based Drug Discovery Using NMR Spectroscopy. *J. Biomol. NMR* **2013**, *56* (2), 65–75. https://doi.org/10.1007/s10858-013-9740-z.

(3) *The rise of fragment-based drug discovery | Nature Chemistry*. https://www.nature.com/articles/nchem.217 (accessed 2026-02-09).

(4) Carr, R. A. E.; Congreve, M.; Murray, C. W.; Rees, D. C. Fragment-Based Lead Discovery: Leads by Design. *Drug Discov. Today* **2005**, *10* (14), 987–992. https://doi.org/10.1016/S1359-6446(05)03511-7.

(5) Hopkins, A. L.; Keserü, G. M.; Leeson, P. D.; Rees, D. C.; Reynolds, C. H. The Role of Ligand Efficiency Metrics in Drug Discovery. *Nat. Rev. Drug Discov.* **2014**, *13* (2), 105–121. https://doi.org/10.1038/nrd4163.

(6) Jhoti, H.; Cleasby, A.; Verdonk, M.; Williams, G. Fragment-Based Screening Using X-Ray Crystallography and NMR Spectroscopy. *Curr. Opin. Chem. Biol.* **2007**, *11* (5), 485–493. https://doi.org/10.1016/j.cbpa.2007.07.010.

(7) Falese, J. P.; Donlic, A.; Hargrove, A. E. Targeting RNA with Small Molecules: From Fundamental Principles towards the Clinic. *Chem. Soc. Rev.* **2021**, *50* (4), 2224–2243. https://doi.org/10.1039/d0cs01261k.

(8) Shortridge, M. D.; Varani, G. Efficient NMR Screening Approach to Discover Small Molecule Fragments Binding Structured RNA. *ACS Med. Chem. Lett.* **2021**, *12* (8), 1253–1260. https://doi.org/10.1021/acsmedchemlett.1c00109.

(9) Carr, H. Y.; Purcell, E. M. Effects of Diffusion on Free Precession in Nuclear Magnetic Resonance Experiments. *Phys. Rev.* **1954**, *94* (3), 630–638. https://doi.org/10.1103/PhysRev.94.630.

(10) Murphy, C. D.; Schaffrath, C.; O'Hagan, D. Fluorinated Natural Products: The Biosynthesis of Fluoroacetate and 4-Fluorothreonine in *Streptomyces Cattleya*. *Chemosphere* **2003**, *52* (2), 455–461. https://doi.org/10.1016/S0045-6535(03)00191-7.

(11) Dalvit, C.; Vulpetti, A. Ligand-Based Fluorine NMR Screening: Principles and Applications in Drug Discovery Projects. *J. Med. Chem.* **2019**, *62* (5), 2218–2244. https://doi.org/10.1021/acs.jmedchem.8b01210.

(12) Lin, X.; Zhan, H.; Li, H.; Huang, Y.; Chen, Z. NMR Relaxation Measurements on Complex Samples Based on Real-Time Pure Shift Techniques. *Molecules* **2020**, *25* (3). https://doi.org/10.3390/molecules25030473.

(13) Vulpetti, A.; Hommel, U.; Landrum, G.; Lewis, R.; Dalvit, C. Design and NMR-Based Screening of LEF, a Library of Chemical Fragments with Different Local Environment of Fluorine. *J. Am. Chem. Soc.* **2009**, *131* (36), 12949–12959. https://doi.org/10.1021/ja905207t.

(14) Maucort, C.; Vo, D. D.; Aouad, S.; Charrat, C.; Azoulay, S.; Di Giorgio, A.; Duca, M. Design and Implementation of Synthetic RNA Binders for the Inhibition of miR-21 Biogenesis. *ACS Med. Chem. Lett.* **2021**, *12* (6), 899–906. https://doi.org/10.1021/acsmedchemlett.0c00682.

(15) Arias-Gómez, A.; Godoy, A.; Portilla, J. Functional Pyrazolo[1,5-a]Pyrimidines: Current Approaches in Synthetic Transformations and Uses As an Antitumor Scaffold. *Molecules* **2021**, *26* (9). https://doi.org/10.3390/molecules26092708.

(16) Vergani-Junior, C. A.; Tonon-da-Silva, G.; Inan, M. D.; Mori, M. A. DICER: Structure, Function, and Regulation. *Biophys. Rev.* **2021**, *13* (6), 1081–1090. https://doi.org/10.1007/s12551-021-00902-w.

CHAPTER 3

CHEMISTRY

Chapter 3: Chemistry

Following the identification of hit compound **1** (**Figure 3.1**) as a promising binder for pre-miR21, initial efforts were directed toward the development of a versatile synthetic route enabling systematic structure–activity relationship (SAR) exploration around the pyrazolo[1,5-a]pyrimidine scaffold. The synthetic design aimed to combine efficiency and modularity, allowing rapid access to analogues through late-stage functionalization. This process led to the synthesis of compounds **1-75**, using the synthetic pathways presented in **Scheme 3.1-3.17**.

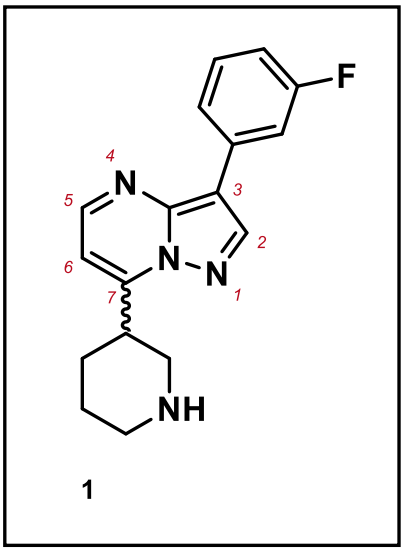

Figure 3.1. *Hit compound identified after the screening pipeline. Scaffold position enumeration is indicated in red.*

Racemic hit compound **1** features a bicyclic pyrazolo[1,5-a]pyrimidine scaffold, bearing a piperidine ring at position 7, linked through a tertiary stereocenter, and a meta-fluorophenyl substituent at position 3. Based on retrosynthetic analysis, positions 2, 3, 5, and 7 of the pyrazolo[1,5-a]pyrimidine core, together with the piperidine nitrogen, were identified as synthetically accessible and thus selected for structure-activity relationship (SAR) exploration around this chemotype. The overall synthetic design focused on preserving the integrity of the pyrazolo[1,5-a]pyrimidine core, while allowing independent and systematic modification of the peripheral substituents.

All new analogues **2-75** were synthesized and tested as racemates, as this work represents an initial investigation of the scaffold, as a potential pre-miR21 binder. All synthesized compounds were characterized by NMR spectroscopy (^{1}H, COSY, and HSQC), for structural confirmation and purity assessment, and by UPLC-MS analysis. All compounds showed an overall 95% minimum purity by LC-MS analysis.

To better understand the SAR analysis, the enumeration of final compounds follows the **Chapter 4** workflow. Final compounds (**2-75**) and their corresponding synthetic intermediates (**76-133**) are reported in ascending order.

As this work is an exploratory approach within this topic, the final compounds (**2-75**) were obtained and characterized as racemic mixtures. An enantiomeric separation on each compound was not pursued, as efforts were prioritized toward the synthesis and evaluation of additional target compounds. Similarly, diastereomeric mixtures that proved difficult to separate were carried forward and characterized without further resolution.

3.1: Initial retrosynthetic analysis

As a starting point in this work, an initial retrosynthetic analysis of hit compound **1** was carried out, outlining a synthetic strategy that could also enable straightforward derivatization at the 3-position (**Scheme 3.1**). This scaffold represents a common chemotype in medicinal chemistry, and several articles reporting its synthesis and derivatization are available in the literature.[1] However, the substitution pattern found in compound **1** was not previously described. The carbon–carbon bond connecting the fluorophenyl moiety to position 3 of the pyrazolo[1,5-a]pyrimidine scaffold was envisaged as the result of a cross-coupling reaction. Assuming a straightforward synthesis of brominated precursor **76** by a well-documented protocol for this class of heterocycles,[2] the retrosynthetic disconnection of compound **77** suggested an α,β-unsaturated intermediate **78** amenable to intramolecular cyclization. Such a key intermediate could be conveniently obtained from the commercially available ketone **79**, identified as a practical and cost-effective starting material for the synthesis. Since the piperidine nitrogen may exhibit undesired nucleophilicity under the described reactions, a *tert*-butoxycarbonyl (Boc) protecting group was selected for this moiety owing to its ease of removal.

Moreover, by employing differently functionalized aminopyrazoles, further modification of the scaffold at position 2 (see **Paragraph 3.3**) or introduction of substituents (see **Paragraph 3.2.4**) could be readily achieved. The identified synthetic pathway appeared amenable to ample scaffold derivatization, proving effective for the hit expansion process.

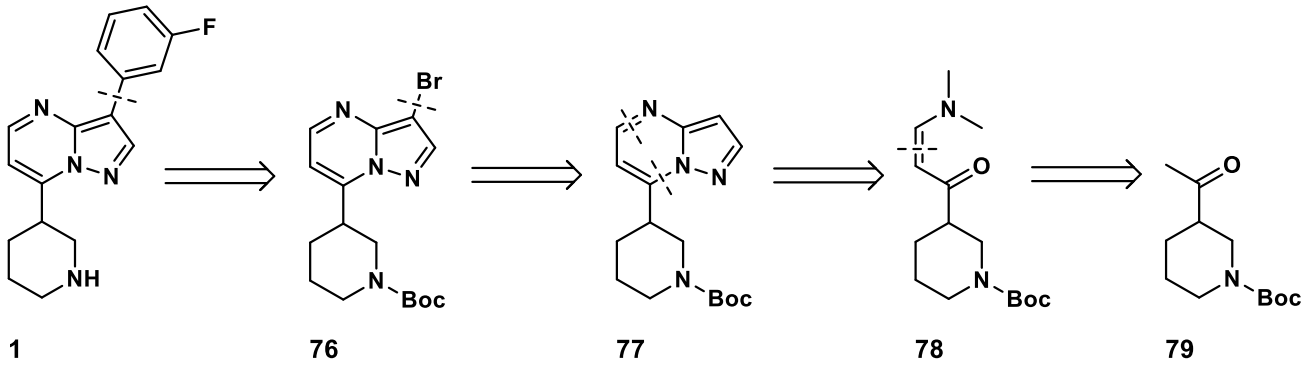

Scheme 3.1. *Retrosynthetic analysis of hit compound **1**.*

3.2: Derivatization of position 3 of the pyrazolo[1,5-a]pyrimidine scaffold

3.2.1: Synthesis of compounds **1-14, 18-23**

Having identified a synthetic pathway able to easily provide the hit compound and obtain some close analogues modified at position 3, this protocol was exploited for yielding compounds **1-14, 18-23** (**Figure 3.2**).

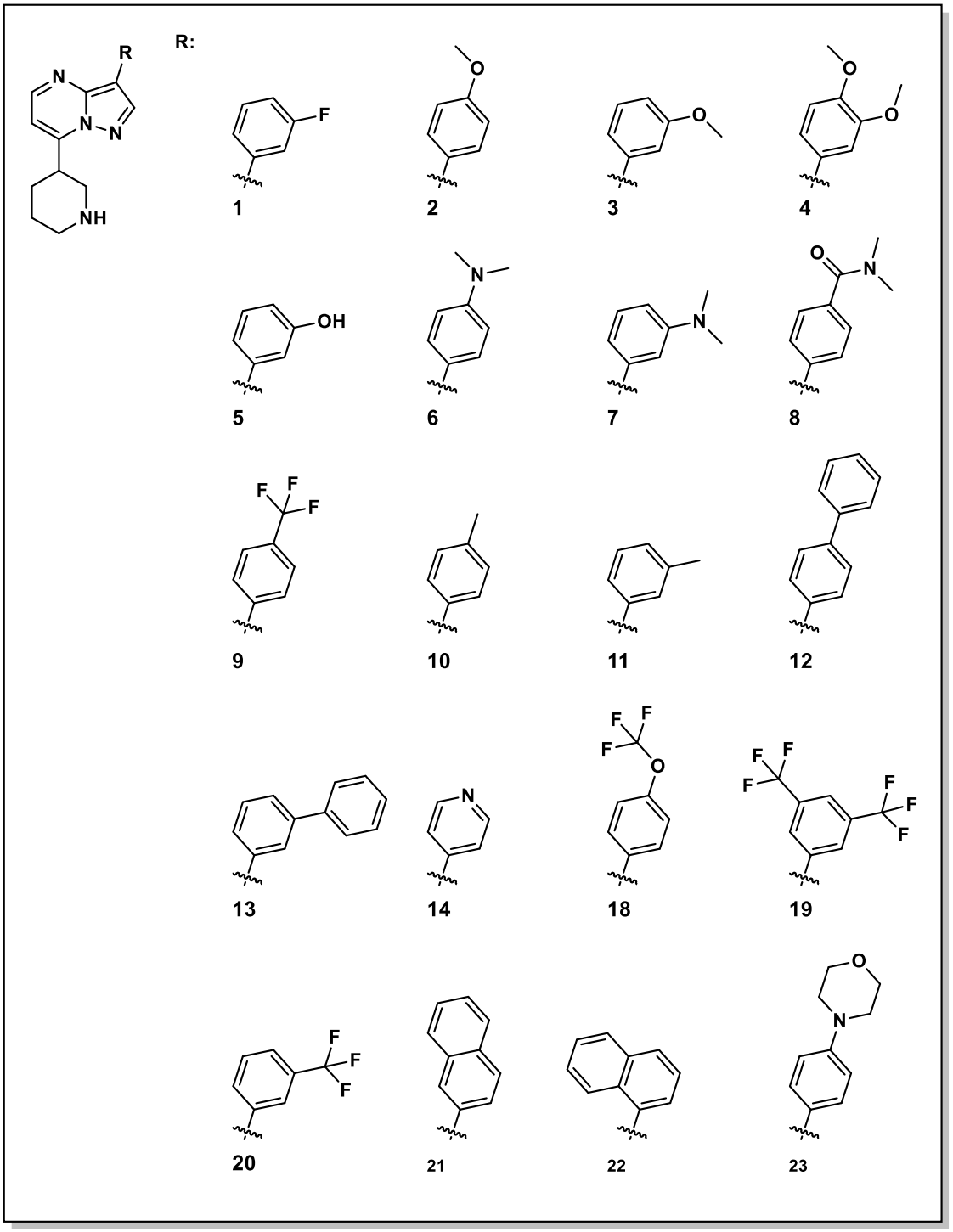

***Figure 3.2**. Synthesized compounds **1-14, 18-23** using the synthetic procedure shown in **Scheme 3.2**.*

In the envisioned synthetic pathway (**Scheme 3.2**), 2-bromopyrazolo[1,5-a]pyrimidine intermediate **76** is the key compound, enabling late-stage diversification and the synthesis of multiple final analogues from a common precursor. To obtain this compound, the commercially available ketone **79** was condensed with N,N-dimethylformamide dimethyl acetal, affording the α,β-unsaturated intermediate **78** in sufficient purity to obviate the need for purification. Since the starting building block **79** is racemic, all intermediates derived from this precursor, also in other synthetic pathways, are obtained as racemic mixtures. Intermediate **78** was not isolated but directly reacted with 3-aminopyrazole in acetic acid, giving compound **77** without Boc-deprotection,[3] in an overall yield of 50–60% over two steps. The

regioselectivity of the reaction was confirmed by the ^{1}H-NMR analysis of **77**, showing doublets J-values consistent with the ones previously reported in the literature for this type of molecule.[4] Starting from **77**, the key-intermediate **76** was obtained by regioselective bromination with N-bromosuccinimide (NBS) in dichloromethane (1:1 stoichiometric ratio), affording the desired compound quantitatively and without the need for purification. This three-step sequence proceeded smoothly (54% overall yield) on a gram-scale with minimal purification, confirming its robustness as a platform for analogue synthesis.

Having obtained bromo-substituted compound **76** as an intermediate prone to cross-coupling reaction, Suzuki–Miyaura reactions[5] were carried out under microwave-assisted conditions, achieving good to complete conversion to the desired products after 1 h of reaction time. As the transformation consistently provided good yields (39%-quantitative) in short reaction times under these conditions, no catalyst screening was deemed necessary. Using a set of commercially available either boronic acids or boronic esters, followed by Boc deprotection under HCl/MeOH conditions, final compounds **1–14** and **18–23** were synthesized and isolated (45%-quantitative), as racemates, as their corresponding salts for subsequent biological evaluation.

Although the final deprotection step generally afforded nearly quantitative yields, an additional purification was introduced to achieve sufficient purity for biological assays. Consequently, a final flash chromatography step was performed to obtain the pure target compounds. This purification resulted in a marginal loss of material, which was accepted as an unavoidable consequence when purifying amines on a small scale by flash chromatography. Similar product loss was also observed during the trituration step in cyclohexane, particularly for more apolar compounds. These considerations apply to all synthesized molecules and will not be reiterated further.

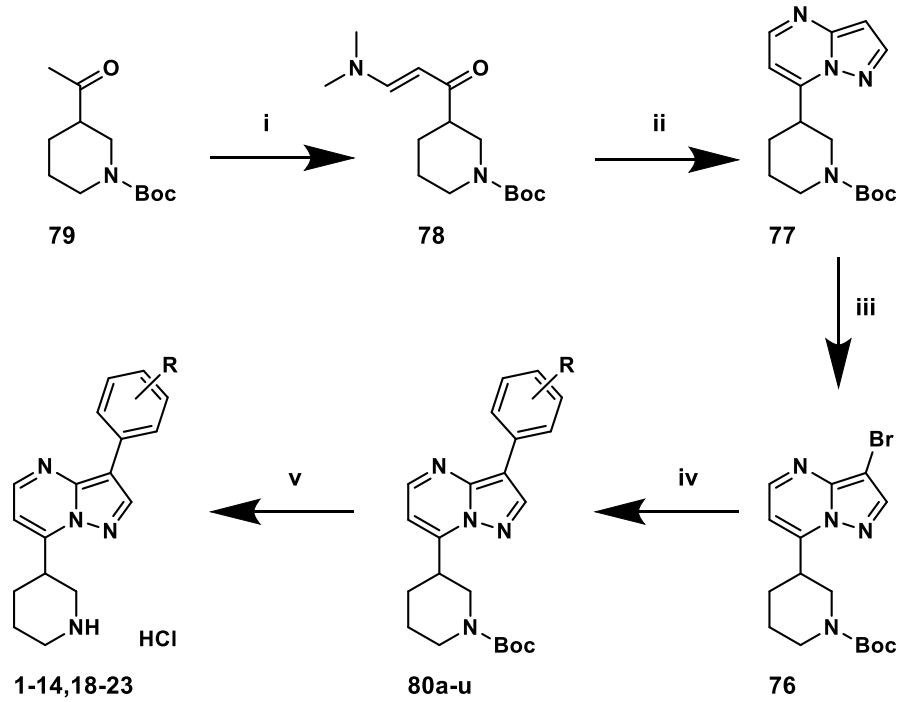

(**i**): 1,1-dimethoxy-N,N-dimethylmethanamine, DMF, 120°C, 24h; not isolated (**ii**) 3-Aminopyrazole, AcOH, 120°C, o.n., 54% over two steps; (**iii**) NBS, DCM, r.t., o.n., quantitative; (**iv**) K_2CO_3, $Pd(PPh_3)_2Cl_2$, boronic acid/boronic esters, THF, H_2O, MW, 110°C, 1h, 39%-quantitative; (**v**) HCl/MeOH, r.t., 1-7h, 45%-quantitative.

***Scheme 3.2**. Synthesis of final compounds **1-14, 18-23**.*

3.2.2: Synthesis of compounds **15-17, 24-26**

Compounds **15-17**, **24-26** (**Figure 3.3**) were designed to probe the effect on biological activity of the phenyl substituent at position 3, by either removing it (i.e., insertion of an aliphatic ring) or increasing its distance from the core scaffold. **Scheme 3.3** outlines the synthetic pathway to obtain these compounds.

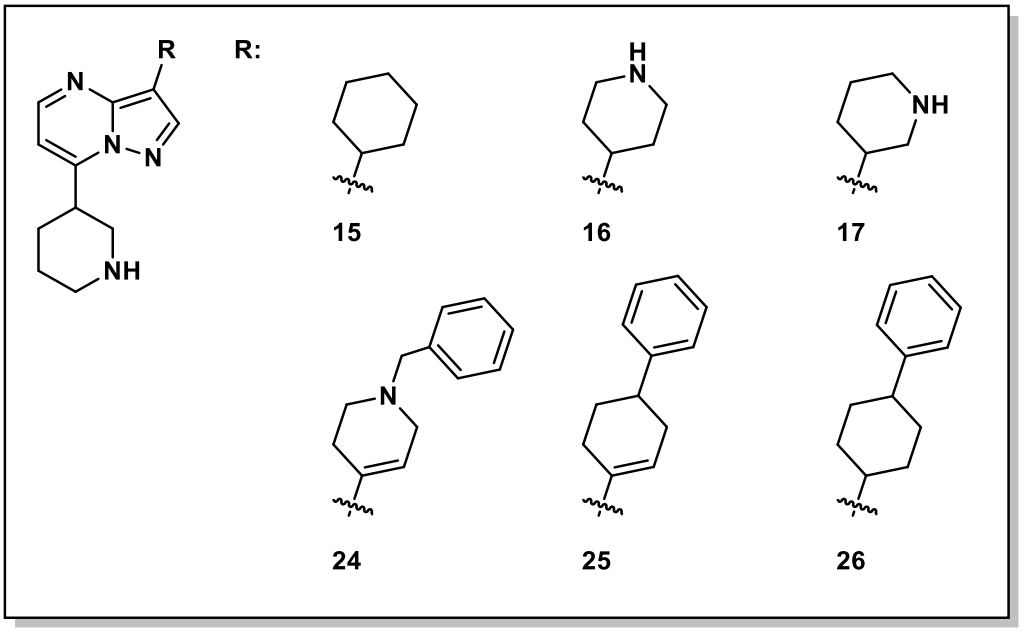

***Figure 3.3**. Synthesized final compounds **15-17, 24-26** using the synthetic procedure shown in **Scheme 3.3**.*

All the designed molecules contained a non-aromatic moiety linked at position 3 of the core scaffold. While Suzuki–Miyaura cross-coupling reactions typically provide good yields when aromatic boronic esters are used, alkyl-substituted boronic esters often suffer from poor catalytic stability, due to the low bond strength between the palladium and the sigma carbon bond, leading to low conversion.[6] Indeed, by applying the same successful coupling conditions used for the aromatic derivatives (even in no-MW-assisted conditions) resulted in only trace amounts of the desired products. To overcome this limitation, following similar conditions described above, mono-unsaturated boronic esters were employed as coupling partners[7] in reactions with racemic intermediate **76**. The corresponding alkenyl intermediates **81a–f** bearing more stable C(sp^2)–C(sp^2) bonds were afforded in good yields and in a time-efficient manner. These intermediates were subsequently reduced using triethylsilane (Et_3SiH) in the presence of Pd/C[8] to obtain the saturated analogues **82a-d,** featuring C(sp^2)–C(sp^3) linkages. To improve the overall yield of the reaction, alternative double-bond reduction conditions, such as the use of formic acid or ammonium formate, were also evaluated. However, with these different conditions hydrogenation of the pyrazolo[1,5-a]pyrimidine core occurred, even at room temperature. This hydrogenation reaction, used also in other pathways in this work, introduces an undefined stereocenter. The formed enantiomers or diastereoisomers were not separated due to the exploratory nature of this work. Boc deprotection under HCl/MeOH conditions led to final compounds **15-17, 26** in high yields (76%-quantitative), as their corresponding salts for subsequent biological evaluation.
In parallel, the corresponding unsaturated derivatives **24–25** were also synthesized and included in the biological evaluation to investigate the influence of the rigidity of the linker on the SAR. In this case, Boc-

deprotection was performed directly on the alkenyl intermediates **81a–f**, affording the final products in good yields.

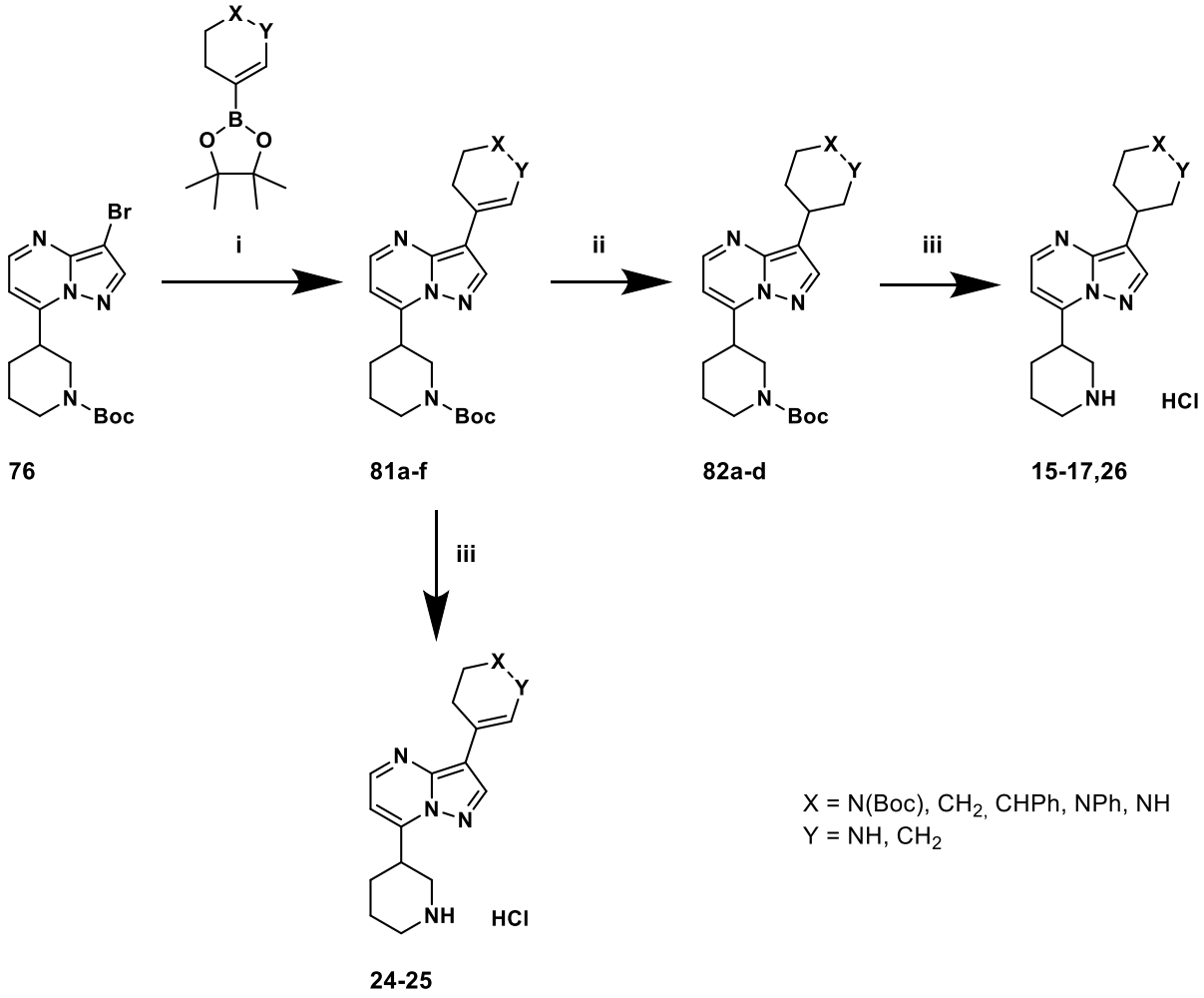

(**i**) K_2CO_3, $Pd(PPh_3)_2Cl_2$, boronic acid/boronic esters, THF, H_2O, MW, 110°C, 1h, 52-77%; (**ii**) Et_3SiH, Pd/C, MeOH, r.t., 1-48h, 32%-quantitative; (**iii**): MeOH/MeOH, r.t., 2h-2days, 76%-quantitative.

Scheme 3.3*. Synthetic pathway followed for the synthesis of final compounds* ***15-17, 24-26.***

While most boronic esters employed in the previously described syntheses were commercially available, boronic ester **85** used for yielding compounds **25** and **26** had to be prepared in-house (**Scheme 3.4**).[9] Starting from the commercially available ketone **83**, the corresponding enolate was generated under kinetic conditions using LDA, which was subsequently trapped as the triflate with triflic anhydride to give the activated intermediate **84** in good yield after chromatographic purification. This intermediate was then subjected to a Miyaura borylation with bis(pinacolato)diboron in the presence of $Pd(dppf)Cl_2$ as the palladium source, giving the desired boronic ester **85**, which was isolated by flash chromatography. Although the yield of this final step was relatively low, no further optimization was pursued, as the amount obtained was sufficient for the synthesis of the corresponding target analogue.

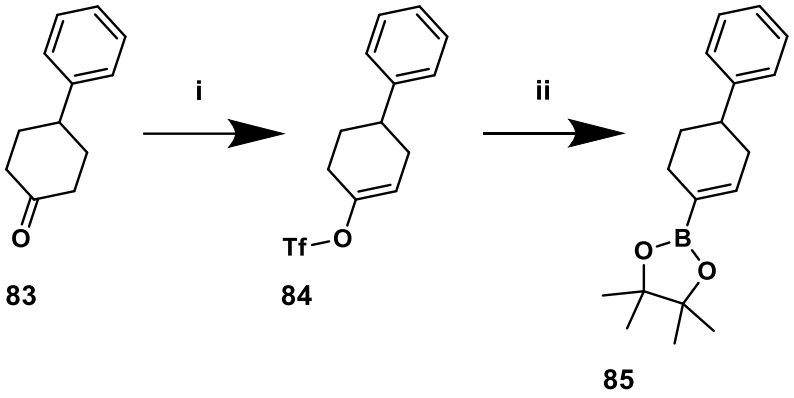

(i): LDA, $PhNTf_2$, THF, -78°C to r.t., on, 65%; (**ii**) Bis(pinacolato)diboron, $Pd(dppf)Cl_2$, AcOK, 1,4-dioxane, 80°C, o.n., 15%.

Scheme 3.4. *In-house synthesis of boronic ester* ***85***.

3.2.3: Synthesis of compound **27**

From the evolving SAR indications (**Chapter 4**), the phenyl ring in position 3 was identified to engage stronger interactions with the biological target when positioned farther from the scaffold's core. Different linkers were evaluated to spatially separate it from the pyrazolo[1,5-a]pyrimidine motif. While apolar linkers had been explored previously (**24-26**), no data were available regarding polar alternatives. Hence, initially, a nitrogen-containing linker was introduced to investigate its potential influence on the binding profile.

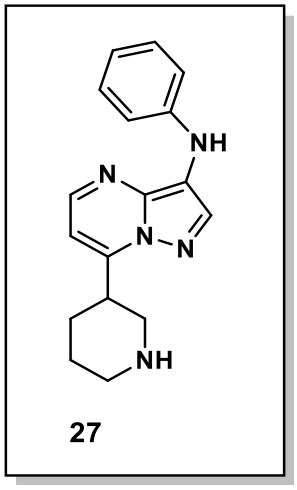

Figure 3.4. *Structure of compound* ***27***.

For this synthesis, a Buchwald–Hartwig amination[5] was carried out using compound **76** as the substrate, tris(dibenzylideneacetone)dipalladium(0) ($Pd_2(dba)_3$) as the palladium source, and tBuXPhos as the supporting ligand **(Scheme 3.5)**. Relatively low yields (ca. 20%) were achieved for product **86**, which was subsequently treated with HCl/MeOH to remove the Boc-moiety, yielding **27**, as a racemic mixture.

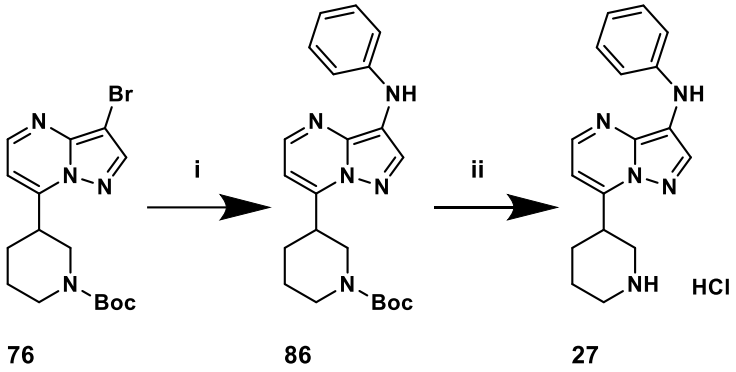

76 86 27

(**i**): NaOtBu, aniline, $Pd_2(dba)_3$, t-BuXPhos. toluene, 90°C, o.n, 20%, (**ii**): HCl/MeOH, 5h, 67%.

Scheme 3.5. *Synthesis of aniline-substituted compounds **27**.*

Under the same Buchwald–Hartwig amination conditions, benzylamine, phthalimide, and benzylalanine were also tested as substrates to expand the chemical space explored within this series. While only trace amounts of product were detected in the reaction with benzylamine, no conversion was observed with the two other substrates. A possible explanation of such a drop in reactivity could be envisaged in the steric hindrance of the reactants and/or the Pd-ligand source tested. Since biological evaluation indicated that the introduction of a nitrogen in this position does not contribute positively to binding affinity, this series was discontinued, and the corresponding reactions were not further investigated.

3.2.4: Synthesis of compounds **28-33**

Building on the findings from the previous study on phenyl influence, an amide linker was introduced in position 3 to connect the phenyl ring to the pyrazolo[1,5-a]pyrimidine scaffold, positioning it further away from the core. This design led to the synthesis of compounds **28–33** (**Figure 3.5**), following the synthetic pathway outlined in **Scheme 3.6**.

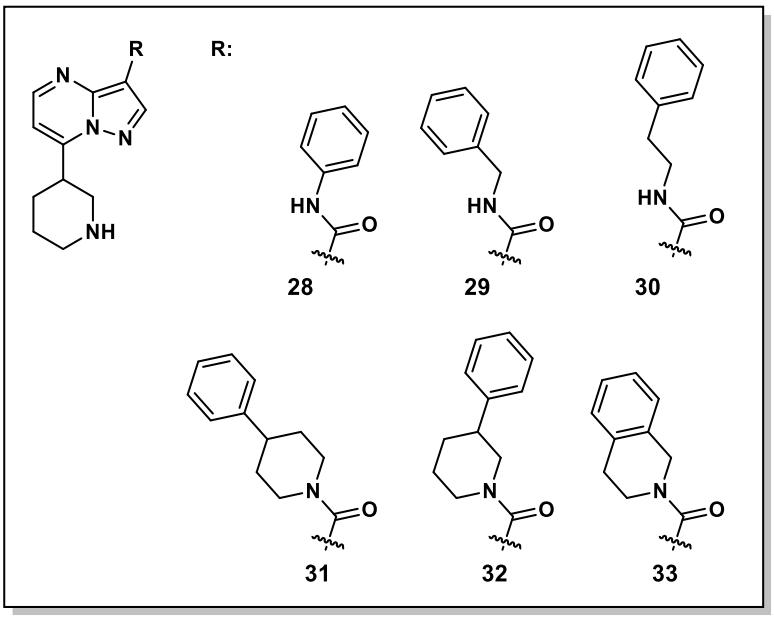

Figure 3.5. *Structure of amide-substituted compounds **28-33**.*

By employing an already functionalized pyrazole, the modular synthetic route previously described in **Scheme 3.2** was adapted for the preparation of compounds **28–33**. Specifically, ethyl 5-amino-1H-pyrazole-4-carboxylate was used to introduce a protected carboxylic functionality during the ring-forming step, carried out in acetic acid at high temperature as previously described. This protocol afforded intermediate **87** in 37% overall yield over two steps. Subsequent ester hydrolysis by standard saponification (LiOH, water, THF for solubility) furnished in good yields the key intermediate **88**, which proved well suited for amide coupling and enabled the rapid generation of diverse analogues with minimal synthetic operations. For the amide bond formation, several coupling reagents were evaluated: while EDC led only to low conversions, HATU in combination with DIPEA in DMF afforded intermediates **89a–f** in good yields after flash chromatography. Final compounds were obtained by Boc-deprotection under HCl/MeOH conditions as racemic (**28-31,33**) or diastereoisomeric (**32**) mixtures **(Scheme 3.6)**. This modular route enabled efficient access to the amide-linked series for subsequent SAR evaluation.

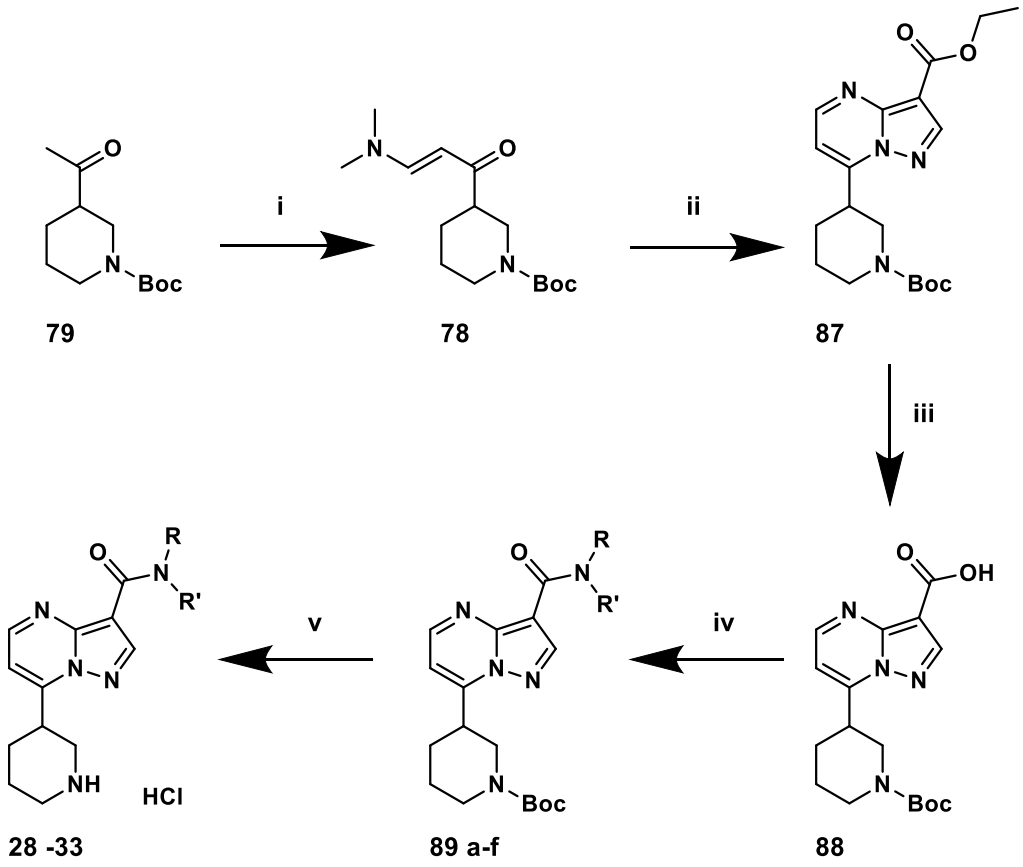

(**i**): 1,1-Dimethoxy-N,N-dimethylmethanamine, DMF, 120°C, 24h; (**ii**) ethyl 5-amino-1H-pyrazole-4-carboxylate, AcOH, 120°C, o.n., 32% (over two steps); (**iii**) LiOH, H_2O, 100° C, o.n., 83%; (**iv**) HATU, DMF, amine, DIPEA, r.t., o.n., 23-87%; (**v**) HCl/MeOH, r.t., 2-5h, 35-70%.

Scheme 3.6*. Synthesis of compounds* ***28-33****.*

3.3: Derivatization of position 2 of the pyrazolo[1,5-a]pyrimidine scaffold: Synthesis of hit-analogues **34-36,38**

To evaluate the SAR in position 2 of the pyrazolo[1,5-a]pyrimidine scaffold compounds **34-36,38** (**Figure 3.6**) were synthesized and evaluated (**Paragraph 4.2**).

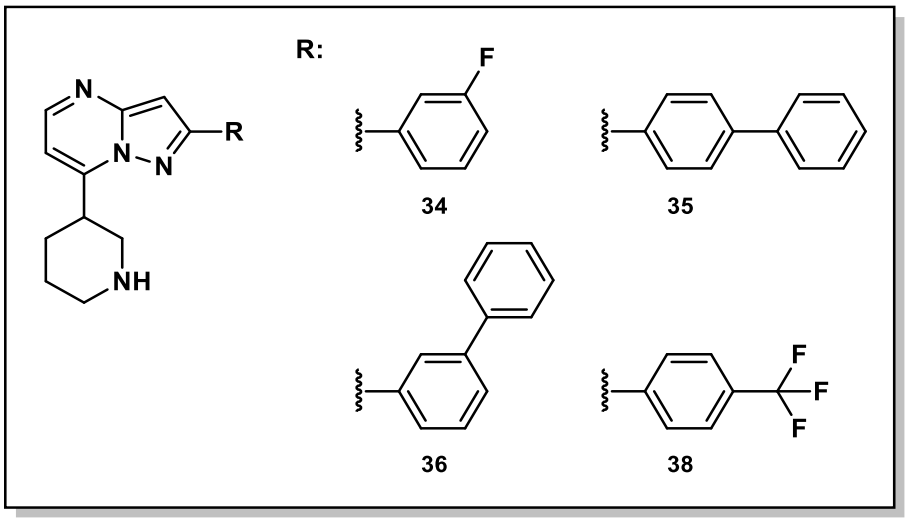

***Figure 3.6**. Synthesis of hit-analogues **34-36,38**.*

As described in **Paragraph 3.1**, the synthetic pathway developed for the preparation of analogues modified at position 3 could be readily adapted for derivatization also at position 2, provided that an aminopyrazole functionalized at position 3 (of the aminopyrazole scaffold) is employed. Following this strategy, the synthetic route depicted in **Scheme 3.2** was applied. This similar synthetic sequence provided key-intermediate **90**, suitable for Suzuki–Miyaura cross-coupling reactions, thus enabling the rapid generation of diverse analogues through a minimal number of synthetic steps.

To access this intermediate, 5-bromo-1H-pyrazol-3-amine was subjected to the cyclization reaction under the conditions previously described (acetic acid, high temperature), affording compound **90** in 70% yield over two steps, after flash chromatography purification. Only one regioisomer was produced under these reaction conditions, thus the same regiochemistry was assumed as for compounds reported in **Scheme 3.2**. Starting from intermediate **90**, the previously optimized microwave-assisted Suzuki–Miyaura reactions ($Pd(PPh_3)_2Cl_2$, K_2CO_3, THF/H_2O) were carried out, providing the corresponding derivatives in yields and reaction times comparable to those obtained for functionalization at position 3. The final compounds (**34–36, 38**) were isolated as their corresponding racemic salts after Boc-deprotection (HCl/MeOH).

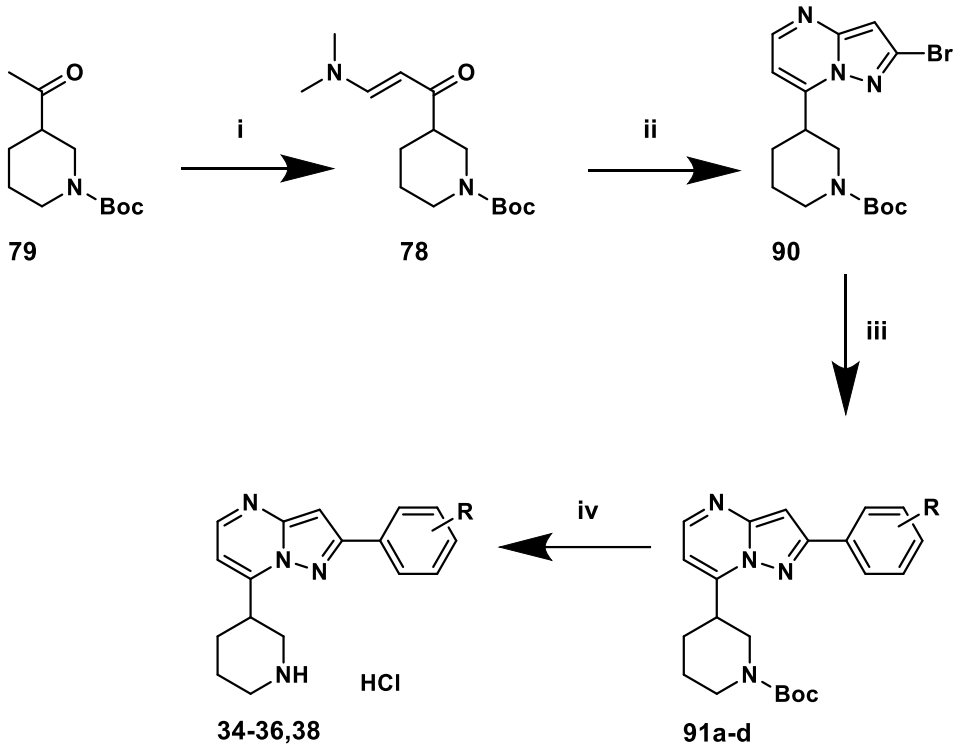

(**i**): 1,1-dimethoxy-N,N-dimethylmethanamine, DMF, 120°C, 24h; (**ii**) 5-bromo-1H-pyrazol-3-amine, AcOH, 120°C, o.n., 74% (over two steps); (**iii**) K_2CO_3, $Pd(PPh_3)_2Cl_2$, boronic acid/boronic esters, THF, H_2O, MW., 110°C, 1h, 42-89%; (i**v**) HCl/MeOH, r.t., 2-4.5h, 23-90%.

Scheme 3.7*. Synthetic pathway for the synthesis of compounds* ***34-36,38.***

3.4: Derivatization of position 5 of the pyrazolo[1,5-a]pyrimidine scaffold

To expand the SAR around this novel scaffold, position 5 of the pyrazolo[1,5-a]pyrimidine core was also investigated by inserting various substituents with distinct physicochemical properties. To do so, a set of novel analogues (**39–51)** of hit compound **1** was designed and synthesized. The corresponding synthetic pathways are illustrated in **Schemes 3.8–3.13**.

Since direct activation of position 5 for final modifications was not feasible as a last step, contrary to the changes introduced at position 3, different selective cross-coupling methodologies (**Paragraph 3.3.1**) and alternative ring-closing strategies (**Paragraph 3.3.4–3.3.5**) were developed to enable derivatization at this position.

3.4.1: Synthesis by regioselective cross-coupling reactions (compounds **43-45, 68**)

To obtain an initial assessment of the SAR at position 5, compounds **43–45** were first synthesized (**Figure 3.7**). In addition, compound **68** was prepared through the same synthetic pathway, as it could be conveniently accessed from a common intermediate and was considered useful for evaluating the influence of substituents on the binding properties of the scaffold.

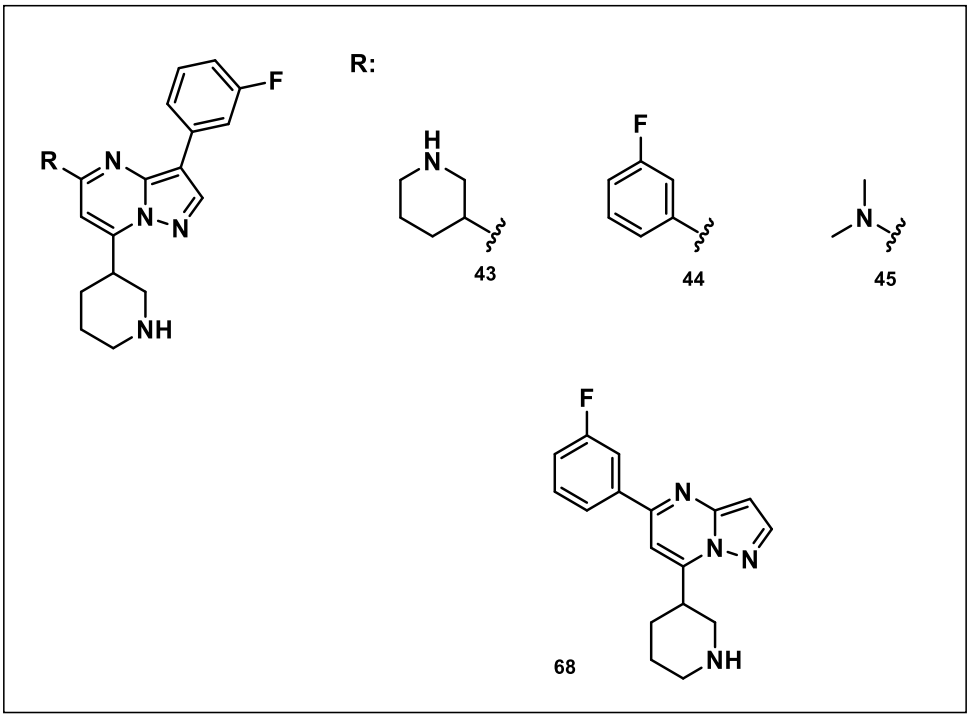

Figure 3.7**. Synthesis of 5-substituted pyrazolo[1,5-a]pyrimidine derivatives **43-45, 68.

As previously reported,[10] 5,7-dichloropyrazolo[1,5-a]pyrimidine **92** underwent regioselective substitution with various amines, displaying a marked preference for reaction at position 7 over position 5, likely due to the higher intrinsic reactivity of the chlorine atom at position 7. Building on this observation, a regioselective Suzuki–Miyaura cross-coupling strategy was envisaged to obtain **93a**, an intermediate suitable for subsequent derivatization at position 5 (**Scheme 3.8)**. Starting from commercially available **92**, several Suzuki–Miyaura cross-coupling conditions were examined. While *tert*-butyl 3-(4,4,5,5-tetramethyl-1,3,2-dioxaborolan-2-yl)piperidine-1-carboxylate failed to provide any detectable product, its unsaturated analogue, *tert*-butyl 3-(4,4,5,5-tetramethyl-1,3,2-dioxaborolan-2-yl)-5,6-dihydropyridine-1(2H)-carboxylate, successfully afforded the desired coupling product, with the double bond being reduced in a later step. To increase regioselectivity, the reaction temperature was lowered to 80 °C (from the 110 °C typically used under microwave irradiation), employing $Pd(PPh_3)_2Cl_2$ as catalyst, K_2CO_3 as base, and THF/H_2O (1:1) as solvent. Under these conditions, the desired regioisomer **93a** was obtained in 57% yield. The other regioisomer **93b** was also detected and isolated (28% yield), further supporting the notion that position 7 is more reactive than position 5. A detailed characterization of regioisomer **93a** is provided in **Paragraph 3.4.3**. No further optimization was carried out, as the route was eventually discontinued following the development of faster synthetic strategies for accessing position-5 derivatives.

Intermediate **93a** was subsequently functionalized at position 5 either through Suzuki–Miyaura cross-coupling under the previously described microwave-assisted conditions ($Pd(PPh_3)_2Cl_2$, THF/H_2O, K_2CO_3), introducing a piperidine (**94a**) substituent (91% yield), or via nucleophilic substitution, introducing dimethylamine (**94c**) in quantitative yield. The resulting intermediates were then brominated with NBS in DCM to give **95a,c** in quantitative yield and without requiring purification. These brominated derivatives were subjected to a second microwave-assisted Suzuki–Miyaura coupling with 3-fluorophenylboronic acid, furnishing **96a,c** quantitatively and in short reaction times. Hydrogenation of the obtained intermediates was performed using Et_3SiH and Pd/C to give compounds **97a,c**. The yields were strongly dependent on the electronic properties of the substrates and ranged from 27% to

83%, but the use of the flow apparatus allowed more reproducibility than the Et_3SiH approach. Racemic, final compounds **43,45** were obtained as their corresponding salts after Boc-deprotection. In the case of compound **43**, the diastereomeric mixture proved difficult to separate and was therefore tested as such.

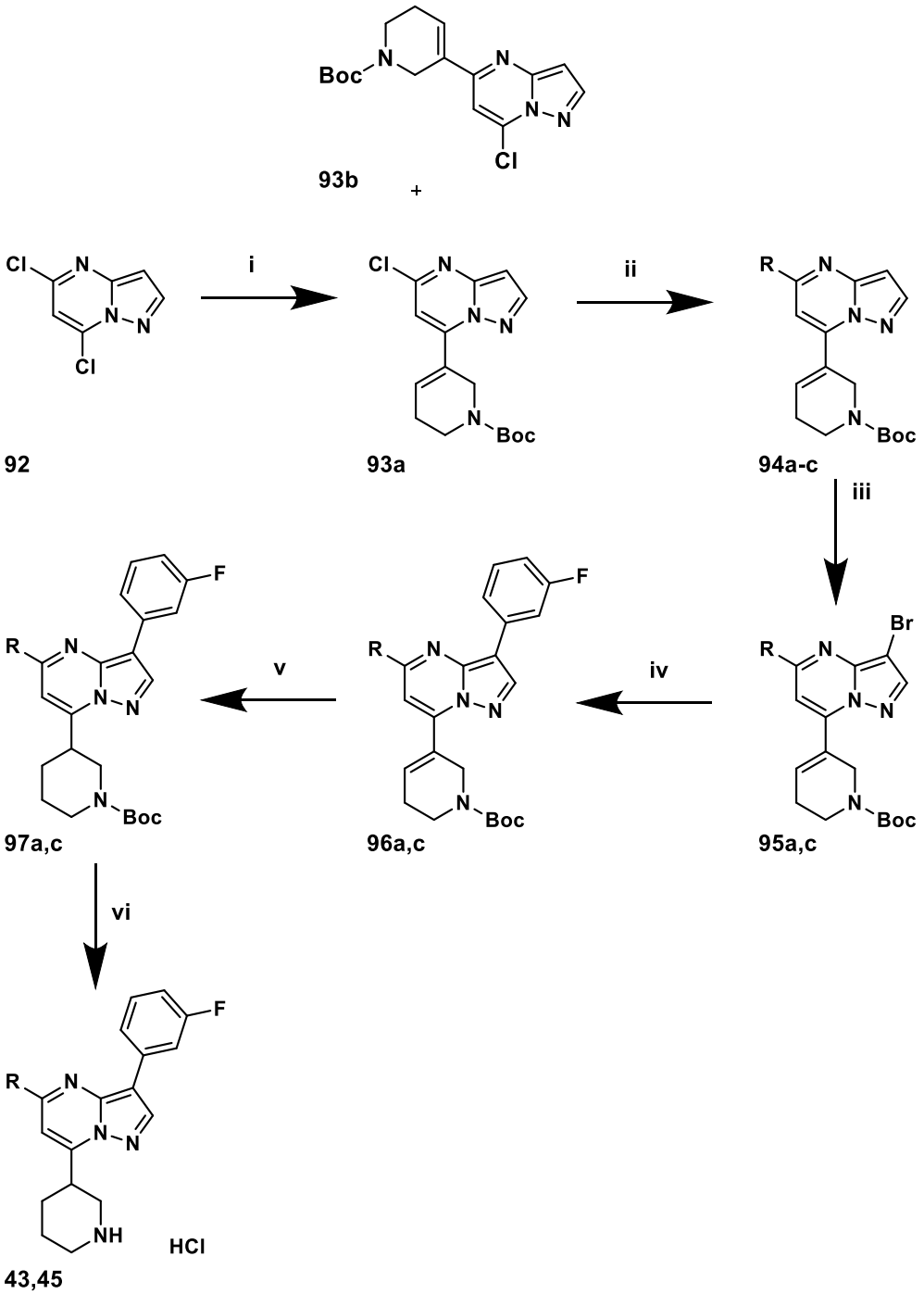

(**i**): K_2CO_3, $Pd(PPh_3)_2Cl_2$, tert-Butyl 3-(4,4,5,5-tetramethyl-1,3,2-dioxaborolan-2-yl)-5,6-dihydropyridine-1(2H)-carboxylate, THF, H_2O, 110°C, o.n., 57%; (**ii**) K_2CO_3, $Pd(PPh_3)_2Cl_2$, boronic acid/boronic esters, THF, H_2O, MW, 110°C, 1h, 91%-quantitative or dimethylamine, CH_3CN, r.t., 3h, quantiattive (**iii**) NBS, DCM, r.t., o.n., 67%-quantitative, (**iv**): K_2CO_3, $Pd(PPh_3)_2Cl_2$, boronic acid/boronic esters, THF, H_2O, MW, 110°C, 1h, 61%-quantitative; (**v**): Et_3SiH, Pd/C, MeOH, r.t., 1-48h, 27-83%; (**vi**) HCl/MeOH, r.t., 5-16 h, 43-65%.

Scheme 3.8*. Synthetic pathway for the synthesis of compounds **43** and **45**.*

To investigate the binding specificity of these novel compounds, a close analogue of the hit compound **1**, featuring shifted positions of the fluorophenyl substituent in position 5, was designed and synthesized. Using a similar synthetic pathway, to enable the synthesis of compound **68** and compound **44,** the order of the steps in the synthetic route described above was inverted (**Scheme 3.9**).
Starting from the previously described intermediate **94b**, H-Cube hydrogenation[11] using Pd/C as a catalyst enabled the formation of intermediate **98** in moderate yield (52%). As anticipated, subsequent Boc deprotection allowed the direct formation of **68** in a satisfactory yield as a racemic mixture (76%). Intermediate **98** also proved to be reactive under bromination conditions using NBS in DCM, affording compound **95b** in quantitative yield without the need for chromatographic purification. Compound **95b** was subsequently subjected to the previously described microwave-assisted coupling conditions ($Pd(PPh_3)_2Cl_2$, THF/H_2O, K_2CO_3), resulting in the introduction of another fluorophenyl group in good yield (83%) and with a short reaction time. Final Boc-deprotection afforded compound **44** in 46% yield as a racemic mixture.

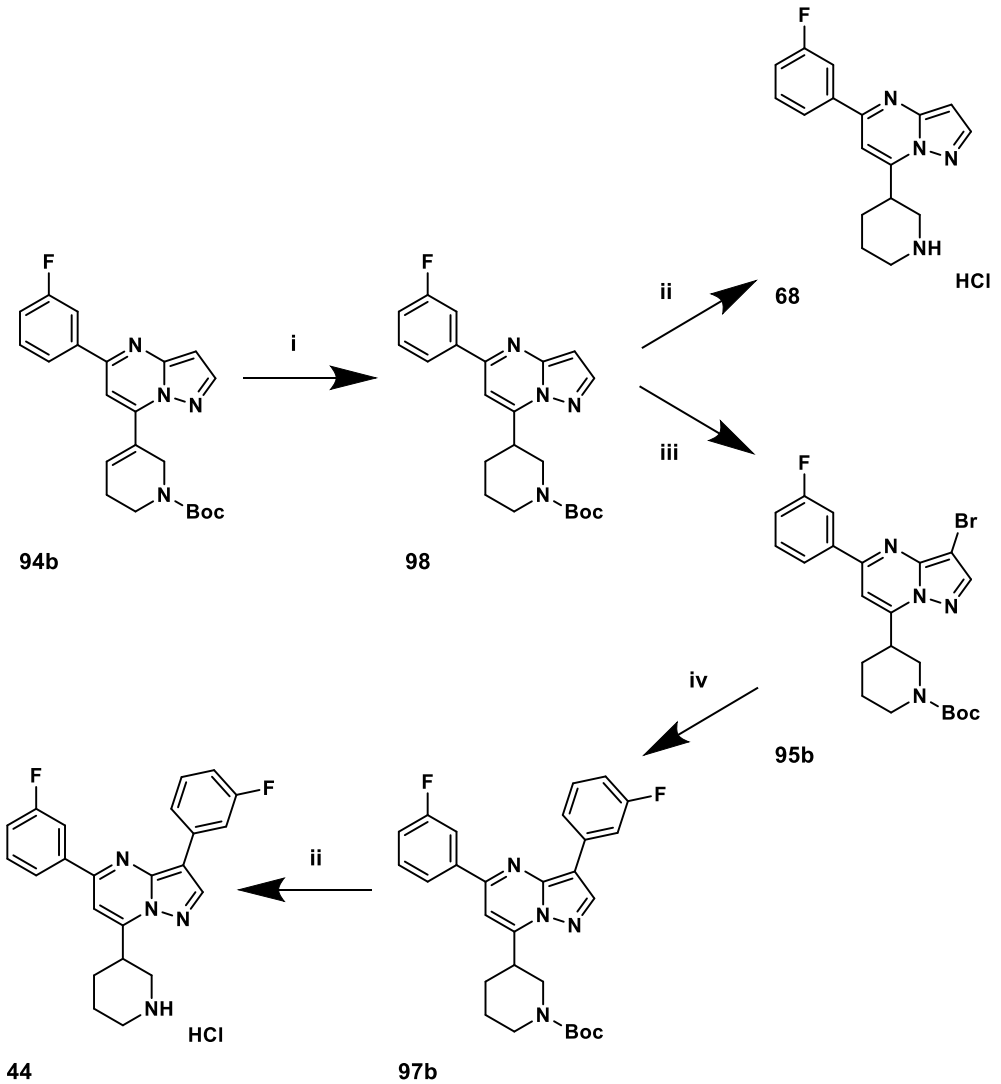

(**i**): H-cube, EtOH, Pd/C, 60 °C, 1.0 bar, 52%; (**ii**) HCl/MeOH, 2h30min, 76%; (**iii**): NBS, DCM, r.t., 6h, quantitative; (**iv**): K_2CO_3, $Pd(PPh_3)_2Cl_2$,3-fluorophenyl boronic acid, THF, H_2O, MW, 110°C, 1h, 83%; (**v**) HCl/MeOH, 15h, 46%.

Scheme 3.9*. Synthesis of compounds **44** and **68.***

3.4.2: Synthesis of compound **69**

Following a similar rational (i.e. switching around the substituents as in hit **1**) behind the design and synthesis of compound **68**, close analogue **69,** featuring the piperidine and the fluorophenyl switched in the corresponding positions was also synthesized (**Figure 3.8**).

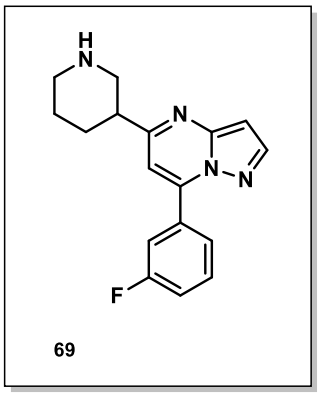

***Figure 3.8**. Structure of 5-pyperidinyl-substituted analogue **69**.*

The cross-coupling reaction described in **Scheme 3.8** was not fully regioselective, also affording the undesired, minor regioisomer **93b**, in 28% yield. This compound could be efficiently exploited as key-intermediate for the synthesis of compound **69** (**Scheme 3.10)**. Specifically, **93b** was subjected to the already described microwave-assisted Suzuki–Miyaura cross-coupling reaction ($Pd(PPh_3)_2Cl_2$, THF/H_2O, K_2CO_3) with 3-fluorophenylboronic acid, affording intermediate **99** in quantitative yields, which was subsequently reduced using an H-Cube system to yield compound **100**. Final Boc-deprotection afforded the target racemic analogue **69** (85% yield)**.**

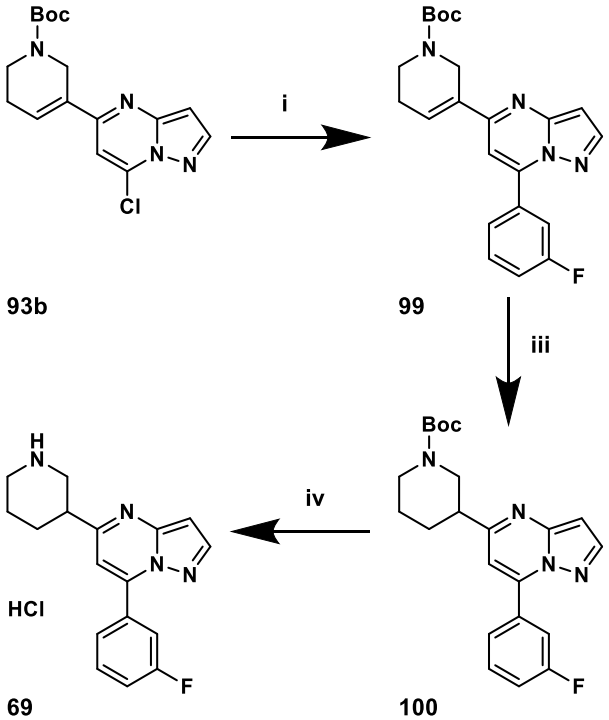

(**i**): (3-fluorophenyl)boronic acid, K_2CO_3, $Pd(PPh_3)_2Cl_2$,THF, H_2O, MW, 110°C, 1h, quantitative; (**ii**): H-cube, EtOH, Pd/C, 60°C, 1bar, 60%; (**iii**) HCl/MeOH, r.t., 7h, 85%.

***Scheme 3.10**. Synthetic pathway for the synthesis of compound **69**.*

3.4.3: ^{19}F-^{1}H HOESY NMR study for the regioselective synthesis of 5-substituted analogues

To investigate the regioselectivity of Suzuki–Miyaura cross-coupling reaction between *tert*-butyl 5-(4,4,5,5-tetramethyl-1,3,2-dioxaborolan-2-yl)-3,6-dihydropyridine-1(2H)-carboxylate and 5,7-dichloropyrazolo[1,5-a]pyrimidine (synthesis of **93a**), a ^{1}H-^{19}F HOESY (Heteronuclear Overhauser Effect SpectroscopY) NMR experiment[12] was conducted on analogues **43** and **44** (**Figure 3.7**), as reference compounds.

The two-dimensional ^{1}H–^{19}F HOESY technique detects through-space dipolar interactions between protons and fluorine atoms typically within ~5 Å, thus allowing the identification of nonbonded spatial proximities. This method enables verification of the reaction's regioselectivity: if the substitution pattern aligns with the literature-reported configuration, a diagnostic HOESY cross-peak is expected due to the close spatial proximity between the proton of the substituent and the fluorine atom of the 3-fluorophenyl ring. As anticipated, compound **44** exhibited the expected cross-peak (**Figure 3.9**), confirming the proposed regioisomeric structure. The fluorophenyl ^{19}F signal at *circa* 112 ppm exhibits cross-peaks with three different protons belonging to two distinct spin systems (two different phenyl rings) from the COSY analysis (not reported). Such correlations can only arise from spatial proximity between the two fluorophenyl substituents, thereby confirming their simultaneous presence at positions 3 and 5. In contrast, compound **43** (3-piperidine in position 5) did not display any detectable cross-peaks with other spin systems for the fluorophenyl fluorine, suggesting that a certain degree of molecular rigidity may be required to observe such dipolar interactions. Furthermore, introduction of a 3-fluorophenyl substituent at position 7 (see **Paragraph 3.5**) did not yield any observable ^{1}H–^{19}F correlations under identical experimental conditions.

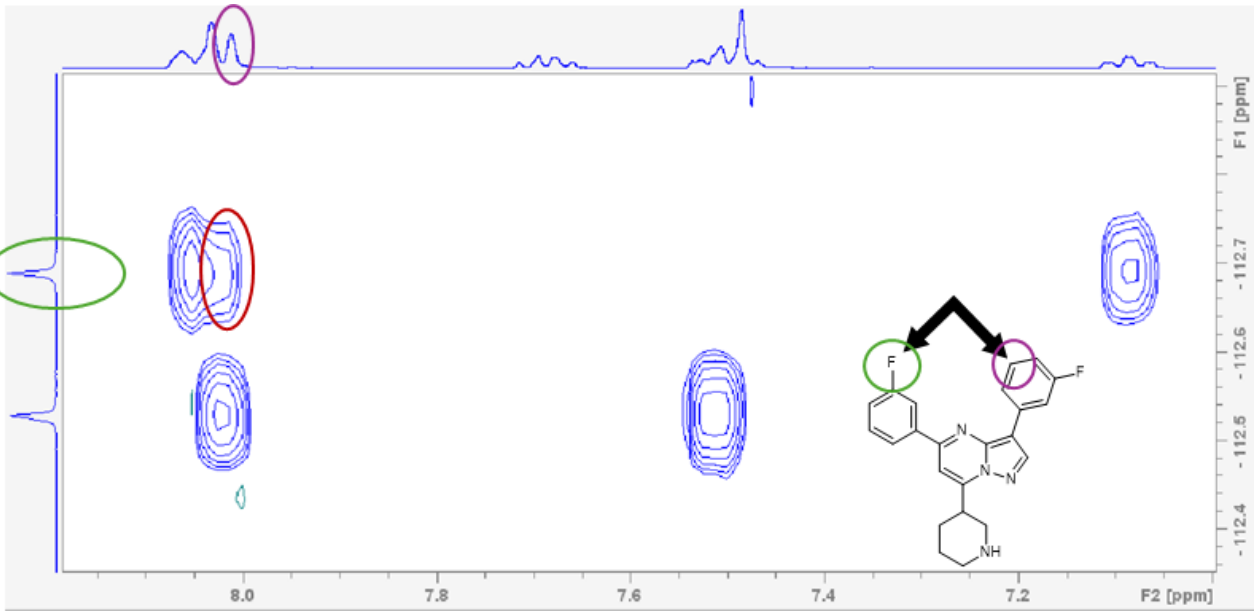

Figure 3.9. *^{1}H-^{19}F HOESY spectrum of compound **43**. Circled in red is the cross-peak with the third proton belonging to the other phenyl ring.*

3.4.4: Synthesis of 5-substituted analogues **39-42** by 1,3-ketoester condensation

Provided that regioselective conditions could be achieved, it would be possible to envision a ring-closing reaction involving differently functionalized α,β-ketoesters, as a strategy to functionalize position 5. With this rationale in mind, a new synthetic pathway was developed, enabling a more scalable synthesis of derivatives functionalized at position 5 (**Scheme 3.11**). Notably, the proposed pathway also allows subsequent functionalization at position 7 of the pyrazolo[1,5-a]pyrimidine scaffold, which was later exploited for the SAR exploration of this position (**Paragraph 3.5**).
By applying this synthetic pathway, compounds **39-42** were obtained (**Figure 3.10**).

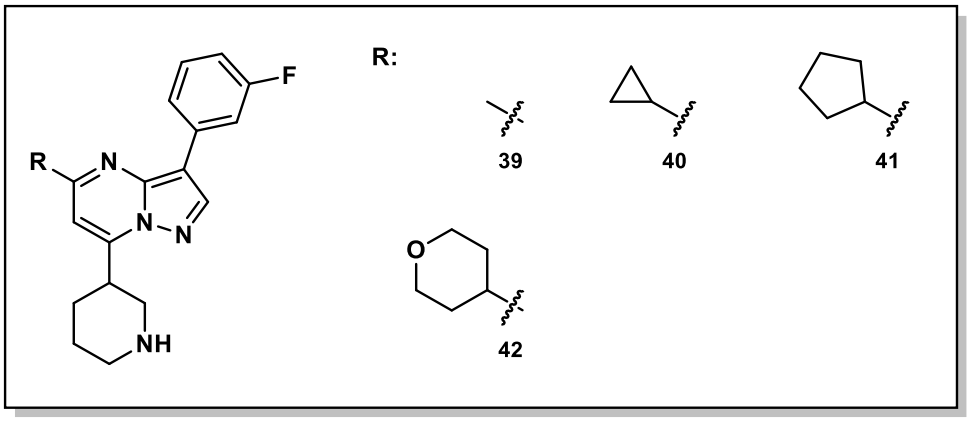

***Figure 3.10**. Structure of new 5-substituted compounds **39-42**.*

The synthetic pathway developed for this series follows a convergent strategy in which a pre-functionalized aminopyrazole,[13] bearing the fluorophenyl substituent to limit the synthetic step required, is condensed with various β-ketoesters during the ring-closing step **(Scheme 3.11)**. To access the functionalized key aminopyrazole, starting material **101** was condensed with the acetal of N,N-dimethylformamide in DMF, affording **102** by precipitation (64% yield), which underwent a ring-forming reaction with hydrazine to give **103** in good yield (84%). Notably, **103** precipitated from the reaction medium as a pure solid, eliminating the need for purification and allowing a low-effort synthesis of this key intermediate. Intermediate **103** was then subjected to cyclization under conditions similar to those employed in the other ring-forming reactions (acetic acid, high temperature).[14] In this case, toluene was added to the reaction mixture to improve the solubility of these reaction products. Remarkably, thanks to this strategy, for all α,β-ketoesters examined, the desired products **104a–d** precipitated directly from the reaction mixture, providing good yields and requiring no chromatographic purification.
Regarding the reaction mechanism, UPLC-MS analysis revealed a transient formation of an imine intermediate on the α,β-ketoester carbonyl functionality, suggesting that an initial nucleophilic attack takes place at this position, followed by intramolecular cyclization involving the ester moiety. This mechanistic proposal was later confirmed by an HOESY analysis (**Paragraph 3.7**) and supported by precedent literature for structurally related analogues.[1] Subsequent $POCl_3$-mediated chlorination of the resulting hydroxyl group furnished intermediates **105a–d** without the need for purification.
Although the use of refluxing $POCl_3$ is typically avoided when milder chlorinating agents can be employed, in this case, the intermediates exhibited extremely poor solubility in most aprotic solvents. Solubility and subsequent reactivity were observed only at elevated temperatures in neat $POCl_3$, which therefore represented the only viable medium to ensure conversion. Intermediates **105a–d** were then subjected to the previously described microwave-assisted Suzuki–Miyaura cross-coupling reaction ($Pd(PPh_3)_2Cl_2$, THF/H_2O, K_2CO_3) with *tert*-butyl 3-(4,4,5,5-tetramethyl-1,3,2-dioxaborolan-2-yl)-5,6-

dihydropyridine-1(2H)-carboxylate, affording unsaturated compounds **106a-d** in quantitative yield. The reduction of these intermediates was performed using either an H-cube flow hydrogenation system or Et_3SiH with 10% Pd/C, as the catalyst, yielding **107a–d** in good yields (55–67%). After Boc-deprotection, the desired final compounds **39–42** were obtained, as racemic hydrochloride salts.

The consistent precipitation of multiple intermediates, together with the straightforward preparation of key building blocks, significantly streamlines the workflow by reducing the number of purification steps and improving overall practicality. However, despite these advantages for potential scale-up, the synthetic route remains suboptimal for the rapid derivatization of the scaffold and allows only C–C bond formation at position 5, thereby limiting the scope of SAR exploration.

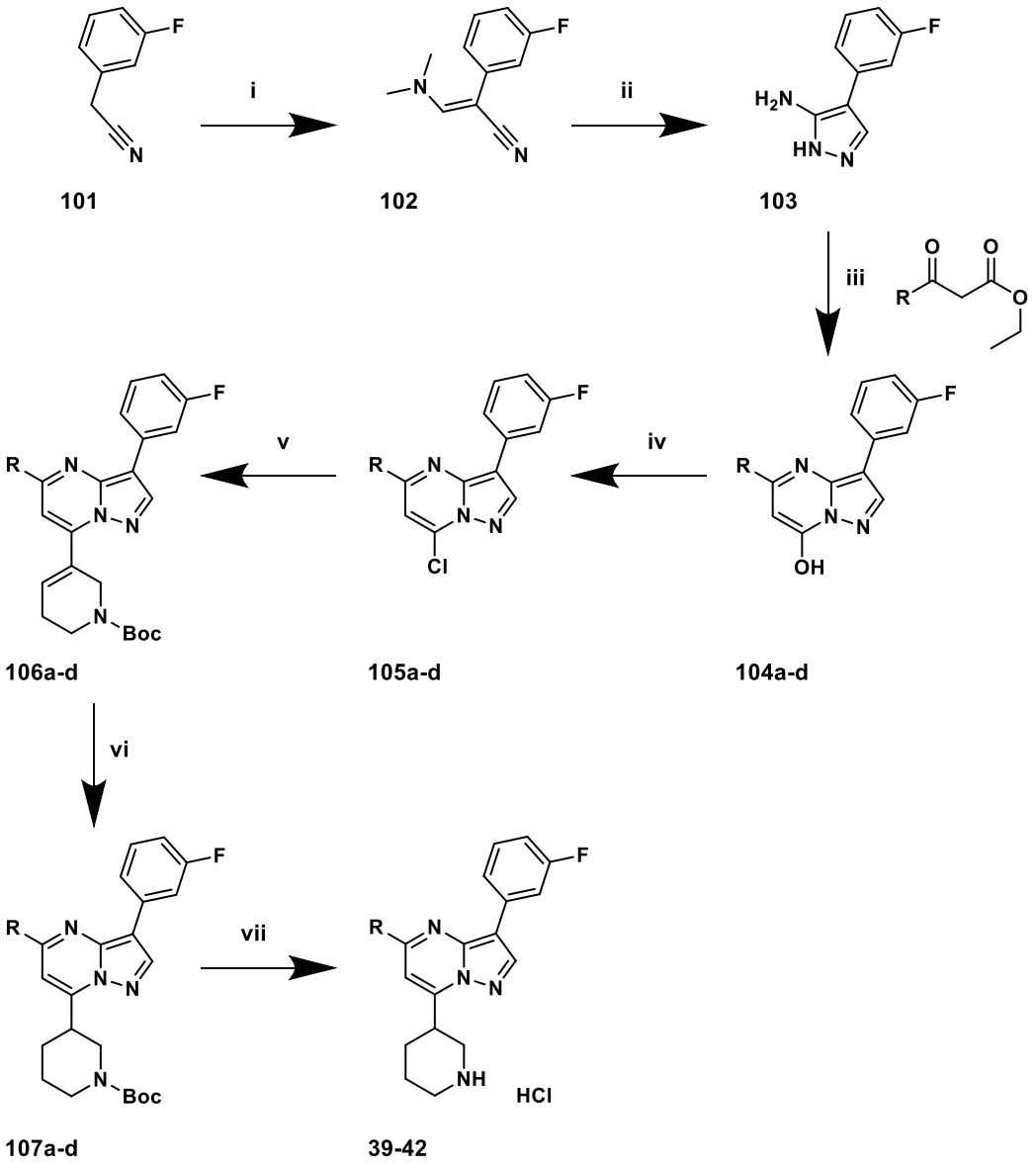

(**i**): 1,1-dimethoxy-N,N-dimethylmethanamine, DMF, 120°C, o.n., 64%; (**ii**) Hydrazine * HCl, EtOH/water, 80°C, o.n., 84% (**iii):**1,3-ketoester, AcOH/toluene 1/1, 120°C, o.n., 62-84%;, (**iv**): $POCl_3$, reflux, o.n., 72-96%; (**v**) K_2CO_3, $Pd(PPh_3)_2Cl_2$, tert-Butyl 3-(4,4,5,5-tetramethyl-1,3,2-dioxaborolan-2-yl)-5,6-dihydropyridine-1(2H)-carboxylate, THF, H_2O, 110°C, 1h, 67-quant%; (**vi**): H-cube, EtOH, Pd/C, 55-67% or Et_3SiH, Pd/C, MeOH, 16h, 55-56%. (**vii**): HCl/MeOH, r.t., 2-16h, 56-87%

Scheme 3.11*. Synthetic pathway for the synthesis of compounds* ***39-42.***

3.4.5: Synthesis of 5-substituted compounds **46-51** by Meldrum's acid condensation

To allow for faster and more flexible derivatization at position 5, a synthetic route was designed in which the key functionalization reactions were carried out at the final stage rather than at the beginning of the sequence. To this end, the synthetic pathway shown in **Scheme 3.12** was developed, enabling late-stage diversification through an intermediate (compound **113**) featuring substituents appropriately inserted at positions 3 and 7, while remaining reactive toward substitution reactions at position 5. This strategy proved particularly advantageous, as it provided a straightforward and convergent route to multiple analogues. Using this approach, compounds **46–51** (**Figure 3.11**) were successfully synthesized.

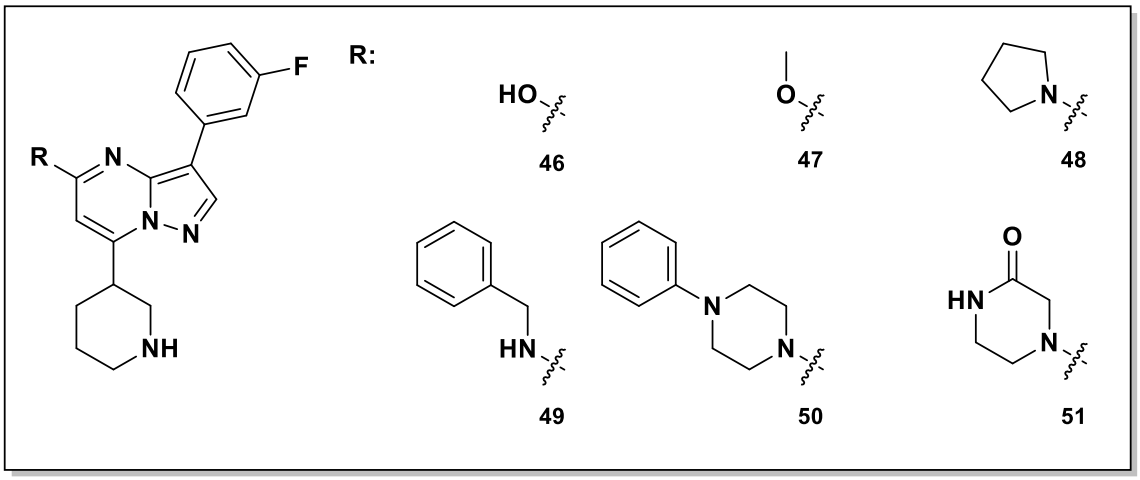

***Figure 3.11**. Structure of compounds **46-51**.*

The synthetic pathway (**Scheme 3.12**) relies on the 1,3-ketoester intermediate **110**, as the key precursor for the condensation reaction. This compound was obtained by activating the carboxylic acid moiety of commercially available **108** with EDC, followed by condensation with Meldrum's acid (**109**).[15] Since **108** was employed as a racemic mixture, all intermediates were obtained as racemates. The desired intermediate **110** was afforded without chromatography purification, in overall good yield (79%). The subsequent cyclization step was performed with a pre-functionalized aminopyrazole already bearing a 3-fluorophenyl substituent (**103**), eliminating the need for a later derivatization step. Low reactivity between the reaction partners was generally observed, and, after an initial reaction screening, high-temperature microwave-assisted conditions with TEA in acetonitrile were selected to obtain the desired intermediate **111**. Poor regioselectivity under these non-thermodynamic (high temperature) conditions was detected, yielding the two regioisomers in an almost 1:1 ratio. Despite this drawback, the ready availability of the reagents, the short reaction times, and the possibility of accessing the alternative regioisomer, **112,** useful for other derivatization routes, made this approach an acceptable strategy for initial scaffold expansion. The regioselectivity characterization of the condensation reaction was performed by analysing the compound derived from these two intermediates, as reported in **Paragraph 3.4.5.1**. Intermediate **111** was activated using PyBrop under basic, non-nucleophilic conditions (TEA, CH_3CN) to afford the key intermediate of this sequence, **113**, in good yield (58%).[16] This species displayed stability and high reactivity toward nucleophilic substitution, enabling the introduction of various heteroaromatic nucleophiles, providing compounds **114a–f**. After Boc-deprotection, the final compounds **46–51** were obtained as racemic mixtures.

Although the initial steps of this synthetic route delivered only moderate yields, partly due to limited regioselectivity and the need for further optimization, the overall pathway represents a substantial improvement over those previously described. It relies on inexpensive and readily available starting materials, avoids hazardous conditions, such as $POCl_3$ at reflux, and unnecessary steps, like hydrogenation of the unsaturated ring at position 7, and finally offers a more efficient diversification at position 5. Furthermore, this methodology not only enables faster analogue generation but also provides a promising framework for stereoselective synthesis, provided that a carboxylic acid (**108**) with predefined stereochemistry is employed as the starting material.

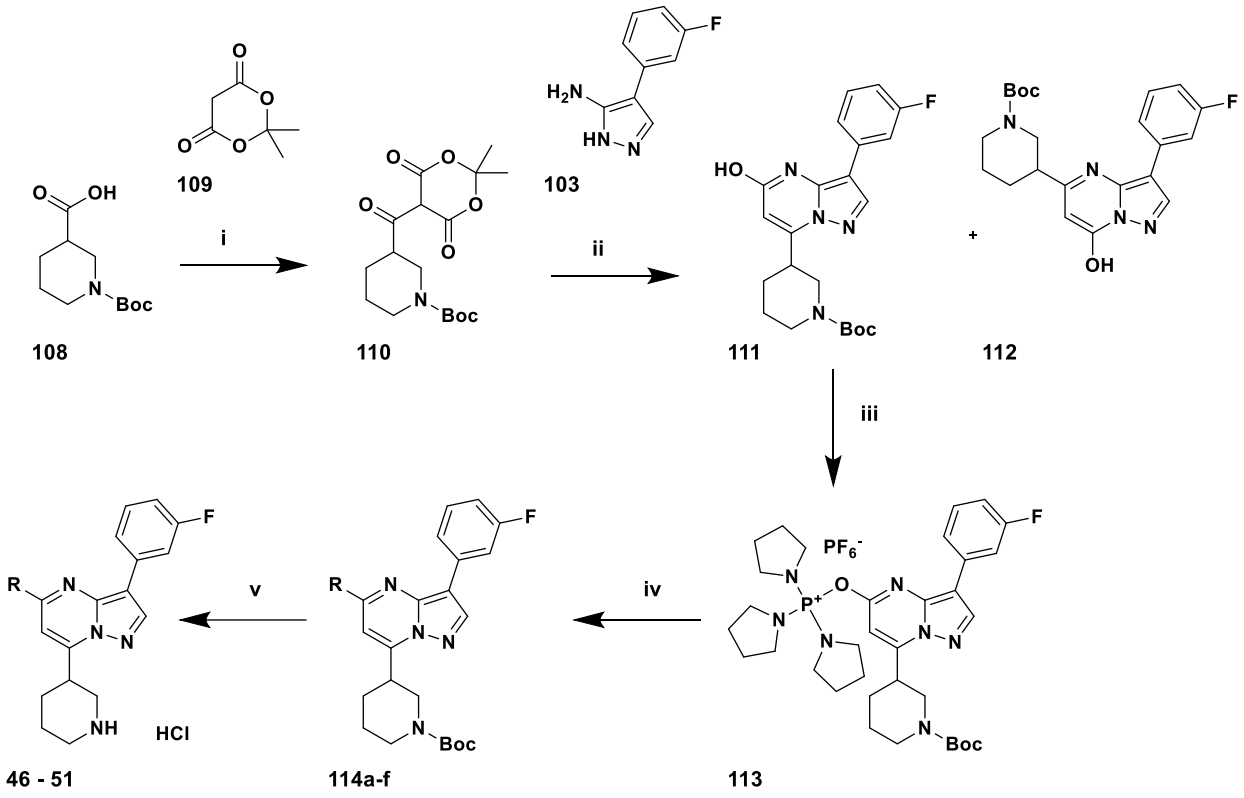

(**i**): DMAP, EDC · HCl, DCM, r.t., o.n., 79%; (**ii**): TEA, CH_3CN, MW, 150°C, 1h, 39%; (**iii**) **:** pyBrop, Et_3N, CH_3CN, r.t., 2h, 58%; (**iv**): RH, CH_3CN or THF, reflux, o.n. 50%-quantitative; (**v**): HCl/MeOH, 1-4h, 61%-quantitative.

Scheme 3.12*. Synthetic pathway for the synthesis of compounds* ***46-51*****.**

3.4.5.1: Regioselectivity assessment of the reported synthetic pathway: synthesis of compound **70**

The regioselectivity of the cyclization reaction reported in **Paragraph 3.4.5** was checked and confirmed by the synthesis of compound **70** (**Figure 3.12**), synthesized starting from the undesired regioisomer (by-product) **112**, following the synthetic pathway outlined in **Scheme 3.13.**

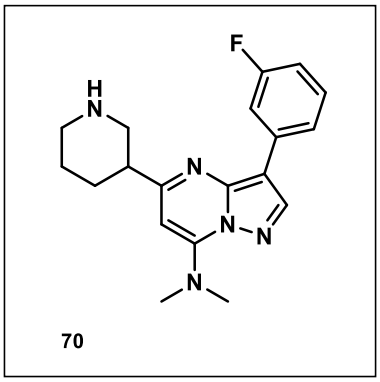

***Figure 3.12**. Structure of compound **70**.*

Starting from compound **112**, the synthesis of compound **70** required only the activation of the hydroxyl group at position 7 toward nucleophilic substitution. To this end, the hydroxyl functionality was converted into a triflate, as a better leaving group, by reaction with trifluoromethanesulfonic anhydride under basic conditions (pyridine, DCM), affording intermediate **115** in good yields (77%). Subsequent substitution with dimethylamine proceeded quantitatively under excess of nucleophile (acting also as base) in CH_3CN, yielding the desired intermediate **116** in quantitative yields, without the need of purification. Final compound **70** was obtained as a racemic mixture after Boc-moiety removal in a quantitative way, without the need for chromatography purification.

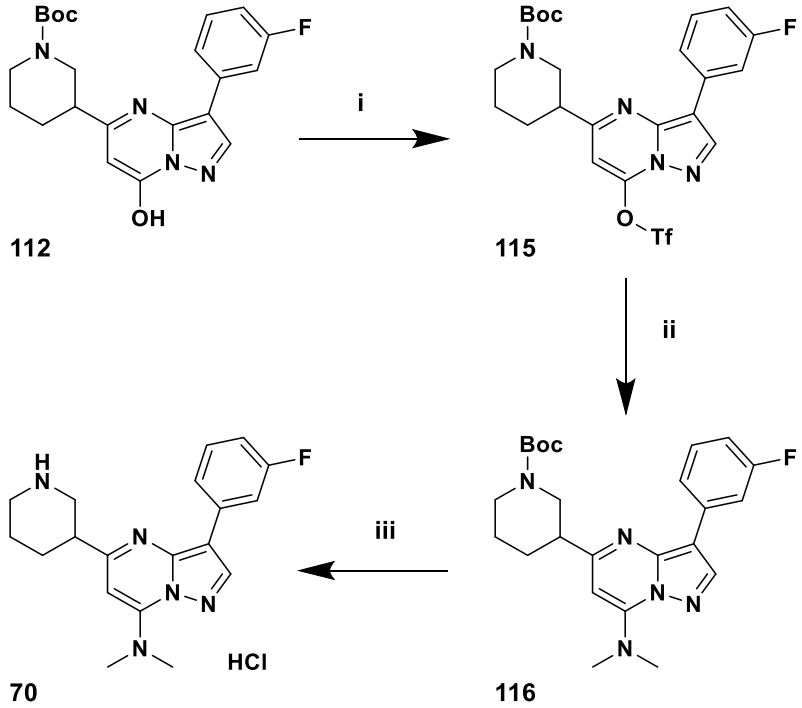

(**i**): pyridine, Tf_2O, DCM, 0°C to r.t., o.n.,77%; (**ii**): NMe_2, CH_3CN, reflux, 2.5h, quantitative (**iii):** HCl/MeOH, r.t., 3h, quantitative

***Scheme 3.13**. Synthetic pathway for the synthesis of compound **70**.*

Compound **70** represents the close analogue of previously synthesized compound **45**, which features the piperidine ring in position 7 and the dimethylamine in position 5 (**Figure 3.13**). For this latter compound, the position of the substituent is well defined, as confirmed by HOESY NMR study presented

in **Paragraph 3.3.2**. [1]H-NMR spectra of these two compounds resulted different, therefore providing confirmation of the hypothesized regioisomery of the compounds shown in **Paragraph 3.4.5**.

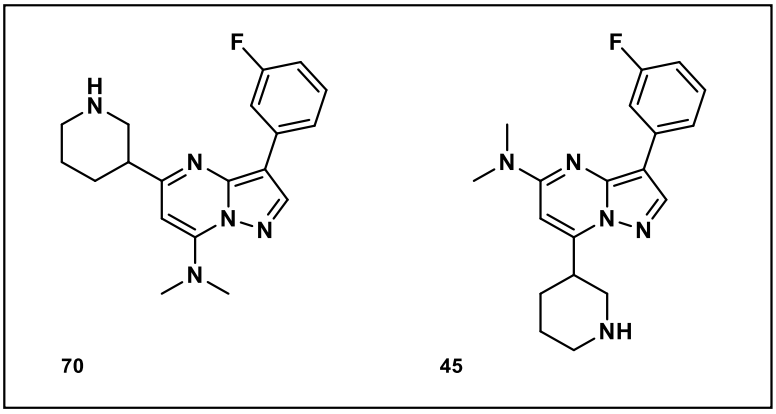

***Figure 3.13**. Structures of isomeric compounds **70** and **45**.*

3.5: Nitrogen derivatization of the piperidine ring of hit **1**: Synthesis of compounds **52-57**

The basic nitrogen of the piperidine ring in hit compound **1** was functionalized to further explore the SAR around this novel scaffold. This process led to the synthesis of compounds **52-57** (**Figure 3.14**).

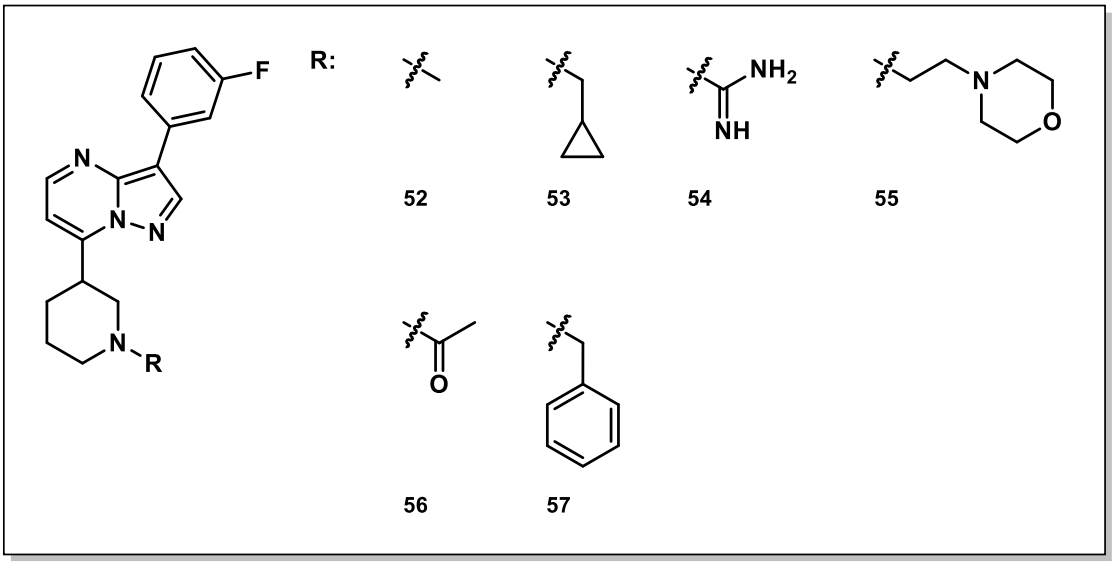

Figure 3.14**. Structures of substituted piperidinyl compounds **52-57.

To accomplish the synthesis of the newly designed compounds, starting from hit **1,** two complementary reaction types were employed (**Scheme 3.14**): a reductive amination[17] or nucleophilic substitutions. The reductive amination reactions were performed using the corresponding aldehydes, together with either formic acid (for formaldehyde) or sodium borohydride (for acetaldehyde and cyclopropanecarbaldehyde), in the presence of catalytic acetic acid and ethanol as solvent, yielding, respectively **52** and **53**. In parallel, substitution reactions were explored employing various activated alkyl chlorides under basic, non-nucleophilic conditions (pyridine or K_2CO_3), with catalytic KI in CH_3CN or DMF, as the reaction medium, yielding compounds **54-57** as racemic mixtures.

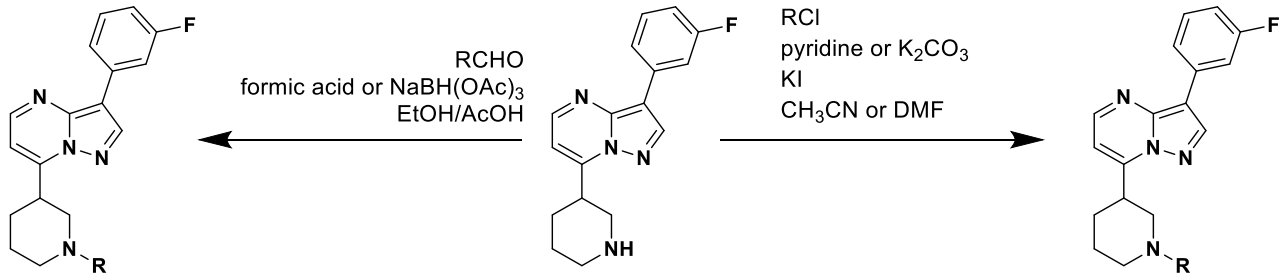

Scheme 3.14**. Synthetic pathways for the synthesis of compounds **52-57.

3.6: Derivatization of position 7 of the pyrazolo[1,5-a]pyrimidine scaffold: Synthesis of compounds **58-67,117**

The direct derivatization of position 7 proved to be difficult to access in a fast manner required for time-effective SAR exploration. Provided the presence of a substituent in position 5, the synthetic pathway presented in **Paragraph 3.3.3** (Synthesis by 1,3-ketoester's condensation (compounds **39-42**) allowed for the functionalization of position 7 in a straightforward manner. To benefit of this finding, in order to further explore the position 7, thanks to reagent availability and chemical stability, the cyclopropyl functionality was selected as a good benchmark for a substitution in position 5 (compound **40**), while different substituents were introduced in position 7. This choice led to the synthesis of compounds **58-67** (**Figure 3.15**).

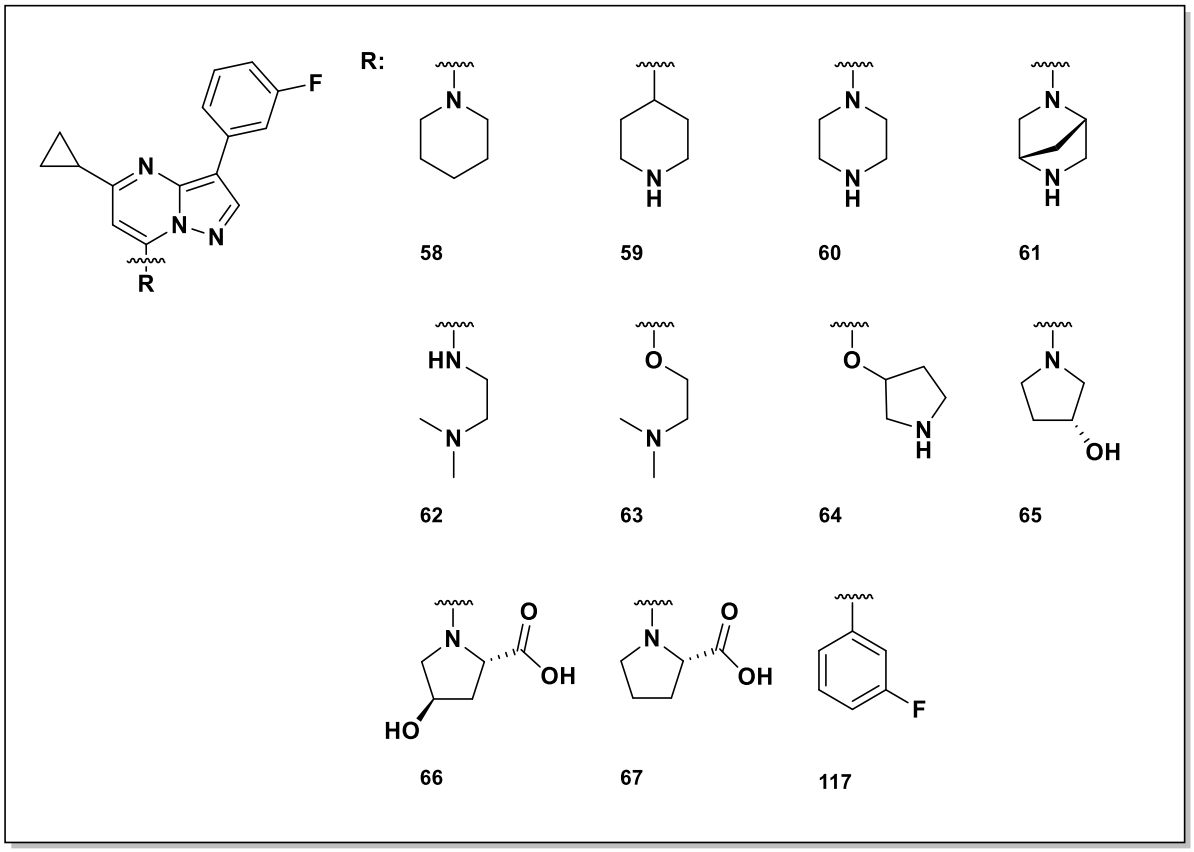

***Figure 3.15**: Structure of compounds **58-67** and **117**.*

The crucial intermediate for the synthesis of this set of compounds is **105b**, obtained following the synthetic pathway outlined in **Scheme 3.11** (**Paragraph 3.3.3**). This compound, bearing a chlorine atom at position 7, is highly versatile, as it participates readily in both cross-coupling and nucleophilic substitution reactions, enabling straightforward structural diversification.

Microwave-assisted Suzuki–Miyaura cross-coupling, performed under the same conditions previously optimized for functionalization at position 3 (K_2CO_3, $Pd(PPh_3)_2Cl_2$, H_2O/THF), was employed to access compounds **59** and **117**. For the preparation of **59**, the unsaturated boronic ester *tert*-butyl 4-(4,4,5,5-tetramethyl-1,3,2-dioxaborolan-2-yl)-3,6-dihydropyridine-1(2H)-carboxylate was used, affording **118** in quantitative yield, which was efficiently reduced via Et_3SiH with Pd/C (90% yield) to give compound **119**. Final Boc-deprotection of the piperidinyl moiety led to the desired analogue **59** in good yields. In contrast, compound **117** was synthesized in low yield starting from intermediate **105b** using 3-fluorophenylboronic acid.

Taking advantage of a nucleophilic substitution reaction, both alkoxy and amino substituents were successfully introduced. In the case of ether substituents, the corresponding oxyanions were generated *in situ* using NaH, followed by reaction with compound **105b**, giving the desired products (**63-64**) in 64–73% yield. Amination was efficiently achieved using a non-nucleophilic base, such as K_2CO_3, and the desired amine, providing the desired compounds (**62,65-67**) with overall good yields. Subsequent Boc-moiety removal following straightforward conditions was performed for **60-61**. All transformations described above are summarized in **Scheme 3.15**.

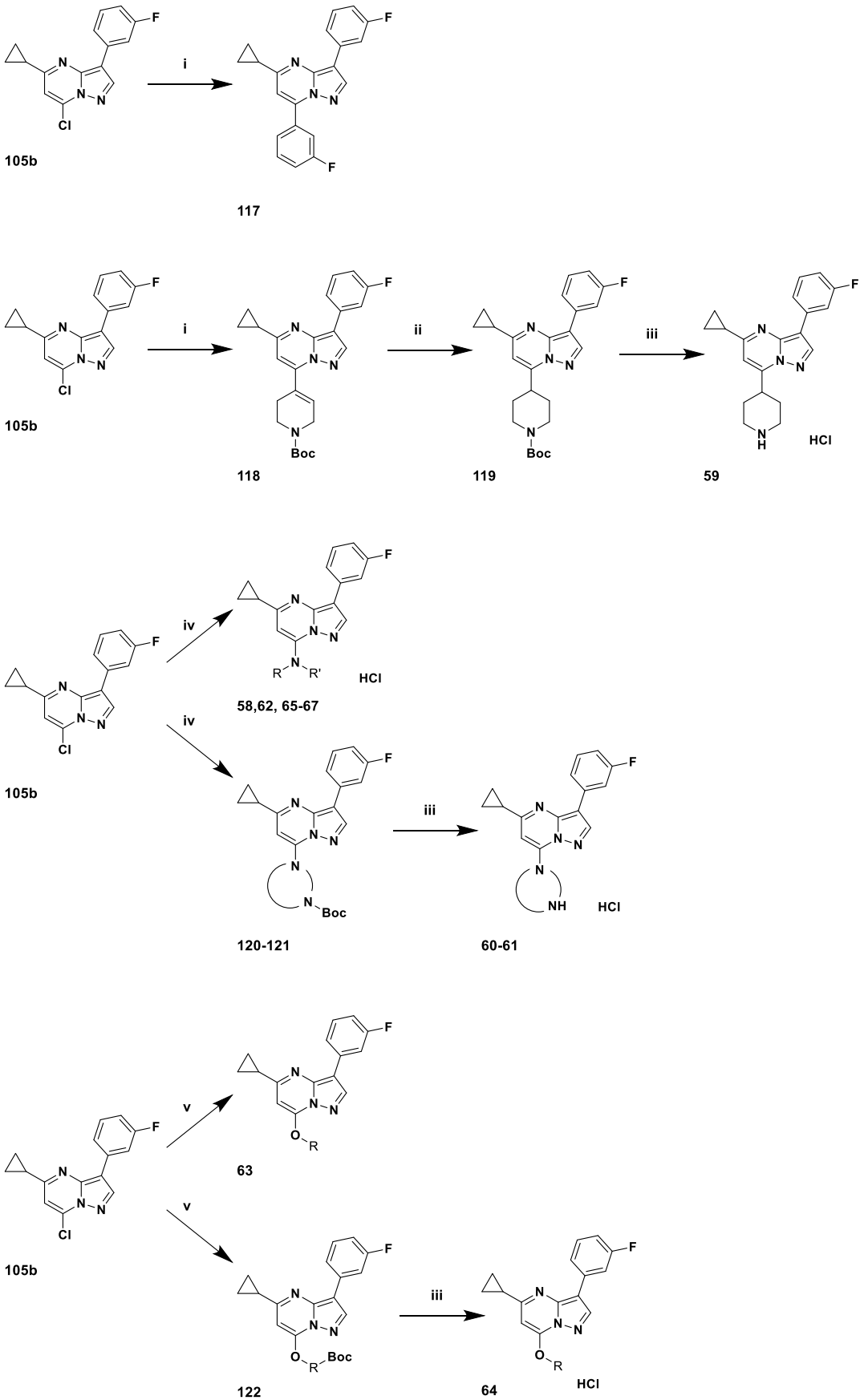

(**i**): K_2CO_3, $Pd(PPh_3)_2Cl_2$,boronic acid/boronic ester, THF, H_2O, 110°C, MW, 1h, quantitatove%; (**ii**) Et_3SiH, Pd/C, MeOH, r.t., 14h, 90%; (**iii**) HCl/MeOH, r.t., 2h, 34%; (**iv**): DIPEA, NRR', CH_3CN, reflux, o.n., 23%-quantitative; (**v**): ROH, NaH, THF, 0°C to r.t., 4h, 64-73%

Scheme 3.15. *Synthetic pathway for the synthesis of compounds* ***58-67*** *and* ***117.***

While compounds **58–67** were selected for biological evaluation, compound **117** was specifically synthesized to investigate the regioselectivity of the ring-forming reaction. This compound was analysed by $^{1}H–^{19}F$ HOESY NMR, under the same experimental conditions used for compound **44**, which bears substituents in positions 3 and 5 and displayed a clear cross-peak. In contrast, no cross-peaks between the F and a different spin system proton were observed for **117**, indicating the absence of spatial proximity between the fluorine and aromatic protons. This result supports the assignment of the phenyl substituent to position 7, thereby confirming the regioselectivity of the ring-closing reaction described in **Paragraph 3.3.3**.

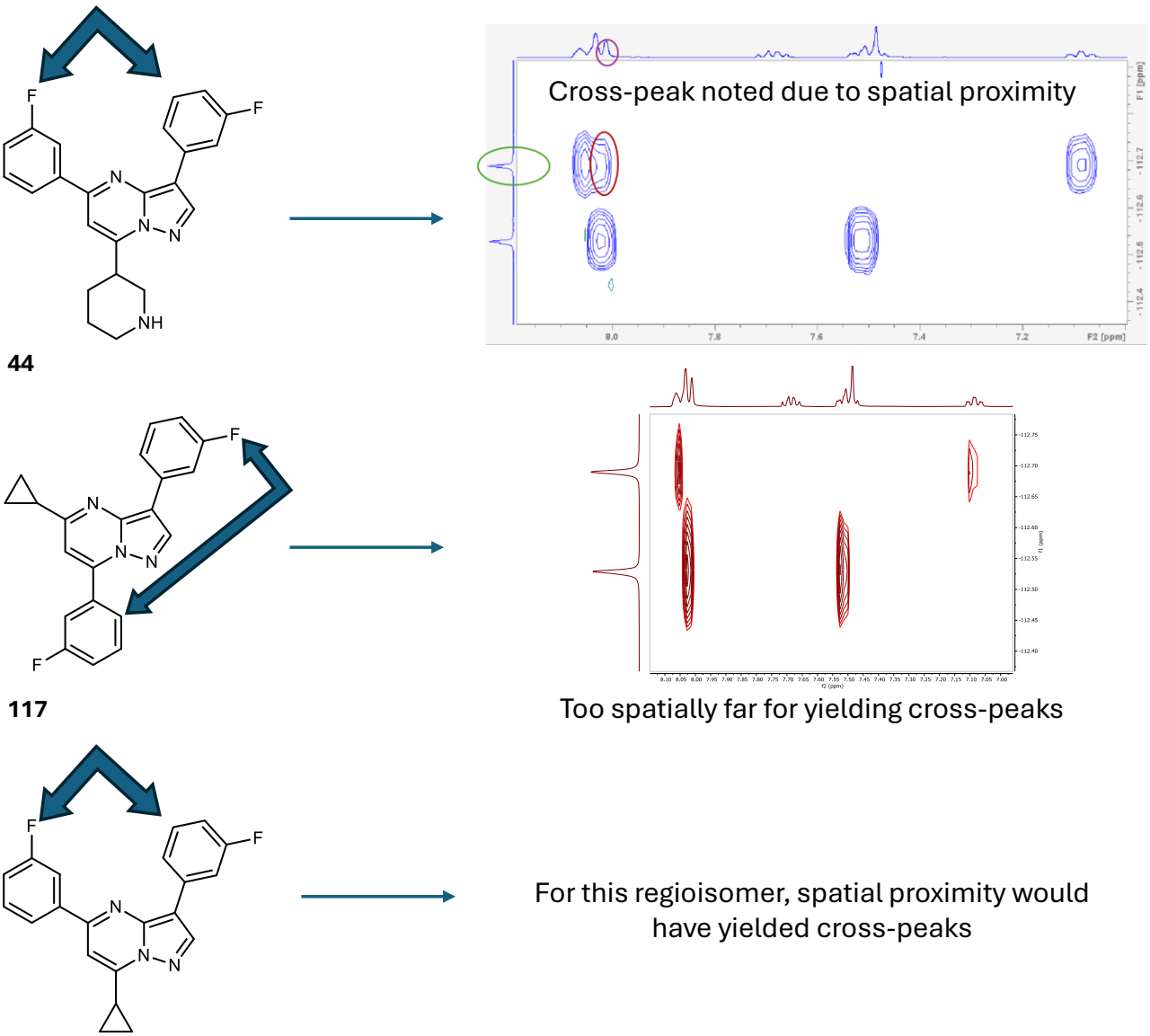

***Figure 3.16**. Representation of the $^{1}H–^{19}F$ HOESY NMR investigation rationale.*

3.7: Three-point functionalization of the pyrazolo[1,5-a]pyrimidine scaffold

Having established synthetic methodologies that enabled functionalization of all accessible positions on the central pyrazolo[1,5-a]pyrimidine scaffold and having derived a preliminary SAR profile, the next challenge was to develop new synthetic protocols capable of introducing triple substitutions onto the pyrazolo[1,5-a]pyrimidine core. A new rationale was then envisaged by combining the most favourable

substituents identified in previous studies to potentially enhance binding affinity. Since the most promising modifications were found at position 3 (i.e., 4-fluorophenyl, biphenyl, and 1,2,3,6-tetrahydro-1,1'-biphenyl groups) and position 5 (i.e., piperidinyl and cyclopentyl groups), new synthetic routes were designed to enable concurrent derivatization at these positions while maintaining the piperidine group in position 7. This strategy led to the synthesis of compounds **71-75** (**Figure 3.17**).

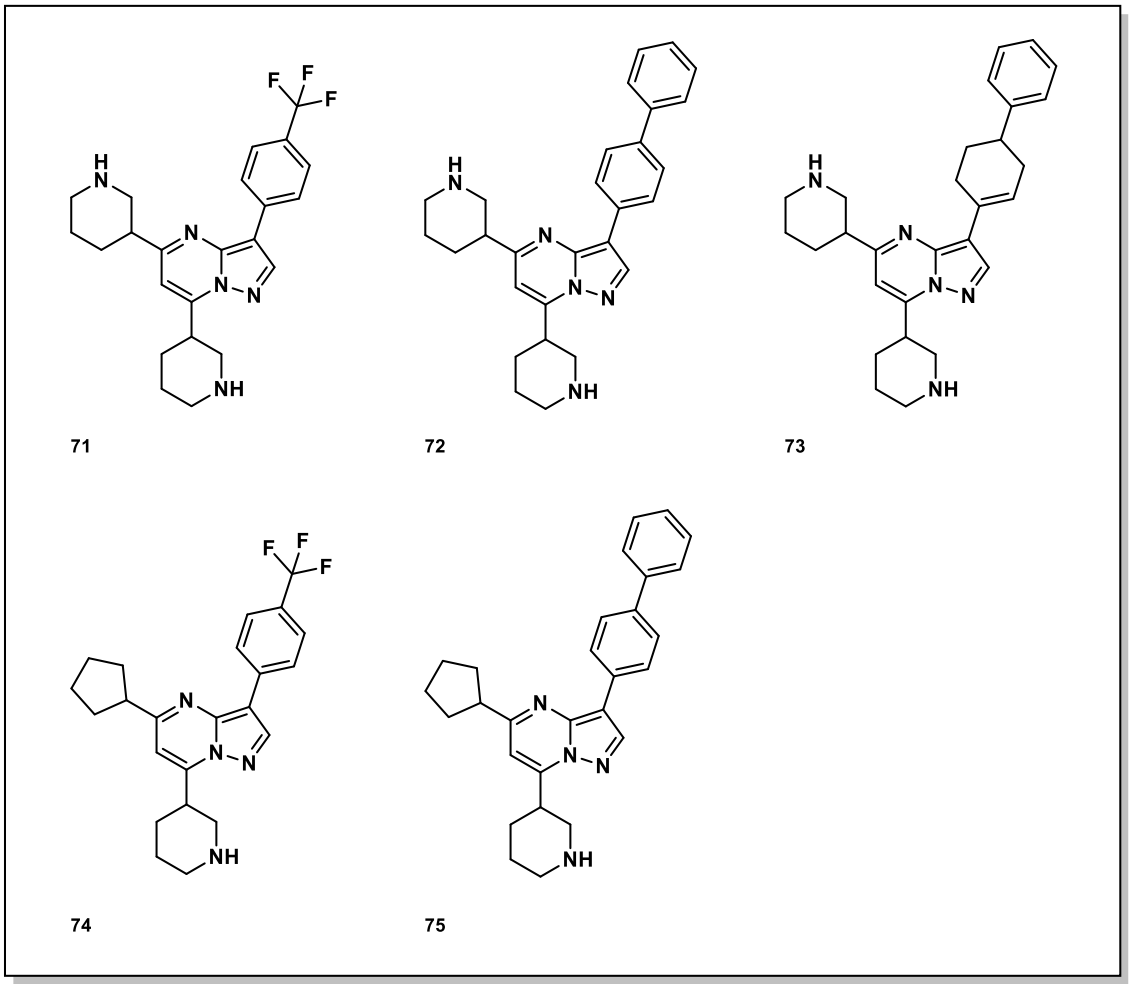

***Figure 3.17**. Structure of compounds **71-75**.*

3.7.1: Synthesis of compounds **71-73**

For the synthesis of compounds **71–73**, the synthetic route outlined in **Scheme 3.16** was developed, taking into account the broad applicability of the functionalization strategy described in **Paragraph 3.3.1** (**Scheme 3.8**). Starting from **93b**, obtained in substantial amounts as a side product in an earlier reaction sequence, a microwave-assisted Suzuki–Miyaura cross-coupling reaction was carried out using K_2CO_3, $Pd(PPh_3)_2Cl_2$, *tert*-butyl 3-(4,4,5,5-tetramethyl-1,3,2-dioxaborolan-2-yl)-5,6-dihydropyridine-1(2H)-carboxylate, and THF under the previously optimized conditions. This transformation enabled efficient functionalization at position 7, providing intermediate **123** in quantitative yield (99%). Intermediate **123** was subsequently reduced via H-cube hydrogenation, affording **124** in moderate yield (56%), primarily due to partial hydrogenation of the heterocyclic scaffold, as previously observed. The resulting intermediate **124** proved highly reactive under iodination conditions: treatment with NIS in DCM furnished the key iodinated intermediate **125** in excellent yield

(94%) without the need for chromatographic purification. Given its suitability for further cross-coupling transformations, **125** was then reacted with a series of boronic acids or boronic esters under microwave-assisted Suzuki–Miyaura conditions identical to those described above, providing intermediates **126a–c** in quantitative yield. Final compounds **71–73** were obtained, as diastereoisomeric mixtures, after Boc-deprotection. Since separation of the diastereomeric mixture proved difficult, the compounds were evaluated biochemically as such.

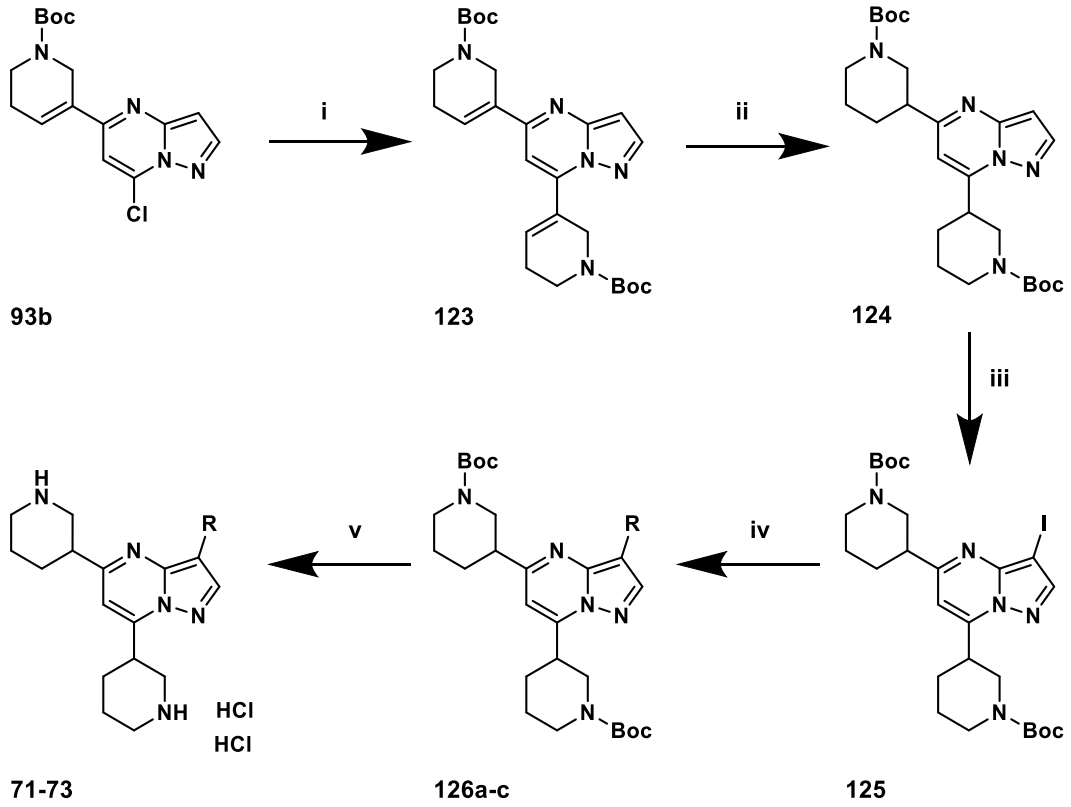

(**i**): K_2CO_3, $Pd(PPh_3)_2Cl_2$, tert-Butyl 3-(4,4,5,5-tetramethyl-1,3,2-dioxaborolan-2-yl)-5,6-dihydropyridine-1(2H)-carboxylate, THF, H_2O, 110°C, MW, 1h, 99%; (**ii**) H-cube, Pd/C, EtOH, 60°C, 1bar, 56% (**iii**) NIS, DCM, r.t., o.n., 94%, (**iv**): K_2CO_3, $Pd(PPh_3)_2Cl_2$, boronic acid/boronic esters, THF, H_2O, MW, 110°C, 1h, 40%-quantitative; (**v**): HCl/MeOH, r.t., 2-4h, 51-79%.

Scheme 3.16*. Synthetic pathway followed for the synthesis of compounds **71-73**.*

3.7.2: Synthesis of compounds **74-75**

Tracing the work developed for the synthetic pathway described in **Paragraph 3.3** (i.e., synthesis of compounds **39–42** by 1,3-ketoester condensation), the same strategy that led to the preparation of compound **41** was adapted to enable late-stage functionalization at position 3 (**Scheme 3.17)**. Starting from the commercially available β-ketoester **127**, bearing the desired cyclopentyl substituent, condensation with 3-aminopyrazole under acidic, high-temperature conditions (AcOH/toluene 1/1) afforded intermediate **128** in good yield (86%), precipitating directly from the reaction mixture and therefore requiring no chromatographic purification. Although functionalization at position 3 could, in principle, be performed at this stage, it was deliberately postponed to the final steps in order to generate a versatile intermediate (**130**) that could support the rapid preparation of multiple analogues. Chlorination of **128** was achieved using refluxing $POCl_3$, affording **129** in adequate purity to avoid

chromatographic purification (36% yield). As previously discussed, the choice of $POCl_3$ under reflux was dictated by the very poor solubility of intermediate **128** in most aprotic solvents, whereas solubility, and thus reactivity, was restored at elevated temperatures in $POCl_3$. The resulting chloride **129**, being suitably activated for cross-coupling, underwent microwave-assisted Suzuki–Miyaura coupling (K_2CO_3, $Pd(PPh_3)_2Cl_2$, *tert*-butyl 3-(4,4,5,5-tetramethyl-1,3,2-dioxaborolan-2-yl)-5,6-dihydropyridine-1(2H)-carboxylate, THF/H_2O), generating **130** in quantitative yield. Subsequent reduction of the double bond by H-cube hydrogenation (90% yield) furnished the corresponding saturated intermediate **131**, which was then halogenated (**132**), and subjected to a second microwave-assisted Suzuki–Miyaura coupling (same conditions as above) with the appropriate boronic acid to yield **144a-b** in 55-58% yield. Final Boc-deprotection afforded the target compounds **74–75** as racemic mixtures.

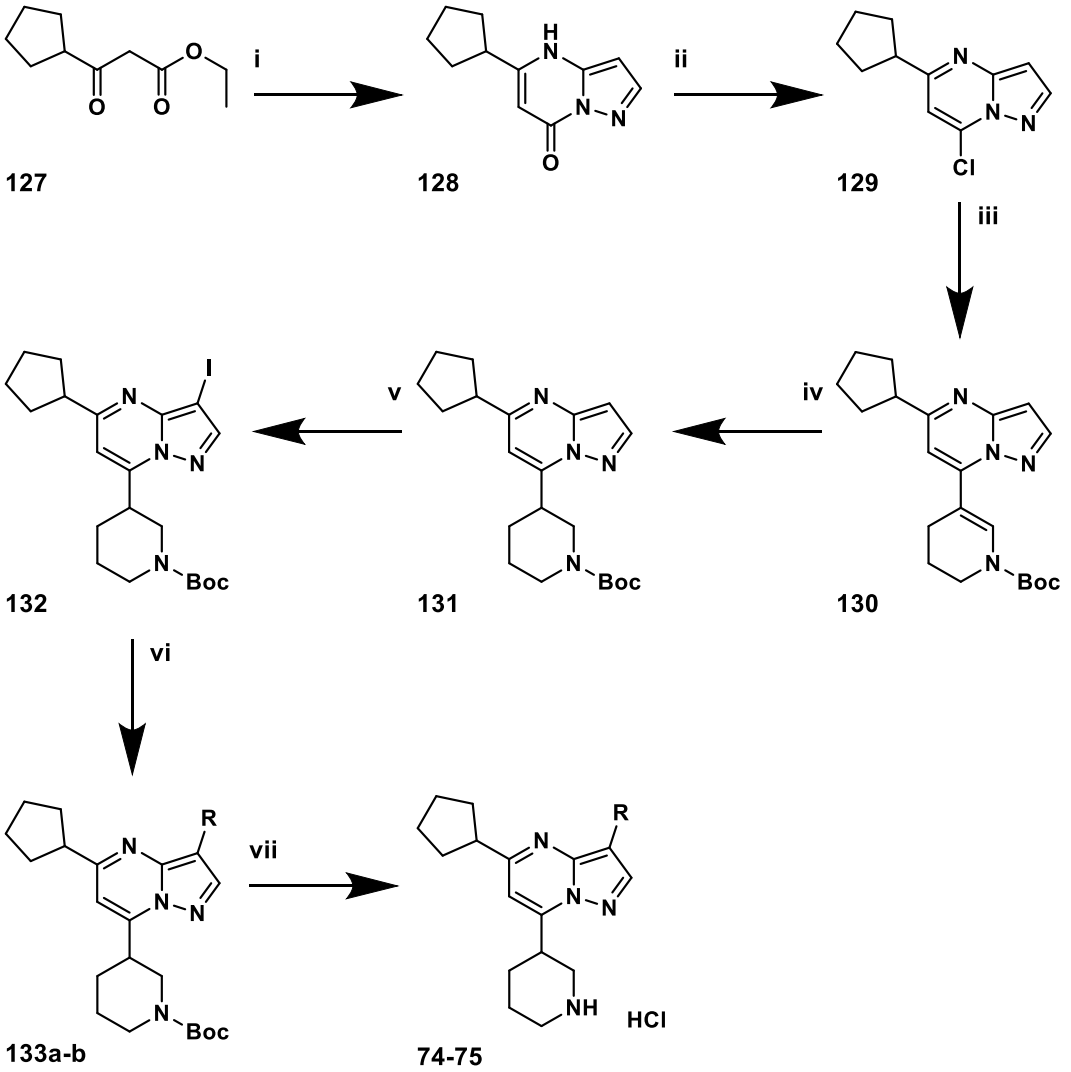

(**i**): 3-Aminopyrazole, AcOH/toluene 1/1, reflux, o.n., 86%; (**ii**) $POCl_3$, reflux, o.n., 36% (**iii**):K_2CO_3, $Pd(PPh_3)_2Cl_2$, tert-Butyl 3-(4,4,5,5-tetramethyl-1,3,2-dioxaborolan-2-yl)-5,6-dihydropyridine-1(2H)-carboxylate, THF, H_2O, 110°C, MW, 1h, quantitative; (**iv**) H-cube, EtOH, 60°C, 1bar, 90%; (**v**): NIS, DCM, r.t., on, 91%; (**vi**): K_2CO_3, $Pd(PPh_3)_2Cl_2$, boronic acid/boronic ester, THF, H_2O, 110°C, 1h, MW 55-58%; (**vii**): HCl/MeOH, r.t., 5.5h, 42-49%.

Scheme 3.17*. Synthetic pathway followed for the synthesis of compounds* ***74-75.***

3.8: Experimental part

All reagents were purchased from commercial sources and, unless otherwise specified, used as received without further purification. Anhydrous solvents were employed directly from the suppliers. Reactions were conducted in round-bottom flasks or sealed tubes and heated using either a metal heating mantle or a sand bath when required. Automated flash chromatography was carried out on a Biotage system, employing pre-packed silica gel cartridges of various dimensions (Redisep or Biotage). Reaction progress was followed by thin-layer chromatography (TLC) using UV/Vis detection (254/366 nm) and/or staining with $KMnO_4$, p-anisaldehyde, ninhydrin, or β-naphthol, as well as by UPLC-MS analysis (see below). NMR spectra were recorded at 300 K on a Bruker Avance III 400 spectrometer (400.13 MHz for ^1H, 100.62 MHz for ^{13}C) equipped with a BBI probe and Z-gradients, and on a Bruker Avance III 600 MHz instrument fitted with a 5 mm CryoProbe™ QCI 1H/19F–13C/15N–D quadruple-resonance probe, a shielded z-gradient coil, and a SampleJet™ automatic sample changer (operating at 400 and 600 MHz for ^1H, 101 and 151 MHz for ^{13}C, and 376 and 565 MHz for ^{19}F). Chemical shifts for ^1H, ^{13}C, and ^{19}F NMR spectra are reported in ppm, referencing the residual non-deuterated solvent signals: 7.26 ppm and 77.16 ppm for $CDCl_3$, 2.50 ppm and 39.52 ppm for DMSO-d_6, and 3.31 ppm and 49.15 ppm for MeOD-d_4. UPLC-MS analyses were performed on an ACQUITY UPLC BEH C_{18} column (100 x 2.1 mm ID, particle size 1.7 µm) with a VanGuard BEH C_{18} pre-column (5 x 2.1 mm ID, particle size 1.7 µm). Mobile phase was 10 mM NH_4OAc in H_2O at pH 5 adjusted with CH_3COOH (phase A) and 10 mM NH_4OAc in CH_3CN–H_2O (95:5) at pH 5.0. Three types of gradients were applied depending on the analysis: gradient “polar” (5 % to 100 % mobile phase B in 3 min) or gradient “generic” (50 % to 100 % mobile phase B in 3 min), or gradient “apolar” (5% to 50% mobile phase B in 3 min). Electrospray ionization in positive and negative modes was applied. HPLC-MS analyses were performed on a Waters ACQUITY UPLC/MS system consisting of a SQD (Single Quadrupole Detector) Mass Spectrometer equipped with an Electrospray Ionization interface and a Photodiode Array Detector. The PDA range was 210-400 nm. Analyses were performed on an ACQUITY UPLC BEH C_{18} column (100 x 2.1 mm ID, particle size 1.7 µm) with a VanGuard BEH C_{18} pre-column (5 x 2.1 mm ID, particle size 1.7 µm). Mobile phase was 10 mM NH_4OAc in H_2O at pH 5 adjusted with AcOH (A) and 10 mM NH_4OAc in MeCN-H_2O (95:5) at pH 5 (B). Generic method: start at 10% B, hold for 0.20 min, then 10-90% B in 6 min, 90-100% B in 0.10 min and 100% B hold for 0.70 min. Total run time: 7 min. Electrospray ionization in positive and negative modes.

3.8.1: General procedure 1 (GP1): NBS Bromination of position 3 of the pyrazolo[1,5-a]pyrimidine scaffold

In a 20 mL vial, the functionalized pyrazolo[1,5-a]pyrimidine (1 eq.) was dissolved in DCM (5 mL/mmol) and the mixture was cooled to 0 °C. NBS (1 eq.) was then added, and the reaction was allowed to stir overnight while warming to room temperature. Progress was monitored by TLC and UPLC-MS. Upon complete consumption of the starting material, the reaction mixture was transferred to a separatory funnel and washed with a saturated aqueous solution of Na_2CO_3. The organic layer was dried over anhydrous Na_2SO_4, filtered, and concentrated under reduced pressure to afford the desired product quantitatively.

3.8.2: General procedure 2 (GP2): General Microwave-Assisted Suzuki–Miyaura Coupling Procedure

In a microwave vial, under a nitrogen atmosphere, the brominated substrate (1 eq.), the coupling partner, a boronic acid or ester (1.2 eq.), $Pd(PPh_3)_2Cl_2$ (0.05 eq.) and K_2CO_3 (3 eq.) were dissolved in a degassed 1:1 water/THF mixture (2 mL/mmol). The reaction was carried out at 110 °C for 1 h in a CEM Discover 2.0 microwave reactor. Reaction progress was monitored by UPLC-MS analysis. Upon

completion, the mixture was filtered through Celite, concentrated under reduced pressure, and purified by automated flash chromatography (Biotage) on silica gel using a cyclohexane/ethyl acetate gradient (0–100%).

3.8.3: General procedure 3 (GP3): Boc removal

In a 7 mL vial, the Boc-protected intermediate (1 eq.) was dissolved in MeOH (25 mL/mmol), and a solution of HCl in MeOH (4 M, 5 mL/mmol) was added at room temperature. The reaction was monitored by TLC until complete disappearance of the starting material. The mixture was concentrated under reduced pressure and the residue was washed with cyclopentane and lyophilized to afford the final product as a salt.

3.8.4: General procedure 4 (GP4): Triethylsilane Reduction Protocol

In a round-bottom flask under a nitrogen atmosphere, the unsaturated olefinic intermediate (1 eq.) and Pd/C (0.1 eq.) were suspended in MeOH (30 mL/mmol). Triethylsilane (10 eq.) was added, and the reaction was monitored by UPLC-MS until complete consumption of the starting material. The crude mixture was then filtered through Celite and purified by automated flash chromatography (Biotage) using a cyclohexane/ethyl acetate gradient (0–100%).

3.8.5: General procedure 5 (GP5): amide coupling on 7-(1-(tert-butoxycarbonyl)piperidin-3-yl)pyrazolo[1,5-a]pyrimidine-3-carboxylic acid

In a vial under a nitrogen atmosphere at room temperature, 7-(1-(tert-butoxycarbonyl)piperidin-3-yl)pyrazolo[1,5-a]pyrimidine-3-carboxylic acid (1 eq.) was dissolved in DMF (10 mL/mmol), and HATU (1 eq.) along with DIPEA (3 eq.) were added. After stirring for 1 h, the desired amine (1 eq.) was added to the reaction mixture. The reaction was stirred overnight and monitored by UPLC-MS. Upon complete consumption of the starting material, the mixture was transferred to a separatory funnel, diluted with ethyl acetate, and washed successively with saturated NH_4Cl and saturated $NaHCO_3$ solutions. The organic layer was dried over anhydrous Na_2SO_4 and concentrated under reduced pressure. The crude mixture was then filtered through Celite and purified by automated flash chromatography (Biotage) using a cyclohexane/ethyl acetate gradient (0–100%).

3.8.6: General procedure 6 (GP6): amino pyrazole cyclization

Into a round-bottom flask, the 1,3-ketoester (1 eq) was solubilized in a 1:1 mixture of acetic acid:toluene (1.0 ml/mmol), and the functionalized aminopyrazole (1 eq) was added. The reaction was stirred at 120°C overnight and monitored by UPLC-MS. The product was obtained by precipitation in reaction media and washed with toluene, obtaining a white solid. This was used in the next reaction without further purification.

3.8.7: General procedure 7 (GP7): substitution reaction on an aromatic activated chlorine (position 7 derivatization)

In a 7 mL vial under a nitrogen atmosphere, the activated chlorinated substrate (1 eq.) was dissolved in dry acetonitrile (10 mL/mmol), and K_2CO_3 (2 eq.) together with the desired nucleophile (1.5 eq.) were added. The reaction was kept stirring at 60°C and monitored by TLC. Upon complete disappearance of the starting material, the reaction mixture was transferred to a separatory funnel, diluted with ethyl acetate, and washed with a saturated NH_4Cl solution. The organic phase was collected, dried over anhydrous Na_2SO_4, and concentrated under reduced pressure.

3.8.8: General procedure 8 (GP8): $POCl_3$ mediated Hydroxy-to-Chloro Conversion

In a round-bottom flask under a nitrogen atmosphere, the hydroxyl-bearing intermediate was dissolved in $POCl_3$ (1 mL/mmol) and stirred at 100 °C overnight, with reaction progress monitored by UPLC. The mixture was cooled to 0 °C and quenched with saturated Na_2CO_3 solution, then transferred to a separatory funnel with DCM and washed again with saturated Na_2CO_3. The organic phase was dried over anhydrous Na_2SO_4 and concentrated under reduced pressure. The resulting crude material was used directly in the next reaction step without further purification.

3.8.9: General procedure 9 (GP9): functionalization of the piperidine nitrogen by substitution reactions

In a round-bottom flask under a nitrogen atmosphere, compound **1** was dissolved in dry DMF (20 mL/mmol), and DIPEA (5 eq.), NaI (1 eq.), and the desired chloride (1.2 eq.) were added. The reaction mixture was heated to 80 °C and stirred overnight, with progress monitored by UPLC-MS. Upon complete consumption of the starting material, the reaction was concentrated by evaporation under a stream of air and purified by automated flash chromatography (Biotage) using a DCM/MeOH (1 M NH_3) gradient (0–20%).

3.8.10: General procedure 10 (GP10): hydroxy functionalization of position 7

In a round-bottom flask under a nitrogen atmosphere at 0 °C, NaH (1 eq.) and the desired alcohol (1 eq.) were suspended in dry THF (10 mL/mmol). After 30 min of stirring, the activated chloride (1 eq.) was added, and the reaction mixture was allowed to warm to room temperature and stirred overnight. Upon complete disappearance of the starting material, the reaction mixture was transferred to a separatory funnel, diluted with ethyl acetate, and washed with saturated NH_4Cl solution. The organic layer was collected, dried over anhydrous Na_2SO_4, and concentrated under reduced pressure.

3.9: Compounds synthesis

3.9.1: Synthesis of compounds **1-14, 18-23**

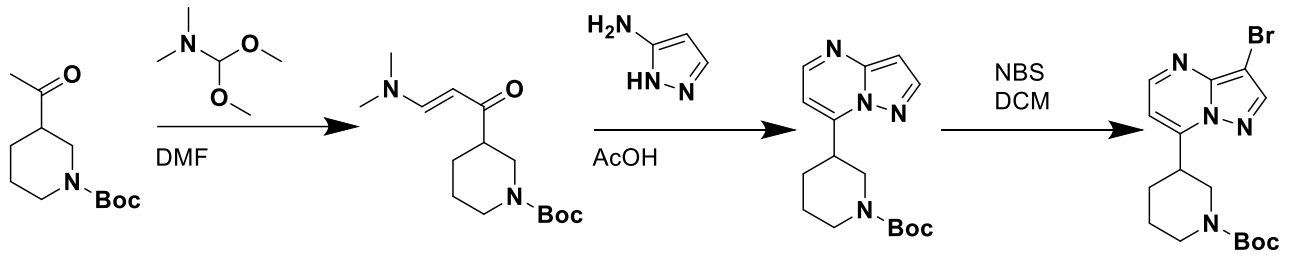

79 **78** **77** **76**

Rac-tert-Butyl (*E*)-3-(3-(dimethylamino)acryloyl)piperidine-1-carboxylate (78). To a solution of *tert*-butyl 3-acetylpiperidine-1-carboxylate (220 mg, 0.97 mmol) in DMF (1 mL) was added 1,1-dimethoxy-N,N-dimethylmethanamine (129 µL, 1.00 mmol). The reaction mixture was stirred at 120 °C for 24 hours in a nitrogen atmosphere. An additional portion of 1,1-dimethoxy-N,N-dimethylmethanamine (63 µL, 0.50 mmol) was then added, and stirring was continued for a further 4 hours. The reaction progress was monitored by UPLC-MS until complete consumption of the starting material was observed (total reaction time 28h). Upon completion, the reaction mixture was concentrated under reduced pressure

to afford a yellow oil, which was used directly in the subsequent step without further purification. **UPLC-MS**: r.t. = 1.83 (generic method). **MS (ESI)** m/z calc [M+H]+: 283.20, found 283.7.

Rac-tert-Butyl 3-(pyrazolo[1,5-a]pyrimidin-7-yl)piperidine-1-carboxylate (77). To a solution of *tert*-butyl (*E*)-3-(3-(dimethylamino)acryloyl)piperidine-1-carboxylate (theoretical, 0.97 mmol) in acetic acid (2 mL) was added 3-aminopyrazole (0.97 mmol). The reaction mixture was stirred under a nitrogen atmosphere at 80 °C for 16 hours. Reaction progress was monitored by UPLC-MS. Upon disappearance of the starting material, the mixture was diluted with ethyl acetate and washed successively with a saturated solution of K_2CO_3 (2 × 10 mL) and a saturated solution of NH_4Cl (2 × 10 mL). The organic layer was collected and concentrated under reduced pressure. The crude product was purified by automated flash column chromatography (gradient elution: pentane/ethyl acetate up to 30% ethyl acetate), affording the desired compound as a yellow oil (163 mg, 54%). **UPLC-MS**: R.t. =2.08 (generic method). **MS (ESI)** m/z calc [M+H]+: 303.18, found 303.2.

Rac-tert-Butyl 3-(3-bromopyrazolo[1,5-a]pyrimidin-7-yl)piperidine-1-carboxylate (76). Starting from **77** (163 mg, 0.54 mmol) and following **GP1**, after 16h reaction time, the title compound was obtained as a yellow oil (205 mg, quantitative). **UPLC-MS: R.t. =**1.27 (generic method). **MS (ESI)** m/z calc [M+H]+: 381.1, found 381.09

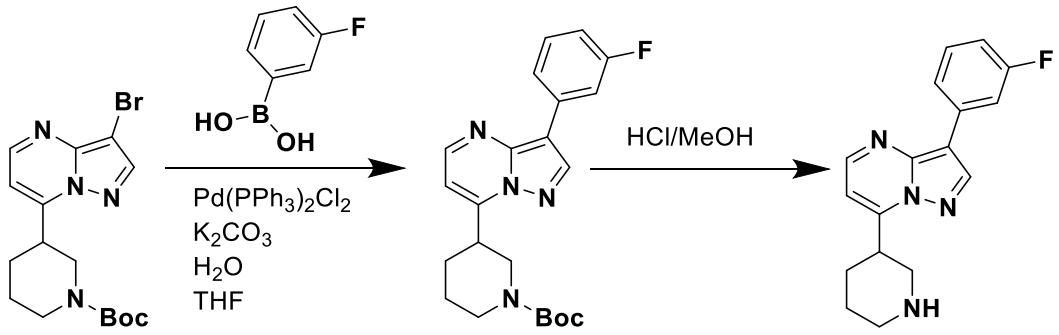

76 **80a** **1**

Rac-tert-Butyl 3-(3-(3-fluorophenyl)pyrazolo[1,5-a]pyrimidin-7-yl)piperidine-1-carboxylate (80a). Starting from **76** (37 mg, 0.1 mmol), following **GP2** and using (3-fluorophenyl)boronic acid as the coupling partner, the title compound was synthesized as a yellow oil (26 mg, 65%). Reaction followed by TLC.

Rac-3-(3-fluorophenyl)-7-(piperidin-3-yl)pyrazolo[1,5-a]pyrimidine (1). Starting from **80a** (25 mg, 0.65 mmol), following **GP3**, after 4h reaction time and automated flash chromatography (Biotage), using silica and as eluent phase DCM/MeOH gradient 0 to 20%, the title compound was synthesized as a yellow powder in its hydrochloride salt form (14 mg, 72%). **HPLC-MS: R.t. =** 2.12 (generic method). **MS (ESI)** m/z calc [M+H]+: 297.15, found 297.05. **^{1}H NMR (400 MHz, DMSO)** δ 8.84 (s, 1H), 8.64 (d, *J* = 4.4 Hz, 1H), 8.08 – 7.98 (m, 2H), 7.47 (td, *J* = 8.1, 6.4 Hz, 1H), 7.11 – 7.01 (m, 2H), 3.67 (tt, *J* = 10.6, 3.5 Hz, 1H), 2.99 (d, *J* = 12.4 Hz, 1H), 2.70 (dd, *J* = 11.9, 10.2 Hz, 1H), 2.58 (td, *J* = 12.0, 3.0 Hz, 1H), 2.13 (d, *J* = 12.4 Hz, 1H), 1.84 – 1.66 (m, 2H), 1.65 – 1.50 (m, 1H). **^{13}C NMR (101 MHz, DMSO)** δ 163.07 (d, *J* = 241.7 Hz), 152.69, 150.89, 145.16, 142.73, 135.01 (d, *J* = 9.0 Hz), 131.00 (d, *J* = 8.8 Hz), 121.97 (d, *J* = 2.6 Hz), 112.85 (d, *J* = 21.1 Hz), 112.40 (d, *J* = 22.8 Hz), 108.26 (d, *J* = 2.5 Hz), 106.13, 49.77, 46.43, 37.68, 28.37, 26.09.

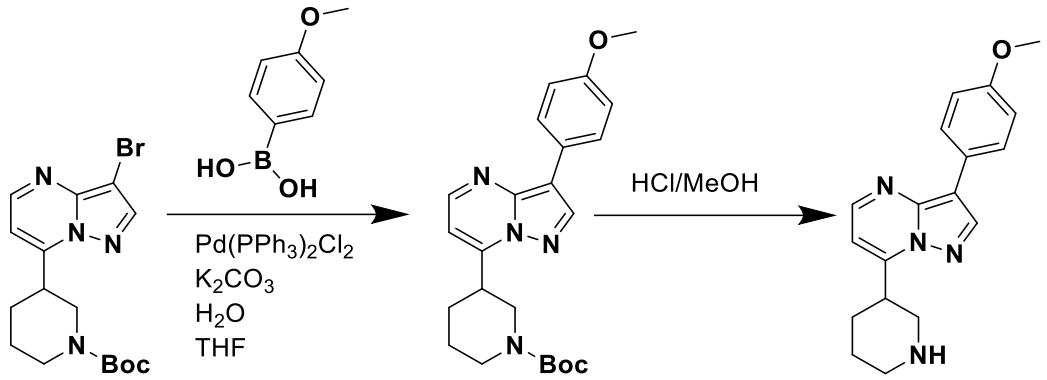

76 **80b** **2**

Rac-t*ert*-Butyl 3-(3-(4-methoxyphenyl)pyrazolo[1,5-a]pyrimidin-7-yl)piperidine-1-carboxylate (80b). Starting from **76** (38 mg, 0.1 mmol), following **GP2** and using (4-methoxyphenyl)boronic acid as the coupling partner, the title compound was synthesized as a yellow oil (16 mg, 39%). **UPLC-MS: R.t. =**1.84 (apolar method). **MS (ESI)** m/z calc [M+H]+: 409.22, found 409.0.

Rac-3-(4-methoxyphenyl)-7-(piperidin-3-yl)pyrazolo[1,5-a]pyrimidine (2). Starting from **80b** (16 mg, 0.039 mmol) and following **GP3**, after 2h reaction time, the title compound was synthesized as a yellow powder in its hydrochloride salt form (14 mg, quantitative). **HPLC-MS**: R.t. =2.83 (generic method). **MS (ESI)** m/z calc [M+H]+: 309.17, found 309.22. **^{1}H NMR (400 MHz, DMSO)** δ 9.24 (s, 1H), 8.66 (s, 2H), 8.56 (d, *J* = 4.3 Hz, 2H), 8.04 – 7.96 (m, 4H), 7.00 – 6.92 (m, 6H), 3.97 (s, 1H), 3.72 (s, 6H), 3.58 (d, *J* = 11.9 Hz, 2H), 3.30 (s, 3H), 3.19 (t, *J* = 12.1 Hz, 4H), 2.93 – 2.83 (m, 2H), 2.14 (d, *J* = 11.2 Hz, 2H), 1.91 – 1.70 (m, 6H). **^{13}C NMR (101 MHz, DMSO)** δ 158.23, 150.07, 149.04, 144.54, 142.08, 127.54, 124.76, 114.64, 110.00, 106.02, 55.59, 44.86, 43.72, 34.17, 26.08, 22.29.

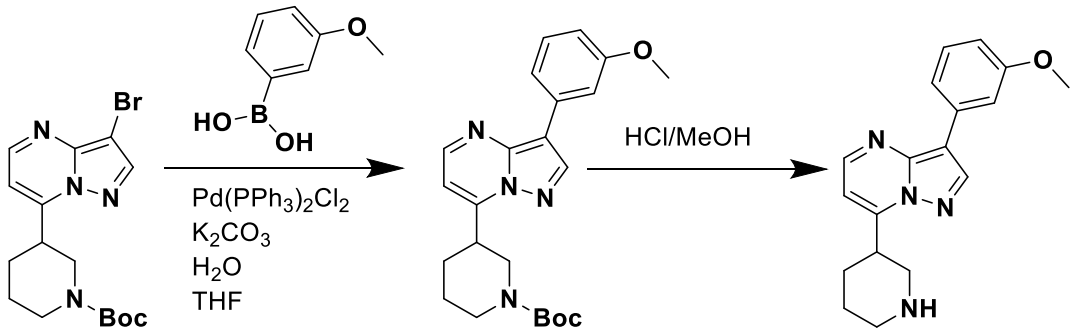

76 **80c** **3**

Rac-t*ert*-Butyl 3-(3-(3-methoxyphenyl)pyrazolo[1,5-a]pyrimidin-7-yl)piperidine-1-carboxylate (80c). Starting from **76** (38 mg, 0.1 mmol), following **GP2** and using (3-methoxyphenyl)boronic acid as the coupling partner, the title compound was synthesized as a yellow oil (41 mg, quantitative). **UPLC-MS**: R.t. =1.84 (apolar method). **MS (ESI)** m/z calc [M+H]+: 409.22, found 409.0.

Rac-3-(3-methoxyphenyl)-7-(piperidin-3-yl)pyrazolo[1,5-a]pyrimidine (3). Starting from **80c** (41 mg, 0.1 mmol) and following **GP3,** after 3h, the title compound was synthesized as a yellow powder in its hydrochloride salt form (29 mg, 56%). **UPLC-MS**: R.t. =1.74 (polar method). **MS (ESI)** m/z calc [M+H]+: 309.17, found 308.9. **1H NMR (400 MHz, DMSO-d6)**: δ 9.27 (s, 1H), 8.77 (s, 2H), 8.61 (d, *J* = 4.3 Hz, 2H), 7.72 – 7.64 (m, 4H), 7.29 (t, *J* = 7.9 Hz, 2H), 7.02 (d, *J* = 4.4 Hz, 2H), 6.77 (ddd, *J* = 8.2, 2.5, 1.0 Hz, 2H), 3.99 (s, 1H), 3.76 (s, 6H), 3.59 (d, *J* = 11.5 Hz, 2H), 3.31 (s, 2H), 3.20 (t, *J* = 12.1 Hz, 4H), 2.94 – 2.83 (m, 2H), 2.14 (d, *J* = 11.5 Hz, 2H), 1.92 – 1.71 (m, 6H). **^{13}C NMR (101 MHz, DMSO)** δ 160.07, 150.60, 149.26,

145.04, 142.79, 133.60, 130.18, 118.69, 112.08, 111.82, 109.80, 106.32, 55.56, 44.84, 43.70, 34.17, 26.10, 22.26.

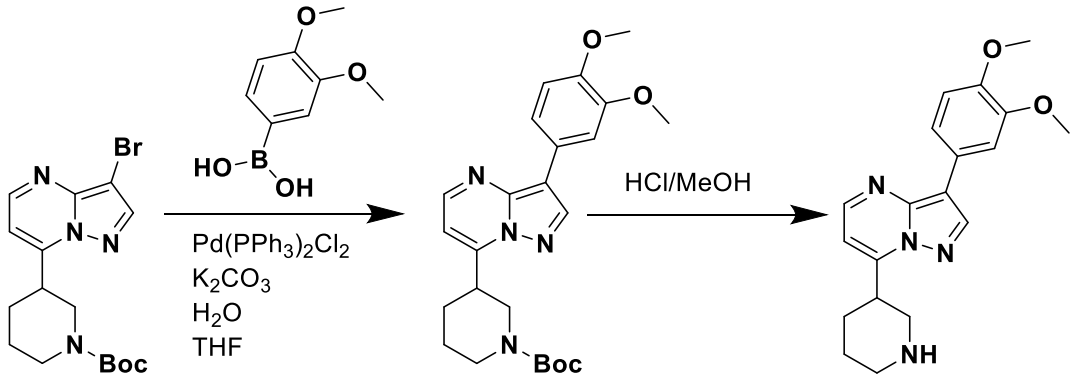

76 **80d** **4**

Rac-t*ert*-Butyl 3-(3-(3,4-dimethoxyphenyl)pyrazolo[1,5-a]pyrimidin-7-yl)piperidine-1-carboxylate (80d). Starting from **76** (38 mg, 0.1 mmol), following **GP2** and using (3,4-dimethoxyphenyl)boronic acid as the coupling partner, the title compound was synthesized as a yellow oil (30 mg, 68%). **UPLC-MS**: R.t. =1.53 (apolar method). **MS (ESI)** m/z calc [M+H]+: 439.23, found 439.0.

Rac-3-(3,4-dimethoxyphenyl)-7-(piperidin-3-yl)pyrazolo[1,5-a]pyrimidine (4). Following **GP3**, starting from **80d** (30 mg, 0.068 mmol), after 1h 30min reaction time, the title compound was synthesized as a yellow powder in its hydrochloride salt form (23 mg, 83%). **UPLC-MS**: R.t. =1.53 (polar method). **MS (ESI)** m/z calc [M+H]+: 339.18, found 338.9. **^{1}H NMR (400 MHz, DMSO)** δ 9.21 (s, 1H), 8.78 (s, 3H), 8.65 (d, J = 4.3 Hz, 3H), 7.77 – 7.68 (m, 6H), 7.08 – 7.01 (m, 6H), 4.04 (s, 2H), 3.85 (s, 9H), 3.79 (s, 9H), 3.66 (d, J = 11.4 Hz, 3H), 3.25 (t, J = 12.1 Hz, 5H), 2.96 (t, J = 11.6 Hz, 3H), 2.21 (d, J = 10.4 Hz, 3H), 1.98 (d, J = 12.1 Hz, 3H), 1.94 – 1.79 (m, 6H). **^{13}C NMR (101 MHz, DMSO)** δ 150.14, 149.40, 147.95, 144.59, 142.31, 125.11, 118.84, 112.73, 110.50, 110.15, 106.02, 56.15, 56.05, 40.61, 40.40, 40.19, 39.98, 39.77, 39.56, 39.36, 34.20, 26.10.

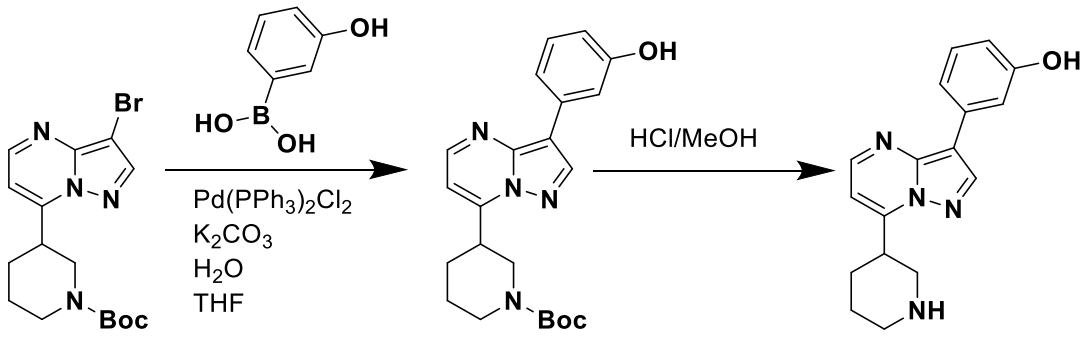

76 **80e** **5**

Rac-*tert*-Butyl 3-(3-(3-hydroxyphenyl)pyrazolo[1,5-a]pyrimidin-7-yl)piperidine-1-carboxylate (80e). Starting from **76** (38 mg, 0.1 mmol), following **GP2** and using (3-hydroxyphenyl)boronic acid as the coupling partner, the title compound was synthesized as a yellow oil. (16 mg, 41%). **UPLC-MS**: R.t. =1.15 (apolar method). **MS (ESI)** m/z calc [M+H]+: 395.20, found 395.0.

Rac-3-(7-(piperidin-3-yl)pyrazolo[1,5-a]pyrimidin-3-yl)phenol (5). Starting from **80e** (16 mg, 0.041 mmol), following **GP3,** after 3h reaction time, the title compound was synthesized as a yellow powder in its hydrochloride salt form (12 mg, quantitative). **UPLC-MS: R.t. =**1.33 (polar method). **MS (ESI)** m/z

calc [M+H]+: 294.15, found 294.9. **^{1}H NMR (400 MHz, DMSO)** δ 9.45 (s, 1H), 9.28 (s, 2H), 8.74 (s, 1H), 8.67 (d, *J* = 4.4 Hz, 1H), 7.64 (t, *J* = 2.0 Hz, 1H), 7.53 (dt, *J* = 7.7, 1.3 Hz, 1H), 7.23 (t, *J* = 7.9 Hz, 1H), 7.08 (d, *J* = 4.3 Hz, 1H), 6.68 (dd, *J* = 8.0, 2.4 Hz, 1H), 4.05 (t, *J* = 11.3 Hz, 1H), 3.66 (d, *J* = 12.0 Hz, 1H), 3.52 (s, 1H), 3.39 (t, *J* = 12.1 Hz, 1H), 3.27 (t, *J* = 10.5 Hz, 1H), 2.97 (d, *J* = 10.8 Hz, 1H), 2.25 – 2.18 (m, 3H). **^{13}C NMR (101 MHz, DMSO)** δ 158.09, 150.39, 149.15, 144.92, 142.62, 133.41, 130.03, 117.18, 113.28, 110.16, 106.23, 44.84, 43.72, 34.17, 26.07, 22.26.

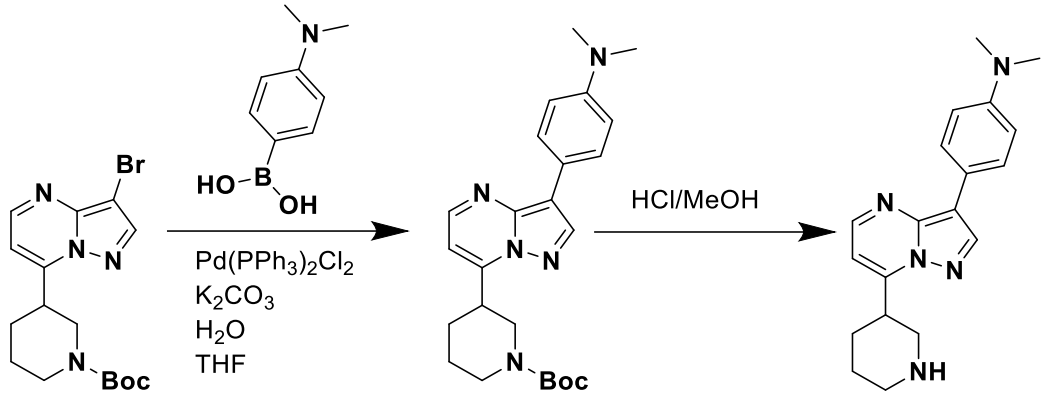

76 **80f** **6**

Rac-*tert*-Butyl 3-(3-(4-(dimethylamino)phenyl)pyrazolo[1,5-a]pyrimidin-7-yl)piperidine-1-carboxylate (80f). Starting from **76** (38 mg, 0.1 mmol), following **GP2** and using (4-(dimethylamino)phenyl)boronic acid as the coupling partner, the title compound was synthesized as a yellow oil (19 mg, 46%). **UPLC-MS**: R.t. =1.99 (apolar method). **MS (ESI)** m/z calc [M+H]+: 422.25, found 422.0.

Rac-N,N-Dimethyl-4-(7-(piperidin-3-yl)pyrazolo[1,5-a]pyrimidin-3-yl)aniline (6). Starting from **80f** (19 mg, 0.046 mmol) and following **GP3**, after 4h reaction time and automated flash chromatography (Biotage), using silica and as eluent phase DCM/MeOH*NH_3 1M gradient 0 to 20%, the title compound was synthesized as a yellow powder in its hydrochloride salt form (5 mg, 47%). **HPLC-MS**: R.t. =3.10 (generic method). **MS (ESI)** m/z calc [M+H]+: 322.11, found 322.20. **^{1}H NMR (400 MHz, DMSO)** δ 8.62 (s, 2H), 8.54 (d, *J* = 4.3 Hz, 2H), 7.99 – 7.90 (m, 4H), 6.97 (d, *J* = 4.3 Hz, 2H), 6.86 – 6.77 (m, 4H), 3.72 (d, *J* = 10.9 Hz, 2H), 3.09 (d, *J* = 8.6 Hz, 2H), 2.93 (s, 11H), 2.83 (t, *J* = 11.3 Hz, 3H), 2.68 (t, *J* = 11.8 Hz, 2H), 2.15 (d, *J* = 11.4 Hz, 2H), 1.76 (t, *J* = 12.9 Hz, 4H), 1.67 (t, *J* = 12.6 Hz, 2H), 1.24 (s, 1H). **^{13}C NMR (101 MHz, DMSO)** δ 149.48, 149.37, 144.25, 141.46, 127.11, 120.44, 113.08, 110.42, 105.38, 48.54, 45.79, 36.74, 27.78, 25.18.

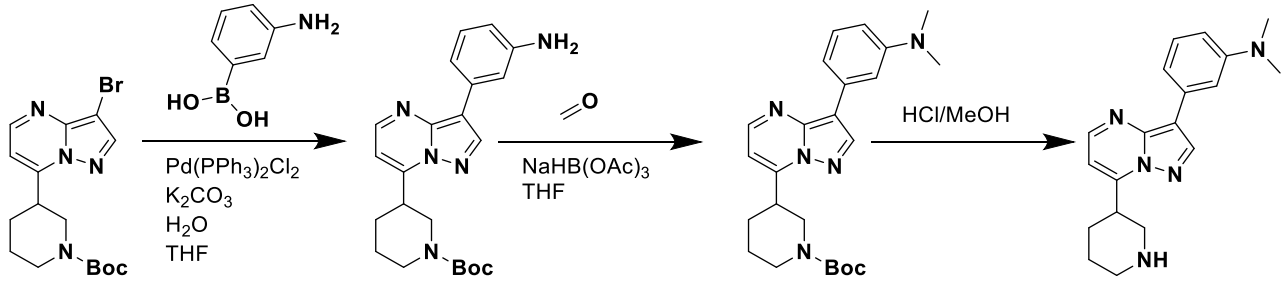

76 **134** **80g** **7**

Rac-*tert*-Butyl 3-(3-(3-aminophenyl)pyrazolo[1,5-a]pyrimidin-7-yl)piperidine-1-carboxylate (134). Starting from **76** (38 mg, 0.1 mmol), following **GP2** and using (3-aminophenyl)boronic acid as the

coupling partner, the title compound was synthesized as a yellow oil (26 mg, 66%). **UPLC-MS: R.t. =**1.16 (apolar method). **MS (ESI)** m/z calc [M+H]+: 394.22, found 394.0.

Rac-*tert*-Butyl 3-(3-(3-(dimethylamino)phenyl)pyrazolo[1,5-a]pyrimidin-7-yl)piperidine-1-carboxylate (80g). In a vial, **134** (26 mg, 0.066 mmol, 1eq) was dissolved in THF (20 mL/mmol). Formaldehyde (10 mg, 0.33 mmol, 5 eq.) and $NaBH(OAc)_3$ (70 mg, 0.33 mmol, 5 eq.) were added. After 6h reaction time, 5 eq of formaldehyde and 5 eq. of $NaBH(OAc)_3$ were again added. The reaction was monitored by UPLC until complete disappearance of the starting material. After 12 h, the reaction was quenched with saturated Na_2CO_3 solution and transferred to a separatory funnel. The mixture was extracted with AcOEt, and the combined organic layers were concentrated under reduced pressure. Purification by automated flash chromatography (Biotage; cyclohexane/AcOEt gradient 0–70%) afforded the title compound as a yellow oil (16 mg, 57%).

Rac-N,N-dimethyl-3-(7-(piperidin-3-yl)pyrazolo[1,5-a]pyrimidin-3-yl)aniline (7). Starting from **80g** (16 mg, 0.038 mmol) and following **GP3**, after 2h reaction time and automated flash chromatography (Biotage), using silica and as eluent phase DCM/MeOH*NH_3 1M gradient 0 to 20%, the title compound was synthesized as a yellow powder in its hydrochloride salt form (10 mg, 73%). **HPLC-MS**: R.t. =3.13 (generic method). **MS (ESI)** m/z calc [M+H]+: 322.22, found 322.30. **^{1}H NMR (400 MHz, DMSO)** δ 9.53 (d, *J* = 11.2 Hz, 1H), 9.27 (d, *J* = 10.5 Hz, 1H), 8.84 (s, 1H), 8.69 (d, *J* = 4.4 Hz, 1H), 7.87 (s, 2H), 7.43 (s, 1H), 7.10 (d, *J* = 4.4 Hz, 1H), 4.08 (t, *J* = 12.1 Hz, 1H), 3.31 (dt, *J* = 34.3, 10.5 Hz, 3H), 3.08 (s, 4H), 2.97 (d, *J* = 11.5 Hz, 1H), 2.22 (d, *J* = 11.6 Hz, 1H), 2.00 – 1.81 (m, 3H). **^{13}C NMR (151 MHz, DMSO)** δ 150.28, 148.83, 144.62, 142.38, 129.75, 105.95, 44.32, 43.21, 33.63, 25.62, 21.76.

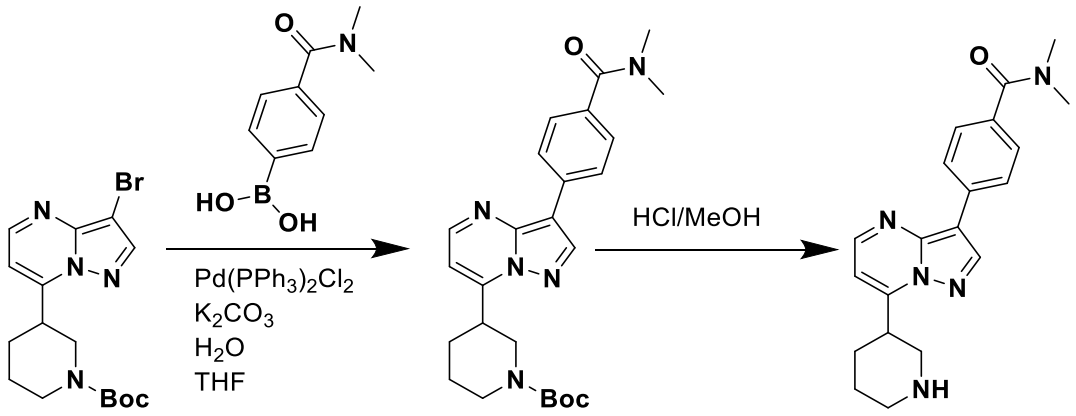

76 **80h** **8**

Rac-*tert*-Butyl 3-(3-(4-(dimethylcarbamoyl)phenyl)pyrazolo[1,5-a]pyrimidin-7-yl)piperidine-1-carboxylate (80h). Starting from **76** (19 mg, 0.05 mmol), following **GP2** and using (4-(dimethylcarbamoyl)phenyl)boronic acid as the coupling partner, the title compound was synthesized as a yellow oil (19 mg, 84%). **UPLC-MS**: R.t. =1.11 (apolar method). **MS (ESI)** m/z calc [M+H]+: 450.25, found 450.3.

Rac-N,N-dimethyl-4-(7-(piperidin-3-yl)pyrazolo[1,5-a]pyrimidin-3-yl)benzamide (8). Starting from **80h** (19 mg, 0.04 mmol), following **GP3**, after 1h30min reaction time and automated flash chromatography (Biotage), using silica and as eluent phase DCM/MeOH gradient 0 to 20%, the title compound was synthesized as a yellow powder in its hydrochloride salt form (11 mg, 68%). **UPLC-MS:** R.t. =1.23 (generic method). **MS (ESI)** m/z calc [M+H]+: 350.19, found 350.2. **^{1}H NMR (400 MHz, DMSO)** δ 9.45 (s, 2H), 8.89 (s, 1H), 8.70 (d, *J* = 4.3 Hz, 1H), 8.27 – 8.19 (m, 2H), 7.53 – 7.45 (m, 2H), 7.12 (d, *J* = 4.4 Hz, 1H), 4.07 (t, 1H), 3.64 (d, *J* = 11.9 Hz, 1H), 3.31 – 3.21 (m, 2H), 2.99 (s, 6H), 2.22 (d, *J* = 11.8 Hz,

1H), 1.97 – 1.94 (m, 1H), 1.94 – 1.80 (m, 2H). **^{13}C NMR (101 MHz, DMSO)** δ 170.54, 150.87, 149.56, 145.20, 142.83, 134.23, 133.48, 128.08, 125.74, 109.24, 106.52, 44.88, 43.70, 40.62, 40.41, 40.20, 39.99, 39.78, 39.57, 39.36, 34.26, 26.22, 22.33.

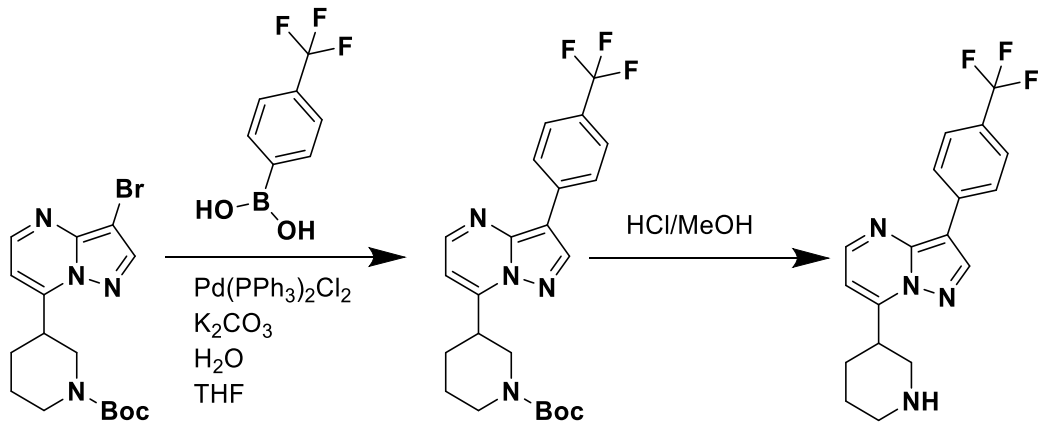

76 **80i** **9**

Rac-*tert*-Butyl 3-(3-(4-(trifluoromethyl)phenyl)pyrazolo[1,5-a]pyrimidin-7-yl)piperidine-1-carboxylate (80i). Starting from **76** (38 mg, 0.1 mmol), following **GP2** and using (4-(trifluoromethyl)phenyl)boronic acid as the coupling partner, the title compound was synthesized as a yellow oil (19 mg, 42%). **MS (ESI)** m/z calc [M+H]+: 447.20, found 447.0.

Rac-7-(piperidin-3-yl)-3-(4-(trifluoromethyl)phenyl)pyrazolo[1,5-a]pyrimidine (9). Starting from **80i** (19 mg, 0.042mmol) and following **GP3**, after 2h reaction time, the title compound was synthesized as a yellow powder in its hydrochloride salt form (15 mg, 93%). **HPLC-MS**: R.t. =3.80 (generic method). **MS (ESI)** m/z calc [M+H]+: 347.14, found 347.27. **^{1}H NMR (400 MHz, DMSO) δ** 9.25 (s, 1H), 8.97 (s, 2H), 8.75 (d, *J* = 4.4 Hz, 2H), 8.42 (d, *J* = 8.2 Hz, 4H), 7.81 (d, *J* = 8.3 Hz, 4H), 7.17 (d, *J* = 4.4 Hz, 2H), 4.07 (s, 1H), 3.66 (d, *J* = 11.9 Hz, 2H), 3.27 (t, *J* = 12.0 Hz, 8H), 2.96 (t, *J* = 11.3 Hz, 2H), 2.22 (d, *J* = 10.1 Hz, 2H), 2.00 – 1.82 (m, 6H). **^{13}C NMR** (101 MHz, DMSO) δ 151.36, 149.66, 143.19, 136.64, 126.36, 126.10, 108.43, 106.86, 44.91, 43.74, 34.25, 26.12, 22.30.

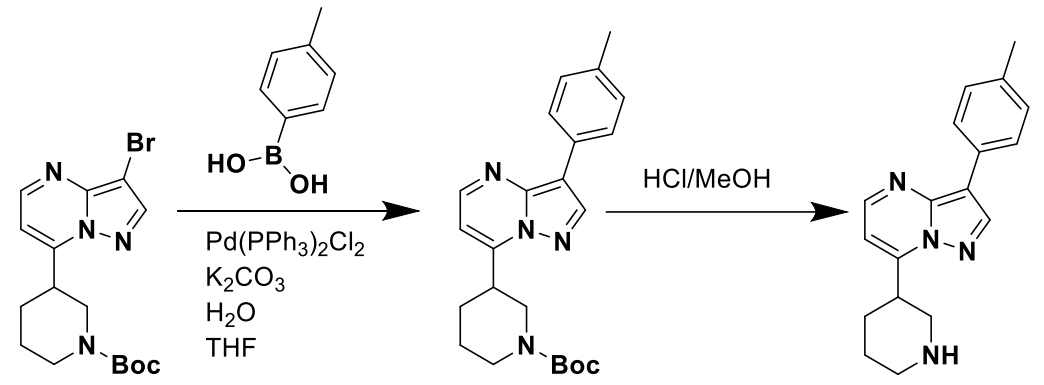

76 **80l** **10**

Rac-tert-butyl 3-(3-(p-tolyl)pyrazolo[1,5-a]pyrimidin-7-yl)piperidine-1-carboxylate (80l). Starting from **76** (38 mg, 0.1 mmol), following **GP2** and using p-tolylboronic acid as the coupling partner, the title compound was synthesized as a yellow oil (29 mg, 73%). **UPLC-MS**: R.t. =2.17 (apolar method). **MS (ESI)** m/z calc [M+H]+: 393.2, found 393.0.

Rac-7-(piperidin-3-yl)-3-(p-tolyl)pyrazolo[1,5-a]pyrimidine (10). Starting from **80l** (29 mg, 0.73 mmol) and following **GP3**, after 3h reaction time and automated flash chromatography (Biotage), using silica and as eluent phase DCM/MeOH*NH_3 1M gradient 0 to 20%, the title compound was synthesized as a yellow powder in its hydrochloride salt form (23 mg, 96%). **UPLC-MS:** R.t. =1.84 (polar method). **MS (ESI)** m/z calc [M+H]+: 293.17, found 293.0. **^{1}H NMR (400 MHz, DMSO)** δ 9.51 (d, *J* = 10.6 Hz, 1H), 9.24 (d, *J* = 11.4 Hz, 1H), 8.70 (s, 1H), 8.58 (d, *J* = 4.3 Hz, 1H), 8.01 – 7.94 (m, 2H), 7.19 (d, *J* = 8.1 Hz, 2H), 7.00 (d, *J* = 4.4 Hz, 1H), 4.04 – 3.94 (m, 1H), 3.58 (d, *J* = 12.0 Hz, 1H), 3.19 (t, *J* = 11.4 Hz, 1H), 2.89 (d, *J* = 11.4 Hz, 1H), 2.26 (s, 3H), 2.14 (d, *J* = 12.0 Hz, 1H), 1.90 (s, 1H), 1.87 – 1.70 (m, 2H). **^{13}C NMR (101 MHz, DMSO)** δ 150.29, 149.11, 144.81, 142.36, 135.69, 129.72, 129.42, 126.18, 110.05, 106.14, 44.74, 43.64, 34.11, 26.08, 22.21, 21.28.

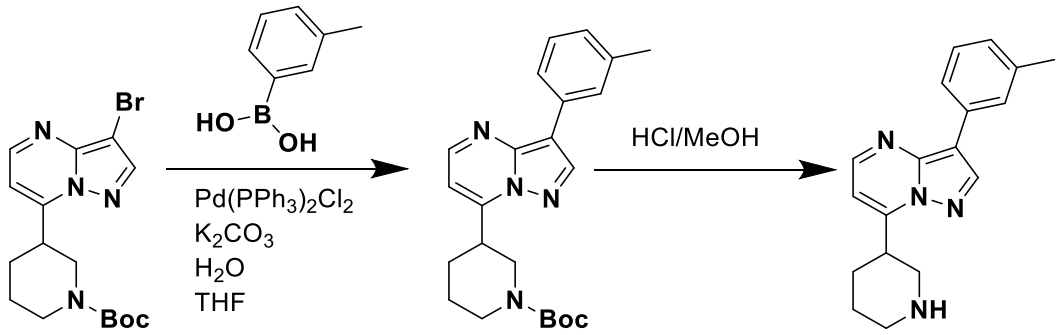

76 **80m** **11**

Rac-*tert*-Butyl 3-(3-(m-tolyl)pyrazolo[1,5-a]pyrimidin-7-yl)piperidine-1-carboxylate (80m). Starting from **76** (38 mg, 0.1 mmol), following **GP2** and using m-tolylboronic acid as the coupling partner, the title compound was synthesized as a yellow oil (19 mg, 48%). **UPLC-MS:** R.t. =2.13 (apolar method). **MS (ESI)** m/z calc [M+H]+: 393.2, found 393.0.

Rac-7-(piperidin-3-yl)-3-(m-tolyl)pyrazolo[1,5-a]pyrimidine (11). Starting from **80m** (19 mg, 0.048 mmol), and following **GP3**, after 2h reaction time, the title compound was synthesized as a yellow powder in its hydrochloride salt form (9 mg, 64%). **HPLC-MS**: R.t. =3.26 (generic method). **MS (ESI)** m/z calc [M+H]+: 293.17, found 293.13. **^{1}H NMR (400 MHz, DMSO)** δ 9.36 (s, 1H), 8.73 (s, 1H), 8.60 (d, *J* = 4.3 Hz, 1H), 7.94 – 7.86 (m, 2H), 7.26 (t, *J* = 7.6 Hz, 1H), 7.04 – 6.97 (m, 2H), 4.05 – 3.94 (m, 1H), 3.59 (dd, *J* = 11.4, 3.5 Hz, 1H), 3.21 (t, *J* = 12.1 Hz, 2H), 2.89 (td, *J* = 12.1, 4.3 Hz, 1H), 2.31 (s, 3H), 2.19 – 2.11 (m, 1H), 1.92 – 1.70 (m, 3H). **^{13}C NMR (101 MHz, DMSO)** δ 150.46, 149.18, 144.97, 142.61, 138.13, 132.21, 129.05, 127.28, 126.77, 123.49, 110.06, 106.23, 44.76, 43.65, 34.12, 26.10, 22.22, 21.74.

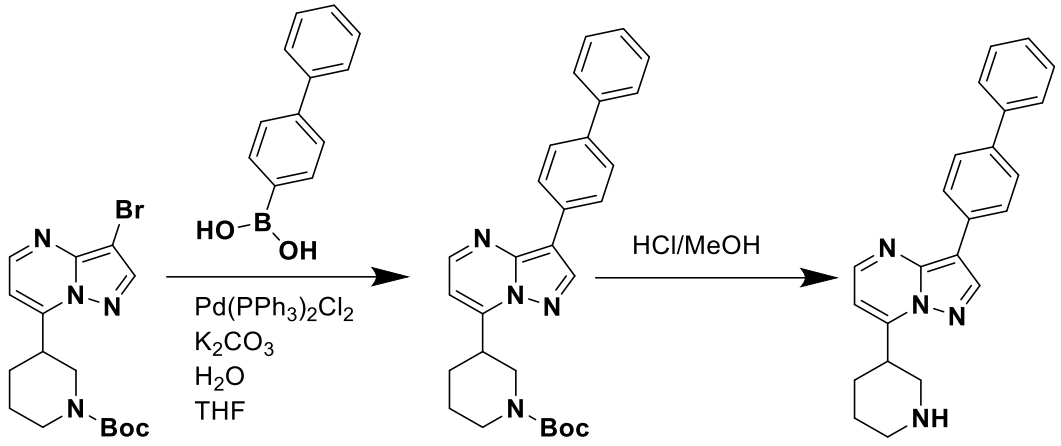

76 **80n** **12**

Rac-*tert*-butyl 3-(3-([1,1'-biphenyl]-4-yl)pyrazolo[1,5-a]pyrimidin-7-yl)piperidine-1-carboxylate (80n). Starting from **76** (38 mg, 0.1 mmol), following **GP2** and using [1,1'-biphenyl]-4-ylboronic acid as the coupling partner, the title compound was synthesized as a yellow oil (33 mg, 72%). **UPLC-MS**: R.t. =2.52 (apolar method). **MS (ESI)** m/z calc [M+H]+: 455.2, found 455.0.

Rac-3-([1,1'-biphenyl]-4-yl)-7-(piperidin-3-yl)pyrazolo[1,5-a]pyrimidine (12). Starting from **80n** (33 mg, 0.072 mmol) and following **GP3**, after 7h reaction time and at 50°C due to an insolubility problem, the title compound was synthesized as a yellow powder in its hydrochloride salt form (21 mg, 82%). **HPLC-MS:** R.t. =4.13 (generic method). **MS (ESI)** m/z calc [M+H]+: 355.19, found 355.33. **^{1}H NMR (400 MHz, DMSO) δ** 9.26 (s, 1H), 8.82 (s, 3H), 8.63 (d, *J* = 4.3 Hz, 3H), 8.24 – 8.17 (m, 6H), 7.73 – 7.62 (m, 12H), 7.42 (t, *J* = 7.7 Hz, 6H), 7.35 – 7.26 (m, 3H), 7.04 (d, *J* = 4.4 Hz, 3H), 4.00 (s, 2H), 3.64 – 3.55 (m, 3H), 3.21 (t, *J* = 12.1 Hz, 11H), 2.94 – 2.83 (m, 3H), 2.16 (d, *J* = 11.1 Hz, 3H), 1.92 – 1.73 (m, 9H). **^{13}C NMR (101 MHz, DMSO)** δ 150.62, 149.36, 145.06, 142.63, 140.33, 138.12, 131.53, 129.43, 127.78, 127.38, 126.89, 126.68, 109.58, 106.38, 44.89, 43.72, 34.24, 26.14, 22.31.

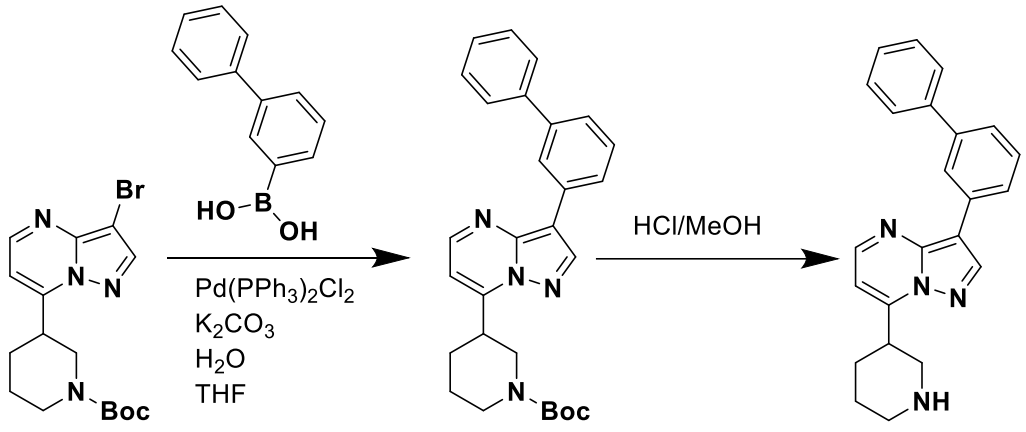

76 **80o** **13**

Rac-*tert*-butyl 3-(3-([1,1'-biphenyl]-3-yl)pyrazolo[1,5-a]pyrimidin-7-yl)piperidine-1-carboxylate (80o). Starting from **76** (38 mg, 0.1 mmol), following **GP2** and using [1,1'-biphenyl]-3-ylboronic acid as the coupling partner, the title compound was synthesized as a yellow oil (34 mg, 74%). **UPLC-MS**: R.t. =2.50 (apolar method). **MS (ESI)** m/z calc [M+H]+: 455.2, found 455.0.

Rac-3-([1,1'-biphenyl]-3-yl)-7-(piperidin-3-yl)pyrazolo[1,5-a]pyrimidine (13). Starting from **80o** (34 mg, 0.074 mmol) and following **GP3**, after 2h30 min reaction time, the title compound was synthesized

as a yellow powder in its hydrochloride salt form (20 mg, 55%). **HPLC-MS**: R.t. =4.11 (generic method). **MS (ESI)** m/z calc [M+H]+: 355.19, found 355.10. **^{1}H NMR (400 MHz, DMSO)** δ 9.15 (s, 1H), 8.95 (s, 3H), 8.71 (d, *J* = 4.4 Hz, 3H), 8.43 (q, *J* = 1.4 Hz, 3H), 8.18 (ddt, *J* = 5.7, 4.1, 2.0 Hz, 3H), 7.78 – 7.71 (m, 6H), 7.60 – 7.48 (m, 11H), 7.46 – 7.37 (m, 3H), 7.11 (d, *J* = 4.4 Hz, 3H), 4.06 (s, 2H), 3.68 (d, *J* = 12.5 Hz, 3H), 3.39 (s, 3H), 3.27 (t, *J* = 12.1 Hz, 8H), 2.97 (t, *J* = 11.4 Hz, 3H), 2.23 (s, 2H), 2.01 – 1.83 (m, 9H), 0.84 (s, 1H). **^{13}C NMR (151 MHz, DMSO)** δ 155.38, 150.79, 150.63, 149.02, 141.89, 140.83, 134.10, 130.50, 130.00, 128.72, 128.51, 127.91, 126.34, 125.57, 106.66, 94.94, 49.57, 45.48, 44.28, 41.03, 34.67, 31.34, 26.45, 22.80.

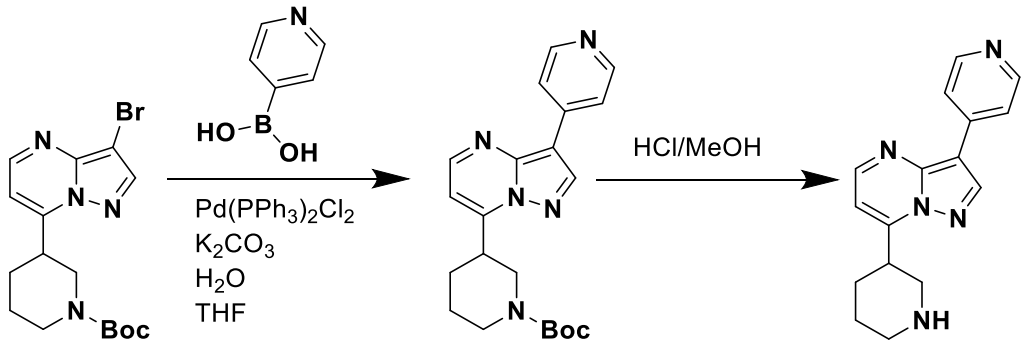

76 **80p** **14**

Rac-*tert*-butyl 3-(3-(pyridin-4-yl)pyrazolo[1,5-a]pyrimidin-7-yl)piperidine-1-carboxylate (80p). Starting from **76** (20 mg, 0.05 mmol), following **GP2,** and using pyridin-4-ylboronic acid as the coupling partner, the title compound was synthesized as a yellow oil (11 mg, 58%). **UPLC-MS**: R.t. =1.06 (apolar method). **MS (ESI)** m/z calc [M+H]+: 380.2, found 380.2.

Rac-7-(piperidin-3-yl)-3-(pyridin-4-yl)pyrazolo[1,5-a]pyrimidine (14). Starting from **80p** (11 mg, 0.29 mmol) and following **GP3**, after 3h reaction time and automated flash chromatography (Biotage), using silica and as eluent phase DCM/MeOH*NH3 1M gradient 0 to 20%, the title compound was synthesized as a yellow powder in its hydrochloride salt form (5 mg, 54%). **HPLC-MS**: R.t. =1.36 (generic method). **MS (ESI)** m/z calc [M+H]+: 280.15, found 380.22. **^{1}H NMR (400 MHz, DMSO)** δ 9.64 (s, 1H), 9.43 (d, *J* = 11.1 Hz, 1H), 9.31 (s, 2H), 8.92 (d, *J* = 4.5 Hz, 2H), 8.83 (d, *J* = 6.3 Hz, 3H), 8.74 – 8.68 (m, 3H), 7.36 (d, *J* = 4.6 Hz, 2H), 4.19 – 4.08 (m, 2H), 3.64 (d, *J* = 12.1 Hz, 2H), 2.97 (d, *J* = 13.0 Hz, 2H), 2.21 (d, *J* = 12.0 Hz, 2H), 1.98 (s, 2H), 1.95 – 1.83 (m, 3H). **^{13}C NMR (151 MHz, DMSO)** δ 153.63, 150.36, 147.74, 147.00, 144.95, 142.94, 121.30, 108.45, 105.56, 63.01, 44.91, 43.88, 34.34, 31.40, 25.84, 22.07.

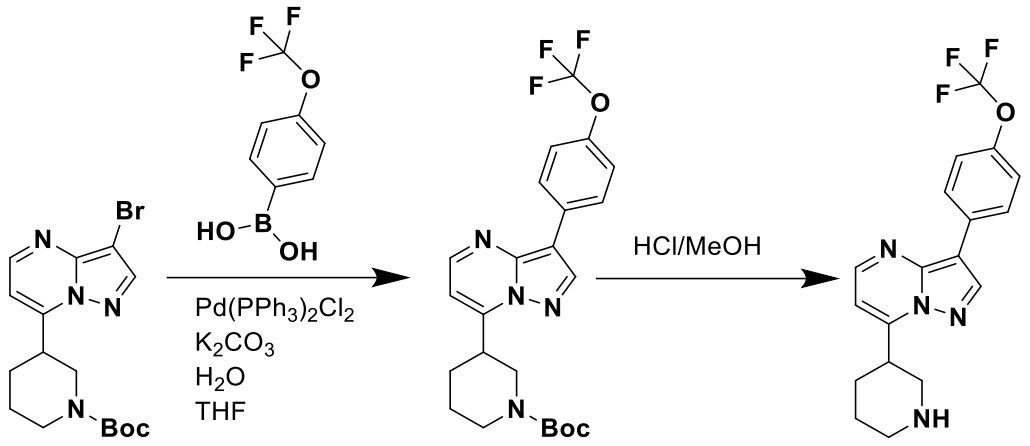

76 **80q** **18**

Rac-*tert*-butyl 3-(3-(4-(trifluoromethoxy)phenyl)pyrazolo[1,5-a]pyrimidin-7-yl)piperidine-1-carboxylate (80q). Starting from **76** (19 mg, 0.05 mmol), following **GP2** and using (4-(trifluoromethoxy)phenyl)boronic acid as the coupling partner, the title compound was synthesized as a yellow oil (16 mg, 70%). **UPLC-MS**: R.t. =2.31 (apolar method). **MS (ESI)** m/z calc [M+H]+: 463.19, found 463.2. **^{1}H NMR (400 MHz, CDCl3)** δ 8.54 (d, *J* = 4.3 Hz, 1H), 8.44 (s, 1H), 8.12 – 8.02 (m, 2H), 7.35 – 7.29 (m, 2H), 6.76 (d, *J* = 4.3 Hz, 1H), 4.46 – 4.37 (m, 1H), 4.06 (d, *J* = 13.3 Hz, 1H), 3.79 (tt, *J* = 9.9, 3.8 Hz, 1H), 3.24 (dd, *J* = 12.9, 9.6 Hz, 1H), 3.06 (ddd, *J* = 13.5, 10.4, 3.4 Hz, 1H), 2.34 (d, *J* = 12.3 Hz, 1H), 1.91 – 1.73 (m, 3H), 1.49 (s, 9H).

Rac-7-(piperidin-3-yl)-3-(4-(trifluoromethoxy)phenyl)pyrazolo[1,5-a]pyrimidine (18). Starting from **80q** (16 mg, 0.035 mmol) and following **GP3**, after 2h reaction time, the title compound was synthesized as a yellow powder in its hydrochloride salt form (9 mg, 65%). **HPLC-MS**: R.t. =3.93 (generic method). **MS (ESI)** m/z calc [M+H]+: 363.14, found 363.26. **^{1}H NMR (400 MHz, DMSO)** δ 9.27 (s, 2H), 8.87 (s, 1H), 8.71 (d, *J* = 4.4 Hz, 1H), 8.33 – 8.25 (m, 2H), 7.47 (d, 2H), 7.13 (d, *J* = 4.4 Hz, 1H), 4.06 (t, 1H), 3.66 (d, *J* = 12.0 Hz, 1H), 3.38 (s, 1H), 3.29 – 3.22 (m, 1H), 2.96 (t, *J* = 11.2 Hz, 1H), 2.22 (d, *J* = 10.7 Hz, 1H), 1.99 – 1.79 (m, 3H).

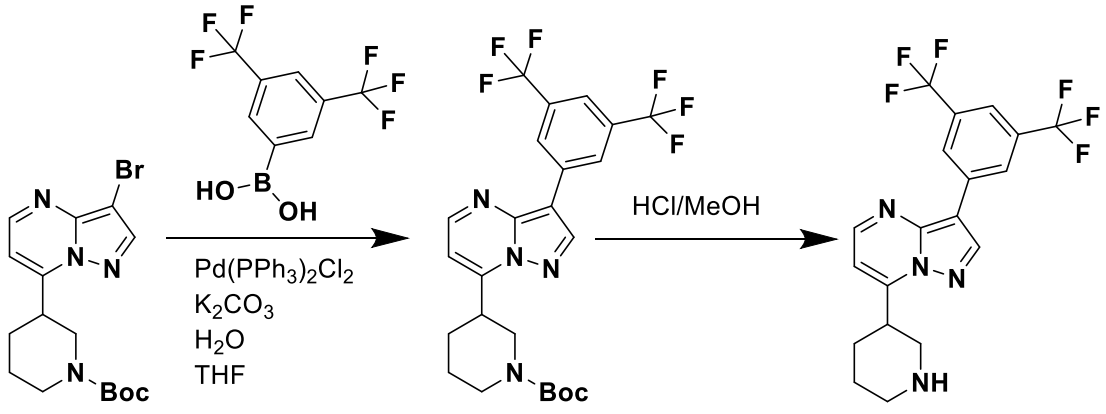

76 **80r** **19**

Rac-*tert*-butyl 3-(3-(3,5-bis(trifluoromethyl)phenyl)pyrazolo[1,5-a]pyrimidin-7-yl)piperidine-1-carboxylate (80r). Starting from **76** (19 mg, 0.05 mmol), following **GP2** and using (3,5-bis(trifluoromethyl)phenyl)boronic acid as the coupling partner, the title compound was synthesized as

a yellow oil (15 mg, 58%). **UPLC-MS**: R.t. =2.59 (apolar method). **MS (ESI)** m/z calc [M+H]+: 515.18, found 515.2.

Rac-3-(3,5-bis(trifluoromethyl)phenyl)-7-(piperidin-3-yl)pyrazolo[1,5-a]pyrimidine (19). Starting from **80r** (15 mg, 0.03 mmol) and following **GP3**, after 3h reaction time and automated flash chromatography (Biotage), using silica and as eluent phase DCM/MeOH*NH3 1M gradient 0 to 20%, the title compound was synthesized as a yellow powder in its hydrochloride salt form (6 mg, 45%). **UPLC-MS**: R.t. =2.28 (generic method). **MS (ESI)** m/z calc [M+H]+: 415.13, found 415.1. **^{1}H NMR (400 MHz, DMSO)** δ 9.33, 9.21, 9.20, 8.90, 8.83, 8.82, 7.94, 7.22, 7.21, 4.09, 3.68, 3.65, 3.51, 3.39, 3.34, 3.28, 3.25, 3.00, 2.97, 2.94, 2.52, 2.51, 2.51, 2.50, 2.50, 2.23, 2.20, 2.00, 1.98, 1.94, 1.91, 1.88, 1.86, 1.24, 1.11, 1.11, 0.86.

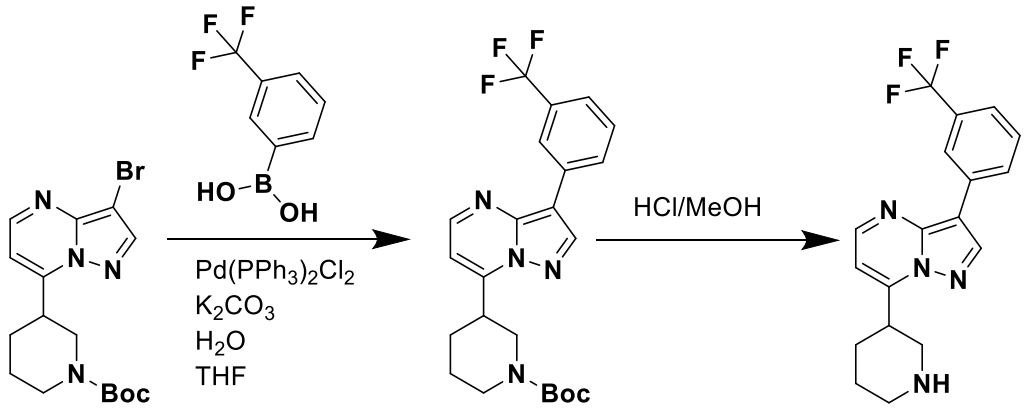

76 **80s** **20**

Rac-*tert*-butyl 3-(3-(3-(trifluoromethyl)phenyl)pyrazolo[1,5-a]pyrimidin-7-yl)piperidine-1-carboxylate (80s). Starting from **76** (19 mg, 0.05 mmol), following **GP2** and using (3-(trifluoromethyl)phenyl)boronic acid as the coupling partner, in 2h reaction time the title compound was synthesized as a yellow oil (20 mg, 88%). **UPLC-MS**: R.t. =2.23 (apolar method). **MS (ESI)** m/z calc [M+H]+: 447.20, found 447.2.

Rac-7-(piperidin-3-yl)-3-(3-(trifluoromethyl)phenyl)pyrazolo[1,5-a]pyrimidine (20). Starting from **80s** (20 mg, 0.05 mmol), following **GP3**, after 2h reaction time, the title compound was synthesized as a yellow powder in its hydrochloride salt form (11 mg, 65%). **HPLC-MS**: R.t. = 3.75 (generic method). **MS (ESI)** m/z calc [M+H]+: 347.14, found 347.23. **^{1}H NMR (400 MHz, DMSO)** δ 9.29 (s, 2H), 9.01 (s, 1H), 8.76 (d, *J* = 4.4 Hz, 1H), 8.58 (d, *J* = 2.2 Hz, 1H), 8.47 (d, *J* = 7.9 Hz, 1H), 7.70 (t, *J* = 7.8 Hz, 1H), 7.61 (d, *J* = 7.8 Hz, 1H), 7.16 (d, *J* = 4.4 Hz, 1H), 4.08 (t, 1H), 3.67 (d, *J* = 11.3 Hz, 1H), 3.42 – 3.35 (m, 1H), 3.32 – 3.23 (m, 1H), 2.97 (t, *J* = 11.0 Hz, 1H), 2.22 (d, *J* = 10.5 Hz, 1H), 2.00 – 1.95 (m, 1H), 1.94 – 1.80 (m, 2H). **^{13}C NMR (151 MHz, DMSO)** δ 151.81, 149.78, 145.74, 143.41, 133.94, 130.81, 130.68, 130.47, 130.30, 126.23, 124.42, 123.46, 123.43, 122.70, 122.67, 122.65, 108.89, 107.26, 45.47, 44.38, 34.72, 26.39, 22.70.

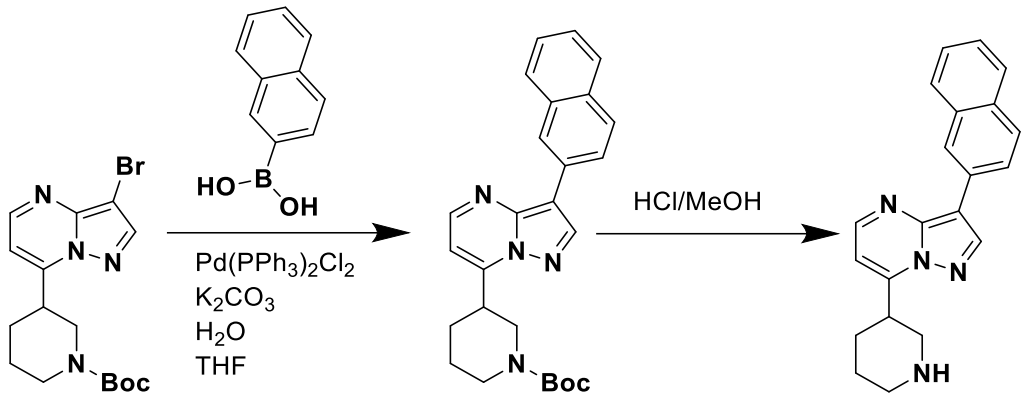

76 **80t** **21**

Rac-*tert*-butyl 3-(3-(naphthalen-2-yl)pyrazolo[1,5-a]pyrimidin-7-yl)piperidine-1-carboxylate (80t). Starting from **76** (50 mg, 0.13 mmol), following **GP2** and using naphthalen-2-ylboronic acid as the coupling partner, the title compound was synthesized as a yellow oil (42 mg, 76%). **UPLC-MS**: R.t. =2.22 (apolar method). **MS (ESI)** m/z calc [M+H]+: 429.22, found 429.2.

Rac-3-(naphthalen-2-yl)-7-(piperidin-3-yl)pyrazolo[1,5-a]pyrimidine (21). Starting from **80t** (42 mg 0.99 mmol) and following **GP3**, in 15h reaction time, after automated flash chromatography (Biotage), using silica and as eluent phase DCM/MeOH gradient 0 to 20%, the title compound was synthesized as a yellow powder in its hydrochloride salt form (13 mg, 36%). **HPLC-MS**: R.t. = 3.48 (generic method). **MS (ESI)** m/z calc [M+H]+: 329.17, found 329.19. **1H NMR (**^{1}**H NMR (400 MHz, DMSO**) δ 8.95 (s, 1H), 8.75 – 8.68 (m, 2H), 8.36 (dd, *J* = 8.6, 1.8 Hz, 1H), 7.99 (d, *J* = 8.7 Hz, 1H), 7.96 – 7.88 (m, 2H), 7.57 – 7.44 (m, 2H), 7.12 (d, *J* = 4.4 Hz, 1H), 3.90 (t, *J* = 11.0 Hz, 1H), 3.53 (d, *J* = 11.9 Hz, 1H), 3.24 – 3.15 (m, 1H), 3.01 (t, *J* = 11.6 Hz, 1H), 2.80 (t, *J* = 11.6 Hz, 1H), 2.20 (d, *J* = 11.3 Hz, 1H), 1.94 – 1.72 (m, 3H). **^{13}C NMR (101 MHz, DMSO)** δ 150.73, 150.67, 145.23, 142.84, 133.89, 132.02, 130.06, 128.54, 128.12, 128.06, 126.82, 125.89, 125.14, 123.90, 109.71, 106.24, 46.90, 44.82, 35.67, 27.10, 23.89.

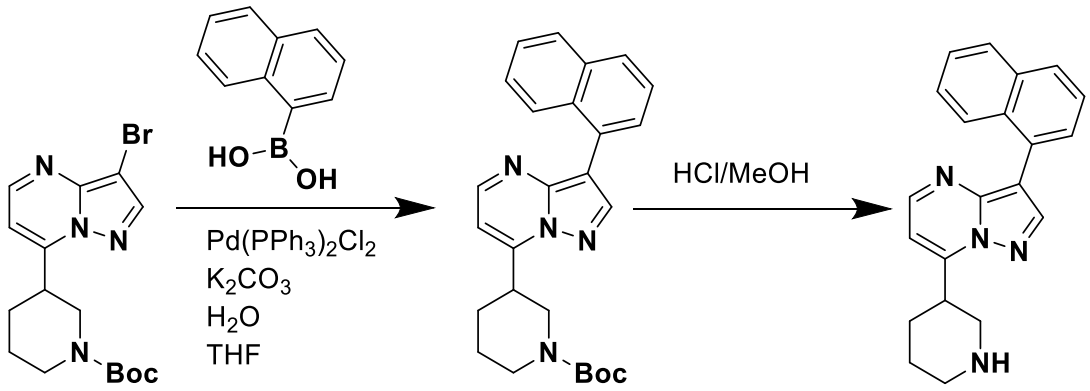

76 **80u** **22**

Rac-t*ert*-butyl 3-(3-(naphthalen-1-yl)pyrazolo[1,5-a]pyrimidin-7-yl)piperidine-1-carboxylate (80u). Starting from **76** (60 mg, 0.16 mmol, 1 eq), following **GP2** and using naphthalen-1-ylboronic acid as the coupling partner, the title compound was synthesized as a yellow oil (35mg, 51%). **UPLC-MS**: R.t. =1.97 (apolar method). **MS (ESI)**, not detectable.

Rac-3-(naphthalen-1-yl)-7-(piperidin-3-yl)pyrazolo[1,5-a]pyrimidine (22). Starting from **80u** (35 mg, 0.08 mmol) and following **GP3**, after 4h reaction time and automated flash chromatography (Biotage),

using silica and as eluent phase DCM/MeOH gradient 0 to 20%, the title compound was synthesized as a yellow powder in its hydrochloride salt form (12 mg, 45%). **HPLC-MS**: R.t. =3.11 (generic method). **MS (ESI)** m/z calc [M+H]+: 329.17, found 329.20. **^{1}H NMR (400 MHz, DMSO)** δ 9.44 (s, 1H), 9.21 (s, 1H), 8.51 (d, *J* = 4.2 Hz, 2H), 7.94 (dd, *J* = 8.2, 1.4 Hz, 1H), 7.93 – 7.84 (m, 2H), 7.61 (dd, *J* = 7.1, 1.3 Hz, 1H), 7.58 – 7.45 (m, 2H), 7.42 (ddd, *J* = 8.3, 6.8, 1.5 Hz, 1H), 7.04 (d, *J* = 4.3 Hz, 1H), 4.06 (s, 1H), 3.66 (d, *J* = 11.8 Hz, 1H), 3.32 (d, *J* = 12.8 Hz, 1H), 2.92 (s, 1H), 2.21 (d, *J* = 10.0 Hz, 1H), 1.95 – 1.77 (m, 3H). **^{13}C NMR (151 MHz, DMSO)** δ 150.51, 149.05, 146.08, 144.85, 134.00, 131.89, 129.56, 128.79, 128.67, 127.96, 126.61, 126.37, 126.16, 126.06, 109.83, 106.44, 46.01, 45.06, 43.85, 26.11, 22.37.

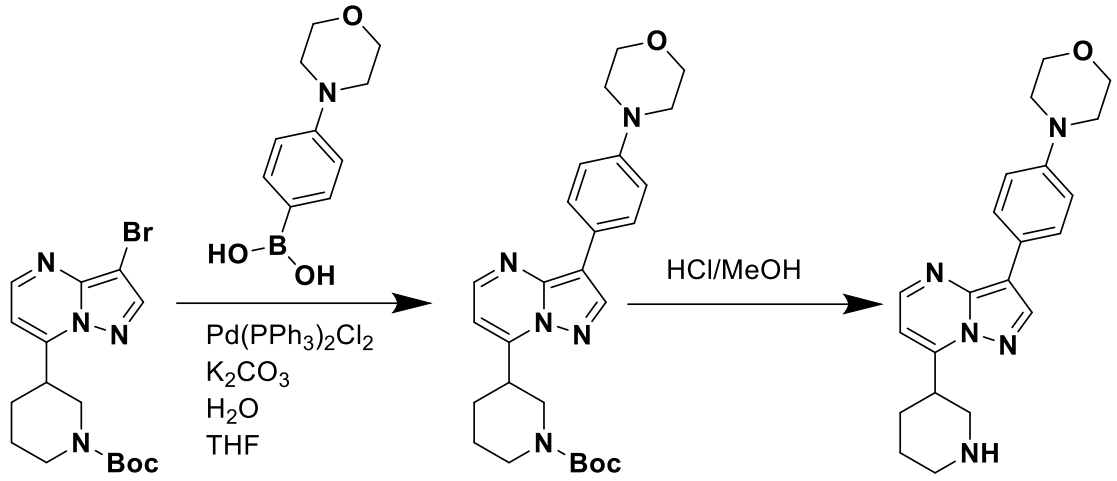

76 **80v** **23**

Rac-*tert*-butyl 3-(3-(4-morpholinophenyl)pyrazolo[1,5-a]pyrimidin-7-yl)piperidine-1-carboxylate (80v). Starting from **76** (19 mg, 0.05 mmol), following **GP2** and using (4-morpholinophenyl)boronic acid as the coupling partner, the title compound was synthesized as a yellow oil (16 mg, 69%). **UPLC-MS**: R.t. =1.58 (apolar method). **MS (ESI)** m/z calc [M+H]+: 464.26, found 464.23.

Rac-4-(4-(7-(piperidin-3-yl)pyrazolo[1,5-a]pyrimidin-3-yl)phenyl)morpholine (23). Starting from **80v** (16 mg, 0.03 mmol) and following **GP3**, after 4h reaction time and automated flash chromatography (Biotage), using silica and as eluent phase DCM/MeOH gradient 0 to 20%, the title compound was synthesized as a yellow powder in its hydrochloride salt form (13 mg, 96%). **UPLC-MS**: R.t. =1.49 (generic method). **MS (ESI)** m/z calc [M+H]+: 364.26, found 364.2. **^{1}H NMR (400 MHz, DMSO)** δ 9.64 (s, 1H), 9.37 (d, *J* = 11.4 Hz, 1H), 8.75 (s, 1H), 8.63 (d, *J* = 4.3 Hz, 1H), 8.08 (d, *J* = 8.4 Hz, 2H), 7.22 (d, *J* = 8.3 Hz, 2H), 7.05 (d, *J* = 4.3 Hz, 1H), 4.06 (t, *J* = 12.1 Hz, 1H), 3.84 (s, 5H), 3.52 – 3.49 (m, 1H), 3.35 (d, *J* = 12.8 Hz, 1H), 3.24 (s, 5H), 3.00 – 2.92 (m, 1H), 2.22 (d, *J* = 12.1 Hz, 1H), 2.02 – 1.79 (m, 4H). **^{13}C NMR (151 MHz, DMSO)** δ 150.57, 149.36, 149.22, 145.03, 142.51, 127.63, 124.94, 117.07, 110.62, 106.55, 66.76, 50.10, 45.39, 44.30, 40.80, 40.68, 40.54, 40.40, 40.26, 40.12, 39.98, 39.85, 34.65, 26.43, 22.70.

3.9.2: Synthesis of compounds **15-17, 24-26**

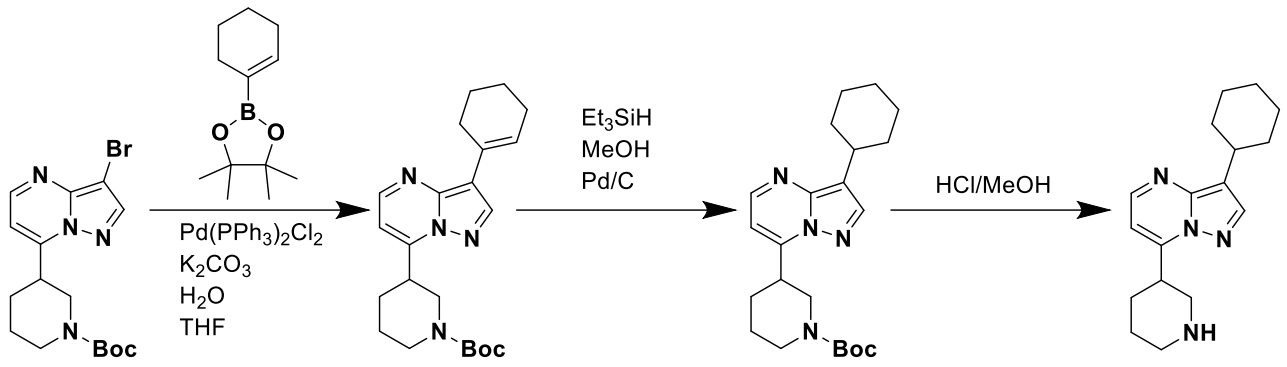

76 **81a** **82a** **15**

Rac-*tert*-butyl 3-(3-(cyclohex-1-en-1-yl)pyrazolo[1,5-a]pyrimidin-7-yl)piperidine-1-carboxylate (81a). Starting from **76** (20 mg, 0.05 mmol), following **GP2** and using 2-(cyclohex-1-en-1-yl)-4,4,5,5-tetramethyl-1,3,2-dioxaborolane as the coupling partner, the title compound was synthesized as a yellow oil (11 mg, 57%). **UPLC-MS**: R.t. =2.30 (apolar method). **MS (ESI)** m/z calc [M+H]+: 383.24, found 383.3.

Rac-*tert*-butyl 3-(3-cyclohexylpyrazolo[1,5-a]pyrimidin-7-yl)piperidine-1-carboxylate (82a). Starting from **81a** (11 mg, 0.029 mmol) and following **GP4**, after 2h reaction time, the tile compound was synthesized as a colourless oil (10.7 mg, 96%). **UPLC-MS**: R.t. =2.24 (apolar method). **MS (ESI)** m/z calc [M+H]+: 385.26, found 385.3.

Rac-3-cyclohexyl-7-(piperidin-3-yl)pyrazolo[1,5-a]pyrimidine (15). Starting from **82a** (10.7 mg, 0.028 mmol) and following **GP3**, after 16h reaction time and automated flash chromatography (Biotage), using silica and as eluent phase DCM/MeOH*NH_3 1M gradient 0 to 20%, the title compound was synthesized as a white powder in its hydrochloride salt form (9 mg, quantitative). **UPLC-MS**: R.t. =1.83 (polar method). **MS (ESI)** m/z calc [M+H]+: 285.26, found 285.2. **^{1}H NMR (400 MHz, MeOD)** δ 8.27 (d, *J* = 4.4 Hz, 1H), 7.92 (s, 1H), 6.69 (d, *J* = 4.4 Hz, 1H), 3.61 (tt, *J* = 11.1, 3.5 Hz, 1H), 3.34 (dt, *J* = 12.7, 2.5 Hz, 1H), 3.25 (s, 1H), 3.01 (dq, *J* = 14.7, 2.6 Hz, 1H), 2.87 (tt, *J* = 11.7, 3.5 Hz, 1H), 2.60 (ddd, *J* = 24.6, 12.5, 10.4 Hz, 2H), 2.18 – 2.08 (m, 1H), 1.94 – 1.85 (m, 2H), 1.75 (dq, *J* = 5.5, 3.0 Hz, 2H), 1.73 – 1.55 (m, 4H), 1.48 (td, *J* = 12.1, 2.9 Hz, 2H), 1.44 – 1.38 (m, 1H), 1.38 – 1.25 (m, 2H), 1.25 – 1.15 (m, 1H). **^{13}C NMR (101 MHz, DMSO)** δ 151.12, 148.34, 145.39, 141.85, 116.09, 104.93, 49.05, 46.09, 37.04, 33.80, 33.48, 28.04, 26.68, 26.19, 25.63.

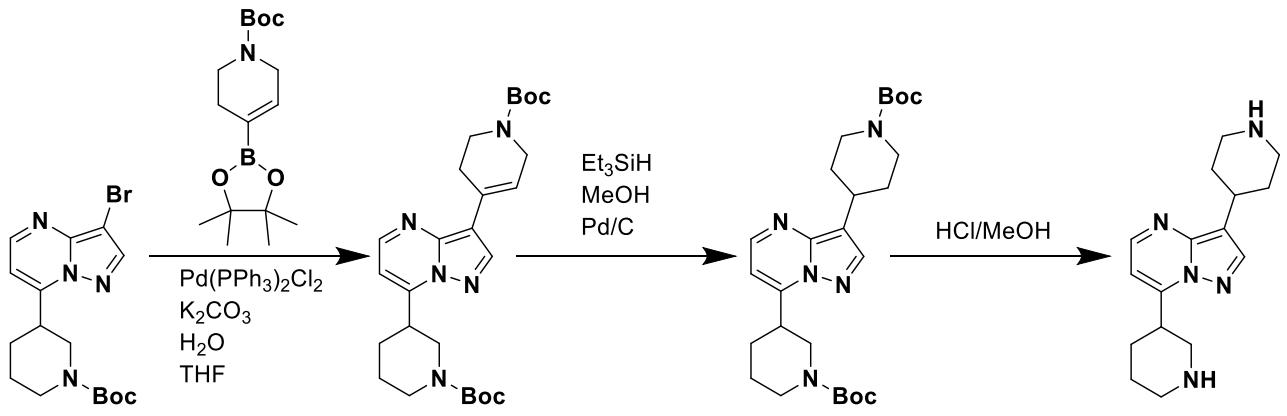

76 **81b** **82b** **16**

Rac-*tert*-butyl 4-(7-(1-(tert-butoxycarbonyl)piperidin-3-yl)pyrazolo[1,5-a]pyrimidin-3-yl)-3,6-dihydropyridine-1(2H)-carboxylate (81b). Starting from **76** (38 mg, 0.1 mmol), following **GP2** and using *tert*-butyl 4-(4,4,5,5-tetramethyl-1,3,2-dioxaborolan-2-yl)-3,6-dihydropyridine-1(2H)-carboxylate as the coupling partner, the title compound was synthesized as a yellow oil (38 mg, 79%). **UPLC-MS**: R.t. =2.06 (apolar method). **MS (ESI)** m/z calc [M+H]+: 484.29, found 484.4.

Rac-*tert*-butyl 3-(3-(1-(tert-butoxycarbonyl)piperidin-4-yl)pyrazolo[1,5-a]pyrimidin-7-yl)piperidine-1-carboxylate (82b). Starting from **81b** (25 mg, 0.05 mmol) and following **GP4**, after 15h reaction time, the tile compound was synthesized as a colourless oil (10 mg, 41%). **UPLC-MS**: R.t. =1.90 (apolar method). **MS (ESI)** m/z calc [M+H]+: 486.30, found 486.4.

Rac-7-(piperidin-3-yl)-3-(piperidin-4-yl)pyrazolo[1,5-a]pyrimidine (16). Starting from **82b** (10 mg, 0.02 mmol) and following **GP3**, after 1h30min reaction time, the title compound was synthesized as a white powder in its hydrochloride salt form (7 mg, quantitative). **HPLC-MS**: R.t. =2.16 (polar method). **MS (ESI)** m/z calc [M+H]+: 286.20, found 286.35. **^{1}H NMR (400 MHz, DMSO)** δ 9.61 (d, *J* = 11.4 Hz, 1H), 9.35 (d, *J* = 11.4 Hz, 1H), 9.17 (s, 1H), 8.91 (d, *J* = 10.3 Hz, 1H), 8.52 (d, *J* = 4.3 Hz, 1H), 8.18 (s, 1H), 6.99 (d, *J* = 4.3 Hz, 1H), 4.01 (dd, *J* = 13.7, 10.0 Hz, 1H), 3.34 (d, *J* = 12.8 Hz, 3H), 3.29 – 3.16 (m, 3H), 3.08 (d, *J* = 11.8 Hz, 1H), 3.02 (d, *J* = 12.2 Hz, 1H), 2.94 (d, *J* = 11.9 Hz, 1H), 2.59 (t, *J* = 6.5 Hz, 1H), 2.22 – 2.10 (m, 3H), 2.09 – 1.96 (m, 3H), 1.93 (d, *J* = 10.4 Hz, 2H), 1.90 – 1.74 (m, 2H).

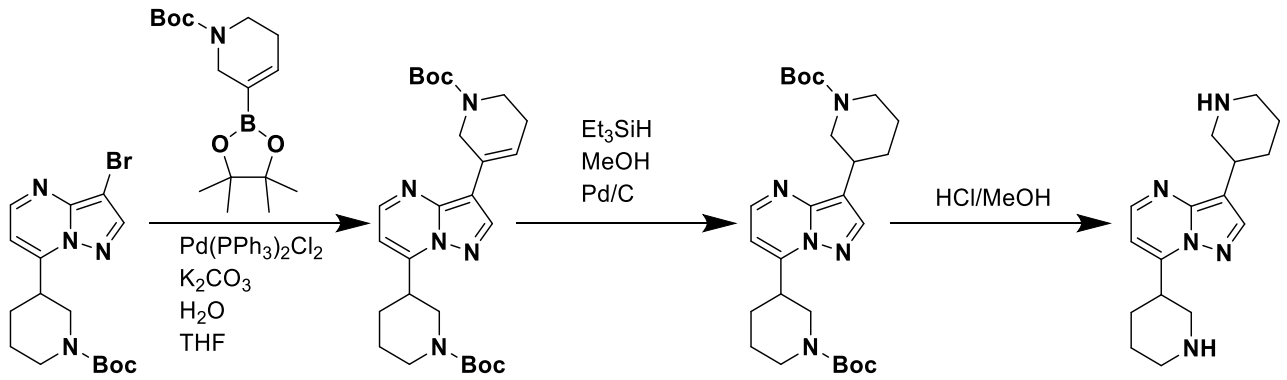

76 **81c** **82c** **17**

Rac-*tert*-butyl 5-(7-(1-(tert-butoxycarbonyl)piperidin-3-yl)pyrazolo[1,5-a]pyrimidin-3-yl)-3,6-dihydropyridine-1(2H)-carboxylate (81c). Starting from **76** (30 mg, 0.08 mmol), following **GP2** and using tert-butyl 5-(4,4,5,5-tetramethyl-1,3,2-dioxaborolan-2-yl)-3,6-dihydropyridine-1(2H)-carboxylate as the coupling partner, the title compound was synthesized as a yellow oil (31 mg, 77%). **UPLC-MS**: R.t. =2.07 (apolar method). **MS (ESI)** m/z calc [M+H]+: 484.29, found 484.5.

Di-*tert*-butyl 3,3'-(pyrazolo[1,5-a]pyrimidine-3,7-diyl)bis(piperidine-1-carboxylate (82c). Starting from **82c** (31 mg, 0.06 mmol) and following **GP4**, after 2days reaction time, the tile compound was synthesized as a colourless oil, as a mixture of diastereoisomers (13 mg, 45%). **UPLC-MS**: R.t. =1.93 (apolar method). **MS (ESI)** m/z calc [M+H]+: 486.30, found 486.5.

3,7-Di(piperidin-3-yl)pyrazolo[1,5-a]pyrimidine (17). Starting from **82c** (13 mg, 0.026 mmol) and following **GP3**, after 1h reaction time and automated flash chromatography (Biotage), the title compound was synthesized as a white powder in its hydrochloride salt form as a 1:1 mixture of diastereoisomers (8 mg, quantitative). **HPLC-MS**: R.t. =2.34, 2.51 (polar method). **MS (ESI)** m/z calc [M+H]+: 286.20, found 286.27 (for both peaks). **^{1}H NMR (400 MHz, DMSO)** δ 9.58 (d, J = 11.0 Hz, 1H), 9.34 (s, 1H), 9.27 (s, 1H), 9.18 (d, J = 10.8 Hz, 1H), 8.55 (d, J = 4.3 Hz, 1H), 8.27 (s, 1H), 7.01 (d, J = 4.4 Hz, 1H), 4.06 – 3.96 (m, 1H), 3.51 (s, 1H), 3.45 (d, J = 11.7 Hz, 3H), 3.35 (d, J = 13.4 Hz, 3H), 3.28 (d, J = 10.1 Hz, 2H), 3.26 – 3.11 (m, 3H), 2.98 – 2.88 (m, 2H), 2.18 (d, J = 12.1 Hz, 1H), 2.05 (s, 1H), 1.97 – 1.76 (m,

7H). **^{13}C NMR (101 MHz, DMSO)** δ 149.37, 148.78, 145.75, 142.63, 110.76, 105.92, 47.72, 44.66, 43.60, 43.51, 34.00, 29.60, 26.05, 22.51, 22.17. N*ote: some ^{1}H signals appear broad and not well resolved, consistent with the presence of two diastereoisomers*.

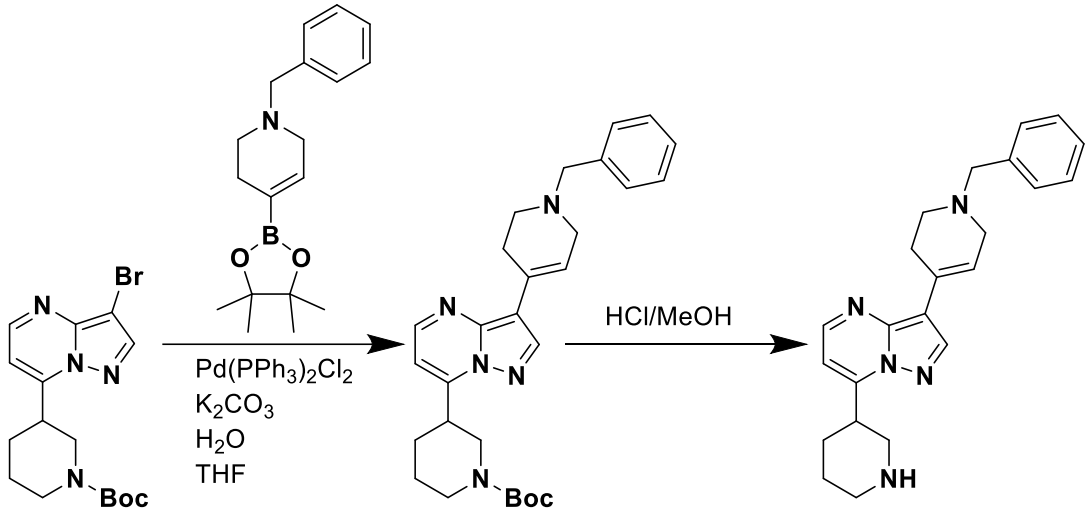

76 **81e** **24**

Rac-*tert*-butyl 3-(3-(1-benzyl-1,2,3,6-tetrahydropyridin-4-yl)pyrazolo[1,5-a]pyrimidin-7-yl)piperidine-1-carboxylate (81e). Starting from **76** (40 mg, 0.1 mmol), following **GP2** and using 1-benzyl-4-(4,4,5,5-tetramethyl-1,3,2-dioxaborolan-2-yl)-1,2,3,6-tetrahydropyridine as the coupling partner, the title compound was synthesized as a yellow oil (19 mg, 52%). **UPLC-MS**: R.t. =1.07 (apolar method). **MS (ESI)** m/z calc [M+H]+: 474.28, found 474.3.

Rac-3-(1-benzyl-1,2,3,6-tetrahydropyridin-4-yl)-7-(piperidin-3-yl)pyrazolo[1,5-a]pyrimidine (24). Starting from **81e** (25 mg, 0.05mmol) and following **GP3**, after 1h30min reaction time and automated flash chromatography (Biotage), using alumina and as eluent phase DCM/MeOH gradient 0 to 20%, the title compound was synthesized as a white powder in its hydrochloride salt form (15 mg, 80%). **UPLC-MS**: R.t. =1.20 (apolar method). **MS (ESI)** m/z calc [M+H]+: 374.23, found 374.2. **^{1}H NMR (600 MHz, DMSO)** δ 11.43 (s, 1H), 9.81 (t, *J* = 10.0 Hz, 1H), 9.56 (q, *J* = 11.1 Hz, 1H), 8.60 (d, *J* = 4.4 Hz, 1H), 8.43 (s, 1H), 7.75 – 7.69 (m, 2H), 7.50 – 7.43 (m, 4H), 7.39 (s, 1H), 7.31 (s, 1H), 7.07 (d, *J* = 4.4 Hz, 1H), 6.66 – 6.61 (m, 1H), 4.48 – 4.42 (m, 1H), 4.42 – 4.36 (m, 1H), 4.06 (tt, *J* = 12.1, 3.7 Hz, 1H), 3.86 – 3.78 (m, 1H), 3.74 (d, *J* = 16.7 Hz, 1H), 3.62 – 3.59 (m, 2H), 3.33 (d, *J* = 12.5 Hz, 1H), 3.31 – 3.22 (m, 2H), 3.11 – 3.02 (m, 1H), 2.99 – 2.89 (m, 2H), 2.20 – 2.14 (m, 1H), 1.94 (qd, *J* = 9.0, 5.1 Hz, 2H), 1.81 (dtd, *J* = 11.8, 8.1, 3.4 Hz, 1H). **^{13}C NMR (151 MHz, DMSO)** δ 150.97, 149.76, 145.33, 142.65, 132.34, 130.92, 130.40, 129.73, 129.54, 127.54, 114.65, 109.63, 106.95, 58.84, 58.81, 49.80, 48.47, 45.06, 44.01, 34.51, 26.62, 25.94, 24.86, 22.61.

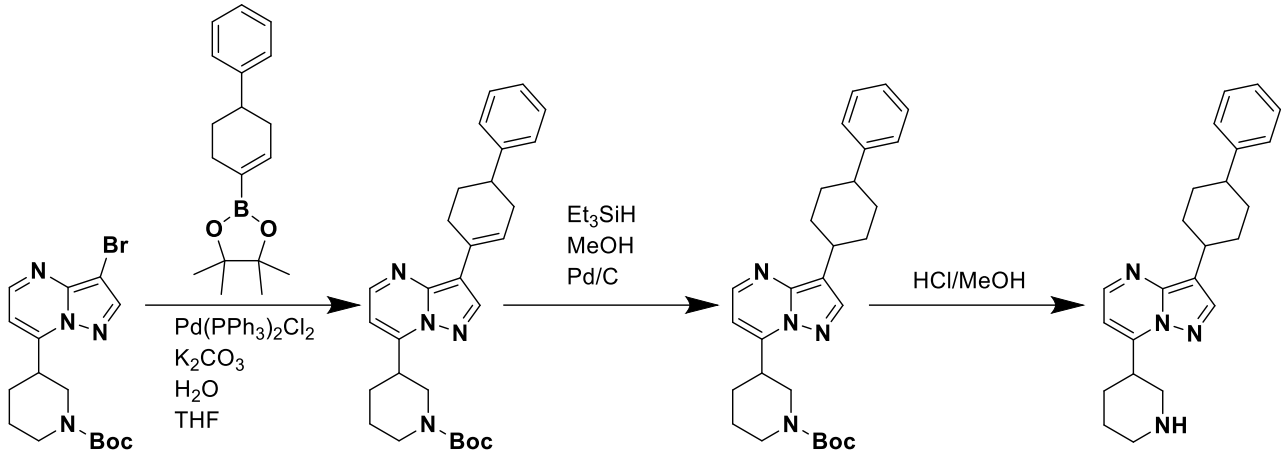

76 **81d** **82d** **26**

***tert*-butyl 3-(3-(1,2,3,6-tetrahydro-[1,1'-biphenyl]-4-yl)pyrazolo[1,5-a]pyrimidin-7-yl)piperidine-1-carboxylate (81d).** Starting from **76** (19 mg, 0.05 mmol), following **GP2** and using 4,4,5,5-tetramethyl-2-(1,2,3,6-tetrahydro-[1,1'-biphenyl]-4-yl)-1,3,2-dioxaborolane as the coupling partner, the title compound was synthesized as a yellow, oil as a mixture of diastereoisomers (16 mg, 70%). **UPLC-MS**: R.t. =2.60 (apolar method). **MS (ESI)** m/z calc [M+H]+: 459.27, found 459.3 (both peaks). **^{1}H NMR (400 MHz, CDCl3)** δ 8.46 (d, *J* = 4.3 Hz, 1H), 8.16 (s, 1H), 7.39 – 7.30 (m, 4H), 7.27 – 7.19 (m, 1H), 6.82 (s, 1H), 6.68 (d, *J* = 4.3 Hz, 1H), 4.40 (d, *J* = 12.9 Hz, 1H), 4.11 – 3.95 (m, 1H), 3.76 (tt, *J* = 10.0, 3.8 Hz, 1H), 3.21 (dd, *J* = 12.9, 9.7 Hz, 1H), 3.09 – 2.91 (m, 2H), 2.86 – 2.71 (m, 2H), 2.62 (dt, *J* = 18.0, 5.3 Hz, 1H), 2.52 – 2.38 (m, 1H), 2.32 (d, *J* = 12.1 Hz, 1H), 2.23 – 2.12 (m, 1H), 2.09 – 1.94 (m, 2H), 1.87 – 1.69 (m, 4H).

***tert*-butyl 3-(3-(4-phenylcyclohexyl)pyrazolo[1,5-a]pyrimidin-7-yl)piperidine-1-carboxylate (82d)**. Starting from **81d** (35 mg, 0.076mmol) and following **GP4**, after 16h reaction time, the title compound was synthesized as a colourless oil, as a mixture of diastereoisomers (16 mg, 32%). Reaction followed by TLC.

3-(4-phenylcyclohexyl)-7-(piperidin-3-yl)pyrazolo[1,5-a]pyrimidine (26). Starting from **82d** (16 mg, 0.025 mmol) and following **GP3**, after 3h reaction time, the title compound was synthesized as a white powder in its hydrochloride salt form, as a 1:1 mixture of diastereoisomers (9 mg, 76%). **HPLC-MS**: R.t. =3.30,3.37 (generic method). **MS (ESI)** m/z calc [M+H]+: 361.23, found 361.52 (both peaks). **^{1}H NMR (600 MHz, DMSO)** δ 9.67 (d, *J* = 11.1 Hz, 1H), 9.40 (q, *J* = 12.0 Hz, 1H), 8.49 (dd, *J* = 4.3, 1.9 Hz, 1H), 8.29 (s, 1H), 8.19 (s, 1H), 7.33 – 7.25 (m, 3H), 7.27 – 7.18 (m, 2H), 7.20 – 7.12 (m, 1H), 6.95 (t, *J* = 3.9 Hz, 1H), 4.02 (qt, *J* = 12.3, 3.6 Hz, 1H), 3.62 (d, *J* = 12.1 Hz, 1H), 3.40 (h, *J* = 4.6 Hz, 1H), 3.33 (s, 1H), 3.30 – 3.21 (m, 1H), 3.00 (tt, *J* = 12.2, 3.7 Hz, 1H), 2.94 (dtd, *J* = 21.3, 11.1, 5.5 Hz, 1H), 2.73 (tt, *J* = 9.5, 4.5 Hz, 1H), 2.63 (tt, *J* = 11.9, 3.5 Hz, 1H), 2.30 (dt, *J* = 13.5, 4.4 Hz, 1H), 2.20 (dt, *J* = 11.7, 3.7 Hz, 1H), 2.14 – 2.05 (m, 1H), 1.92 (tdd, *J* = 12.8, 9.5, 6.1 Hz, 4H), 1.86 – 1.78 (m, 1H), 1.80 – 1.75 (m, 1H), 1.74 (tt, *J* = 8.7, 3.5 Hz, 2H), 1.66 (qd, *J* = 12.7, 3.2 Hz, 1H). **^{13}C NMR (151 MHz, DMSO)** δ 209.02, 149.01, 148.94, 148.90, 148.20, 147.72, 146.28, 146.03, 143.76, 142.60, 129.29, 129.24, 127.78, 127.70, 126.87, 126.67, 116.55, 114.16, 105.95, 105.92, 46.13, 45.21, 45.18, 44.30, 44.10, 34.96, 34.52, 34.50, 34.42, 34.39, 33.54, 30.56, 30.54, 30.51, 30.49, 29.99, 26.61, 26.57, 22.70, 22.20.

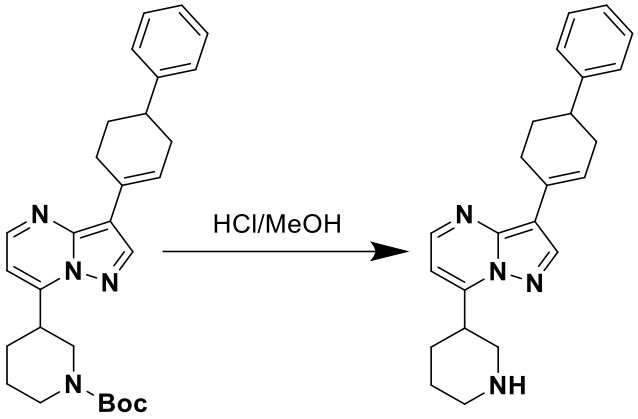

81d **25**

Rac-3-(4-phenylcyclohexyl)-7-(piperidin-3-yl)pyrazolo[1,5-a]pyrimidine (25). Starting from **81d** (16 mg, 0.03 mmol) and following **GP3**, in 2h reaction time and after automated flash chromatography (Biotage), the title compound was synthesized as a yellow powder in its hydrochloride salt form (14 mg, quantitative). **HPLC-MS**: R.t. =4.34 (generic method). **MS (ESI)** m/z calc [M+H]+: 359.34, found 359.22. **^{1}H NMR (400 MHz, DMSO)** δ 9.21 (d, 2H), 8.57 (d, *J* = 4.3 Hz, 1H), 8.36 (s, 1H), 7.32 (d, *J* = 4.4 Hz, 4H), 7.21 (p, *J* = 4.3 Hz, 1H), 7.02 (d, *J* = 4.4 Hz, 1H), 6.81 (s, 1H), 4.00 (d, *J* = 12.0 Hz, 1H), 3.64 (d, *J* = 11.9 Hz, 1H), 3.25 (t, *J* = 12.2 Hz, 2H), 2.97 (d, *J* = 11.0 Hz, 1H), 2.91 – 2.83 (m, 1H), 2.78 (d, *J* = 17.0 Hz, 1H), 2.70 – 2.57 (m, 1H), 2.46 (s, 1H), 2.34 (t, *J* = 14.5 Hz, 1H), 2.19 (d, *J* = 11.9 Hz, 1H), 2.04 – 2.00 (m, 1H), 1.98 – 1.79 (m, 4H). **^{13}C NMR (101 MHz, DMSO)** δ 149.64, 148.68, 147.19, 144.58, 141.83, 128.81, 128.11, 127.29, 126.48, 122.98, 111.83, 105.95, 44.85, 43.77, 34.12, 33.81, 30.01, 28.15, 25.95, 22.23.

3.9.3: Synthesis of compound **85**

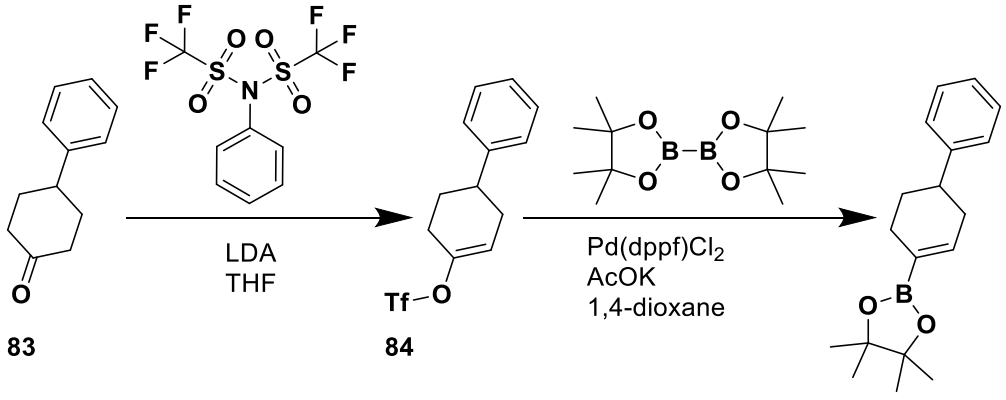

83 **84** **85**

Rac-1,2,3,6-tetrahydro-[1,1'-biphenyl]-4-yl trifluoromethanesulfonate (84). In a round-bottom flask, **83** (174 mg, 1 mmol, 1 eq.) was dissolved in THF (5 mL/mmol). The mixture was cooled to –78 °C, and LDA (1.2 mmol, 1.2 eq.) was added. After 2 h, bis(trifluoromethanesulfonyl)aniline (357 mg, 1 mmol, 1 eq.) was introduced, and the reaction was monitored by UPLC while allowing the mixture to warm to room temperature. After 16 h, the reaction was quenched with water, diluted with DCM, and transferred to a separatory funnel. The organic phase was washed with saturated NH_4Cl, dried over Na_2SO_4, and concentrated under reduced pressure. Purification by automated silica chromatography (Biotage) using a cyclohexane/AcOEt gradient afforded the title compound as a colourless oil (200 mg, 65%). **UPLC-MS**: R.t. =2.02 (apolar method). **MS (ESI)** m/z calc [M+H+H_2O]+: 324.05, found 324.2. **^{1}H NMR (400 MHz,**

CDCl3) δ 7.24 – 7.18 (m, 2H), 7.15 – 7.07 (m, 3H), 5.79 – 5.68 (m, 1H), 2.79 – 2.66 (m, 1H), 2.50 – 2.13 (m, 4H), 2.01 – 1.75 (m, 2H).

Rac-4,4,5,5-tetramethyl-2-(1,2,3,6-tetrahydro-[1,1'-biphenyl]-4-yl)-1,3,2-dioxaborolane (85). In a nitrogen atmosphere and a round-bottom flask, 84 (200 mg, 0.65 mmol, 1 eq.), bis(pinacolato)diboron (181 mg, 0.71 mmol, 1.1 eq.), and AcOK (191 mg, 1.95 mmol, 3 eq.) were dissolved in 1,4-dioxane (5 mL/mmol). The reaction mixture was stirred at 80 °C for 16 h and monitored by UPLC and TLC. After complete disappearance of the starting material, the reaction was filtered through Celite and purified by automated flash silica chromatography (Biotage), using a cyclohexane/AcOEt gradient (0–100%). The title compound was obtained as a white powder (28 mg, 15%). **UPLC-MS**: R.t. =2.02 (apolar method). **^{1}H NMR (400 MHz, CDCl3)** δ 7.24 – 7.17 (m, 2H), 7.14 – 7.06 (m, 3H), 6.61 – 6.55 (m, 1H), 2.75 – 2.63 (m, 1H), 2.38 – 2.23 (m, 2H), 2.20 – 2.06 (m, 2H), 1.91 – 1.81 (m, 1H), 1.68 – 1.53 (m, 1H), 1.19 (s, 12H).

3.9.4: Synthesis of compound **27**

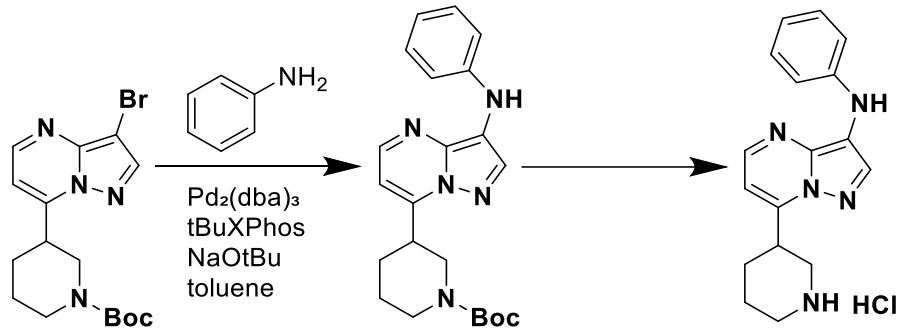

76 **86** **27**

Rac-*tert*-butyl 3-(3-(phenylamino)pyrazolo[1,5-a]pyrimidin-7-yl)piperidine-1-carboxylate (86). In a bottom flask, **76** (40 mg, 0.1 mmol, 1 eq), aniline (0.3 mmol, 27 mg, 3 eq), $Pd_2(dba)_3$ (9 mg, 0.01 mmol, 0.1 eq), tBuXPhos (4 mg, 0.01 mmol, 0.1 eq) were dissolved into degassed toluene. The reaction kept stirring at 90°C and was checked by UPLC. After 16h 2eq of aniline were added to the reaction mixture. After 39h of total stirring time the reaction was filtered through celite using AcOEt as solvent and the title compound was isolated after automated chromatography (Biotage) using as eluent phase petroleum ether and TBME, gradient 0 to 100%, obtaining a colourless oil (8 mg, 20%). **UPLC-MS**: R.t. =1.35 (apolar method). **MS (ESI)** m/z calc [M+H]+: 394.22, found 394.2. **^{1}H NMR (400 MHz, CDCl3)** δ 8.35 (s, 1H), 8.26 (s, 1H), 7.23 (t, *J* = 7.7 Hz, 2H), 6.92 (d, *J* = 8.0 Hz, 2H), 6.83 (t, *J* = 7.5 Hz, 1H), 6.68 (s, 1H), 4.40 (d, *J* = 13.0 Hz, 1H), 4.11 – 3.98 (m, 1H), 3.76 (tt, *J* = 10.1, 3.7 Hz, 1H), 3.24 (dd, *J* = 12.9, 9.6 Hz, 1H), 3.06 (ddd, *J* = 13.5, 10.4, 3.3 Hz, 1H), 2.33 (d, *J* = 12.3 Hz, 1H), 1.93 – 1.67 (m, 3H), 1.49 (s, 9H).

Rac-N-phenyl-7-(piperidin-3-yl)pyrazolo[1,5-a]pyrimidin-3-amine (27). Starting from **86** (8 mg, 0.02 mmol) and following **GP3**, in 5h reaction time, after automated flash chromatography (Biotage), using silica and as eluent phase DCM/MeOH gradient 0 to 20%, the title compound was synthesized as a yellow powder in its hydrochloride salt form (4 mg, 67%). **UPLC-MS**: R.t. =1.41 (generic method). **MS (ESI)** m/z calc [M+H]+: 294.17, found 294.1. **^{1}H NMR (400 MHz, DMSO)** δ 9.39 (d, *J* = 11.5 Hz, 1H), 9.15 (s, 1H), 8.46 (d, *J* = 4.2 Hz, 1H), 8.30 (s, 1H), 7.15 – 7.06 (m, 2H), 6.96 (d, *J* = 4.2 Hz, 1H), 6.81 – 6.74 (m, 2H), 6.64 (t, *J* = 7.3 Hz, 1H), 4.00 (d, *J* = 11.5 Hz, 1H), 3.37 (d, *J* = 12.6 Hz, 1H), 3.27 (m, 2H), 2.96 (d, *J* = 11.8 Hz, 1H), 2.22 (d, *J* = 11.3 Hz, 1H), 2.03 – 1.78 (m, 4H). **^{13}C NMR (151 MHz, DMSO)** δ 150.54, 148.78, 146.03, 144.76, 133.95, 131.84, 129.41, 128.74, 128.70, 128.03, 126.68, 126.52, 126.10, 126.08, 109.88, 106.45, 45.06, 43.92, 34.26, 25.91, 22.22.

3.9.5: Synthesis of compounds **28-33**

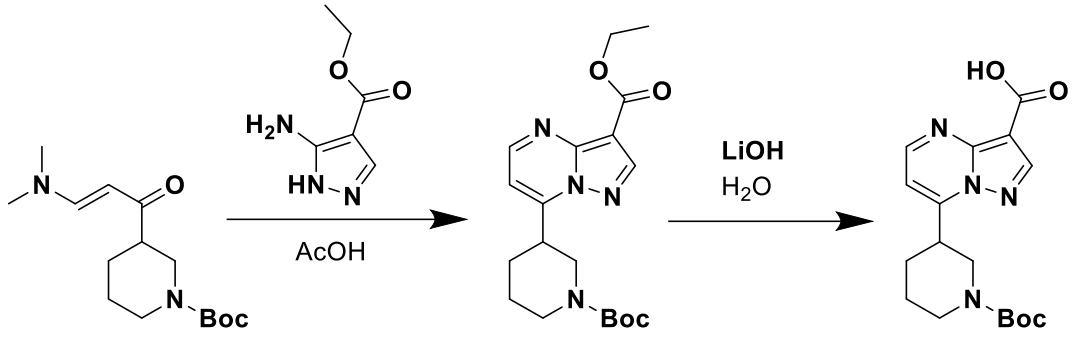

78 **87** **88**

Rac-*tert*-butyl 3-(pyrazolo[1,5-a]pyrimidin-7-yl)piperidine-1-carboxylate (87). In a nitrogen-purged round-bottom flask, **78** (1.0 g, 3.78 mmol, 1.0 equiv) was dissolved in AcOH (10 mL), and ethyl 5-amino-1H-pyrazole-4-carboxylate (585.9 mg, 3.78 mmol, 1.0 equiv) was added. The reaction mixture was stirred for 16 h and monitored by UPLC. Upon complete consumption of 78, the mixture was diluted with EtOAc and transferred to a separatory funnel. The organic layer was washed with aqueous Na_2CO_3, dried over Na_2SO_4, and concentrated under reduced pressure. After automated flash chromatography (Biotage) using silica and cyclohexane/AcOEt gradient from 0 to 37%, the title compound was obtained as a white powder. (467 mg, 32%). Reaction followed by TLC. **^{1}H NMR (400 MHz, DMSO)** δ 8.79 (d, *J* = 4.5 Hz, 1H), 8.66 (s, 1H), 7.24 (d, *J* = 4.5 Hz, 1H), 4.24 (bs, *J* = 29.4 Hz, 2H), 3.86 (bs, 1H), 3.69 – 3.57 (m, 1H), 3.00 (ddd, *J* = 13.6, 11.1, 3.1 Hz, 1H), 2.18 – 2.09 (m, 1H), 1.89 (bs, 1H), 1.77 (bs, 1H), 1.58 – 1.49 (m, 1H), 1.44 – 1.31 (m, 11H).

Rac-7-(1-(*tert*-butoxycarbonyl)piperidin-3-yl)pyrazolo[1,5-a]pyrimidine-3-carboxylic acid (88). In a round-bottom flask, **87** (467 mg, 1.2 mmol) was dissolved in a solution of THF:water 1:1 (2 ml/mmol). LiOH (143 mg, 6 mmol, 5 eq) was added and the reaction kept stirring for 16h at 80°C. The reaction was monitored by TLC. After starting disappearance the reaction mixture was dissolved in AcOEt, transferred in a separatory flask and washed with a saturated solution of NH_4Cl. The organic layer was collected and concentrated under reduced pressure. The title compound was obtained as a white powder (343 mg, 83%). Reaction followed by TLC. **^{1}H NMR (400 MHz, CDCl3)** δ 8.71 (d, *J* = 4.5 Hz, 1H), 8.68 (s, 1H), 6.97 (d, *J* = 4.5 Hz, 1H), 5.32 (s, 1H), 4.38 (dd, *J* = 13.2, 3.8 Hz, 1H), 4.03 (bs, 1H), 3.80 (tt, *J* = 9.5, 3.8 Hz, 1H), 3.31 – 3.21 (m, 1H), 3.11 – 3.00 (m, 1H), 2.32 (d, *J* = 12.8 Hz, 1H), 1.86 – 1.67 (m, 3H), 1.49 (s, 8H).

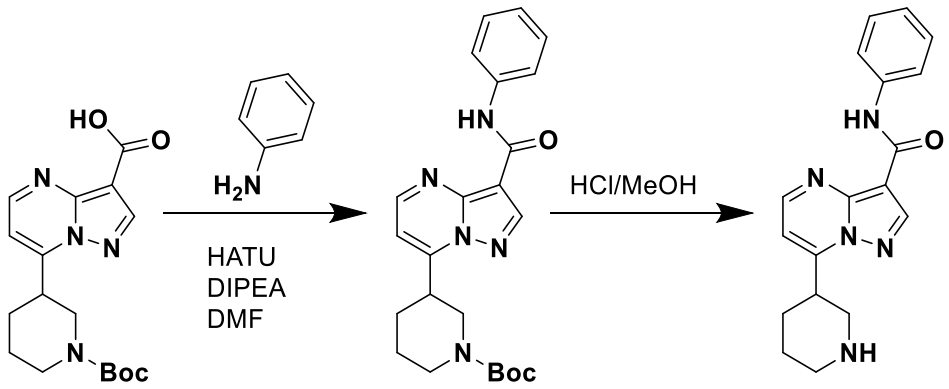

88 **89a** **28**

Rac-*tert*-butyl 3-(3-(phenylcarbamoyl)pyrazolo[1,5-a]pyrimidin-7-yl)piperidine-1-carboxylate (89a). Starting from **88** (30 mg, 0.086 mmol), following **GP5** and using aniline as the coupling partner,

after 16h reaction time, the title compound was synthesized as a yellow oil (30 mg, 82%). **UPLC-MS**: R.t. =1.47 (apolar method). **MS (ESI)** m/z calc [M+H]+: 422.21, found 422.2.

Rac-N-phenyl-7-(piperidin-3-yl)pyrazolo[1,5-a]pyrimidine-3-carboxamide (28). Starting from **89a** (30 mg, 0.071 mmol) and following **GP3**, after 2h reaction time and automated flash chromatography (Biotage), using silica and as eluent phase DCM/MeOH 1M gradient 0 to 20%, the title compound was synthesized as a white powder in its hydrochloride salt form (9 mg, 35%). **HPLC-MS**: R.t. =2.72 (generic method). **MS (ESI)** m/z calc [M+H]+: 322.16, found 322.06. **^{1}H NMR (400 MHz, DMSO)** δ 10.04 (s, 1H), 9.19 (bs, 1H), 8.91 (d, *J* = 4.5 Hz, 1H), 8.81 (s, 1H), 7.74 (d, *J* = 7.6 Hz, 2H), 7.39 (t, *J* = 7.9 Hz, 2H), 7.32 (d, *J* = 4.5 Hz, 1H), 7.12 (t, *J* = 7.4 Hz, 1H), 4.08 (s, 1H), 3.66 (d, *J* = 12.0 Hz, 1H), 3.28 (d, *J* = 12.2 Hz, 1H), 3.02 – 2.92 (m, 1H), 2.23 – 2.18 (m, 1H), 2.01 – 1.96 (m, 1H), 1.93 – 1.84 (m, 2H). **^{13}C NMR (151 MHz, DMSO)** δ 160.46, 153.41, 151.32, 146.61, 146.54, 139.57, 130.01, 124.57, 120.38, 108.37, 106.44, 45.28, 44.21, 40.36, 40.22, 40.08, 34.84, 26.57, 22.69.

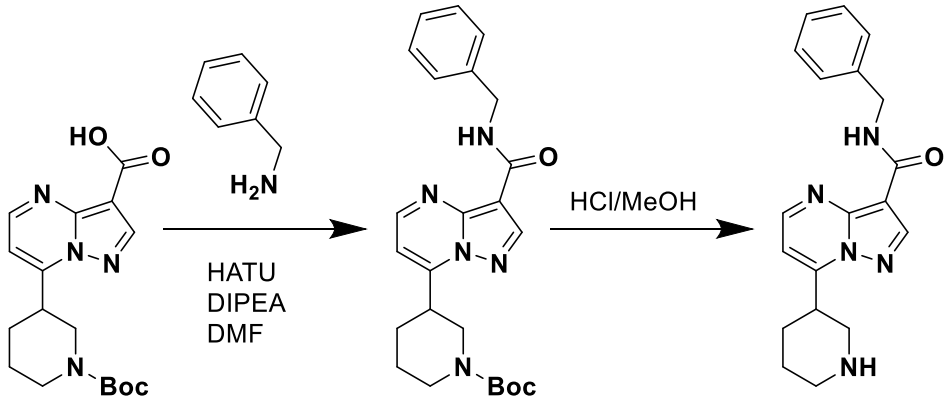

88 **89b** **29**

Rac-*tert*-butyl 3-(3-(benzylcarbamoyl)pyrazolo[1,5-a]pyrimidin-7-yl)piperidine-1-carboxylate **(89b).** Starting from **88 (**20 mg, 0.06 mmol), following **GP5** and using phenylmethanamine as the coupling partner, after 16h reaction time, the title compound was synthesized as a yellow oil (6 mg, 23%). **UPLC-MS**: R.t. =1.20 (apolar method). **MS (ESI)** m/z calc [M+H]+: 436.23, found 436.2.

Rac-*tert*-butyl 3-(3-(benzylcarbamoyl)pyrazolo[1,5-a]pyrimidin-7-yl)piperidine-1-carboxylate (29). Starting from **89b** (6 mg, 0.014 mmol) and following **GP3**, after 4h reaction time and automated flash chromatography (Biotage), using silica and as eluent phase DCM/MeOH gradient 0 to 20%, the title compound was synthesized as a white powder in its hydrochloride salt form (3 mg, 64%). **UPLC-MS**: R.t. =1.44 (generic method). **MS (ESI)** m/z calc [M+H]+: 336.18, found 336.1. **^{1}H NMR (400 MHz, MeOD)** δ 8.56 (d, *J* = 4.5 Hz, 1H), 8.49 (s, 1H), 7.31 – 7.25 (m, 2H), 7.25 – 7.19 (m, 2H), 7.18 – 7.10 (m, 1H), 6.99 (d, *J* = 4.6 Hz, 1H), 4.57 (s, 2H), 3.75 (tt, *J* = 11.3, 3.5 Hz, 1H), 3.41 (dt, *J* = 12.3, 3.2 Hz, 1H), 3.07 (d, *J* = 12.7 Hz, 1H), 2.76 (dd, *J* = 12.2, 11.1 Hz, 1H), 2.65 (td, *J* = 12.4, 2.8 Hz, 1H), 2.14 (d, *J* = 11.3 Hz, 1H), 1.85 – 1.60 (m, 3H). **^{13}C NMR (101 MHz, MeOD)** δ 163.18, 152.63, 151.85, 146.46, 144.99, 138.73, 128.26, 127.11, 126.92, 106.38, 104.60, 47.97, 45.24, 42.44, 37.17, 27.33, 24.83.

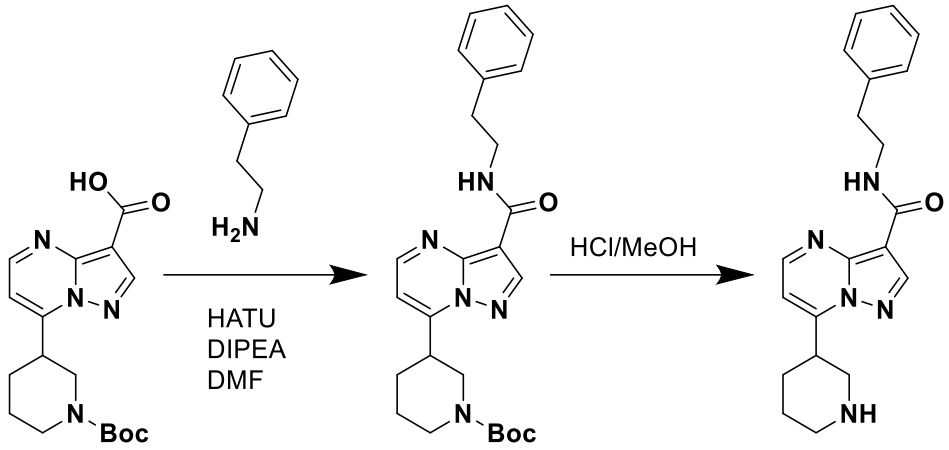

88 89c 30

Rac-*tert*-butyl 3-(3-(phenethylcarbamoyl)pyrazolo[1,5-a]pyrimidin-7-yl)piperidine-1-carboxylate (89c). Starting from **88** (34mg, 0.1mmol), following **GP5** and using 2-phenylethan-1-amine as the coupling partner, after 16h reaction time, the title compound was synthesized as a yellow oil (31mg, 69%). Reaction followed by TLC. **^{1}H NMR (400 MHz, CDCl3)** δ 8.64 (s, 1H), 8.42 (d, *J* = 4.5 Hz, 1H), 8.10 (s, 1H), 8.04 (t, *J* = 5.9 Hz, 1H), 7.32 – 7.11 (m, 3H), 6.78 (d, *J* = 4.5 Hz, 1H), 4.30 (dd, *J* = 13.0, 3.8 Hz, 1H), 3.96 (s, 1H), 3.79 – 3.66 (m, 3H), 3.55 (q, *J* = 6.7 Hz, 2H), 3.20 (s, 1H), 3.01 (s, 1H), 2.93 (t, *J* = 7.2 Hz, 2H), 2.80 (dt, *J* = 11.0, 6.7 Hz, 2H), 2.24 (s, 1H), 1.81 (td, *J* = 13.4, 7.1 Hz, 5H), 1.42 (s, 9H).

Rac-N-phenethyl-7-(piperidin-3-yl)pyrazolo[1,5-a]pyrimidine-3-carboxamide (30). Starting from **89c** (31mg, 0.069mmol) and following **GP3**, after 5h reaction time and automated flash chromatography (Biotage), using silica and as eluent phase DCM/MeOH gradient 0 to 20%, the title compound was synthesized as a white powder in its hydrochloride salt form (13mg, 49%). **HPLC-MS**: R.t. =2.81 (generic method). **MS (ESI)** m/z calc [M+H]+: 350.19, found 350.13. **^{1}H NMR (400 MHz, DMSO)** δ 8.73 (d, *J* = 4.5 Hz, 1H), 8.63 (s, 1H), 8.07 (t, *J* = 5.8 Hz, 1H), 7.36 – 7.17 (m, 7H), 4.01 – 3.91 (m, 1H), 3.61 (q, *J* = 6.8 Hz, 2H), 3.57 – 3.49 (m, 2H), 3.25 (s, 2H), 3.12 (t, *J* = 11.2 Hz, 1H), 2.87 (t, *J* = 7.2 Hz, 3H), 2.18 – 2.13 (m, 1H), 1.94 – 1.83 (m, 2H), 1.83 – 1.80 (m, 1H), 1.24 (bs, 1H). **^{13}C NMR (151 MHz, DMSO)** δ 162.01, 152.82, 151.79, 146.49, 146.13, 140.29, 138.45, 129.74, 129.36, 127.17, 107.84, 106.40, 46.18, 44.62, 41.01, 36.48, 35.49, 27.16, 23.46.

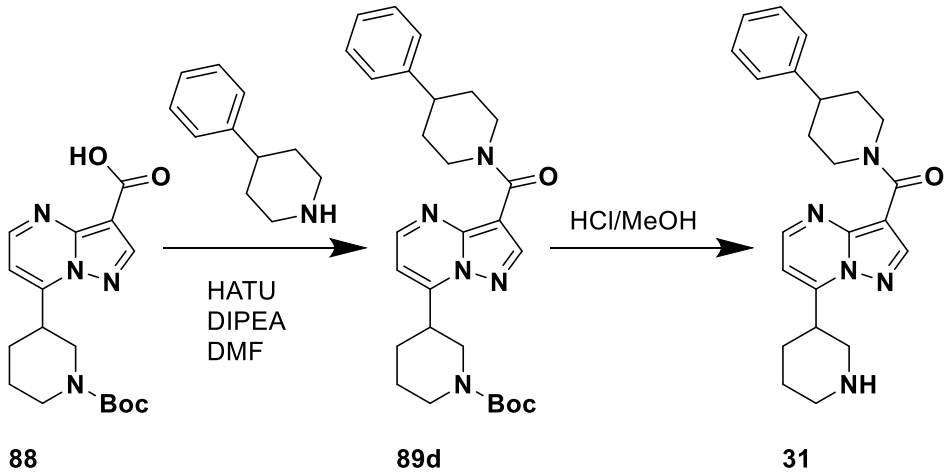

88 89d 31

Rac-*tert*-butyl 3-(3-(4-phenylpiperidine-1-carbonyl)pyrazolo[1,5-a]pyrimidin-7-yl)piperidine-1-carboxylate (89d). Starting from **88** (30mg, 0.086mmol), following **GP5** and using 4-phenylpiperidine as

the coupling partner, after 16h reaction time, the title compound was synthesized as a yellow oil (10mg, 23%). **UPLC-MS**: R.t. =1.44 (apolar method). **MS (ESI)** m/z calc [M+H]+: 490.28, found 490.2.

Rac-*tert*-butyl 3-(3-(4-phenylpiperidine-1-carbonyl)pyrazolo[1,5-a]pyrimidin-7-yl)piperidine-1-carboxylate (31). Starting from **89d** (10mg, 0.02mmol) and following **GP3**, after 5h reaction time, the title compound was synthesized as a white powder in its hydrochloride salt form (6mg, 70%). **UPLC-MS**: R.t. =1.63 (generic method). **MS (ESI)** m/z calc [M+H]+: 390.22, found 390.2. **^{1}H NMR (400 MHz, DMSO)** δ 9.49 (bs, 1H), 9.28 – 9.20 (m, 1H), 8.70 (d, *J* = 4.4 Hz, 1H), 8.50 (s, 1H), 7.36 – 7.18 (m, 6H), 7.14 (d, *J* = 4.4 Hz, 1H), 4.70 (s, 1H), 4.10 – 4.00 (m, 1H), 3.64 (d, *J* = 11.9 Hz, 1H), 3.29 – 3.22 (m, 1H), 3.03 – 2.90 (m, 2H), 2.90 – 2.79 (m, 2H), 2.19 (d, *J* = 10.8 Hz, 1H), 2.01 – 1.73 (m, 6H), 1.72 – 1.59 (m, 2H), 4.00 – 3.90 (m, 1H). **^{13}C NMR (101 MHz, DMSO)** δ 162.52, 151.77, 149.52, 146.14, 145.68, 145.04, 128.91, 127.20, 126.68, 107.07, 106.81, 44.76, 43.62, 42.24, 34.19, 29.83, 26.10, 22.19.

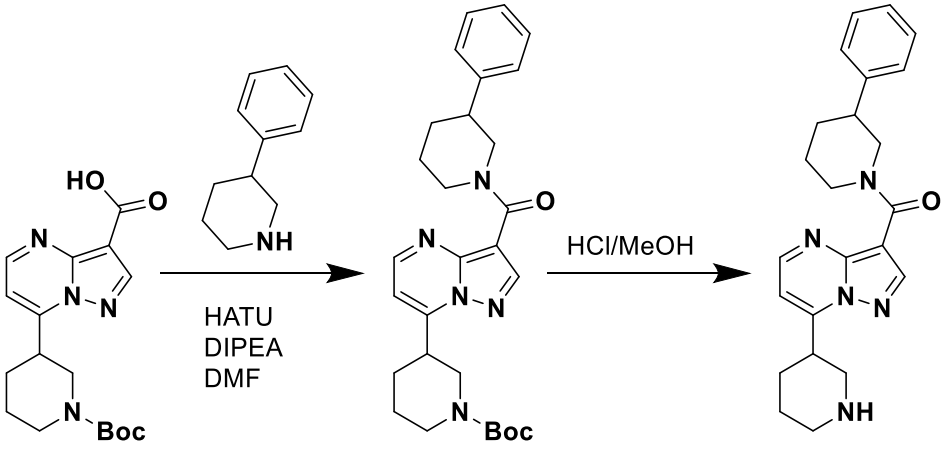

88 **89e** **32**

***Tert*-butyl 3-(3-(3-phenylpiperidine-1-carbonyl)pyrazolo[1,5-a]pyrimidin-7-yl)piperidine-1-carboxylate (89e).** Starting from **88** (34mg, 0.1mmol), following **GP5** and using 3-phenylpiperidine as the coupling partner, after 16h reaction time, the title compound was synthesized as a yellow oil, as a mixture of diastereoisomers (40mg, 81%). **UPLC-MS**: R.t. =1.45 (apolar method). **MS (ESI)** m/z calc [M+H]+: 490.28, found 490.3.

(3-Phenylpiperidin-1-yl)(7-(piperidin-3-yl)pyrazolo[1,5-a]pyrimidin-3-yl)methanone (32). Starting from **89e** (40mg, 0.081mmol) and following **GP3**, after 5h reaction time, the title compound was synthesized as a white powder in its hydrochloride salt form, as a 2:1 mixture of diastereoisomers (22mg, 70%). **HPLC-MS**: R.t. =3.06, 3.08 (generic method). **MS (ESI)** m/z calc [M+H]+: 390.22, found 390.22 (for both peaks). **^{1}H NMR (400 MHz, DMSO)** δ 9.25 (s, 2H), 8.73 (s, 1H), 8.49 (s, 1H), 7.41 – 7.08 (m, 7H), 4.59 (s, 1H), 4.02 (s, 1H), 3.85 (s, 1H), 3.63 (d, *J* = 12.0 Hz, 1H), 3.34 (s, 1H), 3.26 – 3.22 (m, 1H), 2.95 (s, 2H), 2.80 (s, 1H), 2.17 (s, 1H), 2.01 – 1.92 (m, 2H), 1.92 – 1.72 (m, 5H), 1.63 (s, 2H). **^{13}C NMR (101 MHz, DMSO)** δ 162.53, 151.77, 149.66, 145.89, 144.94, 144.00, 128.92, 127.56, 126.99, 106.98, 106.84, 44.63, 43.51, 32.00, 26.16, 22.12. N*ote: some ^{1}H signals appear not well resolved, consistent with the presence of diastereoisomers.*

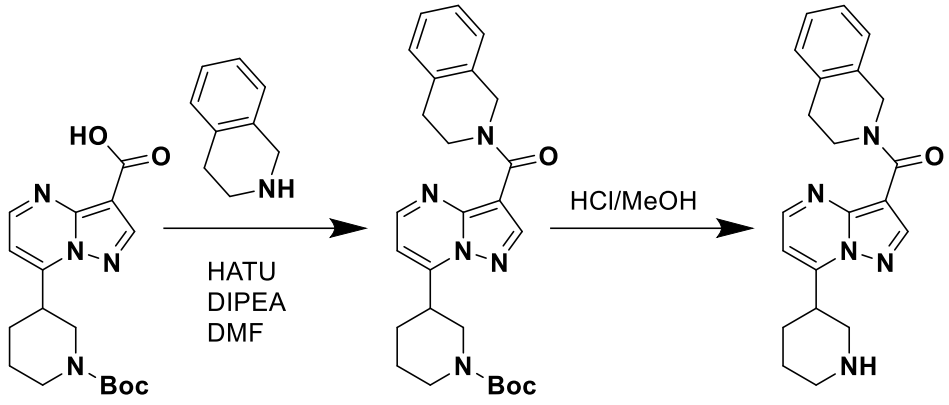

88 89f 33

Rac-tert-butyl 3-(3-(1,2,3,4-tetrahydroisoquinoline-2-carbonyl)pyrazolo[1,5-a]pyrimidin-7-yl)piperidine-1-carboxylate (89f). Starting from **88** (30mg, 0.08mmol), following **GP5** and using 1,2,3,4-tetrahydroisoquinoline as the coupling partner, after 16h reaction time, the title compound was synthesized as a yellow oil (33mg, 87%). **UPLC-MS**: R.t. =1.19 (apolar method). **MS (ESI)** m/z calc [M+H]+: 462.25, found 462.2

Rac-(3,4-dihydroisoquinolin-2(1H)-yl)(7-(piperidin-3-yl)pyrazolo[1,5-a]pyrimidin-3-yl)methanone (33). Starting from **89f** (33mg, 0.071mmol) and following **GP3**, after 2h reaction time and automated flash chromatography (Biotage), using silica and as eluent phase DCM/MeOH 1M gradient 0 to 20%, the title compound was synthesized as a white powder in its hydrochloride salt form (7mg, 23%). **UPLC-MS**: R.t. =1.46 (generic method). **MS (ESI)** m/z calc [M+H]+: 362.19, found 362.19. **1H NMR (400 MHz, DMSO-d6)**: δ 8.69 (d, *J* = 4.4 Hz, 1H), 8.51 (s, 1H), 7.17 (dd, *J* = 11.9, 4.2 Hz, 5H), 4.78 (s, 2H), 4.07 (tt, *J* = 11.9, 3.6 Hz, 1H), 3.84 (bs, *J* = 14.3 Hz, 1H), 3.74 (bs, 1H), 3.61 – 3.55 (m, 1H), 3.33 – 3.27 (m, 1H), 3.27 – 3.21 (m, 1H), 2.96 – 2.85 (m, 3H), 2.23 – 2.14 (m, 1H), 1.93 (tq, *J* = 7.1, 2.9 Hz, 2H), 1.83 (tdd, *J* = 12.4, 9.4, 6.8 Hz, 1H). **13C NMR (101 MHz, DMSO-d6)**: δ 152.38, 150.51, 146.22, 145.80, 135.58, 129.53, 127.39, 127.08, 107.40, 107.38, 45.57, 44.23, 41.03, 34.96, 26.91, 22.96.

3.9.6: Synthesis of compounds **34-38**

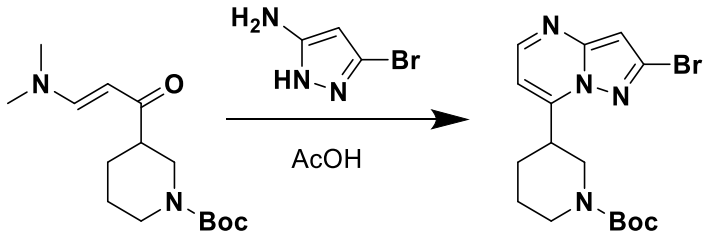

78 90

Rac-tert-butyl 3-(2-bromopyrazolo[1,5-a]pyrimidin-7-yl)piperidine-1-carboxylate (90) In a round-bottom flask, **78** (0.41 mmol theoretical, 1 eq.) was dissolved in AcOH (20 mL/mmol), and 3-bromo-1H-pyrazol-5-amine (107 mg, 0.41 mmol, 1 eq.) was added. The reaction mixture was stirred at 80 °C overnight and monitored by UPLC. After complete disappearance of the starting material (16h reaction time), the mixture was diluted with AcOEt, transferred to a separatory funnel, and washed with saturated Na_2CO_3. The organic layer was collected, dried over Na_2SO_4, and concentrated under reduced pressure. Purification by automated flash chromatography (Biotage) afforded the title compound as a yellow oil (115 mg, 74% over two steps). **UPLC-MS**: R.t. =1.84 (generic method). **MS (ESI)** m/z calc [M+H]+: 283.09, found 283.2.

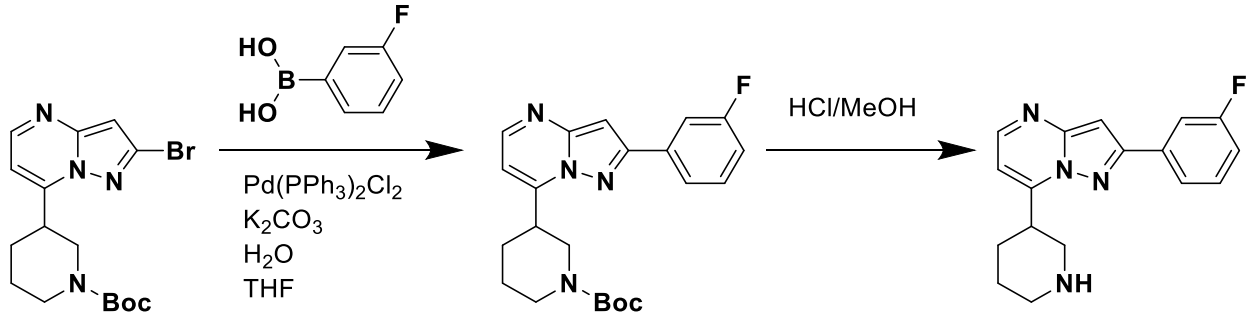

90 **91a** **34**

Rac-tert-butyl 3-(2-(3-fluorophenyl)pyrazolo[1,5-a]pyrimidin-7-yl)piperidine-1-carboxylate (91a). Starting from **90** (96mg, 0.25mmol), following **GP2** and using (3-fluorophenyl)boronic acid as the coupling partner, the title compound was synthesized as a yellow oil (60mg, 60%). **UPLC-MS**: R.t. =1.86 (apolar method). **MS (ESI)** m/z calc [M+H]+: 387.48, found 397.0.

Rac-2-(3-fluorophenyl)-7-(piperidin-3-yl)pyrazolo[1,5-a]pyrimidine (34). Starting from **91a** (60mg, 0.15mmol) and following **GP3**, after 2h reaction time and automated flash chromatography (Biotage), using silica and as eluent phase DCM/MeOH gradient 0 to 20%, the title compound was synthesized as a yellow powder in its hydrochloride salt form (50mg, 90%). **UPLC-MS**: R.t. =1.65 (generic method). **MS (ESI)** m/z calc [M+H]+: 296.35, found 296.9. **^{1}H NMR (400 MHz, DMSO)** δ 9.44 (s, 1H), 9.24 (s, 1H), 8.50 (d, *J* = 4.4 Hz, 1H), 7.93 – 7.83 (m, 2H), 7.50 (td, *J* = 8.0, 6.0 Hz, 1H), 7.31 (s, 1H), 7.22 (td, *J* = 8.6, 2.7 Hz, 1H), 7.09 (s, 0H), 6.97 (d, *J* = 4.4 Hz, 1H), 4.07 – 4.02 (m, 1H), 3.65 (d, *J* = 12.0 Hz, 1H), 3.17 (q, *J* = 11.4 Hz, 1H), 2.95 – 2.87 (m, 1H), 2.15 (d, *J* = 10.9 Hz, 1H), 1.97 – 1.78 (m, 3H). **^{13}C NMR (101 MHz, DMSO)** δ 163.08 (d, *J* = 243.2 Hz), 153.55 (d, *J* = 2.8 Hz), 150.44, 150.07, 148.54, 135.33 (d, *J* = 8.3 Hz), 131.41 (d, *J* = 8.5 Hz), 122.83 (d, *J* = 2.6 Hz), 116.29 (d, *J* = 21.1 Hz), 113.28 (d, *J* = 22.6 Hz), 106.41, 94.50, 44.73, 43.57, 34.16, 25.84, 22.19.

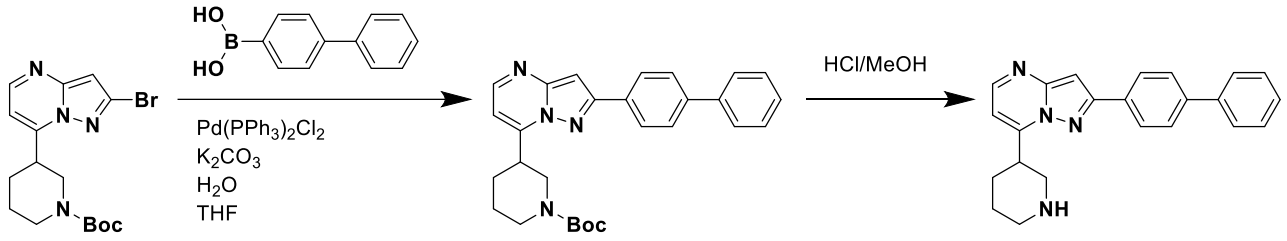

90 **91b** **35**

Rac-tert-butyl 3-(2-([1,1'-biphenyl]-4-yl)pyrazolo[1,5-a]pyrimidin-7-yl)piperidine-1-carboxylate (91b). Starting from **90** (30mg, 0.079mmol, 1eq), following **GP2** and [1,1'-biphenyl]-4-ylboronic acid as the coupling partner, the title compound was synthesized as a yellow oil (23mg, 64%). **UPLC-MS**: R.t. =2.31 (apolar method). **MS (ESI)** m/z calc [M+H]+: 455.24, found 455.3.

Rac-tert-butyl 3-(2-([1,1'-biphenyl]-4-yl)pyrazolo[1,5-a]pyrimidin-7-yl)piperidine-1-carboxylate (35). Starting from **91b** (23mg, 0.06mmol) and following **GP3**, after 2h reaction time and by collecting the product formed directly as a pure solid in the reaction environment, the title compound was synthesized as a white powder in its hydrochloride salt form (7mg, 23%). **UPLC-MS**: R.t. =1.93 (generic method). **MS (ESI)** m/z calc [M+H]+: 355.19, found 355.1. **^{1}H NMR (400 MHz, DMSO)** δ 9.26 – 9.19 (m, 1H), 9.07 – 9.00 (m, 1H), 8.49 (d, *J* = 4.4 Hz, 1H), 8.17 – 8.10 (m, 2H), 7.80 – 7.73 (m, 2H), 7.73 – 7.66 (m, 2H), 7.44 (dd, *J* = 8.4, 6.9 Hz, 2H), 7.37 – 7.31 (m, 1H), 7.29 (s, 1H), 6.95 (d, *J* = 4.4 Hz, 1H), 4.07 – 4.00

(m, 1H), 3.69 (d, *J* = 11.7 Hz, 1H), 3.20 (q, *J* = 11.5 Hz, 2H), 2.92 (t, *J* = 12.1 Hz, 1H), 2.18 (d, *J* = 10.0 Hz, 1H), 1.96 – 1.80 (m, 3H).

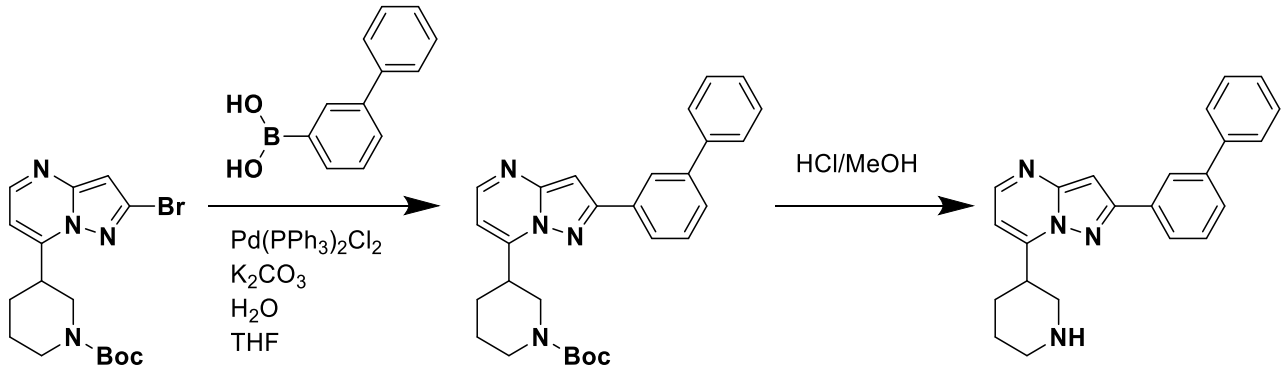

90 **91c** **36**

c

Rac-tert-butyl 3-(2-([1,1'-biphenyl]-3-yl)pyrazolo[1,5-a]pyrimidin-7-yl)piperidine-1-carboxylate (91c). Starting from **90** (30mg, 0.08mmol), following **GP2** and using [1,1'-biphenyl]-3-ylboronic acid as the coupling partner, the title compound was synthesized as a yellow oil (32mg, 89%). **UPLC-MS**: R.t. =2.31 (apolar method). **MS (ESI)** m/z calc [M+H]+: 455.24, found 455.3.

Rac-2-([1,1'-biphenyl]-3-yl)-7-(piperidin-3-yl)pyrazolo[1,5-a]pyrimidine (36). Starting from **91c** (32mg, 0.07mmol) and following **GP3**, after 4h30min reaction time and automated flash chromatography (Biotage), using silica and as eluent phase DCM/MeOH gradient 0 to 20%, the title compound was synthesized as a white powder in its hydrochloride salt form (21mg, 80%). **UPLC-MS**: R.t. =3.82 (generic method). **MS (ESI)** m/z calc [M+H]+: 355.19, found 355.23. **^{1}H NMR (400 MHz, DMSO)** δ 9.39 – 9.00 (m, 2H), 8.56 (d, *J* = 4.4 Hz, 1H), 8.35 (t, *J* = 1.8 Hz, 1H), 8.12 (dt, *J* = 7.7, 1.4 Hz, 1H), 7.84 – 7.79 (m, 2H), 7.75 (dt, *J* = 7.8, 1.4 Hz, 1H), 7.63 (t, *J* = 7.7 Hz, 1H), 7.53 (dd, *J* = 8.4, 6.9 Hz, 2H), 7.47 – 7.39 (m, 2H), 7.03 (d, *J* = 4.4 Hz, 1H), 4.20 – 4.08 (m, 1H), 3.74 (d, *J* = 12.0 Hz, 1H), 3.41 – 3.37 (m, 1H), 3.27 – 3.16 (m, 1H), 2.97 (dd, *J* = 13.7, 9.6 Hz, 1H), 2.24 (d, *J* = 9.8 Hz, 1H), 2.01 – 1.86 (m, 3H). **^{13}C NMR (101 MHz, DMSO)** δ 154.90, 150.31, 150.08, 148.43, 141.41, 140.32, 133.55, 130.04, 129.52, 128.25, 127.38, 125.87, 125.03, 106.17, 94.41, 94.05, 45.13, 43.94, 34.22, 25.87, 22.31.

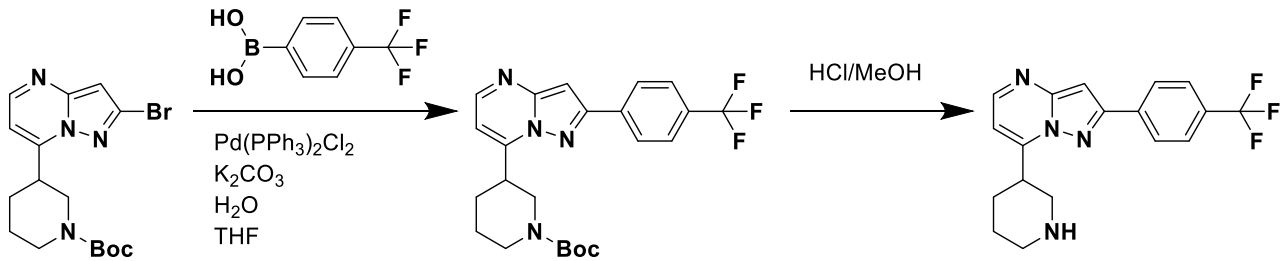

90 **91e** **38**

Rac-tert-butyl 3-(2-(4-(trifluoromethyl)phenyl)pyrazolo[1,5-a]pyrimidin-7-yl)piperidine-1-carboxylate (91e). Starting from **90** (30mg, 0.079mmol), following **GP2** and using (4-(trifluoromethyl)phenyl)boronic acid as the coupling partner, the title compound was synthesized as a yellow oil (15mg, 42%). **UPLC-MS**: R.t. =2.12 (apolar method). **MS (ESI)** m/z calc [M+H]+: 447.2, found 447.2. **^{1}H NMR (400 MHz, CDCl3)** δ 8.45 (d, *J* = 4.4 Hz, 1H), 8.17 (d, *J* = 8.1 Hz, 2H), 7.74 (d, *J* = 8.2 Hz, 2H), 7.07 (s, 1H), 6.73 (d, *J* = 4.4 Hz, 1H), 4.48 – 4.40 (m, 1H), 3.85 (tt, *J* = 10.0, 3.8 Hz, 1H), 3.28 (dd, *J* = 12.9, 9.6 Hz, 1H), 3.13 – 3.02 (m, 1H), 2.35 (d, *J* = 12.8 Hz, 1H), 2.00 – 1.70 (m, 4H), 1.46 (s, 10H).

Rac-7-(piperidin-3-yl)-2-(4-(trifluoromethyl)phenyl)pyrazolo[1,5-a]pyrimidine (38). Starting from **91e** (15mg, 0.033mmol) and following **GP3**, after 2h reaction time and automated flash chromatography (Biotage), using silica and as eluent phase DCM/MeOH gradient 0 to 20%, the title compound was synthesized as a white powder in its hydrochloride salt form (8mg, 63%). **UPLC-MS**: R.t. =1.80 (generic method). **MS (ESI)** m/z calc [M+H]+: 347.14, found 347.1. **^{1}H NMR (400 MHz, DMSO)** δ 9.33 (s, 1H), 9.13 (s, 1H), 8.60 (d, *J* = 4.4 Hz, 1H), 8.33 (d, *J* = 8.1 Hz, 2H), 7.91 (d, *J* = 8.2 Hz, 2H), 7.46 (s, 1H), 7.08 (d, *J* = 4.4 Hz, 1H), 4.11 (d, *J* = 11.9 Hz, 1H), 3.73 (d, *J* = 12.3 Hz, 1H), 3.43 – 3.39 (m, 1H), 3.31 – 3.23 (m, 1H), 2.99 (d, *J* = 11.7 Hz, 1H), 2.24 (d, *J* = 9.9 Hz, 1H), 2.03 – 1.87 (m, 3H). **^{13}C NMR (151 MHz, DMSO)** δ 153.75, 151.17, 150.64, 149.13, 137.35, 127.85, 126.96 – 126.71 (m), 123.61 (q, *J* = 752.5 Hz), 107.20, 95.58, 45.52, 44.39, 34.66, 26.45, 22.82.

3.9.7: Synthesis of compounds **43-45, 68**

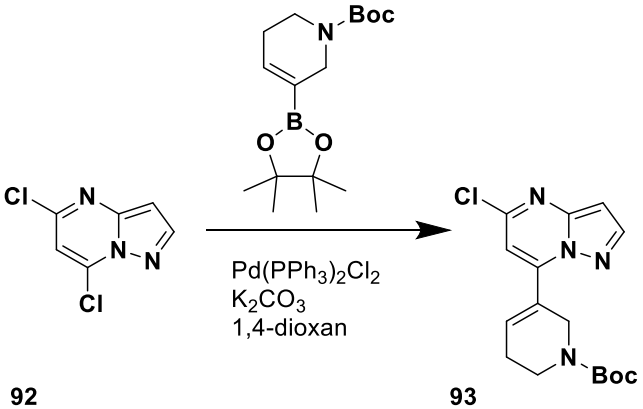

92 93

Tert-butyl 5-(5-chloropyrazolo[1,5-a]pyrimidin-7-yl)-3,6-dihydropyridine-1(2H)-carboxylate (93): In a 7ml vial, **92** (263mg, 1.4mmol, 1eq), tert-butyl 5-(4,4,5,5-tetramethyl-1,3,2-dioxaborolan-2-yl)-3,6-dihydropyridine-1(2H)-carboxylate (430mg, 1.4mmol, 1eq), $Pd(PPh_3)_2Cl_2$ (80mg, 0.07mmol 0.05eq), K_2CO_3 (576mg, 4.2mmol, 3eq) were added and solubilized in degassed 1,4-dioxane (8ml/mmol). The reaction kept stirring at 80°C o.n. and checked by UPLC. After boronic ester disappearance, the reaction mixture was filtered through celite and purified by automated flash chromatography (Biotage system), using cyclhoexane:AcOEt as gradient (0 to 40%) obtaining the title compound (281, 0.8mmol) and the corresponding regioisomer (143mg, 0.4mmol). **UPLC-MS**: R.t. =1.18 (apolar method). **MS (ESI)** m/z calc [M+H]+: 337.12, found 337.0 . **^{1}H NMR (400 MHz, CDCl3)** δ 8.18 (d, *J* = 2.3 Hz, 1H), 7.17 (s, 1H), 6.84 (tt, *J* = 4.3, 1.9 Hz, 1H), 6.76 – 6.72 (m, 1H), 4.49 (s, 2H), 3.60 (t, *J* = 5.7 Hz, 2H), 2.44 (s, 2H), 1.52 (s, 9H).

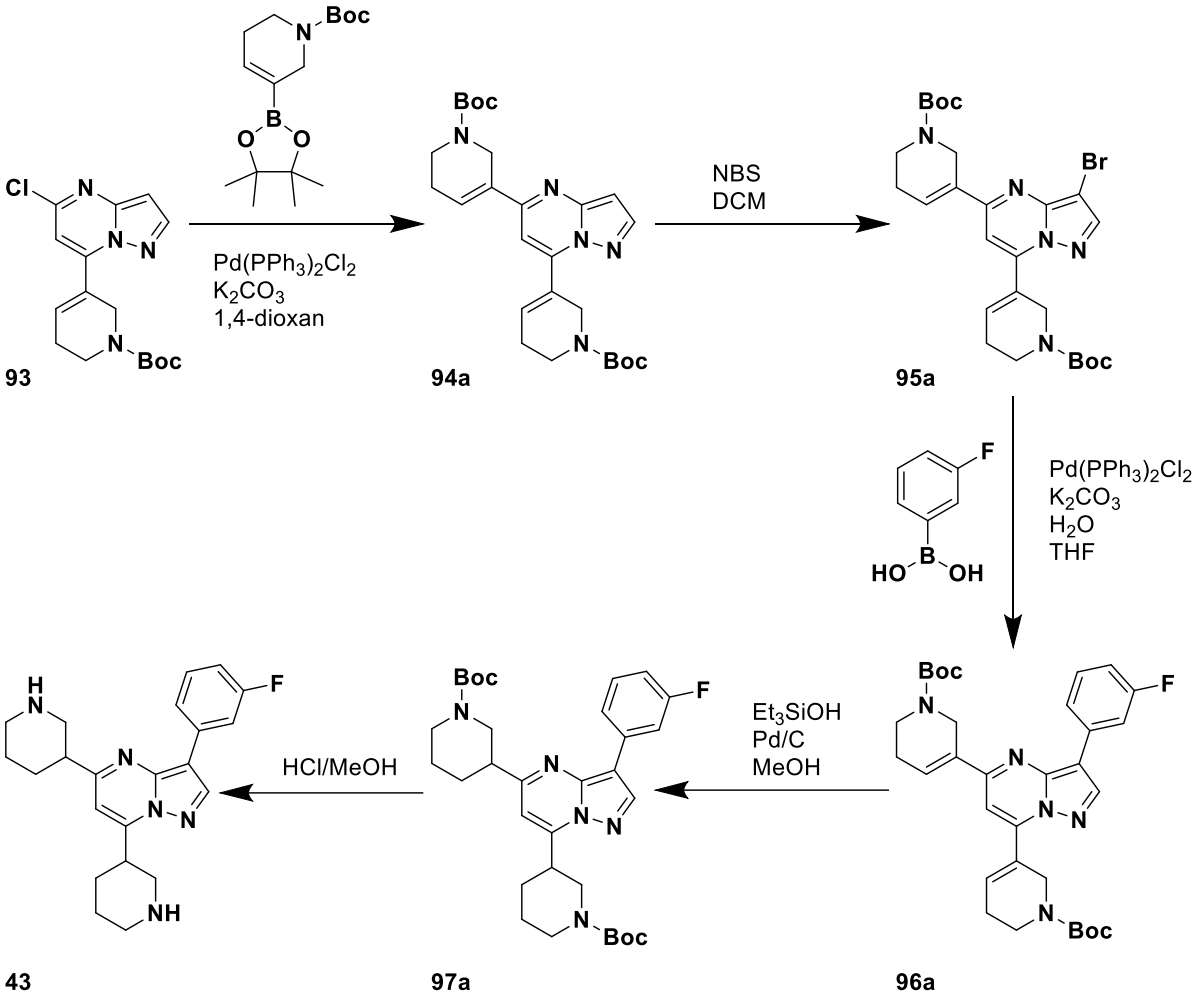

Di-tert-butyl 5,5'-(pyrazolo[1,5-a]pyrimidine-5,7-diyl)bis(3,6-dihydropyridine-1(2H)-carboxylate) (94a): Starting from **93** (43mg, 0.13mmol, 1eq), following **GP2** and using as a coupling partner tert-butyl 5-(4,4,5,5-tetramethyl-1,3,2-dioxaborolan-2-yl)-3,6-dihydropyridine-1(2H)-carboxylate (49mg, 0.16mmol, 1.2eq), the title compound was synthesized as a yellow oil (57mg, 91%). **UPLC-MS**: R.t. =1.99 (apolar method) **MS (ESI)** m/z calc [M+H]+: 482.27, found 482.3.

Tert-butyl 5-(3-bromo-5-(1-(methoxycarbonyl)-1,2,5,6-tetrahydropyridin-3-yl)pyrazolo[1,5-a]pyrimidin-7-yl)-3,6-dihydropyridine-1(2H)-carboxylate (95a). Starting from **94a** (49mg, 0.12mmol, 1eq) and following **GP1,** after 6h reaction time, the title compound was synthesized as a yellow oil (67mg, quantitative). **UPLC-MS**: R.t. =2.42 (apolar method) **MS (ESI)** m/z calc [M+H]+: 562.18, found 562.1.

Di-tert-butyl 5,5'-(3-(3-fluorophenyl)pyrazolo[1,5-a]pyrimidine-5,7-diyl)bis(3,6-dihydropyridine-1(2H)-carboxylate) (96a). Starting from 95a (67mg, 0.12mmol), following **GP2** and using as a coupling partner (3-fluorophenyl)boronic acid, the title compound was synthesized as a yellow oil (42mg, 61%). **UPLC-MS**: R.t. =1.50 (superapolar method) **MS (ESI)** m/z calc [M+H]+: 576.29, found 576.2.

Di-tert-butyl 3,3'-(3-(3-fluorophenyl)pyrazolo[1,5-a]pyrimidine-5,7-diyl)bis(piperidine-1-carboxylate) (97a): starting from **96a** (42mg, 0.07mmol) and following **GP4**, after 4h reaction time, the title compound was synthesized as a colourless oil, as a mixture of diastereoisomers (11mg, 27%). **UPLC-MS**: R.t. =1.50 (superapolar method) **MS (ESI)** m/z calc [M+H]+: 580.33, found 580.3.

3-(3-Fluorophenyl)-5,7-di(piperidin-3-yl)pyrazolo[1,5-a]pyrimidine (43): Starting from **97a** (11mg, 0.02mmol) and following **GP3**, after 16h reaction time and automated flash chromatography (Biotage), using neutral alumina and as eluent phase DCM/MeOH gradient 0 to 20%, the title compound was

synthesized as a white powder in its hydrochloride salt form, as a 3:2 mixture of diastereoisomers (5mg, 65%). **HPLC-MS**: R.t. =2.14, 2.25 (generic method) **MS (ESI)** m/z calc [M+H]+: 380.22, found 380.26 (for both peaks). **^{1}H NMR (400 MHz, DMSO)** δ 9.57 (s, 1H), 9.20 (s, 3H), 8.88 (s, 1H), 8.08 – 7.95 (m, 2H), 7.49 (td, *J* = 8.2, 6.5 Hz, 1H), 7.21 (s, 1H), 7.08 (td, *J* = 9.0, 2.7 Hz, 1H), 4.03 (d, *J* = 12.0 Hz, 1H), 3.63 (d, *J* = 11.4 Hz, 2H), 3.33 (s, 12H), 2.95 (s, 2H), 2.22 (d, *J* = 11.5 Hz, 2H), 1.93 (t, *J* = 15.3 Hz, 5H), 1.74 (d, *J* = 12.4 Hz, 1H). **^{13}C NMR (151 MHz, DMSO)** δ 163.23 (d, *J* = 192.5 Hz), 162.26, 149.47, 144.36, 143.18, 134.83 (d, *J* = 8.8 Hz), 131.12 (d), 121.98, 113.05 (d, *J* = 20.9 Hz), 112.45 (d, *J* = 22.8 Hz), 108.37, 105.87 (d), 46.01, 44.96, 43.81, 43.45, 40.87, 40.84, 34.20, 28.85, 26.25, 22.30, 22.21, 9.02. *Note: some ^{1}H signals appear broad and not well resolved, consistent with the presence of two diastereoisomers.*

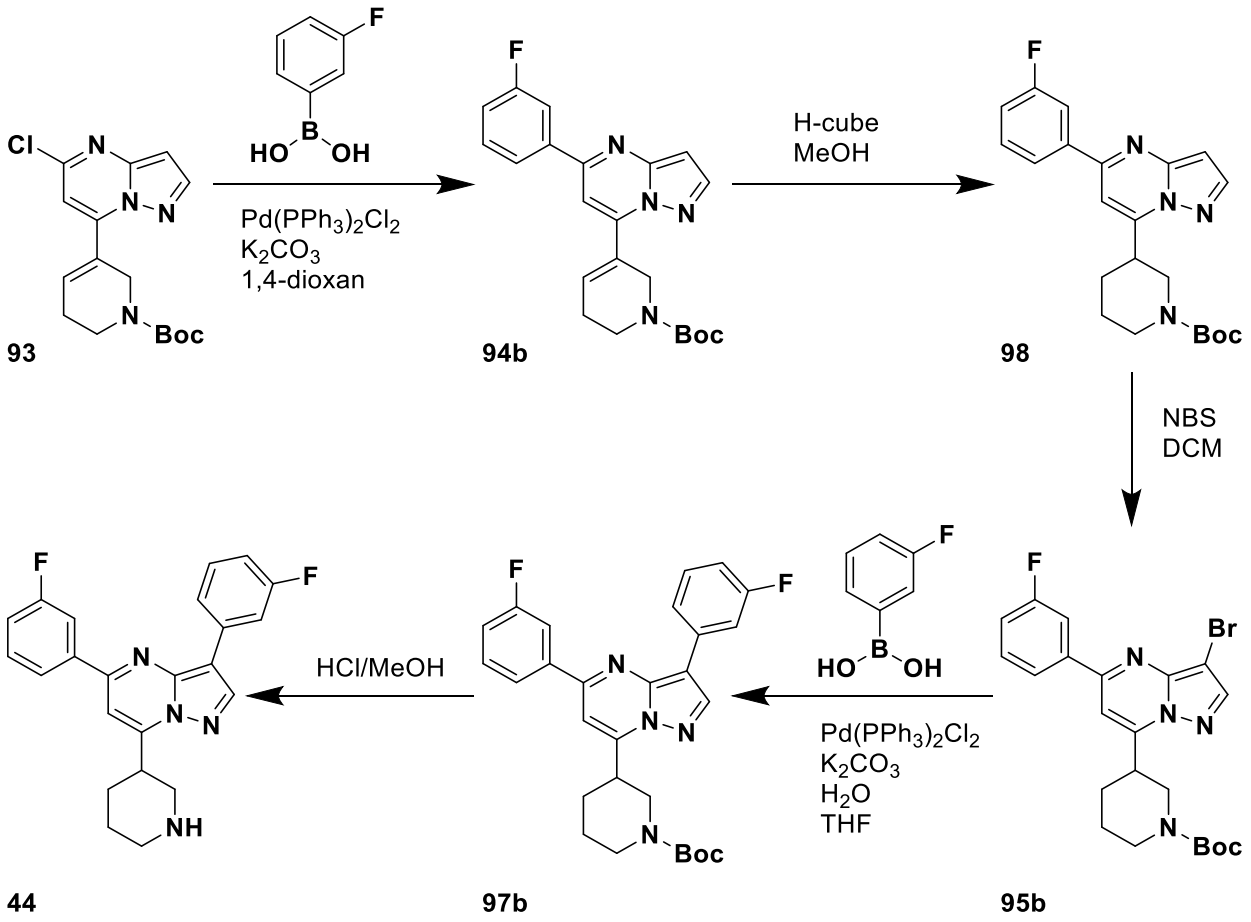

Tert-butyl 5-(5-(3-fluorophenyl)pyrazolo[1,5-a]pyrimidin-7-yl)-3,6-dihydropyridine-1(2H)-carboxylate (94b). Starting from **93** (100mg, 0.3mmol, 1eq), following **GP2** and using as the coupling partner (3-fluorophenyl)boronic acid, the title compound was synthesized as a yellow oil (110mg, 93%). **UPLC-MS**: R.t. =1.80 (apolar method) **MS (ESI)** m/z calc [M+H]+: 395.18, found 395.0.

Rac-tert-butyl 5-(3-bromo-5-(3-fluorophenyl)pyrazolo[1,5-a]pyrimidin-7-yl)-3,6-dihydropyridine-1(2H)-carboxylate (98). **94b** (110 mg, 0.28 mmol) was dissolved in EtOH (0.02 M) and subjected to H-Cube hydrogenation using a 10% Pd/C cartridge at 40 bar, 60 °C, and a flow rate of 0.5 mL/min. The resulting mixture was purified by automated flash chromatography (Biotage) using a cyclohexane/AcOEt gradient (0–100%), affording the product as a yellow oil (58 mg, 52%). **UPLC-MS**: R.t. =1.80 (apolar method) **MS (ESI)** m/z calc [M+H]+: 397.2, found 397.2.

Rac-tert-butyl 5-(3,5-bis(3-fluorophenyl)pyrazolo[1,5-a]pyrimidin-7-yl)-3,6-dihydropyridine-1(2H)-carboxylate (95b). Starting from **98** (43mg, 0.11mmol), following **GP1** and using (3-

fluorophenyl)boronic acid as the coupling partner, after 6h reaction time, the title compound was synthesized as a yellow oil (45mg, quantitative). **UPLC-MS**: R.t. =2.18 (apolar method) **MS (ESI)** m/z calc [M+H]+: 477.11, found 477.0.

Rac-tert-butyl 3-(3,5-bis(3-fluorophenyl)pyrazolo[1,5-a]pyrimidin-7-yl)piperidine-1-carboxylate (97b). Starting from **95b** (45mg, 0.11mmol)**,** following **GP2** and using (3-fluorophenyl)boronic acid as the coupling partner, the title compound was synthesized as a yellow oil (45mg, 83%). **UPLC-MS**: R.t. =2.57 (apolar method) **MS (ESI)** m/z calc [M+H]+: 491.22, found 491.2.

Rac-3,5-bis(3-fluorophenyl)-7-(piperidin-3-yl)pyrazolo[1,5-a]pyrimidine (44). Starting from **135** (45mg, 0.09mmol) and following **GP3**, after 15h reaction time and automated flash chromatography (Biotage), using silica and as eluent phase DCM/MeOH gradient 0 to 20%, the title compound was synthesized as a white powder in its hydrochloride salt form (20mg, 46%). **UPLC-MS**: R.t. =0.84 (apolar method) **MS (ESI)** m/z calc [M+H]+: 391.17, found 391.1. **^{1}H NMR (400 MHz, DMSO)** δ 9.21 (s, 2H), 8.88 (s, 1H), 8.05 (tq, *J* = 8.4, 1.8 Hz, 4H), 7.70 (td, *J* = 8.3, 6.3 Hz, 1H), 7.57 – 7.45 (m, 3H), 7.09 (td, *J* = 8.6, 2.6 Hz, 1H), 3.69 (d, *J* = 11.0 Hz, 1H), 3.49 – 3.37 (m, 2H), 2.99 (d, *J* = 12.2 Hz, 1H), 2.28 (d, *J* = 12.4 Hz, 1H), 1.92 (d, *J* = 22.1 Hz, 2H), 1.87 – 1.75 (m, 1H). **^{13}C NMR (101 MHz, DMSO)** δ 163.84 (d, *J* = 89.0 Hz), 162.84, 161.42 (d, *J* = 90.7 Hz), 145.37, 145.25, 145.22, 143.48, 134.86 (d, *J* = 8.8 Hz), 132.87 (d, *J* = 8.7 Hz), 131.69 – 130.47 (m), 126.35 (d, *J* = 3.0 Hz), 122.08, 118.59 (d, *J* = 21.0 Hz), 117.06 (d, *J* = 24.0 Hz), 113.03 (d, *J* = 21.2 Hz), 112.54 (d, *J* = 22.9 Hz), 108.44, 108.18 (d, *J* = 2.8 Hz), 46.46, 43.67, 41.24, 28.75, 22.58.

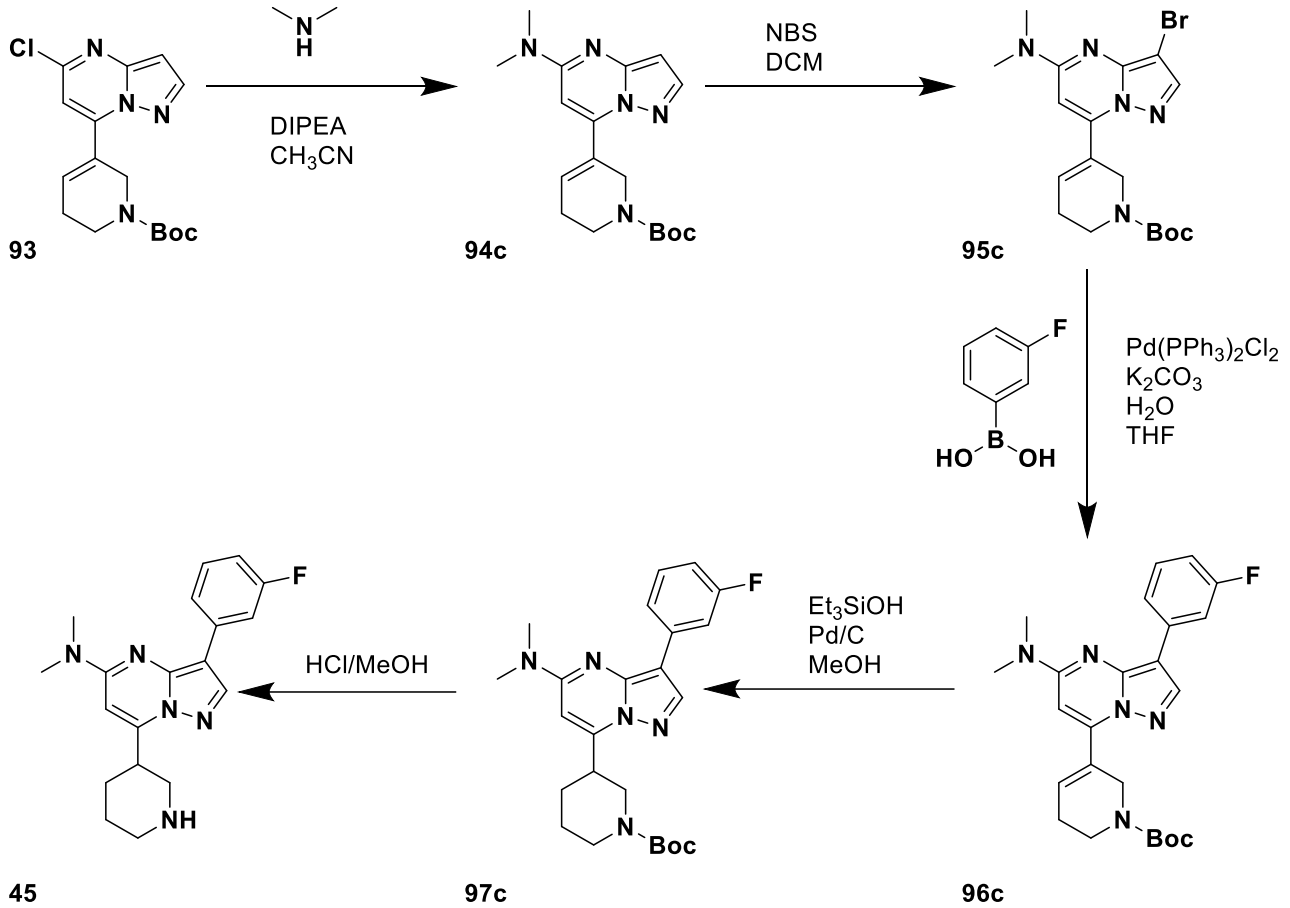

Tert-butyl 5-(5-(dimethylamino)pyrazolo[1,5-a]pyrimidin-7-yl)-3,6-dihydropyridine-1(2H)-carboxylate (94 c). in a 7ml vial, **93** (43mg, 0.13mmol, 1eq), dimethylamine (29mg, 0.65mmol, 5eq) were solubilized in CH_3CN (10ml/mmol). The reaction mixture was stirred at room temperature and monitored by UPLC. After 3 h, complete consumption of the starting material was observed. The mixture

was transferred to a separatory funnel, diluted with water, and extracted with ethyl acetate. The combined organic layers were dried over anhydrous sodium sulfate, filtered, and concentrated under reduced pressure to afford the title compound as a yellow oil (44 mg, quantitative yield). **UPLC-MS**: R.t. =2.32 (generic method) **MS (ESI)** m/z calc [M+2H]+: 345.21, found 345.3.

Tert-butyl 5-(3-bromo-5-(dimethylamino)pyrazolo[1,5-a]pyrimidin-7-yl)-3,6-dihydropyridine-1(2H)-carboxylate (95c). Starting from **94c** (44mg, 0.13mmol) and following **GP1**, after 3h reaction time, and an additional automated flash chromatography purification step (cyclohexane/AcOEt gradient 0 to 60%), the title compound was synthesized as a yellow oil (37mg, 67%). **UPLC-MS**: R.t. =1.77 (apolar method) **MS (ESI)** m/z calc [M+H]+: 424.11, found 424.0. **^{1}H NMR (400 MHz, MeOD)** δ 7.98 (s, 1H), 6.26 (s, 1H), 4.47 (s, 2H), 3.59 (t, J = 5.8 Hz, 3H), 2.40 (dh, J = 8.7, 2.7 Hz, 3H), 1.53 (s, 12H).

Tert-butyl 5-(5-(dimethylamino)-3-(3-fluorophenyl)pyrazolo[1,5-a]pyrimidin-7-yl)-3,6-dihydropyridine-1(2H)-carboxylate (96c). Starting from **95c** (37mg, 0.09mmol), following **GP2** and using (3-fluorophenyl)boronic acid as the coupling partner, the title compound was synthesized as a yellow oil (28mg, 71%). **UPLC-MS**: R.t. =2.25 (apolar method) **MS (ESI)** m/z calc [M+H]+: 438.23, found 438.2.

Rac-tert-butyl 3-(5-(dimethylamino)-3-(m-tolyl)pyrazolo[1,5-a]pyrimidin-7-yl)piperidine-1-carboxylate (97c). Starting from **96c** (28mg, 0.06mmol), following **GP4** (5h reaction time)**,** the title compound was synthesized as a colourless oil (14mg, 53%). **UPLC-MS**: R.t. =2.30 (apolar method) **MS (ESI)** m/z calc [M+H]+: 440.24, found 440.2 . **^{1}H NMR (400 MHz, CDCl3)** δ 8.35 (s, 1H), 7.99 (ddd, J = 11.1, 2.6, 1.5 Hz, 1H), 7.86 (dt, J = 7.8, 1.2 Hz, 1H), 7.38 (td, J = 8.0, 6.3 Hz, 1H), 6.91 (td, J = 8.5, 2.6 Hz, 1H), 6.00 (s, 1H), 4.36 (d, J = 13.1 Hz, 1H), 4.20 (s, 1H), 3.36 (s, 6H), 3.19 – 3.09 (m, 1H), 2.86 (s, 2H), 2.15 (d, J = 12.4 Hz, 1H), 1.83 (d, J = 13.4 Hz, 1H), 1.62 (d, J = 14.5 Hz, 2H), 1.51 (s, 9H).

Rac-3-(3-fluorophenyl)-N,N-dimethyl-7-(piperidin-3-yl)pyrazolo[1,5-a]pyrimidin-5-amine (45). Starting from **97c** (14mg, 0.03mmol), following **GP3**, after 5h reaction time, and using for the final automated flash purification (Biotage) neutral alumina and as eluent phase DCM/MeOH gradient 0 to 20%, the title compound was synthesized as a white powder in its hydrochloride salt form (5mg, 43%). **UPLC-MS**: R.t. =1.83 (generic method) **MS (ESI)** m/z calc [M+3H]+: 342.19, found 341.9 . **^{1}H NMR (400 MHz, DMSO)** δ 9.06 (d, *J* = 20.5 Hz, 2H), 8.70 (s, 1H), 8.10 – 8.01 (m, 1H), 8.01 – 7.94 (m, 1H), 7.43 (td, *J* = 8.1, 6.5 Hz, 1H), 7.01 (td, *J* = 8.3, 2.7 Hz, 1H), 6.32 (s, 1H), 3.56 (d, *J* = 12.3 Hz, 2H), 3.37 (s, 6H), 3.35 – 3.25 (m, 3H), 3.23 (d, *J* = 11.9 Hz, 1H), 2.96 (d, *J* = 12.1 Hz, 1H), 2.16 (d, *J* = 12.4 Hz, 1H), 1.91 (s, 1H), 1.77 (dd, *J* = 13.6, 9.7 Hz, 1H). **^{13}C NMR (151 MHz, DMSO)** δ 162.33, 162.24, 150.99, 147.12, 142.19, 135.64 (d, *J* = 9.1 Hz), 130.80 (d, *J* = 8.7 Hz), 121.56, 112.21 (d, *J* = 21.3 Hz), 112.03 (d, *J* = 22.8 Hz), 105.78 (d), 91.15, 46.57, 43.61, 41.58, 40.95, 29.11, 22.42.

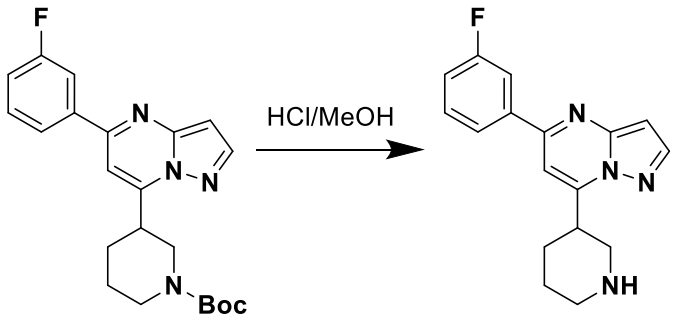

98 **68**

Rac-5-(3-fluorophenyl)-7-(piperidin-3-yl)pyrazolo[1,5-a]pyrimidine (68). Starting from **98** (15mg, 0.04mmol) and following **GP3**, after 2h30min reaction time, the title compound was synthesized as a

yellow powder in its hydrochloride salt form (9mg, 76%). **HPLC-MS**: R.t. =2.55 (generic method) **MS (ESI)** m/z calc [M+H]+: 297.15, found 297.13. **^{1}H NMR (400 MHz, DMSO)** δ 9.09 (s, 1H), 8.99 (s, 1H), 8.29 – 8.27 (m, 1H), 8.09 – 8.01 (m, 2H), 7.68 (td, *J* = 8.1, 6.0 Hz, 1H), 7.53 – 7.47 (m, 1H), 7.41 (s, 1H), 6.79 (d, *J* = 2.4 Hz, 1H), 3.56 (d, *J* = 9.2 Hz, 1H), 3.31 (d, *J* = 11.4 Hz, 3H), 2.94 (d, *J* = 11.7 Hz, 1H), 2.20 (d, *J* = 12.5 Hz, 1H), 1.94 – 1.81 (m, 2H), 1.81 – 1.71 (m, 1H).

3.9.8: Synthesis of compound **69**

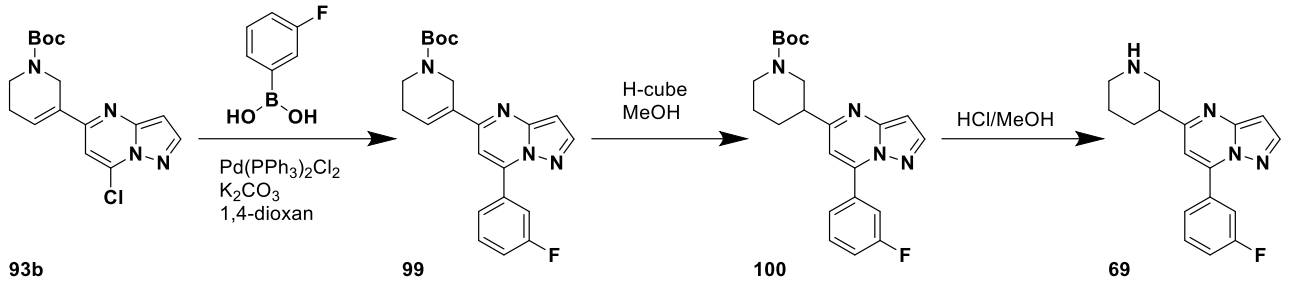

Tert-butyl 5-(7-(3-fluorophenyl)pyrazolo[1,5-a]pyrimidin-5-yl)-3,6-dihydropyridine-1(2H)-carboxylate (99). Starting from **93b** (40mg, 0.1mmol), following **GP2** and using (3-fluorophenyl)boronic acid as the coupling partner, the title compound was synthesized as a yellow oil (39mg, quantitative). **UPLC-MS**: R.t. =1.90 (apolar method) **MS (ESI)** m/z calc [M+H]+: 395.18, found 394.9.

Rac-tert-butyl 3-(7-(3-fluorophenyl)pyrazolo[1,5-a]pyrimidin-5-yl)piperidine-1-carboxylate (100). **94b** (110 mg, 0.28 mmol) was dissolved in EtOH (0.02 M) and subjected to H-Cube hydrogenation using a 10% Pd/C cartridge at 40 bar, 60 °C, and a flow rate of 0.5 mL/min. The resulting mixture was purified by automated flash chromatography (Biotage) using a cyclohexane/AcOEt gradient (0–100%), affording the product as a yellow oil (24 mg, 60%). **UPLC-MS**: R.t. =2.05 (apolar method) **MS (ESI)** m/z calc [M+H]+: 397.20, found 425.1.

Rac-7-(3-fluorophenyl)-5-(piperidin-3-yl)pyrazolo[1,5-a]pyrimidine (69). Starting from **100** (0.6mmol) and following **GP3**, after 7h reaction time and automated flash chromatography (Biotage), using silica and as eluent phase DCM/MeOH gradient 0 to 20%, the title compound was synthesized as a white powder in its hydrochloride salt form (15mg, 85%). **HPLC-MS**: R.t. =2.84 (generic method) **MS (ESI)** m/z calc [M+H]+: 297.15, found 297.20. **^{1}H NMR (400 MHz, DMSO)** δ 9.64 (d, *J* = 11.3 Hz, 1H), 9.25 (d, *J* = 11.7 Hz, 1H), 8.32 (d, *J* = 2.3 Hz, 1H), 8.17 – 8.05 (m, 2H), 7.68 – 7.58 (m, 2H), 7.45 – 7.36 (m, 1H), 6.85 (d, *J* = 2.3 Hz, 1H), 4.13 (s, 1H), 3.65 (d, *J* = 12.0 Hz, 1H), 3.54 – 3.36 (m, 2H), 2.92 (d, *J* = 11.7 Hz, 1H), 2.24 (s, 1H), 2.01 – 1.89 (m, 3H). **^{13}C NMR (101 MHz, DMSO)** δ 149.43, 148.48, 145.49, 135.71 (d, J=7.97 Hz), 131.53, 123.84, 117.84 (d, J=21.78Hz), 114.37 (d, *J* = 23.4 Hz), 103.17, 97.74, 44.90, 43.80, 34.27, 26.58, 22.27.

3.9.9: Synthesis of compounds **39-42**

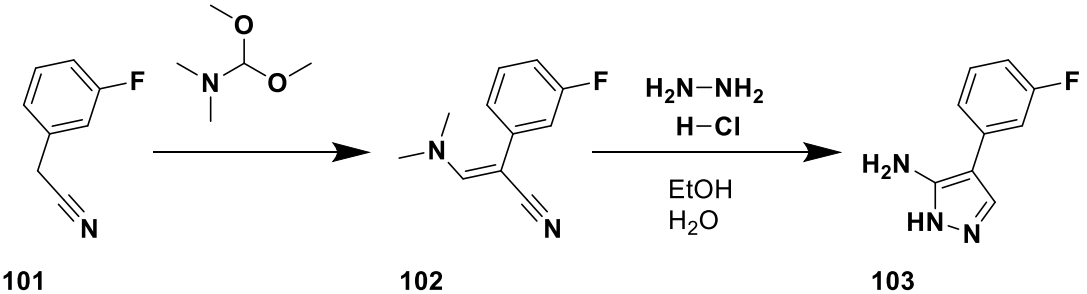

3-(dimethylamino)-2-(3-fluorophenyl)acrylonitrile (102). In a round-bottom flask, **101** (598 µL, 5 mmol, 1 eq.) and 1,1-dimethoxy-N,N-dimethylmethanamine (1.325 mL, 10 mmol, 2 eq.) were combined and stirred for 16 h at 50 °C. The reaction was monitored by UPLC. After complete disappearance of the starting material, the solid formed in the reaction mixture was filtered and washed with cold AcOEt. The mixture was then transferred to a separatory funnel and washed with water. The organic phase was collected, dried over Na_2SO_4, and concentrated under reduced pressure, affording the title compound as a rubine-red powder (625 mg, 64%). **UPLC-MS tR**.: 2.00 (generic method) **MS (ESI)** m/z calc [M+H]+: 191.09, found 191.1. **^{1}H NMR (400 MHz, CDCl3)** δ 7.28 – 7.23 (m, 1H), 7.14 – 7.07 (m, 1H), 7.02 (dt, J = 10.8, 2.2 Hz, 1H), 6.95 (s, 1H), 6.83 (ddd, J = 10.6, 7.9, 2.4 Hz, 1H), 3.28 (s, 6H).

4-(3-Fluorophenyl)-1H-pyrazol-5-amine (103). In a round-bottom flask, **102** (625 mg, 3.2 mmol) was dissolved in an EtOH/water 4:1 mixture (0.64 mL/mmol). Hydrazine hydrochloride (6.4 mmol, 2 eq.) was added, and the reaction mixture was stirred at 80 °C for 16 h and monitored by UPLC. After complete consumption of the starting material (the solution turns red), the mixture was transferred to a separatory funnel, diluted with water, and washed with DCM. The organic layer was dried over Na_2SO_4 and concentrated. The resulting solid was filtered and washed with a cyclohexane/AcOEt 5:1 mixture, affording the title compound as a light-brown powder (480 mg, 84%). **UPLC-MS tR**.: 1.42 (generic method) **MS (ESI)** m/z calc [M+H]+: 191.09, found 177.8. **^{1}H NMR (400 MHz, CDCl3)** δ 7.57 (s, 1H), 7.37 (td, *J* = 8.0, 6.1 Hz, 1H), 7.28 – 7.24 (m, 1H), 7.20 (dt, *J* = 10.2, 2.1 Hz, 1H), 7.01 – 6.91 (m, 1H).

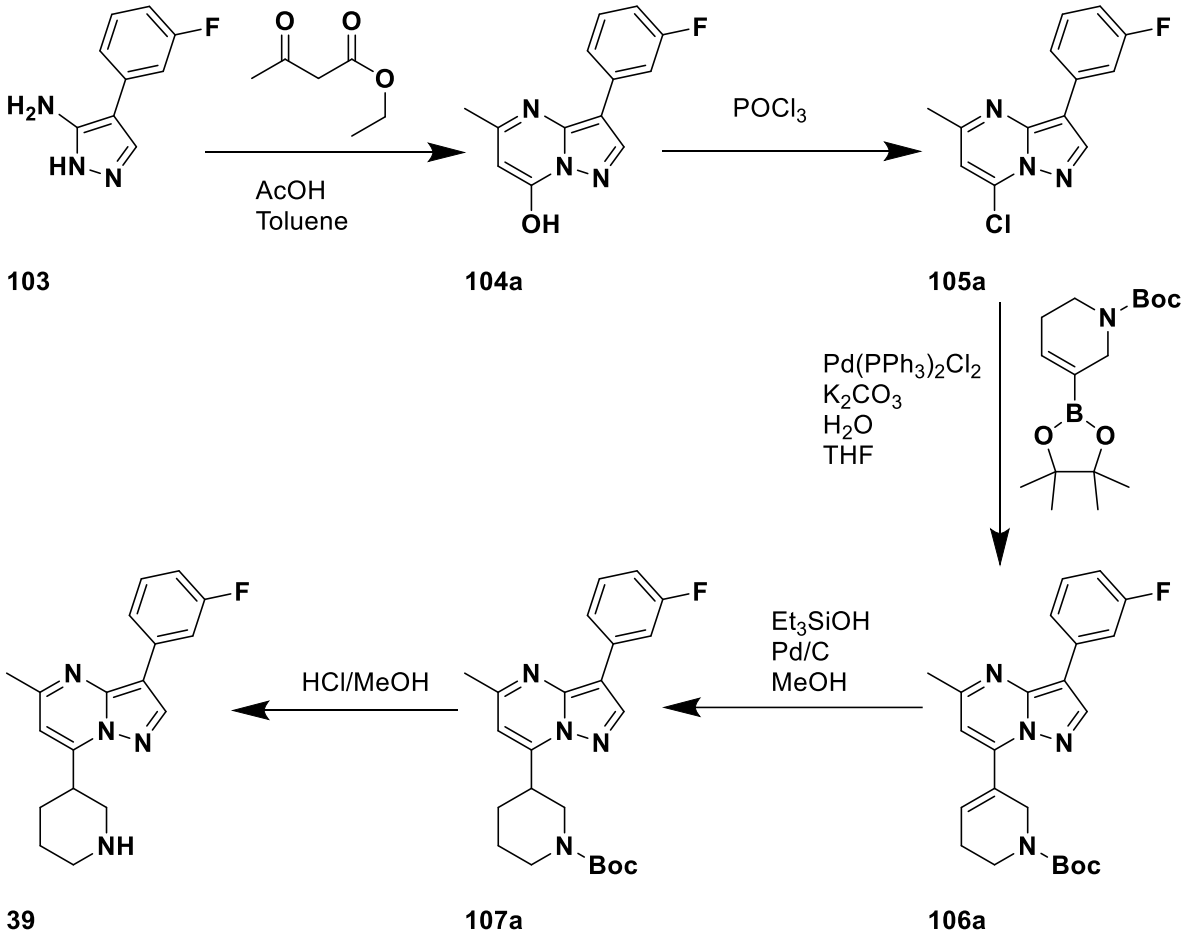

3-(3-Fluorophenyl)-5-methylpyrazolo[1,5-a]pyrimidin-7(4H)-one (104a). Starting from 103 (100mg, 0.56mmol, 1eq) following **GP6**, and using ethyl 3-cyclopropyl-3-oxopropanoate (143ul, 1.12mmol, 2eq) as the α,β-ketoester, after 15h reaction time, the title compound was synthesized as a white powder. (115mg, 84%).**UPLC-MS tR**.: 1.44 (generic method) **MS (ESI)** m/z calc [M+H]+: 244.08, found 244.1. **^{1}H**

NMR (400 MHz, MeOD) δ 8.12 (s, 1H), 7.54 – 7.45 (m, 1H), 7.45 – 7.36 (m, 2H), 7.09 (t, *J* = 8.5 Hz, 1H), 5.79 (s, 1H), 2.46 (s, 3H).

7-Chloro-3-(3-fluorophenyl)-5-methylpyrazolo[1,5-a]pyrimidine (105a). Starting from 104a (0.47mmol, 115mg) and following **GP8**, after 17h reaction time, the title compound was synthesized as a red oil (133mg, 96%).**UPLC-MS tR**.: 2.40 (generic method) **MS (ESI)** m/z calc [M+H]+: 262.05, found 262.0. **^{1}H NMR (400 MHz, CDCl3)** δ 8.49 (s, 1H), 7.91 (ddd, *J* = 10.6, 2.6, 1.6 Hz, 1H), 7.81 (ddd, *J* = 7.8, 1.6, 0.9 Hz, 1H), 7.42 (td, *J* = 8.0, 6.2 Hz, 1H), 6.99 (tdd, *J* = 8.5, 2.6, 1.0 Hz, 1H), 6.93 (s, 1H), 2.70 (s, 3H).

Tert-butyl 5-(3-(3-fluorophenyl)-5-methylpyrazolo[1,5-a]pyrimidin-7-yl)-3,6-dihydropyridine-1(2H)-carboxylate (106a). Starting from **105a** (133mg, 0.45mmol), following **GP2** and using as a coupling partner tert-butyl 5-(4,4,5,5-tetramethyl-1,3,2-dioxaborolan-2-yl)-3,6-dihydropyridine-1(2H)-carboxylate, the title compound was synthesized as a yellow oil (120mg, 67%).**UPLC-MS tR**.: 2.19 (generic method) **MS (ESI)** m/z calc [M+H]+: 409.2, found 409.2 . **^{1}H NMR (400 MHz, CDCl3)** δ 8.36 (s, 1H), 7.90 (ddd, *J* = 10.8, 2.6, 1.5 Hz, 1H), 7.80 (dt, *J* = 7.8, 1.3 Hz, 1H), 7.37 (td, *J* = 8.0, 6.2 Hz, 1H), 6.96 – 6.89 (m, 2H), 6.63 (s, 1H), 4.51 (q, *J* = 2.5 Hz, 2H), 3.66 (t, *J* = 5.8 Hz, 2H), 2.64 (s, 4H), 2.47 (tt, *J* = 6.0, 3.0 Hz, 2H), 1.50 (s, 10H).

Rac-tert-butyl 3-(3-(3-fluorophenyl)-5-methylpyrazolo[1,5-a]pyrimidin-7-yl)piperidine-1-carboxylate (107a). **106a** (120mg, 0.3mmol) was dissolved in EtOH (0.02 M) and subjected to H-Cube hydrogenation using a 10% Pd/C cartridge at 40 bar, 60 °C, and a flow rate of 0.5 mL/min. The resulting mixture was purified by automated flash chromatography (Biotage) using a cyclohexane/AcOEt gradient (0–100%), affording the product as a yellow oil (90mg, 67%).**UPLC-MS tR**.: 2.15 (apolar method) **MS (ESI)** m/z calc [M+H]+: 411.22, found 411.0.

Rac-3-(3-Fluorophenyl)-5-methyl-7-(piperidin-3-yl)pyrazolo[1,5-a]pyrimidine (39). Starting from **107a** (90mg, 0.22mmol) and following **GP3**, after 3h reaction time and automated flash chromatography (Biotage), using silica and as eluent phase CH_3Cl/MeOH gradient 0 to 20%, the title compound was synthesized as a white powder in its hydrochloride salt form (45mg, 66%). **UPLC-MS tR**.: 1.42 (generic method) **MS (ESI)** m/z calc [M+H]+: 311.16, found 311.4. **^{1}H NMR (400 MHz, DMSO)** δ 9.38 (s, 1H), 9.13 (d, *J* = 11.4 Hz, 1H), 8.82 (s, 1H), 8.08 – 7.99 (m, 2H), 7.48 (td, *J* = 8.1, 6.4 Hz, 1H), 7.10 – 7.01 (m, 2H), 4.05 – 3.94 (m, 1H), 3.65 (d, *J* = 12.0 Hz, 1H), 3.36 (s, 1H), 3.25 (q, *J* = 11.6 Hz, 2H), 2.95 (d, *J* = 12.0 Hz, 1H), 2.64 (s, 3H), 2.20 (d, *J* = 11.1 Hz, 1H), 2.02 – 1.78 (m, 3H). **^{13}C NMR (151 MHz, DMSO)** δ 163.02 (d, *J* = 241.9 Hz), 160.78, 148.21, 144.78, 142.73, 134.94 (d, *J* = 8.8 Hz), 131.09 (d, *J* = 8.7 Hz), 121.89, 121.88, 112.85 (d, *J* = 20.9 Hz), 112.26 (d, *J* = 22.8 Hz), 107.56 (d, *J* = 2.8 Hz), 107.44, 45.05, 43.87, 34.06, 26.00, 25.23, 22.17.

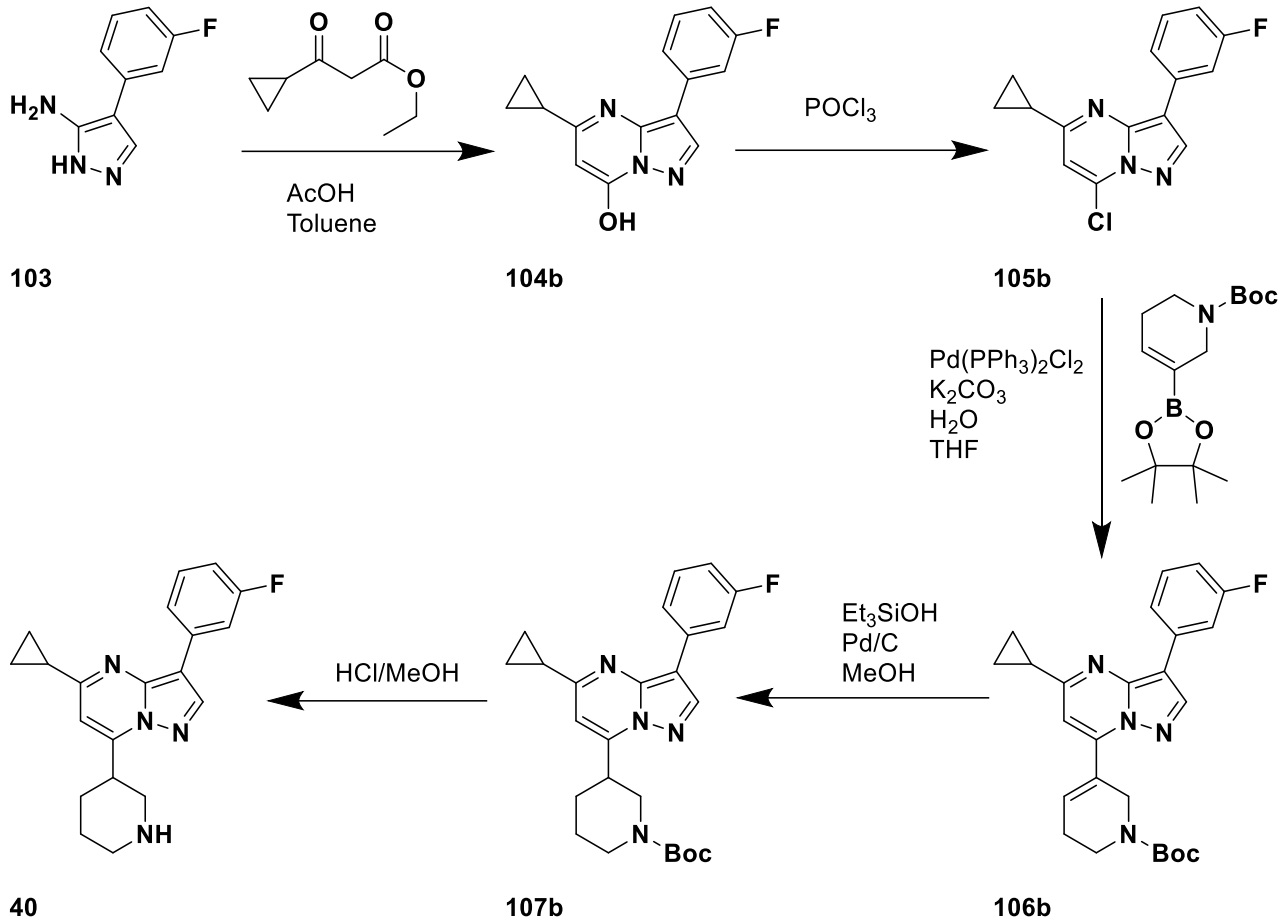

103 **104b** **105b**

40 **107b** **106b**

5-Cyclopropyl-3-(3-fluorophenyl)pyrazolo[1,5-a]pyrimidin-7-ol (104b). Starting from **103** (71mg, 0.4mmol), following **GP6**, and using ethyl 3-oxobutanoate as the α,β-ketoester, after 31h reaction time, the title compound was synthesized as a white powder (67mg, 62%).**UPLC-MS:** tR.: 1.61 (generic method) **MS (ESI)** m/z calc [M+H]+: 270.10, found 270.0.

7-Chloro-3-(3-fluorophenyl)-5-methylpyrazolo[1,5-a]pyrimidine (105b). Starting from **104b** (67mg, 0.25mmol) and following **GP8**, after 20h30min reaction time, the title compound was synthesized as a red oil (63mg, 84%).**UPLC-MS**: tR.: 2.51 (generic method) **MS (ESI)** m/z calc [M+H]+: 290.06, found 290.0. **^{1}H NMR (400 MHz, CDCl3)** δ 8.37 (s, 1H), 7.77 (ddd, J = 10.9, 2.5, 1.6 Hz, 1H), 7.69 (dt, J = 7.8, 1.3 Hz, 1H), 7.32 (td, J = 8.0, 6.2 Hz, 1H), 6.89 (tdd, J = 8.4, 2.6, 1.0 Hz, 1H), 6.82 (s, 1H), 1.30 – 1.08 (m, 6H).

Tert-butyl 5-(3-(3-fluorophenyl)-5-methylpyrazolo[1,5-a]pyrimidin-7-yl)-3,6-dihydropyridine-1(2H)-carboxylate (106b). Starting from **105b** (63mg, 0.21mmol), following **GP2** and using as a coupling partner tert-butyl 5-(4,4,5,5-tetramethyl-1,3,2-dioxaborolan-2-yl)-3,6-dihydropyridine-1(2H)-carboxylate, the title compound was synthesized as a yellow oil (80mg, 87%). Check by TLC, Cyclohexane/AcOEt. **^{1}H NMR (400 MHz, CDCl3)** δ 8.37 (s, 1H), 7.90 (ddd, *J* = 11.0, 2.6, 1.5 Hz, 1H), 7.81 (dt, *J* = 7.9, 1.3 Hz, 1H), 7.39 (td, *J* = 8.1, 6.3 Hz, 1H), 6.94 (tdd, *J* = 8.5, 2.6, 0.9 Hz, 1H), 6.69 (s, 1H), 4.54 (q, *J* = 2.5 Hz, 2H), 3.79 – 3.65 (m, 2H), 2.50 (ddq, *J* = 9.4, 5.3, 2.7 Hz, 2H), 2.14 (tt, *J* = 8.0, 4.7 Hz, 1H), 1.52 (s, 9H).

Rac-tert-butyl 3-(3-(3-fluorophenyl)-5-methylpyrazolo[1,5-a]pyrimidin-7-yl)piperidine-1-carboxylate (107b). **106b** (80 mg, 0.18 mmol) was dissolved in EtOH (0.02 M) and subjected to H-Cube hydrogenation using a 10% Pd/C cartridge at 40 bar, 60 °C, and a flow rate of 0.5 mL/min. The reaction progress was monitored by TLC (cyclohexane/AcOEt as eluent). The crude mixture was purified by automated flash chromatography (Biotage) using a cyclohexane/AcOEt gradient (0–100%), affording a mixture of the desired product and its polyhydrogenated derivative as a yellow oil (80 mg, not fully

purified). **^{1}H NMR (400 MHz, CDCl3)** δ 8.36 (s, 1H), 7.88 (ddd, *J* = 11.0, 2.6, 1.6 Hz, 1H), 7.79 (dt, *J* = 7.8, 1.2 Hz, 1H), 7.37 (td, *J* = 8.0, 6.2 Hz, 1H), 6.91 (tdd, *J* = 8.5, 2.6, 1.0 Hz, 1H), 6.64 (s, 1H), 4.36 (dd, *J* = 12.9, 3.8 Hz, 1H), 4.11 – 3.94 (m, 1H), 3.71 (tdd, *J* = 9.7, 7.3, 4.5 Hz, 1H), 3.27 (dd, *J* = 12.9, 9.5 Hz, 1H), 3.07 (t, 1H), 2.35 – 2.25 (m, 1H), 2.10 (tt, *J* = 8.0, 4.7 Hz, 1H), 1.94 – 1.69 (m, 3H), 1.48 (s, 9H), 1.32 – 1.25 (m, 3H), 1.20 – 1.11 (m, 2H).

Rac-3-(3-fluorophenyl)-5-methyl-7-(piperidin-3-yl)pyrazolo[1,5-a]pyrimidine (40). Starting from **106a** (80mg, 0.18mmol) and following **GP3**, after 16h reaction time and after automated flash chromatography (Biotage), using silica and as eluent phase DCM/MeOH gradient 0 to 20%, the title compound was synthesized as a white powder in its hydrochloride salt form (34mg, 56% over two steps). **UPLC-MS**: tR.: 1.91 (generic method) **MS (ESI)** m/z calc [M+H]+: 337.18, found 337.1. **1H NMR (400 MHz, DMSO)** δ 9.65 (d, J = 10.9 Hz, 1H), 9.33 (d, J = 10.6 Hz, 1H), 8.77 (s, 1H), 7.97 (t, J = 8.8 Hz, 2H), 7.46 (q, J = 7.5 Hz, 1H), 7.08 (s, 1H), 7.02 (td, J = 8.5, 2.5 Hz, 1H), 3.99 (t, J = 12.4 Hz, 1H), 3.63 (d, J = 11.8 Hz, 1H), 3.32 (dd, J = 27.4, 12.3 Hz, 2H), 2.93 (d, J = 11.8 Hz, 1H), 2.34 – 2.25 (m, 1H), 2.20 (d, J = 11.5 Hz, 1H), 2.03 – 1.77 (m, 3H), 1.17 (t, J = 6.5 Hz, 4H). **^{13}C NMR (101 MHz, DMSO)** δ 165.21, 163.05 (d, *J* = 241.6 Hz), 148.30, 144.99, 142.88, 135.24 (d, *J* = 9.0 Hz), 130.99 (d, *J* = 8.7 Hz), 121.67, 112.57 (d, *J* = 20.8 Hz), 112.09 (d, *J* = 22.9 Hz), 106.96 (d, J=2.43Hz), 105.80, 44.84, 43.67, 34.02, 26.30, 22.21, 17.75, 12.18, 12.13.

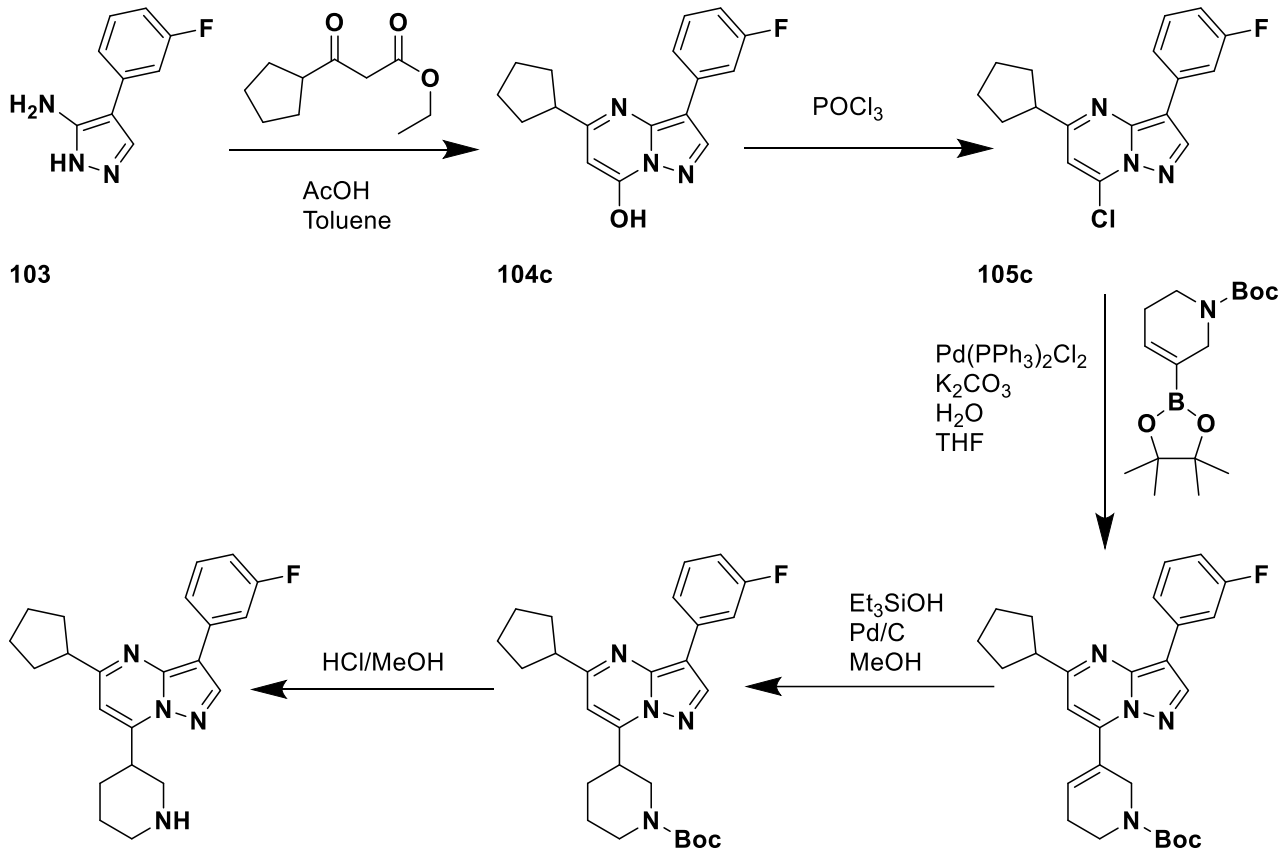

5-Cyclopentyl-3-(3-fluorophenyl)pyrazolo[1,5-a]pyrimidin-7-ol (104c). Starting from **103** (72mg, 0.4mmol), following **GP8**, and using ethyl 3-oxobutanoate as the α,β-ketoester, after 17h reaction time, the title compound was synthesized as a white powder. (not isolated).**UPLC-MS tR**.: 3.16 (apolar method) **MS (ESI)** m/z calc [M+H+H_2O]+: 316.13, found 316.1

7-Chloro-5-cyclopentyl-3-(3-fluorophenyl)pyrazolo[1,5-a]pyrimidine (105c). Starting from **104c** (0.4mmol, theoretical), following **GP7**, after 22h reaction time, the title compound was synthesized as a red oil (91mg, 72% over two steps). Reaction followed by TLC.

Tert-butyl 5-(5-cyclopentyl-3-(3-fluorophenyl)pyrazolo[1,5-a]pyrimidin-7-yl)-3,6-dihydropyridine-1(2H)-carboxylate (106c). Starting from **105c** (81mg, 0.28mmol), following **GP2** and using as a coupling partner tert-butyl 5-(4,4,5,5-tetramethyl-1,3,2-dioxaborolan-2-yl)-3,6-dihydropyridine-1(2H)-carboxylate, the title compound was synthesized as a yellow oil (129mg, quantitative).**UPLC-MS tR**.: 1.78 (superapolar method) **MS (ESI)** m/z calc [M+H]+: 463.25, found 463.3.

Rac-tert-butyl 3-(5-cyclopentyl-3-(3-fluorophenyl)pyrazolo[1,5-a]pyrimidin-7-yl)piperidine-1-carboxylate (107c). Starting from **106c** (129mg, 0.28mmol) and following following **GP4**, adding other 10eq of Et_3SiH after 16h reaction time and letting it stir for in total 30h, the tile compound was synthesized as a colourless oil (73mg, 56%). **UPLC-MS** tR.: 1.65 (superapolar method), **MS (ESI)** m/z calc [M+H]+: 465.26, found 465.3.

Rac-5-cyclopentyl-3-(3-fluorophenyl)-7-(piperidin-3-yl)pyrazolo[1,5-a]pyrimidine (41). Starting from **107c** (73mg, 0.16mmol) and following **GP3**, after 2h reaction time, the title compound was synthesized as a white powder in its hydrochloride salt form (53mg, 82%). **HPLC-MS** tR.: 4.79 (generic method) **MS (ESI)** m/z calc [M+H]+: 365.21, found 365.32. **^{1}H NMR (400 MHz, DMSO)** δ 9.57 (s, 1H), 9.24 (s, 1H), 8.82 (s, 1H), 8.12 – 7.99 (m, 2H), 7.48 (td, J = 8.1, 6.5 Hz, 1H), 7.09 – 7.00 (m, 2H), 4.02 (d, 1H), 3.64 (d, 1H), 3.45 – 3.39 (m, 1H), 3.31 – 3.25 (m, 1H), 2.94 (d, J = 11.9 Hz, 1H), 2.20 (d, J = 10.4 Hz, 1H), 2.16 – 2.04 (m, 2H), 2.02 – 1.76 (m, 8H), 1.75 – 1.68 (m, 2H). **^{13}C NMR (101 MHz, MeOD)** δ 167.10, 164.39, 161.98, 147.41, 144.62, 141.86, 134.70, 134.61, 129.86, 129.78, 121.12, 121.10, 112.21, 112.08, 111.97, 111.87, 108.21, 108.19, 105.59, 60.77, 48.29, 48.08, 47.86, 47.65, 47.53, 47.44, 47.22, 47.01, 45.15, 44.31, 43.92, 34.56, 32.36, 29.50, 28.98, 25.50, 25.44, 21.95.

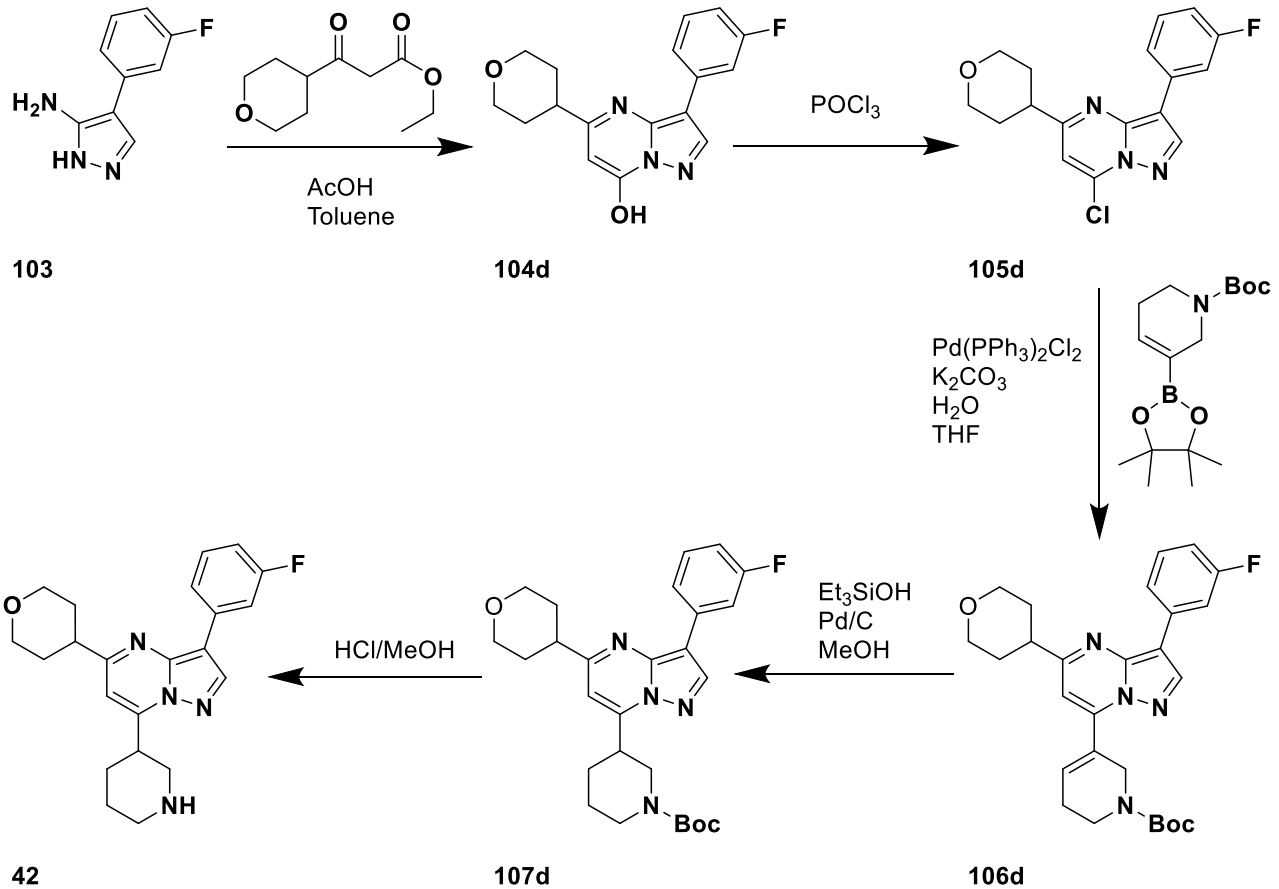

3-(3-Fluorophenyl)-5-(tetrahydro-2H-pyran-4-yl)pyrazolo[1,5-a]pyrimidin-7-ol (104d). Starting from **103** (71mg, 0.4mmol), following **GP6** and using ethyl 3-oxobutanoate as the α,β-ketoester, in 17h reaction time, the title compound was synthesized as a white powder (not isolated). **UPLC-MS tR**.: 1.31 (apolar method) **MS (ESI)** m/z calc [M+H+H_2O]+: 332.13, found 332.1.

7-Chloro-3-(3-fluorophenyl)-5-(tetrahydro-2H-pyran-4-yl)pyrazolo[1,5-a]pyrimidine (105d). Starting from **104d** (theoretical 0.4mmol) and following **GP8**, after 22h reaction time, the title compound was synthesized as a yellow oil (123mg, 0.37mmol theoretical). Reaction followed by TLC.

Tert-butyl 5-(3-(3-fluorophenyl)-5-(tetrahydro-2H-pyran-4-yl)pyrazolo[1,5-a]pyrimidin-7-yl)-3,6-dihydropyridine-1(2H)-carboxylate (106d). Starting from **105d** (theoretical 123mg) Following **GP2** and using as a coupling partner tert-butyl 5-(4,4,5,5-tetramethyl-1,3,2-dioxaborolan-2-yl)-3,6-dihydropyridine-1(2H)-carboxylate, the title compound was synthesized as a yellow oil (120mg, 62% over 3 steps).**UPLC-MS tR**.: 2.20 (generic method) **MS (ESI)** m/z calc [M+H]-: 477.24, found 477.3 .

Rac-tert-butyl 3-(3-(3-fluorophenyl)-5-(tetrahydro-2H-pyran-4-yl)pyrazolo[1,5-a]pyrimidin-7-yl)piperidine-1-carboxylate (107d). Starting from **106a** (120mg, 0.3mmol), and following **GP4**, in 16h reaction time, the tile compound was synthesized as a colourless oil (80mg, 55%). **UPLC-MS tR**.: 2.16 (apolar method), **MS (ESI)** m/z calc [M+H]+: 481.26, found 481.3.

Rac-3-(3-fluorophenyl)-7-(piperidin-3-yl)-5-(tetrahydro-2H-pyran-4-yl)pyrazolo[1,5-a]pyrimidine (42). Starting from **106a** (80mg, 0.16mmol), following **GP3**, after 2h reaction time, the title compound was synthesized as a white powder in its hydrochloride salt form (53mg, 87%). **UPLC-MS tR**.: 0.58 (apolar method) **MS (ESI)** m/z calc [M+H]+: 381.20, found 381.2. **^{1}H NMR (400 MHz, DMSO)** δ 9.54 (s, 1H), 9.28 (s, 1H), 8.84 (s, 1H), 8.11 – 8.01 (m, 2H), 7.49 (td, *J* = 8.3, 6.6 Hz, 1H), 7.13 (s, 1H), 7.06 (dt, 1H), 4.03 (d, 3H), 3.67 – 3.59 (m, 1H), 3.51 (td, *J* = 11.2, 3.2 Hz, 2H), 3.41 – 3.38 (m, 1H), 3.32 – 3.26 (m, 1H), 3.13 (tt, *J* = 9.8, 4.7 Hz, 1H), 2.93 (t, *J* = 11.4 Hz, 1H), 2.21 (d, *J* = 11.2 Hz, 1H), 2.02 – 1.80 (m, 7H). **^{13}C NMR (101 MHz, MeOD)** δ 165.16, 163.05 (d, *J* = 242.6 Hz), 147.68, 147.66, 144.58, 141.84, 134.52 (d, *J* = 8.9 Hz), 129.81 (d, *J* = 8.7 Hz), 121.09, 121.06, 112.08 (d, *J* = 4.7 Hz), 111.86 (d, *J* = 2.9 Hz), 108.30 (d, *J* = 2.5 Hz), 104.92, 74.60, 67.39, 45.13, 43.94, 42.59, 34.53, 34.48, 31.20, 31.16, 25.53, 23.74, 21.98, 21.93.

3.9.10: Synthesis of compounds **46-51**

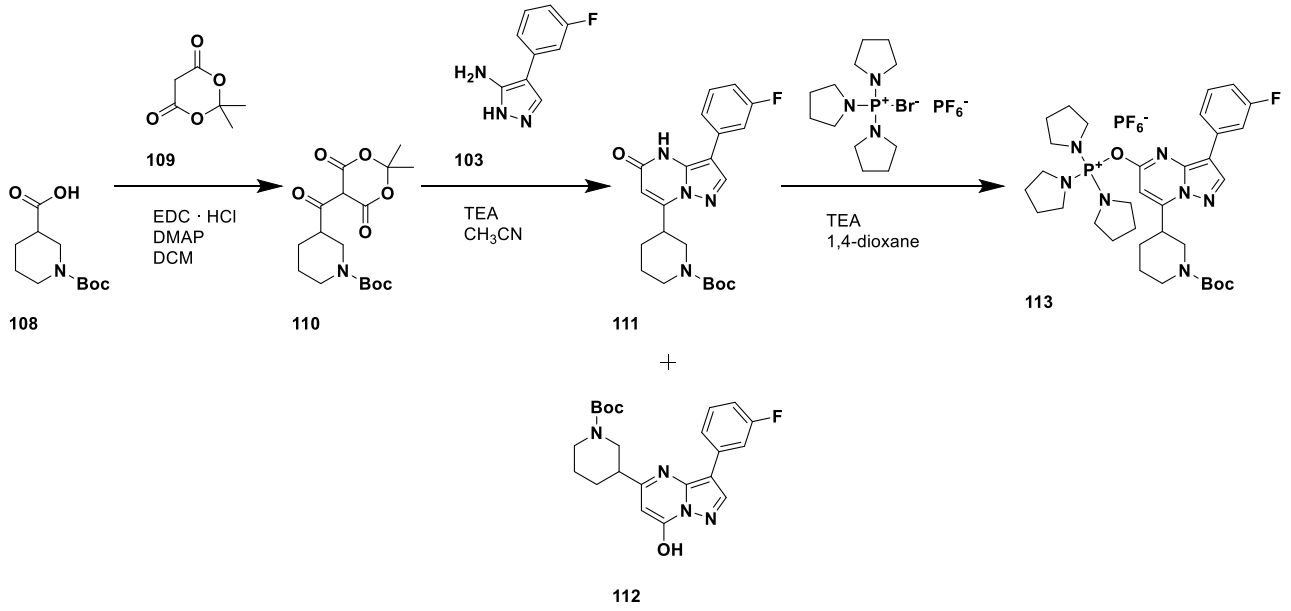

Rac-tert-butyl 3-(2,2-dimethyl-4,6-dioxo-1,3-dioxane-5-carbonyl)piperidine-1-carboxylate (110). In a round-bottom flask, **108** (229 mg, 1 mmol, 1 eq.), **109** (173 mg, 1.2 mmol, 1.2 eq.), and DMAP (305 mg, 2.5 mmol, 2.5 eq.) were dissolved in DCM (5 mL). EDC·HCl (229 mg, 1.2 mmol, 1.2 eq.) was added portionwise, and the reaction was monitored by UPLC. After 2 h, the mixture was transferred to a separatory funnel, diluted with AcOEt, and washed with saturated Na_2CO_3 and NH_4Cl solutions. The organic layer was collected, dried over sodium sulfate, and concentrated under vacuum, affording **110** as a white powder (282 mg, 79%). **UPLC-MS tR**.: 1.38 (generic method) **MS (ESI)** m/z calc [M+H]+: 356.17, found 356.2.

Rac-tert-butyl 3-(3-(3-fluorophenyl)-5-oxo-4,5-dihydropyrazolo[1,5-a]pyrimidin-7-yl)piperidine-1-carboxylate (111) and **rac-tert-butyl 3-(3-(3-fluorophenyl)-7-hydroxypyrazolo[1,5-a]pyrimidin-5-yl)piperidine-1-carboxylate (112)**. In a mw vial, **110** (667mg,1.9 mmol, 1eq.), **103** (332mg, 1.9mmol, 1eq.), and TEA (51µL, 3.8mmol, 2eq.) were dissolved in CH_3CN (5mL). The reaction mixture was subjected to microwave irradiation in a CEM Discovery system at 160 °C for 1 h. The reaction progress was monitored by UPLC. After starting material (**110**) disappearance, the mixture was diluted with AcOEt and washed with cold 3 M HCl. The organic phase was dried over sodium sulfate and concentrated under vacuum. After automated flash chromatography (Biotage) on silica using a cyclohexane/AcOEt gradient (0–100%), the title compound and its regioisomer were obtained as a white powder. (**111**: 170mg, 0.41mmol. **112** 140mg, 0.34mmol. Total yield: 39%). **UPLC-MS:** tR: 2.32 (generic method) **112** tR: 2.08 (generic method) **MS (ESI)** m/z calc [M+H]+: 413.19, found 413.2.

Rac- ((7-(1-(tert-butoxycarbonyl)piperidin-3-yl)-3-(3-fluorophenyl)pyrazolo[1,5-a]pyrimidin-5-yl)oxy)tri(pyrrolidin-1-yl)phosphonium hexafluorophosphate (113). In a round-bottom flask, **111a** (149mg, 0.36mmol, 1eq.), bromotripyrrolidinophosphonium hexafluorophosphate (PyBrop, 168mg, 0.36mmol, 1eq.), and TEA (109mg, 1.08mmol, 3eq.) were dissolved in CH_3CN (5 mL). The reaction mixture was stirred at room temperature for 2 h, until complete starting-material disappearance, as monitored by UPLC. After purification by automated flash chromatography (Biotage) on silica using a cyclohexane/AcOEt gradient (0–80%), the title compound was obtained as a yellow oil (160 mg, 58%). **UPLC-MS tR**.: 1.98 (apolar method) **MS (ESI)** m/z calc [M-$PN_3C_{12}H_{24}$+H]+: 411.1, found 411.1.

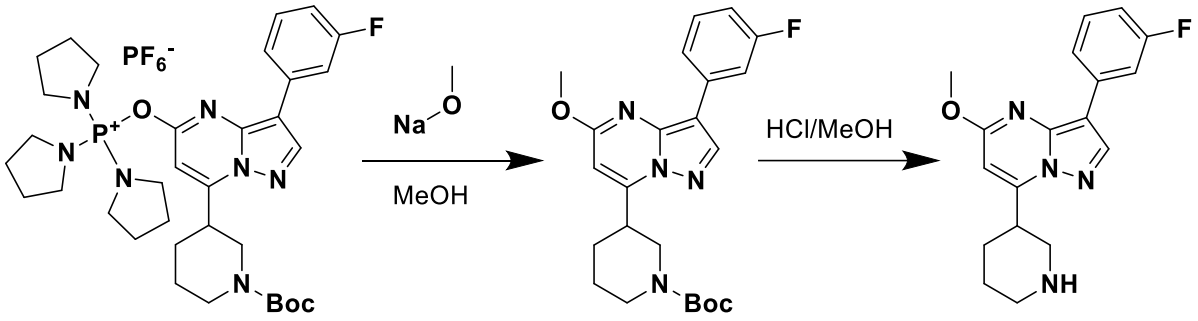

113 **114a** **47**

Rac-tert-butyl 3-(3-(3-fluorophenyl)-5-methoxypyrazolo[1,5-a]pyrimidin-7-yl)piperidine-1-carboxylate (114a). In a 7 mL vial, **113** (15mg, 0.02mmol) and sodium methoxide (8mg, 0.15mmol, 5eq) were dissolved in MeOH (1 mL). The reaction was stirred at 60 °C for 16 h and monitored by UPLC. After disappearance of the starting material, the reaction mixture was transferred into a separatory funnel, diluted with AcOEt, and washed with water. The organic phase was collected and concentrated on a rotavapor. After automated flash chromatography (Biotage) using a cyclohexane/AcOEt gradient (0–15%) as eluent, the title compound was obtained as a colourless oil. (6mg, 70%). **UPLC-MS tR**.: 2.22 (apolar method) **MS (ESI)** m/z calc [M+H]+: 427.21, found 427.2.

Rac-3-(3-fluorophenyl)-5-methoxy-7-(piperidin-3-yl)pyrazolo[1,5-a]pyrimidine (47). Starting from **114a** (6mg, 0.014mmol) and following **GP3**, after 2h reaction time and automated flash chromatography (Biotage), using silica and as eluent phase DCM/MeOH gradient 0 to 20%, the title compound was obtained as a white powder in its hydrochloride salt form (5mg, quantitative). **HPLC-MS tR**.: 3.73 (generic method) **MS (ESI)** m/z calc [M+H]+: 327.13, found 327.02. **^{1}H NMR (400 MHz, DMSO)** δ 8.73 (s, 1H), 7.96 (d, *J* = 7.3 Hz, 2H), 7.47 (td, *J* = 7.8, 6.2 Hz, 1H), 7.08 – 6.99 (m, 1H), 6.64 (s, 1H), 4.06 (s, 3H), 3.99 – 3.91 (m, 1H), 3.62 (d, *J* = 12.3 Hz, 1H), 3.40 – 3.35 (m, 1H), 3.31 – 3.20 (m, 1H), 2.92 (t, *J* = 11.8 Hz, 1H), 2.17 (d, *J* = 11.0 Hz, 1H), 2.00 – 1.76 (m, 3H). **^{13}C NMR (101 MHz, MeOD)** δ 163.20 (d, *J* = 242.5 Hz), 162.56, 149.71, 143.72, 141.80, 134.70 (d, *J* = 8.9 Hz), 129.82 (d, *J* = 8.7 Hz), 120.80 (d, *J* = 2.8 Hz), 111.81 (d, *J* = 3.5 Hz), 111.59 (d, *J* = 5.3 Hz), 107.21 (d, *J* = 2.5 Hz), 97.32, 53.31, 45.33, 43.92, 34.46, 25.53, 21.92.

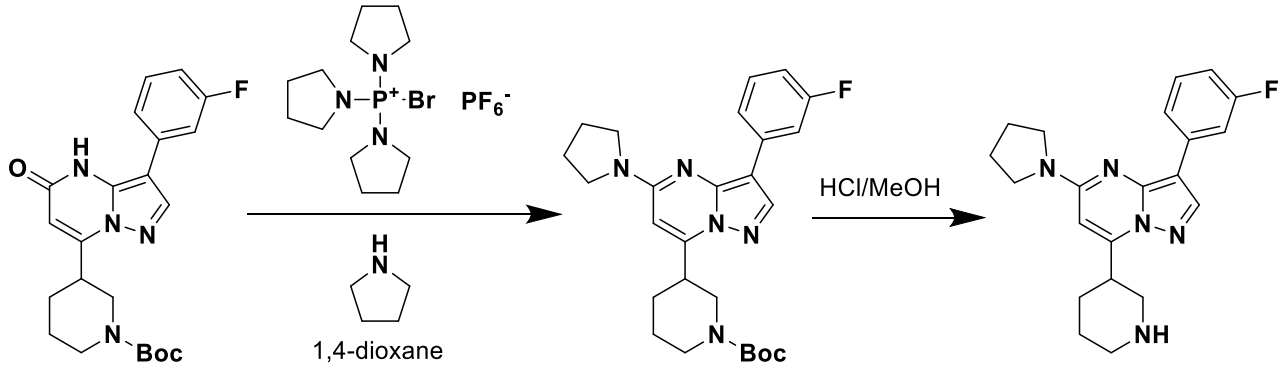

111 **114b** **113**

Rac-tert-butyl 3-(3-(3-fluorophenyl)-5-(pyrrolidin-1-yl)pyrazolo[1,5-a]pyrimidin-7-yl)piperidine-1-carboxylate (114b). In a 7 mL vial, 111 (20mg, 0.026mmol, 1eq) was dissolved in 1,4-dioxane (1mL), and PyBrop (46mg, 0.10mmol, 2eq) and pyrrolidine (17µL, 0.20mmol, 2eq) were added. The reaction mixture was stirred for 2 days and monitored by UPLC. After disappearance of the starting material, the mixture was transferred into a separatory funnel, diluted with AcOEt, and washed with cold 3 M HCl. The organic phase was dried over sodium sulfate and purified by automated flash chromatography (Biotage) on silica, using a cyclohexane/AcOEt gradient (0–20%) as the eluent. The title compound was obtained as a colourless oil (6mg, 50%). **UPLC-MS tR**.: 2.63 (apolar method) **MS (ESI)** m/z calc [M+H]+: 466.23, found 466.3.

Rac-3-(3-fluorophenyl)-7-(piperidin-3-yl)-5-(pyrrolidin-1-yl)pyrazolo[1,5-a]pyrimidine (48). Starting from **114b** (6mg, 0.013mmol) and following **GP3**, after 4h reaction time and automated flash chromatography (Biotage), using silica and as eluent phase DCM/MeOH gradient 0 to 20%, the title compound was obtained as a white powder in its hydrochloride salt form (4.5mg, 64%). **UPLC-MS tR**.: 0.83 (apolar method) **MS (ESI)** m/z calc [M+H]+: 366.20, found 366.2. **^{1}H NMR (400 MHz, DMSO)** δ 8.93 (s, 1H), 8.81 (s, 1H), 8.61 (s, 2H), 8.09 – 8.01 (m, 2H), 7.96 (d, *J* = 7.9 Hz, 2H), 7.42 (q, *J* = 7.7 Hz, 2H), 7.03 – 6.94 (m, 2H), 6.07 (s, 1H), 3.54 (t, *J* = 10.3 Hz, 3H), 3.30 – 3.21 (m, 3H), 3.13 (t, *J* = 11.4 Hz, 2H), 2.96 (d, *J* = 11.5 Hz, 2H), 2.13 (d, *J* = 12.4 Hz, 2H), 1.91 – 1.71 (m, 5H). **^{13}C NMR (101 MHz, DMSO)** δ 163.08 (d, *J* = 240.8 Hz), 154.38, 148.45, 145.67, 142.10, 136.45 (d, *J* = 9.1 Hz), 130.63 (d, *J* = 8.7 Hz), 120.67, 111.25 (d, *J* = 6.9 Hz), 111.03 (d, *J* = 8.5 Hz), 103.39 (d, *J* = 2.5 Hz), 95.44, 47.22, 46.39, 45.08, 43.61, 34.11, 26.73, 26.39, 26.31, 22.24.

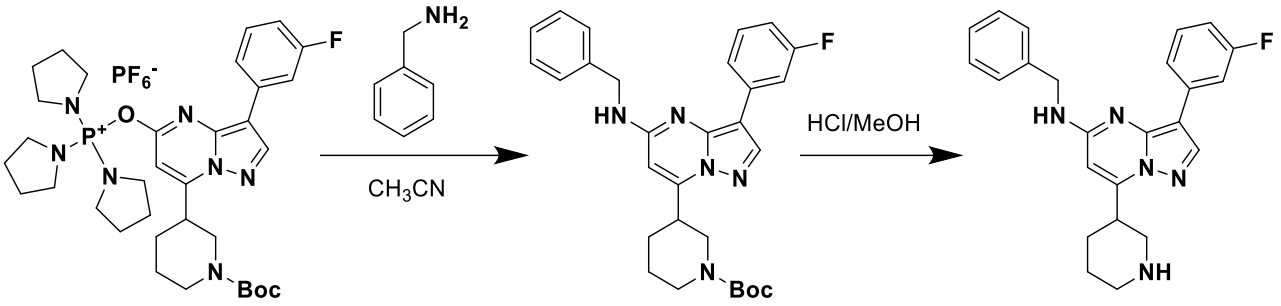

113 **114c** **49**

Rac-tert-butyl 3-(5-(benzylamino)-3-(3-fluorophenyl)pyrazolo[1,5-a]pyrimidin-7-yl)piperidine-1-carboxylate (114c). In a 7 mL vial, **113** (15mg, 0.02mmol) and benzylamine (20ul, 0.15mmol, 5eq) were dissolved in CH_3CN (1 mL). The reaction was stirred at 80 °C for 16 h and monitored by UPLC. After the disappearance of the starting material, the reaction mixture was transferred into a separatory funnel, diluted with AcOEt, and washed with water. The organic phase was collected and concentrated on a rotavapor. After automated flash chromatography (Biotage) using a cyclohexane/AcOEt gradient (0–15%) as eluent, the title compound was obtained as a colourless oil. (10mg, quantitative). **UPLC-MS tR**.: 2.23 (apolar method) **MS (ESI)** m/z calc [M+H]+: 502.26, found 502.2.

Rac-N-benzyl-3-(3-fluorophenyl)-7-(piperidin-3-yl)pyrazolo[1,5-a]pyrimidin-5-amine (49). Starting from **114c** (10mg, 0.02mmol), following **GP3**, after 3h reaction time and automated flash chromatography (Biotage), using neutral alumina and as eluent phase DCM/MeOH gradient 0 to 20%, the title compound was obtained as a white powder in its hydrochloride salt form (7mg, 80%). **HPLC-MS tR**.: 4.40 (generic method) **MS (ESI)** m/z calc [M+H]+: 402.20, found 402.16. **^{1}H NMR (400 MHz, DMSO)** δ 9.34 (d, *J* = 11.1 Hz, 1H), 9.08 (d, *J* = 10.5 Hz, 1H), 8.46 (s, 1H), 8.38 (t, *J* = 5.4 Hz, 1H), 7.93 (dt, *J* = 11.5, 2.0 Hz, 1H), 7.82 (d, *J* = 8.2 Hz, 1H), 7.44 (d, *J* = 7.4 Hz, 2H), 7.41 – 7.30 (m, 3H), 7.29 – 7.20 (m, 1H), 6.91 (td, *J* = 8.7, 2.7 Hz, 1H), 6.31 (s, 1H), 4.62 (d, *J* = 5.7 Hz, 2H), 3.76 (t, *J* = 12.1 Hz, 2H), 3.69 – 3.64 (m, 1H), 3.35 – 3.31 (m, 1H), 3.13 (q, *J* = 11.9 Hz, 2H), 3.01 – 2.93 (m, 1H), 2.17 (d, *J* = 11.6 Hz, 1H), 2.00 – 1.93 (m, 1H), 1.89 – 1.79 (m, 2H), 1.78 – 1.70 (m, 1H). **^{13}C NMR (101 MHz, DMSO)** δ 163.08 (d, *J* = 240.9 Hz), 156.20, 147.81, 145.64, 141.77, 139.98, 136.17 (d, *J* = 9.1 Hz), 130.58 (d, *J* = 8.8 Hz), 128.77, 127.97, 127.31, 120.85 (d, *J* = 2.5 Hz), 111.46 (d, *J* = 7.2 Hz), 111.24 (d, *J* = 8.8 Hz), 104.06, 97.39, 45.26 – 44.93 (m), 44.62, 43.74 – 43.29 (m), 34.12, 26.16, 22.17.

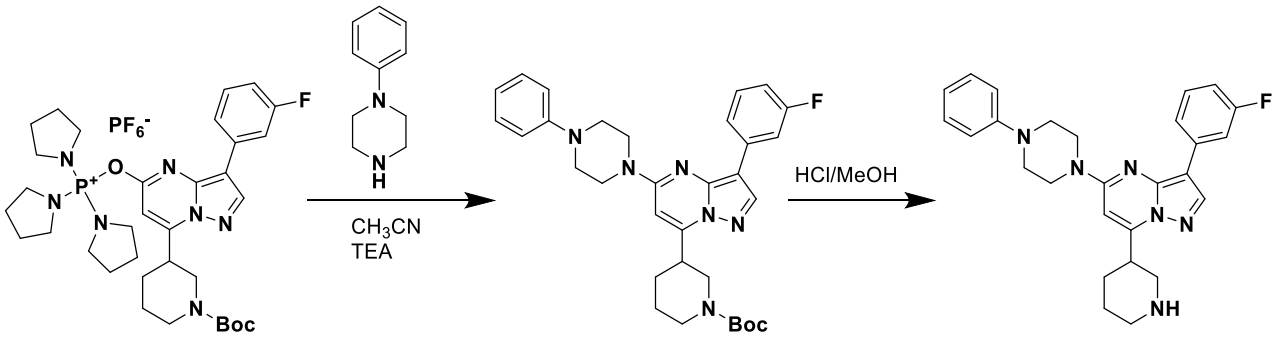

113 **114d** **50**

Rac-tert-butyl 3-(3-(3-fluorophenyl)-5-(4-phenylpiperazin-1-yl)pyrazolo[1,5-a]pyrimidin-7-yl)piperidine-1-carboxylate (114d). In a 7 mL vial, 113 (0.02mmol, 14mg, 1eq), TEA (10µL, 0.06mmol, 2eq), and 1-phenylpiperazine (12µL, 0.09mmol, 3eq) were dissolved in CH_3CN (1 mL). The reaction was stirred at 80 °C for 16 h and monitored by UPLC. After starting disappearance, the reaction mixture was diluted with AcOEt, transferred into a separatory funnel, and washed with cold HCl 3 M. The mixture was

purified by automated flash chromatography (Biotage) using silica and a cyclohexane/AcOEt gradient (0–50%). The title compound was obtained as a colourless oil (11mg, quantitative). **UPLC-MS** tR.: 1.39 (superapolar method). **MS (ESI)** m/z calc [M+H]+: 557.30, found 557.2.

Rac-3-(3-fluorophenyl)-5-(4-phenylpiperazin-1-yl)-7-(piperidin-3-yl)pyrazolo[1,5-a]pyrimidine (50). Starting from **114d** (11mg, 0.02mmol), following **GP3**, after 1h reaction time and automated flash chromatography (Biotage), using neutral alumina and as eluent phase DCM/MeOH gradient 0 to 20%, the title compound was obtained as a white powder in its hydrochloride salt form (6mg, 61%). **UPLC-MS tR**.: 2.40 (generic method) **MS (ESI)** m/z calc [M+H]+: 457.25, found 457.2. **^{1}H NMR (400 MHz, DMSO)** δ 9.41 (bs, 1H), 9.02 (bs, 1H), 8.57 (s, 1H), 7.98 – 7.89 (m, 2H), 7.43 (td, *J* = 8.2, 6.6 Hz, 1H), 7.28 (t, *J* = 7.8 Hz, 2H), 7.10 (d, *J* = 8.1 Hz, 2H), 7.01 – 6.92 (m, 1H), 6.88 (t, *J* = 7.3 Hz, 1H), 6.81 (s, 1H), 3.96 (s, 6H), 3.54 – 3.49 (m, 1H), 3.39 – 3.33 (m, 6H), 2.93 – 2.84 (m, 1H), 2.15 (d, 1H), 2.00 – 1.93 (m, 1H), 1.91 – 1.83 (m, 2H). **^{13}C NMR (101 MHz, MeOD)** δ 163.18 (d, *J* = 242.3 Hz), 155.57, 148.69, 144.55, 141.91, 141.40, 135.18 (d, *J* = 8.7 Hz), 130.50, 130.42, 129.82 (d, *J* = 8.7 Hz), 121.17, 120.67, 111.50 (d, *J* = 7.8 Hz), 111.27 (d, *J* = 6.2 Hz), 94.54, 55.01, 45.48, 43.95, 42.36, 34.85, 25.89, 22.00.

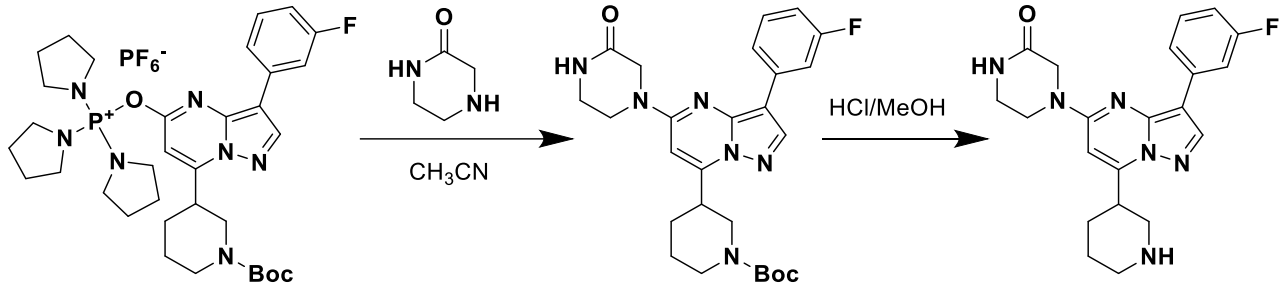

113 **114e** **51**

Rac-tert-butyl 3-(3-(3-fluorophenyl)-5-(3-oxopiperazin-1-yl)pyrazolo[1,5-a]pyrimidin-7-yl)piperidine-1-carboxylate (114e). Starting from **113** (14mg, 0.02mmol), following **GP7** and using piperazin-2-one as a nucleophile, and for the chromatography DCM/MeOH as eluent phase, gradient 0 to 20%, the title compound was obtained as a colourless oil. (6mg, 70%). **UPLC-MS tR**.: 1.26 (apolar method) **MS (ESI)** m/z calc [M+H]+: 495.25, found 495.2.

Rac-4-(3-(3-fluorophenyl)-7-(piperidin-3-yl)pyrazolo[1,5-a]pyrimidin-5-yl)piperazin-2-one (51). Starting from **114e** (6mg, 0.012mmol), following **GP3**, after 4h reaction time, and automated flash chromatography (Biotage), using silica and as eluent phase DCM/MeOH*NH3 1M gradient 0 to 20%, the title compound was obtained as a white powder in its hydrochloride salt form (3mg, 50%). **UPLC-MS tR**.: 1.59 (generic method) **MS (ESI)** m/z calc [M+H]+: 395.25, found 395.2. **^{1}H NMR (400 MHz, MeOD)** δ 8.34 (s, 1H), 7.90 – 7.79 (m, 2H), 7.37 (td, *J* = 8.0, 6.3 Hz, 1H), 6.92 – 6.82 (m, 1H), 6.48 (s, 1H), 4.37 (s, 2H), 4.03 – 3.96 (m, 2H), 3.72 – 3.59 (m, 1H), 3.59 – 3.47 (m, 4H), 3.24 – 3.16 (m, 1H), 2.88 (dd, *J* = 12.3, 11.2 Hz, 1H), 2.77 (td, *J* = 12.6, 2.9 Hz, 1H), 2.24 (d, *J* = 11.9 Hz, 1H), 1.97 – 1.75 (m, 3H).

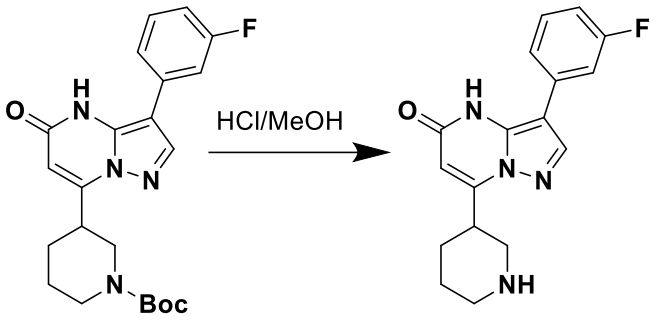

111 46

Rac-3-(3-fluorophenyl)-7-(piperidin-3-yl)pyrazolo[1,5-a]pyrimidin-5(4H)-one (46). Starting from **111** (15mg, 0.036mmol), following **GP3**, after 16h reaction time, the title compound was obtained as a white powder in its hydrochloride salt form (6mg, 37%). **UPLC-MS tR**.: 1.26 (generic method) **MS (ESI)** m/z calc [M+H]+: 313.14, found 313.1. **^{1}H NMR (400 MHz, DMSO)** δ 12.11 (s, 1H), 9.43 (s, 2H), 8.19 (s, 1H), 7.56 – 7.44 (m, 2H), 7.43 (d, *J* = 6.8 Hz, 2H), 7.16 (td, *J* = 8.6, 2.5 Hz, 1H), 5.81 (s, 1H), 3.54 – 3.50 (m, 1H), 3.28 – 3.25 (m, 1H), 3.22 – 3.17 (m, 1H), 2.90 – 2.80 (m, 2H), 2.09 (d, *J* = 12.6 Hz, 1H), 1.90 – 1.61 (m, 3H). **^{13}C NMR (101 MHz, MeOD)** δ 164.23, 161.79, 156.53, 155.38, 138.55, 131.43, 130.61, 130.53, 123.97, 114.85, 114.63, 114.25, 114.03, 106.35, 94.91, 46.13, 43.62, 37.16, 28.15, 21.92, 19.17.

3.9.11: Synthesis of compound **70**

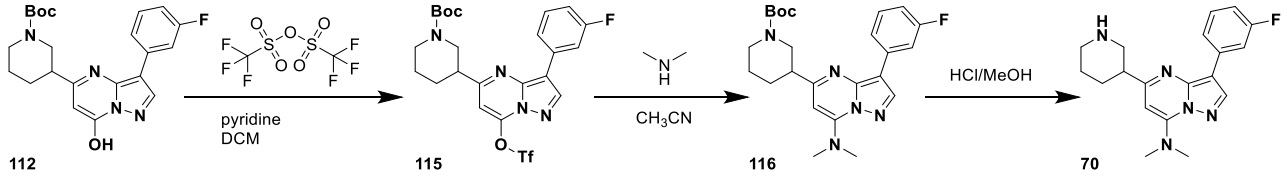

Rac-tert-butyl 3-(3-(3-fluorophenyl)-7-(((trifluoromethyl)sulfonyl)oxy)pyrazolo[1,5-a]pyrimidin-5-yl)piperidine-1-carboxylate (115). In a round-bottom flask, 112 (20mg, 0.05mmol, 1eq.) and pyridine (19µL, 0.25mmol, 5eq.) were dissolved in DCM (0.13M), and the reaction mixture was cooled to 0 °C. Triflic anhydride (42µL, 0.25mmol, 5eq.) was added portionwise, and the mixture was then allowed to warm to room temperature and stirred overnight. The reaction was monitored by UPLC. After complete consumption of the starting material, the solvent was removed by rotary evaporation, and the crude mixture was purified by automated flash chromatography (Biotage) on silica using a cyclohexane/AcOEt gradient as eluent, affording the title compound as an oil (21mg, 77%). **UPLC-MS tR**.: 2.46 (apolar method) **MS (ESI)** m/z calc [M+H]+: 545.14, found 545.2.

Rac-tert-butyl 3-(7-(dimethylamino)-3-(3-fluorophenyl)pyrazolo[1,5-a]pyrimidin-5-yl)piperidine-1-carboxylate (116). In a 7 mL vial, 115 (21mg, 0.038mmol, 1eq) was dissolved in CH_3CN (1mL), and dimethylamine (150µL, 0.25mmol, 5eq) was added. The reaction mixture was stirred at 85 °C for 2h30min and monitored by UPLC until complete disappearance of the starting material. The mixture was then transferred to a separatory funnel, diluted with AcOEt, and washed with cold 3 M HCl. The organic phase was collected, dried over sodium sulfate, and concentrated under vacuum to give the title compound as a colourless oil (17mg, quantitative). **UPLC-MS tR**.: 2.21 (apolar method) **MS (ESI)** m/z calc [M+H]+: 440.24, found 440.3.

Rac-3-(3-fluorophenyl)-N,N-dimethyl-5-(piperidin-3-yl)pyrazolo[1,5-a]pyrimidin-7-amine (70). Starting from **116** (6mg, 0.018mmol) and following **GP3**, after 3h reaction time, the title compound was obtained as a white powder in its hydrochloride salt form (6mg, quantitative). **UPLC-MS tR**.: 1.92

(generic method) **MS (ESI)** m/z calc [M+H]+: 340.24, found 340.2. **^{1}H NMR (400 MHz, DMSO)** δ 9.20 (s, 2H), 8.53 (s, 1H), 7.98 (ddd, *J* = 11.6, 2.7, 1.5 Hz, 1H), 7.91 (d, *J* = 8.1 Hz, 1H), 7.40 (td, *J* = 8.1, 6.5 Hz, 1H), 6.93 (td, *J* = 8.7, 2.7 Hz, 1H), 6.55 (s, 1H), 3.97 – 3.83 (m, 1H), 3.58 (d, *J* = 11.0 Hz, 1H), 3.44 – 3.37 (m, 1H), 3.23 (s, 5H), 2.91 (t, *J* = 10.9 Hz, 1H), 2.18 – 2.10 (m, 1H), 2.02 – 1.81 (m, 3H). **^{13}C NMR (101 MHz, MeOD)** δ 163.15 (d, *J* = 242.6 Hz), 155.75, 148.61, 142.52, 141.00, 134.05 (d, *J* = 9.3 Hz), 129.96 (d, *J* = 8.7 Hz), 121.30, 112.26 (d, *J* = 13.2 Hz), 112.04 (d, *J* = 11.6 Hz), 105.52, 94.83, 45.31, 43.82, 37.93, 34.77, 26.07, 21.89.

3.9.12: Synthesis of compounds **52-57**

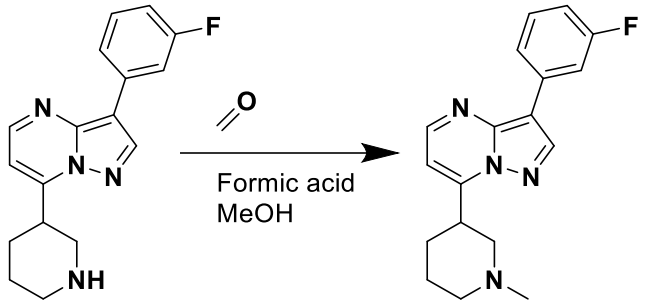

1 **52**

Rac-3-(3-fluorophenyl)-7-(1-methylpiperidin-3-yl)pyrazolo[1,5-a]pyrimidine (52). In a round-bottom flask, **1** (15 mg, 0.05 mmol) was dissolved in MeOH (1 mL, 20 mL/mmol) under a nitrogen atmosphere. Formaldehyde (21 µL, 0.25 mmol) and formic acid (4 µL, 0.1 mmol) were added, and the reaction mixture was stirred at 65 °C for 24 h. After completion, the mixture was diluted with EtOAc and transferred to a separatory funnel, then washed with saturated Na_2CO_3. The organic layer was dried and concentrated. The residue was dissolved in MeOH/HCl to form the hydrochloride salt and precipitated by titration with Et_2O and cyclohexane, affording the title compound as a yellow solid in its hydrochloride salt form (6 mg, 38%). **UPLC-MS tR**.: 1.89 (polar method) **MS (ESI)** m/z calc [M+H]+: 311.16, found 310.9. **^{1}H NMR (400 MHz, DMSO)** δ 8.91 (s, 2H), 8.72 (d, *J* = 4.4 Hz, 2H), 8.09 – 8.00 (m, 4H), 7.50 (td, *J* = 8.1, 6.4 Hz, 2H), 7.14 – 7.03 (m, 4H), 4.08 (s, 1H), 2.88 (s, 1H), 2.73 (s, 4H), 2.19 (dd, *J* = 12.0, 4.8 Hz, 3H), 1.99 – 1.94 (m, 3H), 1.77 (s, 1H), 1.24 (s, 4H).

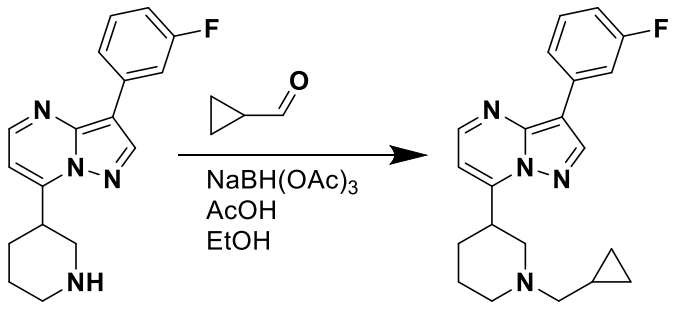

1 **53**

Rac-7-(1-(cyclopropylmethyl)piperidin-3-yl)-3-(3-fluorophenyl)pyrazolo[1,5-a]pyrimidine (53). In a round-bottom flask, **1** (20 mg, 0.07 mmol) was dissolved in MeOH (1 mL, 20 mL/mmol) under a nitrogen atmosphere. Cyclopropanecarbaldehyde (7.5 µL, 0.10 mmol) and $NaBH(OAc)_3$ (32 mg, 0.15 mmol) were added, and the reaction mixture was stirred at room temperature for 18h. After completion, the reaction was quenched with water, diluted with DCM, and transferred to a separatory funnel. The organic phase

was washed with saturated Na_2CO_3, dried, and concentrated under reduced pressure. The crude residue was dissolved in MeOH/HCl to form the hydrochloride salt and precipitated by titration with Et_2O and cyclohexane, then lyophilized to afford the title compound as a yellow solid in its hydrochloride salt form (24 mg, quantitative). **UPLC-MS** tR.: 1.89 (polar method). **^{1}H NMR (400 MHz, DMSO)** δ 10.51 (s, 1H), 8.92 (s, 1H), 8.74 (d, *J* = 4.3 Hz, 1H), 8.08 – 8.00 (m, 2H), 7.50 (td, *J* = 8.1, 6.3 Hz, 1H), 7.16 – 7.04 (m, 2H), 4.21 (s, 1H), 3.93 (s, 1H), 3.65 (s, 2H), 3.38 (s, 7H), 3.33 (s, 3H), 3.04 (s, 1H), 2.23 (s, 2H), 2.05 (s, 1H), 1.84 (s, 1H), 1.24 (d, *J* = 7.8 Hz, 2H), 1.16 (s, 2H).

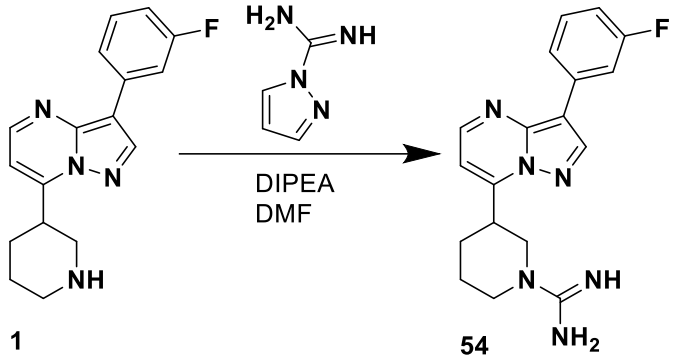

1 54

Rac-3-(3-(3-fluorophenyl)pyrazolo[1,5-a]pyrimidin-7-yl)piperidine-1-carboximidamide (54). In a 7 mL vial, **1** (26 mg, 0.08 mmol, 1 eq.) was dissolved in DMF (15 mL/mmol). 1H-Pyrazole-1-carboximidamide (18 mg, 0.16 mmol, 2 eq.) and DIPEA (41 µL, 0.24 mmol, 3 eq.) were added. The reaction mixture was stirred at 80 °C for 3 days, and another 1eq. of 1H-Pyrazole-1-carboximidamide and 1eq of DIPEA were added. The reaction kept stirring for another 2 days (total stirring time 5 days). After complete disappearance of the starting material, the solvent was removed under a stream of compressed air, and the residue was purified by automated flash chromatography (DCM/MeOH * NM_3 1 M, gradient 0–20%). The purified product was salified, triturated with Et_2O and cyclohexane, and lyophilized to give the title compound as a yellow powder in its hydrochloride salt form (3.5 mg, 12%). **UPLC-MS** tR.: 1.87 (generic method) **MS (ESI)** m/z calc [M+H]+: 339.17, found 339.3. **^{1}H NMR (400 MHz, DMSO)** δ 8.91 (s, 1H), 8.72 (d, *J* = 4.4 Hz, 1H), 8.09 – 8.00 (m, 2H), 7.71 (s, 2H), 7.49 (td, *J* = 8.2, 6.4 Hz, 3H), 7.14 – 7.03 (m, 2H), 4.20 (d, *J* = 12.7 Hz, 1H), 4.03 (d, *J* = 13.7 Hz, 1H), 3.74 (t, *J* = 11.4 Hz, 1H), 3.55 – 3.44 (m, 2H), 3.18 (t, *J* = 12.4 Hz, 1H), 2.28 (d, *J* = 11.1 Hz, 1H), 1.86 (s, 1H), 1.69 (d, *J* = 13.1 Hz, 1H), 1.29 – 1.20 (m, 2H), 0.86 (s, 1H). **^{13}C NMR (151 MHz, DMSO)** δ 163.86, 162.26, 156.48, 151.01, 150.21, 145.08, 142.89, 134.72, 134.66, 131.18, 131.12, 122.07, 113.19, 113.06, 112.56, 112.41, 108.65, 106.35, 63.18, 47.98, 46.65, 40.31, 40.19, 40.17, 40.05, 40.03, 39.91, 39.77, 39.64, 39.50, 39.36, 36.63, 31.67, 27.49, 24.55, 19.17.

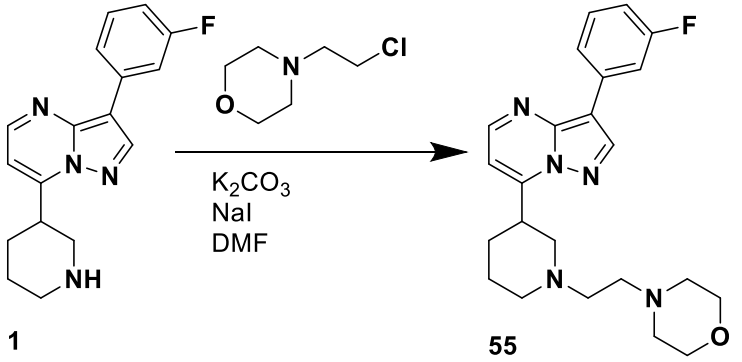

1 55

Rac-4-(2-(3-(3-(3-fluorophenyl)pyrazolo[1,5-a]pyrimidin-7-yl)piperidin-1-yl)ethyl)morpholine (55). In 7ml vial, **1** (23mg, 0.07mmol, 1eq), was dissolved into DMF (15ml/mmol), and K_2CO_3 (50mg, 0.35mmol, 5eq), NaI (10mg, 0.07mmol, 1eq) and 4-(2-chloroethyl)morpholine (15mg, 0.08mmol, 1.2eq) were added. The reaction kept stirring for 3 days at 80°C and monitored by UPLC. After starting disappearance the solvent was stripped by compressed air and the reaction mixture was purified by automated flash chromatography, using DCM/MeOH * NM_3 1M in a gradient from 0 to 20%. The final product was salified, triturated with Et_2O and cyclohexane and liophylized, obtaining the title compound as a yellow powder in its hydrochloride salt form (13mg, 42%). **UPLC-MS** tR.: 1.99 (polar method) **MS (ESI)** m/z calc [M+H]+: 410.23, found 410.3. **^{1}H NMR (400 MHz, DMSO)** δ 8.93 (s, 1H), 8.76 (d, *J* = 4.3 Hz, 1H), 8.09 – 8.01 (m, 2H), 7.50 (td, *J* = 8.2, 6.4 Hz, 1H), 7.14 – 7.04 (m, 2H), 4.25 (t, *J* = 12.2 Hz, 1H), 3.98 (d, *J* = 11.4 Hz, 2H), 3.79 (s, 1H), 3.67 (s, 3H), 3.14 (s, 1H), 2.28 (d, *J* = 12.5 Hz, 1H), 2.08 (d, *J* = 8.6 Hz, 2H), 1.83 (s, 1H).

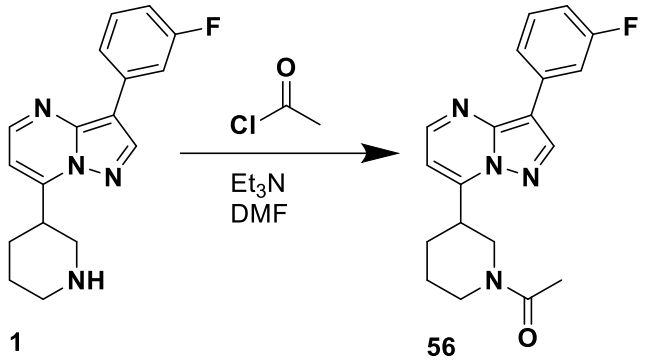

Rac-1-(3-(3-(3-fluorophenyl)pyrazolo[1,5-a]pyrimidin-7-yl)piperidin-1-yl)ethan-1-one (56). In a 7 mL vial cooled to 0 °C, **1** (15 mg, 0.05 mmol, 1 eq.) was dissolved in DMF (15 mL/mmol). Acetyl chloride (7 µL, 0.10 mmol, 2 eq.) and Et_3N (10 µL, 0.07 mmol, 1.3 eq.) were added. The reaction mixture was stirred for 5 h 30 min and monitored by UPLC. After complete disappearance of the starting material, the reaction was quenched with saturated Na_2CO_3 solution and transferred to a separatory funnel. The mixture was extracted with DCM, and the organic layer was dried and concentrated. The crude product was salified, triturated with Et_2O and cyclohexane, and lyophilized to afford the title compound as a yellow powder (12 mg, 71%). **UPLC-MS** tR.: 2.18 (generic method) **MS (ESI)** m/z calc [M+H]+:339.16 found 338.9**. ^{1}H NMR (400 MHz, DMSO)** δ 8.83 (s, 0H), 8.79 (s, 0H), 8.63 (d, *J* = 4.3 Hz, 1H), 8.61 (d, *J* = 4.4 Hz, 0H), 7.96 (dd, *J* = 9.7, 7.3 Hz, 2H), 7.47 – 7.36 (m, 1H), 7.07 – 6.95 (m, 2H), 4.56 (d, *J* = 13.2 Hz, 1H), 4.38 (d, *J* = 13.1 Hz, 1H), 4.21 (d, *J* = 13.2 Hz, 1H), 3.79 (d, *J* = 13.4 Hz, 0H), 3.63 – 3.49 (m, 1H), 3.24 – 3.09 (m, 1H), 3.01 – 2.91 (m, 1H), 2.65 – 2.54 (m, 1H), 2.12 (d, *J* = 12.7 Hz, 1H), 2.02 (d, *J* = 8.8 Hz, 3H), 1.95 – 1.81 (m, 1H), 1.78 – 1.70 (m, 1H), 1.58 (d, *J* = 13.0 Hz, 0H), 1.45 (d, *J* = 12.9 Hz, 1H). (A splitting in the signal due to two different conformations caused by the amide introduction is noted). **^{13}C NMR (101 MHz, $CDCl_3$)** δ 169.50, 169.32, 164.48, 162.05, 150.40, 149.45, 149.28, 149.23, 145.33, 145.24, 142.22, 142.13, 134.29, 134.20, 134.12, 134.03, 130.26, 130.18, 130.10, 126.45, 121.77, 121.75, 113.26, 113.22, 113.06, 113.03, 113.01, 112.84, 109.97, 109.71, 105.11, 105.03, 49.59, 46.99, 43.96, 42.29, 37.77, 36.40, 27.89, 27.50, 25.11, 24.54, 21.65, 21.60. (A splitting in the signal due to two different conformations caused by the amide introduction is noted).

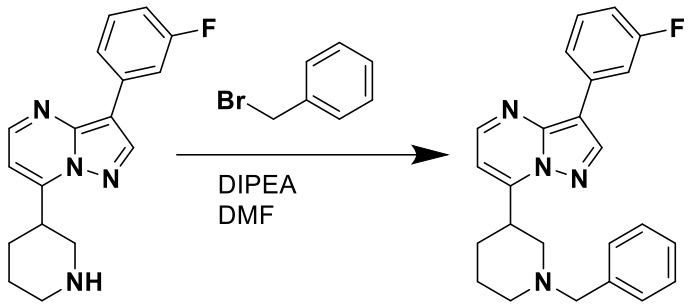

1 **57**

Rac-7-(1-benzylpiperidin-3-yl)-3-(3-fluorophenyl)pyrazolo[1,5-a]pyrimidine (57). In a 7 mL vial, **1** (20 mg, 0.07 mmol, 1 eq.) was dissolved in DMF (15 mL/mmol). (bromomethyl)benzene (10ul, 0.08 mmol, 1.2 eq.) and DIPEA (40 µL, 0.28 mmol, 4 eq.) were added. The reaction mixture was stirred at r.t. for 20h and monitored by UPLC. After complete disappearance of the starting material, the solvent was removed under a stream of compressed air, and the residue was purified by automated flash chromatography (DCM/MeOH * NM_3 1 M, gradient 0–20%). The purified product was salified, triturated with Et_2O and cyclohexane, and lyophilized to give the title compound as a yellow powder in its hydrochloride salt form (17 mg, 62%). **UPLC-MS** tR.: 1.92 (apolar method) **MS (ESI)** m/z calc [M+H]+:387.19 found 387.2. **^{1}H NMR (400 MHz, DMSO)** δ 11.11 (s, 1H), 8.79 (s, 1H), 8.63 (d, *J* = 4.3 Hz, 1H), 8.00 – 7.91 (m, 2H), 7.56 (s, 2H), 7.46 – 7.35 (m, 4H), 7.05 – 6.95 (m, 2H), 4.29 (s, 2H), 4.18 (s, 1H), 3.66 (s, 1H), 3.38 (s, 1H), 2.96 (s, 1H), 2.13 (d, *J* = 12.5 Hz, 1H), 1.94 (d, *J* = 14.3 Hz, 2H), 1.83 – 1.69 (m, 1H). **^{13}C NMR (101 MHz, DMSO)** δ 163.07 (d, *J* = 241.9 Hz), 151.01, 145.16, 142.89, 134.74 (d, *J* = 9.0 Hz), 132.05, 131.08 (d, *J* = 8.7 Hz), 130.20 – 129.55 (m), 129.22, 122.06, 113.07 (d, *J* = 20.8 Hz), 112.49 (d, *J* = 23.1 Hz), 108.69, 106.61, 34.57.

3.9.13: Synthesis of compounds **58-63**

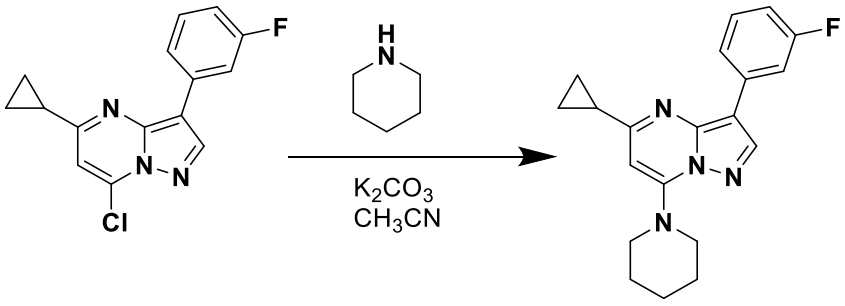

105b **58**

5-Cyclopropyl-3-(3-fluorophenyl)-7-(piperidin-1-yl)pyrazolo[1,5-a]pyrimidine (58). Starting from **105b** (28mg, 0.1mmol), following **GP7**, and using piperidine as the nucleophile, after 14h reaction time the title compound was obtained as a white powder (17mg, 37%). **UPLC-MS** tR.: 2.38 (apolar method) **MS (ESI)** m/z calc [M+H]+: 337.18, found 337.1. **^{1}H NMR (400 MHz, DMSO)** δ 8.56 (s, 1H), 7.94 (ddd, *J* = 11.6, 2.7, 1.5 Hz, 1H), 7.86 (dt, *J* = 7.9, 1.2 Hz, 1H), 7.35 (td, *J* = 8.1, 6.5 Hz, 1H), 6.94 – 6.85 (m, 1H), 6.39 (s, 1H), 3.68 – 3.61 (m, 4H), 2.12 (tt, *J* = 7.9, 4.9 Hz, 1H), 1.68 – 1.59 (m, 6H), 1.08 – 0.95 (m, 4H). **^{13}C NMR (101 MHz, DMSO)** δ 164.85, 161.85 (d, *J* = 242.1 Hz), 150.18, 147.43, 141.92, 135.96 (d, *J* = 9.2 Hz), 130.75 (d, *J* = 8.9 Hz), 121.32, 111.93 (d, *J* = 12.6 Hz), 111.71 (d, *J* = 13.7 Hz), 105.08 (d, *J* = 2.8 Hz), 93.02, 49.38, 25.54, 24.37, 17.43, 11.12.

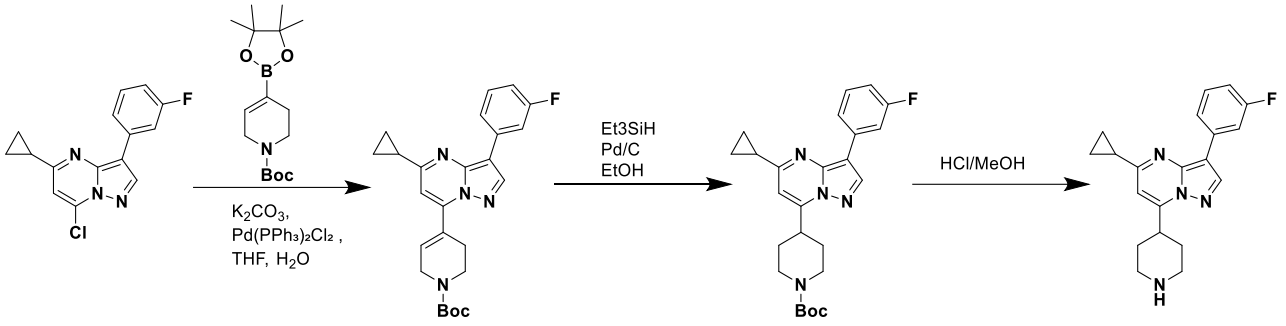

105b 118 119 59

Tert-butyl 4-(5-cyclopropyl-3-(3-fluorophenyl)pyrazolo[1,5-a]pyrimidin-7-yl)-3,6-dihydropyridine-1(2H)-carboxylate (118). Starting from **105b** (40mg, 0.14mmol), following **GP2** and using as the coupling partner tert-butyl 4-(4,4,5,5-tetramethyl-1,3,2-dioxaborolan-2-yl)-3,6-dihydropyridine-1(2H)-carboxylate, the title compound was synthesized as a yellow oil (60mg, quantitative). **UPLC-MS** tR.: 1.22 (superapolar method) **MS (ESI)** m/z calc [M+H]+: 435.22, found 435.2.

Tert-butyl 4-(5-cyclopropyl-3-(3-fluorophenyl)pyrazolo[1,5-a]pyrimidin-7-yl)piperidine-1-carboxylate (119). Starting from **118** (60mg, 0.14mmol) and following **GP4**, after 14h reaction time, the title compound was obtained as a yellow oil (55mg, 90%). **UPLC-MS** tR.: 2.44 (apolar method) **MS (ESI)** m/z calc [M+H]+: 437.23, found 437.3.

5-Cyclopropyl-3-(3-fluorophenyl)-7-(piperidin-4-yl)pyrazolo[1,5-a]pyrimidine (59). Starting from **119** (55mg, 0.13mmol) and following **GP3**, after 2h reaction time and after automated flash chromatography (Biotage), using neutral alumina and as eluent phase toluene/MeOH gradient 0 to 20%, the title compound was obtained as a yellow powder in its hydrochloride salt form (15mg, 34%). **UPLC-MS** tR.: 0.73 (apolar method) **MS (ESI)** m/z calc [M+H]+: 337.18, found 337.1. **^{1}H NMR (400 MHz, DMSO)** δ 9.02 (s, 3H), 8.77 (s, 1H), 8.03 – 7.93 (m, 2H), 7.46 (td, *J* = 8.1, 6.4 Hz, 1H), 7.07 – 6.98 (m, 2H), 3.77 (t, *J* = 11.9 Hz, 1H), 3.44 (d, *J* = 12.6 Hz, 2H), 3.15 (t, 2H), 2.42 – 2.32 (m, 1H), 2.29 (d, *J* = 13.4 Hz, 2H), 2.09 – 1.95 (m, 2H), 1.18 (dt, *J* = 8.3, 2.2 Hz, 4H). **^{13}C NMR (101 MHz, DMSO)** δ 165.29, 163.05 (d, *J* = 241.5 Hz), 150.98, 145.09, 142.81, 135.33 (d, *J* = 9.1 Hz), 130.98 (d, *J* = 8.5 Hz), 121.63, 112.50 (d, *J* = 21.3 Hz), 112.04 (d, *J* = 22.8 Hz), 106.75 (d, *J* = 2.4 Hz), 105.25, 49.06, 46.03, 44.07, 34.96, 26.86, 17.54, 12.22, 10.51.

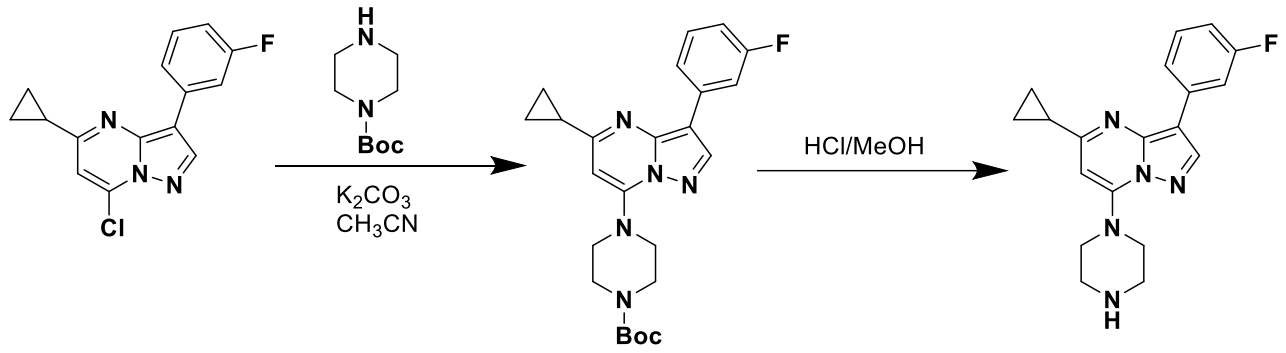

105b 120 60

5-Cyclopropyl-3-(3-fluorophenyl)-7-(piperazin-1-yl)pyrazolo[1,5-a]pyrimidine (120). Starting from **105b** (15mg, 0.05mmol), following **GP7** and using tert-butyl piperazine-1-carboxylate as the nucleophile, after 16h reaction time, the title compound was obtained as a white oil (22mg, quantitative). **UPLC-MS** tR.: 2.32 (generic method). **MS (ESI)** m/z calc [M+H]+: 438.23, found 438.2.

5-Cyclopropyl-3-(3-fluorophenyl)-7-(piperazin-1-yl)pyrazolo[1,5-a]pyrimidine (60). Starting from **120** (22mg, 0.05mmol) and following **GP3**, after 3h reaction time and automated flash chromatography (Biotage), using neutral alumina and as eluent phase DCM/MeOH gradient 0 to 20%, the title compound was obtained as a white powder in its hydrochloride salt form (19mg, quantitative). **HPLC-MS** R.t.: 3.69 (generic method). **MS (ESI)** m/z calc [M+H]+: 338.17, found 338.22. **^{1}H NMR (400 MHz, DMSO)** δ 9.47 (s, 1H), 8.69 (s, 1H), 8.06 – 7.99 (m, 1H), 7.99 – 7.93 (m, 1H), 7.44 (td, *J* = 8.1, 6.5 Hz, 1H), 6.99 (td, *J* = 8.5, 2.6 Hz, 1H), 6.63 (s, 1H), 4.00 (t, *J* = 5.1 Hz, 4H), 3.34 (s, 5H), 2.23 (ddd, *J* = 12.8, 7.8, 5.1 Hz, 1H), 1.17 – 1.06 (m, 4H). **^{13}C NMR (151 MHz, DMSO)** δ 165.48, 163.01 (d, *J* = 241.2 Hz), 149.07, 147.08, 142.20, 135.47 (d, *J* = 8.8 Hz), 130.93 (d, *J* = 8.7 Hz), 121.46 (d, *J* = 2.0 Hz), 112.26 (d, *J* = 21.3 Hz), 111.86 (d, *J* = 23.0 Hz), 105.66 (d, *J* = 2.5 Hz), 93.75, 45.08, 42.83, 17.57, 11.49.

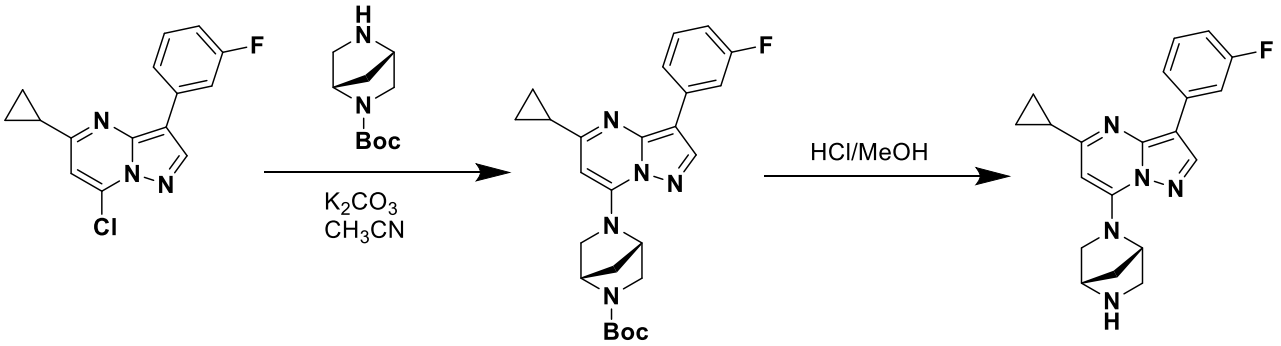

105b **121** **61**

Tert-butyl (1S,4S)-5-(5-cyclopropyl-3-(3-fluorophenyl)pyrazolo[1,5-a]pyrimidin-7-yl)-2,5-diazabicyclo[2.2.1]heptane-2-carboxylate (121). Starting from **105b** (28mg, 0.1mmol), following **GP7**, and using tert-butyl (1S,4S)-2,5-diazabicyclo[2.2.1]heptane-2-carboxylate as the nucleophile, after 29h reaction time the title compound was obtained as a colourless oil (45mg, quantitative). **UPLC-MS** tR.: 2.30 (apolar method) **MS (ESI)** m/z calc [M+H]+: 450.23, found 450.2.

7-((1S,4S)-2,5-diazabicyclo[2.2.1]heptan-2-yl)-5-cyclopropyl-3-(3-fluorophenyl)pyrazolo[1,5-a]pyrimidine (61). Starting from **105b** (45mg, 0.1mmol) and following **GP3**, after 6h reaction time and after automated flash chromatography (Biotage), using silica and as eluent phase DCM/MeOH gradient 0 to 20%, the title compound was obtained as a white powder in its hydrochloride salt form (11mg, 29%). **UPLC-MS** tR.: 0.83 (apolar method), **MS (ESI)** m/z calc [M+H]+: 350.17, found 350.0. **^{1}H NMR (400 MHz, DMSO)** δ 10.08 (s, 1H), 9.50 (s, 1H), 8.60 (s, 1H), 8.00 (dt, *J* = 11.3, 2.0 Hz, 1H), 7.92 (d, *J* = 7.8 Hz, 1H), 7.41 (td, *J* = 8.1, 6.5 Hz, 1H), 6.96 (td, *J* = 8.6, 2.6 Hz, 1H), 6.28 (s, 1H), 4.52 (s, 1H), 4.09 (s, 2H), 3.51 – 3.41 (m, 1H), 3.41 – 3.29 (m, 1H), 2.23 (d, *J* = 11.0 Hz, 1H), 2.13 (td, *J* = 7.7, 3.9 Hz, 1H), 2.06 (d, *J* = 11.0 Hz, 1H), 1.15 – 1.01 (m, 4H). **^{13}C NMR (101 MHz, DMSO)** δ 164.84, 161.82 (d, *J* = 241.0 Hz), 147.42, 142.37, 135.82, 130.74 (d, *J* = 9.1 Hz), 121.28, 112.05 – 111.51 (m), 104.56 (d, *J* = 2.0 Hz), 89.42, 57.41, 43.68, 35.70, 17.35, 10.91, 10.87.

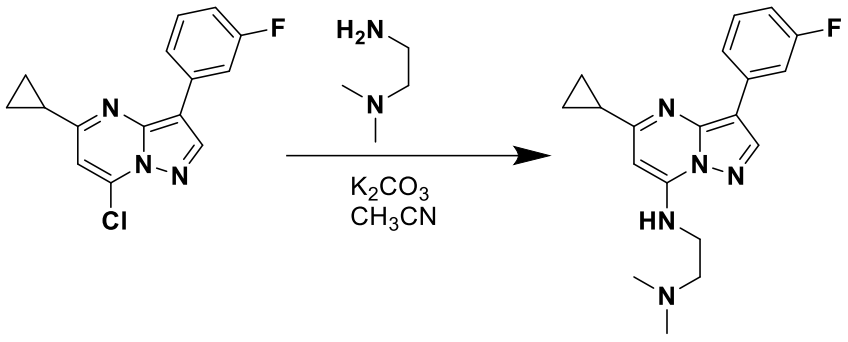

105b **62**

N1-(5-cyclopropyl-3-(3-fluorophenyl)pyrazolo[1,5-a]pyrimidin-7-yl)-N2,N2-dimethylethane-1,2-diamine (62). Starting from **105b** (28mg, 0.1mmol), following **GP7** and using N1,N1-dimethylethane-1,2-diamine as the nucleophile, by adding 1eq of N1,N1-dimethylethane-1,2-diamine after 16h reaction time and in 39h and automated flash chromatography (Biotage), using neutral alumina and as eluent phase DCM/MeOH gradient 0 to 20%, total reaction time the title compound was obtained as a white powder in its hydrochloride salt form (26mg, 69%). **UPLC-MS** tR.: 2.13 (generic method), **MS (ESI)** m/z calc [M+H]+: 340.19, found 340.1. **^{1}H NMR (400 MHz, DMSO)** δ 10.68 (s, 1H), 8.66 (s, 1H), 8.27 (s, 1H), 7.99 (dt, *J* = 11.7, 2.0 Hz, 1H), 7.93 (d, *J* = 7.9 Hz, 1H), 7.42 (td, *J* = 8.1, 6.5 Hz, 1H), 6.97 (td, *J* = 8.5, 2.6 Hz, 1H), 6.51 (s, 1H), 3.86 (q, *J* = 6.4 Hz, 2H), 3.36 (q, *J* = 6.2 Hz, 2H), 2.85 (s, 3H), 2.84 (s, 3H), 2.16 (td, *J* = 8.0, 4.0 Hz, 1H), 1.19 – 1.04 (m, 4H). **^{13}C NMR (101 MHz, DMSO)** δ 165.00, 163.04 (d, *J* = 240.9 Hz), 146.73, 142.26, 130.79 (d, *J* = 9.1 Hz), 121.35, 113.02 – 111.01 (m), 105.40, 85.38, 54.83, 42.74, 37.09, 17.66, 11.07.

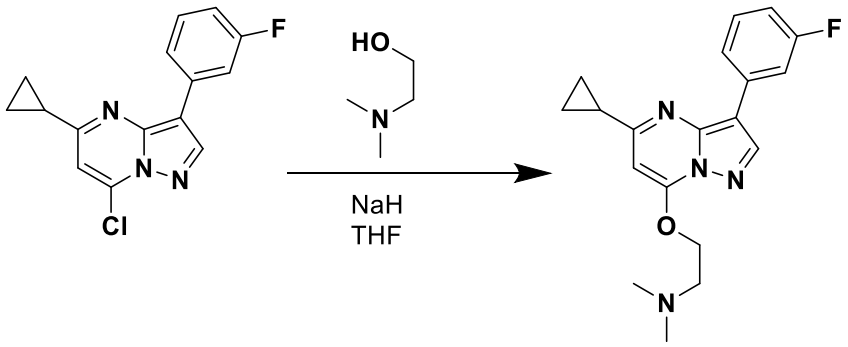

105b **63**

2-((5-Cyclopropyl-3-(3-fluorophenyl)pyrazolo[1,5-a]pyrimidin-7-yl)oxy)-N,N-dimethylethan-1-amine (63). Starting from **105b** (28mg, 0.1mmol), following **GP10** and using 2-(dimethylamino)ethan-1-ol as the nucleophile, after 29h reaction time and after automated flash chromatography (Biotage), using silica and as eluent phase DCM/MeOH gradient 0 to 20%, the title compound was obtained as a white powder in its hydrochloride salt form (22mg, 64%). **UPLC-MS** tR.: 1.99 (generic method), **MS (ESI)** m/z calc [M+H]+: 341.17, found 341.6. **^{1}H NMR (400 MHz, DMSO)** δ 10.97 (s, 1H), 8.71 (s, 1H), 8.04 – 7.92 (m, 2H), 7.45 (td, *J* = 8.0, 6.4 Hz, 1H), 7.01 (td, *J* = 8.5, 2.6 Hz, 1H), 6.83 (s, 1H), 4.95 – 4.88 (m, 2H), 3.72 (dd, *J* = 9.2, 4.5 Hz, 3H), 2.94 (s, 3H), 2.92 (s, 3H), 2.33 – 2.22 (m, 1H), 1.24 – 1.09 (m, 5H). **^{13}C NMR (101 MHz, DMSO)** δ 167.14, 163.00 (d, *J* = 242.2 Hz), 153.97, 146.65, 143.45, 135.31 (d, *J* = 8.9 Hz), 131.02 (d, *J* = 10.1 Hz), 121.52, 112.53 (d, *J* = 21.2 Hz), 111.83 (d, *J* = 23.2 Hz), 106.19, 88.64, 65.67, 55.02, 43.48, 18.05, 11.80.

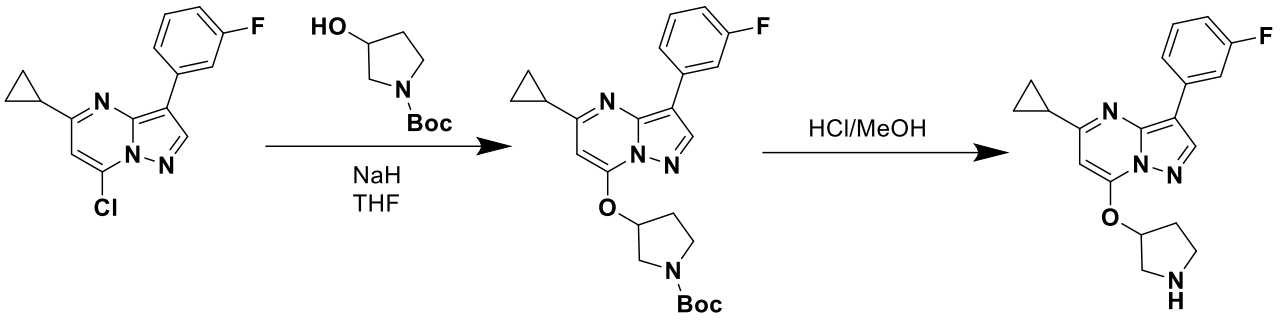

105b **122** **64**

Rac-tert-butyl 3-((5-cyclopropyl-3-(3-fluorophenyl)pyrazolo[1,5-a]pyrimidin-7-yl)oxy)pyrrolidine-1-carboxylate (122). Starting from **105b** (28mg, 0.1mmol), following **GP10** and using tert-butyl 3-hydroxypyrrolidine-1-carboxylate as the nucleophile, after 4h 30min reaction time, the title compound was obtained as a colourless oil (32mg, 73%). **UPLC-MS** tR.: 1.76 (apolar method), **MS (ESI)** m/z calc [M+H]+: 439.21, found 439.2.

Rac-5-cyclopropyl-3-(3-fluorophenyl)-7-(pyrrolidin-3-yloxy)pyrazolo[1,5-a]pyrimidine (64). Starting from **122** (32mg, 0.07mmol), following **GP3**, after 2h reaction time and automated flash chromatography (Biotage), using silica and as eluent phase DCM/MeOH gradient 0 to 20%, the title compound was obtained as a white powder in its ammonia salt form (8mg, 32%). **UPLC-MS** tR.: 1.96 (generic method), **MS (ESI)** m/z calc [M+H]+: 339.16, found 339.1. **^{1}H NMR (400 MHz, DMSO)** δ 9.78 (s, 1H), 9.44 (s, 1H), 8.69 (s, 1H), 8.04 – 7.92 (m, 2H), 7.45 (td, *J* = 8.1, 6.5 Hz, 1H), 7.01 (td, *J* = 8.7, 2.7 Hz, 1H), 6.82 (s, 1H), 5.66 (d, *J* = 4.1 Hz, 1H), 3.75 – 3.65 (m, 1H), 3.63 (s, 1H), 3.45 – 3.40 (m, 1H), 3.38 – 3.27 (m, 1H), 2.40 (ddd, *J* = 9.3, 6.3, 3.5 Hz, 2H), 2.27 (p, *J* = 6.4 Hz, 1H), 1.20 – 1.09 (m, 4H). **^{13}C NMR (101 MHz, DMSO)** δ 167.02, 161.84 (d, *J* = 230.0 Hz), 153.23, 146.77, 143.23, 135.35 (d, *J* = 8.9 Hz), 130.90 (d, *J* = 8.4 Hz), 121.48, 112.30 (d, *J* = 21.9 Hz), 111.93 (d, *J* = 23.3 Hz), 106.33 (d, *J* = 2.7 Hz), 89.35, 79.49, 50.24, 44.22, 31.14, 18.02, 11.93, 11.86.

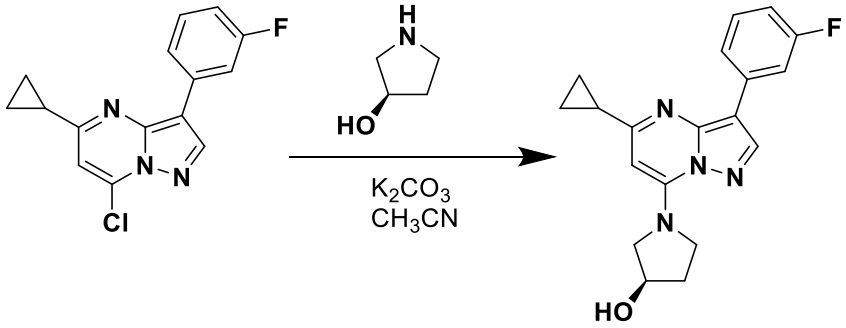

105b **65**

(R)-1-(5-cyclopropyl-3-(3-fluorophenyl)pyrazolo[1,5-a]pyrimidin-7-yl)pyrrolidin-3-ol (65). Starting from **105b** (20mg, 0.07mmol), following **GP7**, and using (R)-pyrrolidin-3-ol as the nucleophile, after 16h reaction time, the title compound was obtained as a white powder (26mg, quantitative). **UPLC-MS** tR.: 1.36 (apolar method), **MS (ESI)** m/z calc [M+H]+: 339.16, found 339.1. **^{1}H NMR (400 MHz, DMSO)** δ 8.54 (s, 1H), 8.02 (ddd, *J* = 11.7, 2.7, 1.5 Hz, 1H), 7.95 – 7.88 (m, 1H), 7.39 (td, *J* = 8.1, 6.6 Hz, 1H), 7.22 (s, 1H), 6.93 (td, *J* = 8.5, 2.6 Hz, 1H), 6.07 (s, 1H), 5.12 (d, *J* = 3.5 Hz, 1H), 4.42 (s, 1H), 4.08 – 4.00 (m, 1H), 3.96 (s, 2H), 2.16 – 2.06 (m, 1H), 2.06 – 1.98 (m, 1H), 1.98 – 1.89 (m, 1H), 1.14 – 0.97 (m, 4H). **^{13}C NMR (101 MHz, DMSO**) δ 164.48, 163.04 (d, *J* = 240.9 Hz), 147.91, 147.25, 141.99, 136.22 (d, *J* = 9.1 Hz), 130.63

(d, *J* = 8.7 Hz), 121.01 (d, *J* = 2.0 Hz), 111.58, 111.35, 103.88, 88.91, 69.15, 59.46, 48.98, 33.40, 17.30, 10.51, 10.47.

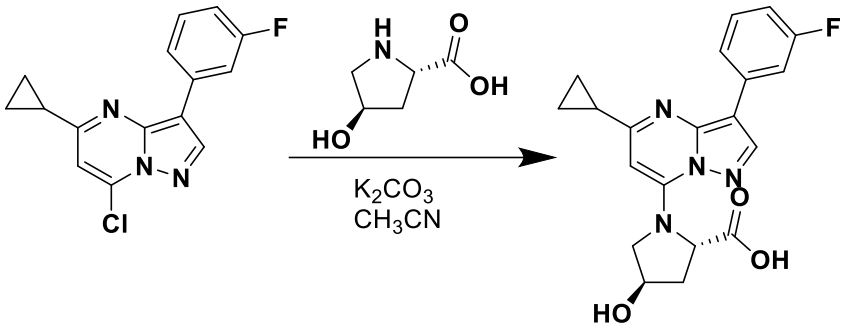

105b **66**

1-((2S,4R)-1-(5-cyclopropyl-3-(3-fluorophenyl)pyrazolo[1,5-a]pyrimidin-7-yl)-4-hydroxypyrrolidin-2-yl)ethan-1-one (66). Starting from **105b** (22mg, 0.08mmol), following **GP7**, and using 1-((2S,4R)-4-hydroxypyrrolidin-2-yl)ethan-1-one as the nucleophile, after 19h reaction time, the title compound was obtained as a white powder (7mg, 23%). **UPLC-MS** tR.: 1.62 (generic method), **MS (ESI)** m/z calc [M+H]+: 381.17, found 381.3. **^{1}H NMR (400 MHz, DMSO)** δ 8.49 (s, 1H), 8.01 (dt, *J* = 11.4, 2.2 Hz, 1H), 7.91 (d, *J* = 8.0 Hz, 1H), 7.39 (td, *J* = 8.1, 6.6 Hz, 1H), 6.92 (td, *J* = 8.6, 2.6 Hz, 1H), 6.06 (s, 1H), 5.27 – 5.08 (m, 1H), 4.41 (s, 1H), 4.11 – 3.73 (m, 2H), 2.32 – 2.22 (m, 1H), 2.16 – 2.02 (m, 2H), 1.09 – 0.99 (m, 4H). **^{13}C NMR (151 MHz, DMSO)** δ 164.48 (d, *J* = 42.3 Hz), 162.74, 148.21, 142.20, 136.78, 131.11, 121.47, 111.91 (d, *J* = 22.1 Hz), 104.26, 90.49, 64.01, 52.29, 17.85, 11.07.

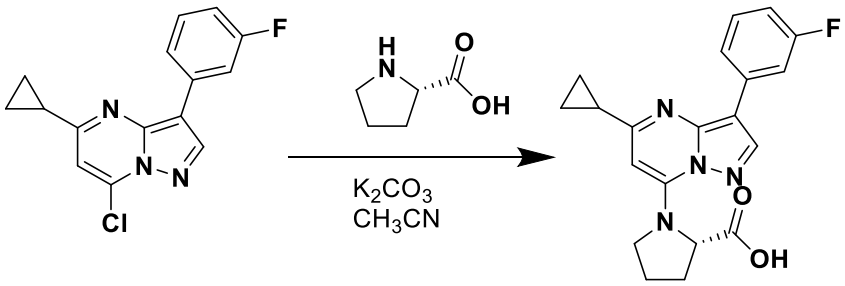

105b **67**

(5-Cyclopropyl-3-(3-fluorophenyl)pyrazolo[1,5-a]pyrimidin-7-yl)-L-proline (67). Starting from **105b** (28mg, 0.1mmol), following **GP7**, and using L-proline as the nucleophile, after 24h reaction time, the title compound was obtained as a white powder in its ammonia salt form (21mg, 57%). **UPLC-MS** tR.: 3.10 (generic method), **MS (ESI)** m/z calc [M+H]+: 367.15, found 367.1. **^{1}H NMR (400 MHz, DMSO)** δ 8.51 (s, 1H), 8.00 (ddd, *J* = 11.6, 2.7, 1.5 Hz, 1H), 7.95 – 7.89 (m, 1H), 7.40 (td, *J* = 8.1, 6.6 Hz, 1H), 6.94 (td, *J* = 8.4, 2.8 Hz, 1H), 6.17 (s, 1H), 5.72 – 5.67 (m, 1H), 3.70 (t, *J* = 6.8 Hz, 2H), 2.47 – 2.34 (m, 1H), 2.19 – 1.89 (m, 4H), 1.14 – 1.00 (m, 4H). **^{13}C NMR (101 MHz, DMSO)** δ 164.83, 163.04 (d, *J* = 241.2 Hz), 150.17, 147.43, 141.89, 135.92 (d, *J* = 9.1 Hz), 130.71 (d, *J* = 8.7 Hz), 121.30, 121.28, 111.80 (dd, *J* = 22.0, 10.5 Hz), 105.12, 105.09, 93.00, 49.37, 25.53, 24.36, 17.43, 11.11.

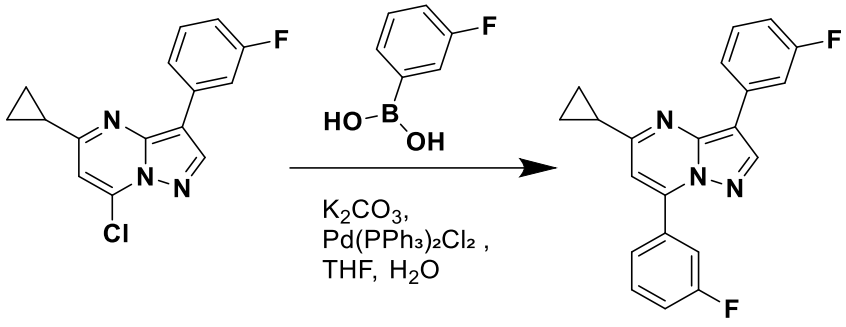

105b **117**

5-Cyclopropyl-3,7-bis(3-fluorophenyl)pyrazolo[1,5-a]pyrimidine (117). Starting from **105b** (29mg, 0.1mmol), following **GP2** and using 3-fluorophenyl boronic acid as the coupling partner, the title compound was synthesized as a yellow oil (4mg, 11%). Reaction followed by TLC. **^{1}H NMR (400 MHz, CDCl3)** δ 8.41 (s, 1H), 7.96 – 7.90 (m, 1H), 7.86 – 7.76 (m, 3H), 7.62 – 7.53 (m, 1H), 7.44 – 7.36 (m, 1H), 7.33 – 7.25 (m, 2H), 6.96 (tdd, *J* = 8.5, 2.6, 1.0 Hz, 1H), 6.86 (s, 1H), 2.20 (tt, *J* = 8.0, 4.7 Hz, 1H), 1.38 – 1.32 (m, 2H), 1.25 – 1.17 (m, 2H).

3.9.14: Synthesis of compounds **71-73**

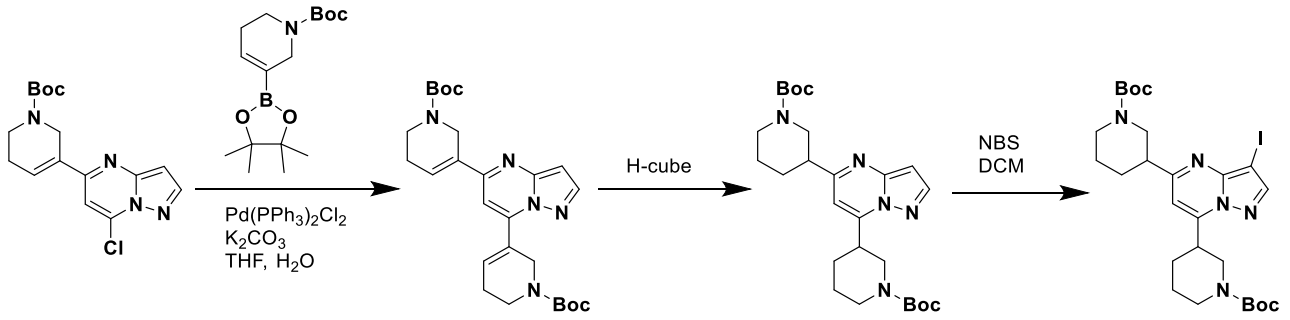

93b **123** **124** **125**

Di-tert-butyl 5,5'-(pyrazolo[1,5-a]pyrimidine-5,7-diyl)bis(3,6-dihydropyridine-1(2H)-carboxylate) (123). Starting from **93b** (334mg, 0.84mmol), following **GP2** and using tert-butyl 5-(4,4,5,5-tetramethyl-1,3,2-dioxaborolan-2-yl)-3,6-dihydropyridine-1(2H)-carboxylate as the coupling partner, the title compound was synthesized as a yellow oil (400mg, 99%). **UPLC-MS** tR.: 2.05 (apolar method) **MS (ESI)** m/z calc [M+H]+: 482.27, found 482.4.

Di-tert-butyl 3,3'-(pyrazolo[1,5-a]pyrimidine-5,7-diyl)bis(piperidine-1-carboxylate) (124). **106a** (400mg, 0.83mmol) was dissolved in EtOH (0.02 M) and subjected to H-Cube hydrogenation using a 20% Pd/C cartridge at 40 bar, 60 °C, and a flow rate of 0.5 mL/min. The resulting mixture was purified by automated flash chromatography (Biotage) using a cyclohexane/AcOEt gradient (0–100%), affording the product as a colourless oil, as a mixture of diastereoisomers (262mg, 56%). **UPLC-MS** tR.: 1.97 (apolar method) **MS (ESI)** m/z calc [M+H]+: 586.30, found 486.4.

Di-tert-butyl 3,3'-(3-iodopyrazolo[1,5-a]pyrimidine-5,7-diyl)bis(piperidine-1-carboxylate) (125). In a round-bottom flask, **124** (262 mg, 0.46 mmol) was dissolved in DCM (20 mL/mmol), and the reaction mixture was cooled to 0 °C. NIS (104 mg, 0.46 mmol, 1 eq.) was added, and the mixture was stirred for 16 h while being monitored by UPLC. After complete disappearance of the starting material, the reaction mixture was diluted with DCM, transferred to a separatory funnel, and washed with saturated Na_2CO_3 solution. The title compound was obtained as a yellow powder, as a mixture of diastereoisomers (267mg, 94%). **UPLC-MS** tR.: 2.52 (apolar method), **MS (ESI)** m/z calc [M+H]+: 612.2, found 612.3.

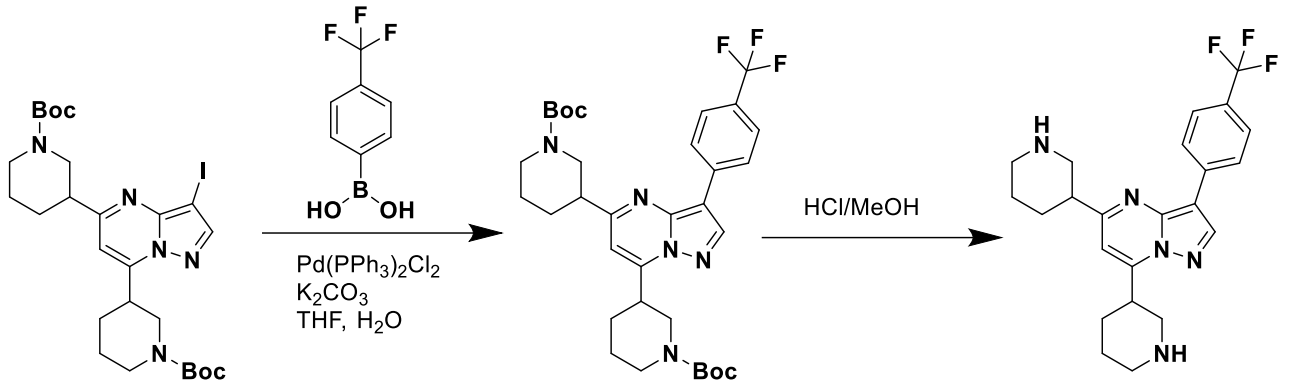

125 126a 71

Di-tert-butyl 3,3'-(3-(4-(trifluoromethyl)phenyl)pyrazolo[1,5-a]pyrimidine-5,7-diyl)bis(piperidine-1-carboxylate) (126a). Starting from **125** (61mg, 0.1mmol)**,** following **GP2** and using (4-(trifluoromethyl)phenyl)boronic acid as the coupling partner, the title compound was synthesized as a yellow oil, as a mixture of diastereoisomers (64mg, quantitative). **UPLC-MS** tR.: 1.90 (superapolar method), **MS (ESI)** m/z calc [M+H]+: 630.32, found 630.4.. *Note: the UPLC peak appears broad, consistent with the presence of a diastereomeric mixture of co-eluting compounds.*

5,7-Di(piperidin-3-yl)-3-(4-(trifluoromethyl)phenyl)pyrazolo[1,5-a]pyrimidine (71). Starting from **126a** (0.1mmol), following **GP3**, after 4h reaction time and automated flash chromatography (Biotage), using neutral alumina and as eluent phase DCM/MeOH gradient 0 to 20%, the title compound was obtained as a white powder in its hydrochloride salt form, as a 1:1 mixture of diastereoisomers (22mg, 51%). **HPLC-MS** tR.: 2.80, 2.92 (generic method), **MS (ESI)** m/z calc [M+H]+: 430.22, found 430.37 for both peaks). **^{1}H NMR (400 MHz, MeOD)** δ 9.87 (d, *J* = 11.1 Hz, 1H), 9.51 (dt, *J* = 23.7, 10.7 Hz, 3H), 8.91 (s, 1H), 8.38 (d, *J* = 8.2 Hz, 2H), 7.78 (d, *J* = 8.3 Hz, 2H), 7.26 (d, *J* = 1.6 Hz, 1H), 4.15 – 4.03 (m, 1H), 3.65 – 3.55 (m, 2H), 3.34 (q, *J* = 11.6 Hz, 5H), 3.01 – 2.88 (m, 2H), 2.20 (dd, *J* = 11.1, 6.5 Hz, 2H), 1.95 (qq, *J* = 8.1, 3.9 Hz, 4H), 1.85 (s, 1H), 1.77 (s, 1H). **^{13}C NMR (101 MHz, DMSO)** δ 163.03, 163.01, 149.74, 144.76, 143.35, 136.73, 126.36, 126.28 (d, *J* = 5.1 Hz), 126.00 (q, *J* = 3.8 Hz), 123.61 (q, J = 300.0 Hz) 108.05, 106.10, 46.03, 44.76, 43.62, 43.34, 40.88, 40.86, 34.10, 28.77, 28.70, 26.42, 22.13. *Note: some ^{1}H signals appear broad and not well resolved, consistent with the presence of two diastereoisomers.*

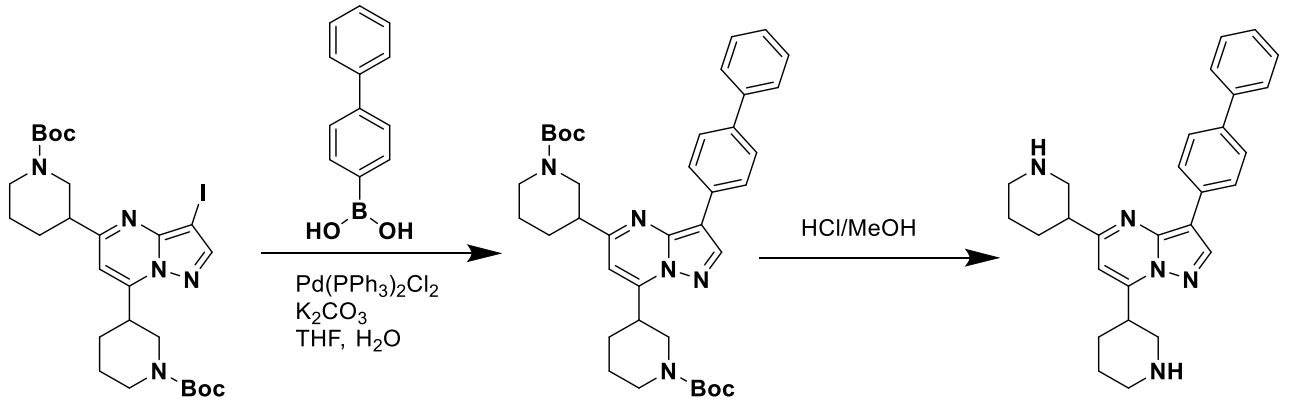

125 126b 72

Di-tert-butyl 3,3'-(3-([1,1'-biphenyl]-4-yl)pyrazolo[1,5-a]pyrimidine-5,7-diyl)bis(piperidine-1-carboxylate) (126b). Starting from **125** (61mg, 0.1mmol), following **GP2** and using [1,1'-biphenyl]-4-ylboronic acid as the coupling partner, the title compound was synthesized as a yellow oil, as a mixture

of diastereoisomers (55mg, 86%). **UPLC-MS** tR.: 2.14 (superapolar method) **MS (ESI)** m/z calc [M+H]+: 638.37, found 638.15.

3-([1,1'-Biphenyl]-4-yl)-5,7-di(piperidin-3-yl)pyrazolo[1,5-a]pyrimidine (72). Starting from **126b** (55mg, 0.09mmol), following **GP3**, after 3h reaction time and automated flash chromatography (Biotage), using neutral alumina and as eluent phase DCM/MeOH gradient 0 to 20%, the title compound was obtained as a white powder in its hydrochloride salt form, as a 1:1 mixture of diastereoisomers (30mg, 79%). **HPLC-MS** tR.: 3.16, 3.28 (generic method), **MS (ESI)** m/z calc [M+H]+: 438.26, found 438.43 (for both peaks). **^{1}H NMR (400 MHz, DMSO)** δ 9.66 (s, 1H), 9.32 (s, 3H), 8.78 (s, 1H), 8.19 (d, *J* = 8.7 Hz, 2H), 7.72 – 7.63 (m, 4H), 7.42 (dd, *J* = 8.4, 7.0 Hz, 2H), 7.35 – 7.26 (m, 1H), 7.12 (s, 1H), 4.00 (t, *J* = 12.0 Hz, 1H), 3.55 (t, *J* = 9.6 Hz, 2H), 3.33 (d, *J* = 8.0 Hz, 2H), 3.25 – 3.16 (m, 2H), 2.87 (s, 2H), 2.15 (d, *J* = 12.1 Hz, 2H), 1.96 – 1.64 (m, 7H). **^{13}C NMR (101 MHz, DMSO)** δ 162.21, 149.45, 144.32, 142.90, 140.32, 138.06, 131.64, 129.47, 127.79, 127.37, 126.87, 126.61, 109.19, 105.60, 46.11, 44.84, 43.70, 43.39, 40.94, 34.15, 28.81, 26.37, 22.20. N*ote: some ^{1}H signals appear broad and not well resolved, consistent with the presence of two diastereoisomers.*

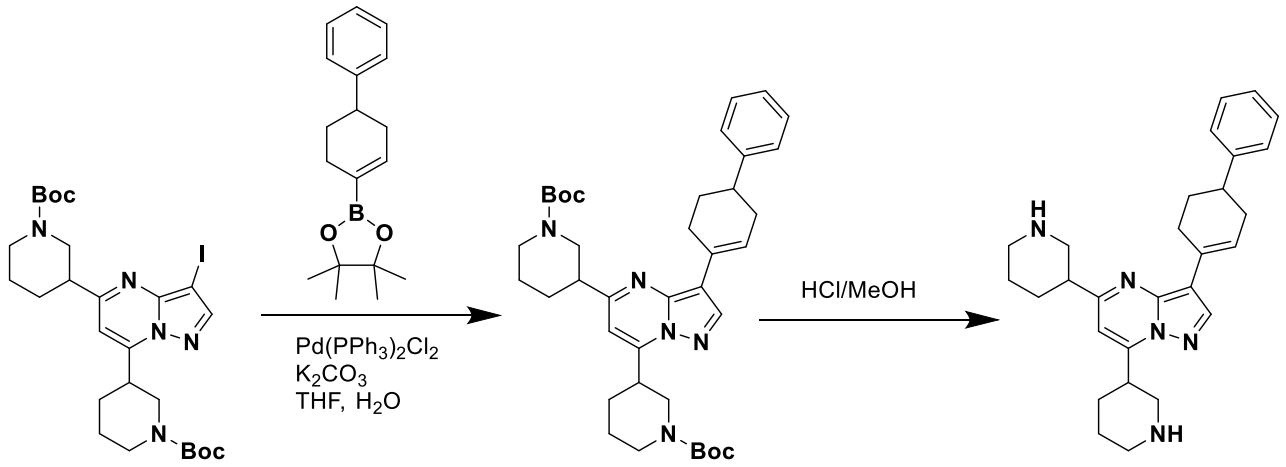

125 **126c** **73**

Di-tert-butyl 3,3'-(3-(1,2,3,6-tetrahydro-[1,1'-biphenyl]-4-yl)pyrazolo[1,5-a]pyrimidine-5,7-diyl)bis(piperidine-1-carboxylate) (126c). Starting from **125** (60mg, 0.1mmol)**,** following **GP2** and using 4,4,5,5-tetramethyl-2-(1,2,3,6-tetrahydro-[1,1'-biphenyl]-4-yl)-1,3,2-dioxaborolane as the coupling partner, the title compound was synthesized as a yellow oil, as a mixture of diastereoisomers (26mg, 40%). **UPLC-MS** tR.: 2.44 (superapolar method) **MS (ESI)** m/z calc [M+H]+: 642.40, found 642.4.

5,7-Di(piperidin-3-yl)-3-(1,2,3,6-tetrahydro-[1,1'-biphenyl]-4-yl)pyrazolo[1,5-a]pyrimidine (73). Starting from **126c** (26mg, 0.04), following **GP3**, after 2h reaction time and automated flash chromatography (Biotage), using silica and as eluent phase DCM/MeOH*NH_3 1M gradient 0 to 20%, the title compound was obtained as a white powder in its hydrochloride salt form, as a 4:5 mixture of diastereoisomers (11mg, 57%). **HPLC-MS** tR.: 3.30 (generic method), **MS (ESI)** m/z calc [M+H]+: 442.29, found 442.21. **1H NMR (400 MHz, DMSO-d6)**: δ 9.38 (s, 1H), 8.32 (s, 1H), 7.32 (d, *J* = 4.3 Hz, 4H), 7.21 (dt, *J* = 8.6, 4.3 Hz, 1H), 7.11 (d, *J* = 3.0 Hz, 1H), 6.78 – 6.74 (m, 1H), 4.02 (tt, *J* = 12.0, 3.6 Hz, 1H), 3.59 (d, *J* = 12.2 Hz, 1H), 3.56 – 3.49 (m, 1H), 3.30 (t, *J* = 12.9 Hz, 3H), 3.24 (d, *J* = 11.7 Hz, 1H), 2.97 – 2.83 (m, 4H), 2.80 – 2.72 (m, 1H), 2.68 – 2.58 (m, 1H), 2.50 (d, *J* = 1.9 Hz, 2H), 2.49 – 2.43 (m, 1H), 2.35 (ddd, *J* = 17.5, 10.7, 3.1 Hz, 1H), 2.18 (t, *J* = 13.2 Hz, 2H), 2.05 – 1.98 (m, 1H), 1.97 – 1.89 (m, 5H), 1.89 – 1.86 (m, 1H), 1.81 (qd, *J* = 12.0, 4.7 Hz, 1H), 1.68 (ddp, *J* = 12.5, 8.8, 4.2 Hz, 1H). **^{13}C NMR (151 MHz, DMSO)** δ 161.65, 149.50, 147.72, 144.32, 142.60, 129.33, 128.79, 127.79, 126.98, 123.11, 111.89, 105.58, 46.56, 45.28, 44.17, 43.83, 41.32, 41.30, 34.58, 34.40, 30.60, 29.36, 29.33, 29.29, 29.27, 28.66, 26.86, 22.68. N*ote:*

some ^{1}H signals appear broad and not well resolved, consistent with the presence of two diastereoisomers.

3.9.15: Synthesis of compounds **74-75**

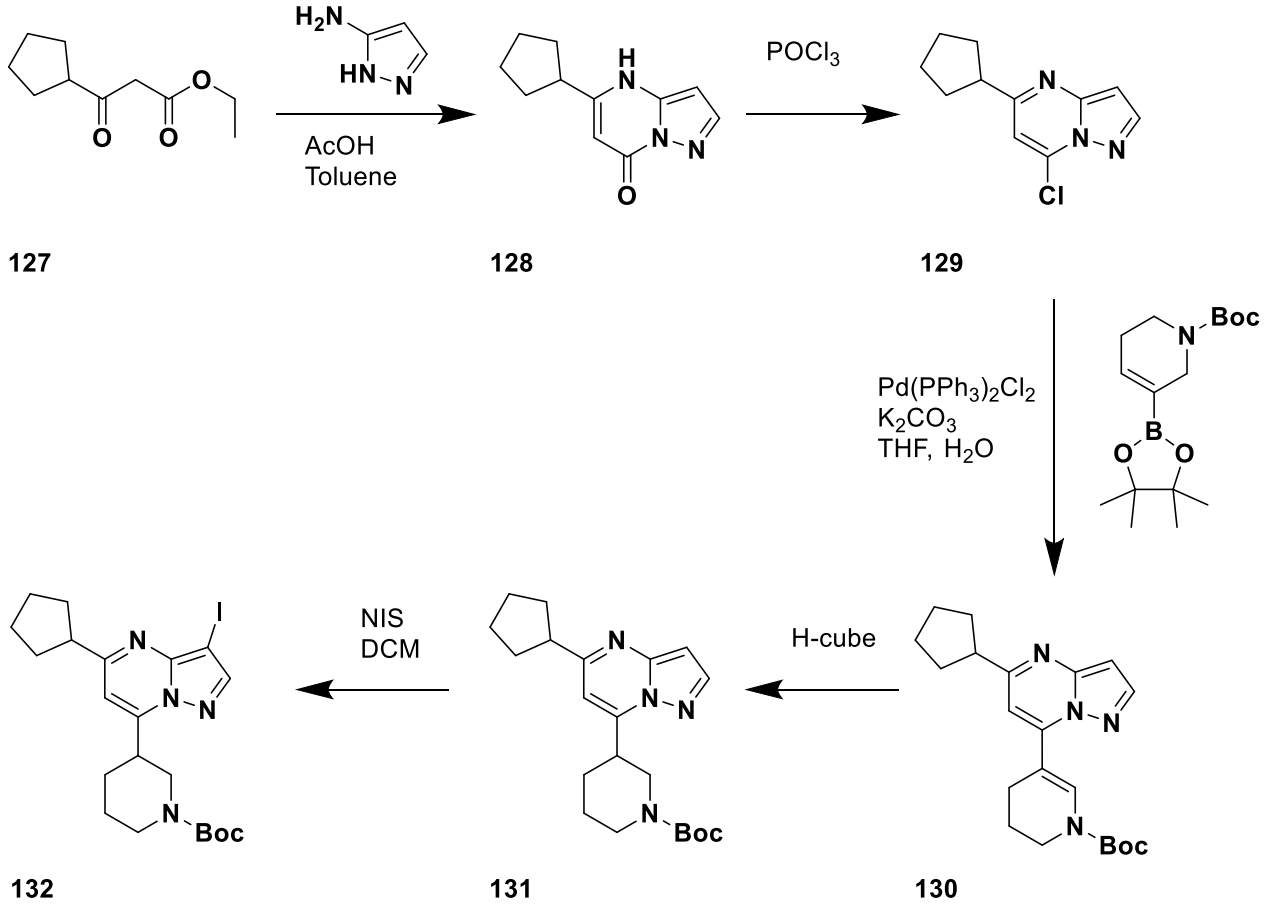

5-Cyclopentylpyrazolo[1,5-a]pyrimidin-7(4H)-one (128). Starting from **127** (184mg, 1mmol), following **GP6**, after 16h reaction time, the title compound was obtained as a white powder (175mg, 86%). **UPLC-MS** tR.: 1.28 (generic method), **MS (ESI)** m/z calc [M+H]+: 204.11, found 204.0.

7-Chloro-5-cyclopentylpyrazolo[1,5-a]pyrimidine (129). Starting from **128** (115mg, 0.56mmol), following **GP8**, after 16h reaction time, the title compound was obtained as a red oil (70mg, 36%). **UPLC-MS** tR.: 2.15 (generic method), **MS (ESI)** m/z calc [M+H]+: 222.08, found 222.0.

Tert-butyl 5-(5-cyclopentylpyrazolo[1,5-a]pyrimidin-7-yl)-3,4-dihydropyridine-1(2H)-carboxylate (130). Starting from **129** (70mg, 0.3mmol)**,** following **GP2** and using tert-butyl 5-(4,4,5,5-tetramethyl-1,3,2-dioxaborolan-2-yl)-3,6-dihydropyridine-1(2H)-carboxylate as the coupling partner, the title compound was synthesized as a yellow oil (114mg, quantitative). **UPLC-MS** tR.: 1.87 (apolar method) **MS (ESI)** m/z calc [M+H]+: 369.22, found 369.4.

Rac-tert-butyl 3-(5-cyclopentylpyrazolo[1,5-a]pyrimidin-7-yl)piperidine-1-carboxylate (131). (114mg, 0.3mmol) was dissolved in EtOH (0.02 M) and subjected to H-Cube hydrogenation using a 10% Pd/C cartridge at 40 bar, 60 °C, and a flow rate of 0.5 mL/min. The resulting mixture was purified by automated flash chromatography (Biotage) using a cyclohexane/AcOEt gradient (0–100%), affording the product as a colourless oil (104mg, 90%). **UPLC-MS** tR.: 1.81 (apolar method), **MS (ESI)** m/z calc [M+H]+: 371.24, found 370.9.

Rac-tert-butyl 3-(3-bromo-5-cyclopentylpyrazolo[1,5-a]pyrimidin-7-yl)piperidine-1-carboxylate (132). In a round-bottom flask, **131** (104 mg, 0.28 mmol) was dissolved in DCM (20 mL/mmol), and the reaction mixture was cooled to 0 °C. NIS (63mg, 0.28 mmol, 1 eq.) was added, and the mixture was stirred for 16 h while being monitored by UPLC. After complete disappearance of the starting material, the reaction mixture was diluted with DCM, transferred to a separatory funnel, and washed with saturated Na_2CO_3 solution. The title compound was obtained as a yellow powder (120mg, 91%). **UPLC-MS** tR.: 2.48 (apolar method), **MS (ESI)** m/z calc [M+H]+: 497.14, found 497.1.

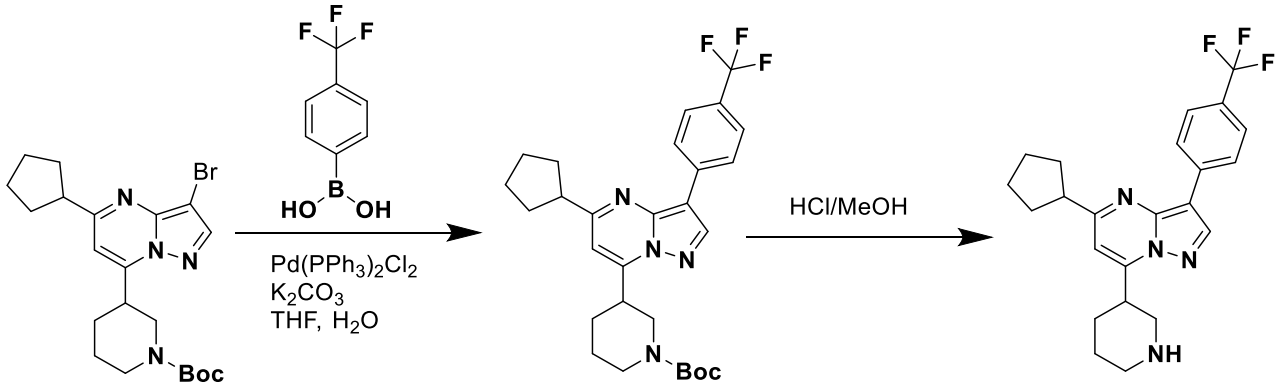

132 **133a** **74**

Rac-tert-butyl 3-(5-cyclopentyl-3-(4-(trifluoromethyl)phenyl)pyrazolo[1,5-a]pyrimidin-7-yl)piperidine-1-carboxylate (133a). Starting from **132** (40mg, 0.08mmol), following **GP2** and using (4-(trifluoromethyl)phenyl)boronic acid as the coupling partner, the title compound was synthesized as a yellow oil (24mg, 58%). **UPLC-MS** tR.: 2.10 (superapolar method), **MS (ESI)** m/z calc [M+H]+: 515.26, found 515.2.

Rac-5-cyclopentyl-7-(piperidin-3-yl)-3-(4-(trifluoromethyl)phenyl)pyrazolo[1,5-a]pyrimidine (74). Starting from **133a** (24mg, 0.046mmol), following **GP3**, after 5h30min reaction time and automated flash chromatography (Biotage), using silica and as eluent phase DCM/MeOH gradient 0 to 20%, the title compound was obtained as a white powder in its hydrochloride salt form (9mg, 49%). **UPLC-MS** tR.: 2.57 (generic method), **MS (ESI)** m/z calc [M+H]+: 415.21, found 415.1. **^{1}H NMR (400 MHz, DMSO)** δ 9.05 (bs, 2H), 8.81 (s, 1H), 8.34 (d, *J* = 8.2 Hz, 2H), 7.73 (d, *J* = 8.3 Hz, 2H), 7.01 (s, 1H), 3.99 – 3.88 (m, 1H), 3.58 (d, *J* = 12.1 Hz, 1H), 3.35 – 3.31 (m, 1H), 3.22 – 3.18 (m, 1H), 2.91 – 2.83 (m, 1H), 2.16 – 2.08 (m, 1H), 2.08 – 1.98 (m, 2H), 1.95 – 1.72 (m, 8H), 1.66 (dd, *J* = 7.4, 4.7 Hz, 2H). **^{13}C NMR (101 MHz, MeOD**) δ 167.31, 150.45, 145.13, 141.85, 136.67, 127.02, 126.70, 125.97, 125.49, 124.98, 124.94, 107.53, 105.01, 45.32, 37.13, 32.40, 27.51, 25.44, 25.11.

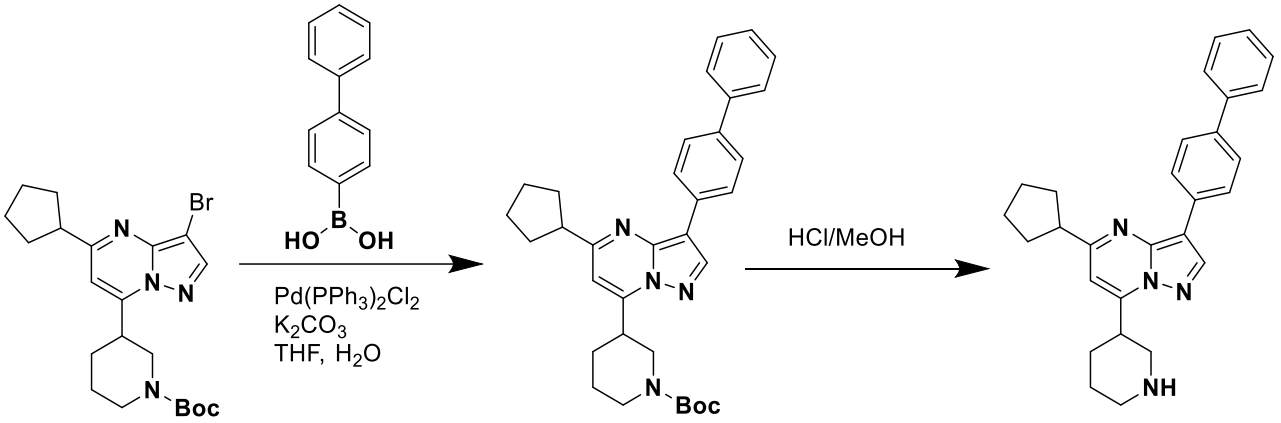

132 **133b** **75**

Rac-tert-butyl 3-(3-([1,1'-biphenyl]-4-yl)-5-cyclopentylpyrazolo[1,5-a]pyrimidin-7-yl)piperidine-1-carboxylate (133b). Starting from **132** (40mg, 0.08mmol), following **GP2** and using [1,1'-biphenyl]-4-ylboronic acid as the coupling partner, the title compound was synthesized as a yellow oil (23mg, 55%). **UPLC-MS** tR.: 2.32 (superapolar method), **MS (ESI)** m/z calc [M+H]+: 523.3, found 523.3.

Rac-3-([1,1'-biphenyl]-4-yl)-5-cyclopentyl-7-(piperidin-3-yl)pyrazolo[1,5-a]pyrimidine (75). Starting from **133b** (23mg, 0.04mmol), following **GP3**, after 5h30min reaction time and automated flash chromatography (Biotage), using silica and as eluent phase DCM/MeOH gradient 0 to 20%, the title compound was obtained as a white powder in its hydrochloride salt form (8mg, 42%). **UPLC-MS** tR.: 1.77 (apolar method), **MS (ESI)** m/z calc [M+H]+: 423.25, found 423.2. **^{1}H NMR (400 MHz, MeOD)** δ 8.52 (s, 1H), 8.22 (d, *J* = 8.1 Hz, 2H), 7.66 (d, *J* = 7.9 Hz, 4H), 7.44 (t, *J* = 7.6 Hz, 2H), 7.33 (t, *J* = 7.3 Hz, 1H), 6.81 (s, 1H), 3.84 (s, 1H), 3.67 (d, *J* = 12.2 Hz, 1H), 3.40 – 3.29 (m, 2H), 3.03 (t, *J* = 11.9 Hz, 1H), 2.90 (t, *J* = 11.5 Hz, 1H), 2.30 – 2.23 (m, 1H), 2.19 – 2.11 (m, 2H), 2.04 – 1.86 (m, 7H), 1.83 – 1.75 (m, 2H). **^{13}C NMR (101 MHz, MeOD**) δ 166.42, 148.79, 144.69, 141.51, 140.78, 138.27, 131.53, 128.47, 126.73, 126.58, 126.28, 125.95, 108.96, 104.84, 44.74, 36.04, 32.35, 26.62, 25.44, 23.83.

3.10: References

(1) Arias-Gómez, A.; Godoy, A.; Portilla, J. Functional Pyrazolo[1,5-a]Pyrimidines: Current Approaches in Synthetic Transformations and Uses As an Antitumor Scaffold. *Molecules* **2021**, *26* (9). https://doi.org/10.3390/molecules26092708.

(2) Yin, L.; Liebscher, J. Convenient Synthesis of Substituted 3-Alkenylpyrazolo[1,5-a]Pyrimidines via Heck Cross-Coupling Reaction. *Synthesis* **2004**, *2004* (14), 2329–2334. https://doi.org/10.1055/s-2004-831189.

(3) Tigreros, A.; Aranzazu, S.-L.; Bravo, N.-F.; Zapata-Rivera, J.; Portilla, J. Pyrazolo[1,5-a]Pyrimidines-Based Fluorophores: A Comprehensive Theoretical-Experimental Study. *RSC Adv.* **2020**, *10* (65), 39542–39552. https://doi.org/10.1039/D0RA07716J.

(4) Chimichi, S.; Cosimelli, B.; Bruni, F.; Selleri, S. 1H and 13C NMR Study of the Pyrazolo[1,5-a]Pyrimidine System. *Can. J. Chem.* **1992**, *70* (4), 1093–1097. https://doi.org/10.1139/v92-144.

(5) Martin, R.; Buchwald, S. L. Palladium-Catalyzed Suzuki−Miyaura Cross-Coupling Reactions Employing Dialkylbiaryl Phosphine Ligands. *Acc. Chem. Res.* **2008**, *41* (11), 1461–1473. https://doi.org/10.1021/ar800036s.

(6) Ahmed, A.; Mushtaq, I.; Chinnam, S. Suzuki–Miyaura Cross-Couplings for Alkyl Boron Reagent: Recent Developments—a Review. *Future J. Pharm. Sci.* **2023**, *9* (1), 67. https://doi.org/10.1186/s43094-023-00520-1.

(7) Verner, E. V.; Vashchenko, B. V.; Sosunovych, B.; Frolov, A. I.; Subotin, V. V.; Kozytskiy, A.; Grygorenko, O. O.; Ryabukhin, S. V.; Volochnyuk, D. M.; Kolotilov, S. V. Novel Approach to Saturated Amino Acid Derivatives with Isolated (Hetero)Cyclic Rings via the Hydrogenation of Dienes. *Chem. Heterocycl. Compd.* **2023**, *59* (6), 442–448. https://doi.org/10.1007/s10593-023-03214-x.

(8) Mandal, P. K.; McMurray, J. S. Pd−C-Induced Catalytic Transfer Hydrogenation with Triethylsilane. *J. Org. Chem.* **2007**, *72* (17), 6599–6601. https://doi.org/10.1021/jo0706123.

(9) *TERT-BUTYL 5-(4,4,5,5-TETRAMETHYL-1,3,2-DIOXABOROLAN-2-YL)-3,6-DIHYDROPYRIDINE-1(2H)-CARBOXYLATE CAS#: 885693-20-9*. https://m.chemicalbook.com/ProductChemicalPropertiesCB62454647_EN.htm (accessed 2026-03-02).

(10) Yamamoto, T.; Andou, A.; Hayakawa, N.; Noguchi, M.; Kuribayashi, K.; Eviryanti, A.; Yokoyama, R.; Fukuda, S.; Sugiura, T.; Kageyama, S.; Shima, Y.; Noguchi, M. Pyrazolo-Pyrimidine Compounds. US2011294781A1, December 1, 2011.

(11) Poznansky, B.; Thompson, L.; Reeve, H.; Vincent, K. Accelerating Biocatalytic Hydrogenations Using the H-Cube Flow Reactor. **2020**. https://doi.org/10.26434/chemrxiv.12532301.v1.

(12) Rinaldi, P. L. Heteronuclear 2D-NOE Spectroscopy. *J. Am. Chem. Soc.* **1983**, *105* (15), 5167–5168. https://doi.org/10.1021/ja00353a071.

(13) Sun, L.; Bera, H.; Chui, W. K. Synthesis of Pyrazolo[1,5-*a*][1,3,5]Triazine Derivatives as Inhibitors of Thymidine Phosphorylase. *Eur. J. Med. Chem.* **2013**, *65*, 1–11. https://doi.org/10.1016/j.ejmech.2013.03.063.

(14) Manetti, F.; Stecca, B.; Santini, R.; Maresca, L.; Giannini, G.; Taddei, M.; Petricci, E. Pharmacophore-Based Virtual Screening for Identification of Negative Modulators of GLI1 as Potential Anticancer Agents. *ACS Med. Chem. Lett.* **2020**, *11* (5), 832–838. https://doi.org/10.1021/acsmedchemlett.9b00639.

(15) Donzel, M.; Chorell, E. Access to Pyrazolo[1,5-a]Pyrimidinone Regioisomers from Acylated Meldrum's Acids. *Org. Lett.* **2026**, *28* (1), 157–162. https://doi.org/10.1021/acs.orglett.5c04435.

(16) Jismy, B.; Tikad, A.; Akssira, M.; Guillaumet, G.; Abarbri, M. Efficient Access to 3,5-Disubstituted 7-(Trifluoromethyl)Pyrazolo[1,5-a]Pyrimidines Involving SNAr and Suzuki Cross-Coupling Reactions. *Molecules* **2020**, *25* (9). https://doi.org/10.3390/molecules25092062.

(17) Abdel-Magid, A. F.; Carson, K. G.; Harris, B. D.; Maryanoff, C. A.; Shah, R. D. Reductive Amination of Aldehydes and Ketones with Sodium Triacetoxyborohydride. Studies on Direct and Indirect Reductive Amination Procedures1. *J. Org. Chem.* **1996**, *61* (11), 3849–3862. https://doi.org/10.1021/jo960057x.

CHAPTER 4

HIT EXPANSION PROCESS

Chapter 4: Hit expansion process

Hit compound **1** was re-synthesized and evaluated to confirm its binding affinity to pre-miR21 using the biochemical assay described in **Paragraph 2.2**. For this molecular entity (**Figure 4.1**), the k_d was estimated to be 8.61 ± 0.49 μM, and no IC_{50} was detected.
As outlined in **Figure 4.1**, starting from this structure, five positions were identified as potential sites for structural derivatization to explore the SAR. Accordingly, single-point modifications were introduced at each position (**Paragraph 4.1-4.6**) and, later on, the most promising ones were also preliminary combined into newly designed analogues (**Paragraph 4.7**).

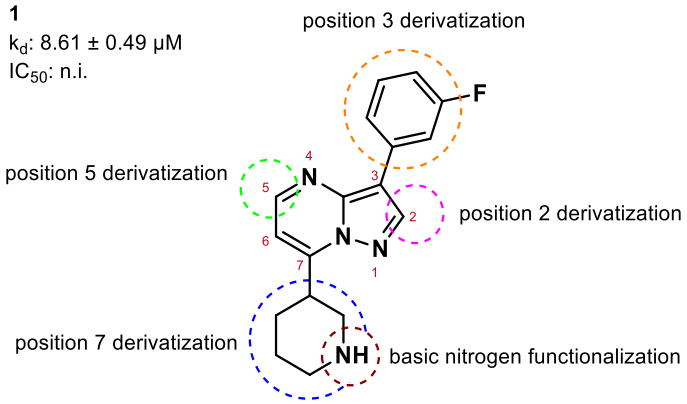

***Figure 4.1**. Hit compound **1** and identified vectors for the hit expansion.*

As described in **Chapter 2**, the fluorescence-based assay performed at University of Nice (Dr. Duca's lab) guided the development of this chemotype by evaluating both affinity and inhibition of the Dicer-mediated cleavage process. Briefly, for affinity determination, a 5'-fluorescently labeled pre-miR21 was titrated with increasing concentrations of each compound.[1] Changes in fluorescence intensity, resulting from conformational alterations upon binding, were monitored to assess affinity.
For IC_{50} determination, a pre-miR21 construct labeled with a fluorophore at the 5' end and a quencher at the 3' end was used. Upon Dicer-mediated cleavage, an increase in fluorescence is normally observed due to the separation of the fluorophore and the quencher, which abolishes quenching.[1] In contrast, when the Dicer-mediated cleavage is inhibited, fluorescence remains low or decreases relative to the control. Experimental details are provided in **Paragraph 4.9**.
As stated in **Chapter 2**, since this is an exploratory work, all compounds were evaluated as racemic or diastereoisomeric mixtures.

4.1: Structure-activity relationship (SAR) exploration: modification of position 3 of the pyrazolo[1,5-a]pyrimidine scaffold

Due to the ease of chemical derivatization, position 3 of the pyrazolo[1,5-a]pyrimidine core was selected for initial exploration of the chemical series (**Figure 4.1**). In a preliminary scaffold-expansion study, various substituents, with distinct structural and physicochemical properties, were introduced at this position to enhance ligand affinity toward the target and to establish a preliminary SAR.
To this end, the phenyl ring was functionalized with groups exhibiting different characteristics, i.e., featuring hydrogen-bond donors and acceptors (**2-8**), halogen-containing moieties (**9**), apolar aliphatic (**10-11**) and aromatic substituents (**12-13**). Along with it, to assess its contribution to target affinity, the phenyl ring itself was replaced with heteroaromatic (**14**) and aliphatic (**15-17**) groups.

The initial series of derivatives is reported in **Figure 4.2** and the biochemical data in **Table 4.1**.

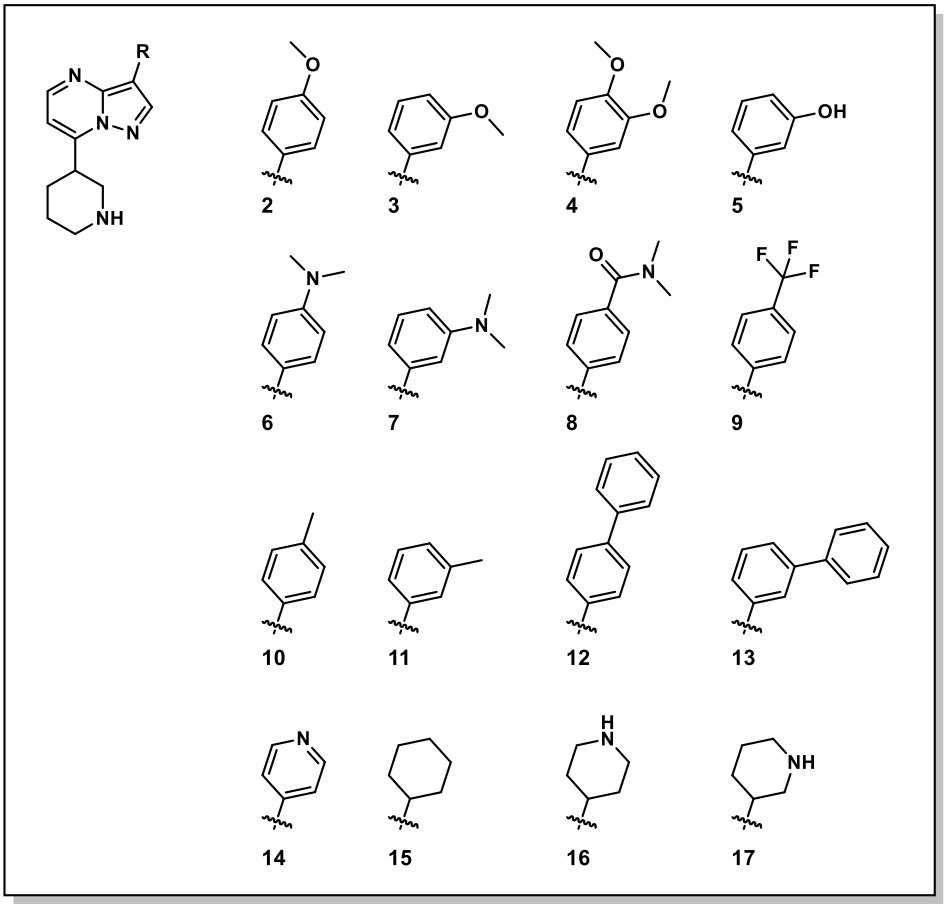

Figure 4.2. *Synthesized compounds for the SAR study of position 3 of the pyrazolo[1,5-a]pyrimidine core.*

Table 4.1*. Biochemical data of the initially synthesized compounds for the SAR study of position 3 of the pyrazolo[1,5-a]pyrimidine core.*

compound	K_d (μM)	IC_{50} (μM)
1 (hit compound)	8.61 ± 0.49	n.i.
2	13.3 ± 2.8	169
3	11.7 ± 1.15	n.i.
4	28.8 ± 5.2	44.7 ± 12
5	14.8 ± 3.8	73.03
6	7.55 ± 0.86	> 50
7	9.84 ± 1.3	> 50
8	n.b.	n.t.
9	0.41 ± 0.05	6.24 ± 1.36
10	7.53 ± 0.58	> 50
11	7.88 ± 0.13	n.i.
12	0.36 ± 0.01	6.30 ± 0.93
13	0.64 ± 0.03	9.43 ± 1.65
14	n.b.	n.t.
15	28.8 ± 2.3	n.t.
16	46.2 ± 10	n.t.
17	69.5 ± 28	n.t.

Compounds highlighted in yellow represent those exhibiting the most promising data, both in terms of k_d and IC_{50}. (n.t. = not tested, n.b.= no binding, n.i. = no inhibition).

As a result of the initial scaffold expansion study, a SAR could be derived, identifying this series as a potential chemotype for pre-miR21 binding. Analysing the same substituent shifted in different positions on the phenyl ring (e.g., meta or para), the same group seemed to work better when in para position (**2-3**, **4-5**, **6–7**, **10-11**,**12–13**), thus identifying this position as a preferred vector for scaffold functionalization (**Table 4.1**). Furthermore, since both the hydrogenated version (**15**) and the introduction of another aromatic group (**14**) resulted in no-binding activity, the phenyl ring was identified as a crucial element for scaffold interaction (**Table 4.1**).

In this initial phase, the increase in IC_{50} of the tested compounds seemed to be concomitant with the increase of the affinity toward the target, since the most potent compounds (**9**, **11-12**) also showed the best inhibitory activity. Compounds with modest affinities (**4-7**) showed, in fact, a less potent inhibitory activity (IC_{50} overall > 50μM).

This preliminary exploration highlighted two substituents of particular interest for their affinity and inhibitory activity: the trifluoromethyl group (**9**) and the biphenyl residue (para- (**12**) and meta- (**13**) substituted). These moieties were subsequently investigated in greater detail to improve the physicochemical properties of the resulting compounds and potentially enhance the biochemical activity.

Starting from compound **9**, three new analogues were synthesized to expand the trifluoromethyl series. This motif was either moved further away from the scaffold core (**18**) or shifted to the meta position to understand directionality (**20**) and possibly boost the binding affinity toward the target. Furthermore, to possibly exploit the effect of double CF_3 substitution in terms of affinity, the corresponding bis-trifluoromethyl-analogue **19** was also investigated. The structures of the obtained derivatives and their biochemical data are shown in **Figure 4.3** and **Table 4.2**, respectively.

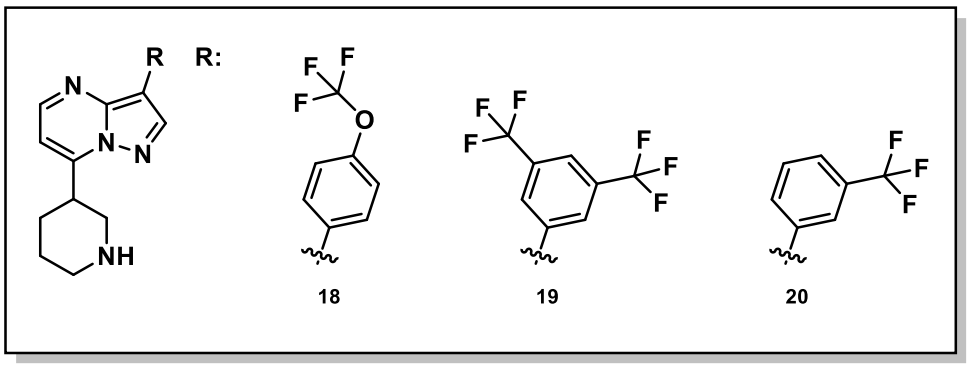

***Figure 4.3**. Analogues of compound **9** for the SAR investigation around the trifluoromethyl series.*

***Table 4.2**. Biochemical data of the trifluoromethyl analogues of compound **9**.*

compound	K_d (μM)	IC_{50} (μM)
1 (hit compound)	8.61 ± 0.49	n.i.
9	0.41 ± 0.05	6.24 ± 1.36
18	2.73 ± 0.27	n.t.
19	2.15 ± 0.29	n.t.
20	3.18 ± 0.56	n.t.

Compounds highlighted in yellow represent those exhibiting the most promising data, both in terms of k_d and IC_{50}. (n.t. = not tested, n.b.= no binding, n.i. = no inhibition).

As reported in **Table 4.2**, no improvement in affinity was noted for the analogues of compound **9**, both meta- (**20**) and di-substituted (**19**). This finding is consistent with the preference for the para rather than

the meta orientation in the substitution shown in the initial SAR exploration of position 3. Additionally, the shift of the trifluoromethyl moiety further from the scaffold's core of compound **18**, through an ether linker, also didn't yield any improvement in affinity, possibly identifying the need for either no linker or a non-polar linker between the trifluoromethyl and the phenyl ring.

The biphenyl-bearing compounds, **12** and **13**, despite showing good affinity, were associated with putative strong intercalating capabilities, due to their extended aromatic planar surface. Aiming to overcome this liability, new derivatives were synthesized to obtain compounds featuring other substitution patterns to replace the biphenyl motif. To this aim, the biphenyl ring was collapsed to a naphthyl group (**21**, **22**) and, to assess which one of the two aromatic rings of the biphenyl group was crucial for the interaction, either the second (**23**) or the first (**24**, **25**) aromatic ring was substituted with an aliphatic moiety. The derivatives of compound **12** are shown in **Figure 4.4** and their biochemical data in **Table 4.3**:

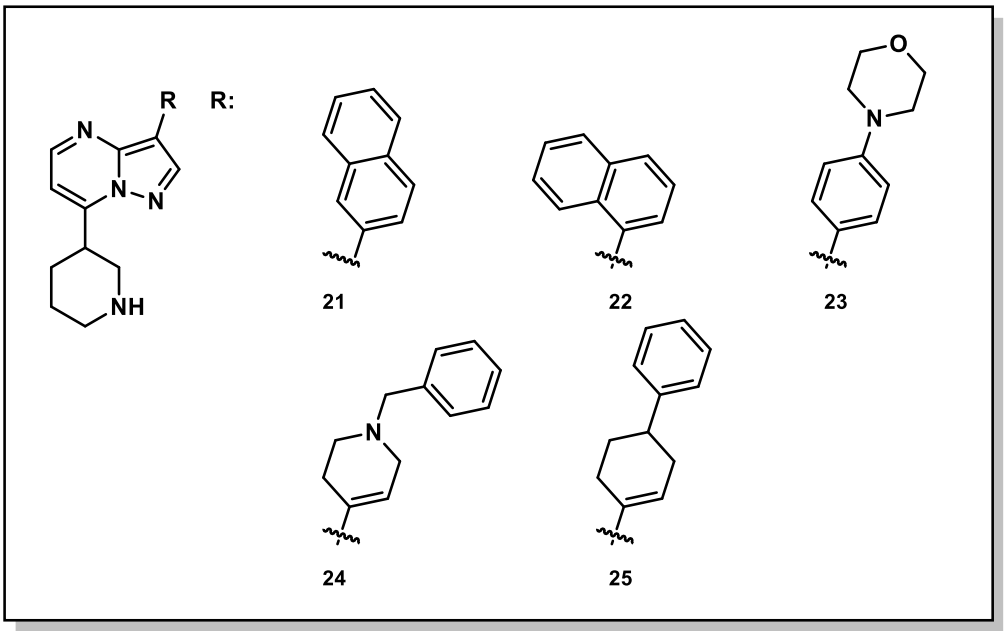

Figure 4.4. *Initial synthesized analogues of compound **12**.*

Table 4.3. *Biochemical data of the initial derivatives of compound **12**.*

compound	K_d (μM)	IC_{50} (μM)
1 (hit compound)	8.61 ± 0.49	n.i.
12	0.36 ± 0.01	6.30 ± 0.93
21	2.58 ± 0.68	15.23
22	6.37 ± 1.18	n.i.
23	28.7 ± 0.6	n.t.
24	9.92 ± 2.17	> 100
25	0.14 ± 0.02	34.0 ± 0.10

Compounds highlighted in yellow represent those exhibiting the most promising data, both in terms of k_d and IC_{50}. (n.t. = not tested, n.b.= no binding, n.i. = no inhibition).

As shown in **Table 4.3**, an increase in affinity was observed for compound **25**. Due to the presence of a more flexible cyclohexenyl ring, this newly synthesized analogue could exhibit more drug-like properties and potentially improved solubility. However, its inhibitory activity appeared to be reduced compared to that of the parent compound. The other compounds in the series showed neither an increase in affinity

nor inhibitory activity. This outcome could be ascribed to the removal (**23**) or the shift (**21**, **22**) of the phenyl ring further from the core, identifying in this motif an important element for this series' interaction with the target. Surprisingly, compound **24** also didn't show an increase in affinity, suggesting the presence of an apolar binding pocket in this region, a hypothesis that remains to be confirmed.
Having identified the distal aromatic ring as an important contributor to the scaffold-target interaction, a series of different linkers was explored to potentially enhance affinity. Aliphatic (**26**), amine (**27**), and differently flexible amide (**28-33**) linkers were investigated for this purpose. The amide series was particularly explored due to both the chemical accessibility of starting materials and to confirm the importance of a rigid linker in terms of inhibitory activity. The synthesized derivatives' structures are shown in **Figure 4.5**, and the corresponding biochemical data are reported in **Table 4.4**.

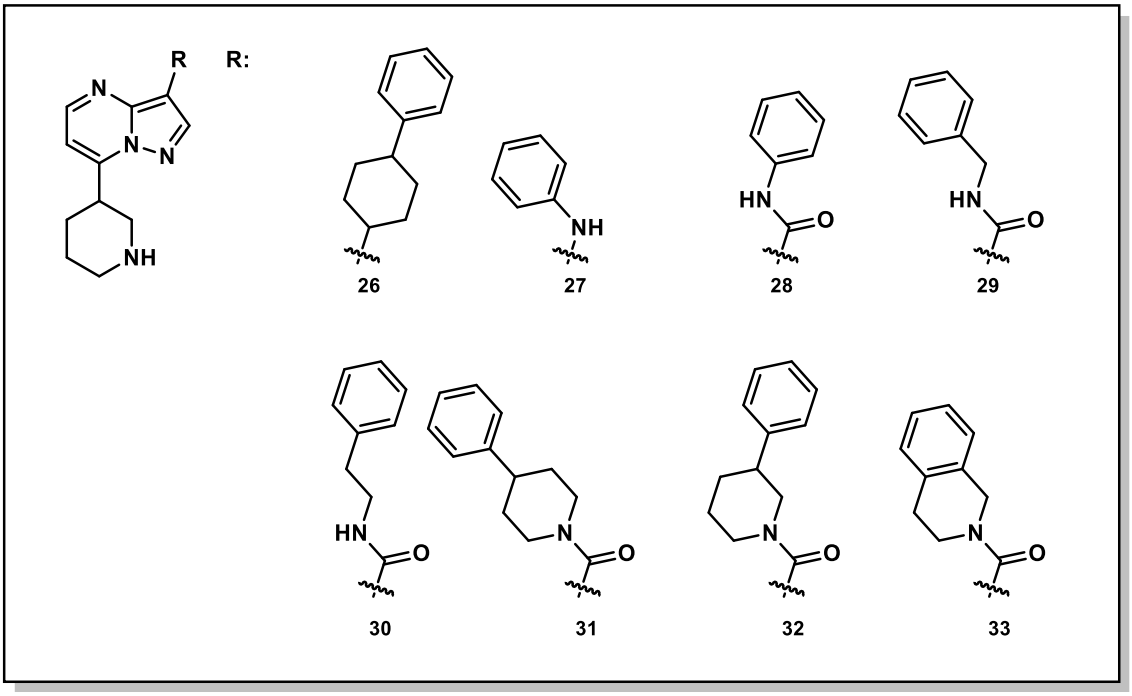

Figure 4.5. *Second-generation synthesized derivatives of compound **12**.*

Table 4.4. *Biochemical data of the second-generation derivatives of compound **12**.*

compound	K_d (μM)	IC_{50} (μM)
1 (hit compound)	8.61 ± 0.49	n.i.
12	0.36 ± 0.01	6.30 ± 0.93
25	0.14 ± 0.02	34.0 ± 0.10
26	0.57 ± 0.07	n.i.
27	28.1 ± 4.1	>100
28	8.47 ± 0.78	n.t.
29	n.b.	n.t.
30	8.26 ± 0.83	n.t.
31	7.34 ± 1.27	n.t.
32	16.59 ± 1.83	n.t.
33	18.14 ± 1.05	n.t.

Compounds highlighted in yellow represent those exhibiting the most promising data, both in terms of k_d and IC_{50}. (n.t. = not tested, n.b.= no binding, n.i. = no inhibition).

As shown in **Table 4.4**, only compound **26**, the reduced analogue of **25** (featuring a cyclohexenyl linker) exhibited a noteworthy biochemical affinity. The introduction of either polar or heteroatom-containing linkers, as in compounds **27–33**, resulted in a decrease in affinity. The SAR analysis suggests the presence of a hydrophobic pocket in this region, with an aromatic area located further on from the scaffold's core.

It is noteworthy that for all the biphenyl compounds tested for IC_{50} (**Tables 4.3-4.4**), no compound with significant activity emerged. By comparing **12** with its progressively hydrogenated derivatives (compounds **25** and **26**), a decrease in IC_{50} was observed as the rigidity of the scaffold was reduced, thus denoting a trend. The inhibitory phenomenon is, however, complex, and without further structural studies, only mere speculative considerations can be made. A more rigid group, however, seems to be more effective for this purpose.

Starting from screening hit **1**, the exploration of position 3 yielded four different compounds exhibiting improved affinity (**9**, **12**, **13**, **25**) and, for two of them (**9**, **25**), possible enhanced drug-like properties due to the removal of the planar and possible intercalating structures. All these compounds feature groups capable of engaging in aliphatic interactions or interactions with a π system (either via π–π stacking or C–F···π interactions), potentially suggesting that they interact with the nucleobases rather than the sugar moiety of the target. While the trifluoromethyl series has been extensively explored, further investigation of the 1,2,3,6-tetrahydro-[1,1'-biphenyl]-4-yl group could yield compounds with improved affinity, as functionalization of the phenyl ring in this series remains unexplored.

4.2: Structure-activity relationship (SAR) exploration: modification of position 2 of the pyrazolo[1,5-a]pyrimidine scaffold

To gain an initial insight into the SAR at position 2, the groups that demonstrated the most promising interactions at position 3 were also investigated at this position. The synthesized compounds and their corresponding biochemical data are presented in **Figure 4.6** and **Table 4.5**, respectively. As for **37**, the compound was already present in an IIT library and was not synthesized, but just directly tested.

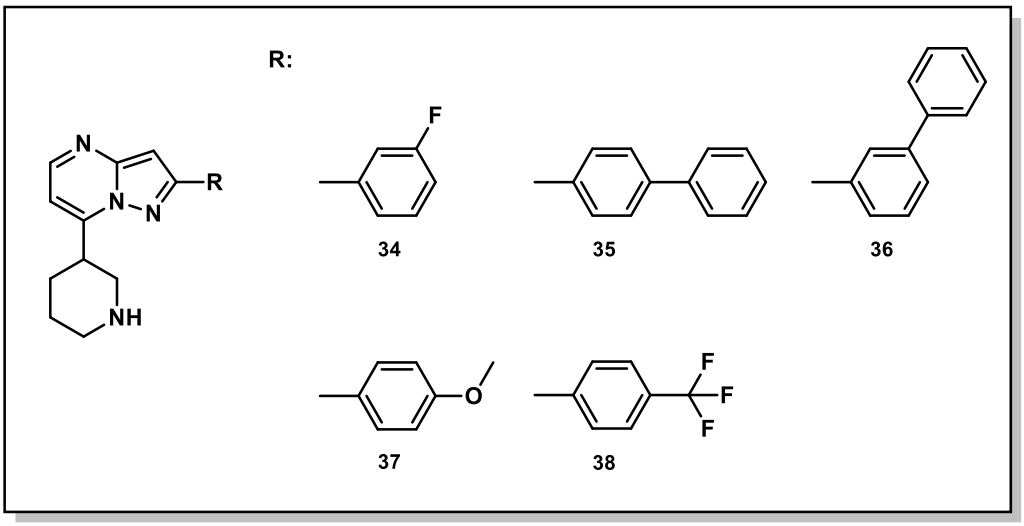

Figure 4.6. *Synthesized compounds for the SAR study of position 2 of the pyrazolo[1,5-a]pyrimidine core.*

***Table 4.5**. Biochemical data of the synthesized compounds for the study of the SAR of position 2 of the pyrazolo[1,5-a]pyrimidine core.*

compound	K_d (μM)	IC_{50} (μM)
1 (hit compound)	8.61 ± 0.49	n.i.
34	6.5 ± 0.6	n.i.
35	0.38 ± 0.07	25.9 ± 2.7
36	0.96 ± 0.02	36.7 ± 4.0
37	12.1 ± 1.2	6.59
38	11.9 ± 2.0	n.t.

Compounds highlighted in yellow represent those exhibiting the most promising data, both in terms of k_d and IC_{50}. (n.t. = not tested, n.b.= no binding, n.i. = no inhibition).

The 2-substituted analogue of the hit compound (**34**), featuring the 3-fluoro-phenyl ring in position 2 instead of position 3 of the pyrazolo[1,5-a]pyrimidine core, exhibited slightly improved affinity compared to the hit compound. Although this observation appears to identify position 2 as an interesting vector for scaffold evolution, substituents that showed good affinity in position 3, such as the 4-trifluoromethylphenyl group (compound **9**, K_d = 0.41 ± 0.05 μM), resulted in reduced affinity when shifted to position 2 (**38**). Concerning the biphenyl moiety, the affinities of compounds **35** and **36** were comparable to those of their analogues in position 3 (compounds **12** and **13**, respectively), although a decrease in IC_{50} values was observed (compound **12**, IC_{50} = 6.30 ± 0.93 μM; compound **13**, IC_{50} = 9.43 ± 1.65 μM). These findings may suggest that position 3 could represent a more favourable vector for scaffold growth. Furthermore, since derivatization at position 3 could be envisaged as more synthetically accessible, position 2 of the pyrazolo[1,5-a]pyrimidine core was not pursued for further scaffold expansion.

4.3: Structure-activity relationship (SAR) exploration: modification of position 5 of the pyrazolo[1,5-a]pyrimidine scaffold

In order to explore the chemical space of position 5 of the pyrazolo[1,5-a]pyrimidine scaffold, the hit compound was functionalized with groups having different stereo-electronic properties, in a similar fashion as for position 3 of the pyrazolo[1,5-a]pyrimidine core. The synthesized compounds are shown in **Figure 4.7**, and the biochemical data are presented in **Table 4.6**.

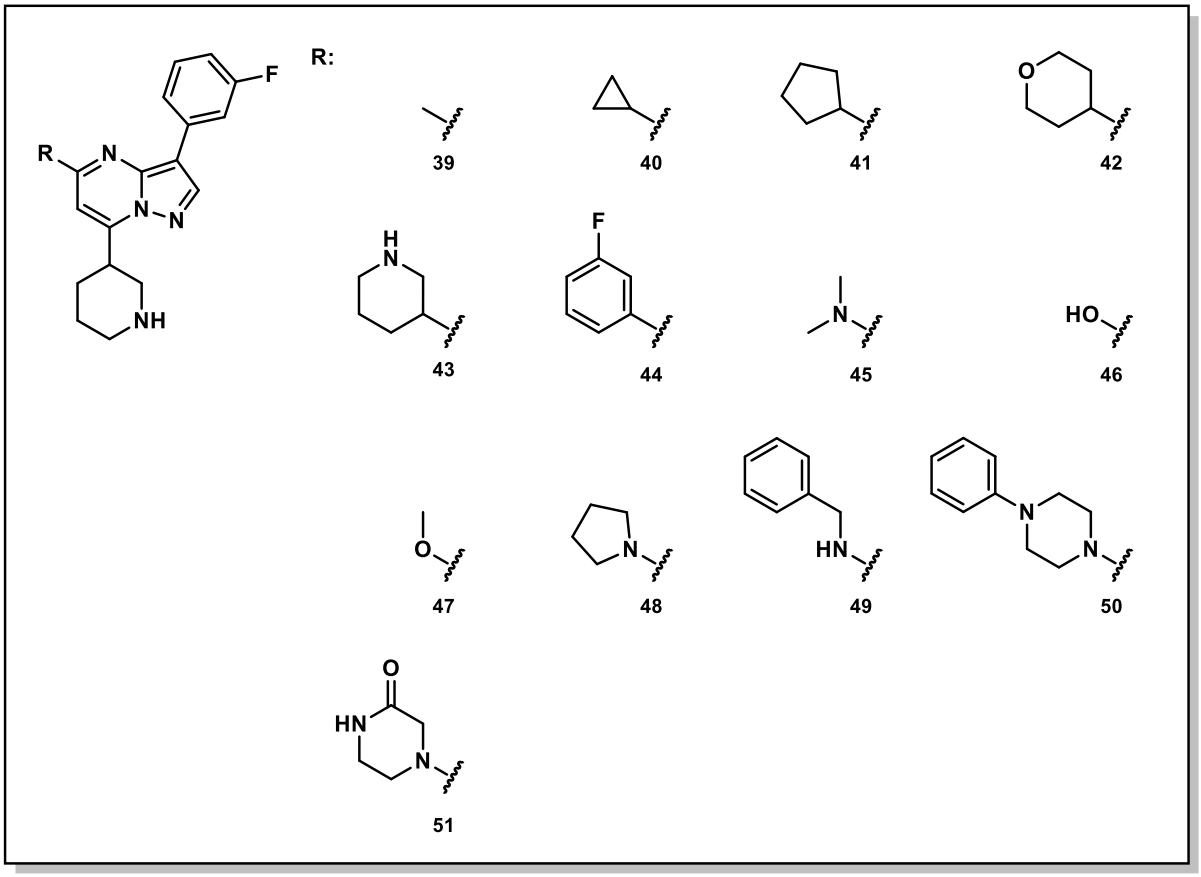

***Figure 4.7**. Synthesized compounds for the study of the SAR of position 5 of the pyrazolo[1,5-a]pyrimidine core.*

***Table 4.6**. Biochemical data of the synthesized compounds for the study of the SAR of position 5 of the pyrazolo[1,5-a]pyrimidine core.*

compound	K_d (μM)	IC_{50} (μM)
1 (hit compound)	8.61 ± 0.49	n.i.
39	5.2 ± 1.2	> 100
40	1.01 ± 0.12	29.94
41	0.59 ± 0.05	23.9 ± 0.66
42	2.67 ± 0.17	n.t.
43	1.63 ± 0.26	9.40 ± 1.54
44	0.67 ± 0.12	5.67 ± 2.26
45	4.96 ± 0.13	n.i.
46	n.b.	n.t.
47	0.42 ± 0.10	n.i.
48	0.60 ± 0.06	n.t.
49	0.42 ± 0.12	31.27 ± 4.09
50	0.56 ± 0.18	13.18
51	0.87 ± 0.08	n.i.

Compounds highlighted in yellow represent those exhibiting the most promising data, both in terms of k_d and IC_{50}. (n.t. = not tested, n.b.= no binding, n.i. = no inhibition).

As reported in **Table 4.6**, an increase in biochemical affinity was observed for most of the derivatives, except for compound **46**, which showed no measurable binding to the target. Both aliphatic (**41**, **47-48**) and aromatic (**44**, **49-50**) groups in this region appeared to enhance affinity, although such modifications may negatively impact the overall drug-likeness of the derivatives. This finding seemed to

highlight the presence of a hydrophobic pocket in this area, and no direct dependency on the nature of the atom linked to the scaffold's core. Such indication appeared to be confirmed when apolar groups were substituted on the scaffold (for example, compounds **41** and **48** showed a similar affinity). Consistent with the observed trend in affinity, increases in inhibitory activity (IC_{50}) were also recorded for the most active compounds of this series. Interestingly, compound **43** exhibited good inhibitory activity despite being a weaker binder than most other analogues in this series. This deviation from the general trend further highlighted the complexity of the relationship between affinity and inhibition.

4.4: Structure-activity relationship (SAR) exploration: basic nitrogen substitutions of the piperidine ring of the pyrazolo[1,5-a]pyrimidine scaffold

The role of the basic nitrogen of the piperidine ring of hit **1** was also investigated by thorough functionalization, thanks to its chemical accessibility. As in the initial exploration of the other positions, the basic nitrogen was decorated with groups bearing different structural and physicochemical properties to probe possible interactions. The synthesized analogues and their corresponding biochemical data are presented in **Figure 4.8** and **Table 4.7**.

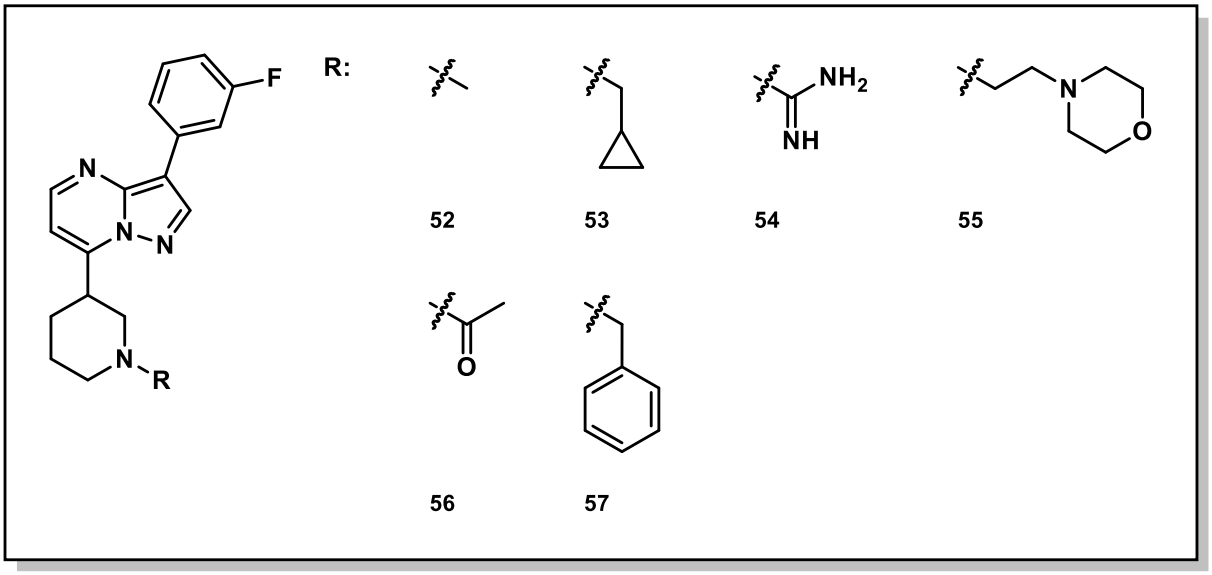

***Figure 4.8**. Synthesized compounds for the study of SAR of the piperidine nitrogen substitutions.*

***Table 4.7**. Biochemical data of the synthesized compounds for the SAR study of the piperidine nitrogen substitutions.*

compound	K_d (μM)	IC_{50} (μM)
1 (hit compound)	8.61 ± 0.49	n.i.
52	11.70 ± 0.35	n.i.
53	7.51 ± 1.90	n.i.
54	6.2 ± 2.2	n.i.
55	6.38 ± 0.40	n.i.
56	n.b.	n.i.
57	> 100	n.t.

(n.t. = not tested, n.b.= no binding, n.i. = no inhibition).

Upon derivatization of the nitrogen atom, no significant increase in affinity was observed, and the SAR appeared particularly flat at this position. Moreover, when the amine was converted into an amide (**56**), no binding was detected, possibly suggesting that the presence of a positively charged nitrogen is a crucial determinant for interaction with the target. Considering that nearly all modifications led to a worsening of the K_d, this indication may reasonably suggest the presence of a narrow binding pocket in this region, discouraging further exploration of this position.

4.5: Structure-activity relationship (SAR) exploration: modification of position 7 of a 5-substituted pyrazolo[1,5-a]pyrimidine scaffold

To validate the hypothesis that the nitrogen atom of the piperidine ring plays a crucial role in the interaction with the target, a series of additional analogues was synthesized. Three different structural changes were investigated: *I)* shift of the ring nitrogen position (**58-61**, **64**), *II)* ring opening (**62-63**), and *III)* substitution of the nitrogen with alternative hydrogen-bond donors or acceptors (**65-67**).
Since the direct modification in position 5 appeared to be synthetically demanding, a substituent was kept in position 5, achieving easy chemical derivatization useful for an initial SAR exploration of the position. For this purpose, the cyclopropyl substituent was retained at position 5, as its introduction only slightly affected the affinity for the target (compound **40** K_d = 1.01 ± 0.12 μM). The structures of the synthesized derivatives are shown in **Figure 4.9**, and their corresponding biochemical data are summarized in **Table 4.8**.

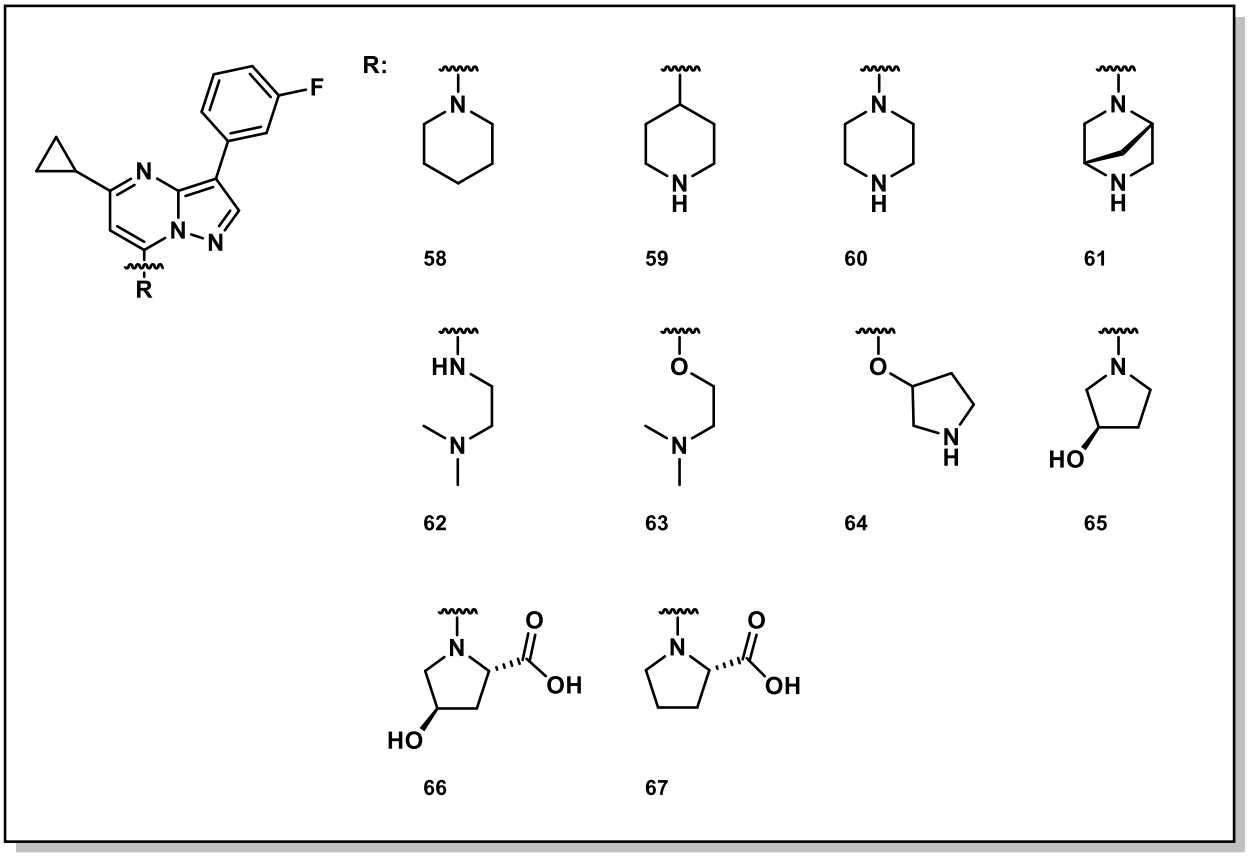

***Figure 4.9**. Synthesized compounds for the study of SAR of position 7 of the 5-cyclopropyl pyrazolo[1,5-a]pyrimidine core.*

***Table 4.8**. Biochemical data of the synthesized compounds for the study of the SAR of position 7 of the 5-cyclopropyl pyrazolo[1,5-a]pyrimidine core.*

compound	K_d (μM)	IC_{50} (μM)
1 (hit compound)	8.61 ± 0.49	n.i.
40	1.01 ± 0.12	29.94
58	n.b.	n.t.
59	1.29 ± 0.32	n.t.
60	1.83 ± 0.29	n.t.
61	1.19 ± 0.29	n.t.
62	6.4 ± 2.4	n.t.
63	6.11 ± 0.43	n.t.
64	1.97 ± 0.11	62.7 ± 4.1
65	n.b.	n.t.
66	n.b.	n.t.
67	n.b.	n.t.

(n.t. = not tested, n.b.= no binding, n.i. = no inhibition).

For all synthesized compounds, no increase in affinity was observed when compared to compound **40**. While no significant change in affinity was detected when the ring nitrogen was shifted from position 3 to position 4 of the piperidine ring (**59**), or when an additional nitrogen was introduced at position 1 (**60–61**), shifting the nitrogen from position 4 to position 1 of the ring resulted in a complete loss of binding (**58**). This finding seemed to highlight the need for a nitrogen atom located away from the scaffold core for an effective interaction with the target, while no significant effect was registered for the nature of the atom in position 1. Ring opening also led to a partial decrease in affinity (**62–63**), possibly indicating the requirement for a linker with a specific degree of rigidity and directionality, such as a ring connecting the nitrogen to the scaffold's core. Finally, replacement of the nitrogen with a hydroxyl group (**65–66**) also resulted in no detectable binding, suggesting that a positively charged residue at this position is essential. Based on these preliminary affinity data, which somehow align with the findings presented in **Paragraph 4.5**, this position was excluded from further investigations.

4.6: Structure-activity relationship (SAR) exploration: inverting substitution patterns in positions 5, 7 and 3 of the pyrazolo[1,5-a]pyrimidine scaffold

To further investigate the influence of substitution patterns on activity, the positions of the substituents on the pyrazolo[1,5-a]pyrimidine core of the hit compound **1**, i.e., the piperidine ring and the 3-fluorophenyl ring, were systematically varied. Two series were investigated: in the first one, the piperidine ring was retained at position 7 while the aromatic ring was shifted among the available positions. Additionally, the effect of the shift of the piperidine ring from position 7 to position 5 was also examined. While the first attempt led to the synthesis of compound **68**, thereby completing the series comprising the hit compound and compound **34**, the second approach led to the synthesis of compounds **69** and **70**. The structures of the compounds are shown in **Figure 4.10**, and the biochemical data are reported in **Table 4.9**.

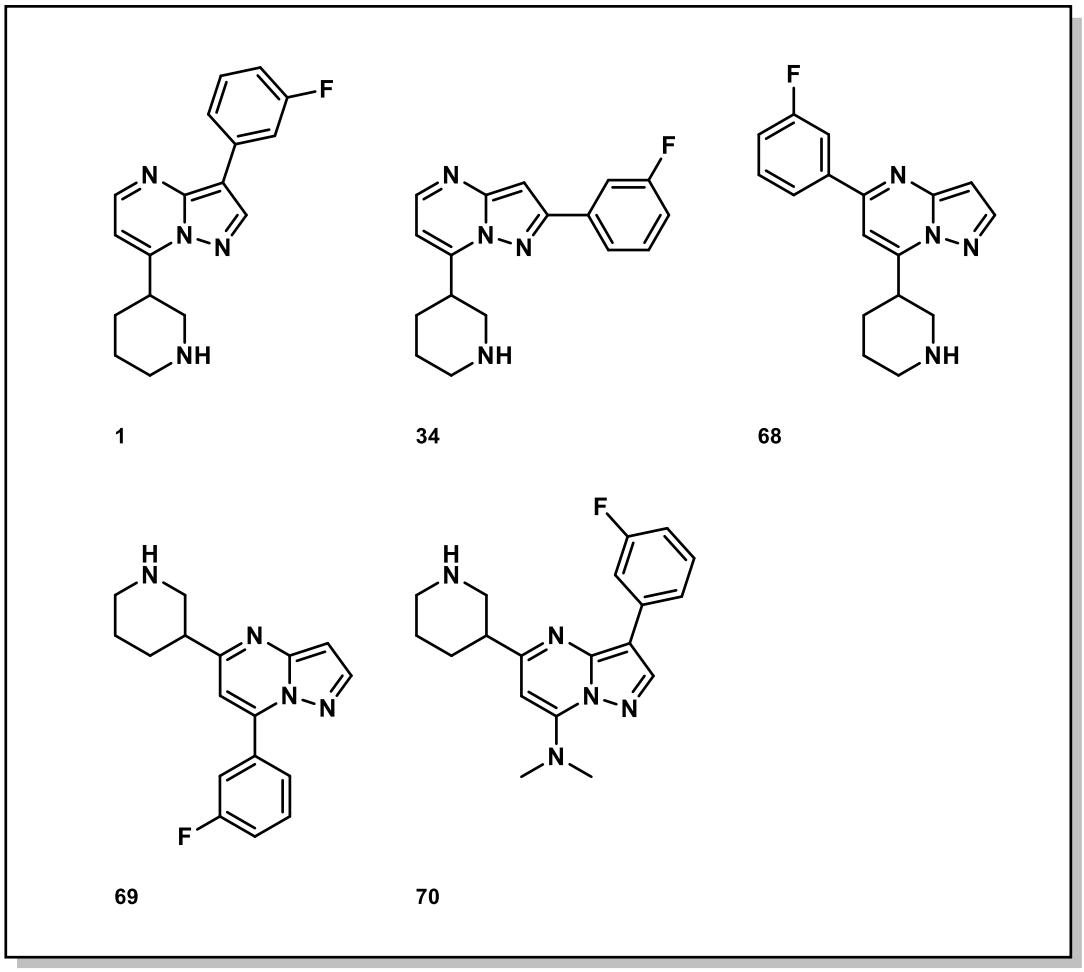

***Figure 4.10**. Synthesized compounds for the study of the inversion of the substituent of positions 3, 5 and 7 of the pyrazolo[1,5-a]pyrimidine core.*

***Table 4.9**. Biochemical data of the synthesized compounds for the study of the inversion of the substituent of positions 3, 5 and 7 of the pyrazolo[1,5-a]pyrimidine core.*

compound	K_d (μM)	IC_{50} (μM)
1 (hit compound)	8.61 ± 0.49	n.i.
34	6.50 ± 0.60	n.i.
68	n.b.	n.i.
69	26.2 ± 3.8	n.i.
70	0.65 ± 0.02	126.85 ± 23.95

Compounds highlighted in yellow represent those exhibiting the most promising data, both in terms of k_d and IC_{50}. (n.b.= no binding, n.i. = no inhibition).

As shown in **Table 4.9**, in the first series, the highest affinities were observed for compounds bearing a phenyl ring at positions 3 and 2 (**1**, **34**), whereas shifting this group to position 5 resulted in a compound with no detectable binding to the target (**68**). The observed decrease in affinity upon this substitution pattern's change suggested a certain degree of directionality in the interaction with the target, while no clear preference between positions 2 and 3 was identified. In the second series, an improvement in affinity was observed when the phenyl ring was retained at position 3 (**70**), identifying this combination (piperidine at position 5 and phenyl ring at position 3) as a favourable vector for scaffold derivatization.

Interestingly, it must be noted, however, that this introduction caused a drop in inhibitory activity, which could highlight the preference for keeping the piperidine in position 5 instead of 7.

4.7: Structure-activity relationship (SAR) exploration: combination of the most active identified substituents

Having identified positions 3 and 5 of the pyrazolo[1,5-a]pyrimidine core as suitable vectors for scaffold derivatization, the best substituents at each position were combined to assess the potential additivity of the structural changes on the pyrazolo[1,5-a]pyrimidine core.

At position 3, three motifs were identified as favourable for binding affinity: the 4-trifluoromethylphenyl group (**9**), the biphenyl group (**12**), and the more drug-like 1,2,3,6-tetrahydro-1,1'-biphenyl group (**25**). At position 5, the most notable increases in both affinity and IC_{50} were observed for the cyclopentyl (**41**), phenylmethylamine (**49**), and 4-phenylpiperazide (**50**) substituents. However, due to the pronounced hygroscopicity observed in the latter two compounds, these were initially excluded from further development. Since compound **70**, which features a piperidine ring in position 5, showed a good affinity toward the target, the 3-piperidine ring substituent was also selected for the combination process. The combination of these motifs led to the synthesis of the compounds **71-75**, shown in **Figure 4.11**. Their biochemical data are reported in **Table 4.10**.

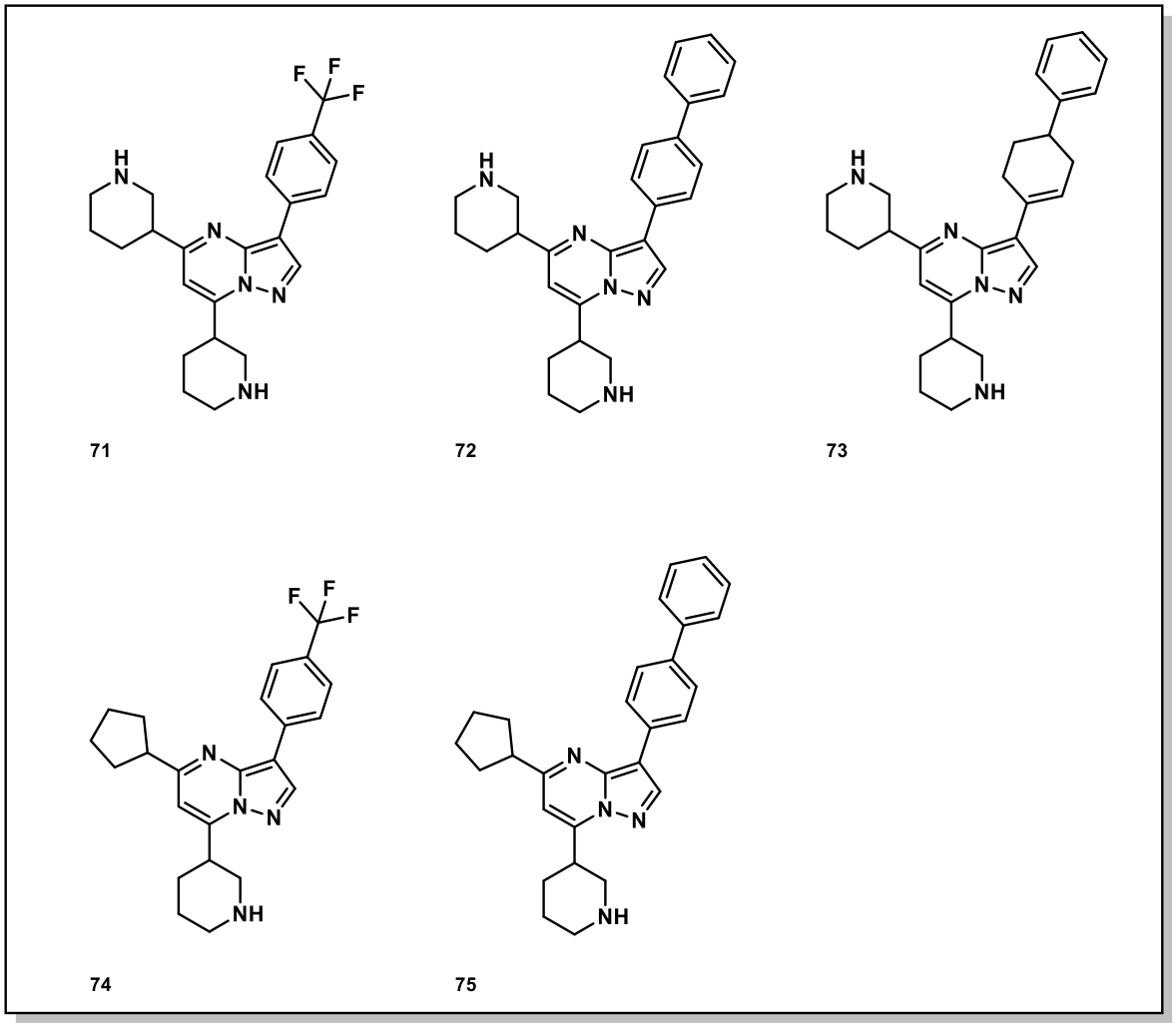

Figure 4.11. *Synthesized compounds combining the best substitutions in positions 3 and 5 of the pyrazolo[1,5-a]pyrimidine core.*

***Table 4.10**. Biochemical data of the synthesized compounds combining the best substitutions in positions 3 and 5 of the pyrazolo[1,5-a]pyrimidine core.*

compound	K_d (μM)	IC_{50} (μM)
1 (hit compound)	8.61 ± 0.49	n.i.
71	0.078 ± 0.050	31.64 ± 3.87
72	0.141 ± 0.014	11.41 ± 1.5
73	0.197 ± 0.003	14.86 ± 0.54
74	0.537 ± 0.017	73.43 ± 12.49
75	0.432 ± 0.161	n.t.

Compounds highlighted in yellow represent those exhibiting the most promising data, both in terms of k_d and IC_{50}. (n.t. = not tested, n.i. = no inhibition).

As shown in **Table 4.10**, all synthesized compounds exhibited promising affinity toward the target. While the combination of the piperidine ring with other substituents led to an increase in affinity (**71-73**), the incorporation of a cyclopentyl ring (**74-75**) did not result in a significant enhancement of binding affinity (**41**, K_d = 0.590 ± 0.05 μM). Although the additivity effect of the substitutions was not strictly preserved, the absence of any reduction in affinity in this initial set of compounds remained quite encouraging. To further investigate this rationale additional combinations of the best substituents at position 3 and 5 should be explored.

Compound **71** displayed favourable affinity, possible improved solubility, and overall drug-like properties. It complies with "*Lipinski's Rule of Five*" and lacks structural motifs associated with potential intercalation. Its analogues, compounds **72** and **73**, exhibited lower, yet still appreciable, affinity for the target, but also reduced drug-likeness; in particular, **72** may act as an intercalator due to the presence of the extended planar aromatic surface.

During the position 3 investigation, an increase in both affinity and inhibitory activity was observed. However, this trend did not continue in the current series, where the highest affinities were found but only modest inhibitory activities were observed. Despite this, compounds **71** and **74**, owing to their putative favourable drug-like properties and high affinities, represent promising candidates for in-cell testing.

4.8: Conclusions

Through the systematic derivatization of the different positions of the pyrazolo[1,5-a]pyrimidine scaffold, reasonable SAR indications were preliminary established. By designing and synthesizing a set of new analogues of hit **1** the affinity was improved from the low micromolar (**1**, k_d = 8.61 ± 0.49 μM) to the mid-low nanomolar (**71**, k_d = 0.078 ± 0.05 μM) range. The findings outlined in **Paragraphs 4.1-4.7** are summarized hereafter and analysed for each modified position. The best compounds for each position and the obtained SAR are reported in **Figure 4.12**.

Concerning position 3 modifications, a hydrophobic pocket with high directionality seems to be present. The presence of a phenyl group appears to be a crucial element for the interaction with the target, as its removal leads to an overall binding decrease. Shifting the phenyl moiety further away from the core scaffold is generally quite tolerated. When linked to the core scaffold, substitutions at the para position (position 4) of the phenyl ring prove more favourable for affinity compared to meta substitution, identifying a directionality preference for the binding affinity. Different physicochemical groups have also been explored at this position, with the best activities achieved for the 4-(trifluoromethyl)phenyl, the biphenyl, and the 1,2,3,6-tetrahydro-1,1'-biphenyl group motifs. Among the best motifs, the 4-(trifluoromethyl)phenyl, despite presenting lower affinity, emerges as the most promising candidate for

in-cell testing, due to its improved solubility and biological properties with respect to the other two strong binders.
As position 2 modifications are concerned, aromatic groups seem to improve the overall binding, reaching comparable affinities to position 3 when the same biphenyl rings have been studied. While this data could possibly represent the identification of a hydrophobic pocket in this area, lower affinities have been observed with respect to position 3, causing suspension of further investigation in this area.
Concerning position 5 derivatization, a general increase in affinity has been found for almost all studied groups. However, bulkier substituents result in improved affinities compared to less sterically demanding groups. In this position, aliphatic or aromatic groups seem to yield better activities than the others, identifying a possible hydrophobic binding pocket in this region.
Derivatization of the piperidine nitrogen has not led to any improvement in binding affinity and, in some cases, results in a complete loss of binding, particularly when the nitrogen is converted into an amide. These findings suggest that the presence of a basic nitrogen is crucial for interaction with the target. When the position of this nitrogen has been changed during the exploration of position 7 substitutions, no enhancement in affinity was observed. These findings seem to highlight the specificity of the nitrogen interaction with a defined linker, such as the piperidine one.
It should be noted that all compounds were tested as racemic mixtures. If the interaction with the target is stereochemistry-dependent, it is reasonable to expect an increase in binding affinity for one of the two stereoisomers.
While a SAR pattern could be outlined for the affinity of the tested compounds, the IC_{50} analysis does not highlight any trend useful for further investigations.

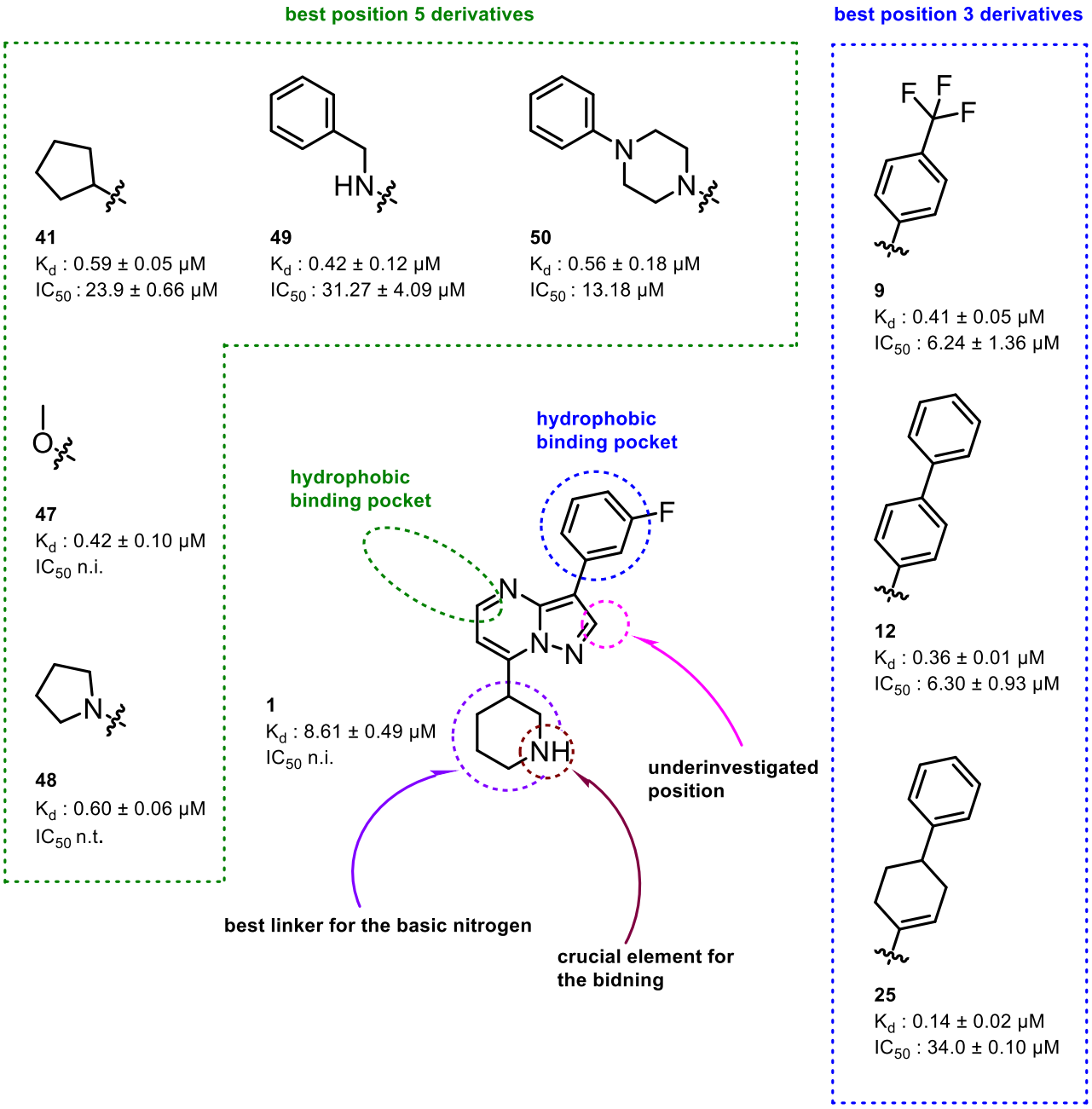

Figure 4.12*. SAR analysis: best substitutions identified for each investigated position of the pyrazolo[1,5-a]pyrimidine scaffold (n.t. = not tested, n.i. = no inhibition).*

4.9: Experimental Part and Methods

Fluorescence-based assay

For k_d and IC_{50} determinations, assays were performed in a buffer containing 20 mM Tris·HCl (pH 7.4), 12 mM NaCl, 2.5 mM $MgCl_2$, and 1 mM DTT. The buffer was filtered through 0.22 µm Millipore ExpressPLUS membrane filters prior to use. RNA refolding was carried out using a ThermoStat Plus thermocycler (Eppendorf). Samples were heated to 90 °C for 2 min, rapidly cooled to 4 °C for 10 min, and subsequently incubated at 25 °C for 20 min.

All assays were performed in 384-well black plates (Greiner Bio-One) using a 5070 EpMotion automated pipetting system (Eppendorf). Each experiment was conducted in duplicate and independently repeated three times. RNA was diluted to a working concentration of 50 nM for FRET-Dicer assays or 10 nM for binding assays using the appropriate buffer.

For binding experiments, 30 µL of 5'-FAM-pre-miR21 solution (10nM) was added to each well containing 30 µL of ligand solution (final volume 60 µL). Ligands were tested in 15 serial dilutions ranging from 61 nM to 1 mM. Plates were incubated overnight at 4 °C prior to fluorescence measurement.

For FRET-Dicer assays, 10 µL of 5'-FAM-pre-miR21-3'-DAB solution (50nM) was added to each well containing 5 µL of ligand solution at the desired concentration (488 nM to 1 mM). Reaction mixtures were pre-incubated at room temperature for 30 min. Subsequently, 0.25 U of Dicer and 0.25 µM TARBP2 protein (BioCat GmbH) in 5 µL were added to reach a final volume of 20 µL. Plates were incubated at 37 °C for 20 h.

Compound dilutions were performed from the same stock without DMSO normalization.

Fluorescence measurements were performed using a Genios Pro plate reader (Tecan) with excitation at 485 ± 10 nm and emission at 535 ± 15 nm. Each well was measured 10 times with a 500 µs integration time, and the values were averaged.

Binding data were fitted using a simple 1:1 binding model to determine dissociation constants.

4.10: References

(1) Shcheholeva, I.; Fernández-Remacha, D.; Estrada-Tejedor, R.; Duca, M.; Michelet, V. De-Novo Design of Pre-miR-21 Maturation Inhibitors: Synthesis and Activity Assessment. *Chem. – Eur. J.* **2023**, *29* (40), e202300825. https://doi.org/10.1002/chem.202300825.

CHAPTER 5
STRUCTURAL STUDIES

Chapter 5: Structural Studies.

Following the described pipeline (**Chapter 2-4**), starting from hit **1**, several fragments featuring a bicyclic pyrazolo[1,5-a]pyrimidine core scaffold were identified binding to pre-miR21. Based on these preliminary outcomes, an initial structure–activity relationship (SAR) was established (**Chapter 4**). However, the binding mode remained uncharacterized, and the possibility of having unspecific interactions could not be excluded. To further validate these initial hits and assess their potential for future development, a structural investigation of the ligand-target interaction was required. To achieve this, I spent 6 months at the biophysics department of AstraZeneca (AZ) in Gothenburg (Sweden).

5.1: Pre-miR21 available structural studies

As reported in **Chapter 1**, pre-miR21 comprises 72 nucleotides. From a structural perspective, this biomolecule represents a challenging target: it is too short and conformationally dynamic to be characterized by cryo-EM, yet too long for easy NMR analysis, since for such a structure spectral overlap and limited resolution are expected due to its length. Despite these intrinsic difficulties, several structural investigations of pre-miR21 have already been carried out, providing a foundation for subsequent studies. In particular, Varani's group deposited a structural model of pre-miR21[1] in the Protein Data Bank (PDB), which has since served as a common starting point for computational investigations of this target. A representation of this structural model of pre-miR21 is reported in **Figure 5.1**.

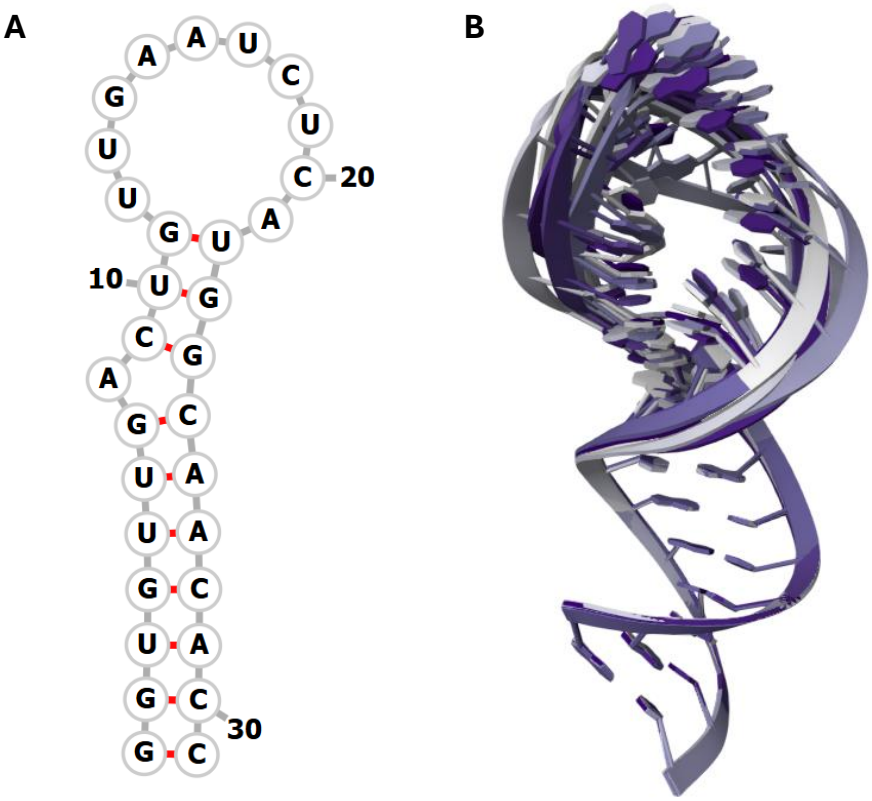

Figure 5.1. ***A****: Proposed structural models of pre-miR21 by Varani's group.*[1] ***B****: pre-miR21 proposed tertiary structure, as an ensemble composed of 10 different conformational superimposed models*.[1]

The reported model corresponds to a truncated 31-nucleotide construct (5'-GGUGUUGACUGUUGAAUCUCAUGGCAACACC-3') relative to the full-length pre-miR21, presenting a base substitution (A23 to G23) compared to the native sequence. Although this truncation enabled structure determination, it might also have introduced structural bias. Due to the high RNA dynamicity, the truncation of its structure could indeed alter the conformational landscape of the obtained construct with respect to the native one, potentially yielding a model not properly describing the target dynamics. This is indeed the case of pre-miR21.

Varani's group also reported a 60-nucleotide construct (sequence: 5'-GAGCUUAUCAGACUGGUGUUGACUGUUGAAUCUCAUGGCAACACCAGUCGAUGGGCUU-3') more closely resembling the full-length pre-miR21.[2] This construct shows different dynamics with respect to the shorter one, whose structure is deposited in the PDB. The difference casts doubts on the reliability of the results that can be obtained when using the PDB-deposited structure to model the full-length pre-miR21. However, as the 60 nucleotides construct was not fully solved, most likely due to resolution limitations, the shorter construct remains, to date, the most detailed three-dimensional structural model available for pre-miR21.

An alternative approach to investigating the structure of pre-miR21 is chemical probing: the RNA dynamicity can also be studied by interaction with selective chemical reagents, yielding information on the target secondary structure indirectly. In this context, Selective 2'-Hydroxyl Acylation analyzed by Primer Extension (SHAPE) analysis,[3,4] represents an efficient and cost-effective method. This methodology is grounded on the chemical reactivity of the 2'-hydroxyl group of the ribose, which is highly sensitive to the local nucleotide environment and backbone flexibility,[5] as illustrated in **Figure 5.2A**. To exploit this property, several electrophilic reagents have been developed, such as isatoic anhydride, *N*-methyl isatoic anhydride (*NMIA*), 1-methyl-7-nitroisatoic anhydride, and benzoyl chloride (**Figure 5.2C**) to allow selective reactions with the 2'-hydroxy functionality. These reagents are reported to react with RNA in a concentration-dependent manner or undergo hydrolysis in water (**Figure 5.2B**), thus rendering the analysis simpler.[4]

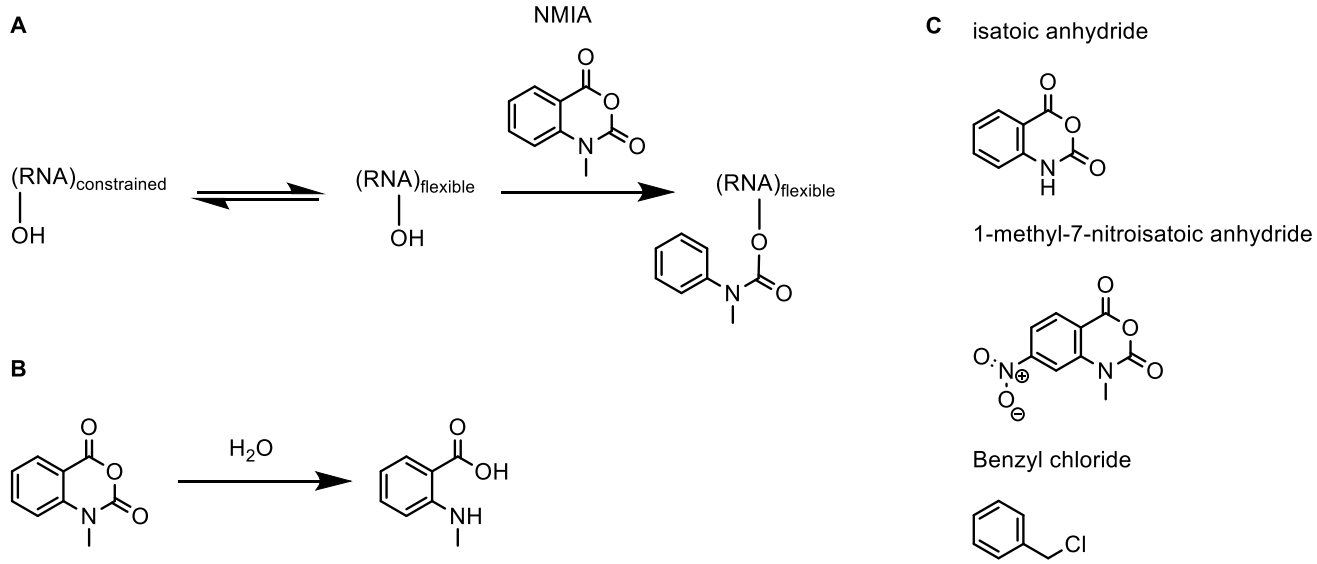

***Figure 5.2**. **A**: Simplified mechanism for the reaction of NMIA with a generic RNA strand. **B**: Chemical inactivation of NMIA with water. **C**: Example of reagents used in SHAPE.*

In a typical SHAPE experiment, following reaction with the electrophile, the RNA is subjected to reverse transcriptase-mediated primer extension (**Figure 5.3**). The reverse transcription process generally terminates one nucleotide prior to the modified position, generating complementary DNAs (cDNAs) of varying lengths. By analyzing the distribution and relative abundance of these cDNAs, commonly through gel electrophoresis, it is possible to infer RNA reactivity and, consequently, obtain information about the secondary structure.[4] Due to its relative simplicity and scalability, SHAPE methodology can be applied in a high-throughput manner, enabling the structural characterization of long and dynamic RNA molecules for which other high-resolution structural techniques are often unsuitable.[6]

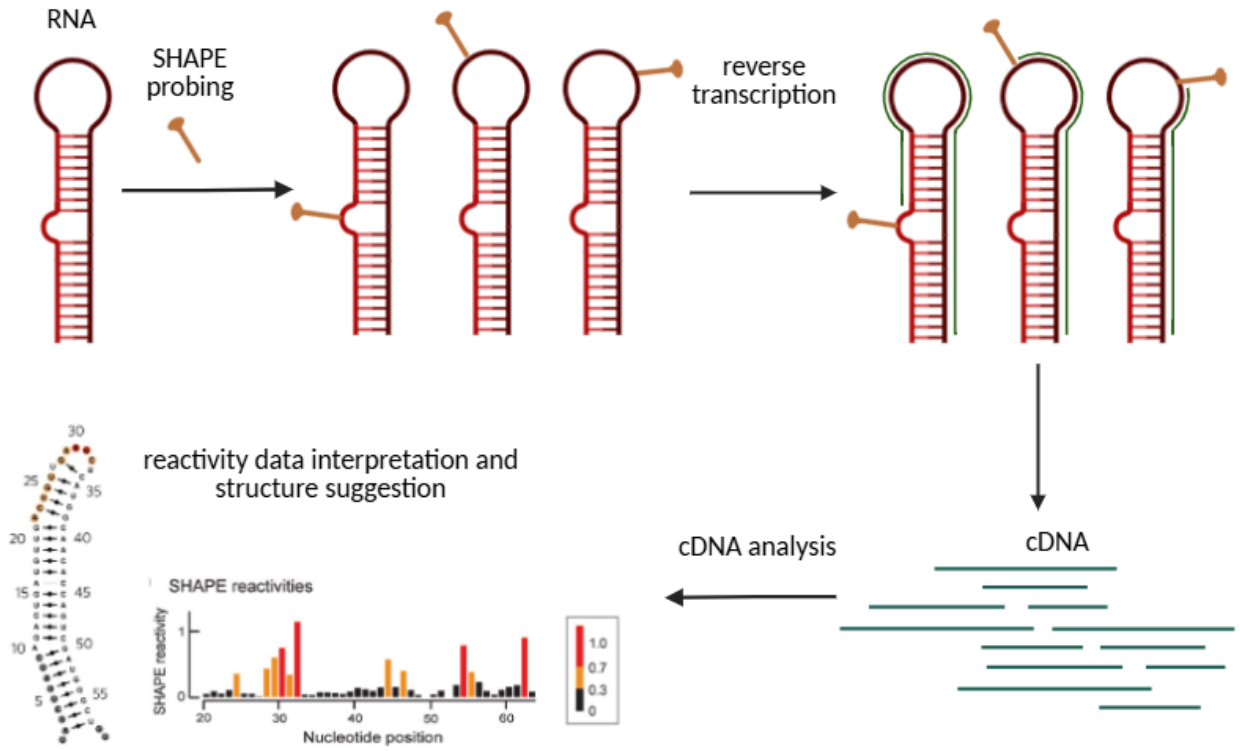

***Figure 5.3**. Schematization of the SHAPE approach workflow. Adapted from reference 4 and generated with biorender.com.*

Examples of SHAPE analysis applied to pre-miR21 were initially reported by Varani's group[7] (**Figure 5.4A**). In this study, taking into account the intrinsic limitations associated with reverse transcription-based readout, the apical loop appears more extended, with increased flexibility at its apex. It remains unclear whether bases 33 to 38 are actually paired or whether their lower reactivity results from bias introduced during the SHAPE process. According to the hypothesis of an extended apical loop and integrating the information obtained from the pre-miR21 SHAPE analysis[6] (**Figure 5.4B**), describing this area, a possible structural model is proposed, representing a possible interpretation of the reactivity profile (**Figure 5.4C)**. In particular, the 5' region appeared to be more reliably characterized than the 3' terminus. The assignment of nucleotides 33–38 as unpaired was partly arbitrary and made to maintain complementarity with the opposite strand of the RNA. Although SHAPE analysis is rapid and experimentally accessible, it primarily provides indirect information based on nucleotide reactivity and does not yield quantitative structural parameters.

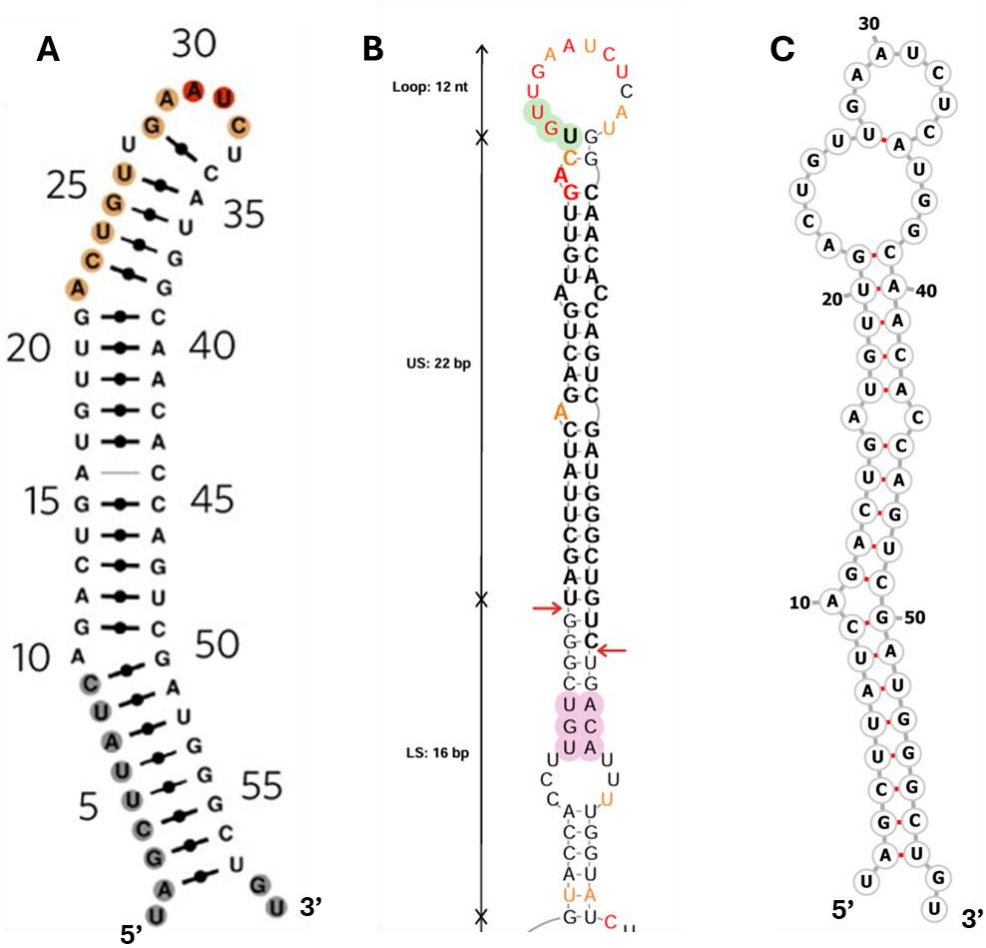

Figure 5.4. ***A****: SHAPE analysis of pre-miR21 as reported by Varani and co-workers (Adapted from Ref.*7*).* ***B****: SHAPE analysis of pri-miR21 proposed by Baek and colleagues (Adapted from Ref.*6*).* ***C****: Proposed secondary structure derived from the SHAPE data.*[7]

Based on the literature data already reported, the presence of a large apical loop emerges as a distinctive structural feature of pre-miR21, both in the NMR and in the SHAPE analysis. In the shorter PDB construct,[1] this region exhibits a certain degree of structural organization. It remains unclear whether such ordering is preserved in the context of the full-length sequence, particularly in light of the altered dynamics reported for longer constructs. SHAPE analyses appear to support the existence of an extended loop region, although the data are predominantly qualitative and do not provide definitive information regarding the conformational populations of the different structural states. Furthermore, the stem region has not been comprehensively characterized, and the possibility of uncharacterized binding sites also in this area cannot be excluded.

Taken all together, considering the current structural evidence available, proposing a specific binding site appears quite premature, as the existing data do not provide sufficiently detailed information to support assignments.

5.2. Application of fluorinated probes to pre-miR21: Aim of the structural studies

The structural characterization of pre-miR21 remains incomplete, with high-resolution information currently limited to truncated constructs and SHAPE data, which require interpretation and do not provide atomic-level resolution. To more accurately characterize the interaction between pre-miR21

and the novel chemotype identified during my PhD work, more robust and well-defined structural data were required.

The incorporation of ^{19}F-containing nucleosides as NMR-spectroscopy probes may offer a promising strategy to address this limitation. The use of fluorinated labels in RNA for structural investigation by NMR analysis has been previously reported.[8,9] However, these studies have generally focused on probing the local dynamics of individual nucleosides. Systematic incorporation of ^{19}F probes into a full-length RNA construct has not yet been extensively explored and could represent an innovative approach for describing RNA secondary structure and conformational dynamics. Moreover, ^{19}F labeling presents several advantages, including the absence of a natural background and high NMR sensitivity.[10]

To enable site-specific incorporation of ^{19}F-containing NMR probes within the RNA sequence, solid-phase synthesis[11] represents a suitable strategy for medium-length RNAs such as pre-miR21. According to this approach, protected nucleoside phosphoramidites (**Paragraph 5.3**) were sequentially coupled in an automated manner to assemble the desired RNA constructs. For this purpose, all commercially available and literature-reported[9] phosphoramidite-functionalized nucleosides were selected and systematically incorporated into a structural model of pre-miR21 (**Figure 5.5**).

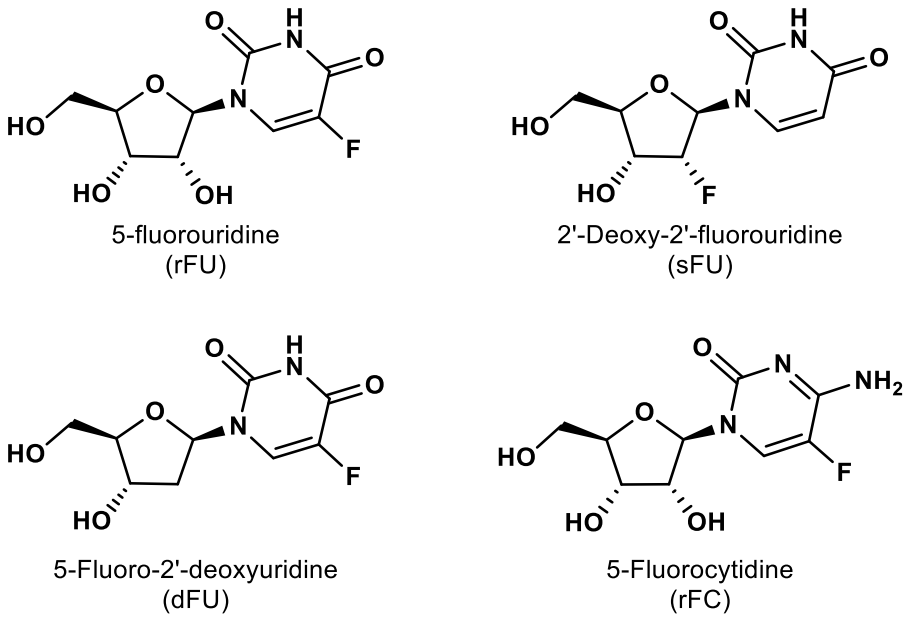

***Figure 5.5**. Fluorinated nucleosides incorporated into the pre-miR21 sequence.*

Although the complete pre-miR21 construct is made of 72 nucleotides, to facilitate the chemical synthesis, a 60-nucleotide truncated variant was envisaged. This way-out approach was based on the assumption that removal of five base pairs from the stem would not substantially affect the conformational behaviour of the terminal loop. The sequence investigated in this work, hereafter referred to as the wild type (w.t.), is:

5'-UAGCUUAUCAGACUGAUGUUGACUGUUGAAUCUCAUGGCAACACCAGUCGAUGGGCUGUC-3'

Although the previously reported structural studies may not fully capture the native conformation of pre-miR21, several putative binding regions have been suggested, with the apical loop identified as a likely site of interaction.[1,2,12] Based on these considerations, it was hypothesized that the developed compounds would interact with pre-miR21 in the same region. This hypothesis justified trimming 5 nucleotides from each terminus of the stem.

To probe distinct structural regions, 12 uridine residues distributed across the sequence were selected for substitution with modified fluorinated nucleoside analogues (i.e., rFU, sFU, or dFU, see **Figure 5.5** for acronym). The modified positions were *8, 14, 17, 19, 20, 24, 27, 31, 33, 36, 48,* and *52*, respectively. In addition, dFU substitutions were also introduced at positions *6* and *26*. Cytidine residues (rFC, see **Figure 5.5** for acronym) were examined at positions *23, 34, 39, 42, 45, 46,* and *49*, respectively.
In contrast to uridine, which was substituted at multiple positions to assess the robustness of the method, cytidine modifications were restricted to the positions necessary to complete the structure investigation. A schematic representation of the applied mutations/modifications is shown in **Figure 5.6**. Each RNA variant was identified using the format "*Xn*," where *X* indicates the type of modification (dFU, rFC, rFU, or sFU) and *n* denotes the nucleotide position (e.g., rFU14 stands for substitution of uridine at position 14 with rFU in the wild-type sequence).

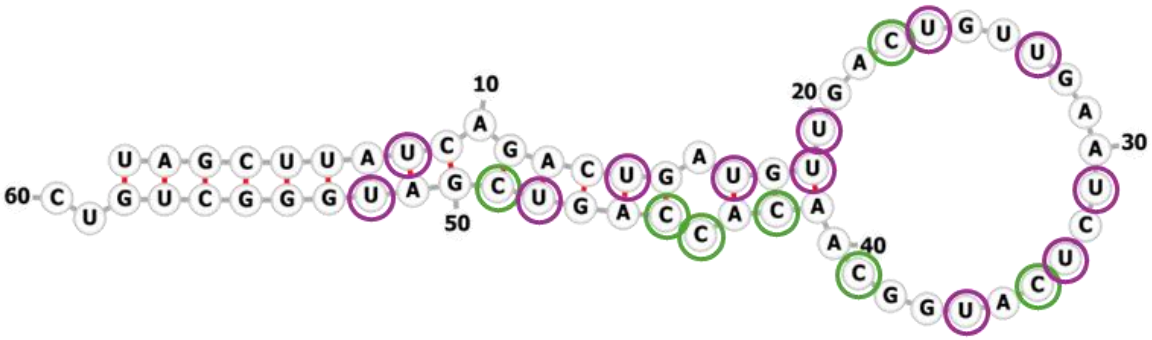

***Figure 5.6**. Secondary structure of pre-miR21 derived for [19]F-NMR-probe analysis. The substituted positions highlighted refer to nucleosides replaced with sFU, dFU, or rFU (in purple for the positions 8, 14, 17, 19, 20, 24, 27, 31, 33, 36, 48, and 52), and with rFC (in green for the positions 23, 34, 39, 42, 45, 46, and 49), respectively. Structure generated using viennafold.com.*

The experiments described in this Chapter, with the exception of the phosphoramidite synthesis, were carried out at AZ in Sweden.

5.3: Solid phase synthesis of fluorinated RNAs

To produce a wide range of fluorinated RNAs, solid-phase synthesis was chosen as the most practical and efficient approach. RNA solid-phase synthesis is a well-established technique for the preparation of RNA oligonucleotides.[13] Oligonucleotide synthesis is a multi-step process for each incorporated nucleoside in the RNA chain. Due to this complexity, the process is typically performed using automated synthesizers. While also in-cell or in-vitro production could achieve RNA synthesis, solid phase synthesis presents the advantage of being able to have precise control over the sequence, allowing for modification of the RNA in every part deemed interesting for the structural elucidation. Phosphoramidites protected nucleosides are the building blocks of solid-phase RNA synthesis,[13] presenting a reactive part (the phosphoramidite, in green in **Figure 5.7**) and a cleavable group (the dimethoxytritylphenyl group, in blue in **Figure 5.7**), unreactive in the coupling conditions. Moreover, the other nucleophilic groups of the nucleoside are protected to avoid undesired secondary reactivity. An example of the structures of the mainly used protected nucleosides is shown in **Figure 5.7**.

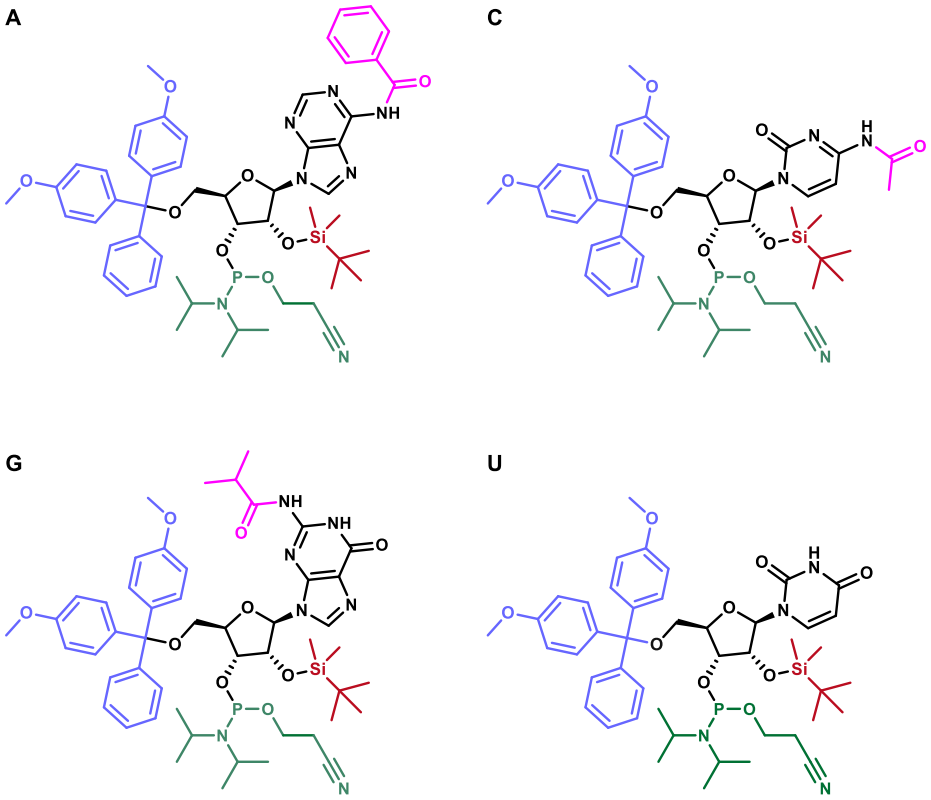

***Figure 5.7**. Protected nucleosides used for solid-phase RNA synthesis. The 5'-O-dimethoxytrityl (DMT) group is shown in blue, the phosphoramidite moiety in green, and the 2'-O-dimethylisopropylsilyl protecting group in red. The protecting groups employed for the nucleophilic functionalities of the individual nucleobases are highlighted in pink.*

5.3.1: rFU and rFC Phosphoramidites synthesis

For introducing the fluorinated probes into the pre-miR21 structure, the protected corresponding fluorinated phosphoramidites were needed. As stated in **Paragraph 5.2** four different nucleosides were selected for incorporation: rFU, rFC, sFU and dFU. While sFU and dFU phosphoramidites are commercially available, the corresponding rFU (**134**) and rFC (**135**) phosphoramidites are not and had to be in-house synthesized before oligonucleotide assembly (**Figure 5.8**). This activity was carried out at D3P-IIT prior to relocating the project to AZ.

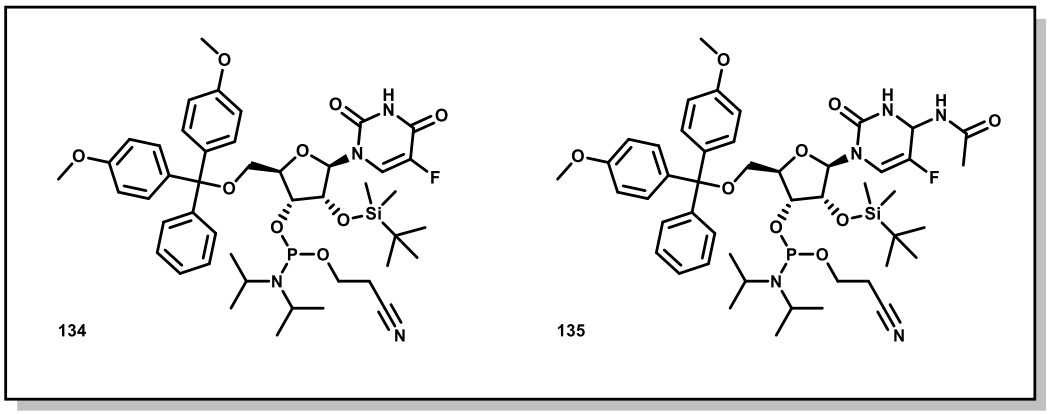

***Figure 5.8**. Structures of the synthesized rFU (**134**) and rFC (**135**) phosphoramidites.*

Starting from the unprotected, commercially available fluorinated nucleosides, the synthesis followed the methodology reported by Puffer and colleagues.[8] Since the synthesis of these two molecules has been previously reported, it is only briefly described here (**Scheme 5.1)**.

For solid-phase oligonucleotide synthesis, free hydroxyl and other nucleophilic functional groups must be appropriately protected. The proposed synthetic strategy exploits the differences in reactivity among the nucleophilic atoms, namely the oxygen atoms of the sugar moiety and the nitrogen atom of rFC, to regioselectively functionalize the nucleoside.

For the synthesis of rFU phosphoramidite **134**, the synthetic pathway is outlined in **Scheme 5.1**. Primary alcohols (5'-hydroxyl group) are more reactive than secondary alcohols (2'- and 3'-hydroxyl groups), enabling selective functionalization of the primary position. This is done by exploiting a substitution reaction performed at room temperature using a stoichiometric amount of 4,4'-dimethoxytrityl chloride, resulting in selective protection of the 5'-hydroxyl group, affording the desired product in 89% yield. Regioselection between the two equally reactive secondary hydroxy groups is performed by masking the reactivity of the one in 3', by means of silver nitrate. Silver ions can, in fact, chelate between the 3'- and 5'-hydroxyl groups, thereby hindering these groups from reacting with the electrophilic tert-butylchlorodimethylsilane. In these conditions, functionalization of the 2' hydroxyl group is achieved in good yields (81%). Finally, with only one unprotected hydroxyl group remaining, the phosphoramidite moiety can be introduced at the free position with a substitution reaction, providing the fully functionalized building block in high yield (92%) (**Scheme 5.1)**.

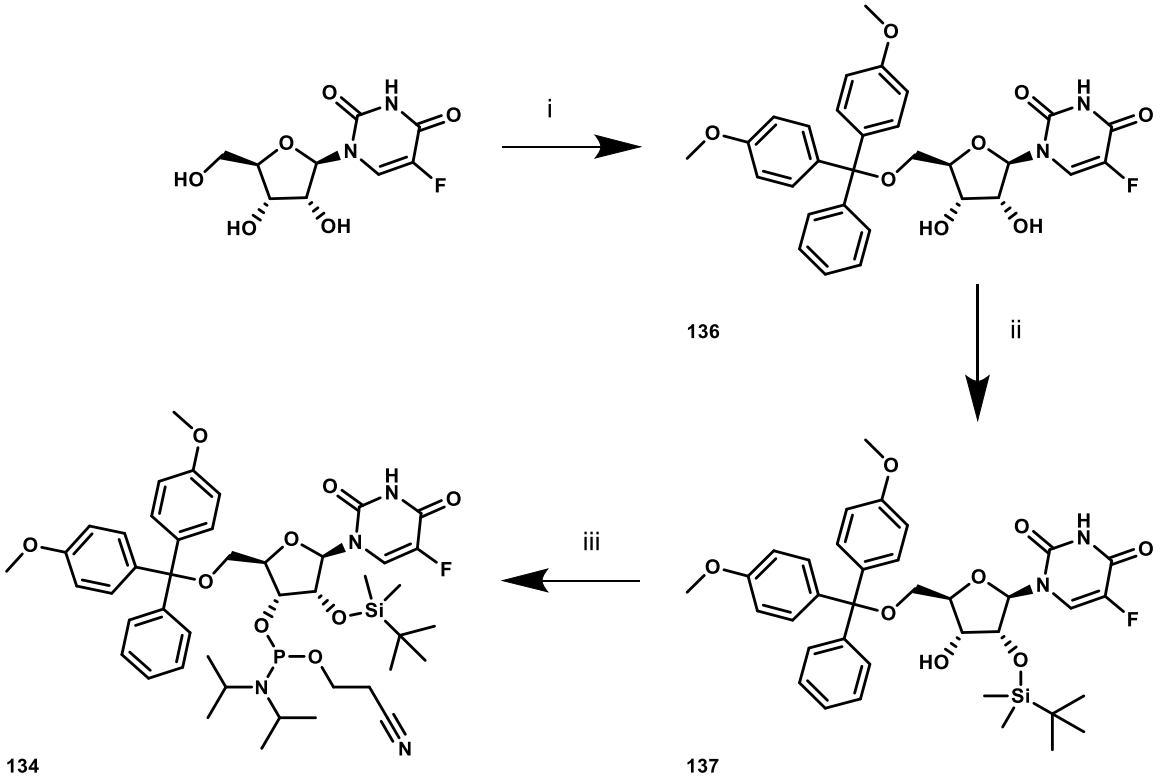

(**i**) 4,4′-Dimethoxytrityl chloride, pyridine, r.t., 16h, 71%; (**ii**) $AgNO_3$, pyridine, tert-Butyldimethylsilyl chloride, THF, r.t., 16h, 81%; (**iii**) DIPEA, 2-Cyanoethyl N,N-diisopropylchlorophosphoramidite, THF, 0°C to r.t., 16h, 92%.

Scheme 5.1. *Synthetic pathway for the synthesis of rFU phosphoramidite **134**.*

The synthesis of the protected rFC phosphoramidite **135** follows the same general strategy described for rFU. The corresponding synthetic pathway is presented in **Scheme 5.2**.
In contrast to rFU, rFC contains an additional nucleophilic site that requires protection, namely the exocyclic base nitrogen. In the absence of a base, this nitrogen represents the most nucleophilic site, enabling its regioselective functionalization prior to modification of the hydroxyl groups. Selective protection of the nucleobase was achieved by reaction with an acidic anhydride at 85°C in DMF. The desired product was isolated by crystallization from toluene in high yield (89%). Subsequent transformations, including selective hydroxyl protection and installation of the phosphoramidite functionality, were carried out following the same procedure described for rFU and are therefore not described (**Scheme 5.2)**.

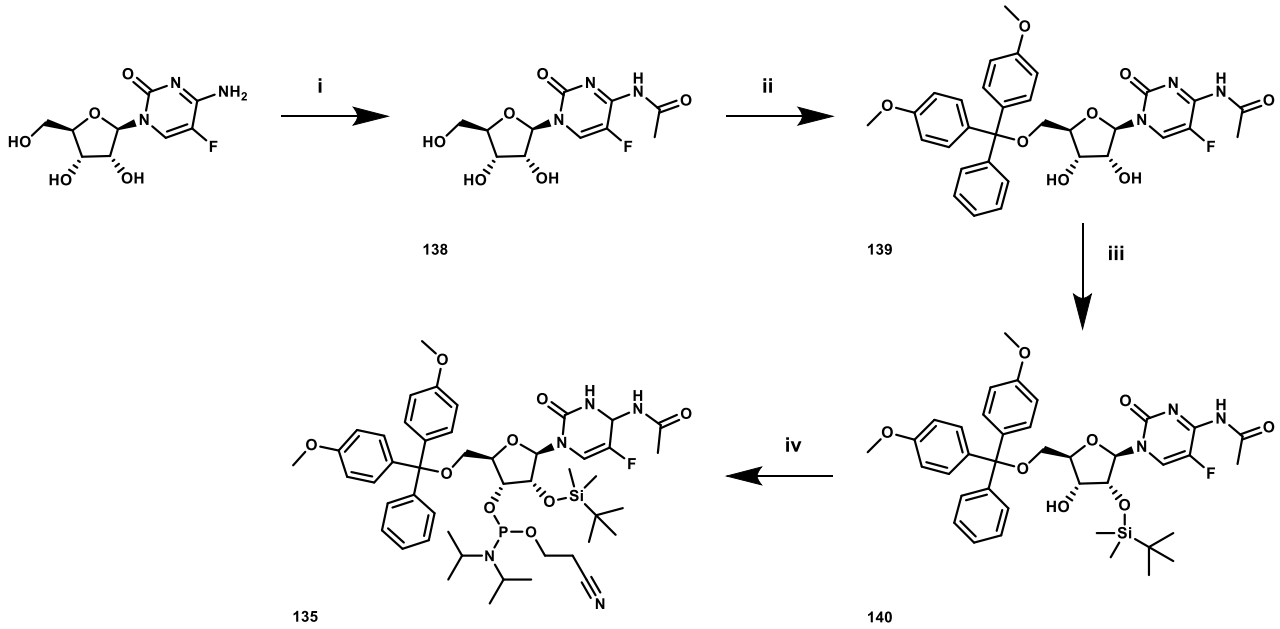

(**i**) Acetic anhydride, DMF, 85°C, 2h, 89%; (**ii**) 4,4′-Dimethoxytrityl chloride, pyridine, r.t., 16h, 49%; (**iii**) $AgNO_3$, pyridine, tert-Butyldimethylsilyl chloride, THF, r.t., 16h, 45%; (**iv**) 2-Cyanoethyl N,N-diisopropylchlorophosphoramidite, DIPEA, THF, 0°C to r.t., 16h, 85%.

Scheme 5.2*. Synthetic pathway for the synthesis of rFU phosphoramidite **135**.*

The detailed protocol for the synthesis of the rFU (**134**) and rFC (**135**) phosphoramidites is reported in the Experimental part (**Paragraph 5.6.1**).

5.3.2: Fluorinated RNA synthesis

A schematic representation of the solid-phase synthesis process employed for the preparation of the fluorinated oligonucleotides is shown in **Scheme 5.3**.

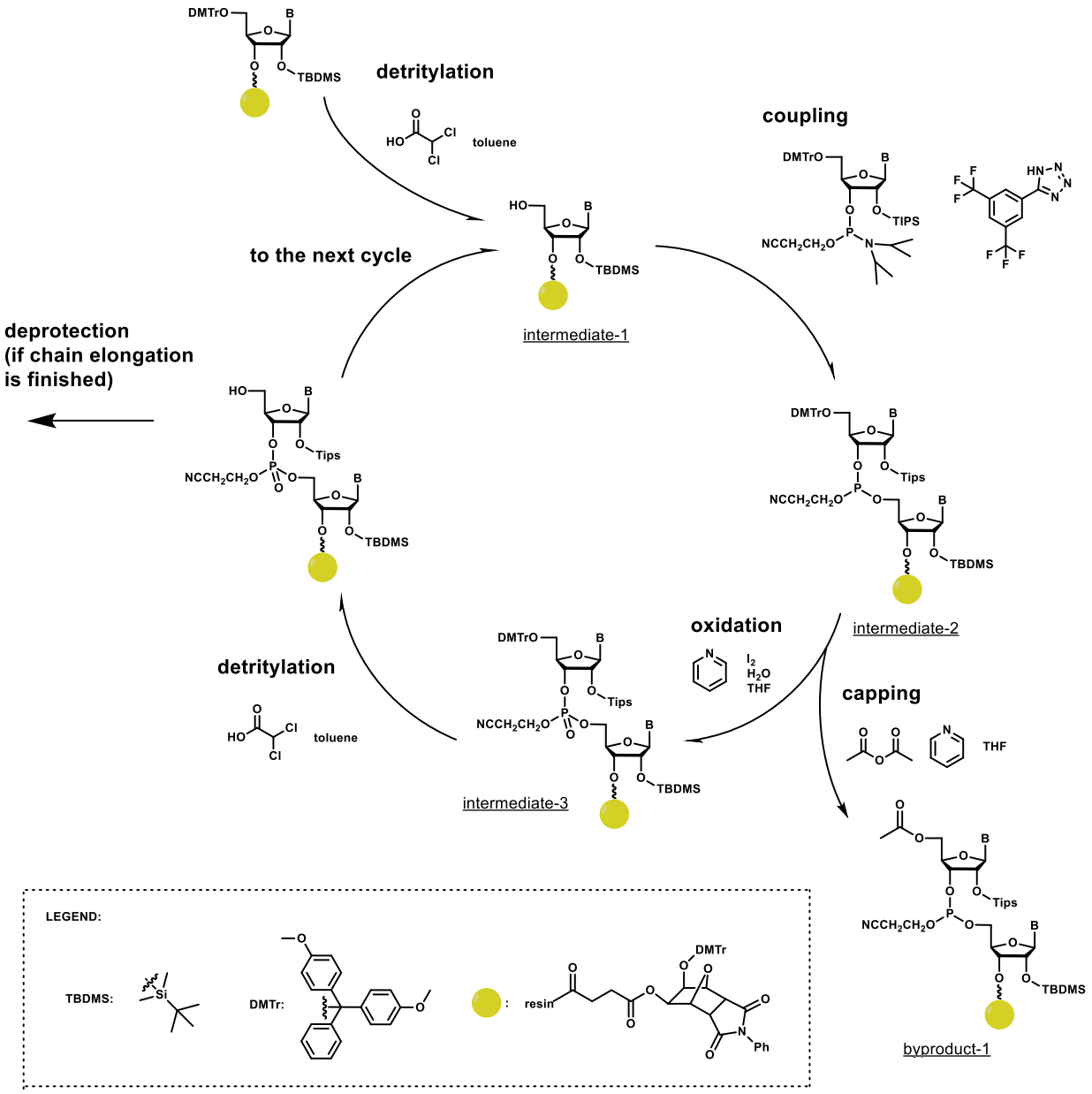

***Scheme 5.3**. Solid-phase synthesis of the fluorinated oligonucleotides.*

The elongation of the RNA chain can be divided into four main steps (**Scheme 5.3**):

1. **DMT removal:** The dimethoxytrityl (DMTr) protecting group of the first nucleotide is removed by acid treatment, exposing the free reactive 5'-hydroxyl group, obtaining *intermediate-1*.

2. **Coupling reaction:** The 5'-hydroxyl group reacts with the incoming phosphoramidite, which is activated with a tetrazole. This forms a phosphite triester linkage between the growing chain and the new nucleotide, obtaining *intermediate-2*.

3. **Capping of unreacted ends:** Any unreacted 5'-hydroxyl groups in the previous step are capped to prevent further elongation of incomplete chains and the formation of undesired sequences. This process leads to the synthesis of *byproduct-1*.

4. **Oxidation and deprotection:** The phosphite triester is oxidized to a more stable phosphate triester, yielding *intermediate-3*.

High yields are required at each step of the chain assembly because the process is linear, and several equivalents of reagents are typically used at each stage to drive the reactions to completion. After oxidation, another detritylation step can take place, thus continuing the chain elongation process or, if chain elongation is complete, the β-cyanoethyl protecting groups on the phosphate moieties can be removed using diisopropylethylamine (DIPEA), yielding a fully protected oligonucleotide still attached to the solid support (**Scheme 5.3**).
Due to the high number of oligonucleotides needed to be synthesized, the overall described process was performed on a MerMade48 automated synthesizer (Biosearch Technologies), allowing for the parallel synthesis of up to 12 oligonucleotides, thereby significantly accelerating the overall production process. Following the protocol reported in the Experimental Part (**Paragraph 5.6.2**), in *circa* two days a set of 12 fluorinated pre-miR21 could be produced.
After completion of the solid-phase synthesis, the resin-bound oligonucleotides were cleaved from the solid support under aqueous basic conditions, which simultaneously removed also the nucleobase protecting groups. The reaction mixture was subsequently lyophilized to eliminate residual reagents and byproducts, being all volatile. In a second step, removal of the 2'-O-silyl protecting groups was achieved by treatment with TBAF at room temperature for 24 hours. Precipitation of the RNA in ethanol enabled removal of the reagents used in this step, yielding a crude mixture containing the full-length product together with shorter, capped shorter subproducts, to purify by reverse-phase chromatography.
Separation of oligonucleotides by reverse-phase chromatography is challenging due to the minimal differences in physicochemical properties between the full-length product and truncated sequences. To facilitate purification, the crude sample was first subjected to dialysis using centrifugal filter columns with an appropriate molecular weight cutoff. This step allowed removal of shorter oligonucleotides below a defined molecular weight threshold, thereby simplifying the chromatographic separation. Subsequently, the crude RNA products were purified by reverse-phase high-performance liquid chromatography (RP-HPLC). For this purpose, ion-pairing chromatography conditions were employed to achieve effective resolution of the desired full-length RNA from remaining impurities. Purity and characterization were assessed by LC-MS analysis.
The detailed protocol for the synthesis and purification, and the resulting chromatograms assessing the purity of the constructs, is reported in the Experimental Part (**Paragraph 5.6.2**).

5.4: ^{1}H- and ^{19}F-NMR secondary structure deconvolution

The synthesized fluorinated oligonucleotides were folded in buffer (see the Experimental Part in **Paragraph 5.6**), and both ^{1}H- and ^{19}F-NMR spectra were recorded. Comparison of the obtained spectra with the wild-type one provided insights into the secondary structure of the RNA and elucidation of the conformational states of this target.
In general, paired imino protons give rise to signals in the characteristic imino region of the ^{1}H-NMR spectrum (approximately 10–15 ppm), whereas unpaired imino protons appear at lower chemical shifts. Monitoring these imino signals is a standard approach for assessing proper folding of RNA constructs, since the same imino signals are expected for the same conformation obtained upon folding. From the paired imino protons, it should be possible to deconvolute the number of paired bases; however, in practice, the imino peaks frequently overlap, and integration is not reliable for quantifying the extent of base pairing. Improved resolution can be achieved by spreading the signals into two dimensions using [^{1}H,^{15}N]-HSQC experiments,[14] thus helping to identify the overlapped peaks. As an example, the [^{1}H,^{15}N]-HSQC experiment of pre-miR21 is reported in **Figure 5.9**. Additional structural information can

be inferred from the chemical shifts of the nitrogen signals, which are sensitive to the type of nucleobase. For instance, paired uridine residues produce signals between 165 and 157 ppm, while guanine pairs appear in the region of 150 to 142 ppm, allowing identification of the kind of base pairings that occur in the structure.

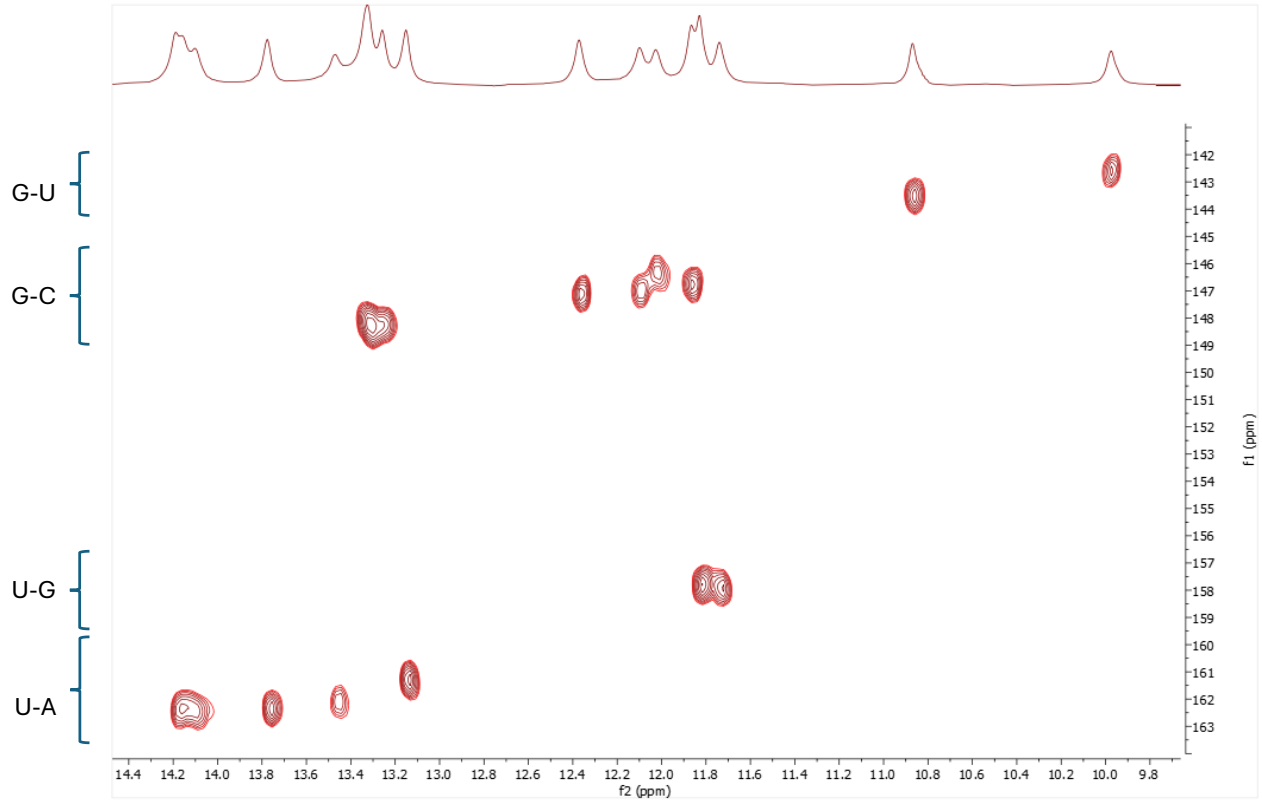

***Figure 5.9**. [^{1}H, ^{15}N]HSQC spectrum of 60nt model of pre-miR21 studied.*

Analysis of the spectra revealed approximately sixteen distinct imino resonances: five corresponding to U–A base pairs, six to C–G pairs, two to U–U interactions, and two to U–G pairs (assignment based on the peaks' chemical shift). Although direct integration of these signals was not strictly quantitative, and some resonances may overlap within the same spectral regions and thus remain unresolved, this preliminary observation indicated that the pre-miR21 construct is less structured than predicted by SHAPE analysis (**Paragraph 5.1**), which anticipates at least nineteen distinct imino peaks (**Figure 5.10**). Even from this basic comparison, it is apparent that the SHAPE-based model does not fully capture the actual folding of pre-miR21, emphasizing the need to complement this method with additional structural probing techniques.

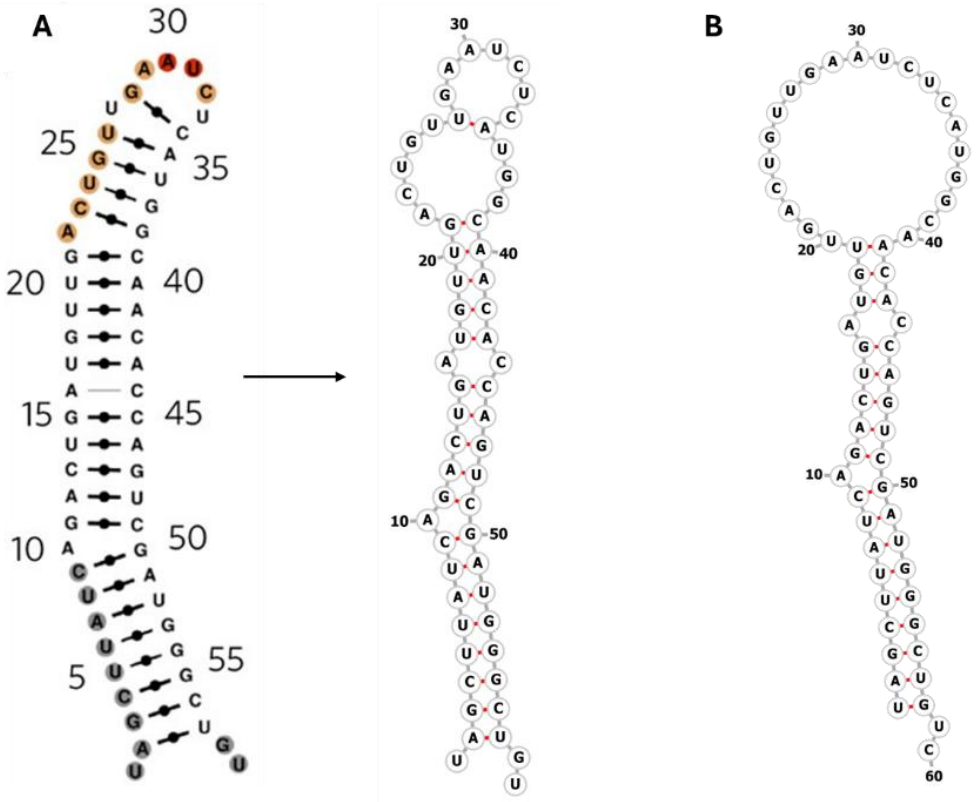

Figure 5.10. ***A****: SHAPE-derived secondary structure of pre-miR21 by Varani and colleagues*[7] *and its interpretation. Adapted from reference 7.* ***B****: Secondary structure derived from the* ^{19}F *probe application, as for my PhD work.*

5.4.1: rFU introduction

As described in the Experimental Part (**Paragraph 5.6.1**), rFU probes were individually introduced at positions *8, 14, 17, 19, 20, 24, 27, 31, 33, 36, 48,* and *52*, respectively, to sample the structure (**Figure 5.11**).

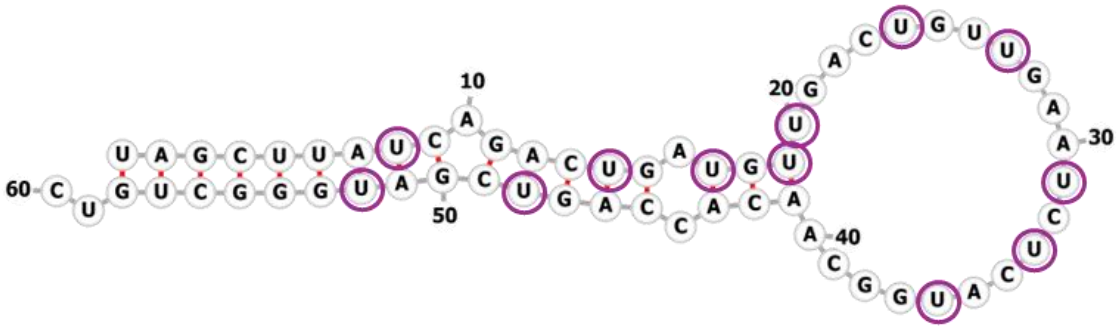

Figure 5.11. *Schematic representation of the introduced rFU probes. The different positions where rFU substitutions were introduced are highlighted in purple. Based on the experimentally derived secondary structure, the figure was generated using the ViennaRNA package*.

To evaluate the structural impact of fluorine incorporation, the ^{1}H-NMR spectra of the rFU constructs, focusing on the paired imino region (from now on imino spectra), were compared with those of the wild-type. This allowed for secondary structure deconvolution. Initially, to create a reference method allowing for structure elucidation, the effect of the rFU substitution on a paired base and an unpaired

one was studied. To this aim, according to SHAPE analysis data (**Figure 5.10**), rFU14 (stem) and rFU31 (apical loop) were chosen. Their spectra, compared with the wild type, are displayed in **Figure 5.12**. At first glance, the overall spectral pattern of the displayed modified RNAs appeared largely similar to that of the wild-type¸however, in the rFU14 spectrum (in green in **Figure 5.12**), the w.t. pre-miRs signal at 13.13 ppm was no longer detectable. As previously reported by Henning and colleagues,[9] incorporation of a fluorine atom at position 5 of uridine can lead to broadening of the corresponding imino resonance, likely due to alterations in the local pK_a, rendering it undetectable by NMR. Since only a single peak was deemed missing, it was reasonable to assign the signal at 13.13 ppm to base *14*. U31, located in the apical loop according to SHAPE analysis, was likely unpaired. Introduction of rFU at position U31, as shown in the purple spectrum in **Figure 5.12**, did not produce any detectable changes in the imino spectra. From this initial observation, it could be concluded that paired bases generally showed peak disappearance upon fluorine substitution, whereas unpaired bases remained unaltered. This behavior provided a useful framework for interpreting the full set of imino spectra.

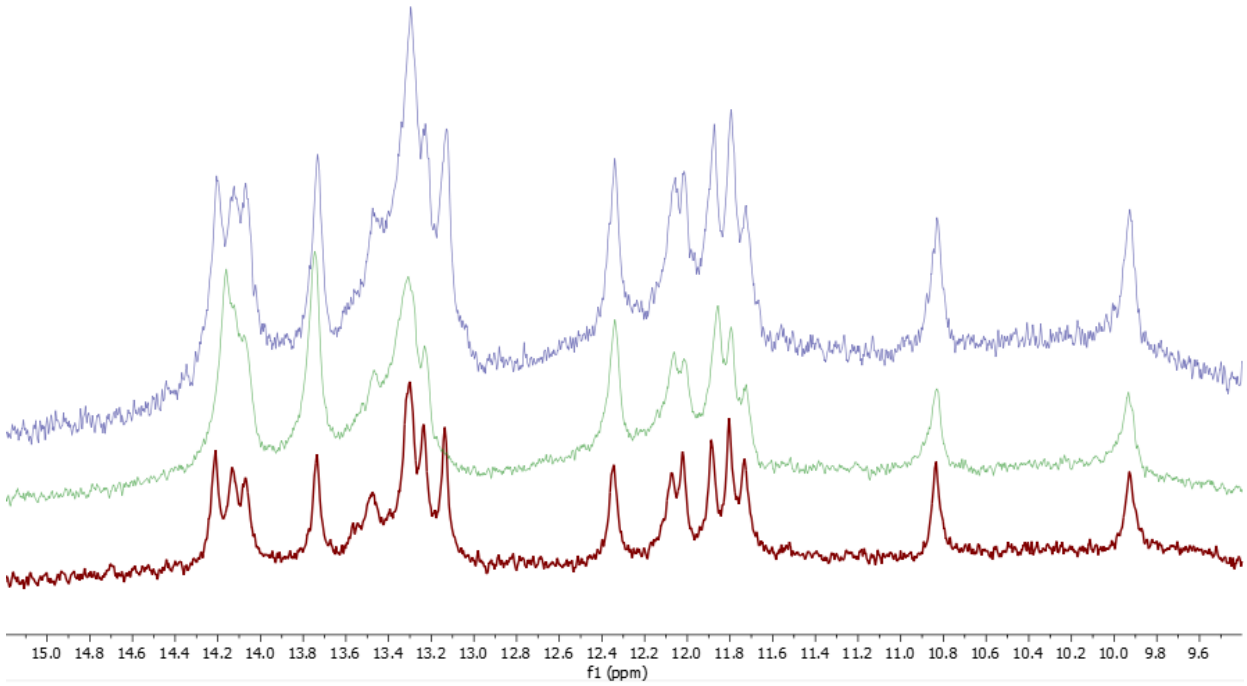

***Figure 5.12**. Superimposition of the wild-type (red), rFU14 (green) and rFU31 (purple) imino spectra of pre-miR21.*

Secondary shifts of other imino peaks were noted alongside peak disappearance, for example, those at 11.89 or 13.74 ppm for rFU14 (**Figure 5.12**). These changes were deemed likely due to the spatial proximity of neighbouring base pairs to the site of fluorine substitution, providing a means to assign adjacent nucleotides. To create a model to interpret this secondary peak shift, two nearby bases, rFU14 and rFU17, were analyzed.

The w.t., rFU14, and rFU17 imino spectra are reported in **Figure 5.13**. The comparison of the rFU17 imino spectrum with that of the wild-type highlighted three key observations: (1) the disappearance of the peak at 13.74 ppm, corresponding to the imino proton of the paired base, allowing peak assignment; (2) a slight upfield shift of the peak at 13.13 ppm (previously assigned to U14), reflecting its close proximity to the perturbed site; and (3) a downfield shift of the peak at 11.89 ppm **(Figure 5.13)**. Because this latter shift was also present in the rFU14 spectrum, the affected signal could be attributed to a nucleotide positioned between the two substituted residues, presumably G15. This assignment was further

corroborated by the rFC45 spectrum (**Paragraph 5.4.2**). Since from these secondary peaks shifts reasonable assignments could be made, they were not considered artifacts caused by the fluorine introduction but used for structure elucidation, following the rationale just described.
In general, both upfield and downfield secondary shifts were observed in all spectra, without a consistent directional trend.

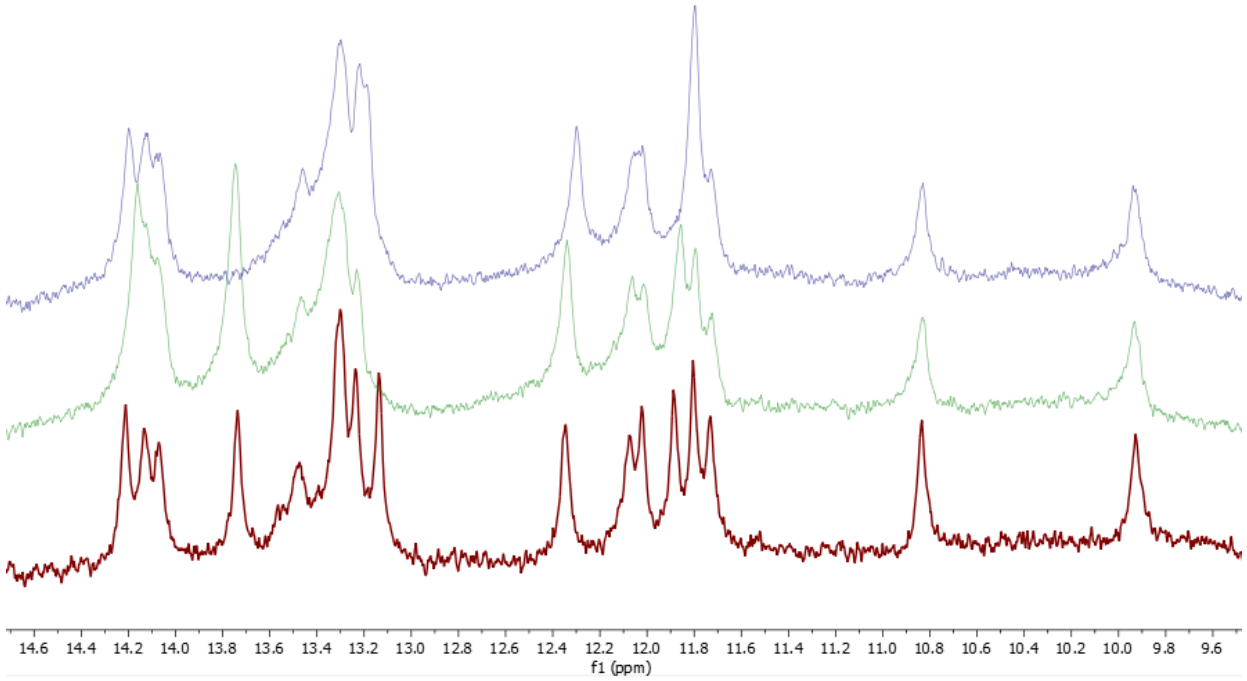

***Figure 5.13**. Superimposition of the wild-type (red), rFU14 (green), and rFU17 (purple) spectra.*

By systematically analyzing peak disappearance and secondary peak shifts, it was possible to reconstruct the overall secondary structure of the RNA. In particular, peak broadening provided a rapid and unambiguous way to correlate a paired base with a specific signal, thus offering a practical starting point for structural assignment. Secondary chemical shift variations presented a more time-consuming analysis and were evaluated subsequently to peak broadening. However, they offered the advantage of reporting on more than one nucleoside at a time, thereby enabling the assignment of multiple base-pairing interactions from a single spectrum.
The comparison of the wild type with the twelve rFU-substituted imino spectra is presented in **Figure 5.14**. For bases *6, 14, 17, 19, 48,* and *52* (**Figure 5.14A**), noticeable shifts were observed in the imino region, whereas bases *20, 24, 27, 31, 33,* and *36* (**Figure 5.14B**) showed no significant changes, indicating these nucleotides as likely unpaired. For rFU20, a slight shift in ppm was noted at *circa 14.15ppm*. This was deemed consistent with the influence of the fluorine atom incorporation on the neighbouring U19. Based on these observations, a revised secondary structure model was derived, revealing a larger apical loop than predicted by SHAPE analysis, extending from base *20* to *40* (**Figure 5.14C**).
The rFU substitutions enabled assignment of certain imino peaks in the wild-type spectrum, although the rFU data alone were insufficient to assign all resonances, necessitating complementary analysis using rFC substitutions for confirmation (**Figure 5.14D**).

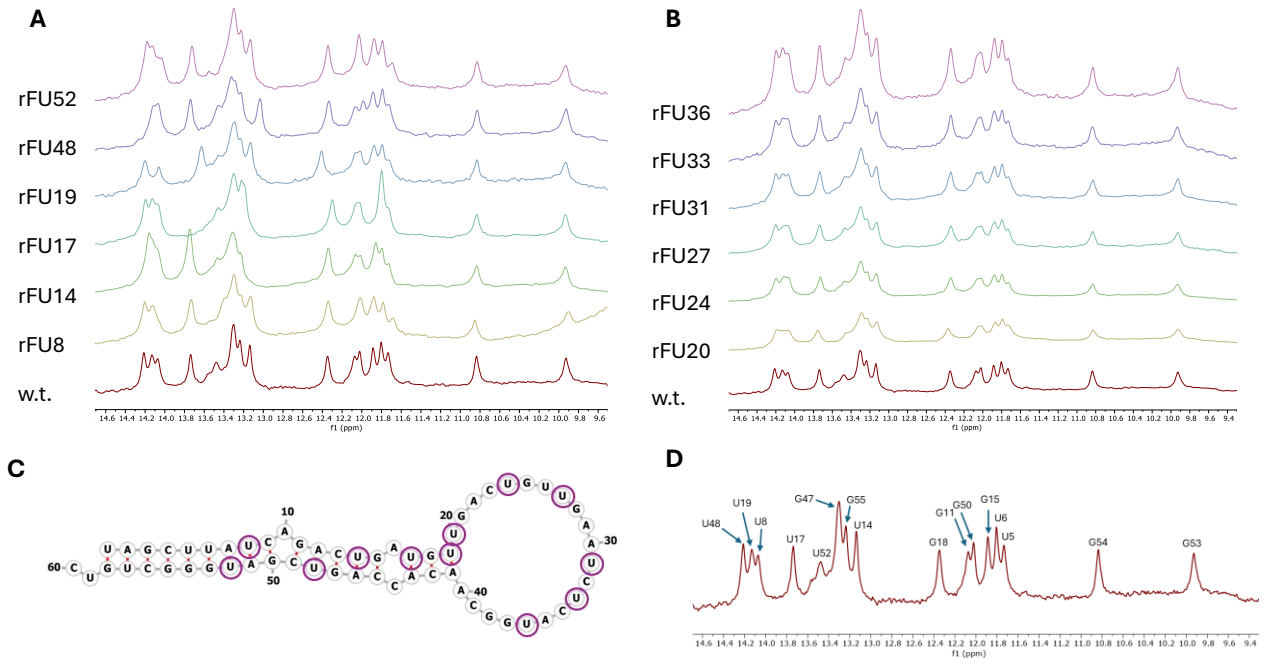

Figure 5.14. ***A****: Superimposition of the imino spectra obtained by NMR-probe introduction on a paired base.* ***B****: Superimposition of the imino spectra obtained by NMR-probe introduction on an unpaired base.* ***C****: Proposed pre-miR21 secondary structure derived by ^{19}F NMR-probes analysis, with rFUs substitutions shown in purple.* ***D****: Assignment of pre-miR21 imino peaks.*

Having sampled the secondary structure by imino analysis, the focus of the study moved to the investigation of the conformational population, enabled by ^{19}F-NMR spectroscopy. When a single conformation is present in a structure, a single fluorine atom is expected to give rise to a single resonance in a decoupled spectrum. However, RNA molecules can adopt multiple conformations, generating distinct local magnetic environments and, consequently, possibly multiple ^{19}F-NMR-signals. This phenomenon has been previously observed by Puffer and colleagues.[8] The application of this approach to an entire, uncharacterized RNA construct enabled the characterization of structure dynamics.

^{19}F-decoupled NMR spectra, recorded for all twelve rFU-substituted oligonucleotides, are reported in **Figure 5.15A** with their intensities represented in **Figure 5.15B**. The intensities, as for all the ^{19}F-NMR reported spectra, are displayed scaled to the proton intensities, making them comparable to one another.

As a general guideline for signal interpretation, high peak intensity was deemed to indicate the presence of a dominant conformational species, reflecting a relatively high degree of structural order. Peak shape, on the other hand, was evaluated as providing information about the nature of the conformational ensemble in solution: a single, sharp resonance was deemed characteristic of a predominant state, whereas peak splitting could suggest the presence of multiple slowly exchanging conformational states. For the stem region, a certain degree of order was expected due to the defined conformation, as seen in the ^{19}F-NMR spectra analysis: rFU8, rFU14, rFU17, rFU19, rFU48, rFU52 were observed to present single well-defined sharp peaks, with high intensities. rFU17 appeared as an exception, being broader than the other peaks, hinting at probably higher conformational dynamicity in that area, as would be expected by the first paired base above a less conformationally defined mismatched pair. The loop region, instead, appeared to display three different typed of conformational dynamics: 1) well-defined sharp peaks (rFU20), which could be explained by a certain degree of pairing, 2) signals split in

two peaks with moderate intensities (rFU31, rFU33), characteristic of a two-state conformation quite defined, 3) peaks with low intensity (rFU24, rFU36), characteristic of a high exchange situation for the corresponding base. From this analysis, pre-miR21 seemed to present a structure with a rather rigid stem and a loop composed of a fast exchange area and a more ordered one.

In the ^{19}F-NMR signal analysis, the method appeared to confirm itself to be rather robust toward impurities. As reported in **Paragraph 5.6.2**, the synthesized RNAs were not entirely pure. The fact that well-resolved singlet peaks were still observed for many stem-region rFU constructs indicates that, for this type of ^{19}F-NMR analysis, minor impurities have little impact on the overall spectral interpretation, making the method more practical and cost-effective. Confirmation of this with other experiments is currently ongoing in the AZ laboratories.

In **Figure 5.15B**, the chemical shifts of all fluorine signals are reported, scaled according to the intensities of the corresponding ^{1}H signals. A clustering pattern was identified in the chemical shifts: fluorine atoms in base-paired regions were noted to locate at lower ppm, while those in unpaired regions were observed at higher ppm. This trend was hypothesized to reflect differences in solvent exposure. Within the stem, a relatively hydrophobic environment was expected, as base–base interactions reduce solvent accessibility. Notably, rFU17, despite being paired, appeared in the "unpaired" chemical shift region, consistent with its location above a solvent-exposed bulge. Similarly, the chemical shift of rFU20 fell between the paired and unpaired regions, which could reflect its position as the first unpaired base above the more protected stem or a degree of transient pairing that was not resolved under room-temperature NMR conditions.

This interpretation could provide a framework for understanding loop signal splitting: signals showing two peaks may represent a fluorine experiencing both transient interactions with neighbouring bases and interactions with solvent or less tightly paired residues. This interpretation was further supported, even if confirmation is still lacking, by ^{19}F-NMR analysis of sFU-substituted constructs (**Paragraph 5.4.3**).

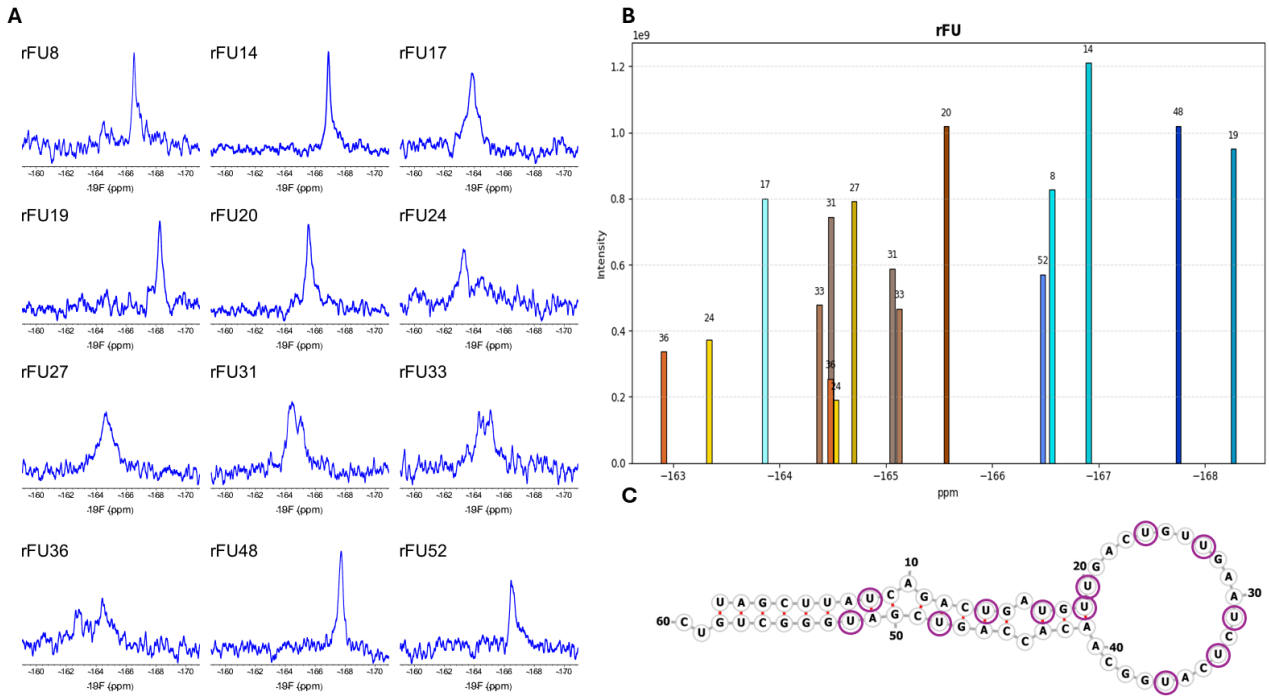

***Figure 5.15**. **A**: rFU ^{19}F-NMR signals, not scaled by their intensity. **B**: Schematization of the intensity and position of the rFU ^{19}F-NMR signals*. **C**: Substituted positions within the modified miR21.

5.4.2: rFC introduction in modified pre-miR21

Having probed the secondary structure through rFU incorporation, rFC mutations were also introduced at positions *23, 34, 39, 42, 45, 46,* and *49*, respectively, of pre-miR21 to confirm the assignments based on secondary chemical shift variations and to gain further insight into the molecule's dynamics (**Figure 5.16**).

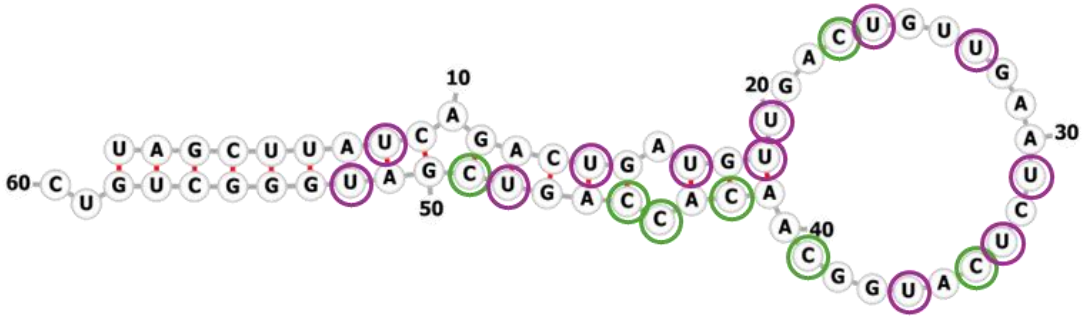

***Figure 5.16**. Schematization of the individually introduced rFC (green) and rFU (purple) mutations.*

The imino spectra obtained by the introduction of rFC are reported in **Figure 5.17A** (paired) and **B** (unpaired). The introduction of different probes brought different effects in the imino spectra. In particular, rFC introduction did not cause signal broadening but instead led to a strong upfield shift for the substituted peak and secondary, smaller shifts to the neighbouring bases. This is consistent with what was also reported by other groups for this nucleoside incorporation.[9] In some cases, minor additional chemical shift perturbations, both upfield and downfield, were observed in neighbouring imino peaks, reflecting, as for rFU, the influence of the fluorine on the other RNA bases.

Unpairing was noted for rFC23, rFC34, rFC39, and rFC45 (**Figure 5.17B**), allowing better characterization of the loop and the unpaired areas of the stem. Moreover, rFC42, rFC45 and rFC49 helped confirm the secondary peak assignment hypothesis derived by rFU substitutions (**Figure 5.17A**).

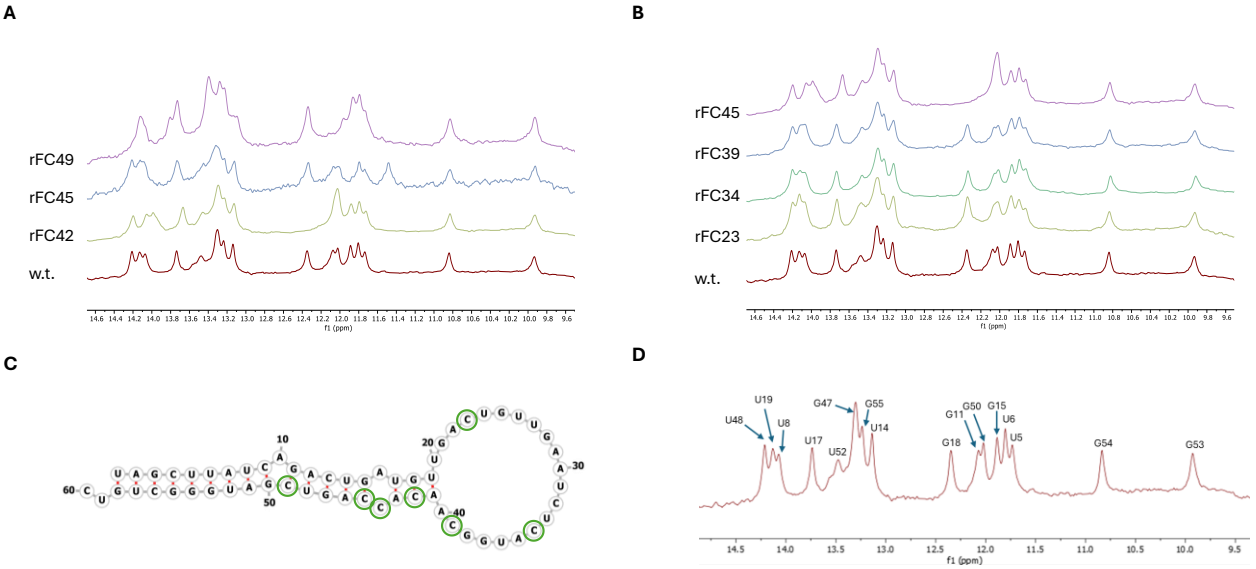

***Figure 5.17**. **A**: Superimposition of the imino spectra obtained by NMR-probe introduction on a paired base. **B**: Superimposition of the imino spectra obtained by NMR-probe introduction on an unpaired base. **C**: Proposed pre-miR21 secondary structure derived by 19F-NMR probes analysis, with rFCs substitutions shown in green. **D**: Assignment of pre-miR21 imino peaks.*

The ^{19}F-NMR spectra of the rFC-substituted oligonucleotides are shown in **Figure 5.18A**. Analysis of these signals provides additional insights into loop dynamics. In the loop region, structured behaviour was evident for some residues: rFC23 exhibited a two-state dynamic, even if in fast exchange, whereas rFC39 showed a dominant high intensity conformation and a minor secondary state. In contrast, rFC34 was characterized by a very broad and weak signal, consistent with a lack of well-defined structure and reflecting a more disordered loop region.
Within the stem, rFC42 and rFC45 displayed sharp singlet resonances, characteristic of stable, base-paired residues, while rFC44 presented a broader signal, in agreement with its assignment as a bulged-out nucleotide. The rFC49 signal was difficult to detect, suggesting more complex dynamics than predicted from the imino spectra. This may be influenced by the proximity of a nearby bulged region, although further investigations are needed to fully understand the underlying conformational behaviour.
In **Figure 5.18B**, the chemical shifts of all fluorine signals are reported, scaled according to the intensity of the corresponding ^{1}H signals. No clear trend was observed in the chemical shifts of the modified bases; however, with only seven positions analysed, this dataset remains too limited to draw definitive conclusions.

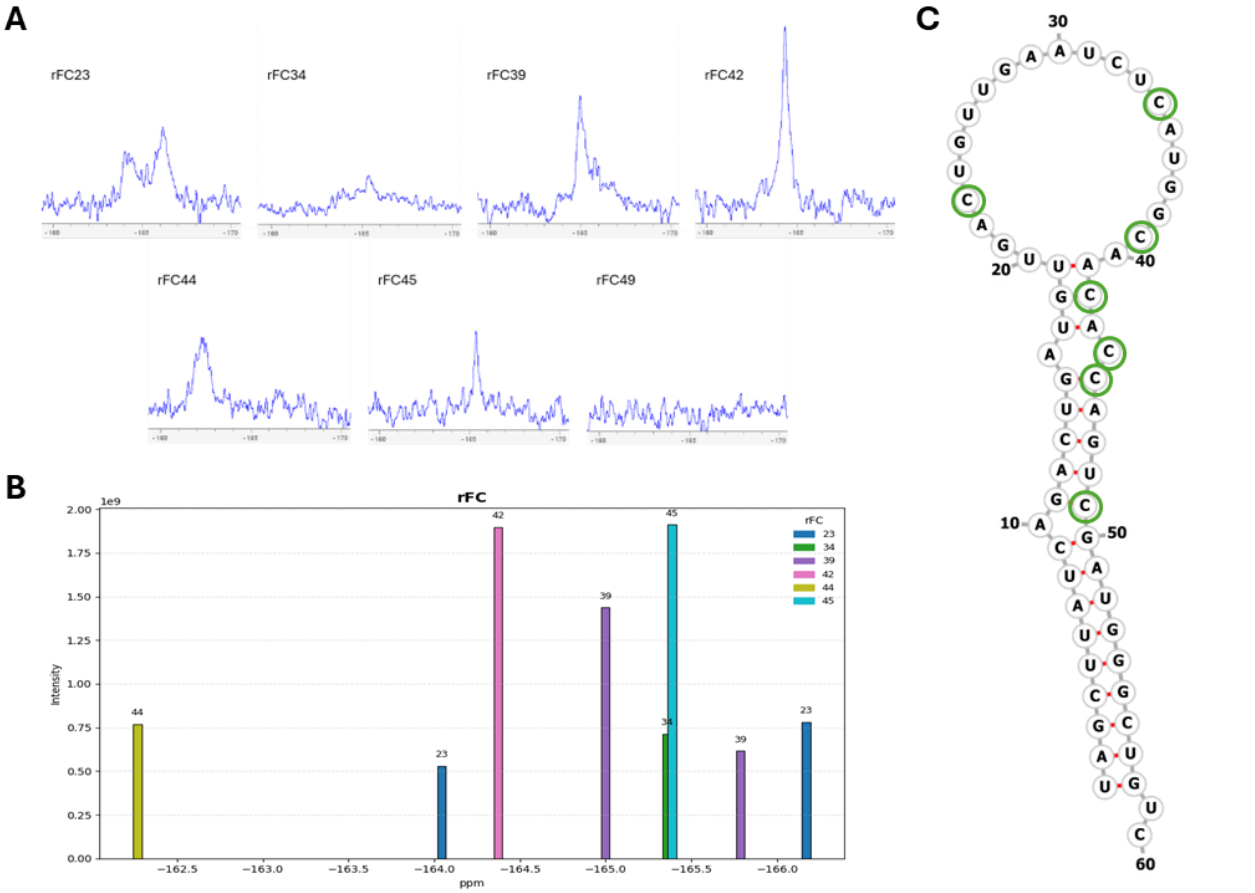

***Figure 5.18**. **A**: ^{19}F-NMR rFC signals. **B**: Schematization of the intensity and position of rFC ^{19}F-NMR signal. **C**: Proposed pre-miR21 secondary structure derived by F-probes analysis, with rFCs substitutions shown in green.*

5.4.3: sFU introduction in modified pre-miR21

To determine the most suitable probe for imino spectral analysis, sFU substitutions were introduced at the same twelve positions previously studied with rFU. Direct comparison of the corresponding imino spectra was expected to allow evaluation of how fluorine incorporation affects the RNA structure: if similar structural information were obtained, this would indicate that the substitution does not substantially perturb the overall dynamics, highlighting the method as robust.

When fluorine was incorporated on the sugar moiety rather than the base, no broadening of the imino signals corresponding to paired, substituted nucleotides was observed. In general, upfield shifts were noted, consistent with the introduction of an electronegative atom near the imino proton and the resulting change in its local electronic environment. As for the case of rFC, larger shifts were noted for certain peaks with respect to the overall spectra, making it possible to assign these peaks (**Figure 5.19**). The imino spectra of the sFU-substituted constructs are reported in **Figure 5.19** (**A** and **B**). Comparable assignments could be made for the substituted peaks relative to the rFU spectra, indicating that the presence of the fluorine atom did not significantly alter the RNA secondary structure. Differences were instead noted for the secondary peak shifts: under this area, sFU appeared as a complementary probe to rFU. The same secondary shift obtained upon rFU introduction, for example, at base 14 (rFU14), was not noted upon sFU introduction, and vice versa. The number of affected secondary peaks resulted, however, lower, probably due to the higher distance from the base-pairing area of the stem, thus affecting less the chemical shift of the paired imino protons.

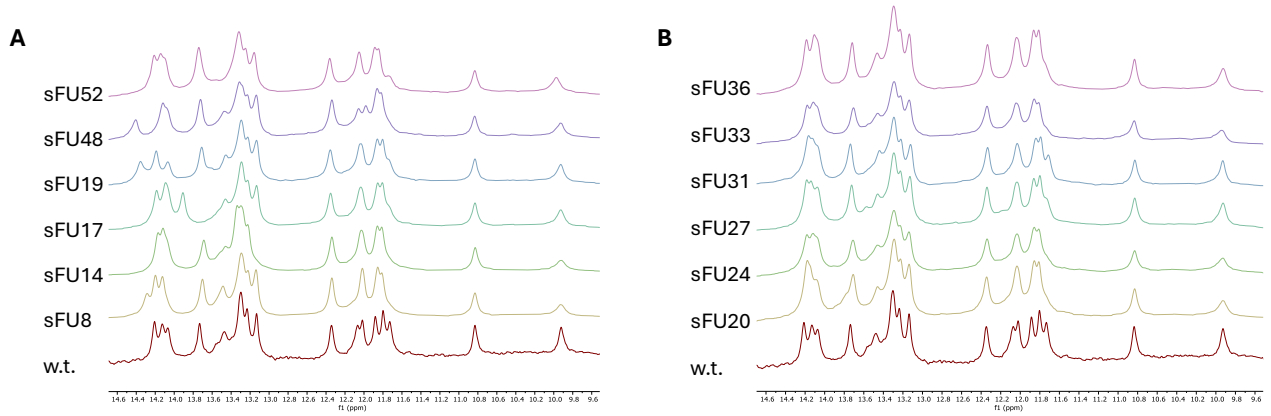

***Figure 5.19**. **A**: Superimposition of the imino spectra obtained by NMR-probe introduction on a paired base. **B**: Superimposition of the imino spectra obtained by probe introduction on an unpaired base.*

sFU probes displayed the fluorine atom in the sugar moiety of the nucleoside, providing insights into the backbone dynamics of the RNA. This makes sFU a complementary probe to rFU for conformational population analysis by ^{19}F-NMR. sFUs spectra are reported in **Figure 5.20**. For sFU ^{19}F signals, a similar behaviour to rFU ones was observed. Paired nucleotides gave rise to sharp high-intensity singlets (sFU8, sFU14, sFU17, sFU19, sFU48, and sFU52), whereas unpaired ones exhibited faster exchange dynamics, with an overall low intensity. sFU27 resulted as an outlier in this trend, presenting a major high-intensity conformational state and highlighting the presence of some structural order also for the backbone in this area, while the rest of the loop appeared to be in exchange between different states.

In **Figure 5.20B**, the chemical shifts of all fluorine signals are reported, scaled according to the intensity of the corresponding ^{1}H signals. Regarding chemical-shift dispersion, sFU signals were noted to cluster near –200 ppm, with a narrower range compared to rFU. Paired bases were observed to occupy the same ppm range, while unpaired bases showed a greater dispersion. This could reflect a relatively uniform

solvent exposure for the sugar-attached fluorine in the stem area, causing a similar resonance frequency. The reason why some residues shifted to higher ppm and others to lower remains to be understood.

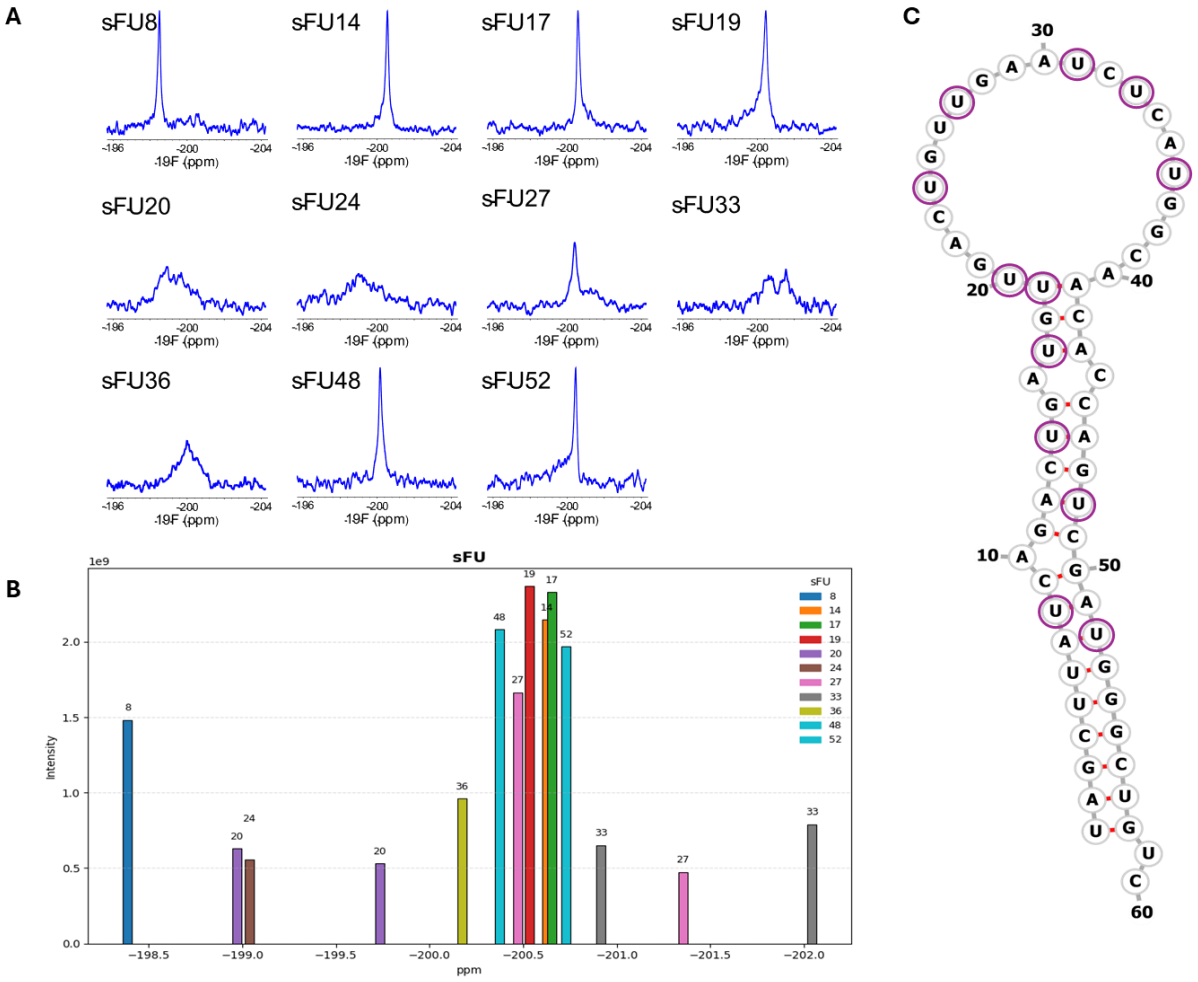

***Figure 5.20**. **A**: [19]F-NMR spectra of the synthesized sFUs. **B**: Schematization of the intensity and position of sFU [19]F signals. **C**: Substituted positions.*

5.4.4: dFU introduction in modified pre-miR21

As a potential, commercially available alternative to rFU, dFU was also investigated. Substitutions were introduced at all the positions previously studied with rFU, with the addition of positions *8* and *26*.
The imino spectra of the dFU-modified constructs are reported in **Figure 5.21** (**A** and **B**). Incorporation of dFU at paired nucleotides produced peak broadening comparable to that observed for rFU, allowing rapid assignment of paired residues and yielding the same conclusions regarding stem and loop structure. Regarding neighbouring chemical-shift perturbations, dFU substitution affected a larger number of nearby peaks than rFU, suggesting increased local mobility of the modified residues. Additional minor resonances, not present in the wild-type spectrum, were also observed (e.g., signals at 13.59 ppm for dFU24 and dFU31). The origin of these signals remains unclear, but they may reflect either the unmasking of previously overlapping resonances or subtle structural perturbations introduced by the 2'-deoxy modification.

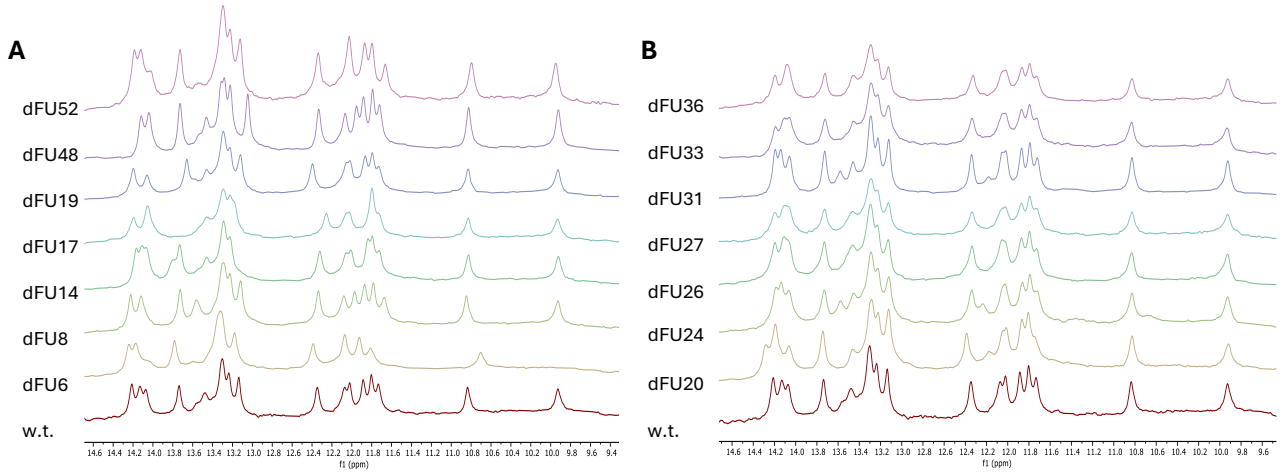

***Figure 5.21**. **A**: Superimposition of the imino spectra obtained by probe introduction on a paired base. **B**: Superimposition of the imino spectra obtained by probe introduction on an unpaired base.*

The ^{19}F-NMR spectra of the dFU-modified constructs are shown in **Figure 5.22A**. A different pulse sequence was used for these measurements, producing sharper peaks with reduced noise. In the stem region, the overall ^{19}F-NMR signals appeared similar to the rFU ones, with comparable shapes. This observation further demonstrated the robustness of the method: despite potential differences in synthesis and the presence of impurities, the stem conformational signals remained consistent, indicating that the technique is indeed tolerant to minor sample heterogeneity.

In the loop region, however, discrepancies between dFU and rFU signals were noted, with different peak shapes for the same base (**Figure 5.23B**). Coupled with the perturbations observed in the imino spectra upon dFU incorporation, dFU was evaluated to be less preserving of the native RNA conformational behaviour. The absence of the 2'-hydroxy group in dFU was deemed to likely perturb local structure, causing deviations from the native dynamics, particularly in more flexible regions such as loops. dFU probes, therefore, did not appear to be suitable tools to probe disordered areas, while for ordered ones, the influence of the absence of the 2'-OH group did not seem to be so impactful, given the already high degree of order.

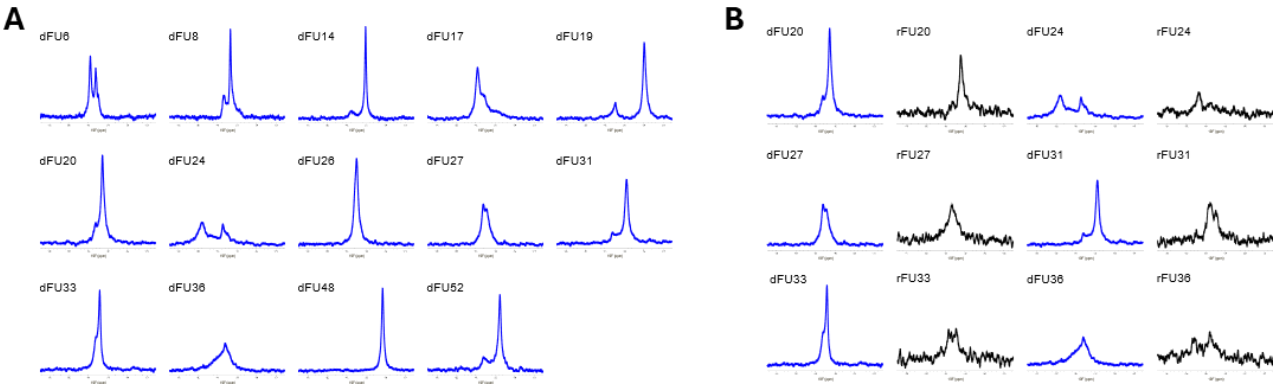

***Figure 5.22**. **A**: ^{19}F-NMR spectra of the 14 dFU modified oligonucleotides synthesized. **B**: Comparison of the 19F dFU signals and rFU signals. For all the shown positions, differences in shape are noted.*

5.4.5: Pre-miR21 structural studies: preliminary conclusions

A novel approach has been demonstrated to probe the overall structural features of an RNA construct even in the absence of prior structural information. Provided that an automated oligonucleotide synthesizer is available, this method allows for rapid acquisition of reliable data regarding RNA secondary structure and the distribution of conformational populations. Importantly, this approach does not suffer from the resolution limitations encountered with standard NMR or cryo-EM techniques for medium-length RNAs. The method is robust to sample impurities, and the presence of fluorine appears not to significantly perturb the native folding. While the method provides rapid and reliable secondary structure information, full coverage of all nucleotides, particularly adenines and guanines in loops, requires additional probe development, which would make this approach even more robust.

Application of the fluorinated probe strategy enabled the proposal of a new secondary structure model for pre-miR21. Based on the ^{19}F probe data, the stem consists of 17 base pairs, featuring a stacked-out nucleotide (A10) and a bulge (A16–C44). The stem appears relatively rigid, exhibiting a single principal conformational population as indicated by the ^{19}F spectra. A large loop spans bases 20 to 40; although not completely disordered, it displays multiple distinguishable conformational states, reflecting a moderate degree of structural organization. By combining information from sugar-modified sFU probes (reporting backbone dynamics) and base-modified rFU and rFC probes (reporting base dynamics), a more comprehensive description of loop behavior is achievable. A full characterization, however, would require fluorinated substitutions of the adenine and guanine residues within the loop.

Analysis of the loop reveals that its backbone exhibits a broad conformational ensemble, suggesting limited interactions within this region, with notable exceptions such as sFU27, which shows a single well-defined peak, likely due to interactions with nearby residues. The lower degree of order in the backbone relative to the bases is consistent with a flexible loop in which the backbone is largely solvent-exposed, while base interactions are transient. Individual bases display variable dynamics: some regions show fast exchange with broad ^{19}F resonances (e.g., rFC23, rFU24, rFC34, rFU36, highlighted in pink in **Figure 5.23**), whereas other nucleotides exhibit clearly defined two-state populations (e.g., dFU26, rFU27, rFU31, rFU33, shown in green in **Figure 5.23**). The lower portion of the loop displays well-ordered ^{19}F signals for the bases (e.g., rFU20, rFC39), reflecting a more structured region between the rigid stem and the dynamic apical loop. Overall, the loop appears to be ordered in the apical part, in exchange between two defined states, with a flexible area linking the loop to the highly ordered stem.

Some areas of the loop, such as bases 28-30, are still to be investigated. These regions correspond to G or A nucleosides that could not be substituted, as suitable fluorinated analogues are currently not available. Nevertheless, it is unlikely that these residues are stably paired, since their complementary bases (U or C) in that area were observed in an unpaired state. Transient non-canonical interactions, however, cannot be excluded.

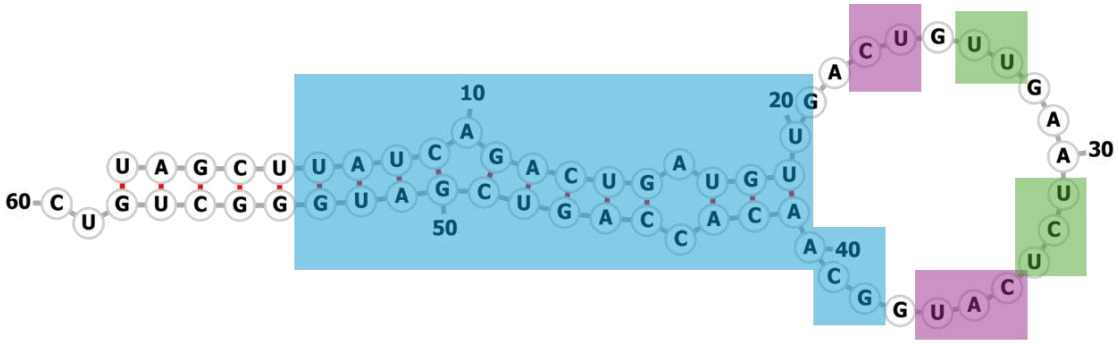

***Figure 5.23**. Putative analysis of the dynamics of pre-miR21. Nucleobases conformations are color-coded: well-defined (blue), certain degree of order (green) and broad conformational state (pink).*

Overall, this model provides a more detailed and accurate description of pre-miR21 than previously reported SHAPE analysis (**Paragraph 5.1**). SHAPE methodology is, however, less time-consuming than the fluorinated samples approach, and I think it should still be the first choice when dealing with an uncharacterized secondary structure analysis. The fluorinated probe analysis would come as a second, deeper analysis, enabling the characterization of the difficult-to-capture dynamic areas.

5.5: Binding site studies

To evaluate binding specificity and gain further insights into the interaction site of the in-house synthesized hit **1** analogues, all dFU-modified pre-miR21 constructs were titrated with compound **41** (**Figure 5.24**), a promising compound synthesized during the hit expansion process and selected for its binding affinity for the target (**Paragraph 4.3**).
The results of these titrations are summarized in **Figure 5.24**. As discussed in **Paragraph 5.4.4**, dFU probes were demonstrated not to fully capture the native conformational landscape of RNA. Nonetheless, the corresponding phosphoramidites are commercially available, making the synthesis of dFU-modified RNAs more accessible and cost-effective compared to rFU and rFC, which require in-house preparation. Importantly, this preliminary dFU-based binding study may well serve as a proof-of-concept investigation. In fact, more biologically relevant studies, using alternative probes, are currently underway in collaboration with AZ biophysics laboratories.

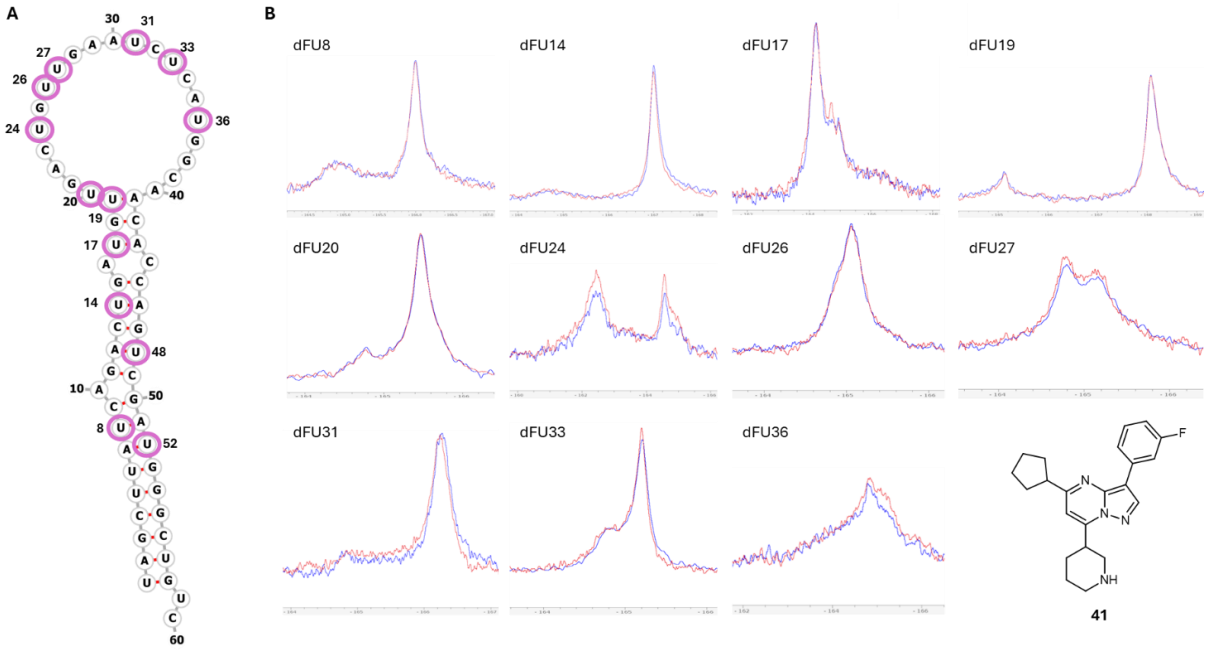

***Figure 5.24**. **A**: Pre-miR21 secondary structure with the substituted dFU bases circled in pink. **B**: dFU ^{19}F-NMR signals upon titration with **41**. In blue, the native free RNA state is shown (*100 µM dFRNA), while in red the signal obtained upon addition of **41** (100 µM).*

Comparison of the free RNA state (blue trace, **Figure 5.24B**) with the spectrum recorded upon addition of **41** (100 µM, red trace, **Figure 5.24B**) revealed three distinct patterns of base dynamics. For residues dFU8, dFU14, dFU17, dFU19, dFU20, and dFU26, the spectra of the free and ligand-bound states were largely overlapping, indicating these nucleotides were not directly involved in the binding event.

A second group of positions, dFU24, dFU27, dFU33, and dFU36, showed an increase in signal intensity upon ligand addition. This behaviour likely reflected a redistribution of conformational populations, consistent with stabilization of the dominant state induced by binding of **41**. Finally, dFU31 exhibited a small chemical shift perturbation, suggesting a change in its local environment and indicating close proximity to the ligand. Taken together, these results pointed to the apical region of the loop as the probable binding site.

Notably, the observed effects extended beyond a single nucleotide, suggesting that ligand binding may induce a broader reorganization of the loop architecture. Similar perturbations would be expected if other biologically relevant probes, such as rFU, sFU, or rFC, are used, with differences primarily reflected in spectral line shapes rather than the identity of affected residues.

From a medicinal chemistry perspective, this study provided two key insights:

1) *Specificity of interaction*: the stem region remained largely unaffected. This indicates that **41** does not intercalate non-specifically, but rather engages in targeted interactions, likely centered around dFU31, where a high degree of order was identified by ^{19}F-probes analysis.
2) *Loop rearrangement and binding mechanism*: multiple positions in the loop showed spectral changes, suggesting a significant structural reorganization upon binding. This observation is compatible with an entropy-driven binding mechanism, potentially involving the release of structural water. Consequently, increasing the size or functional footprint of the chemotype may enhance its interaction with pre-miR21, further promoting loop rearrangement and potentially improving binding affinity.

While these initial findings are indeed valuable for understanding how the new compounds affecr pre-miR21 conformational changes, they do not provide a sufficiently strong foundation for structure-based drug design. Further studies, such as integrating these data with Saturation Transfer Difference (STD) experiments or solving the ligand–target structure based on the ^{19}F-derived data, could represent a reasonable, valuable continuation of this project.

5.6: Experimental part

5.6.1: Phosphonamidites synthesis

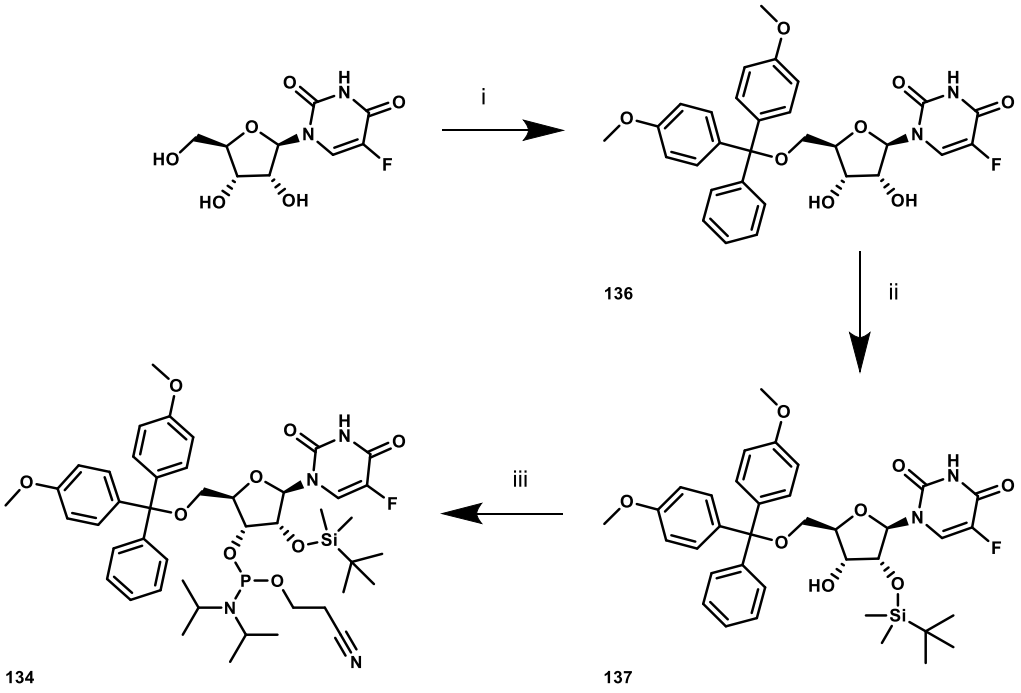

(**i**) 4,4′-Dimethoxytrityl chloride, pyridine, r.t., 16h, 71%; (**ii**) $AgNO_3$, pyridine, tert-Butyldimethylsilyl chloride, THF, r.t., 16h, 81%; (**iii**) DIPEA, 2-Cyanoethyl N,N-diisopropylchlorophosphoramidite, THF, 0°C to r.t., 16h, 92%.

1-((2*R*,3*R*,4*S*,5*R*)-5-((Bis(4-methoxyphenyl)(phenyl)methoxy)methyl)-3,4-dihydroxytetrahydrofuran-2-yl)-5-fluoropyrimidine-2,4(1H,3H)-dione (**136**). In a round-bottom flask under a nitrogen atmosphere, 5-fluorouridine (2.4 g, 9.20 mmol, 1.0 eq) was dissolved in dry pyridine (20 mL, 0.40 M). 4,4'-Dimethoxytrityl chloride (3.42 g, 10.1 mmol, 1.1 eq) was added portionwise, and the reaction mixture was stirred at room temperature for 16 h. Reaction progress was monitored by UPLC–MS. Upon complete consumption of the starting material, the reaction mixture was transferred to a separatory funnel, diluted with ethyl acetate, and washed with saturated aqueous ammonium chloride. The organic layer was collected, dried over anhydrous sodium sulfate, filtered, and concentrated under reduced pressure. The crude product was purified by automated flash chromatography (Biotage) using dichloromethane/methanol as the eluent (0-10% MeOH gradient) to afford the title compound as a white solid (3.7 g, 71%). **MS (ESI)** m/z calc. [M-H]-: 563.19, found 563.1. **^{1}H NMR (400 MHz, $CDCl_3$)** δ 7.91 (d, *J* = 5.8 Hz, 1H), 7.74 – 7.64 (m, 1H), 7.33 – 7.16 (m, 8H), 6.86 – 6.77 (m, 4H), 5.91 (s, 1H), 5.29 (s, 1H), 4.44 – 4.35 (m, 2H), 4.23 – 4.18 (m, 1H), 3.75 (s, 1H), 3.73 (s, 6H), 3.47 – 3.42 (m, 2H).

1-((2*R*,3*R*,4*R*,5*R*)-5-((Bis(4-methoxyphenyl)(phenyl)methoxy)methyl)-3-((tert-butyldimethylsilyl)oxy)-4-hydroxytetrahydrofuran-2-yl)-5-fluoropyrimidine-2,4(1H,3H)-dione (**137**). In a round-bottom flask under an argon atmosphere, **136** (3.7 g, 6.54 mmol, 1.0 eq) was dissolved in dry THF (13 mL, 0.5 M). Pyridine (2.3 mL, 7.19 mmol, 1.1 eq) and silver nitrate (1.22 g, 7.19 mmol, 1.1 eq) were added sequentially, and the reaction mixture was stirred for 20 min. *tert*-Butyldimethylsilyl chloride (1.08 g, 7.19 mmol, 1.1 eq) was then added, and the mixture was stirred at room temperature in the dark for 16 h. Reaction progress was monitored by UPLC–MS. Upon complete consumption of the

starting material, the reaction mixture was filtered through a pad of Celite® and concentrated under reduced pressure. The crude product was purified by automated flash chromatography (Biotage) on silica gel using a cyclohexane/ethyl acetate gradient (0–30% EtOAc) to afford the title compound as a white solid (2.0 g, 81%). **MS (ESI)** m/z calc [M-H]-: 677.28, found 677.3. **^{1}H NMR (400 MHz, DMSO)** δ 7.86 (d, *J* = 6.7 Hz, 1H), 7.32 (d, *J* = 8.0 Hz, 2H), 7.27 – 7.11 (m, 7H), 6.82 (d, *J* = 8.8 Hz, 4H), 5.69 – 5.63 (m, 1H), 5.07 (d, *J* = 6.2 Hz, 1H), 4.19 (t, *J* = 4.5 Hz, 1H), 4.04 – 3.97 (m, 1H), 3.97 – 3.90 (m, 2H), 3.66 (s, 5H), 3.30 (d, *J* = 4.6 Hz, 1H), 3.13 (dd, *J* = 10.7, 2.4 Hz, 1H), 0.79 (s, 9H), -0.00 (d, *J* = 2.2 Hz, 6H).

(2R,3R,4R,5R)-2-((Bis(4-methoxyphenyl)(phenyl)methoxy)methyl)-4-((tert-butyldimethylsilyl)oxy)-5-(5-fluoro-2,4-dioxo-3,4-dihydropyrimidin-1(2H)-yl)tetrahydrofuran-3-yl (2-cyanoethyl) diisopropylphosphoramidite (**134**). In a round-bottom flask under a nitrogen atmosphere, **137** (1.385 g, 2.05 mmol, 1.0 eq) and *N,N*-diisopropylethylamine (2.14 mL, 12.28 mmol, 6.0 eq) were dissolved in dry THF (26 mL, 0.04 M). The reaction mixture was cooled to 0 °C, and 2-cyanoethyl *N,N*-diisopropylchlorophosphoramidite (1.83 mL, 8.18 mmol, 4.0 eq) was added portionwise. The reaction mixture was allowed to warm to room temperature and stirred for 16 h. Reaction progress was monitored by UPLC–MS. Upon complete consumption of the starting material, the reaction was quenched at 0 °C by the addition of methanol, transferred to a separatory funnel, and washed with water. The organic layer was dried over anhydrous sodium sulfate, filtered, and concentrated under reduced pressure. The crude product was purified by automated flash chromatography on silica gel using a hexane/ethyl acetate gradient (0–100% EtOAc) to afford the title compound as a white powder (1.65 g, 92%). **MS (ESI)** m/z calc [M-H]-: 877.39, found 877.6. **^{31}P NMR (202 MHz, CD_3CN)** δ 149.52, 149.14.

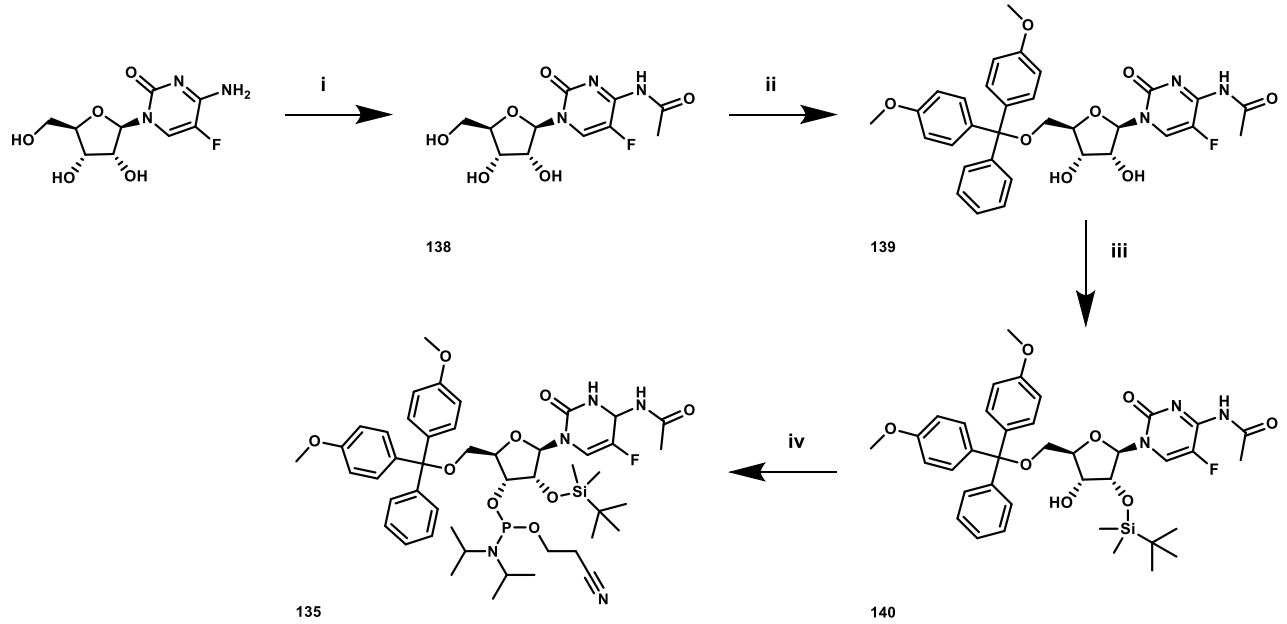

(**i**) Acetic anhydride, DMF, 85°C, 2h, 89%; (**ii**) 4,4′-Dimethoxytrityl chloride, pyridine, r.t., 16h, 49%; (**iii**) $AgNO_3$, pyridine, tert-Butyldimethylsilyl chloride, THF, r.t., 16h, 45%; (**iv**) 2-Cyanoethyl N,N-diisopropylchlorophosphoramidite, DIPEA, THF, 0°C to r.t., 16h, 85%.

***N*-(1-((2*R*,3*R*,*4S*,5*R*)-3,4-Dihydroxy-5-(hydroxymethyl)tetrahydrofuran-2-yl)-5-fluoro-2-oxo-1,2-dihydropyrimidin-4-yl)acetamide** (**138**). Under a nitrogen atmosphere, 5-fluorocytidine (2.0 g, 7.66 mmol, 1.0 eq) was dissolved in *N,N*-dimethylformamide (DMF, 10 mL) at room temperature with stirring. Acetic anhydride (0.78 g, 7.66 mmol, 1.0 eq) was added, and the reaction mixture was heated to 85°C. Reaction progress was monitored by UPLC–MS and thin-layer chromatography (TLC) using

dichloromethane/methanol (80:20, v/v) as the eluent. After 2 h, the reaction mixture was cooled to room temperature, and the product was isolated by precipitation into toluene. The resulting solid was collected and washed with cold methanol to afford the title pure compound, as a white foam (2.06 g, 89%). **MS (ESI)** m/z calc [M-H]-: 302.09, found 302.1**. ^{1}H NMR (400 MHz, DMSO)** δ 10.57 (bs, 1H), 8.70 (d, *J* = 6.8 Hz, 1H), 5.72 – 5.67 (m, 1H), 5.55 (d, *J* = 4.5 Hz, 1H), 5.35 (t, *J* = 4.8 Hz, 1H), 5.05 (d, *J* = 5.7 Hz, 1H), 4.05 – 3.95 (m, 2H), 3.95 – 3.87 (m, 1H), 3.83 – 3.74 (m, 1H), 3.67 – 3.57 (m, 1H), 2.23 (s, 3H).

***N*-(1-((2*R*,3*R*,4*S*,5*R*)-5-((Bis(4-methoxyphenyl)(phenyl)methoxy)methyl)-3,4-dihydroxytetrahydrofuran-2-yl)-5-fluoro-2-oxo-1,2-dihydropyrimidin-4-yl)acetamide** (**139**). Under a nitrogen atmosphere, **138** (2.06 g, 6.80 mmol, 1.0 eq) was dissolved in dry pyridine (17 mL) with stirring. 4,4'-(Chloro(phenyl)methylene)bis(methoxybenzene) (2.3 g, 6.8 mmol, 1.0 eq) was added portionwise over 1 h. Reaction progress was monitored by UPLC–MS. After stirring at room temperature for 16 h, the reaction mixture was diluted with ethyl acetate (20 mL) and washed with saturated aqueous ammonium chloride (2 × 10 mL). The organic layer was dried over anhydrous sodium sulfate, filtered, and concentrated under reduced pressure. The crude material was purified by automated flash chromatography (Biotage) using a 24 g silica gel column (Looknova) and a dichloromethane/methanol gradient. The product eluted at 10% MeOH to afford the title compound, as a yellow oil (2.03 g, 49%). **MS (ESI)** m/z calc [M-H]-: 604.22, found 604.2**. ^{1}H NMR (400 MHz, $CDCl_3$)** δ 8.66 – 8.60 (m, 1H), 8.08 (d, *J* = 5.8 Hz, 1H), 7.86 (bs, 1H), 7.37 – 7.15 (m, 9H), 6.88 – 6.73 (m, 4H), 5.78 (d, *J* = 4.2 Hz, 1H), 4.57 (t, *J* = 4.7 Hz, 1H), 4.52 – 4.41 (m, 2H), 3.80 (d, *J* = 3.7 Hz, 6H), 3.44 – 3.30 (m, 2H), 2.69 (s, 3H), 2.06 (s, 6H).

***N*-(1-((2*R*,3*R*,4*R*,5*R*)-5-((Bis(4-methoxyphenyl)(phenyl)methoxy)methyl)-3-((tert-butyldimethylsilyl)oxy)-4-hydroxytetrahydrofuran-2-yl)-5-fluoro-2-oxo-1,2-dihydropyrimidin-4-yl)acetamide** (**140**). Under an inert atmosphere, **139** (1.887 g, 3.34 mmol, 1.0 eq) was dissolved in pyridine (10 mL) and stirred in the dark. Silver nitrate (0.622 g, 3.68 mmol, 1.1 eq) was added, and the reaction mixture was stirred for 30 min. *tert*-Butyldimethylsilyl chloride (TBSCl) (0.601 g, 4.01 mmol, 1.2 eq) was then added, and reaction progress was monitored by UPLC–MS. After stirring at room temperature in the dark for 16 h, the reaction mixture was filtered through a pad of Celite® using ethyl acetate as the eluent. The filtrate was washed with saturated aqueous ammonium chloride (2 × 10 mL) and saturated aqueous sodium bicarbonate (2 × 10 mL). The organic layer was dried over anhydrous sodium sulfate, filtered, and concentrated under reduced pressure at room temperature. The crude product was purified by automated flash chromatography (Biotage) using a 25 g silica gel column (Looknova) and a cyclohexane/ethyl acetate gradient. The product eluted at 30% EtOAc to afford the title compound, as a white foam (1.02 g, 45%). **MS (ESI)** m/z calc [M-H]-: 718.30, found 718.3**. ^{1}H NMR (400 MHz, DMSO)** δ 10.46 (bs, 1H), 8.11 (d, *J* = 6.1 Hz, 1H), 7.36 – 7.29 (m, 2H), 7.27 – 7.10 (m, 8H), 6.85 – 6.77 (m, 4H), 5.55 (t, *J* = 1.7 Hz, 1H), 5.05 (d, *J* = 6.2 Hz, 1H), 4.15 – 4.10 (m, 1H), 4.10 – 4.03 (m, 1H), 4.03 – 3.95 (m, 1H), 3.65 (s, 6H), 3.31 (dd, *J* = 11.0, 4.4 Hz, 1H), 3.19 (dd, *J* = 11.0, 2.1 Hz, 1H), 2.15 (s, 3H), 0.80 (s, 8H), 0.80 (d, *J* = 5.9 Hz, 1H).

(2*R*,3*R*,4*R*,5*R*)-5-(4-Acetamido-5-fluoro-2-oxo-3,4-dihydropyrimidin-1(2H)-yl)-2-((bis(4-methoxyphenyl)(phenyl)methoxy)methyl)-4-((tert-butyldimethylsilyl)oxy)tetrahydrofuran-3-yl (2-cyanoethyl) diisopropylphosphoramidite (**135**). In a round bottom flask, under nitrogen atmosphere, **140** (0.75 g, 1.05, 1.0 eq) and N,N-diisopropylethylamine (1.1 mL, 6.29 mmol, 6 eq) were dissolved in THF (28 mL, 0.04 M). Temperature was lowered to 0°C and 2-cyanoethyl N,N-diisopropylchlorophosphoramidite (0.94 mL, 4.2 mmol, 4.0 eq) was added portionwise to the reaction mixture. The reaction was kept stirring for 16h, reaching room temperature. After disappearance of the starting material, the reaction was quenched at 0°C with MeOH, transferred into a separatory funnel and washed with water. The organic layer was dried with sodium sulfate, concentrated under vacuum and purified by automated flash chromatography, using silica and as eluent phase hexane/ethyl acetate

gradient from 0 to 100%. The final product was obtained as a white powder (0.825 g, 85%). **MS (ESI)** m/z calc [M-H]-: 920.43, found 918.6 (major), 920.6 (minor)**. ^{31}P NMR (202 MHz, CD_3CN)** δ 149.69, 148.61.

5.6.2: Purity analyses of synthesized RNAs

All reagents and commercial phosphoramidites were procured from Sigma-Aldrich (Merck Group), TCI Chemicals, and WuXi AppTec, and were employed without further purification unless explicitly noted. The phosphoramidites of 5-fluorouridine (rFU) and 5-fluorocytidine (rFC) were prepared in-house as described in **Paragraph 5.4.2**. Commercially available phosphoramidites were used for 2'-fluorouridine (sFU) and 5-fluoro-2'-deoxyuridine (dFU). Acetonitrile (LiChrosolv grade) utilized for oligonucleotide synthesis was purchased from Sigma-Aldrich and further dried and purified immediately prior to use by passing through an MBRAUN SPS Compact solvent purification system under a nitrogen atmosphere. Fluorinated RNA sequences were synthesized on a MerMade48 automated synthesizer (Biosearch Technologies) at a 5 µmol scale using universal linker-functionalized CPG resin (CUTAG CPG, Sigma-Aldrich). Phosphoramidites were prepared as 0.1 M solutions in anhydrous acetonitrile. Coupling reactions were carried out using 0.25 M 5-[3,5-bis(trifluoromethyl)phenyl]-1H-tetrazole in acetonitrile over four consecutive 9-minute cycles.

Oxidation of the phosphite intermediates was performed with 0.02 M iodine in tetrahydrofuran/water/pyridine (90.54:9.05:0.41, v/v/v) for 1 minute. Unreacted 5'-hydroxyl groups were capped with Cap A (acetic anhydride/tetrahydrofuran, 9.1:90.9, v/v) and Cap B (tetrahydrofuran/N-methylimidazole/pyridine, 8:1:1, v/v) for 1 minute. Detritylation was achieved using 3% dichloroacetic acid in toluene. After the final detritylation, 2-cyanoethyl protecting groups were removed by treatment with 20% diethylamine in acetonitrile. The resin-bound oligonucleotides were then subjected to a mixture of 30% ammonium hydroxide and 40% aqueous methylamine (1:1, v/v) at 65 °C for 60 minutes to effect base deprotection and cleavage from the solid support. Following addition of 200 µL of 1 M Tris–HCl, the solution was lyophilized. The intermediate oligonucleotide was subsequently treated with tetrabutylammonium fluoride in tetrahydrofuran at room temperature for 24 hours to remove 2'-protecting groups. Afterward, 200 µL of sodium acetate buffer (pH 5.2) was added, and the RNA was precipitated using a tert-butanol/ethanol mixture, followed by dialysis through a 10 kDa molecular weight cutoff spin column. Crude RNA products were purified by reverse-phase high-performance liquid chromatography (RP-HPLC) on a Waters LC 150 system equipped with an XBridge BEH C18 OBD Prep column (130 Å, 5 µm, 10 × 250 mm). Ion-pairing chromatography was performed using 0.1 M triethylammonium acetate buffer, with a linear gradient from 5% to 20% acetonitrile in water over 30 minutes. The identity and purity of the synthesized oligonucleotides were confirmed by LC–MS analysis using an Acquity I-Class LC system equipped with a PDA detector coupled to an RDa mass detector via heated electrospray ionization (BioAccord, Waters Corporation). Oligonucleotide concentrations and overall yields were determined spectrophotometrically using a NanoDrop instrument.

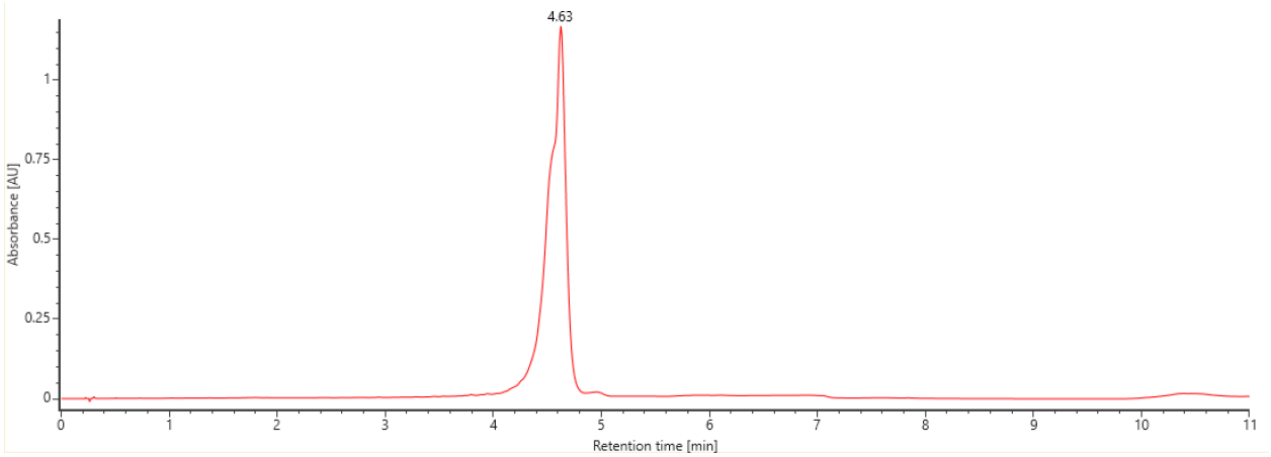

***Figure 5.25**. Purified rFU8. HRMS (ESI-) calculated: 19221.317, observed deconvoluted: 19221.183. UV Purity at 260 nm: 51%.*

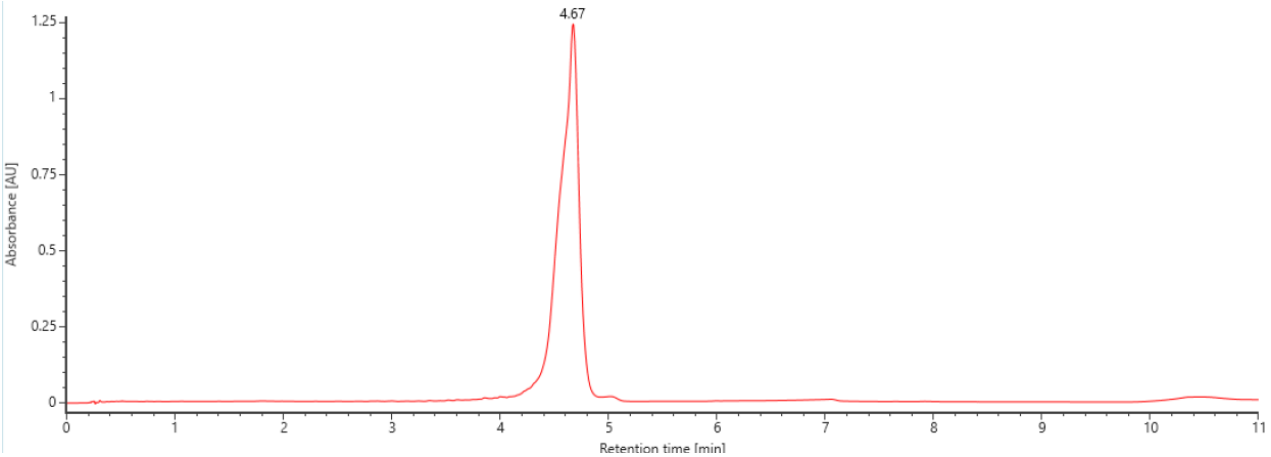

***Figure 5.26**. Purified rFU14. HRMS (ESI-) HRMS (ESI-) calculated 19221.317, observed deconvoluted 19221.183. UV Purity at 260 nm: 55%.*

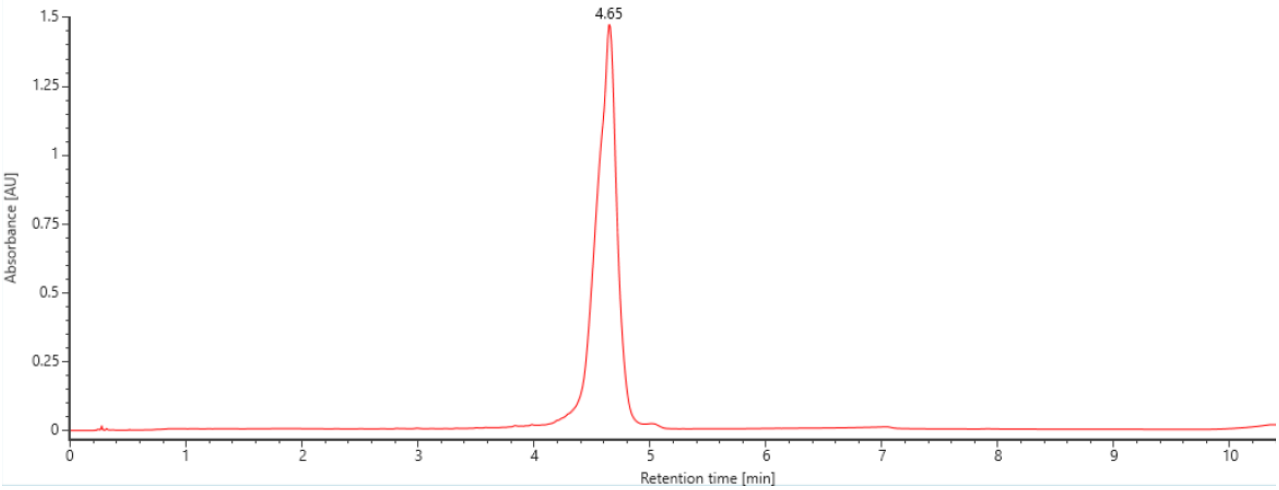

***Figure 5.27**. Purified rFU17. HRMS (ESI-) HRMS (ESI-) calculated 19221.317, observed deconvoluted 19221.582. UV Purity at 260 nm: 63%.*

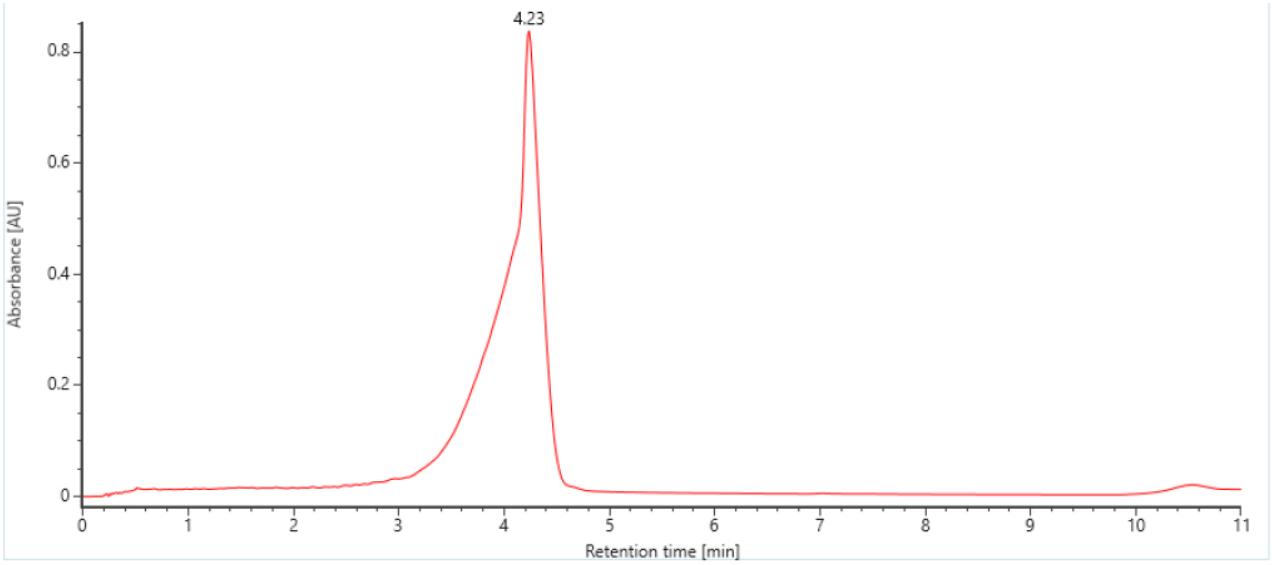

***Figure 5.28**. Purified rFU19. HRMS (ESI-) HRMS (ESI-) calculated 19221.317, observed deconvoluted 19221.004. UV Purity at 260 nm: 53%.*

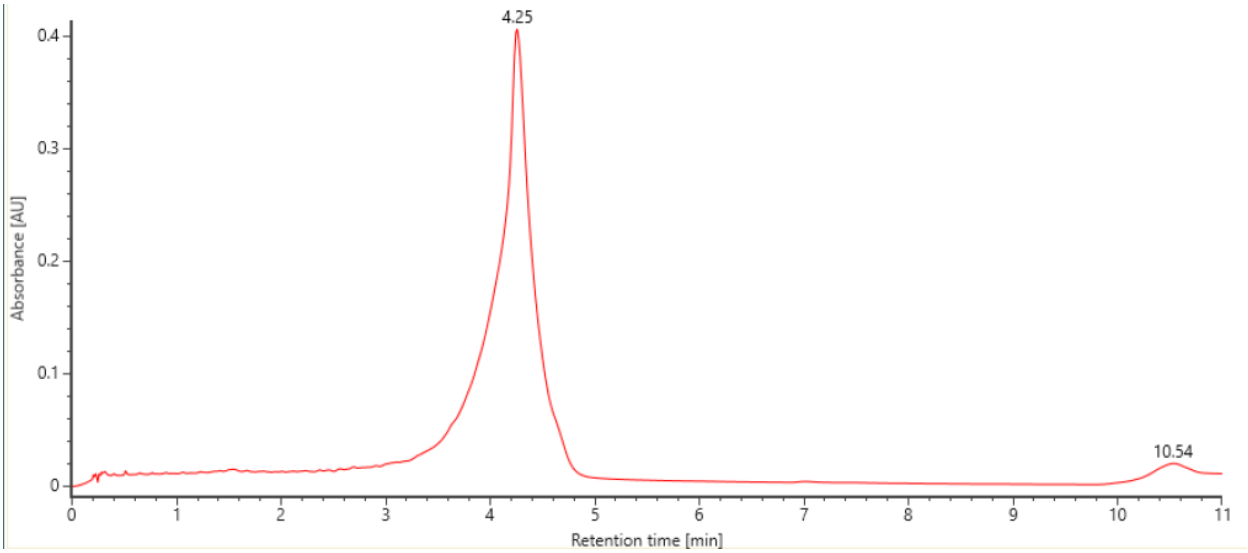

***Figure 5.29**. Purified rFU20. HRMS (ESI-) HRMS (ESI-) calculated 19221.317, observed deconvoluted 19221.563. UV Purity at 260 nm: 81%.*

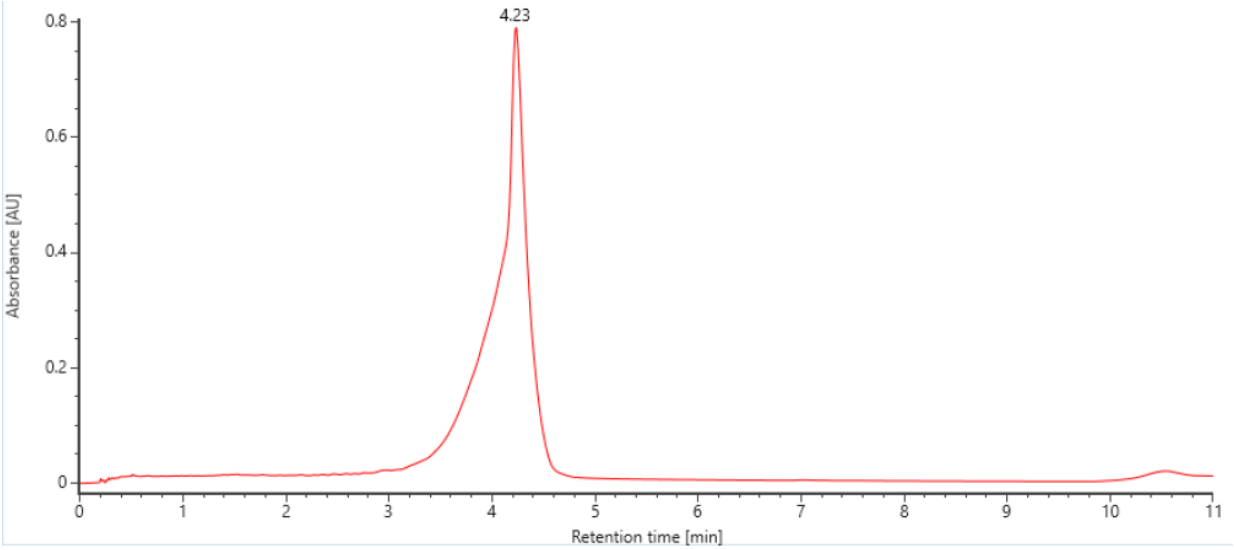

***Figure 5.30**. Purified rFU24. HRMS (ESI-) HRMS (ESI-) calculated 19221.317, observed deconvoluted 19221.183. UV Purity at 260 nm: 54%.*

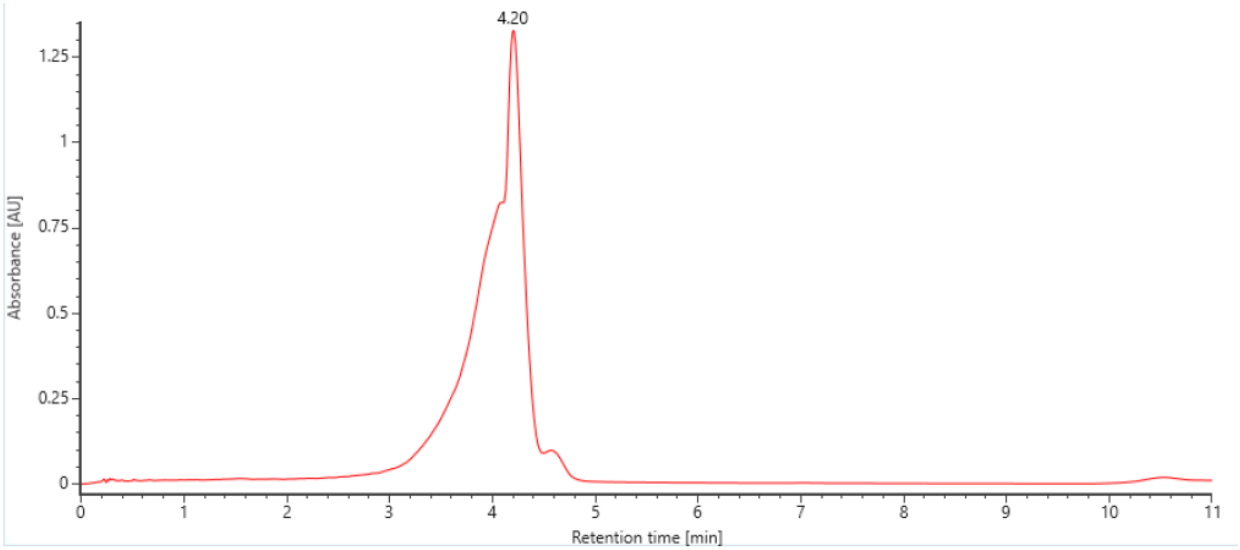

***Figure 5.31**. Purified rFU27. HRMS (ESI-) HRMS (ESI-) calculated 19221.317, observed deconvoluted 19221.183. UV Purity at 260 nm: 51%.*

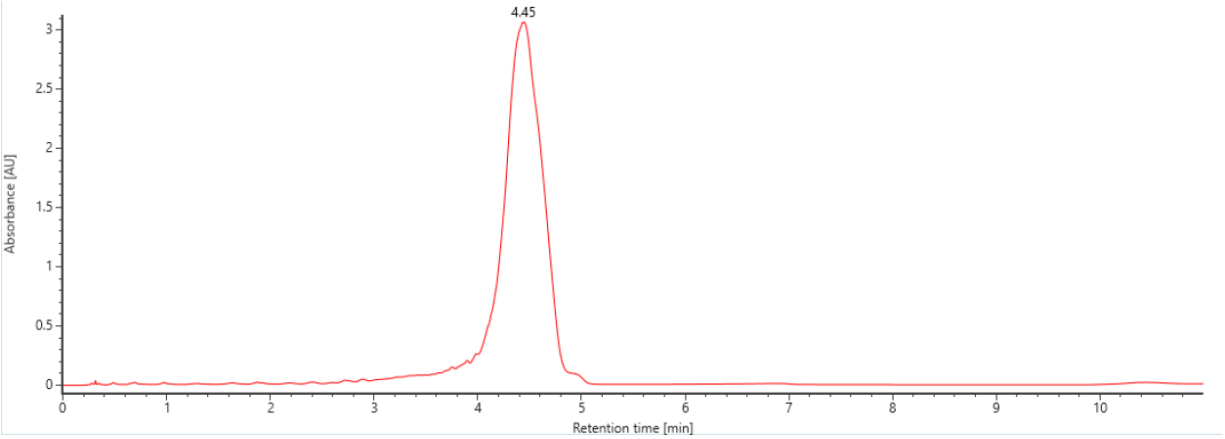

***Figure 5.32**. Purified rFU31. HRMS (ESI-) HRMS (ESI-) calculated 19221.317, observed deconvoluted 19221.416. UV Purity at 260 nm: 78%.*

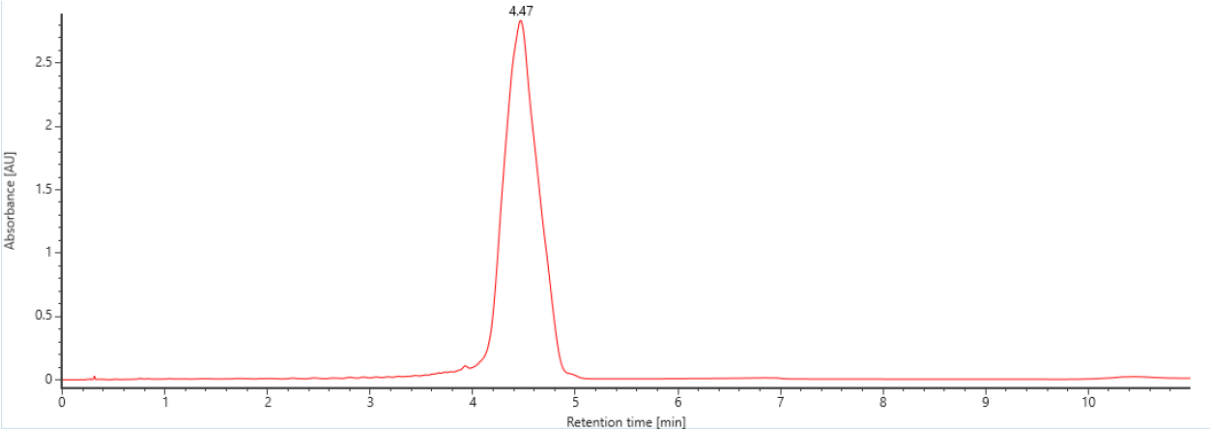

***Figure 5.33**. Purified rFU33. HRMS (ESI-) HRMS (ESI-) calculated 19221.317, observed deconvoluted 19221.563. UV Purity at 260 nm: 84%.*

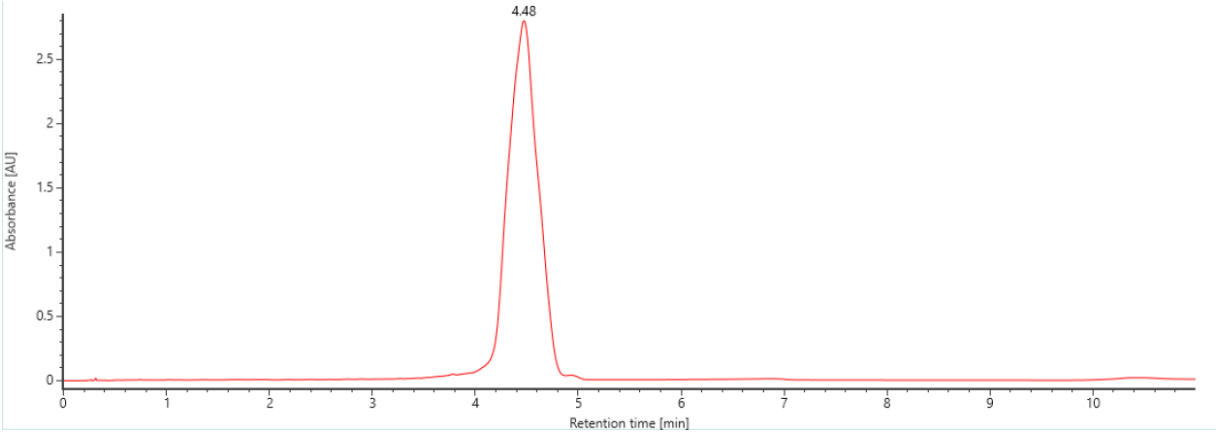

***Figure 5.34**. Purified rFU36. HRMS (ESI-) HRMS (ESI-) calculated 19221.317, observed deconvoluted 19221.183. UV Purity at 260 nm: 72%.*

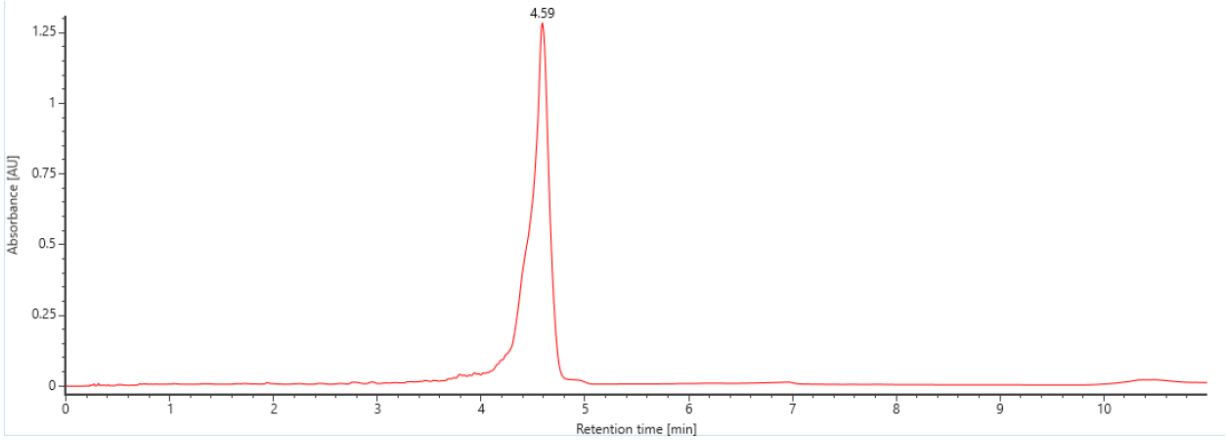

***Figure 5.35**. Purified rFU48. HRMS (ESI-) HRMS (ESI-) calculated 19221.317, observed deconvoluted 19221.416. UV Purity at 260 nm: 71%.*

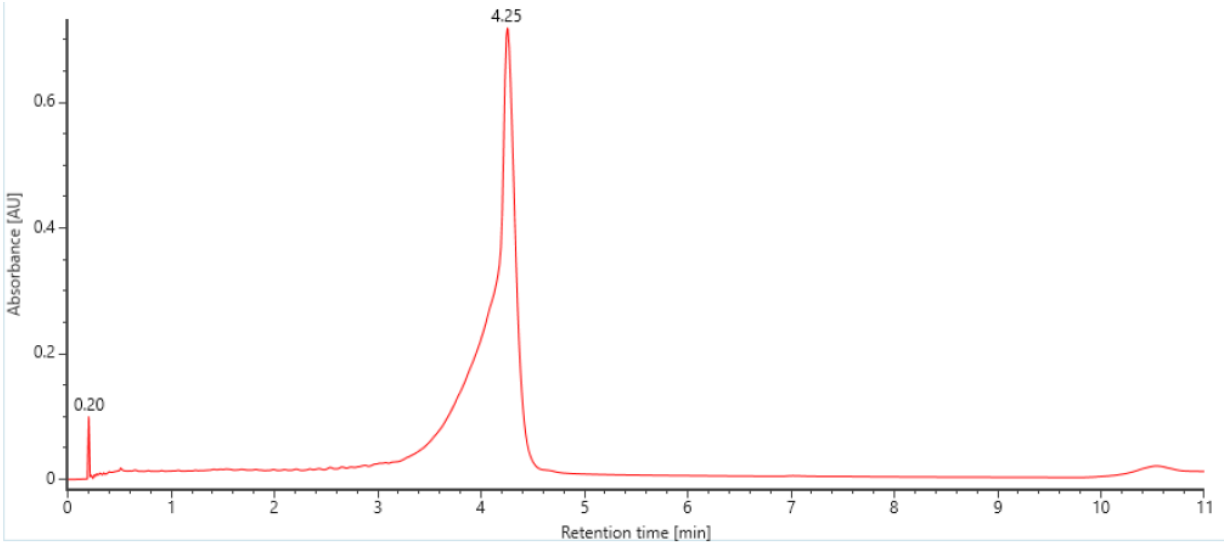

***Figure 5.36**. Purified rFU52. HRMS (ESI-) HRMS (ESI-) calculated 19221.317, observed deconvoluted 19221.426. UV Purity at 260 nm: 56%.*

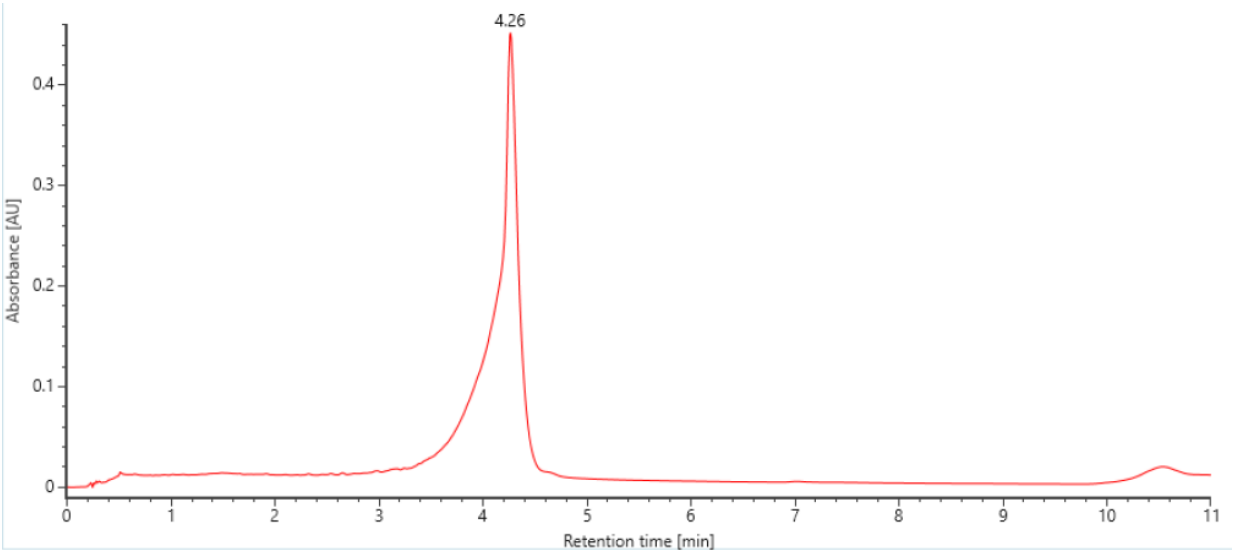

***Figure 5.37**. Purified rFC23. HRMS (ESI-) HRMS (ESI-) calculated 19221.317, observed deconvoluted 19221.183. UV Purity at 260 nm: 60%.*

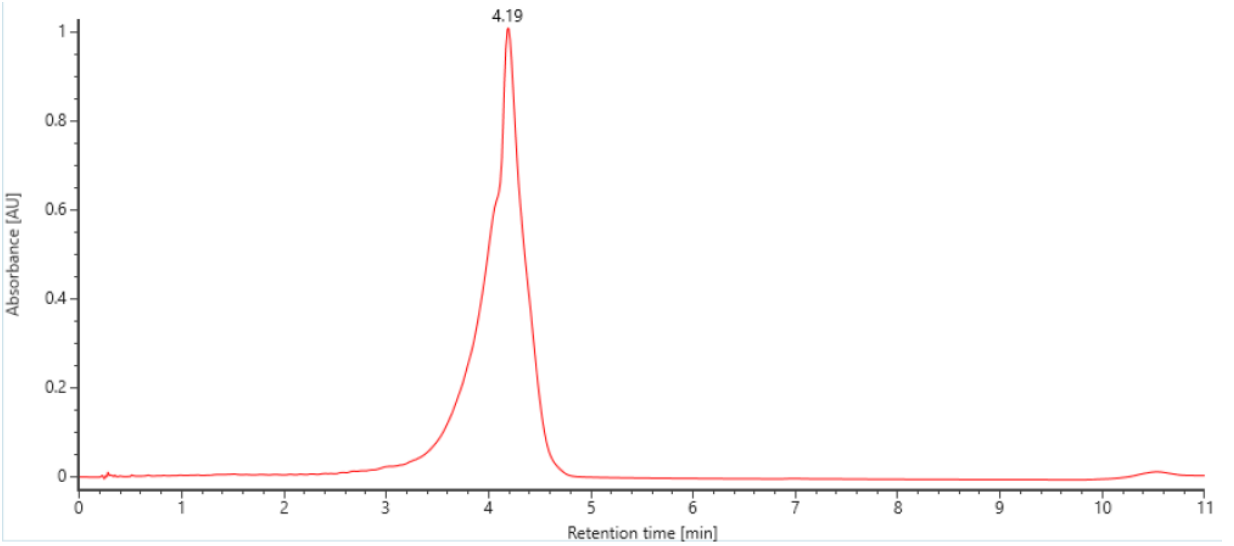

***Figure 5.38**. Purified rFC34. HRMS (ESI-) HRMS (ESI-) calculated 19221.317, observed deconvoluted 19221.144. UV Purity at 260 nm: 61%.*

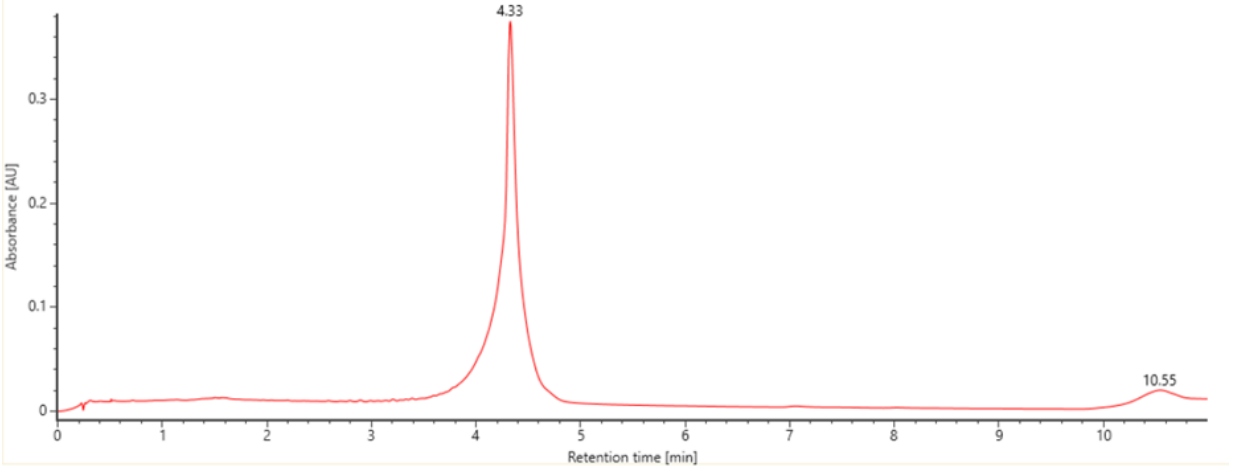

***Figure 5.39**. Purified rFC39. HRMS (ESI-) HRMS (ESI-) calculated 19221.317, observed deconvoluted 19221.183. UV Purity at 260 nm: 59%.*

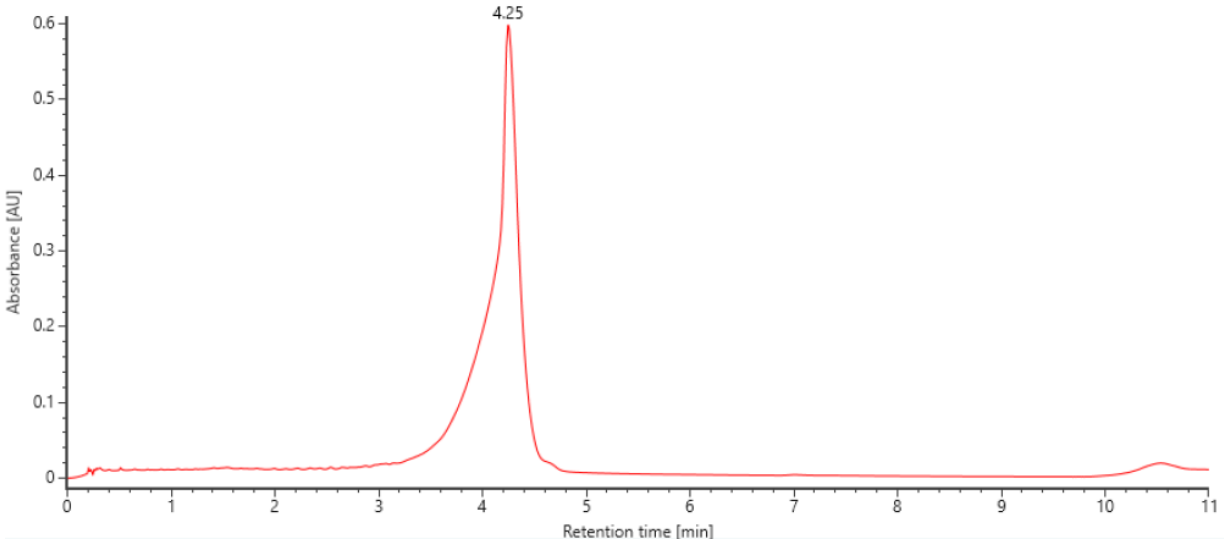

Figure 5.40. *Purified rFC42. HRMS (ESI-) HRMS (ESI-) calculated 19221.317, observed deconvoluted 19220.849. UV Purity at 260 nm: 62%.*

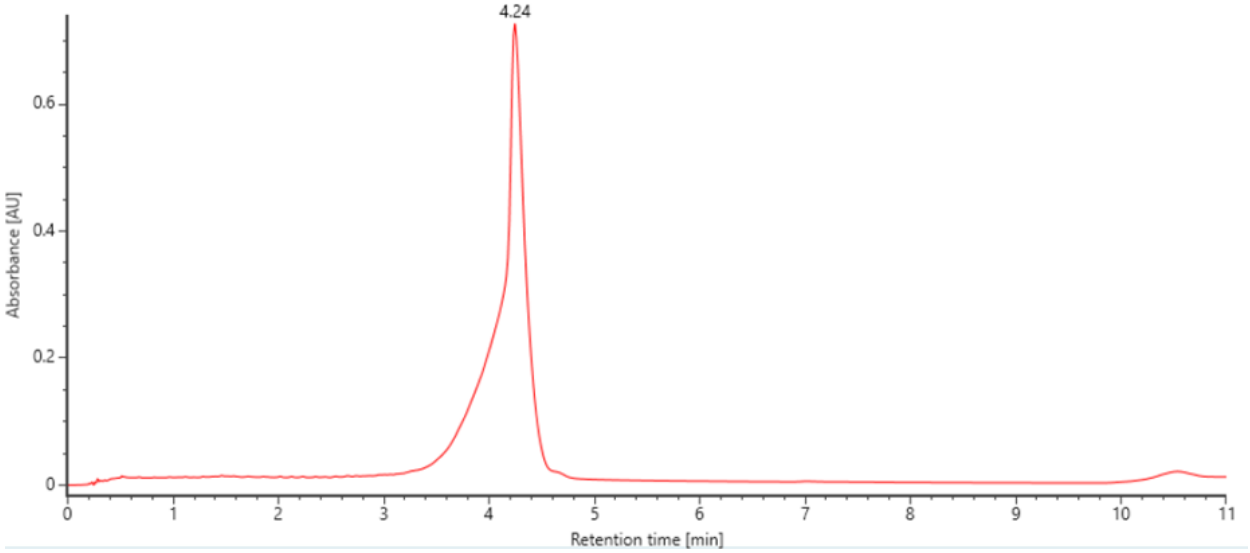

Figure 5.41. *Purified rFC44. HRMS (ESI-) HRMS (ESI-) calculated 19221.317, observed deconvoluted 19220.386. The discrepancy in the mass deconvolution is due to wrong peak selection in the MS spectra. UV Purity at 260 nm: 56%.*

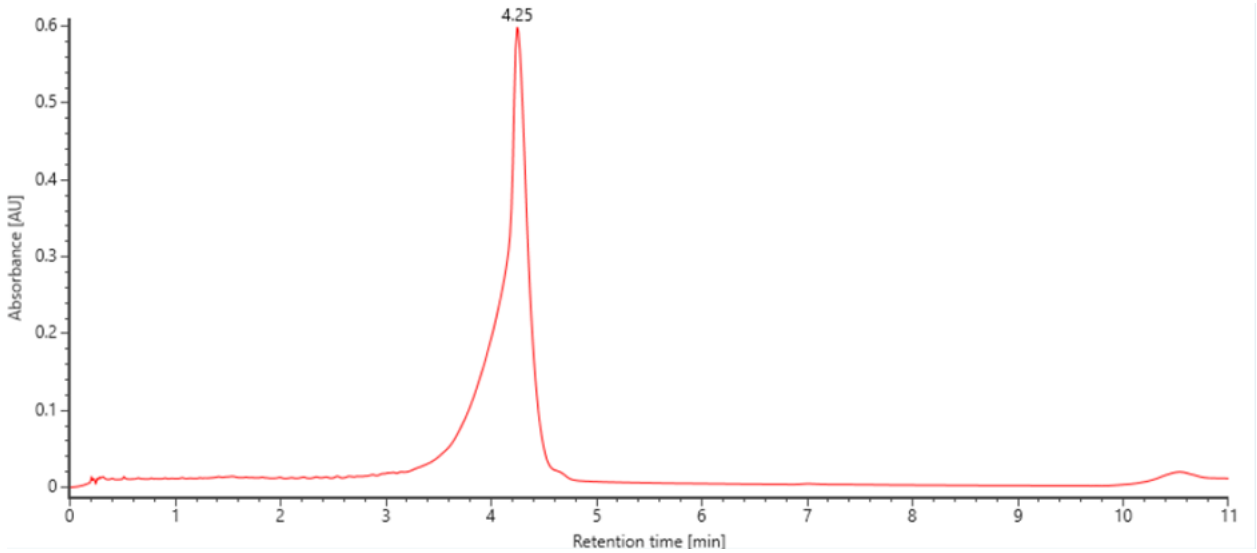

***Figure 5.42**. Purified rFC45. HRMS (ESI-) HRMS (ESI-) calculated 19221.317, observed deconvoluted 19221.183. UV Purity at 260 nm: 57%.*

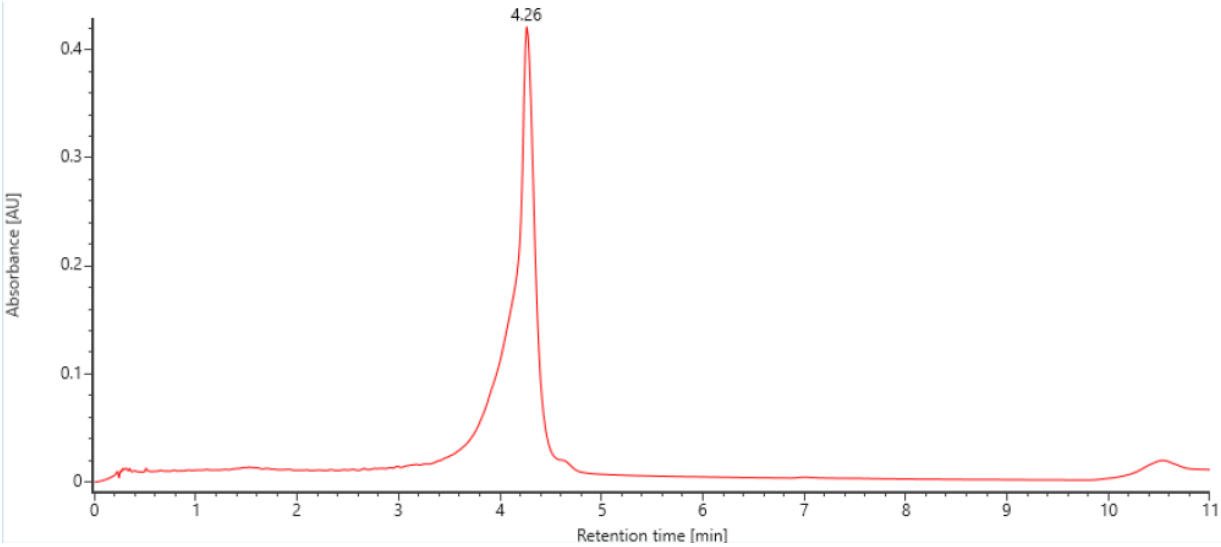

***Figure 5.43**. Purified rFC49. HRMS (ESI-) HRMS (ESI-) calculated 19221.317, observed deconvoluted 19221.416. UV Purity at 260 nm: 65%.*

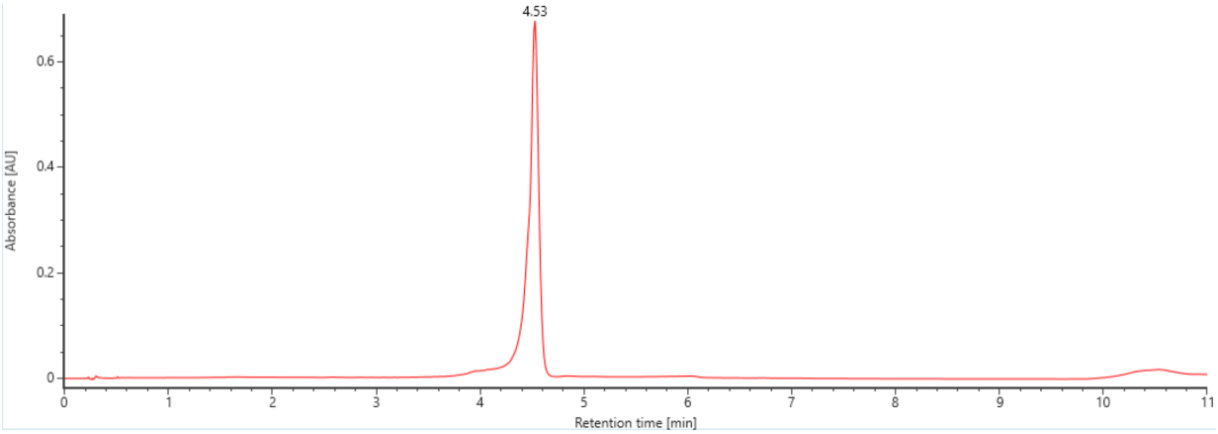

***Figure 5.44**. Purified sFU8. HRMS (ESI-) HRMS (ESI-) calculated 19205.308, observed deconvoluted 19205.363. UV Purity at 260 nm: 69%.*

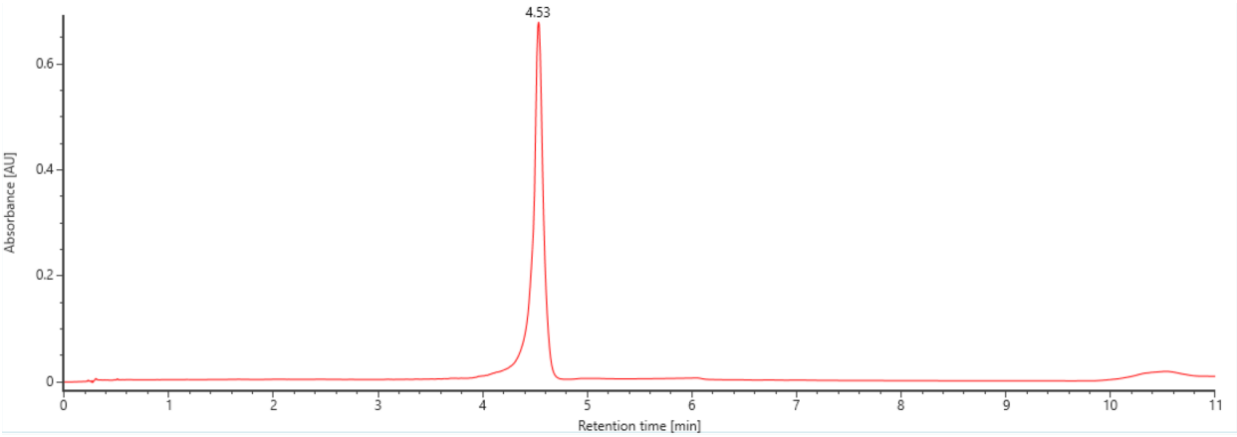

***Figure 5.45**. Purified sFU14. HRMS (ESI-) HRMS (ESI-) calculated 19205.308, observed deconvoluted 19205.364. UV Purity at 260 nm: 81%.*

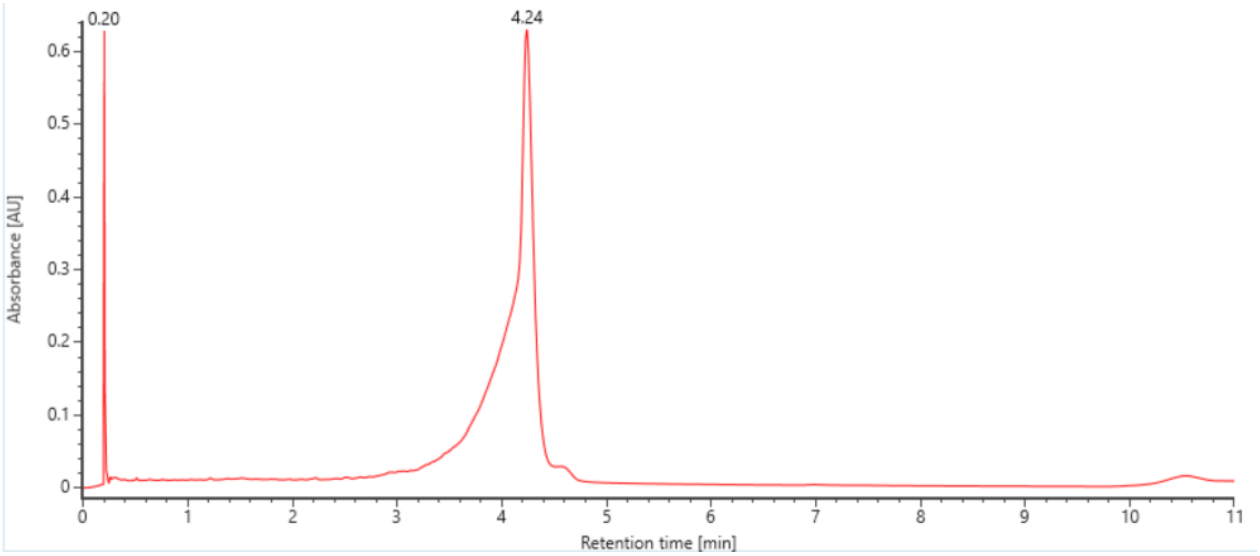

***Figure 5.46**. Purified sFU17. HRMS (ESI-) HRMS (ESI-) calculated 19205.308, observed deconvoluted 19205.101. UV Purity at 260 nm: 59%.*

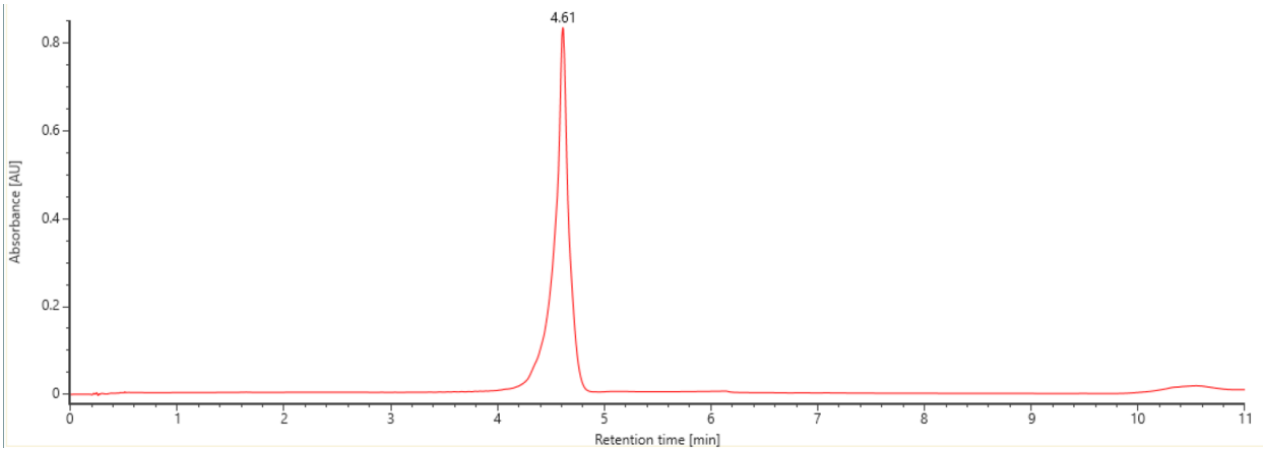

***Figure 5.47**. Purified sFU20. HRMS (ESI-) HRMS (ESI-) calculated 19205.308, observed deconvoluted 19205.776. UV Purity at 260 nm: 84%.*

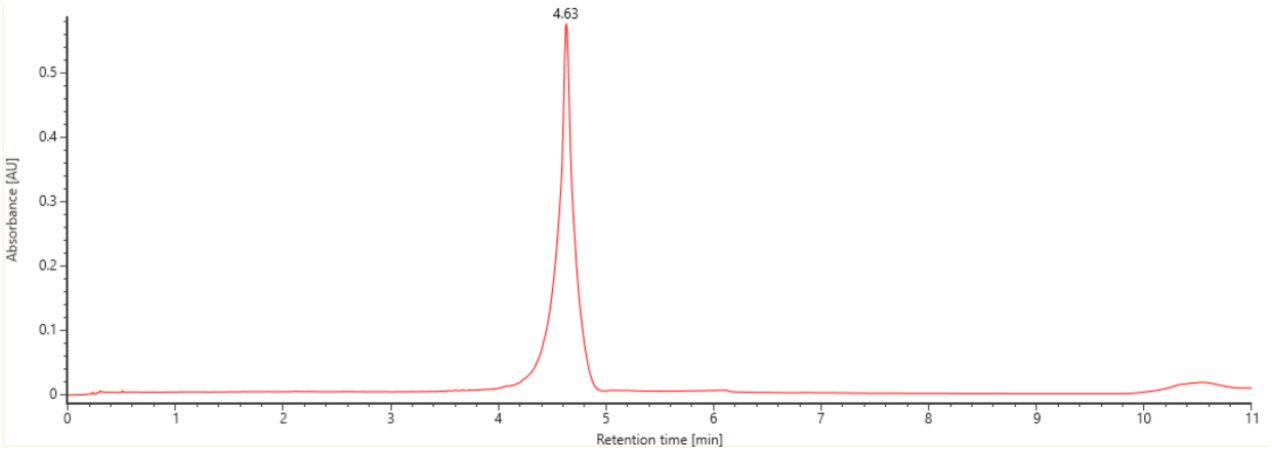

***Figure 5.48**. Purified sFU24. HRMS (ESI-) HRMS (ESI-) calculated 19205.308, observed deconvoluted 19204.844. UV Purity at 260 nm: 86%.*

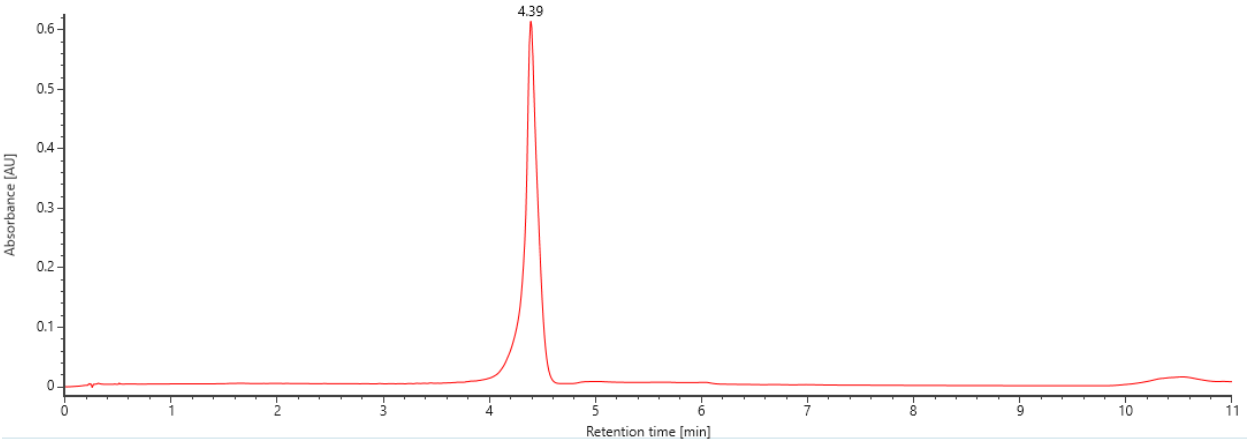

***Figure 5.49**. Purified sFU27. HRMS (ESI-) HRMS (ESI-) calculated 19205.308, observed deconvoluted 19204.446. UV Purity at 260 nm: 83%.*

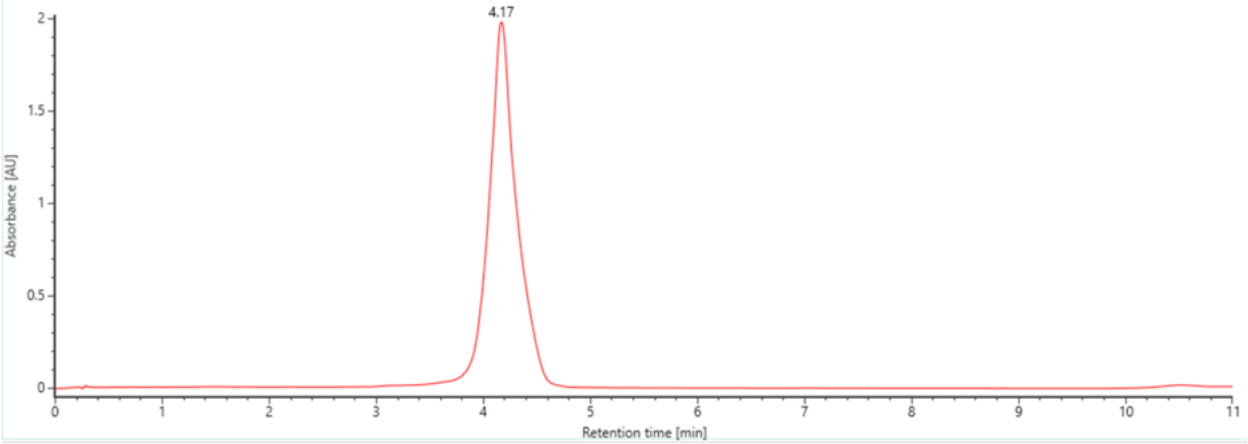

***Figure 5.50**. Purified sFU31. HRMS (ESI-) HRMS (ESI-) calculated 19205.308, observed deconvoluted 19205.363. UV Purity at 260 nm: 85%.*

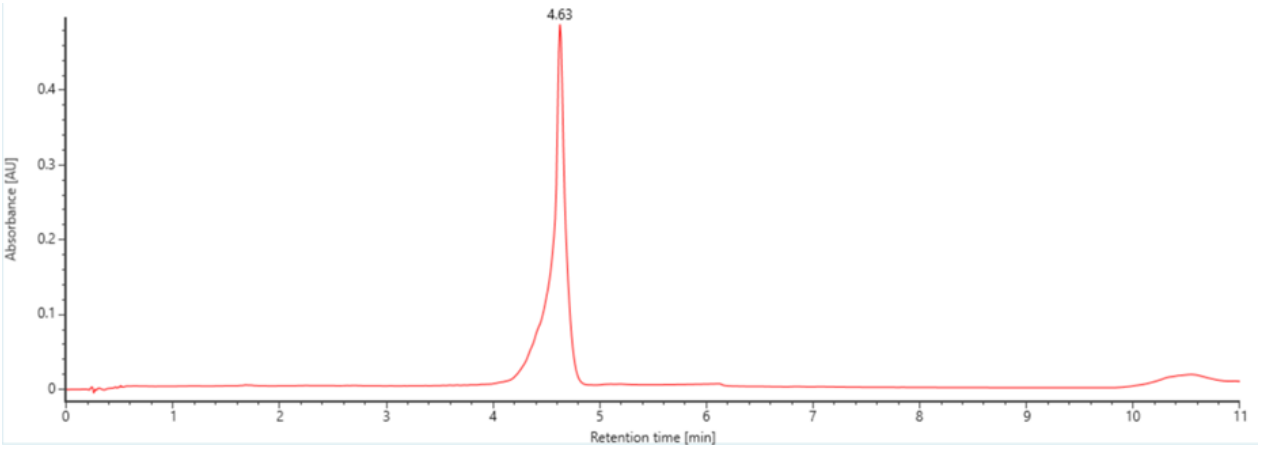

Figure 5.51. *Purified sFU33. HRMS (ESI-) HRMS (ESI-) calculated 19205.308, observed deconvoluted 19205.235. UV Purity at 260 nm: 74%.*

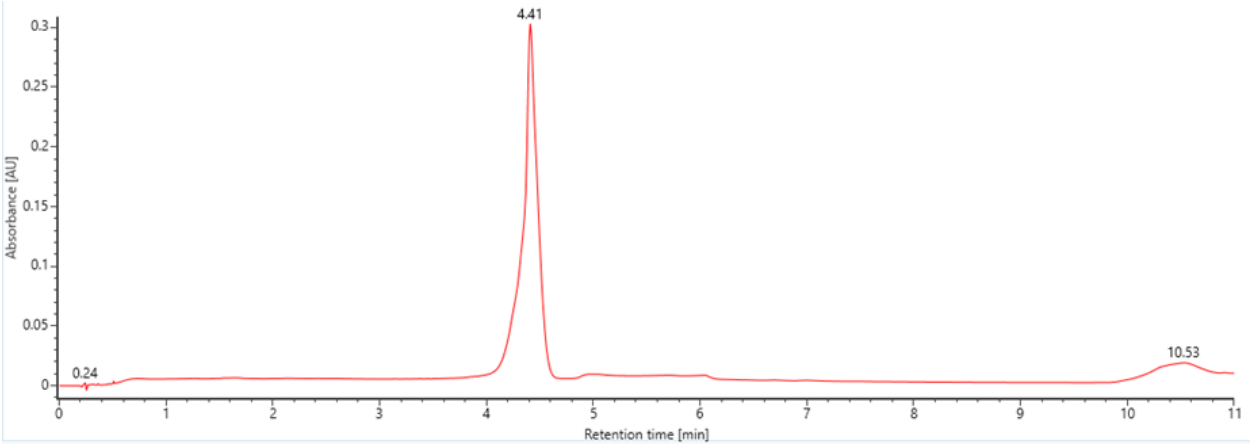

Figure 5.52. *Purified sFU36. HRMS (ESI-) HRMS (ESI-) calculated 19205.308, observed deconvoluted 19205.243. UV Purity at 260 nm: 65%.*

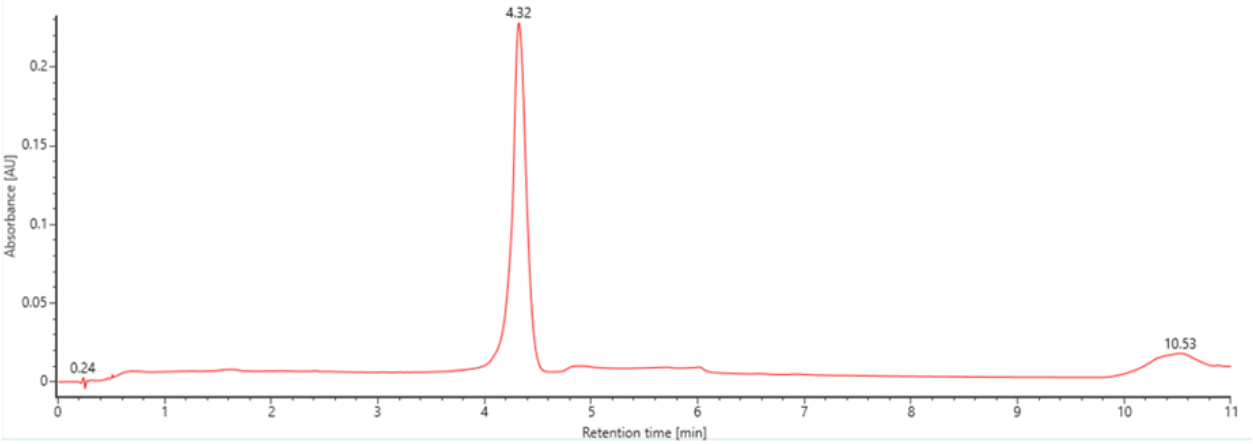

Figure 5.53. *Purified sFU48. HRMS (ESI-) HRMS (ESI-) calculated 19205.308, observed deconvoluted 19205.363. UV Purity at 260 nm: 78%.*

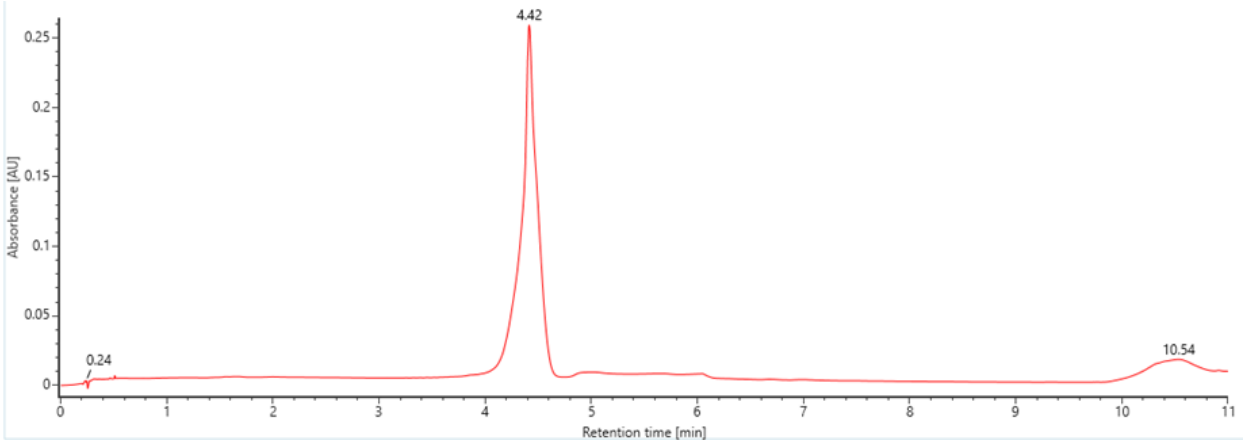

***Figure 5.54**. Purified sFU52. HRMS (ESI-) HRMS (ESI-) calculated 19205.308, observed deconvoluted 19204.362. UV Purity at 260 nm: 50%.*

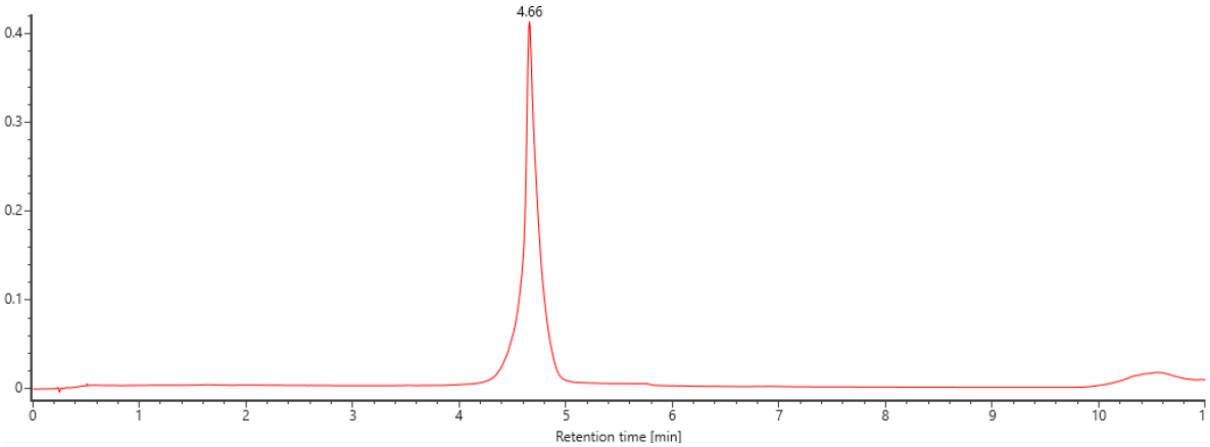

***Figure 5.55**. Purified dFU6. HRMS (ESI-) HRMS (ESI-) calculated 19205.308, observed deconvoluted 19205.644. UV Purity at 260 nm: 60%.*

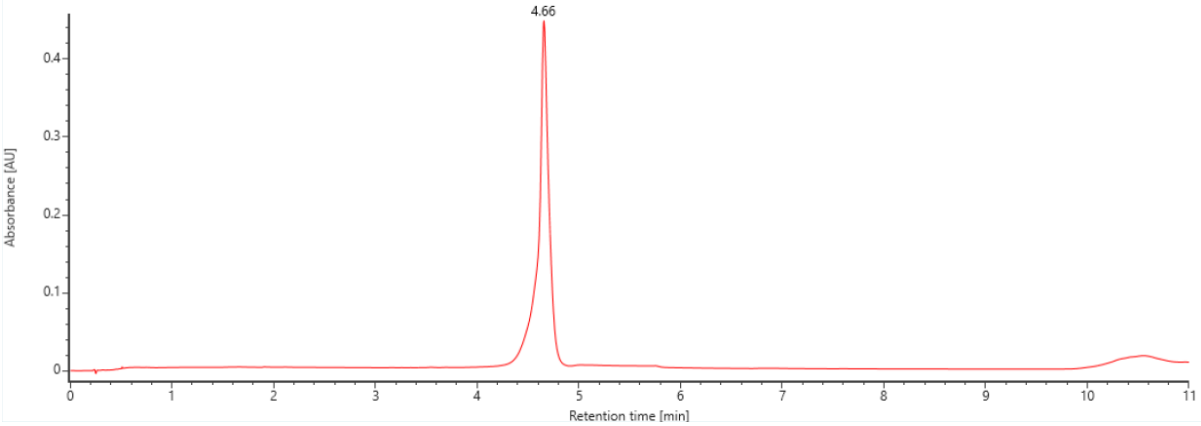

***Figure 5.56**. Purified dFU8. HRMS (ESI-) HRMS (ESI-) calculated 19205.308, observed deconvoluted 19204.973. UV Purity at 260 nm: 67%.*

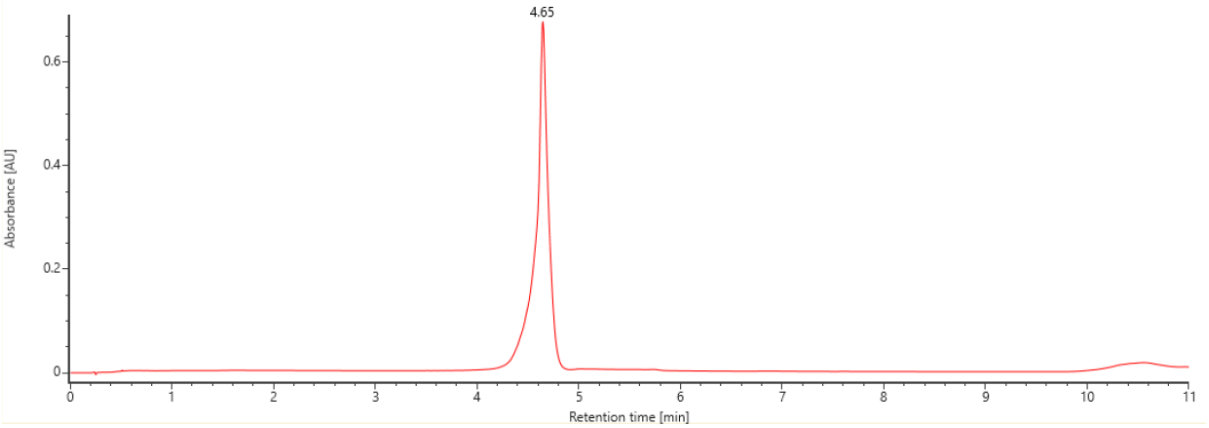

***Figure 5.57**. Purified dFU14. UV Purity at 260 nm: 70%.*

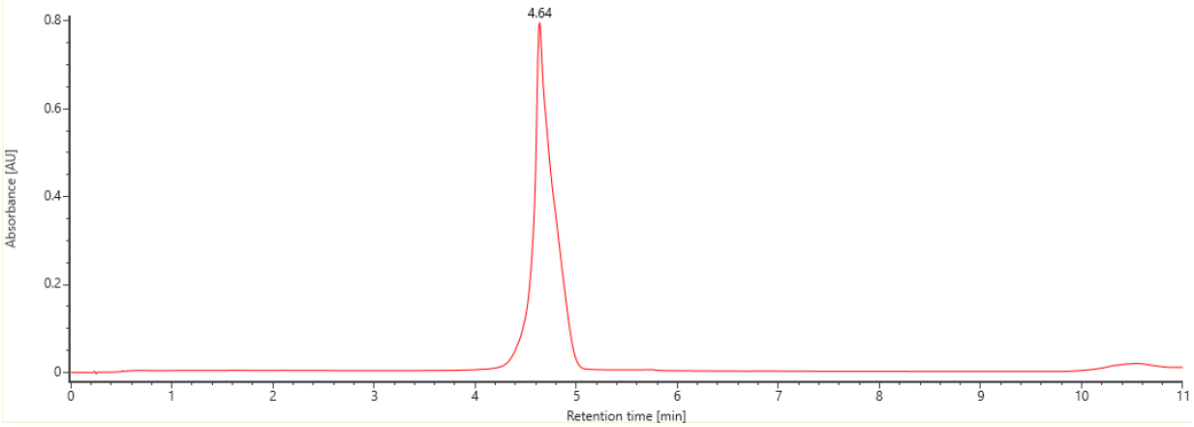

***Figure 5.58**. Purified dFU17. HRMS (ESI-) HRMS (ESI-) calculated 19205.308, observed deconvoluted 20805.387. UV Purity at 260 nm: 50%.*

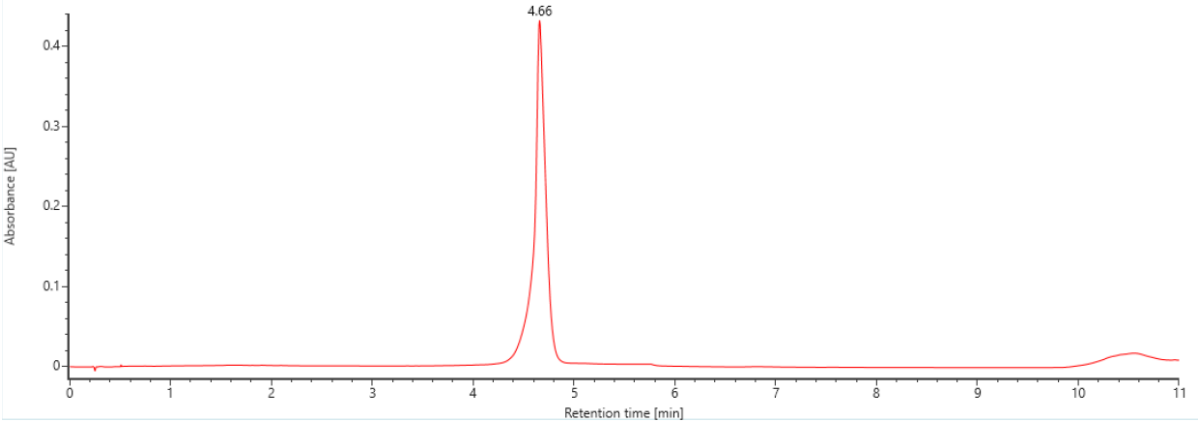

***Figure 5.59**. Purified dFU19. HRMS (ESI-) HRMS (ESI-) calculated 19205.308, observed deconvoluted 19205.753. UV Purity at 260 nm: 63%.*

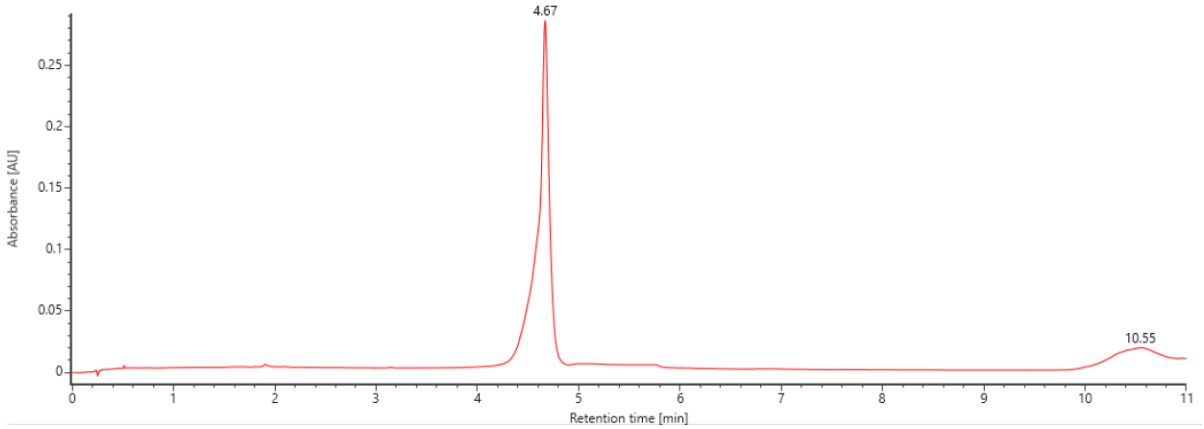

Figure 5.60. *Purified dFU20. HRMS (ESI-) HRMS (ESI-) calculated 19205.308, observed deconvoluted 19204.889. UV Purity at 260 nm: 62%.*

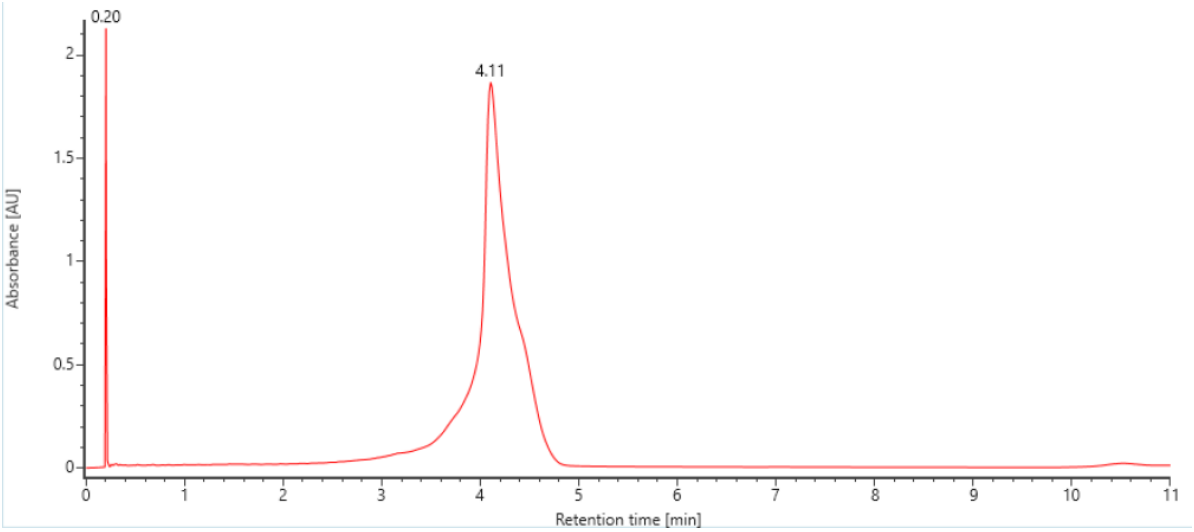

Figure 5.61*. Purified dFU24. HRMS (ESI-) HRMS (ESI-) calculated 19205.308, observed deconvoluted 19205.394. UV Purity at 260 nm: 66%.*

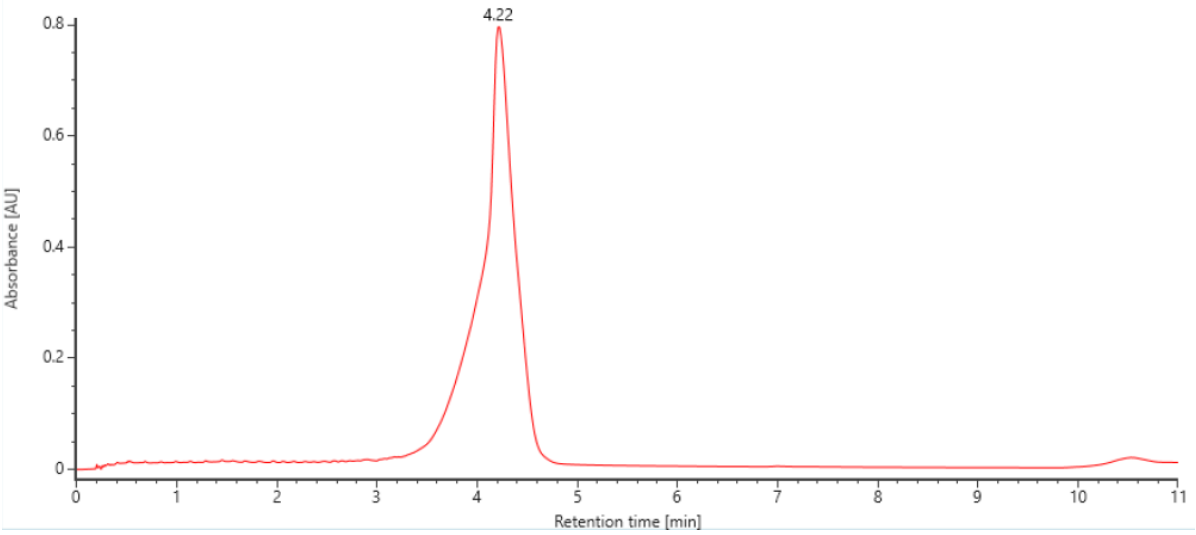

Figure 5.62*. Purified dFU26. UV Purity at 260 nm: 70%.*

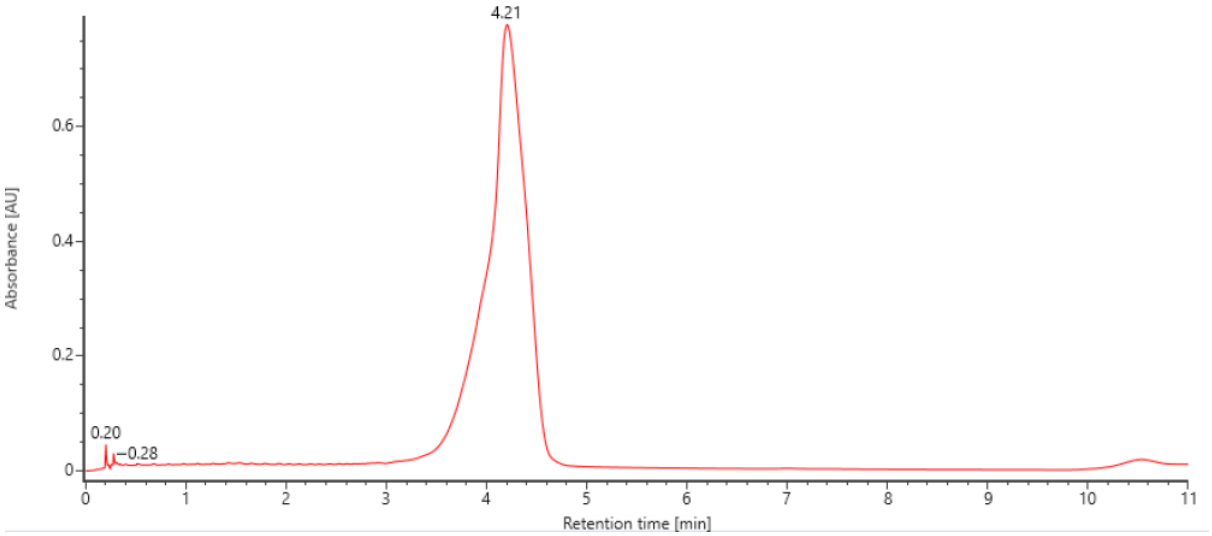

***Figure 5.63**. Purified dFU27. HRMS (ESI-) HRMS (ESI-) calculated 19205.308, observed deconvoluted 19205.644. UV Purity at 260 nm: 77%.*

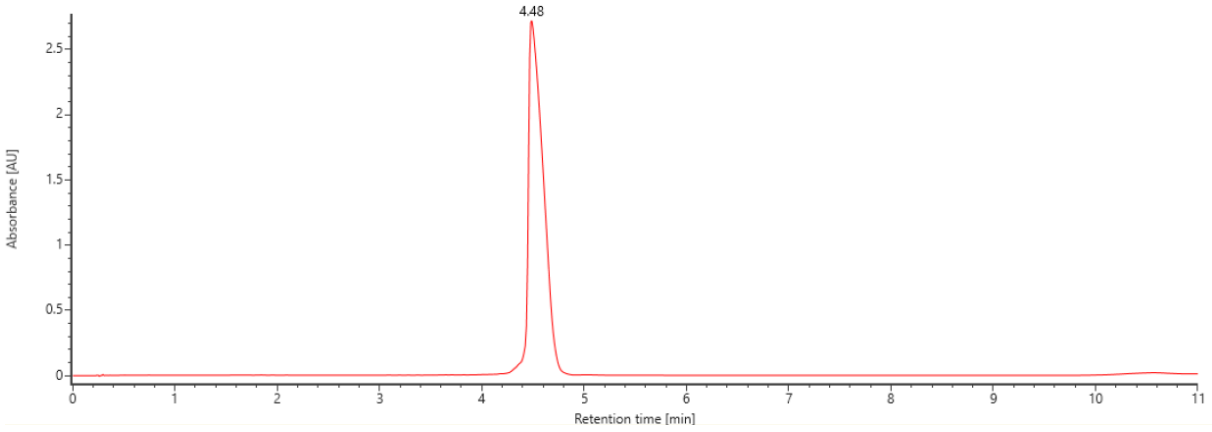

***Figure 5.64**. Purified dFU31. HRMS (ESI-) HRMS (ESI-) calculated 19205.308, observed deconvoluted 19205.604. UV Purity at 260 nm: 71%.*

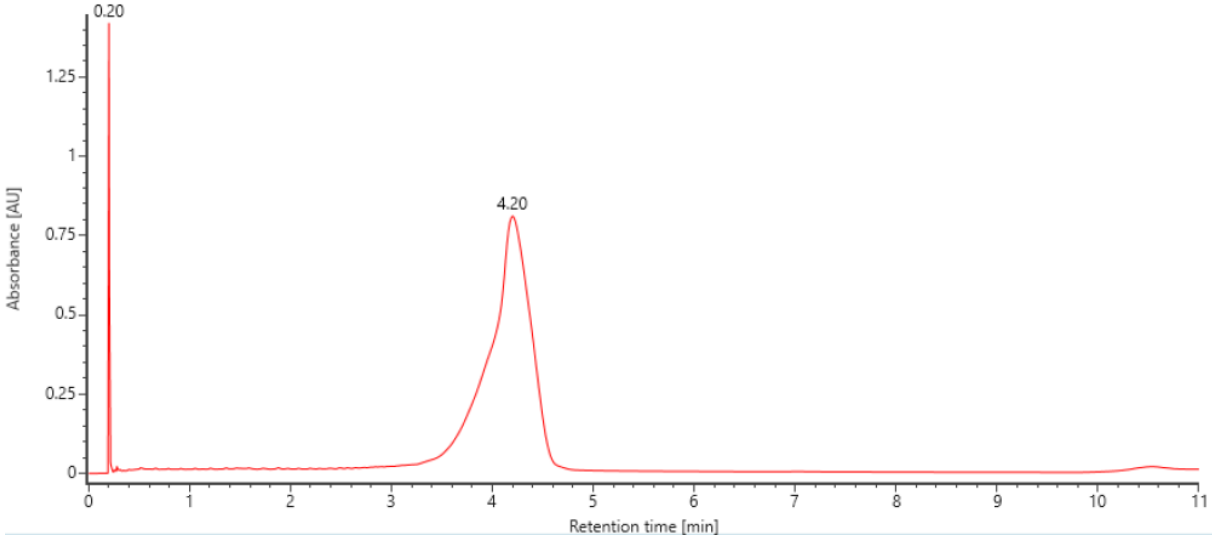

***Figure 5.65**. Purified dFU33. HRMS (ESI-) HRMS (ESI-) calculated 19205.308, observed deconvoluted 19206.438. UV Purity at 260 nm: 72%.*

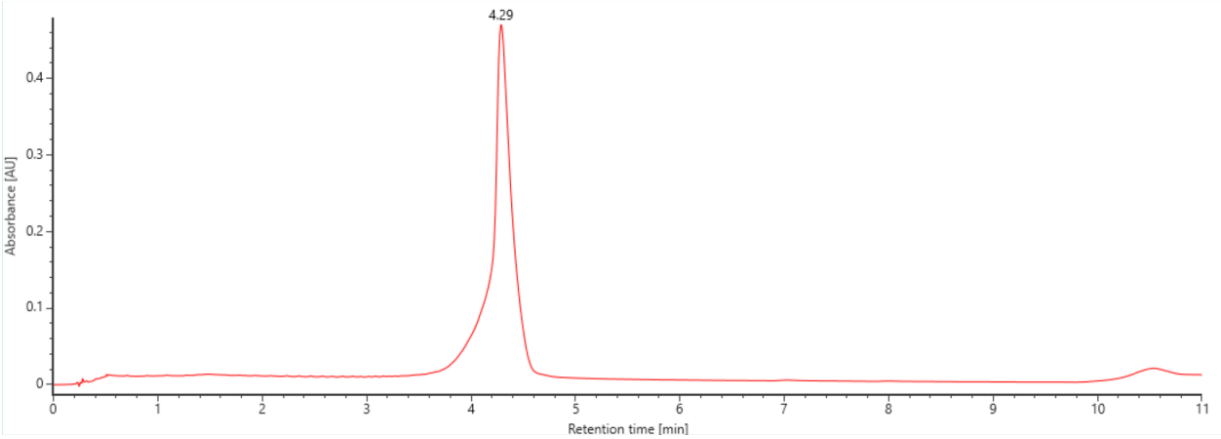

***Figure 5.66**. Purified dFU36. HRMS (ESI-) HRMS (ESI-) calculated 19205.308, observed deconvoluted 19205.549. UV Purity at 260 nm: 66%.*

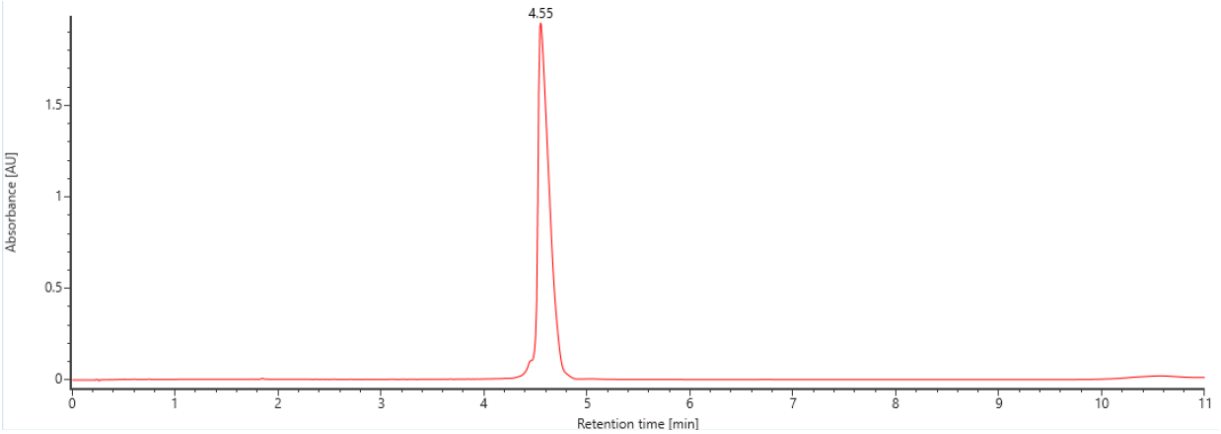

***Figure 5.67**. Purified dFU48. HRMS (ESI-) HRMS (ESI-) calculated 19205.308, observed deconvoluted 19205.495. UV Purity at 260 nm: 81%.*

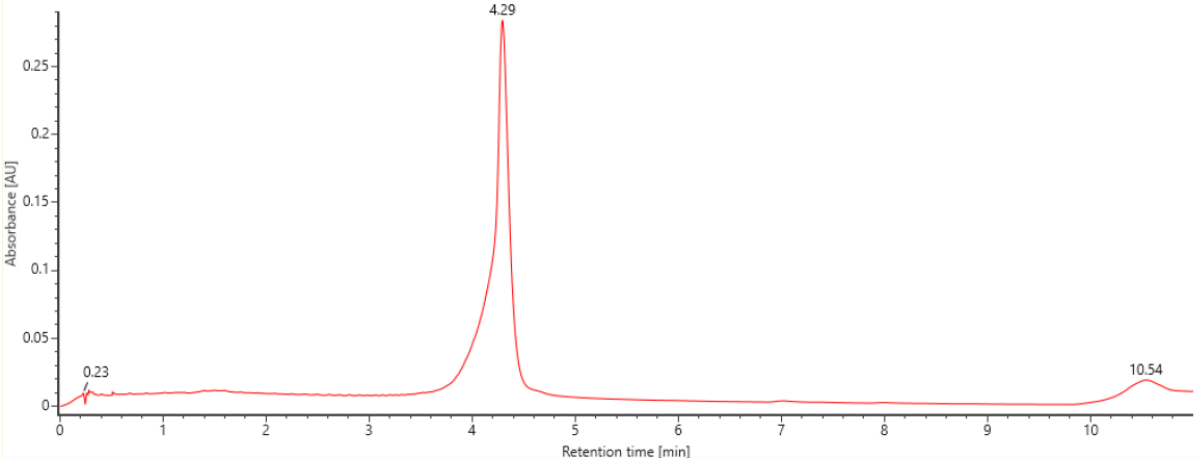

***Figure 5.68**. Purified dFU52. HRMS (ESI-) HRMS (ESI-) calculated 19205.308, observed deconvoluted 19205.843. UV Purity at 260 nm: 61%.*

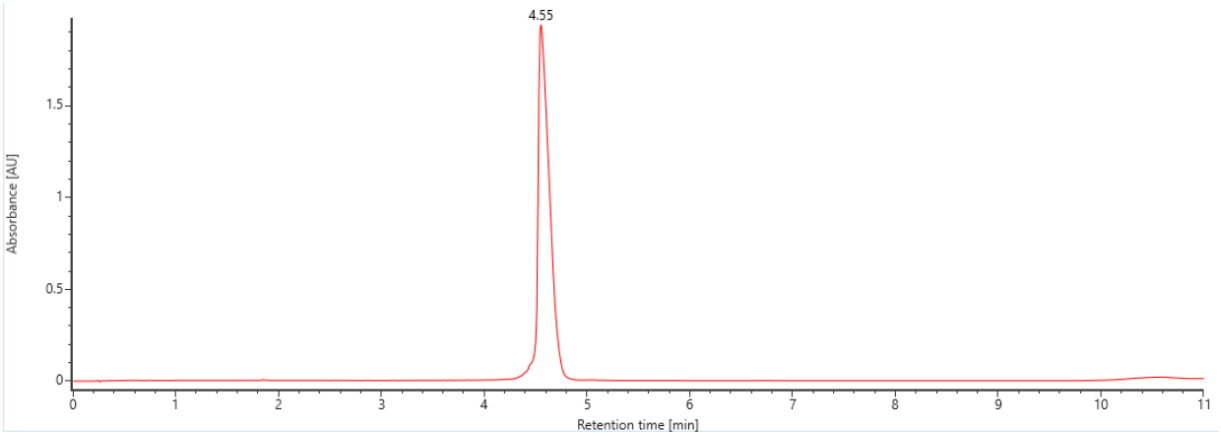

***Figure 5.69**. Purified w.t. HRMS (ESI-) HRMS (ESI-) calculated 19203.317, observed deconvoluted 19203.704. UV Purity at 260 nm: 96%.*

5.6.3: NMR experiments

The fluorinated RNA oligonucleotides were folded by heating the samples at 95 °C for 5 minutes in buffer, followed by rapid cooling on ice. The buffer consisted of 90% H_2O and 10% D_2O, 25 mM potassium phosphate (pH 6.2), 50 mM KCl, 5 mM $MgCl_2$, and 10 µM sodium 2,2-dimethyl-2-silapentane-5-sulfonate (DSS), which served as an internal chemical shift reference. dFU, rFU, and rFC-modified RNAs were studied at 100 µM, whereas sFU-modified constructs were prepared at 250 µM. For HSQC experiments, the wild-type RNA was prepared at 800 µM. All samples were loaded into 3 mm NMR Bruker tubes with a final volume of 140 µL.

NMR experiments were performed on a 600 MHz Bruker spectrometer at the AstraZeneca NMR Centre of Excellence in Gothenburg (Sweden). A 5 mm CryoProbe™ QCI $^{1}H/^{19}F–^{13}C/^{15}N–D$ with a shielded z-gradient coil was used in combination with the automated SampleJet™ system for temperature-controlled sample handling. All spectra were recorded at 298 K. Detailed acquisition parameters are summarized in **Table 5.1.**

***Table 5.1**. NMR acquisition parameters for the reported spectra.*

spectrum	**T (K)**	**Pp (Bruker)**	**td**	**ns**	**D1(s)**	**Aq (s)**	**SW ^{1}H**	**SW hetero atom**	**O1 (Hz)**	**O2 (Hz)**	**O3 (Hz)**
Imino	298	1D SOFAST	32768	2048	1	1.11	24.5ppm	-	2819.35	-	9729.70Hz
^{19}F spectra (s,rFU, rFC)	298	zgig30	262144	4096	1	5.77	-	40.25ppm	-90349.82	2820.61	
^{19}F spectra (dFU)	298	zg19f	131072	4096	1	2.88	-	40.25 ppm	-90349.82		
HSQC	298	sfhmqcf3gpph	2048	8192	0.25	0.070 (f1) – 0.015(f2)	24.5ppm	60.00ppm	2820.61 (^{1}H), 9729.70 (^{15}N)	22937.23	9729.70

NMR data were processed using Topspin. Proton chemical shifts were internally referenced to Sodium trimethylsilylpropanesulfonate (DSS), while fluorine chemical shifts were indirectly referenced relative

to the proton shifts. The data were multiplied with an exponential window function with 3 Hz (imino) and 50Hz (^{19}F) line broadening prior to Fourier transformation.

5.7: References

(1) Shortridge, M. D.; Walker, M. J.; Pavelitz, T.; Chen, Y.; Yang, W.; Varani, G. A Macrocyclic Peptide Ligand Binds the Oncogenic MicroRNA-21 Precursor and Suppresses Dicer Processing. *ACS Chem. Biol.* **2017**, *12* (6), 1611–1620. https://doi.org/10.1021/acschembio.7b00180.

(2) Shortridge, M. D.; Chaubey, B.; Zhang, H. J.; Pavelitz, T.; Vidadala, V.; Tang, C.; Olsen, G. L.; Calin, G. A.; Varani, G. Drug-Like Small Molecules That Inhibit Expression of the Oncogenic MicroRNA-21. *ACS Chem. Biol.* **2023**, *18* (2), 237–250. https://doi.org/10.1021/acschembio.2c00502.

(3) Wilkinson, K. A.; Merino, E. J.; Weeks, K. M. Selective 2'-Hydroxyl Acylation Analyzed by Primer Extension (SHAPE): Quantitative RNA Structure Analysis at Single Nucleotide Resolution. *Nat. Protoc.* **2006**, *1* (3), 1610–1616. https://doi.org/10.1038/nprot.2006.249.

(4) Weeks, K. M.; Mauger, D. M. Exploring RNA Structural Codes with SHAPE Chemistry. *Acc. Chem. Res.* **2011**, *44* (12), 1280–1291. https://doi.org/10.1021/ar200051h.

(5) Chamberlin, S. I.; Weeks, K. M. Mapping Local Nucleotide Flexibility by Selective Acylation of 2‘-Amine Substituted RNA. *J. Am. Chem. Soc.* **2000**, *122* (2), 216–224. https://doi.org/10.1021/ja9914137.

(6) Baek, S. C.; Kim, B.; Jang, H.; Kim, K.; Park, I.-S.; Min, D.-H.; Kim, V. N. Structural Atlas of Human Primary microRNAs Generated by SHAPE-MaP. *Mol. Cell* **2024**, *84* (6), 1158-1172.e6. https://doi.org/10.1016/j.molcel.2024.02.005.

(7) Chen, Y.; Yang, F.; Zubovic, L.; Pavelitz, T.; Yang, W.; Godin, K.; Walker, M.; Zheng, S.; Macchi, P.; Varani, G. Targeted Inhibition of Oncogenic miR-21 Maturation with Designed RNA-Binding Proteins. *Nat. Chem. Biol.* **2016**, *12* (9), 717–723. https://doi.org/10.1038/nchembio.2128.

(8) Puffer, B.; Kreutz, C.; Rieder, U.; Ebert, M.-O.; Konrat, R.; Micura, R. 5-Fluoro Pyrimidines: Labels to Probe DNA and RNA Secondary Structures by 1D 19 F NMR Spectroscopy. *Nucleic Acids Res.* **2009**, *37* (22), 7728–7740. https://doi.org/10.1093/nar/gkp862.

(9) Hennig, M.; Scott, L. G.; Sperling, E.; Bermel, W.; Williamson, J. R. Synthesis of 5-Fluoropyrimidine Nucleotides as Sensitive NMR Probes of RNA Structure. *J. Am. Chem. Soc.* **2007**, *129* (48), 14911–14921. https://doi.org/10.1021/ja073825i.

(10) Murphy, C. D.; Schaffrath, C.; O’Hagan, D. Fluorinated Natural Products: The Biosynthesis of Fluoroacetate and 4-Fluorothreonine in *Streptomyces Cattleya*. *Chemosphere* **2003**, *52* (2), 455–461. https://doi.org/10.1016/S0045-6535(03)00191-7.

(11) Mohammed, A. A.; AlShaer, D.; Al Musaimi, O. Oligonucleotides: Evolution and Innovation. *Med. Chem. Res.* **2024**, *33* (12), 2204–2220. https://doi.org/10.1007/s00044-024-03352-7.

(12) Shcheholeva, I.; Fernández-Remacha, D.; Estrada-Tejedor, R.; Duca, M.; Michelet, V. De-Novo Design of Pre-miR-21 Maturation Inhibitors: Synthesis and Activity Assessment. *Chem. – Eur. J.* **2023**, *29* (40), e202300825. https://doi.org/10.1002/chem.202300825.

(13) Flemmich, L.; Bereiter, R.; Micura, R. Chemical Synthesis of Modified RNA. *Angew. Chem. Int. Ed.* **2024**, *63* (22), e202403063. https://doi.org/10.1002/anie.202403063.

(14) Bodenhausen, G.; Ruben, D. J. Natural Abundance Nitrogen-15 NMR by Enhanced Heteronuclear Spectroscopy. *Chem. Phys. Lett.* **1980**, *69* (1), 185–189. https://doi.org/10.1016/0009-2614(80)80041-8.

CHAPTER 6

NMR ASSAY

Chapter 6: NMR assay

The objective of this work extends beyond biochemical binding characterization and aims toward the identification of compounds active in cells and capable of modulating miR21 in a cellular context. In cell-based systems, off-target interactions and secondary pathway effects complicate the interpretation of a compound's activity, as the biological response may not necessarily result from direct target engagement. Therefore, establishing a validated biochemical affinity test before in-cell evaluation is essential for a first selection of compounds worth being tested in cells. A well-characterized interaction at the biochemical level increases confidence that any subsequent cellular effects might be ascribed to specific target engagement rather than indirect or off-target mechanisms.
False positives and negatives represent a recurrent challenge in medicinal chemistry campaigns. Although the fluorescence-based assay described in **Chapter 4** is a medium-throughput method that enables rapid assessment of multiple compounds' affinity, it remains susceptible to aggregation-related and fluorescence interference artefacts, which can compromise the reliability of the obtained data.
The use of two independent methods, based on distinct physical principles (orthogonal methods), increases confidence in the observed binding event. If both techniques yield consistent affinity rankings, the measured k_d are more likely to reflect ligand–target interactions rather than assay-specific artefacts. To this end, an NMR-based assay, complementary to the fluorescence assay for affinity measurement, was established by applying already developed techniques to the studied target.
In NMR spectroscopy, the transverse relaxation time (T_2) describes the decay of magnetization due to spin–spin dephasing.[1] It is known that T_2 strongly depends on molecular size and tumbling rate: small molecules, which tumble rapidly in solution, typically exhibit long T_2 values and therefore sharp signals, whereas larger biomolecules display shorter T_2 values, resulting in broader peaks.[1]
When a small molecule binds to a biomolecule, its relaxation rate is influenced by the presence of the macromolecule, resulting in slower tumbling rates and enhanced dipolar relaxation mechanisms, leading to a decrease in T_2. For a ligand under fast exchange conditions (low-affinity ligand, up to high nanomolar range), the observed signals represent a population-weighted average of the free (sharp signal) and bound (broad signal) states. Application of a Carr–Purcell–Meiboom–Gill (CPMG)[2] NMR pulse sequence allows selective attenuation of signals with short T_2 values, effectively acting as a T_2 filter. In the case of a fast-exchanging ligand, application of the T_2 filter will broaden the bound ligand signal, causing a general apparent decrease in the overall compound's peak intensity. Since the broadening is proportional to the amount of bound ligand, it is possible to derive affinities from the T_2 filter application.
Based on this rationale, this principle was exploited to measure the affinity of the synthesized small molecules toward the biological target both in a direct way, assessing the affinity of a molecule alone with the receptor (**Paragraph 6.1**) or in an indirect way, by using a molecule with known affinity and displacing it with another with unknown affinity (**Paragraph 6.2**).

6.1: Direct affinity measurement

The fraction of ligand bound to its target is directly linked to its affinity. As stated before, for a bound compound, if a T_2 experiment is used, the signal decreases during the dephasing period. This decrease is proportional to the amount of bound compound. By changing this parameter, it is possible to deconvolute the affinity. For fast exchange compounds, used in large excess with respect to the target, it is possible to measure the affinity as proposed by Dalvit and colleagues.[3] For achieving that, the target

is titrated at different compound concentrations, thus changing the amount of bound ligand and making it possible to deconvolute the k_d. Applying T_2 filters with different lengths (τ) enables robust measurement of the affinity, since more data can be obtained from the same sample.
In the proposed experimental setup,[3] ligand-target interaction is studied by starting from the compound alone, without the target, at a certain concentration (L_0). A second sample, with the ligand at a concentration (L_0) and the target at a low concentration (T_0), is prepared. In a third sample, the concentration of the ligand is increased (L), with no change in target concentration (T_0). The affinity of the compound to the target can be calculated using **Equation 6.1**.

(6.1) $$K_d = \frac{\left\{\ln\left[\frac{I_{L_0}(\tau)}{I_{L_0}(0)}\right]_{-T_0+L_0} - \ln\left[\frac{I_{L_0}(\tau)}{I_{L_0}(0)}\right]_{+T_0+L_0}\right\} * [L_0] - \left\{\ln\left[\frac{I_{L_0}(\tau)}{I_{L_0}(0)}\right]_{-T_0+L_0} - \ln\left[\frac{I_L(\tau)}{I_L(0)}\right]_{+T_0+L}\right\} * [L]}{\left\{\ln\left[\frac{I_{L_0}(\tau)}{I_{L_0}(0)}\right]_{+T_0+L_0} - \ln\left[\frac{I_L(\tau)}{I_L(0)}\right]_{+T_0+L}\right\}}$$

Where:

- $\left[\frac{I_{L_0}(\tau)}{I_{L_0}(0)}\right]_{-T_0+L_0}$ is the ratio between the compound signal without the target, with (τ), and without (0) the T_2 filter of length τ, and the compound at low concentration
- $\left[\frac{I_{L_0}(\tau)}{I_{L_0}(0)}\right]_{+T_0+L_0}$ is the ratio between the compound signal with the target, with (τ), and without (0) the T_2 filter of length τ, and the compound at low concentration
- $\left[\frac{I_L(\tau)}{I_L(0)}\right]_{+T_0+L}$ is the ratio between the compound signal with the target, with (τ), and without (0) the T_2 filter of length τ, and the compound at high concentration

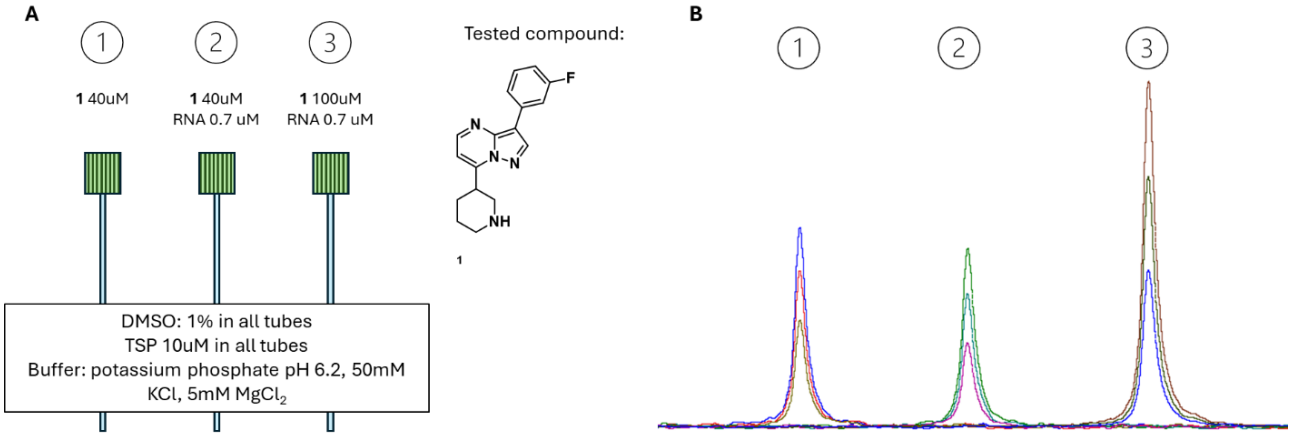

***Figure 6.1**. **A**: Experimental setup for the affinity measurement. **B**: Resulted spectra, using τ 0.08 and 0.160 μs. The reported intensity of the fluorine signal in tube 3 is 50% of the measured one to allow fitting into the image. The intensity of the fluorine signal in tube 3 is 50% of the real intensity, due to fitting into the image.*

To derive its affinity, hit compound **1** was tested at 40 (L_0) and 100 μM (L), with 0.7 μM of the 60nt pre-miR21 (T_0). For studying the change in intensity, ^{19}F-NMR spectroscopy was used, studying the change in intensity of the fluorine in compound **1**, thus achieving easy data processing. The experimental setup is reported in **Figure 6.1A**.

By following the described setup, the signals reported in **Figure 6.1B** were obtained for **1.** For affinity calculation, **Equation 6.1** was applied, employing the intensity of the fluorine without T_2 filter as a control. This process, using the same buffer used for the structural studies, brought to an affinity estimation of 72.35 ± 8.38 μM for compound **1**. It must be noted that this is a preliminary result, and more studies are ongoing to confirm this data.

6.2: Indirect affinity measurement: displacement experiments

Direct affinity measurements, although more accurate, are time-consuming and therefore not suitable for the evaluation of all 75 synthesized compounds. For this reason, a faster approach was employed. As discussed previously, under conditions of ligand in excess and fast exchange, affinities can be determined by changing the fraction of ligand bound to the target: the bound fraction becomes an observable parameter when a T_2 filter experiment is applied, allowing for the deconvolution of affinities. The amount of bound molecule can also be altered by using a second molecule with a stronger affinity to displace the first one.

In the proposed setup,[3] a molecule with a known affinity to the target is incubated with the target. A T_2 filter experiment is acquired for both the free molecule and the bound molecule with the target. A second molecule, with unknown affinity, is then added to the sample. If the two molecules share the same binding pocket (competitive binding scenario), the amount of the first ligand (spy) displacement will be proportional to the displacer affinity. Since the spy's affinity is known, it is possible to deconvolute the displacer's affinity by studying how the spy signal recovers in the T_2 filter experiment. This approach enables rapid, even if less accurate, affinity calculation, since only one T_2 filter is necessary, provided that a control molecule is used. At the same time, structural information can be indirectly obtained, since the effective displacement is binding-site dependent.

According to Dalvit and colleagues,[3] knowing the affinity of the spy, it is possible to deconvolute the affinity of the displacer using **Equation 6.2**:

(6.2) $$K_d = \frac{(100-F)*[D]*K_S}{F*\{[S]+K_S\}}$$

Where:

- F is the displacement factor, calculated according to **Equation 6.3**
- $[D]$ is the displacer concentration
- K_S is the measured spy's k_d
- $[S]$ is the spy concentration

The displacement factor of **Equation 6.2** can be expressed as a function of the intensity of the spy signals according to **Equation 6.3**:

(6.3) $$F = 100 * \left\{ 1 - \frac{\ln\left[\frac{I_S(\tau)}{I_C(\tau)}\right]_{-T_0} * \ln\left[\frac{I_S(\tau)}{I_C(\tau)}\right]_{+T_0+D}}{\ln\left[\frac{I_S(\tau)}{I_C(\tau)}\right]_{-T_0} * \ln\left[\frac{I_S(\tau)}{I_C(\tau)}\right]_{+T_0}} \right\}$$

Where:

- $\left[\frac{I_S(\tau)}{I_C(\tau)}\right]_{-T_0}$ is the ratio of the signal between the spy and the control without RNA and without displacer,
- $\left[\frac{I_S(\tau)}{I_C(\tau)}\right]_{+T_0+I}$ is the ratio of the signal between the spy and the control with the RNA and the displacer,
- $\left[\frac{I_S(\tau)}{I_C(\tau)}\right]_{+T_0}$ is the ratio of the signal between the spy and the control molecule with only the RNA.

The affinity of the spy molecule is normally derived by another technique or by k_d measurement with NMR (**Paragraph 6.1**). Having obtained the affinity of **1** by NMR, it was possible to evaluate all the other synthesized compounds using **1** as a spy.

The experimental setup was optimized by considering the general solubility of the compounds, the amount of pre-miR21 required for effective signal broadening, and the T_2 filter length. To facilitate straightforward data deconvolution of both the free and bound states, the spy ligand's signals need to be well above the noise level. This parameter is influenced by both the amount of target and the τ length of the T_2 filter. At the same time, solubility must also be considered. A maximum concentration of 100 μM was established as a threshold for the other analogues to ensure solubility. The displacer must be used at a higher concentration than the spy, so a low amount of the latter should be used. At the same time, a low concentration of spy results in long acquisition times and inefficient use of the NMR instrument. By considering these parameters, 30 μM of spy, 0.7 μM of the 60nt model of pre-miR21, and 60 and 100 μM of displacer were employed. For compounds capable of quantitative displacement at 60 μM, additional concentrations of 13.5 and 30 μM were also tested.

The same buffer used in the structural studies was employed for these experiments. As previously discussed, displacement experiments are effective only if the spy and the displacer share the same binding pocket. Since a putative binding site was identified for a displacer (compound **41**), using the same 60nt pre-miR construct and the same buffer also facilitates structural characterization of the entire compound series. Indeed, the spy is effectively displaced by compound **41**, which was used in the structural studies of **Chapter 5**, and for which a binding site can be hypothesized. DMSO concentration was set to the minimum value required for compound solubilization, corresponding to 1%. This standardization was considered necessary since for some RNAs, such as tau, DMSO was reported to strongly bind the RNA, thus changing the conformation and altering the binding process with other ligands.[4] The experimental setup is schematically represented in **Figure 6.2A**.

While direct affinity measurements were conducted by looking at the fluorine, for these displacement experiments, the proton was studied. The choice was due to the fact that ^{1}H was deemed more sensitive than ^{19}F for describing this particular binding process, having tested both conditions initially. Trimethylsilylpropanoic acid (TSP) was used as a control molecule, necessary for the affinity calculation, but also for monitoring the effective amount of displacer present in solution, thus obtaining an indication about the compounds' solubility. This was done by registering a ^{1}H-NMR spectrum to verify the effective concentrations of the spy and displacer in the NMR tube.

In **Equation 6.3**, the TSP integral was used as a standard and set to 1, and the ^{1}H-NMR spy signal at 8.41 ppm (referenced to the TSP signal) was monitored. The overall setup is reported in **Figure 6.2A**. The free spy signal intensity was measured from tube 1, the spy + target from tube 2, and the spy + displacer from tubes 3 and 4. Compound **1** was used as the spy ligand, while analogue **41** served as a control to ensure reproducibility between measurements.

An example of a displacement experiment is shown in **Figure 6.2B**. After selecting a peak in the spy's ^{1}H-NMR spectrum, its intensity is monitored under the different experimental conditions. The spy signal

alone (30µM) is sharp and minimally affected by the T_2 filter. Upon addition of the RNA target (0.7µM), the signal intensity decreases due to ligand–target binding. Subsequent addition of the displacer (60µM) leads to partial recovery of the spy signal, indicating displacement. A second addition of the displacer (100µM) results in further recovery, consistent with increased displacement of the spy ligand.

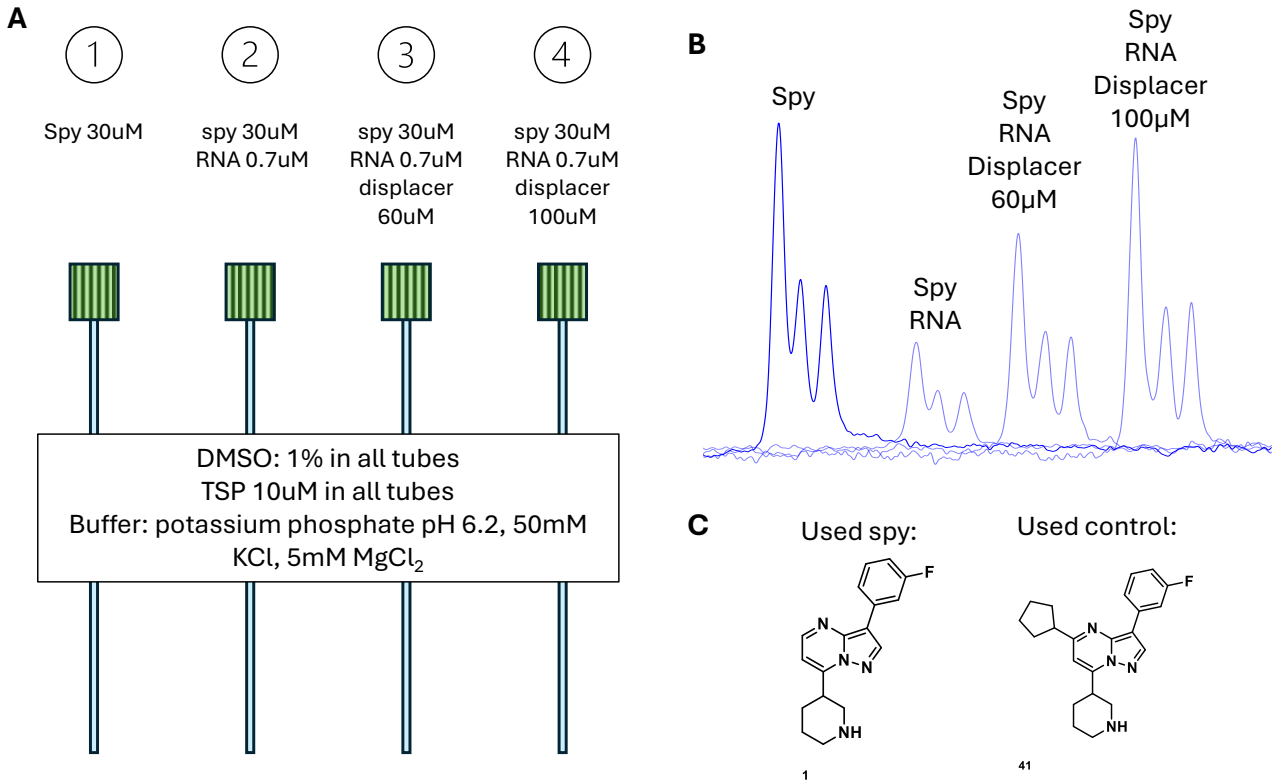

***Figure 6.2**. **A.** Experimental setup for the displacement experiments. **B**: Example of the behaviour of the spy signal in different conditions in the displacement experiments. **C**: used spy and control for the displacement experiments.*

6.2.1: Affinities obtained by displacement experiments

All synthesized final compounds were tested as displacers toward compound **1**. The results can be grouped into four different categories: low, medium, and strong displacement, as well as allosteric behaviour. This classification is illustrated in **Figure 6.3**. For 16 compounds, very low or negligible displacement was observed. Because the change in the spy signal was minimal in these cases, the derived K_d values are not reliable, and K_d values above 100 µM are not reported due to the high error. Other 29 compounds showed a moderate but non-quantitative increase in the spy signal. This scenario represents the optimal range for this type of assay, as the signal increase is above the noise level, allowing for accurate K_d determination. The strongest compounds, which also showed high activity in the biochemical assay, displaced the spy quantitatively at 60 µM. In these cases, the spy concentration was reduced to enable accurate affinity estimation. Finally, for a subset of compounds, a decrease in the spy signal was observed upon compound addition. Under fast exchange conditions, this decrease indicates enhanced binding of the spy, likely arising from allosteric interactions induced by the displacing compound, as discussed in **Paragraph 6.2.6**.

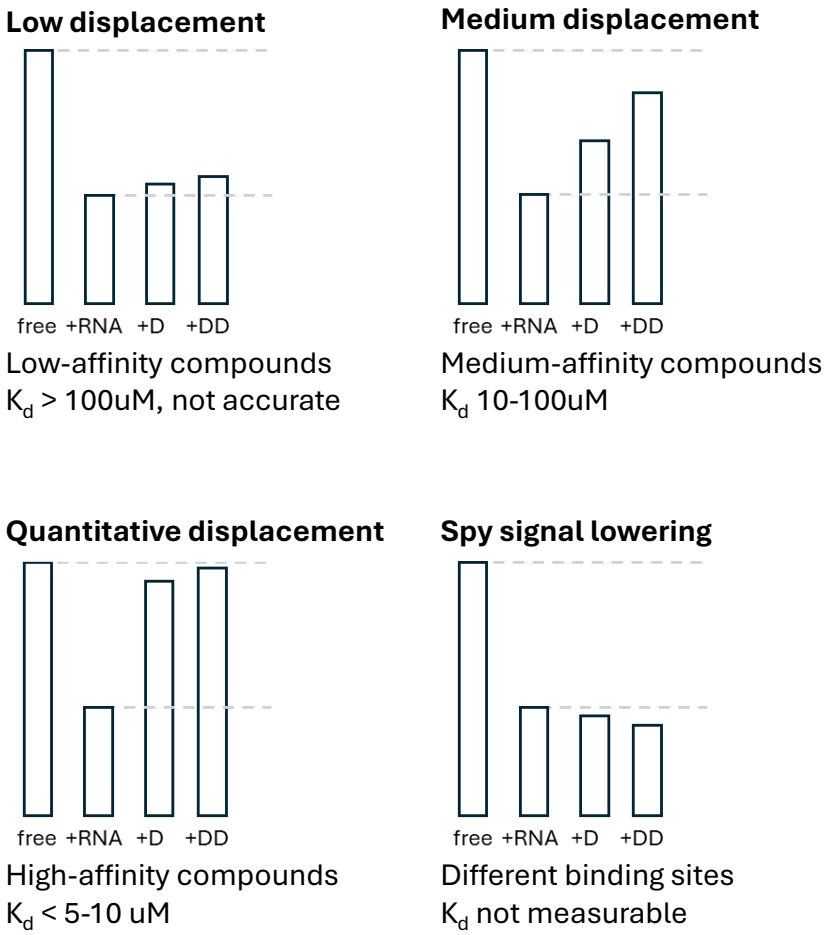

***Figure 6.3**. Schematization of the results of the NMR assay.*

The overall results of the displacement experiments are summarized in **Table 6.1**. While all 75 synthesized derivatives were tested, for some compounds, peak overlapping was noted; therefore, they couldn't be tested and are not reported in the table.

Solubility estimations were also obtained while performing these experiments. Not all compounds resulted soluble in the assay conditions. In **Equation 6.2**, the concentration of the compound detected in solution was used, and all the affinities were reported as insolubility and thus aggregate presence does not influence the analysis. However, aggregates or precipitates can affect the assay, creating false positives, thus overestimating the compound's affinity. Compounds exhibiting good affinity were retested at a concentration lower than their solubility in the buffer.

It must be noted that this test has a structural bias, since competitive binding is assumed. If the displacer binds the target in a different binding pocket than **1**, without influencing the spy binding, it will result in non-binding in the assay while still retaining an activity toward pre-miR21. All reported non-binders with this assay should be confirmed with another biophysical technique to exclude the multiple binding pocket hypothesis.

It should be noted that all compounds were evaluated as racemic or diastereomeric mixtures. If the interaction with the target is stereochemistry-dependent, an increase in binding affinity for one of the stereoisomers can reasonably be expected.

***Table 6.1**. Results of the displacement experiments.*

compound	affinity (μM)	compound	affinity (μM)	compound	affinity (μM)
1	72.35 ± 8.38	**26**	84.72 ± 4.85	**48**	20.32
2	71.67 ± 10.80	**27**	>100	**49**	12.86 ± 7.90
5	70.41 ± 15.72	**28**	n.b.	**50**	2.52 ± 0.16
6	70.41 ± 15.72	**29**	>100	**51**	26.09 ± 3.62
7	71.67 ± 10.80	**30**	n.b.	**58**	>100
8	>100	**31**	>100	**59**	50.83 ± 4.05
9	39.99 ± 2.16	**32**	n.b.	**61**	47.89 ± 7.17
10	87.93 ± 15.24	**33**	>100	**62**	114.80 ± 15.63
11	>100	**34**	>100	**63**	>100
12	18.63 ± 0.39	**35**	43.40 ± 4.20	**64**	60.06 ± 1.32
13	32.25 ± 6.70	**36**	35.49 ± 11.51	**65**	n.b.
15	79.89 ± 22.69	**38**	>100	**66**	n.b.
17	>100	**39**	44.98 ± 5.29	**67**	n.b.
19	78.01 ± 10.73	**40**	28.87 ± 0.10	**68**	allosteric
20	38.04 ± 2.87	**41**	17.96 ± 9.47	**69**	allosteric
21	36.74 ± 5.36	**42**	48.38 ± 1.03	**70**	30.08 ± 6.54
22	>100	**44**	84.71 ± 15.88	**71**	26.30 ± 2.08
23	>100	**45**	>100	**72**	3.54 ± 2.49
24	>100	**46**	n.b.	**73**	2.50 ± 0.70
25	9.89 ± 5.44	**47**	42.91 ± 2.72	**74**	5.54 ± 0.51

Data are expressed as the mean of two experiments (compounds tested both at 60 and 100μM). n.a.: not analyzed (because of peak overlapping); n.b.: no binding detected.

6.2.2: NMR-based SAR at position 3 of the pyrazolo[1,5-a]pyrimidine scaffold

A SAR at position 3 of the synthesized compounds can be derived also from the NMR-based assay, as shown in **Figure 6.4**. All deductions here presented were made by comparing the resulting affinity with that of the hit compound **1**, used as a spy.

Overall, these considerations could be preliminarily outlined:

- A generally flat SAR was observed upon substitution with different groups, with only aromatic moieties (**12**, **13**, **21**, **25**) and trifluoromethyl-bearing derivatives (**9**, **20**) showing increased affinity. These data could suggest that specific interactions may take place. It must be noted, however, that for the first set of compounds (the ones featuring an aromatic moiety in position 3), a moderately low solubility was measured (maximum solubility around 20-30 μM), thus the corresponding affinities could have been affected by the presence of aggregates in the sample.
- *Meta*- and *para*-substitution on the phenyl ring did not appear to significantly affect affinity, with the exception of compounds **12** and **13** that bear a biphenyl group. For this substituent, a clear directionality effect was observed: the *para* biphenyl showed a k_d of 18.63 ± 0.39 μM, while the *meta* biphenyl displays a k_d of 32.25 ± 6.70 μM.
- The phenyl group maintained favourable interactions even when positioned further from the scaffold core (**25**, k_d = 9.89 ± 5.44 μM), provided that an appropriate linker was used. Indeed,

when the cyclohexenyl moiety of **25** was converted to a saturated cyclohexyl ring to give analogue **26** (k_d = 84.72 ± 4.85 μM), the affinity markedly decreased.

Overall, SAR analysis of the position 3 of the pyrazolo[1,5-a]pyrimidine scaffold identified the trifluoromethylphenyl group (**9** and **20**) and the biphenyl group (**12** and **13**) as the most favourable substituents, reaching affinities of around 40 μM and 20 μM, respectively. These compounds, except for **20**, were also identified as good binders in the fluorescence-based assay.

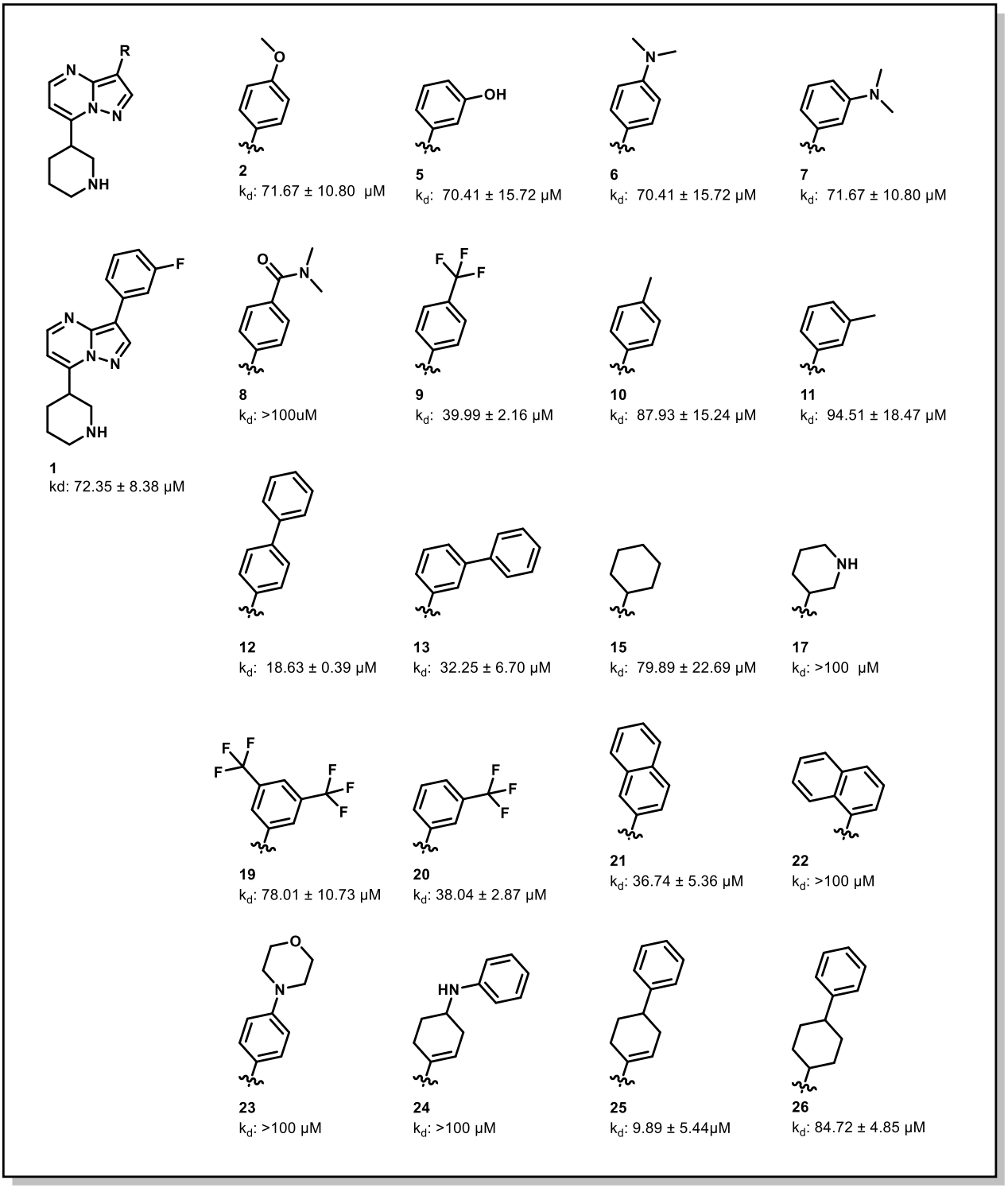

***Figure 6.4**. Binding affinity to pre-miR21 of compound **1** analogues as determined by NMR.*

While the SAR trend at position 3 of the pyrazolo[1,5-a]pyrimidine scaffold derived from the NMR-based assay appeared similar to that obtained with the fluorescence-based assay, the corresponding amide derivatives (**Figure 6.5**) showed a different trend in the two assays. NMR-derived analysis identified a lack of binding for this class of compounds, while a low affinity was found with the fluorescence-based assay (**Paragraph 4.1**). This discrepancy could be explained by the presence of a different binding pocket for these compounds and the hit, given the bias in the NMR-based assay, or by their overall low solubility, possibly influencing the fluorescence-based assay.

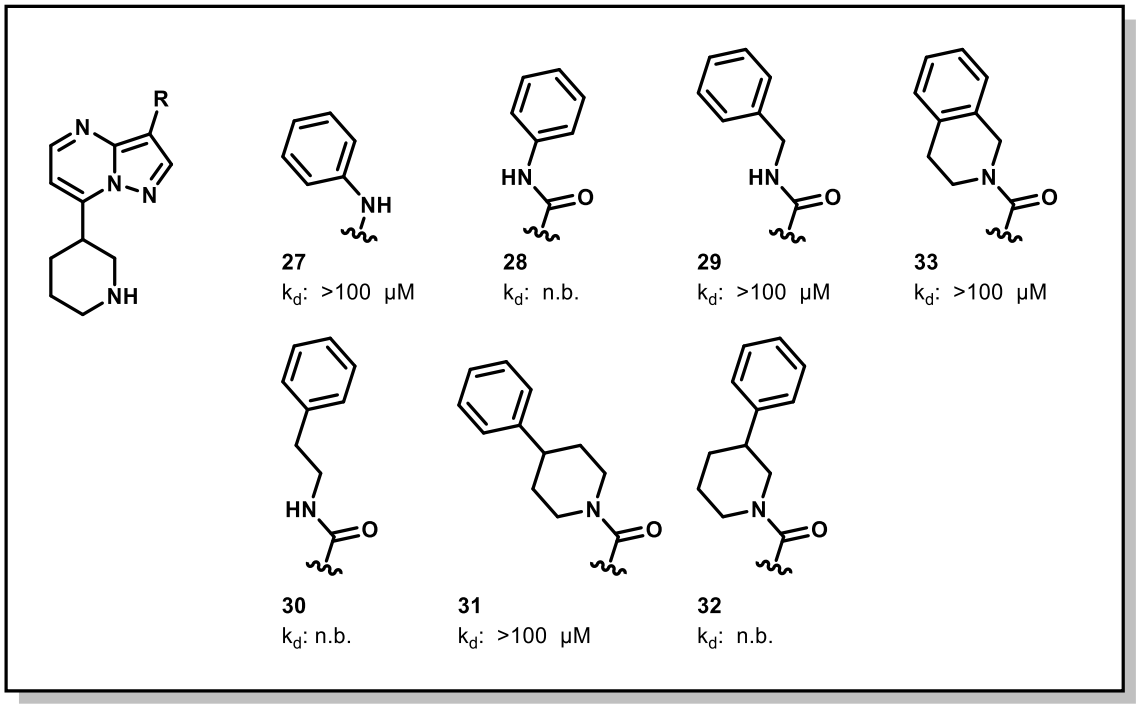

***Figure 6.5**. Binding affinity to pre-miR21 of amide analogues of compound **1** as determined by NMR.*

6.2.3: NMR-based SAR at position 2 of the pyrazolo[1,5-a]pyrimidine scaffold

The exploration of the SAR at position 2 was performed with the synthesis of a small number of compounds, shown in **Figure 6.6**. As stated in **Chapters 3-4**, the most active groups identified at position 3 were introduced at position 2 to compare the affinity at the two sites. For the *p*-trifluoromethylphenyl group, a complete loss of affinity was observed in the NMR-based assay for **38** (k_d >100 µM), whereas its regioisomer at position 3 (**9**) displayed a modest, still detectable k_d of 39.99 ± 2.16 µM (**Paragraph 6.2.1**). A similar trend was observed for the biphenyl moiety, where the affinity to pre-miR21 was lower than that at position 3. While **35** presented a relatively low affinity (k_d = 43.40 ± 4.20 µM), for the corresponding regioisomer **12**, a k_d of 18.63 ± 0.39 µM was measured (**Paragraph 6.2.1**). Despite differences in k_d values, a similar trend in SAR could be observed in the two assays.

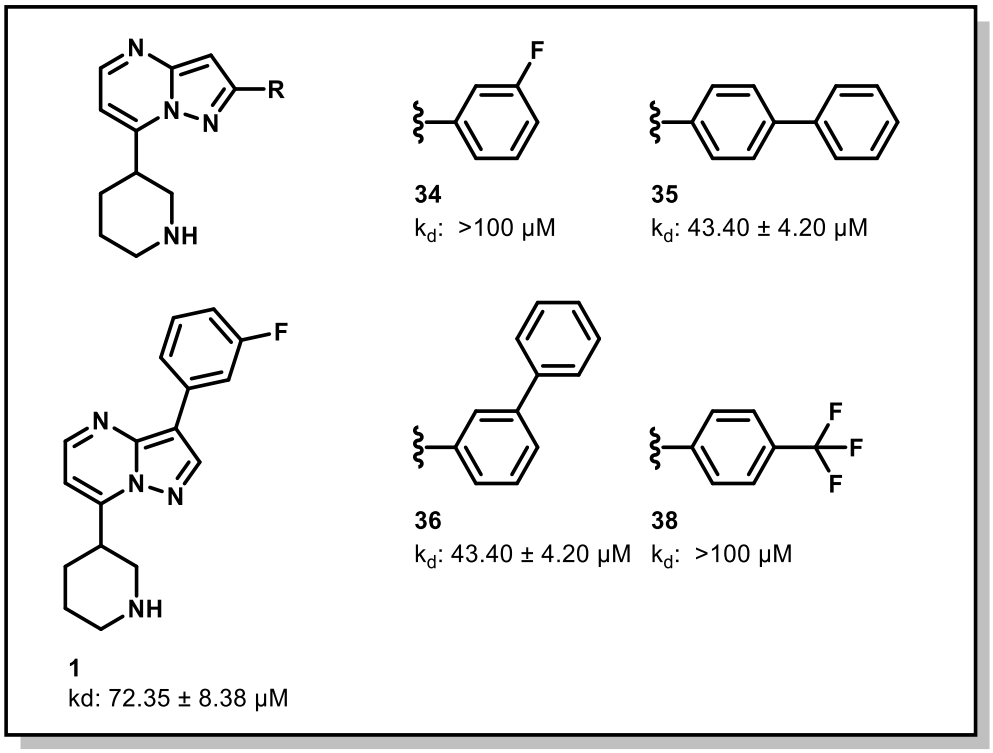

Figure 6.6. *Binding affinity to pre-miR21 of compounds bearing different substituents at position 2 as derived by the NMR-based assay*.

6.2.4: NMR-based SAR at position 5 of the pyrazolo[1,5-a]pyrimidine scaffold

Concerning the SAR analysis of hit **1** derivatives substituted at position 5, apolar and aromatic groups emerged as the most promising for affinity (**Figure 6.7)**. Compounds **39**, **40**, and **41** contain different aliphatic groups with increasing steric hindrance, ranging from a methyl (**39**) to a cyclopropyl (**41**). The affinity appeared to increase with the size of the substituent, reaching a k_d of 17.96 ± 9.47 µM for **41**. Aliphatic residues seemed to be favoured at this position since, when an oxygen atom was introduced into the substituent, as in compound **42**, a decrease in affinity was observed (k_d = 48.38 ± 1.03 µM).
Compounds bearing an aromatic substituent were also found to be strong binders in the NMR-based assay. Compounds **49** and **50**, bearing a phenyl group separated from the scaffold core, resulted among the best binders of this series, with K_d values of 12.86 ± 7.90 and 2.52 ± 0.16 µM, respectively. Relevant binding for these molecules was also detected in the fluorescence-based assay. It must be noted, however, that low solubility was measured for these compounds (up to *circa* 30 µM), making them less appealing for the subsequent in-cell testing.
The presence of a polar group at position 5, such as a dimethylamino (**45**) or a hydroxyl residue (**46**), appeared to significantly decrease the affinity. Indeed, a k_d > 100µM was found for **45,** and no binding was observed for **46**. Compounds with bulky substituents at position 5 retained affinity, as observed with compounds **48-51**, even if a polar group was present in 5.
Still taking into account the SAR evaluation around this position, in contrast to the other compounds bearing a polar residue, the piperazinone analogue **51** showed good interaction with pre-miR21 (k_d = 26.09 ± 3.62µM).

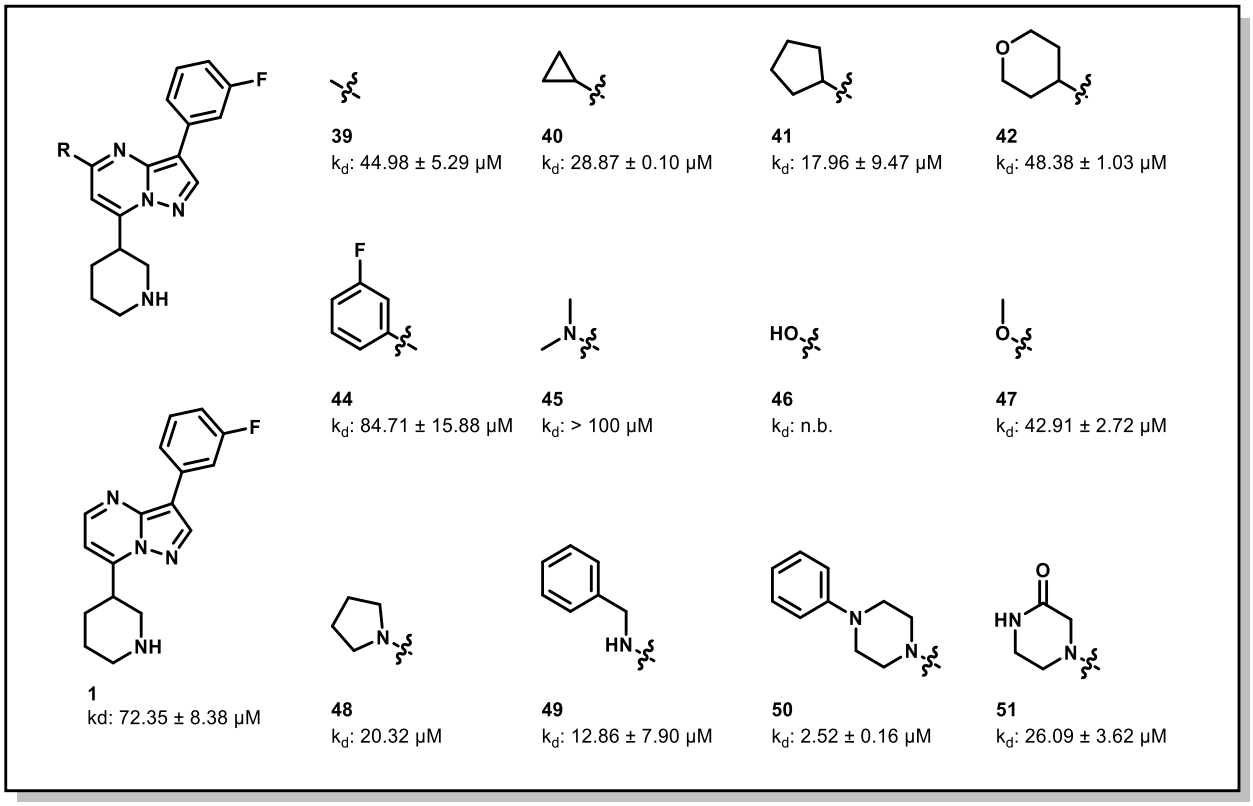

***Figure 6.7**. Binding affinity to pre-miR21 of 5-substituted pyrazolo[1,5-a]pyrimidine derivatives of compound **1** as determined by NMR-based assay.*

6.2.5: NMR-based SAR at position 7 of the pyrazolo[1,5-a]pyrimidine scaffold

NMR-derived affinities for compounds substituted at position 7 of the pyrazolo[1,5-a]pyrimidine scaffold are reported in **Figure 6.8**. For synthetic reasons, as stated in **Paragraphs 3.6** and **4.5**, these compounds were derived from **40**. Therefore, the obtained affinities should be compared to **40** (k_d = 28.87 ± 0.10 μM), as reference molecule.

Among the 9 synthesized derivatives, no increase in affinity with respect to **40** was observed. Compounds **58, 62, 63**, and **65-67** showed low or non-detectable binding to pre-miR21. These findings suggest the importance of the piperidine nitrogen for the binding activity. For compounds **58**, **65-67**, the absence of a basic nitrogen led to a low or no-detectable binding, supporting this hypothesis. When instead the nitrogen was shifted to other positions of the piperidine ring, as in **59** and **61**, a decrease in affinity was registered with respect to **40.** Considering also compounds **62** and **63**, speculations about the importance of a restricted conformational freedom could be made, identifying the 3-piperidinyl group as the group presenting the best orientation and rigidity for the binding. Additional compounds bearing specific substituents should be prepared and tested to support this hypothesis, but the results obtained with the compounds within this series appear to confirm the SAR derived from the fluorescence-based assay.

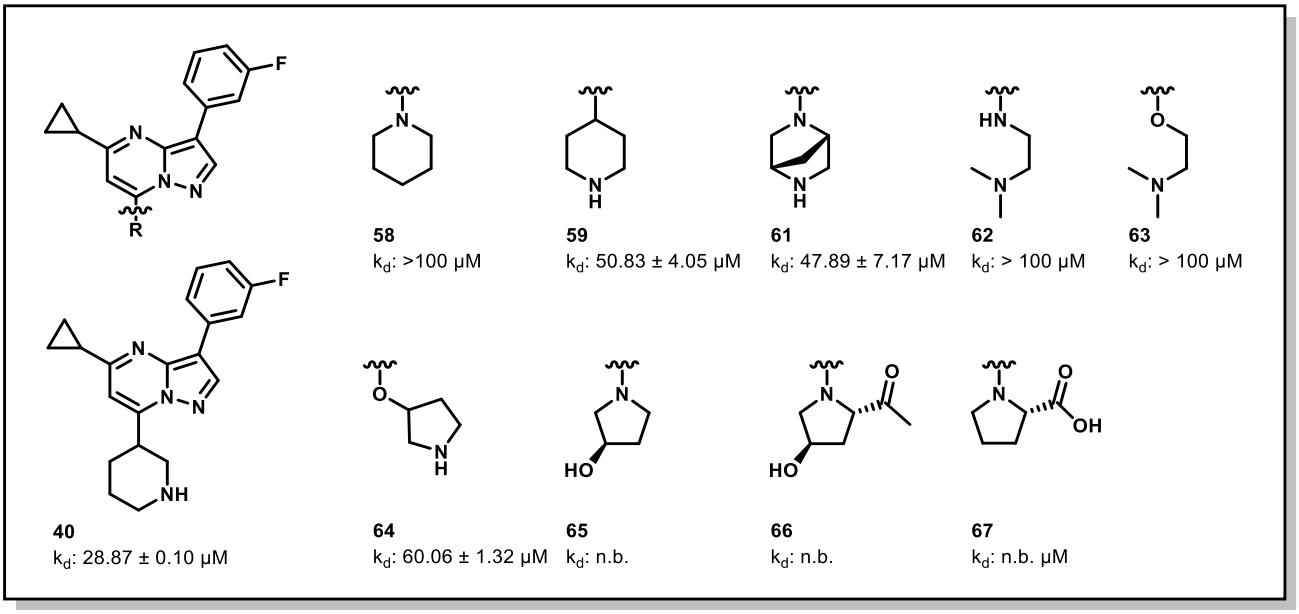

Figure 6.8. *Binding affinity to pre-miR21 of 7-substituted pyrazolo[1,5-a]pyrimidine derivatives of compound **1** as determined by NMR-based assay.*

6.2.6: NMR-derived data for compounds **68** and **69**

Compounds **68** and **69** (**Figure 6.9)** showed a peculiar behaviour when tested in the NMR-based assay. For these compounds, in fact, a decrease of the spy signal in the presence of the displacer was observed. For fast-exchange compounds as these ones, this is consistent with an improvement of the binding upon addition of the compounds, since more free spy binds the RNA (hence the decrease in signal) upon the addition of the displacer. Aggregation or precipitation phenomena could be excluded since these compounds are soluble at the tested concentration. The observed behaviour could be consistent with a possible positive modulation effect of the interaction of the spy molecule with pre-miR21. Most likely, compounds **68** and **69** bind to a different binding pocket with respect to hit **1**, as a result of moving the 3-fluorophenyl residue from position 3 to position 5 of the pyrazolo[1,5-a]pyrimidine scaffold (for **68**) and placing the 3-fluorophenyl at position 7 and the piperidin-3-yl at position 5 (for **69**), improving the affinity of **1** toward the target.

From a medicinal chemistry perspective, this finding is particularly interesting, as it further highlights the importance of these two substituents for specific binding to pre-miR21 and suggests a potential strategy for further development of this chemotype. In particular, one could hypothesize that linking one of these allosteric compounds to fragment **1** could represent an approach to obtain compounds with enhanced affinity.

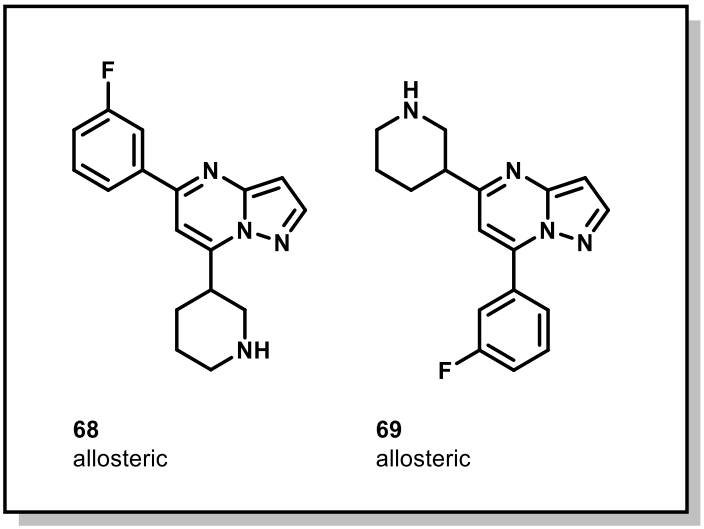

***Figure 6.9**. Structure of compounds **68** and **69** and proposed interaction with pre-miR21 derived from the NMR-based assay.*

6.2.7: NMR-derived SAR of trisubstituted pyrazolo[1,5-a]pyrimidines

To complete the SAR investigation, a small set of 2,5,7-tri-substituted pyrazolo[1,5-a]pyrimidines was synthesized: their structures and affinity to pre-miR21 are reported in **Figure 6.10**. In general, the affinity of each of these compounds resulted higher than that of the corresponding di-substituted analogues.
For compounds **72** (k_d = 3.54 ± 2.49 μM) and **73** (k_d = 2.50 ± 0.70 μM) an increase in affinity was detected with respect to their position 3 substituted precursors **12** (k_d = 18.63 ± 0.39 μM) and **25** (k_d 9.89 ± 5.44 μM), respectively. The piperidine ring at position 5 (k_d of the precursor not available due to signal overlap) appears to be beneficial for affinity and for solubility. However, the solubility improvement (calculated by NMR) was quite modest, being *ca*. 30 μM for **72**, and *ca*. 40μM for **73**, respectively. Due to the low solubility, these compounds were not selected for follow-up studies.
Instead, the introduction of a second piperidin-3-yl ring at position 5, leading to **71** (k_d = 26.30 ± 2.08 μM) increased the affinity with respect to the precursor **9** (**Paragraph 6.2.2**, k_d = 39.99 ± 2.16 μM), although not as much as observed with compounds **72** and **73**. While this compound was identified as the one with the highest affinity in the fluorescence-based assay, in the NMR assay, its affinity appeared to be not so noteworthy. The reasons for this discrepancy are still under investigation.
Compound **74** represents the combination of two quite promising residues: a cyclopentyl ring at position 5 (precursor **41**: k_d = 17.96 ± 9.47 μM) and a 4-trifluorophenyl moiety at position 3 (**9**: k_d = 39.99 ± 2.16 μM). Interestingly, this compound displayed a remarkable k_d of 5.54 ± 0.51 μM and showed a relatively good solubility (ca. 150 μM, as measured by NMR). Overall, analogue **74** appears as the most interesting one among those synthesized within this new set of pyrazolo[1,5-a]pyrimidines.

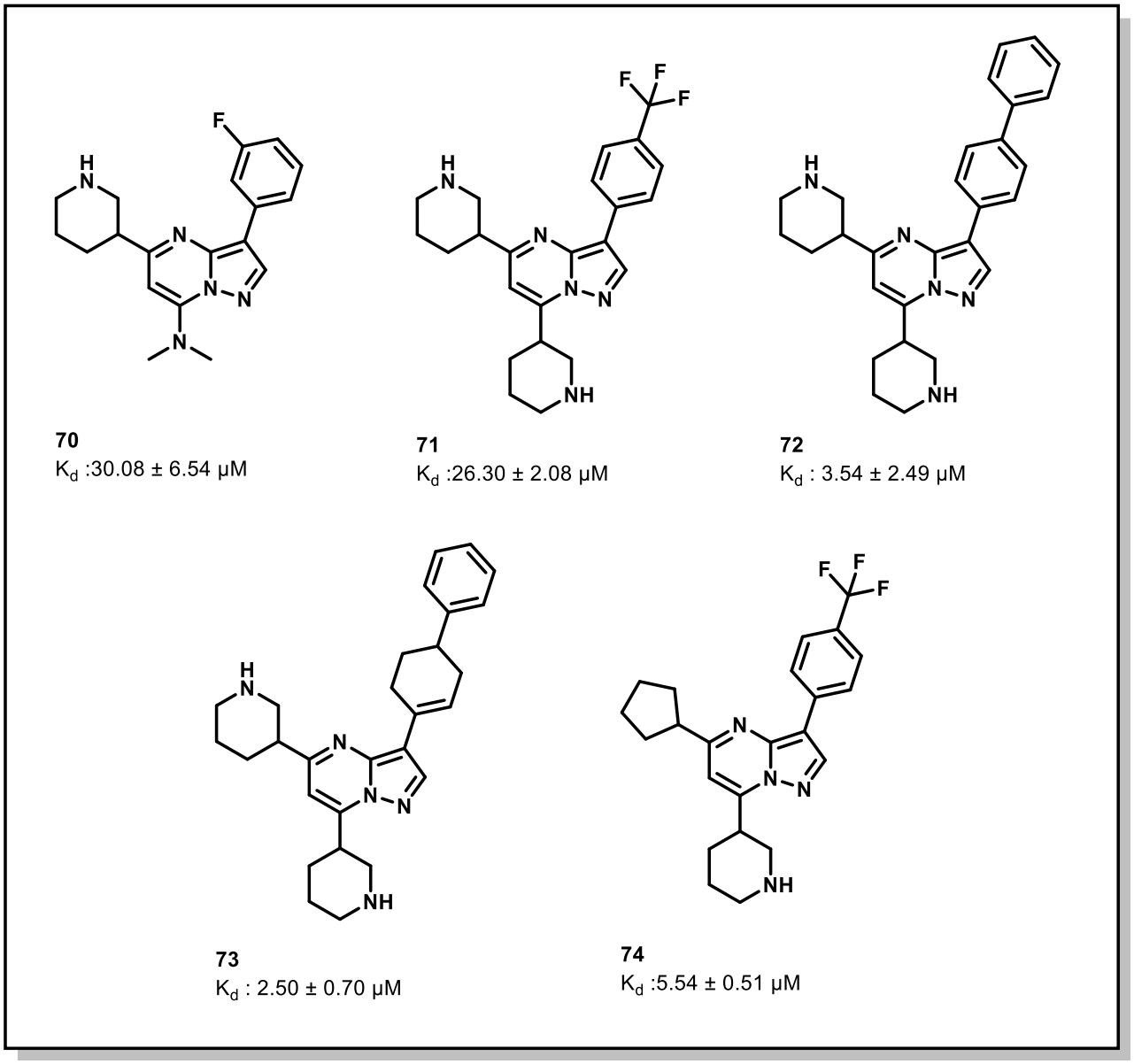

***Figure 6.10**. Binding affinity to pre-miR21 of trisubstituted pyrazolo[1,5-a]pyrimidines as determined by NMR-based assay.*

6.2.8: Conclusions

NMR displacement experiments allowed drawing further SAR indications for the investigated chemotype, which are summarized in **Figure 6.11**.

Concerning substitutions at position 3 of the pyrazolo[1,5-a]pyrimidine scaffold, compounds bearing extended aromatic groups or a fluorine-substituted phenyl group exhibited higher affinities, suggesting the presence of a hydrophobic binding pocket. Introduction of substituents at position 2 resulted generally detrimental for affinity, often resulting in compounds with lower binding affinity than the hit compound or only a marginal improvement. Compounds substituted at position 5 with aromatic or bulky aliphatic groups showed good activity, suggesting that the substituent can be accommodated in a hydrophobic pocket. Finally, the piperidin-3-yl moiety at position 7 was confirmed as crucial element for the affinity toward pre-miR21, since its modification led to a lowering of the binding.

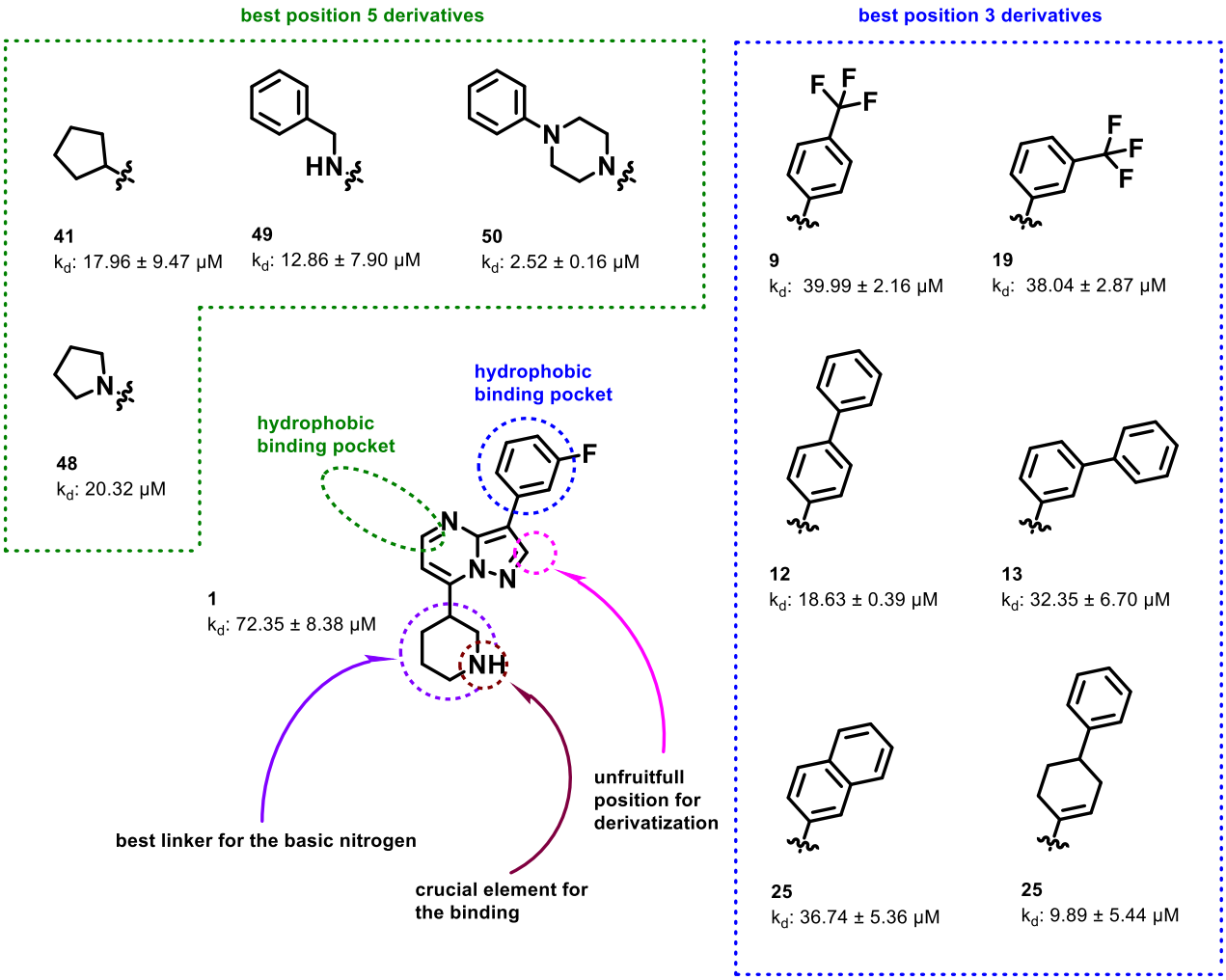

Figure 6.11. *Schematic SAR of pyrazolo[1,5-a]pyrimidines derived from NMR displacement experiments.*

6.3: Comparison between NMR- and fluorescence-derived affinities

Overall, the SAR indications derived from either the fluorescence-based or NMR-based assays appear to be in reasonable agreement. Both approaches identify similar best derivatives in terms of affinity to pre-miR21. Discrepancies are found in the tri-substituted compounds series, where the fluorescence-based assay identified **71** as the best analogue in terms of affinity, while **74** emerged as the most potent binder in the NMR-based assay.

Differences in the two assays are, however, found when considering the plain affinity values: the fluorescence-based assay measured K_ds from low micromolar to mid-nanomolar, whereas the NMR-based assay returned K_ds in the mid- to low-micromolar. The derived k_ds, plotted against each other, are shown in **Figure 6.12**. Although no clear correlation is apparent, a logarithmic trend may be identified. The most potent binders do cluster in the same region of the plot. Compounds from this region were selected for subsequent in-cell testing (**Chapter 7**) by filtering out those that lacked drug-like properties.

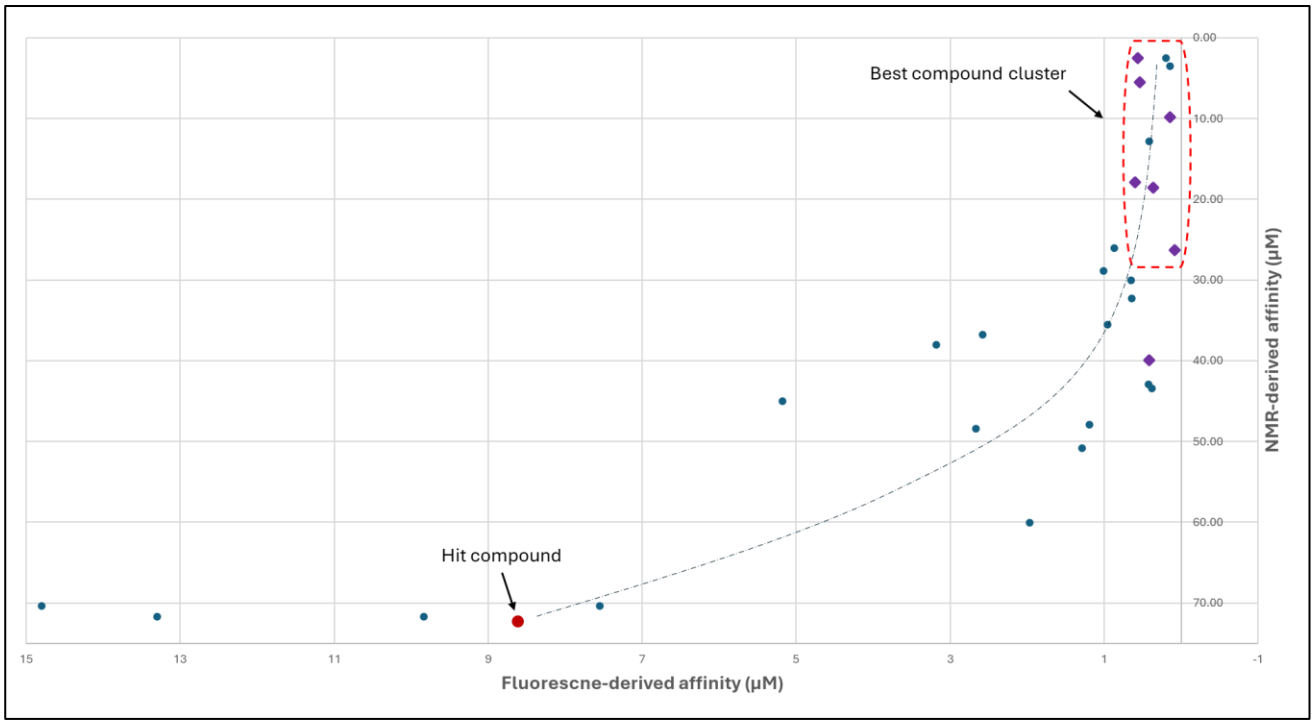

***Figure 6.12**. Plot of the fluorescence- vs. NMR-derived affinities to pre-miR21 of the synthesized pyrazolo[1,5-a]pyrimidines.*

The reason why the k_d values are widely different for some compounds is still under investigation. Several differences in the experimental setup may account for this discrepancy:

- The test buffers are different, which could influence the compounds' affinities.
- The two pre-miR21 constructs used in the experiments differ in length: the NMR displacement assay employs a 60-nt RNA, whereas the fluorescence assay uses a 72-nt RNA. Differences in length may lead to different conformations in solution, potentially affecting binding affinities.
- The fluorescence-based biochemical assay relies on changes in fluorescence resulting from conformational rearrangements near the dye. From the compound binding studies (**Chapter 5**), it is known that binding does not significantly affect this region of pre-miR21, as no changes in the ^{19}F-NMR spectra were observed. Placing the dye at the 5' end, as in this assay, may therefore not fully capture the true affinity of the compounds.
- Solubility bias could affect the results in both assays.
- The final percentage of DMSO in the fluorescence-based assay is not the same in all experiments. It has been reported that DMSO alters the conformation of some RNAs, making this variable worth further investigation.[4]

A third biophysical technique to measure the K_d of the compounds is currently being applied in an attempt to understand which technique provides the best estimate of the compounds' affinity to pre-miR21.

6.4: Experimental Part and Methods

NMR experiments were performed on a 600 MHz Bruker spectrometer in IIT. A 5 mm CryoProbe™ QCI $^{1}H/^{19}F–^{13}C/^{15}N–D$ with a shielded z-gradient coil was used in combination with the automated SampleJet™ system for temperature-controlled sample handling. All spectra were recorded at 298 K. Detailed acquisition parameters are summarized in **Table 6.2.**

Table 6.2*. NMR acquisition parameters for the reported spectra.*

spectrum	**Pp (Bruker)**	**td**	**ns**	**D1 (s)**	**Aq F1 (s)**	**Aq F2 (s)**	**SW ^{1}H (ppm)**	**SW ^{19}F (ppm)**	**O1 (Hz)**	**O2 (Hz)**	**τ (μs)**
^{1}H spectra	cpmgesgppr	16384	256	1	0.90	-	15.15	-	2819.05	-	-
T_2 filter	noesygppr1d	16384	256	1	0.90	-	15.15	-	2819.05	-	67
T_2 filter (^{19}F)	cpmgigsp	16384	96	5	2.88	0.72	10	20.1261	-64938.93	4440.96	4/8/12/16

NMR data were processed using Topspin. Proton chemical shifts were internally referenced to trimethylsilylpropanoic acid (TSP). The data were multiplied by an exponential window function with 0.1 Hz line broadening prior to Fourier transformation.

6.4: References

(1) *Elementi Di Risonanza Magnetica*; Coriasco, M., Rampado, O., Bradac, G. B., Eds.; Springer Milan: Milano, 2014. https://doi.org/10.1007/978-88-470-5641-1.

(2) Carr, H. Y.; Purcell, E. M. Effects of Diffusion on Free Precession in Nuclear Magnetic Resonance Experiments. *Phys. Rev.* **1954**, *94* (3), 630–638. https://doi.org/10.1103/PhysRev.94.630.

(3) *Fast NMR Methods for Measuring in the Direct and/or Competition Mode the Dissociation Constants of Chemical Fragments Interacting with a Receptor - Dalvit - 2019 - ChemMedChem - Wiley Online Library*. https://chemistry-europe.onlinelibrary.wiley.com/doi/10.1002/cmdc.201900152 (accessed 2026-03-10).

(4) Lee, J.; Vogt, C. E.; McBrairty, M.; Al-Hashimi, H. M. Influence of Dimethylsulfoxide on RNA Structure and Ligand Binding. *Anal. Chem.* **2013**, *85* (20), 9692–9698. https://doi.org/10.1021/ac402038t.

CHAPTER 7
IN-CELL COMPOUND EVALUATION

Chapter 7: In-Cell Compound Evaluation

Through the pipeline described in **Chapters 2–6**, starting from a hit compound and proceeding through a systematic hit expansion campaign, some binders of pre-miR21 were identified. Thus, having achieved a well-defined SAR at the biochemical level, the evaluation of miR21 levels' modulation in a cellular context was subsequently undertaken. To this end, the identified most active compounds were selected for in-cell testing, together with additional analogues to allow the assessment of an initial SAR also in cells. These studies were carried out in collaboration with Dr. Debora Russo and Dr. Ilaria Penna at IIT, who performed the experimental design and testing in cells.

miR21 expression level varies depending on the cancer cell line. To this end, a panel of six cancer cell lines was identified from different tissues (e.g., PANC-1, pancreatic cancer; U87MG, glioblastoma; HeLa, cervical carcinoma; MDA-MB-231, breast cancer; DU145, prostate cancer; and A549, non-small cell lung cancer), reported to overexpress miR21, and verified for their relative expression levels. From this analysis, the PANC-1 line was selected for its aberrant overexpression of miR21, a finding also reported by other groups.[1] Pancreatic cancer also represents a particularly relevant model from a clinical perspective due to its poor prognosis, with a low 5-year survival rate of approximately 12-13%,[2] and the limited availability of effective therapeutic options. Accordingly, PANC-1 cell line provides a biologically and clinically meaningful system for evaluating compounds aimed at modulating miR21 levels.

Among the synthesized 75 small molecules, only 10 compounds (**9**, **12**, **25**, **29**, **41**, **43**, **50**, **70**, **71**, **74**), shown in **Figure 7.1**, were selected for in-cell testing. The compounds were selected according to these three criteria:

- Affinity. Among the compounds displaying favourable drug-like properties, **71** and **74** emerged as the highest-affinity ligands, respectively, in the fluorescence and NMR assays. Other high-affinity compounds were discarded due to the extended aromaticity and possible intercalating properties. Compounds **25, 50,** and **12**, showing good affinities, were also tested to represent the discarded compounds.
- SAR. Having identified compounds **71** and **74** as the most promising candidates, their precursors, **43** (for **71**), **41** (for **74**), and **9** (for both), were tested to investigate a possible in-cell preliminary SAR.
- Structural difference. Compound **70**, identified as a potential starting point for the development of a new chemical series, was tested to assess its in-cell activity and evaluate its suitability for further optimization.

Moreover, compound **29**, a non-binder in the fluorescent-based assay and only slightly active in the NMR-based assay, was tested as a negative control.

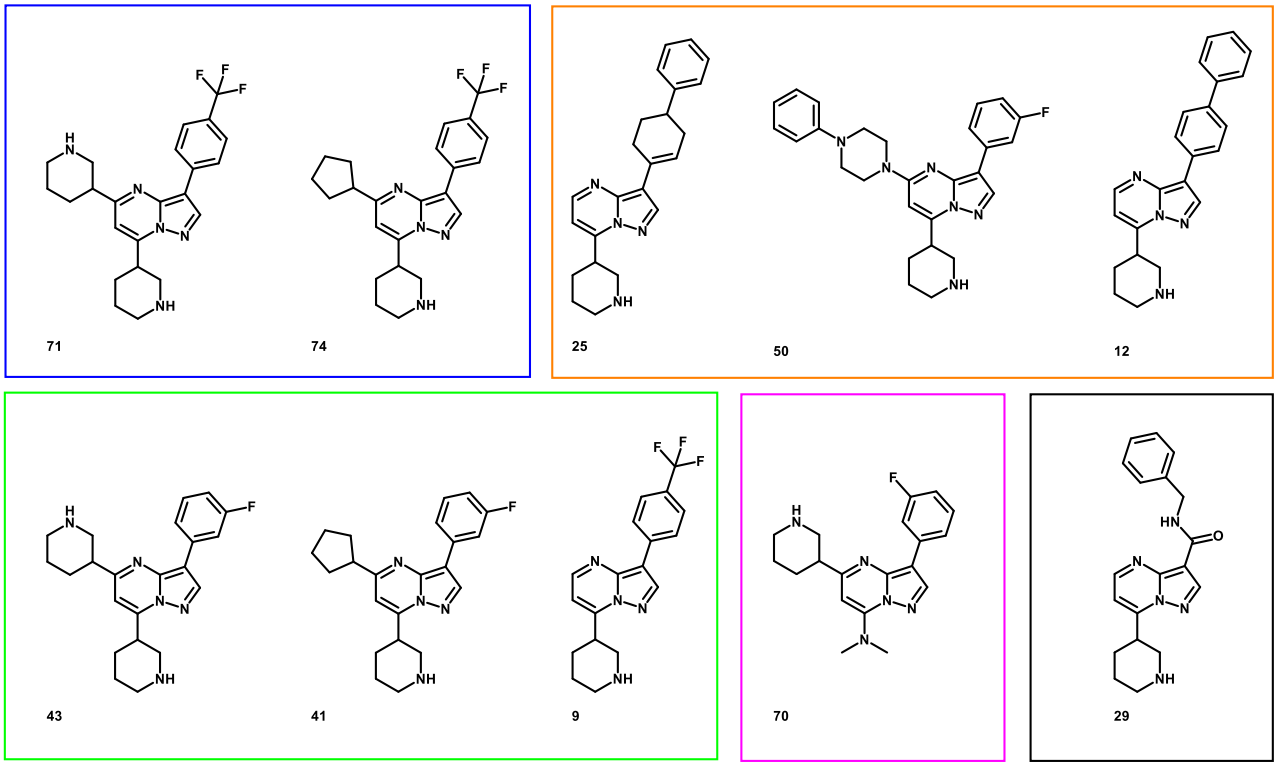

Figure 7.1. *Structures of compounds tested in PANC-1 cell line. Compounds within the blue frame were selected based on their affinity to pre-miR21 and their drug-like properties. Compounds within the orange frame were selected for their affinity. Compounds within the green frame correspond to synthetic precursors of the derivatives exhibiting the highest affinity to pre-miR21. The compound within the pink frame represents a potential starting point for the development of a new chemical series. The compound within the black frame represents a low-affinity binder, for which a low modulation of miR21 levels in cells is expected.*

7.1: miR21 antisense oligonucleotide in-cell testing.

No reference compound is currently available for the modulation of miR21 levels in PANC-1 cells. To validate the proposed cell model system and describe the cellular response to the miR21 level decrease, commercial antisense oligonucleotide inhibitors were employed. Antisense oligonucleotides are chemically modified, single-stranded oligonucleotides with a secondary structure designed to specifically bind to and inhibit endogenous RNAs.[3] For an oligonucleotide complementary to his target miRNA, high selectivity is expected, enabling the probing of the desired biological response. To this end, using antisense oligonucleotides designed to selectively target miR21-3p and -5p (miR21-5p or miR21-3p inhibitors), the downstream target and the precursors of miR21, programmed cell death gene 4 (PDCD4), and the upstream precursors pre-miR21 and primiR21 (**Chapter 1**), were evaluated, alongside the levels of mature miR21, both the 3p and 5p species. For compounds targeting pre-miR21, and thus indirectly modulating miR21, a downstream response similar to that observed with the antisense oligonucleotides is expected.

PANC-1 cells were transiently transfected with 50 nM miR21-5p or miR21-3p inhibitors to downregulate miR21 levels. MirVana™ miRNA Inhibitor Negative Control (Anti-miR-Control; grey bars in **Figure 7.2**) was used to normalize miR21 expression levels. Expression levels of miR21-5p and miR21-3p, as well as the mRNA of PDCD4, were evaluated at 24, 48, and 72h after transfection.

As seen in **Figure 7.2**, the transfection with the antisense oligonucleotides led to an overall decrease of the miR21 levels, more marked for the 5p than the 3p species. miR21-5p downregulation was more substantial (up to 55% reduction at 24h) than that of miR21-3p, only slightly modulated (around 30% decrease). In cells transfected with miR21-5p inhibitor, the decrease of its expression levels was maintained up to 72h, while for miR21-3p inhibitor, its reduction was detected only at 24h after transfection. Right now, no experimentally supported explanation can be given for this observation.
PDCD4 levels were seen to increase with the modulation of miR21, as expected for one of its downstream targets upon inhibition of miR21.

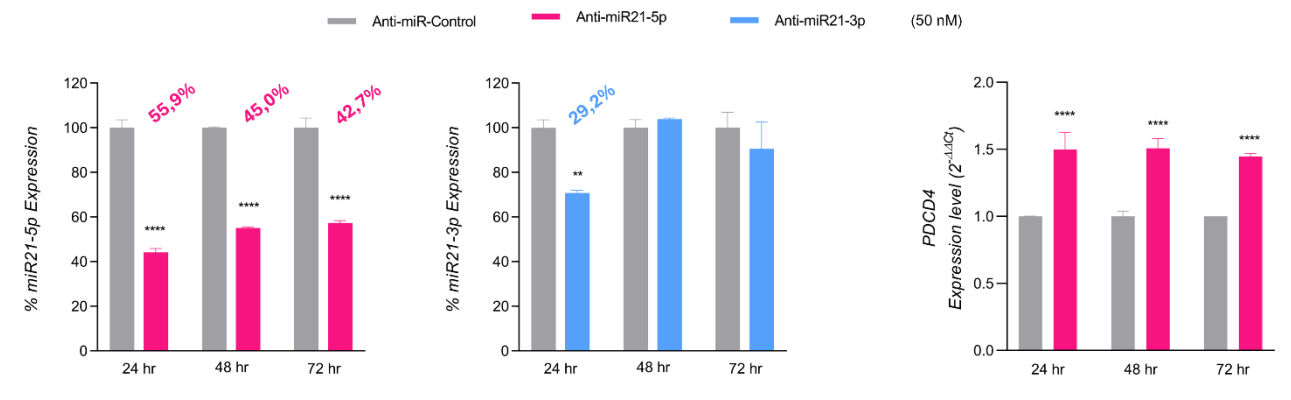

Statistical analysis: Two-Way ANOVA followed by the Bonferroni's post-hoc test (**p<0.001, **** p<0.0001; * vs Anti-miR-Control)

***Figure 7.2**. Expression levels of miR21-5p and miR21-3p in PANC-1 cells after treatment with anti miR21-5p and anti miR21-3p antisense oligonucleotides.*

Levels of pri-miR21 and pre-miR21, evaluated upon transfection, are reported in **Figure 7.3**. Their modulation seems to be consistent with the overall biological response, correlating with the miR-5p decrease shown in **Figure 7.3**. pre-miR21 levels increased upon treatment and exhibited a slight decrease at the 72h timepoint, while miR21 levels remained down-modulated in a dose-dependent manner (30 vs 50 nM inhibitor). Interestingly, pri-miR21 levels seem to increase upon transfection, suggesting a potential autoregulatory feedback loop to counteract the inhibition and sustain miR21 expression in this cell line.

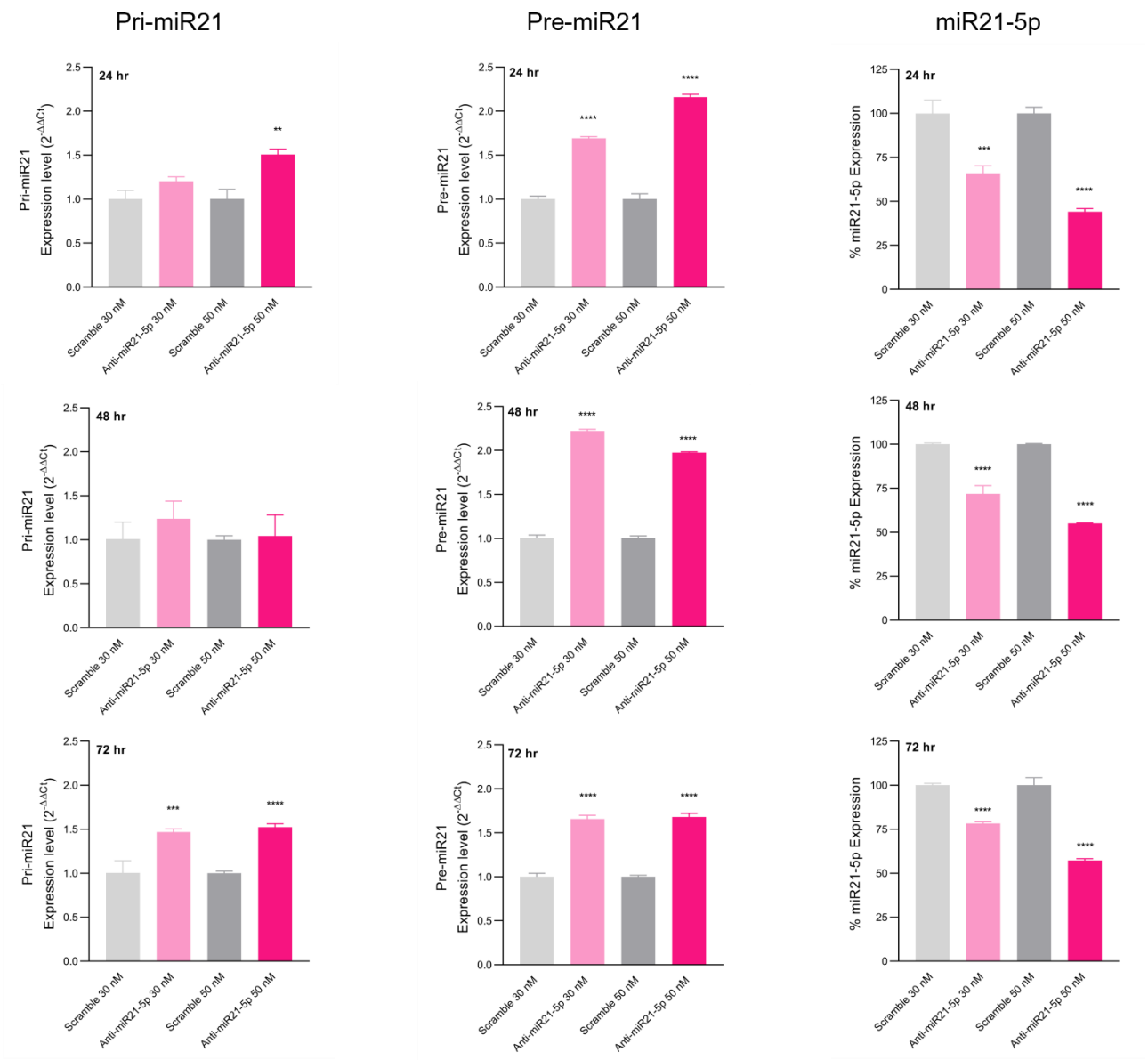

***Figure 7.3**. Level of pri-, pre-miR21 and mature miR21 following mirVana™-5p inhibitor transfection at different time points.*

While these experiments are functional to understanding the biology behind miR21 inhibition, for the purpose of this work, they present a model system for comparing the results obtained with the developed compounds. For a small molecule inhibiting the Dicer-mediated cut of pre-miR21 and thus reducing miR21 levels, a similar cellular response is expected. If any of the reported modulated biomolecules (PDCD4, pre-miR21, and pri-miR21) is not modulated in the expected way despite the decrease in miR21 levels, the observed effect is likely linked to an off-target rather than specific engagement of pre-miR21.

7.2: miR21 level reduction upon compounds' treatment.

After the validation of the system with antisense oligonucleotides, PANC-1 cells were treated with the selected compounds, reported in **Table 7.1**, at two concentrations (5 and 10 μM), and miR21 levels were evaluated (both -5p and -3p) after 24 and 48h exposure.

Table 7.1. *Compounds tested in cellular assays and their corresponding effects on miR21 levels.*

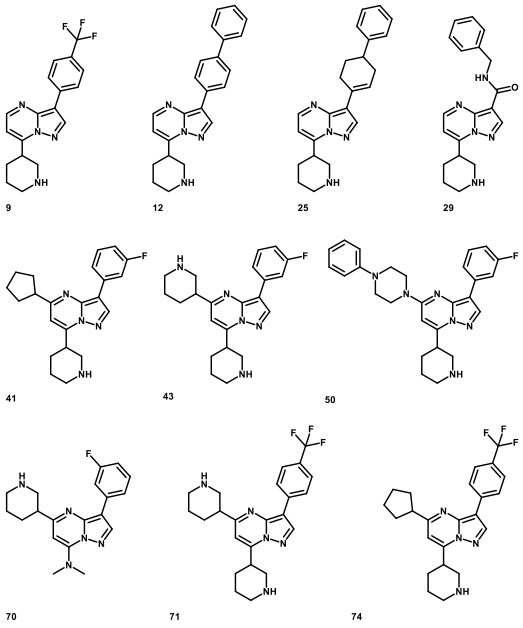

	miR21-5p decrease (%)		miR21-3p decrease (%)	
Compound / Dose (μM)	24h	48h	24h	48h
9 / 5	-	32,9 ± 0,6	-	19,0 ± 1,4
9 / 10	-	21,9 ± 0,3	-	38,3 ± 1,4
12 / 5	10,7 ± 1,2	11,7 ± 2,2	-	29,6 ± 1,1
12 / 10	10,0 ± 2,4	20,1 ± 0,02	13,4 ± 0,2	37,5 ± 0,9
25 / 5	42,5 ± 0,8	24,4 ± 1,3	76,7 ± 0,6	35,7 ± 1,8
25 / 10	-	30,8 ± 0,1	40,4 ± 2,3	56,45± 2,3
29 / 5	15,1 ± 1,8	-	12,2 ± 4,2	-
29 / 10	10,1 ± 0,8	-	14,6 ± 0,2	11,2 ± 3,9
41 / 5	-	10,0 ± 4,9	44,5 ± 1,8	32,5 ± 1,3
43 / 5	25,8 ± 2,0	25,0 ± 0,1	38,0 ± 1,2	32,5 ± 3,1
43 / 10	24,6 ± 1,6	35,4 ± 2,9	47,0 ± 2,0	49,1 ± 0,1
50 / 5	11,9 ± 1,8	43,6 ± 0,9	41,2 ± 0,9	53,3 ± 2,2
70 / 5	27,6 ± 2,4	-	57,1 ± 2,0	20,9 ± 1,1
70 / 10	31,4 ± 0,6	15,1 ± 0,3	65,8 ± 2,7	40,0 ± 2,6
71 / 5	70,2 ± 1,5	55,5 ± 0,1	85,1 ± 0,8	76,4 ± 1,3
74 / 5	23,0 ± 5,0	14,1 ± 2,5	42,3 ± 2,3	33,9 ± 3,6
74 / 10	51,2 ± 1,2	59,1 ± 1,4	67,2 ± 2,1	80,5 ± 1,1

Rows highlighted in yellow indicate compounds that exhibited the most relevant reduction in miR21 expression.

An overall reduction in miR21 levels was observed for the selected compounds; however, compounds **41**, **50**, and **71** exhibited toxicity at the highest dose (10 μM), and the corresponding data are therefore not reported. For the latter compounds, toxicity was also observed at the lowest dose of 5 μM, but this did not compromise the RNA recovery and the following analysis.
Based on the antisense oligonucleotide model as a reference for interpreting the results, the following conclusions can be drawn:

- Dose dependence: a dose-dependent effect on miR21 levels was observed for compounds **12**, **43**, **70,** and **74**. Compounds **25** and **29**, not showing dose-dependent modulation, were deemed not interesting for miR21 levels modulation and are not discussed further.
- Modulation of both 3p and 5p: in general, the compounds exhibited stronger inhibition of miR21-3p than miR21-5p, with some molecules affecting only the -3p species. Since inhibition of the pre-miR21 Dicer-mediated cut should inhibit the two species almost equally, compounds inhibiting both species in a similar way were deemed more relevant under a target engagement profile. This analysis identified **43**, **71**, and **74** as the most interesting compounds.
- Consistency over time (24 vs 48h): the antisense oligonucleotide maintained a similar effect on miR21-5p levels at 24 and 48h, showing a continued effect over time. Among the tested compounds, only **43**, **71,** and **74** displayed this trend, reinforcing their potential as interesting modulators.

From an analysis of the results, compounds **43** and **74** emerged as the most promising candidates. Compound **71** also stood out for its miR21 level inhibition, already at the lowest dose of 5 µM, showing a comparable modulation of -5p and -3p species and a similar effect after 24 and 48h exposure.
The negative control, compound **29**, was found inactive in the fluorescence-based assay and only moderately active in the NMR one. In the PANC-1 cells model, only a slight reduction of the levels of both miR21-5p and -3p (up to 15%) and a lack of dose-dependency was observed, as expected from its weak binder profile, further supporting the idea of possible in cell target engagement for the other compounds.
From the presented analysis, **74** appeared as the most promising compound for subsequent studies. It effectively decreases miR21 levels, achieving 60% and 80% level decrease for the 5p and 3p species, respectively, after 48h treatment. In addition, it shows a dose-dependent decrease of mir2R levels and stable activity over time, supporting its selection for subsequent evaluation. Moreover, a preliminary cellular SAR could be established. Its precursors, compounds **9** and **41**, showed in fact moderate modulation of miR21 levels. The modulation capability resulted increased when the structural features of these compounds were combined, as highlighted in **Figure 7.4**. The same preliminary SAR can also be seen by analysing compound **71** and its precursors **9** and **43** (**Table 7.1**).

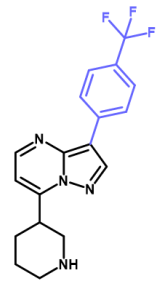

9

	miR21-5p decrease (%)		miR21-3p decrease (%)	
Compound / Dose (µM)	24h	48h	24h	48h
9 / 5	-	32,9 ± 0,6	-	19,0 ± 1,4
9 / 10	-	21,9 ± 0,3	-	38,3 ± 1,4

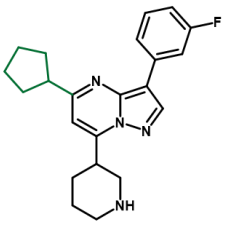

41

	miR21-5p decrease (%)		miR21-3p decrease (%)	
Compound / Dose (µM)	24h	48h	24h	48h
41 / 5	-	10,0 ± 4,9	44,5 ± 1,8	32,5 ± 1,3

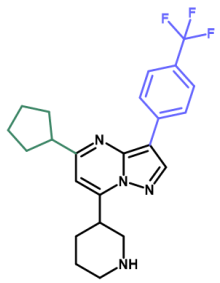

74

	miR21-5p decrease (%)		miR21-3p decrease (%)	
Compound / Dose (µM)	24h	48h	24h	48h
74 / 5	23,0 ± 5,0	14,1 ± 2,5	42,3 ± 2,3	33,9 ± 3,6
74 / 10	51,2 ± 1,2	59,1 ± 1,4	67,2 ± 2,1	80,5 ± 1,1

***Figure 7.4**. Preliminary in cellulo SAR indication for the identified analogues of hit **1**. By combining two low modulation substituents, the trifluoromethylphenyl in position 3 (as in **9**) and the cyclopropyl in position 5 (as in **41**), a more potent miR21 level modulator (**74**) is obtained.*

7.3: Target engagement

While a decrease in miR21 levels by the compounds provides an indication of the modulation of the desired target (i.e., pre-miR21 processing), it could also result from the activation of alternative cellular pathways. The results obtained with the antisense oligonucleotides described in **Paragraph 7.1** represent an important reference for evaluating the target-specific effects of a tested compound. For a specific modulation of miR21 biogenesis, impairing the production of mature miR21, an increase in PDCD4 as well as pre-miR21 levels is expected (**Paragraph 7.1**). Since this analysis is more time-consuming than measuring mature miR21 levels alone, it was performed on a single compound.
From the overall in-cell compound screening, two compounds, **71** and **74**, emerged for their ability to modulate miR21 levels. However, compound **74** also showed a dose-dependent effect and low toxicity, making it more suitable than **71** for a detailed characterization. Following the detection of mature miR21

decrease, the expression of PDCD4 and pre-miR21 was evaluated from the same RNA sample. All the results obtained for compound **74** are reported in **Figure 7.5**.

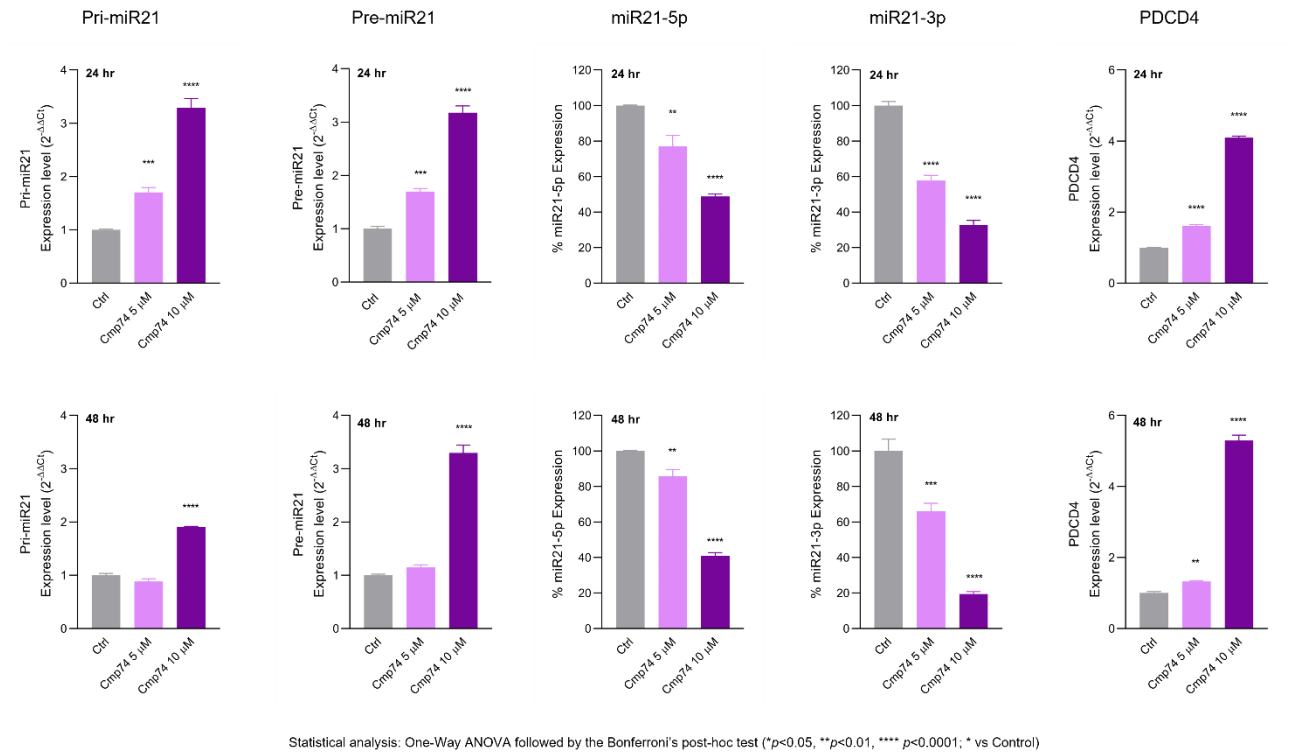

***Figure 7.5**. Pri- and pre-miR21, mature miR21-5p and -3p, PDCD4 expression levels in PANC-1 cells following 24 and 48 hr treatment with **74** (5 and 10 µM). The graphs show expression levels for each target, compared to vehicle control (Ctrl), set at 100%. Statistically significant variations in expression levels were calculated by One-way ANOVA, followed by Bonferroni's post-hoc test (*p<0.05, **p<0.01, ****p<0.0001 vs Ctrl).*

Compound **74** appears to behave in a similar way to the antisense oligonucleotide, as shown by the dose-dependent increased levels of PDCD4, pri-, and pre-miR21. Moreover, time-dependent activity was observed, in agreement with the reference model.

At 24h, PDCD4 levels increased approximately fourfold compared to the control, while pre-miR21 levels rose approximately threefold. PDCD4 continued to accumulate over time, as observed at 48h. These findings are consistent with the proposed inhibition of the Dicer-mediated cut of pre-miR21, leading to an accumulation of the pre-miR21 and a corresponding increase in the expression of downstream targets normally suppressed by miR21, such as PDCD4. Dose-response relationship is also seen in the extent of modulation, with a slighter modulation for the lowest dose of 5 µM after 48h treatment.

Pri-miR21 levels were observed to accumulate, showing an increase of more than threefold compared to the control, and remained relatively stable over time. This behaviour is consistent with the expected mechanism of inhibition. Similar to the antisense oligonucleotide model, pri-miR21 levels were upregulated at 24h and 48h. The magnitude of the increase in the target and precursor levels is greater than with the oligonucleotide; however, it should be noted that substantially higher concentrations of **74** (5–10 µM) were used compared to the antisense oligonucleotide (30–50 nM).

7.4: Conclusions

The in-cell evaluation of a selection of the most promising compounds, identified during SAR evolution, confirmed their activity and potency for miR21 modulation and provided preliminary insights into their mode of action. Among the tested molecules, **71** and **74** emerged as the most effective miR21 modulators, with **74** showing dose-dependent activity and modulation of downstream and upstream targets. Taking into account that these two compounds were tested as either a mixture of diastereoisomers (**71**) or a racemate (**74**), their resolution into single, pure stereoisomers could potentially enhance their activity, also in cells, provided that the binding phenomenon is stereochemistry-dependent.

Notably, these compounds were also previously identified as the most active molecules biochemically. The observed correlation between high biochemical affinity to pre-miR21 and in-cell activity suggests that these compounds might engage pre-miR21 in cell with a certain degree of selectivity, although further investigations are needed to confirm this conclusion. Analysis of downstream targets further supports this hypothesis: PDCD4 levels increased significantly, consistent with the miR21 levels reduction. Pre- and pri-miR21 also accumulated, as expected from the inhibition of pre-miR21 cleavage. Overall, these findings agree with what was observed with the antisense oligonucleotides model, further supporting the hypothesized mode of action of the compounds

In conclusion, the investigated chemotype appears as a valuable source of miR21 modulators in pancreatic cancer cells. As stated before, modified hit analogues **71** and **74** display activity both biochemically and in cells, highlighting the strength of the rational approach employed for the identification of these compounds. Moreover, these two compounds still have relatively low molecular weight, leaving space for further evolution and derivatization in the search for more potent modulators of miR21 levels in cells.

7.5: Experimental part and Methods

7.5.1: Cell culture conditions

PANC-1 (ATCC CRL-1469) cell line was obtained from American Tissue Cell Culture (ATCC, Manassas, VA, USA) and cultured in Dulbecco's Modified Eagle's Medium (DMEM) supplemented with heat-inactivated fetal bovine serum (FBS) to a final concentration of 10% (v/v), at 37°C in a 5% CO_2 atmosphere.

7.5.2: Transfection of miRNA inhibitors and compounds treatment

For transfections experiments, PANC-1 were seeded in 6-well plates 24 hr before transfection with either 50 nM mirVana™ has-miR21-5p, hsa-miR21-3p inhibitors (ID: MH10206 and MH12979, respectively, Thermo Fisher Scientific) or mirVana™ miRNA Inhibitor Negative Control #1 (ID: 4464076, Thermo Fisher Scientific), using Lipofectamine™ RNAiMAX Transfection Reagent (13778075, Thermo Fisher Scientific), in OptiMem-reduced serum media (31985070, Thermo Fisher Scientific). The effect of transfection of miR21 inhibitors was assessed at 24, 48, and 72 hours after transfection using Real Time-PCR of miR21-5p, miR21-3p, and PDCD4 levels.

To evaluate the effect of compound 74 on mature miR21, its precursors (Pri- and Pre-miR21) and its target (PDCD4) expression levels, cells were seeded in 6-well plates 24 hr before treatment with DMSO only (vehicle control) or with 5 or 10 µM compound 74. After 24 and 48 hr treatment, cells were harvested in 700 µL QIAzol Lysis Reagent (79306, Qiagen) by scraping, homogenized by vortexing, and stored at -80°C until RNA extraction.

After both transfections and compounds' treatment, total RNA, enriched with small RNA, was isolated with mirVana™ miRNA isolation kit (AM1561, Thermo Fisher Scientific), following the manufacturer's instructions. Spike-in cel-miR-39 (10620310, ThermoFisher Scientific) was used as the normalization control for quantification of microRNA expression levels.

For the evaluation of mature miR21, 10 ng of total RNA were reverse transcribed using the TaqMan™ MicroRNA Reverse Transcription Kit (4366597, Applied Biosystems), whereas for the precursors and the PDCD4 target, 500 ng of total RNA were reverse transcribed using Super-Scripts™ VILO™ cDNA Synthesis Kit (11754050, Thermo Fisher Scientific), as indicated by manufacturer instructions.

The resulting cDNA was amplified using the specific TaqMan MicroRNA assays (Applied Biosystems) for miR21-5p, miR21-3p, and cel-miR-39-3p or TaqMan primer/probe sets (ThermoFisher Scientific) for Pri-miR21, Pre-miR21, PDCD4, and HPRT1, used as housekeeping gene. Reactions were performed using TaqMan™ Fast Advanced Master Mix (4444557, Applied Biosystems) on the ViiA™ 7 Real-Time PCR System (Applied Biosystems).

Samples were amplified in triplicate, and the relative quantification of the targets, respect to the vehicle control, was calculated using the $2^{-\Delta\Delta Ct}$ method.

Statistically significant variations in expression levels were calculated by One-way ANOVA, followed by Bonferroni's post-hoc test. GraphPad Prism 8 was used for statistical analysis (GraphPad Software Inc. San Diego, CA, USA). P values less than 0.05 were considered significant.

7.6: References

(1) Lieber, M.; Mazzetta, J.; Nelson-Rees, W.; Kaplan, M.; Todaro, G. Establishment of a Continuous Tumor-Cell Line (PANC-1) from a Human Carcinoma of the Exocrine Pancreas. *Int. J. Cancer* **1975**, *15* (5), 741–747. https://doi.org/10.1002/ijc.2910150505.

(2) Hale, J.; Gilbert, T.; Stott, M.; Whelan, P.; Jackson, R.; Wong, H.; McKay, M.; Ghaneh, P.; Halloran, C.; Faluyi, O.; Dunne, D.; Neoptolemos, J. P.; Palmer, D. Real-World Outcomes Following Adjuvant Chemotherapy for Resected Pancreatic Cancer in a Centralised Oncology Service. *Br. J. Cancer* **2026**, 1–7. https://doi.org/10.1038/s41416-026-03341-0.

(3) Çakan, E.; Lara, O. D.; Szymanowska, A.; Bayraktar, E.; Chavez-Reyes, A.; Lopez-Berestein, G.; Amero, P.; Rodriguez-Aguayo, C. Therapeutic Antisense Oligonucleotides in Oncology: From Bench to Bedside. *Cancers* **2024**, *16* (17), 2940. https://doi.org/10.3390/cancers16172940.

CHAPTER 8
CONCLUSIONS

Chapter 8: Conclusions

The identification of compounds able of modulating miR-21 levels represents an expanding frontier in drug discovery. This microRNA has been implicated in the progression of various malignancies, making it an increasingly attractive potential therapeutic target.

As discussed in **Chapter 1**, several strategies have been proposed to achieve the modulation of miR-21 levels in cells, providing the scientific community with multiple approaches to address this biomolecule. The present work adds to the existing scientific literature on this target by reporting a fragment-based drug discovery approach as a strategy to achieve miR-21 modulation by small molecules binding to the precursor of miR-21 and thereby preventing its cleavage by the cytosolic enzyme Dicer.

In drug discovery, the use of fragments as a starting point of a medicinal chemistry project offers several advantages in screening, hit expansion, and in the optimization of drug-like and biological activity properties. In screening, the small size and reduced complexity of fragments minimize unfavourable steric clashes, often achieving high ligand efficiency, making them ideal starting points for the hit-to-lead campaign. Hit expansion is facilitated starting from fragments, as they are generally synthetically accessible through multiple synthetic pathways and, due to the reduced molecular weight, they provide ample opportunities for fragment growing to achieve good binding or inhibition activity. Moreover, starting from low molecular weight compounds increases the likelihood of obtaining leads compliant with Lipinski's rule of five.

This work provides another example of the advantages of fragment-based drug discovery. The ^{19}F-NMR-based screening campaign enabled the rapid identification of several potential binders to pre-miR21, some of which were confirmed in a fluorescence-based assay (**Chapter 2**). Among the hits identified in the screening campaign, compound **1**, featuring a pyrazolo[1,5-a]pyrimidine core scaffold, was selected as the starting point for hit expansion and exploration of the Structure Activity Relationships (SAR) within the class.

The hit compound **1** was easily modified by means of several synthetic routes, which enabled the preparation of new analogues. By optimizing previously reported synthetic methodologies, different types of substituents were introduced at positions 2, 3, 5, and 7 of the pyrazolo[1,5-a]pyrimidine. The rational approach described in **Chapter 3** allowed the design and synthesis of 75 new compounds.

The changes in affinity (K_d value), measured by a fluorescence-based assay, guided the hit evolution (**Chapter 4**). The scaffold was systematically substituted at multiple positions with groups having different stereo-electronic properties in order to explore the important structural features for binding to pre-miR21. A clear SAR was obtained for each position, a finding that was later confirmed by testing the compounds in an NMR-based assay (**Chapter 6**). Among the 75 synthesized molecules, compounds **71** and **74** were deemed the most interesting ones. These derivatives originate from the combination of the best substituent at positions 3 and 5 of the pyrazolo[1,5-a]pyrimidine scaffold.

Target engagement of the compounds was also investigated using both direct and indirect approaches. As described in **Chapter 5**, a new structural model of the pre-miR21 was obtained by fluorine-enabled secondary structure analysis. Direct target engagement was evaluated by incubating the compounds with selectively fluorinated pre-microRNA21 constructs and analysing the RNA structure by ^{19}F-NMR spectroscopy. This approach enabled the identification of a binding site and the assessment of ligand-induced structural rearrangements. Overall, the synthesized compounds appear to bind selectively to the apical region of the loop of pre-miR21, promoting a rearrangement of the global RNA structure toward a more ordered conformation, likely associated with loop closure. Moreover, no change in the stem signals was observed, suggesting that these compounds do not intercalate with the RNA but interact selectively in a defined area.

Having a good indication of target engagement, some compounds, selected for their affinity and acceptable drug-like properties, were tested in a pancreatic cancer cell line, PANC-1 (**Chapter 7**). In these cells, the compounds were able to modulate miR21 levels in a dose-dependent way, showing also modulation of miR21's downstream targets and precursors. These findings are in agreement with a possible in-cell target engagement, although additional studies are required to increase confidence in the mechanism of action of these compounds. Notably, among the tested compounds, those with

higher affinity to pre-miR21 in the biochemical assays proved the most effective in the reduction of the miR-21 levels in cells.

In conclusion, the overall PhD work highlights the power of fragment-based drug discovery for identifying effective hit compounds that can be ameliorated in their biological activity and drug-like properties and advanced to validation in cells. The best compounds exhibit promising affinities to pre-miR21 and demonstrate activity in cellular assays. While these preliminary results are encouraging, the obtained molecules are not yet lead-like and require relatively high concentrations for efficacy in cells. Nevertheless, their low molecular weight provides broad opportunities for scaffold expansion, making them a good starting point for a drug discovery campaign aimed at developing more potent modulators of miR21 levels in cells.